Oceanic Anoxic Event Conundrums: Reconciling Palaeontology and Geochemistry.

Connor Sean O'Keeffe

Submitted in accordance with the requirements for the

degree of Doctor of Philosophy

University of Leeds,
School of Earth and Environment

September, 2023

Acknowledgments

Writing this thesis has been an incredible 4-year journey, and I could not have made it to the end without the guidance and support of so many amazing tutors and colleagues. First and foremost, I would like to thank my outstanding supervisor Professor Crispin Little. The help that Cris provided, from tutorials on the fossil macrofauna of the Cleveland Basin, to collecting additional samples, and, above all, outstanding comments and criticisms on my chapter drafts, were all vital to the completion of my project. Our many wonderful conversations on earth science, and life at Leeds, have also truly made my project a fantastic experience. I could not possibly thank my wider supervisory team enough, with Dr. Christian März, Dr. Fiona Gill, and Professor Simon Poulton, all going above and beyond to help me reach my full potential. In addition, I would like to sincerely thank Dr. Christopher Vane, who carried out the Rock-Eval analysis of my samples, and Professor Lorenz Schwark, for carrying out the TLE and GCMS analysis, double-checking my TIC peak integrations, and for providing invaluable supervision on organic geochemistry. I also wish to acknowledge Dr. Ian Bull and Dr. Helen Whelton for performing the compound-specific isotopic analysis, Max Page for the acid digestion step of the palynological preparations (and for being a helpful and encouraging lab technician), and Dr. Jim Riding for excellent supervision on lower Jurassic palynology.

The rigorous scientific analysis reported in this thesis required many hours of lab work, none of which would have been possible without the invaluable training and guidance of Dr. Andrew Hobson and Fiona Keay, of the SEE Cohen Laboratories. I would like to thank Stephen Reid for performing the ICPMS/OES analysis for major and trace elements, as well as Richard Walshaw, for much appreciated guidance on SEM operation.

Outstanding encouragement and help was not only provided by my supervisory team, but also the many amazing academic staff and postgraduate researchers from the University of Leeds. Above all, I would like to thank Dr. Jed Atkinson for many stimulating conversations on the British lower Jurassic, driving me to Hawsker Bottoms prior to sampling for a much-appreciated field trip, and for simply being a wonderful friend. I would also like to acknowledge Professor Tianchen He for showing all the amazing work done on the Mochras core and JET project, Associate Professor Satoshi Takahashi for being excellent company on the sample collection field trip, Associate Professor Rob Newton and Professor Paul Wignall for providing brilliant advice on the project, and for being such great company.

Thank you to all my wonderful colleagues for making my time studying at Leeds so exciting and memorable. I would especially like to acknowledge Dr. Bob Jamieson, Dr. Amy McGuire, Amy

Shipley, Dr. Andy Mair, Dr. Adam Woodhouse, Dr. Bethany Allen, Grace Lamyman, Francis Procter, Chiara Krewer, Ailsa Roper, and Dr. Yijun “Mark” Xiong.

Special thanks go to Dr. Sam Parsons, Dr. James Woodman, Dr. Dorothy Drayton, Dr. Andy Cooke, Dr. Delia Cangelosi and Bobbie, for welcoming me into office on level 7.

During the project, I had the amazing opportunity to network with a wide range of academics, postgraduate researchers and technical staff at the conferences which I attended. They have also rewarded me with stimulating conversations on earth science, and have made the experience of conference attendance truly sensational. Special thanks go to Dr. Wolfgang Ruebsam, Dr. Bryony Caswell, Dr. Ian Boomer, Dr. Kevin Page, Dr. Clemens Ullmann, Dr. Ricardo Silva, Dr. Calum Fox, Professor Richard Pancost, Dr. Sargent Bray and Professor John Marshall.

Of all the academics I have had the pleasure of working with, I would, above all, like to thank my former masters project supervisor, Dr. Jessica Whiteside, both for staying in touch well after my degree, and for giving me the confidence to become the impassioned young researcher I am today.

Finding a home for my one-month placement at BGS Keyworth, was always going to be stressful, and so I am eternally grateful to Suzanne and Steve Whitling, for providing wonderful accommodation in Keyworth, and for being two of the most hospitable and welcoming people I have ever had the pleasure to meet.

Finally, I would love to thank my parents, brother, auntie, cousins, and all my wonderful family for being unfailing in their love, support, and encouragement, both through this project, and always.

This work is dedicated to the memory of Bernard William Twiddy, and Jenifer Marjorie Twiddy.

Abstract

The lower Jurassic (Toarcian) mudstones of the Cleveland Basin (Yorkshire, UK), record a mass extinction of marine organisms triggered by widespread anoxia (the Toarcian Oceanic Anoxic Event – TOAE). A long history of geochemical study has shown that the black shales of the Whitby Mudstone Formation were deposited under anoxic conditions, and these are widely assumed to have been persistent throughout the section. However, the black shales also contain paleontological features implying deposition under oxygenated conditions. These include thin laminae rich in bivalves (*Pseudomytiloides dubius* and *Bositra radiata*), and highly bioturbated intervals. In addition, the underlying sediments of the Cleveland Ironstone Formation contain a decimetre-scale black shale unit called the Lower Sulphur Band (LSB). It is possible that its presence foreshadows the later development of anoxia in the overlying Whitby Mudstone Formation, and that it is also synchronous with an episode of global carbon cycle disruption at the Pliensbachian-Toarcian boundary. To reconcile palaeontology and geochemistry within these intervals, I have employed a high resolution (≤1 cm) multiproxy approach, utilising sedimentological, macropalaeontological, palynological, pyrite framboid, inorganic geochemical, organic geochemical, and isotopic methods. I collected samples from the LSB, and three shell pavements from the *Dactyloceras tenuicostatum* and *Harpoceras serpentinum* zones, at Hawsker Bottoms. I subjected samples from all four intervals to palynological preparation, SEM analysis, Fe speciation, total digest, Rock Eval, total lipid extraction, and compound-specific isotopic analyses. I have demonstrated that the LSB was deposited under hydrodynamically restricted conditions (implied by a high degree of Mn enrichment), and marks a 10 – 15 thousand year interval (or half a precession cycle) where the Cleveland Basin was characterised by highly frequent anoxia. This system shift was triggered by an enhanced nutrient flux concomitant with a humid climatic episode, as implied by the presence of a silty lens immediately preceding the interval of maximum organic carbon preservation. The LSB also contains evidence for high energy deposition despite the accumulation of organic matter, and intervals of bioturbation. This was found to shift the values of redox proxies (notably Fe_{HR}/Fe_T), yielding an apparently anoxic signal. This finding has important implications for the high-resolution study of black shales, and implies that in bioturbated and reworked sediments, redox proxies must not be treated as a direct function of redox, but rather as a function of anoxia frequency. I have also demonstrated that the shell pavements are likely to have been formed in situ (due to the presence of pyrite encrustation of the shells), representing brief periods of reoxygenation. I speculate that these periods can be attributed to interannual variability in ocean circulation during the TOAE, possibly driven by episodic declines in the rate of carbon dioxide injection into the earth surface system.

Overall, my work demonstrates the highly dynamic nature of black shale deposition in the lower Jurassic, and highlights the vulnerability of shallow marine ecosystems in hydrographically restricted settings to earth system perturbations.

Table of contents

Table of figures

Chapter 1 – Introduction:

Chapter 2 – Methods (sample collection, preparation and analysis):

Chapter 3 – High-resolution inorganic redox proxy, and Rock-Eval analysis of the Lower Sulphur Band:

Chapter 4 – Palynology and Palynofacies of the Lower Sulphur Band:

Chapter 5 – An organic geochemical and isotopic study of the Lower Sulphur Band:

Chapter 6 – A multiproxy analysis of thin Shell Pavements from the Whitby Mudstone Formation:

Table index

Chapter 1 – Introduction

1.0 Oxygen depletion in modern coastal waters – an ongoing environmental problem

One of the many deleterious environmental effects the coastal ocean will experience over the coming decades is the expansion of coastal dysoxia (defined by Tyson & Pearson, 1991, where dissolved water-column oxygen drops below 2.0 mL/L; see 1.2). One of the driving factors behind the expansion of coastal dysoxia is the enhanced anthropogenic nutrient loading of river catchment systems, which is predicted to increase throughout the 21st century (Rabalais *et al.*, 2014; Sinha *et al.*, 2017). Dysoxic conditions generally lead to many adverse effects on the physiology of marine organisms, which often cope by slowing down or ceasing costly metabolic functions such as growth and reproduction (Diaz & Rosenberg, 2008; Rabalais *et al.*, 2010; Breitburg *et al.*, 2018; Galic *et al.*, 2019). The Danish Straits are one example of a shallow marine environment highly sensitive to oxygen depletion (Ærtebjerg *et al.*, 2003, Conley *et al.*, 2009). In 2002, a period of unusually high surface runoff on the surrounding land, followed by a relatively warm, still summer, resulted in the area of the seafloor of the Danish Straits exposed to oxygen concentrations <2 mg/L increasing by 17 % relative to the previous year (Conley *et al.*, 2007). Understanding the impact of coastal dysoxia on marine ecosystems is crucial to planning for the future impact on fish stocks and economically significant marine invertebrate communities. Most of the studies of the response of benthic communities have been conducted over a period of days (e.g. Stachowitsch *et al.* 2007), and it is unclear whether the results of these studies are representative of the response to persistent dysoxia (decades to centuries in duration). However, multiple periods of extensive oceanic oxygen depletion occurred during the Earth's geological past (notably in the Mesozoic; Jenkyns, 2010), and these provide a vast fossil archive, documenting the response of benthic communities to severe oxygen depletion, albeit over timescales of hundreds of thousands to millions of years.

2.0 Oxygen depletion-related terms defined

It is essential at the outset to clarify terms used in the literature to describe dissolved oxygen content in seawater, and the response of biological communities to oxygen depletion, as these terms will be used frequently throughout this work. Different sets of terms are required to distinguish the oxygen content of marine waters versus the response of the biological community. This is because, historically, bottom water oxygen concentrations were measured 0.5-1.0 m above the sediment/water interface, with later work demonstrating that the actual oxic/anoxic transition (often referred to as the chemocline) is typically very sharp, and confined to the bottom 0.05-0.25 m of the water column (Jørgensen, 1980). If organisms are kept in cages 0.4 m above the sediment/water interface, there is also no net mortality due to oxygen depletion lower in the water column (Arntz & Rumohr, 1986). Furthermore, the terms "oxia, dysoxia, and anoxia" are defined in relation to redox potentials. While seafloor sediments can exceed the redox threshold for oxia, that does not necessarily mean that oxygen penetrates the sediment (i.e. factors limiting diffusion play a more important role) and, therefore, that a biological community can become established there. The oxygen demand of different benthic species also varies greatly, and is dependent on a wide range of physiological and behavioural

	O_2 > 2.0 mL/L	**O_2 2.0-0.2 mL/L**	**O_2 0.2-0.0 mL/L**	**O_2 0.0 mL/L**
Water column O_2 level	Oxic	Dysoxic	Suboxic	Anoxic
Biological community	Aerobic	Dysaerobic	Quasi-anaerobic	Anaerobic
Organism physiology	Normoxic	Hypoxic		Anoxic
+ sulphide	N/A			Euxinic

Table 1.1 Definitions of various oxygen depletion-related terms, including those referring to water oxygen content (row 1), and biofacies (row 2). Note that herein, the term "Hypoxia" is restricted to describing responses on the level of an individual organism to oxygen depletion, to avoid the use of a hybrid term when discussing water oxygen content (after Tyson & Pearson, 1991).

factors (feeding rate, growth rate, reproduction, etc.; Theede *et al.*, 1969; Thomas *et al.*, 2019). These observations led to the realisation that bottom water O_2 measurements do not necessarily reflect the oxygen limitation on the organisms inhabiting the benthic environment, and that a separate set of criteria for defining the biological response to oxygen depletion was required (Tyson & Pearson, 1991). Table 1 summarises the above distinctions.

3.0 Thin black shales

The Toarcian Oceanic Anoxic Event (T-OAE) was a period of widespread oxygen depletion in shallow marine settings, occurring in the Toarcian stage of the Lower Jurassic ca.183 Ma (Ogg *et al.*, 2016). This event has been tied to a disruption of the global exogenic carbon cycle (Hesselbo *et al.*, 2000; French *et al.*, 2014), with proposed sources of ^{12}C injection ranging from methane hydrate dissociation (Hesselbo *et al.*, 2000; Kemp *et al.*, 2005), to volcanism in the Karoo-Ferrar large igneous province (McElwain *et al.*, 2005; Svensen *et al.*, 2007), to permafrost destabilisation at the end of the preceding Pliensbachian icehouse (Ruebsam *et al.*, 2019; 2020a) – although locally dominant processes such as upwelling often effect the $\delta^{13}C$ signature of bulk organic carbon in sediments spanning this event (Küspert, 1982; Sælen *et al.*, 1996; van de Schootbrugge *et al.*, 2013; Suan *et al.*, 2015). Famous black shale successions associated with this event include the Posidonia Shale of Southern Germany (Röhl *et al.*, 2001) and the Mulgrave Shale Member of the Whitby Mudstone Formation in the Cleveland Basin (Yorkshire, UK; Hesselbo & Jenkyns, 1995; Simms *et al.*, 2004). However, three decimetre-scale black shale units within the underlying Grey Shale Member, as well as in the Cleveland Ironstone Formation (in the Cleveland Basin; see the stratigraphic column in Fig. 1.1) remain relatively understudied. One of these is the Lower Sulphur Band (hereafter LSB). It is a black shale unit 0.15 m thick that marks the upper boundary of the Cleveland Ironstone Formation (*Pleuroceras spinatum* zone, *Pleuroceras hawskerense* subzone; Howarth, 1973; Powell, 1984). It is bed number 43 of the Hawsker Bottoms section of Howarth (1955 – although the term LSB had not yet been conceived), and bed number 26 of the ironstone series of Howarth (1973). It could also be equivalent to the OMPI P-Toa of Silva *et al.* (2021). The name "Sulphur Band" is a vernacular term and refers to the sulphurous appearance of the unit when weathered, due to its high pyrite content (see 2.0). The processes responsible for the formation of this unit may foreshadow the later development of more extensive black shale deposition (in the Mulgrave Shale Member), and the

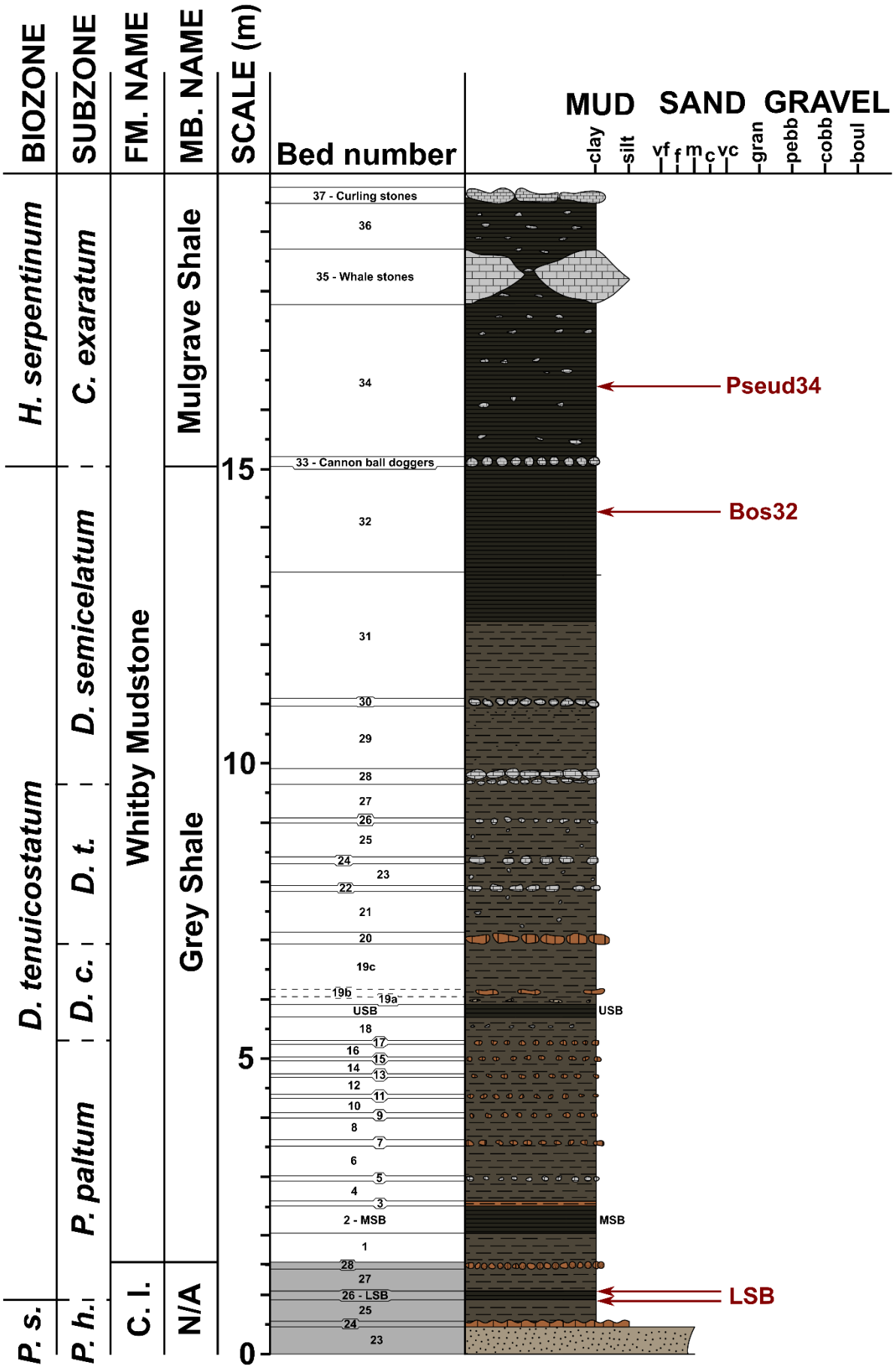
BIOZONE
SUBZONE
FM. NAME
MB. NAME
SCALE (m)
Bed number
MUD
SAND
GRAVEL
clay
silt
vf
f
m
c
vc
gran
pebb
cobb
boul
H. serpentinum
C. exaratum
D. semicelatum
D. t.
D. c.
P. paltum
D. tenuicostatum
P. s.
P. h.
Whitby Mudstone
C. l.
Mulgrave Shale
Grey Shale
N/A
37 - Curling stones
36
35 - Whale stones
34
33 - Cannon ball doggers
32
31
30
29
28
27
26
25
24
23
22
21
20
19c
19b
19a
USB
18
17
16
15
14
13
12
11
10
9
8
7
6
5
4
3
2 - MSB
1
28
27
26 - LSB
25
24
23
15
10
5
0
Pseud34
Bos32
USB
MSB
LSB

Fig. 1.1

widespread extinctions in the benthic community associated with the T-OAE (Little & Benton, 1995; Danise *et al.*, 2013). Decimetre-scale black shales are by no means limited to the Lower Jurassic of the Cleveland Basin. Similar units are also found, for example, in the Kimmeridgian and Tithonian-aged Kimmeridge Clay of the UK and the north coast of France, where TOC can be enriched by up to 52.1 wt.% (the Blackstone Band; Oschmann, 1988; van Kaam-Peters *et al.*, 1998; Atar *et al.*, 2019; 2020). However, in contrast to the Blackstone Band, the LSB reaches 0.15 m in thickness (Howarth, 1973), while the black shales of the Kimmeridge Clay can reach 0.4 – 1 m in thickness (Tribovillard *et al.*, 1994). The palaeoenvironment of the Kimmeridge Clay black shales was also far more laterally extensive, spanning thousands of kilometres rather than just the width of a single basin (Oschmann, 1988). The black shales also occur in regular, orbitally forced cycles (400kyr long eccentricity modulated; Armstrong *et al.*, 2016), rather than at three distinct stratigraphic horizons (as in the Sulphur Bands; Newton, 2001). Oschmann (1988) attributed the formation of these shales to regular variation in chemocline stability, as a consequence of alternating monsoon-driven currents through the North Atlantic Shelf Sea. Later work by Armstrong *et al.* (2016) suggested that the placement of a Hadley Cell over the European Epicontinental Seaway (hereafter EES) was accompanied by alternating episodes of dry/wet climate,with the black shales being associated with northward migration of the intertropical convergence zone (i.e. monsoons).

The thin black shales of the Kimmeridge Clay are also associated with a change in the marine benthic community. Wignall & Newton (1998) showed how the Kimmeridge Clay is mostly bioturbated, with no lamination, and 4-8 benthic species are typically present. However, periodic fissile/laminated intervals are associated with a decrease in the number of benthic species to between 1 and 4. Occasionally, the fissile intervals indicate anaerobic conditions, with no benthos, for example, in the Blackstone Band.

Figure 1.1 (page 4). Stratigraphic column from the upper part of the Cleveland Ironstone Formation to the top of the Mulgrave Shale Member. Bed numbers are from Howarth (1955; 1962; 1973), with the beds belonging to the Ironstone Series shaded in grey. The locations of the Sulphur Bands, and two of the shell pavements analysed in my study (Chapter 2) are also indicated. Broken lines reflect uncertainty in the positions of the subzones. Abbreviations: C. I. – Cleveland Ironstone Fomration; *P. s.* – *Pleuroceras spinatum* zone; *P. h.* – *Pleuroceras hawskerense* subzone; *D. c.* – *Dactylioceras clevelandicum* subzone; *D. t.* – *Dactylioceras tenuicostatum* subzone.

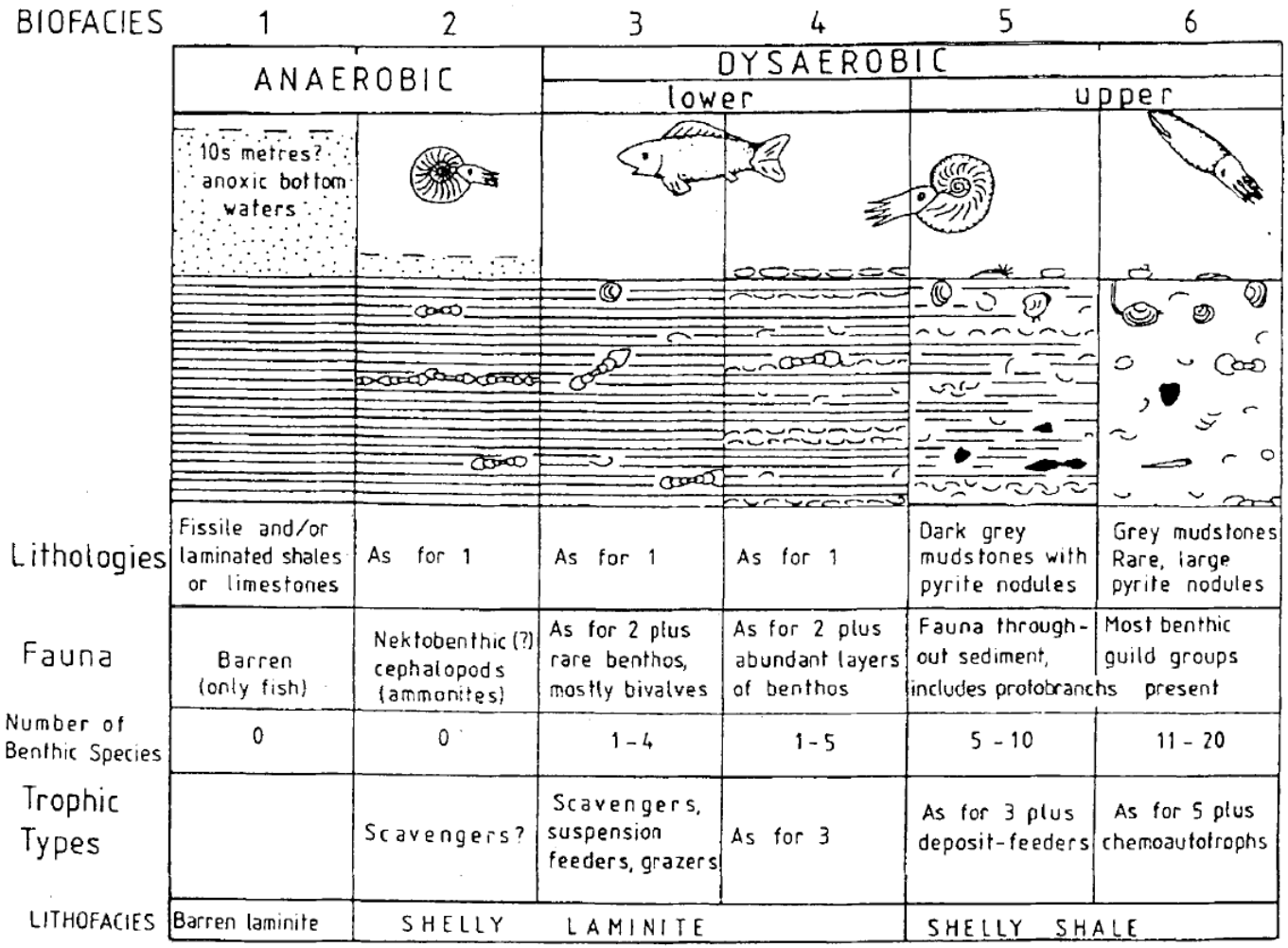

Figure 1.2. Graphical representation of the sedimentological and palaeoecological characteristics of the ORBs. Taken from Wignall & Hallam (1991).

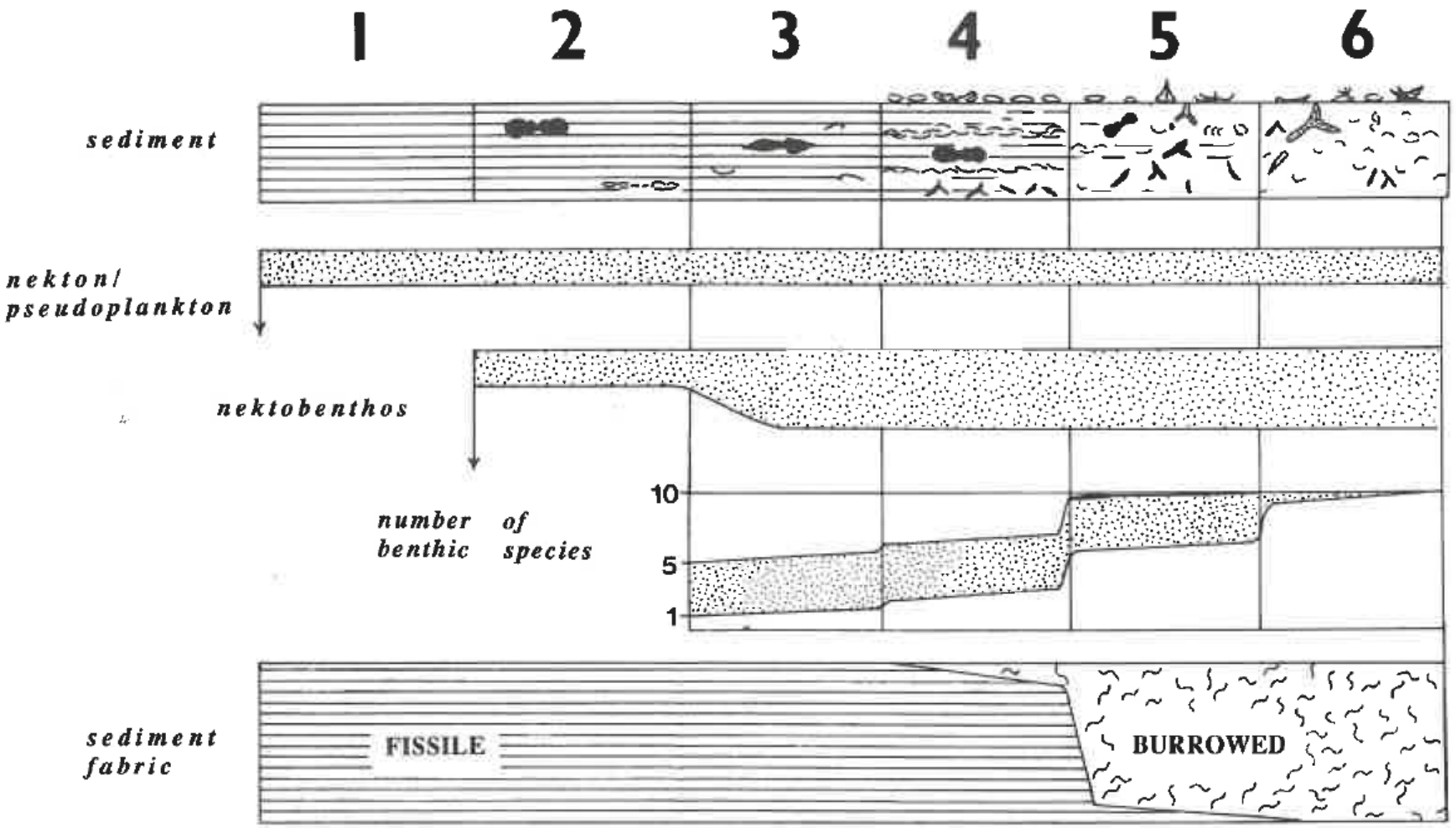

Figure 1.3. Figure taken from Wignall (1994), relating the ORBs to the relative intensity of bioturbation. The presence/absence of nekton and pseudoplankton, nektobenthos, and the number of benthic species characteristic of each ORB are also included. While only ORBs 5 and 6 are characterised by intense bioturbation, bioturbation does not disappear until ORB3 is reached.

4.0 Oxygen Restricted Biofacies

To succinctly describe changes in the marine benthic community, Wignall & Newton (1998) used the Oxygen Restricted Biofacies (ORB) model of shallow marine palaeoecology, originally developed by Wignall & Hallam (1991; their Fig. 7 – reproduced here in Fig. 1.2), and briefly described here. This model relies on the combination of macropalaeontological, sedimentological and ichnological observations of a rock unit, in order to assess how severely the environment was impacted by the lack of dissolved oxygen. Six "biofacies" (here labelled ORB1-6) are defined. ORB 1 is characterised by fissile/laminated shale (or plattenkalk), without bioturbation (Figs 1.2 and 1.3), and with no in situ benthos present (only the fossils of planktonic, and nektonic organisms such as fish are found). The biological community inferred from ORB1 is anaerobic (see Tyson & Pearson, 1991), and it is likely that ORB1 indicates that the anoxic/oxic redox boundary lies 10s of meters above the sediment/water interface. ORB2 is also characterised by finely laminated sediments, but may contain the body fossils of nektobenthic organisms and ammonites. Obligate benthos are nonetheless still absent. The inferred biological community type is also anaerobic, and it is likely that the position of the anoxic/oxic chemocline, while still in the water column, is much closer to the sediment/water interface than it is in ORB1. ORB3 marks the lower limit of the lower dysaerobic biological community and is probably indicative of the point where the anoxic/oxic chemocline drops below the sediment/water interface. While the sediments are still finely laminated, 1-4 species of benthos (occasionally occurring in shell pavements; see 1.6) may be preserved in addition to the nektobenthos. ORB4 sediments are still laminated but contain far more abundant shelly benthos than ORB3 (1 to 5 species) and are associated with a lower dysaerobic biological community. In ORB5, the sediment fabric becomes distorted by bioturbating organisms, and 5-10 benthic species (including deposit feeders) are represented. This biofacies represents the lower limit of the upper dysaerobic biological community. Finally, ORB6 is characterised by intensely bioturbated, massive mudstones, with most benthic groups represented (11-20 species present), and corresponds with the upper limit of the upper dysaerobic biological community.

5.0 Previous work on the LSB

A high-resolution study of the LSB, comparable to that of the Blackstone Band (e.g. Tribovillard, 1994), and of the Toarcian black shales of the Dutch Central Graben (Trabucho-Alexandre *et al.*,

2012), has not yet been performed, and so the comparison between these three deposits remains poorly constrained.

Newton (2001) did much to illuminate the geochemical character of the LSB. Based on low-resolution Fe-redox data, he determined that the Sulphur Bands were formed under anoxic to euxinic conditions (on the basis of Fe_{HR}/Fe_T and TOC/S_{py}), with the relatively high Fe_{HR}/Fe_T signature of the LSB being attributed to the presence of siderite. It was also argued that the LSB was generated partly due to a restriction in the supply of silt to the basin depocentre due to the inundation of deltaic settings by a marine transgression. This explanation is supported by the uniform thickness and lateral continuity of the LSB, which imply that it was deposited under sediment-starved conditions. The LSB also contained high levels of apatite-associated phosphorus, indicative of slow sedimentation rates. However, multiple suggested pathways of highly reactive iron (Fe_{HR}) enrichment were proposed: including infrequent storm events remobilising (possibly unlithified) siderite colloids from the marginal ironstones to the northwest; or (by contrast) background rates of erosion of the marginal facies supplying a steady stream of easily reducible Fe to the shelf, which was subsequently reduced to Fe^{2+} in sediment porewaters, and enriched below the redoxcline via the anoxic shuttle (see 1.8.1.4).

In a subsequent unpublished study, Salem (2013), revealed that the Sulphur Bands, rather than representing episodes of persistent anoxia (as is often assumed for black shales), represented periods of widely oscillating redox conditions in basinal bottom waters, from fully oxic, to fully euxinic (as corroborated by patterns of enrichment and depletion in Mo, and of presence and absence of isorenieratane – a carotenoid biomarker for the presence of brown-coloured green sulphur bacteria, that require both light, and free sulphide; see 1.8.1.6). In the LSB, it was noted that conditions cycled from fully euxinic at the base, to fully oxic, then back to fully euxinic at the top of the unit, all within a stratigraphic height of 0.15 m. The reactive iron redox proxies, and levels of isorenieratane evaluated by Salem (2013), also show significant lateral variation along the Sulphur Bands (i.e. from Port Mulgrave to Hawsker Bottoms), implying that the periods of anoxia they record were localised in bathymetric lows on the basin floor. It was concluded that the deposition of the Sulphur Bands could have been caused by a combination of high basinal restriction, and water column stratification.

Sediment starvation through the Cleveland Basin during the deposition of the LSB is supported by the LSB's lateral continuity and uniform thickness throughout the Cleveland Basin (14 – 26 cm over 18.75 km; Newton, 2001). However, the sedimentary architecture contains features typically associated with higher energy deposits (e.g. scour marks and hummocky cross-stratification – HCS). Ghadeer & McQuaker (2011, 2012) proposed a higher-energy formation mechanism for organic-rich mudstones in the Cleveland Basin, remarking on the similarity of the HCS-lamination-bioturbation triplet (seen in the LSB as well as in thin sections of the Whitby Mudstone Formation) to the "lam-scram" style textures of some turbidites (Goldring *et al.*, 1991). The authors suggest that such units

within the Cleveland Ironstone Formation and the Grey Shale Member of the Whitby Mudstone Formation can be explained by episodes of shelf-to-basin transport, followed by the rapid development of a laminated mud profile, and a spell of brief benthic colonisation prior to emplacement of the next turbidite. In this model, elevated TOC within the laminated muds is a consequence of enhanced primary production in surface waters (i.e. not necessarily due to enhanced preservation under anoxic conditions; MacQuaker *et al.*, 2010). However, the extent to which these processes are responsible for the deposition of the LSB has not yet been studied in detail, and therefore, the presence of high-energy sedimentary structures in the LSB has not yet been reconciled with its apparent lateral continuity.

6.0 Thin shell pavements

The early Toarcian-aged Grey Shale, and Mulgrave Shale members of the Whitby Mudstone Formation, despite showing paleontological (Little & Benton, 1995) and geochemical (Raiswell & Berner, 1985; Pearce *et al.*, 2008; French *et al.*, 2014) evidence for frequent oxygen depletion, contain frequent, mm-scale beds of in situ (no evidence of fracture or imbrication) bivalves (hereafter referred to as shell pavements; Caswell & Coe, 2013). Frequent occurrences of bivalve-rich shelly laminae have been noted from the Whitby Mudstone Formation, including as many as five occurrences in the *C. exaratum* subzone – corresponding with black shales that yield between 4.0-8.0 wt.% Sulphur (mainly pyrite-hosted; Raiswell & Berner, 1985; Danise *et al.*, 2013), Mo content up to 15.57 ppm (Pearce *et al.*, 2008), and an isorenieratane content of up to 17.54 µg/gTOC (French *et al.*, 2014).

The bivalve species found in these pavements are *Pseudomytiloides dubius* (hereafter *P. dubius*) and *Bositra radiata* (hereafter *B. radiata*), which both possess valves 59 – 104 mm^2, and 166 – 298 mm^2 in area, respectively (Caswell & Coe, 2013), that generally appear flat in hand specimen. In *P. dubius*, the umbone is located near the hinge line (at the anterior), and the valves have a trigonal "teardrop" outline. While often found flattened, the valves were originally strongly convex (Oschmann 1993). *B. radiata*, by contrast, has a much shorter hinge line (narrower than the shell width), and a less pronounced umbone. The shells also show a circular outline and concentric circular ribs, with a second set of very thin ribs (often only visible in well-preserved specimens) radiating from the umbone (Conti and Monari 1992, Jefferies & Minton, 1965).

While *P. dubius* is stratigraphically limited to the lower to middle Jurassic of Europe, and the genus *Bositra* extends from the Triassic to the end of the Albian (early Cretaceous; Pan *et al.*, 2014; Palaeobiology Database, 2022), many bivalve and brachiopod genera from the Mesozoic, and Paleozoic, show strong morphological similarity and are assumed to have shared similar

palaeoecology (i.e., these disparate organisms demonstrate convergent evolution; Wignall, 1994). The palaeoecology of thin-shelled bivalves of Paleozoic/Mesozoic age (often described as "paper pectens", or "flat clams" - even though the morphology was not restricted to the Pectinidae or even to bivalves; Wignall, 1994), has been a subject of intense debate, and over the decades, multiple modes of life have been suggested for these organisms (summarised in Fig. 1.4). This debate has been exacerbated by the apparent lack of modern analogues for the paper pectens. The extant bivalves

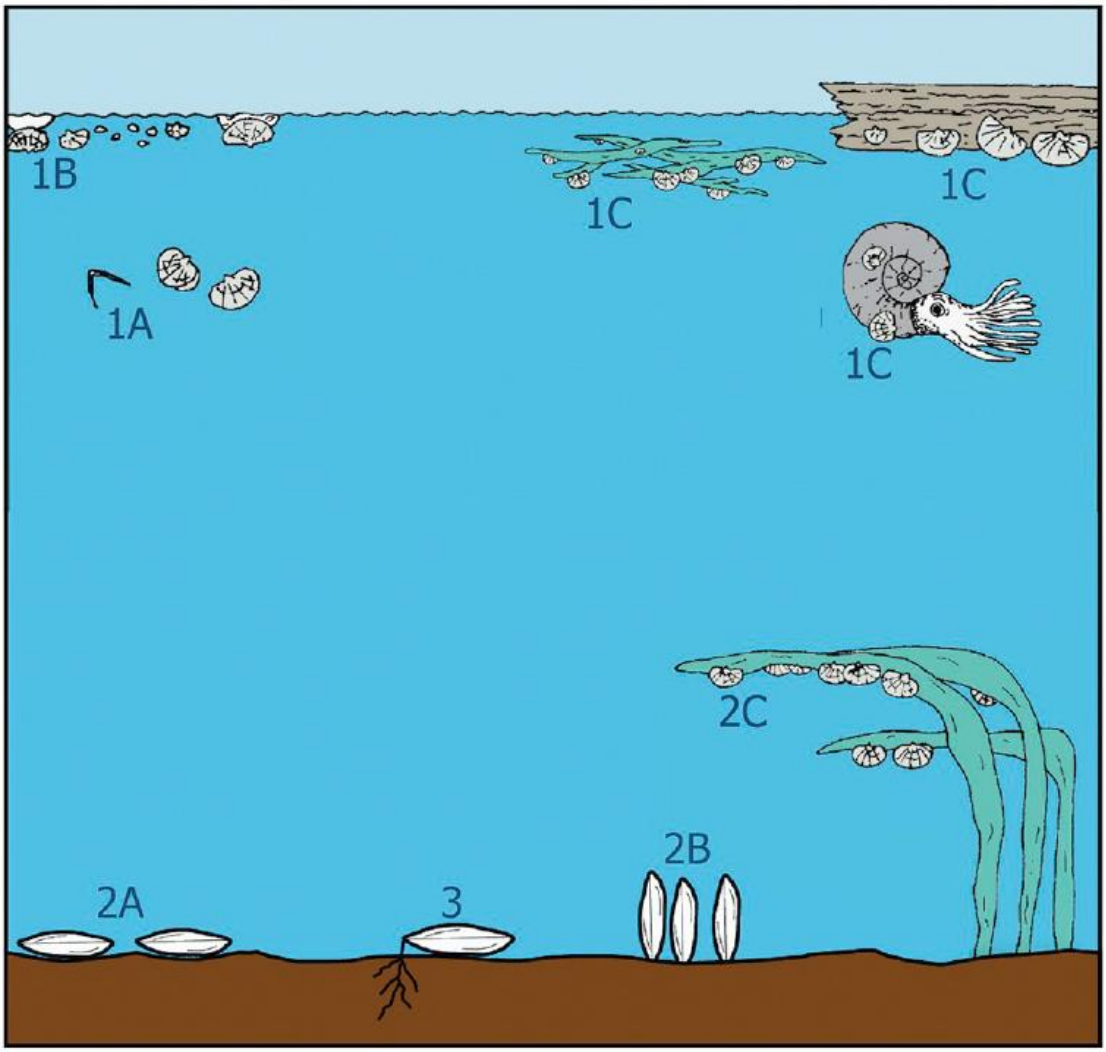

Figure 1.4. Proposed modes of life for the paper pectens. Taken from Del Piero *et al.* (2020) – modified after Wignall (1994) and Schatz (2005): 1A – nektonic; 1B – holoplanktonic; 1C – pseudoplanktonic; 2A – epibenthic recliners; 2B – mudstickers; 2C – attached to benthic macroalage; 3 – chemosymbiotic.

Amygdalum anoxicolum, and *Placuna palacenta*, have been likened to the paper pectens due to their thin shells and occasional occurrence in oxygen-depleted marine environments (Yonge, 1977; Oliver, 2001; Del Piero *et al.*, 2020). However, unlike the paper pectens, these bivalves do not form monospecific pavements that cover the sediment-water interface.

The paper pectens were probably primarily benthic organisms (Fig. 1 4, 2A). The thin profile and wide surface area of the shells would have made the organisms well adapted to a sessile palaeoecology – particularly on a fine-grained, soupy substrate, where the shells would have acted as snowshoes, keeping the animal from sinking into the substrate (Wignall, 1994). If indeed, paper pecten pavements were developed in situ, in the benthic environment, a sediment-stabilisation effect could occur once the pavement reached sufficient lateral coverage: as more paper pectens appear on the sediment-water interface, and as their mean shell diameter grows, a greater area of the sea floor becomes covered by the hard, calcified surfaces of their valves, rather than the softer, less cohesive substrate. This is a preferable growing surface for more bivalves - both the pavement-forming bivalves, and other bivalves that share a commensalistic relationship with the pavement-former. This initiates a positive feedback loop, in which a greater area of seafloor covered by bivalves, leads to a greater rate of increase in the coverage of the seafloor by bivalves. Doyle & Witham (1991) have argued that pavements of the posidoniid bivalve genus *Aulacomyella*, could make the sediment/water interface stable enough to support the growth of larger benthos such as *Buchia* sp.

Savrda & Bottjer (1987) documented shell pavements of the bivalve *Anadara montereyana* in the Miocene Monterey formation of California. Based on the location of these pavements (of intact, non-fractured shells) on the boundaries between laminated, and *Chondrites*-rich sediments, they argued that this bivalve grew in situ on the sediment/water interface. Given that these pavements were limited to between the lower dysaerobic/anaerobic divisions of the oxygen-restricted biofacies (where calcification was believed to be impossible; Rhoads & Morse, 1971), the workers further suggested that in situ accumulations of *Anadara montereyana* characterised a new oxygen-restricted biofacies, distinct from lower dysaerobic, and anaerobic – the "exaerobic" biofacies. Savrda & Bottjer (1991) later expanded on this concept, distinguishing exaerobic facies from quasi-anaerobic due to the presence of in situ benthic macrofauna, and from lower dysaerobic due to the absence of bioturbation. However, this biofacies requires the close juxtaposition of oxia and anoxia, since all benthic macrofauna require at least some oxygen, and the lack of bioturbation in sediments belonging to this biofacies implies accumulation under conditions too harsh to support diverse benthic communities. . Savrda & Bottjer (1991) suggested that the exaerobic biofacies, therefore, was characterised by the oxic/anoxic chemocline being positioned precisely on the sediment/water interface, allowing for dysaerobic benthos to survive, whilst discouraging the development of a more biodiverse oxygen-restricted biofacies. It was further suggested that exearobic biofacies are characterised by the growth of benthic microbial mats: these thin layers of glutinous material would have acted as a barrier to

diffusion of oxygen and sulphide across the sediment/water interface, and might have offered a stable growing surface for epifaunal benthos due to a substrate-stabilising effect. The close proximity of oxic and euxinic environments suggested by this model would be particularly favourable to the growth of microbial mats, since strains of mat-forming bacteria such as *Beggiatoa* and *Thioploca* require both oxygen (supplied from the water column in this case) and sulphide from the sediment (Williams & Reimers, 1983).

Despite the evidence supporting a primarily benthic mode of life for paper pectens, some of these bivalves (*P. dubius* in particular) were also clearly facultative pseudoplankton (Fig. 14, 1C), as demonstrated by the frequent close association with macrofossil wood, particularly in the Posidonia Shale of the SW German Basin (Röhl *et al.*, 2001). Some workers have argued, however, that the wide distribution of abundant paper pecten valves, demonstrates that attachment of these organisms to floating wood, ammonites, macroalgae, or floating fragments of algal mats (Duff, 1975; McRoberts & Stanley, 1989) was the rule rather than the exception. However, this ignores that, with the notable exception of the filamentous red limestones of the Rosso Amonitico Formation (central Italy) – where *Bositra buchi* occurs within a succession of clayey marls and limestones, occasionally showing redeposition (Conti & Monari, 1992) – paper pectens are only found on fine-grained siliciclastic substrates (i.e. in shales). If paper pectens were truly obligate pseudoplankton, there would be no such facies control on their distribution (Kauffman, 1982). Oschmann (1993) went further, speculating that the small size and thin shells of paper pectens indicate a holoplanktonic mode of life (Fig. 14, 1B). While this mode of life is, in fact, unlikely for the adult forms of paper pectens (since they are calcified), it is almost certain (as also suggested by Oschmann, 1993) that the spat of bivalves such as *P. dubius* and *B. radiata* were planktonic, possessing a thinner, proteinaceous shell like that of the modern *Planktomya henseni* (Allen & Scheltema, 1972). However, no extant holoplanktonic bivalve has been discovered (see review in Del Piero *et al.*, 2020), and the assumption that the palaeoenvironment inhabited by *P. dubius* and *B. radiata* suffered anoxia persistently enough to necessitate this mode of life is questionable (see below). It has even been suggested that *Bositra buchi* and *B. radiata* were capable of free-swimming and had a primarily nektonic mode of life (Jefferies & Minton, 1965; Fig. 14, 1A). While free-swimming is observed in the extant bivalve *Argopecten irradians* (Winter & Hamilton, 1985), this bivalve is nonetheless predominantly sessile, resorting to free swimming (a very energetically demanding activity; Chih & Ellington 1983) only when threatened. This hypothesis is, therefore, incapable of explaining the wide distribution of paper pectens, and, again, does not address the clear facies control.

In addition to macrofossil wood, *P. dubius* is occasionally found growing on the shells of ammonites. The occurrence of many such examples in the Posidonia Shale led Kauffman (1978, 1982) to formulate a controversial hypothesis for the palaeoenvironment of the formation. In this model, anoxia was limited to the sediment, or, at the very most, the lower few cm of the water column.

Therefore, while most of the sediment-water interface was uninhabitable, the flat-lying, seafloor-parallel shells of dead ammonites acted as "benthic islands", with bivalves colonising only the upper surface, which protruded above the chemocline. However, the ammonites preserved in the Posidonia Shale have been subject to a high degree of compaction, so it is often difficult to tell which side of the conch the *P. dubius* shells grew from. Furthermore, Schmid-Röhl & Röhl (2003) documented ammonite specimens appearing to show *P. dubius* growing on both sides of the conch – an observation inconsistent with Kauffman's model, and one that implies the bivalves were pseudoplankton, and grew on the ammonite while it was alive.

In some well-preserved specimens of paper pectens such as *Halobia* sp., a small hole can be found along the hinge line. It has frequently been suggested that this marks a byssal attachment site (Campbell, 1985), although the function of the byssus (if present), has also been a matter of debate. Some workers have argued that the byssus would have facilitated shell pavement formation (Hollingworth & Wignall, 1992), while proponents of a pseudoplanktonic mode of life have suggested that the byssus was used to anchor the bivalve to macroalgae (Fig. 14, 2C; McRoberts & Stanley, 1989). The few fossil examples of the latter mode of life, however, are assemblages of multiple bivalve species, and the bedding-parallel pavements of paper pectens are frequently monospecific (for example in the Cleveland Basin). This, again, implies that even though many of these bivalves are clearly facultative pseudoplankton, they could also adopt a distinct benthic recliner mode of life.

In the Carboniferous (Namurian) aged Edale Shales formation (central England), specimens of *Posidonia* sp. are frequently found, and not strongly associated with macrofossil wood. Anita & Wood (1977), being sceptical of Jefferies & Minton's (1965) free-swimming mode of life, argued it was just as likely (based on the same observations; occasional vertical orientation in the sediment, and the possible presence of a nonplanar commissure) that these paper pectens were mudstickers – protruding their open valves just perpendicular to the sediment-water interface (Fig. 14, 2B). The flat, circular morphology of paper pectens, however, is very atypical of mudstickers, and so this hypothesis is also highly unlikely for the mode of life of the majority of the paper pectens (Wignall, 1994).

The close association between many thin-shelled bivalves and black shales, has also led some workers to suggest that these organisms harboured symbionts capable of sulphide chemosynthesis. Seilacher (1990), for example, has argued that the hole located on the hinge line of the shells of the Triassic paper pecten *Halobia* (see above), accommodated a tube foot capable of burrowing into sulphidic sediment, and thus directing free sulphide towards chemosymbionts located within the valves (Fig. 14, 3). Such a strategy can be observed in the modern Thyasiridae (Dufour & Felbeck, 2003). However, sulphide farmers need a ready supply of dissolved oxygen, in order for their chemosymbionts to quickly carry out the oxidation of the sulphide, before this incredibly toxic

chemical endangers the host. As such, chemosymbiosis is far less likely to have been utilised in ancient ORBs than in more oxic environments (e.g. hydrothermal vent communities; Wignall, 1994).

As the above review demonstrates, several non-benthic modes of life have been suggested for the paper pectens, even though many such models are poorly supported by evidence. A key assumption held by palaeoecologists who argue against a primarily benthic mode of life for *P. dubius* and *B. radiata* is that the sediments in which they are found were deposited under persistent anoxia, with no fluctuations back to oxic conditions, and therefore, no opportunities for dysoxia-intolerant organisms to colonise the benthic environment (Oschmann 1993). However, multiple lines of evidence suggest that this assumption is incorrect. Firstly, in modern environments, persistently anoxic conditions are very rarely observed (apart from in the Black Sea). Oxygen-depletion can occur across a wide range of spatial and temporal scales (Rabalais *et al.*, 2010), and, in many shallow marine settings, is mediated by seasonal changes in stratification and primary productivity (Tyson & Pearson, 1991; Testa *et al.*, 2018). Secondly, even the thinnest black shale sequences (Oschmann 1988; Chapter 3 of this volume) represent extensive periods of time, particularly in condensed sequences. The LSB, for example, encompasses a period of time sufficiently long to include multiple episodes of reoxygenation, despite being a thin black shale. I will consider two established age models for the Cleveland Basin (where the LSB is located). One age model is from McArthur *et al.* (2000), which, relies on the $^{87}Sr/^{86}Sr$ value of seawater, and the sedimentation rate remaining constant. This model implies that the *tenuicostatum* zone has a duration of 300 kyr. This is in poor agreement with the estimate of 1.74 Myr based on the average biozone durations of Page (1995, 2004), and implies that the two assumptions of the model are questionable. The sedimentation rate in the Cleveland Basin is unlikely to have remained constant over 300 kyr, and the occurrence of thin silty laminations within the upper Grey Shale and Mulgrave Shale members indicate that (for brief periods) it, in fact, did not. This, in fact, undermines the formation of any age model with sub-kyr precision for the mudrocks of the Cleveland Basin. In a modelling study constrained with sedimentological data from the upper Grey Shale member, Kemp *et al.* (2018) argue that the mm-scale scours described by MacQuaker *et al.* (2011; 2012) are accompanied by hiatuses, and consequently impose a lower limit of 2 kyr on the temporal resolution of cm-scale studies on this lithology. Furthermore, changes in the rate of continental weathering through the T-OAE (Cohen *et al.*, 2004) would have delivered large quantities of ^{87}Sr to the oceans, meaning that the $^{87}Sr/^{86}Sr$ composition of seawater was not in a steady state. An alternative age model is based on the length of the T-OAE CIE, as deduced from spectral analysis (see discussion in Chapter 3, section 4.3). Using an estimate of 561 – 1500 kyr for the duration of the T-OAE CIE (Huang & Hesselbo, 2014; Boulila & Hinnov, 2017; Thibault *et al.*, 2018), encompassing around 10.75 m of the Whitby Mudstone Formation, this yields a sedimentation rate of 7.17×10^{-3} – 0.02 mm/yr. While it is unlikely that this sedimentation rate would have remained constant throughout the underlying grey shales formation (especially since the *D. tenuicostatum* and *H. sperpentinum*

zones are characterised by a transgression; Hesselbo, 2008; Thibault *et al.*, 2018), an estimate for the duration of the LSB using this age model (8 – 20 Ka), roughly agrees with an estimate using the biozone durations of Page (1995, 2004; ~30 Ka), and with the estimate of duration for the same unit using the McArthur *et al.* (2000; 2008) model (5 – 10 Ka, note that post-depositional compaction was not factored into either of these calculations). If, indeed, oxygen depletion occurred on a cyclic, seasonal basis during the deposition of the LSB (as I will argue in Chapters 3, 4 and 5), then the environment (despite generally being harsh), would have offered many opportunities for colonisation, particularly by organisms already adapted to low oxygen conditions. Even though the absolute durations of the beds in question cannot be accurately quantified, various age models all imply that the LSB was deposited over a period of time on the order of 10 kyr in duration.

If paper pecten shell pavements indeed grew in situ, then their presence within black shales implies that brief oxic to dysoxic episodes occurred, in an interval generally characterised by anoxia. The causes of such oxic episodes are, however, poorly understood, with some workers suggesting a link with variability in ocean current regimes, driven by climate. Röhl *et al.* (2001), for example, presented a climate-driven model for the formation of the Inoceramenbank (a shell pavement in the Toarcian aged Posidonia Shale of SW Germany), involving a strong meridional atmospheric circulation system with pronounced seasonality. The high contrast in temperature and moisture levels of the atmosphere over the continent of Pangea led to the strengthening of the trade and monsoon winds. This resulted in two distinct seasonal circulation regimes in the SW German Basin. In summer, a more humid climate with greater surface runoff resulted in the emplacement of a low salinity surface layer, and, therefore, strong water column stratification. C_{org} fixed by new production in the surface layer was exported below the chemocline, and resulted in very reducing conditions in the benthic environment. During winter, by contrast, an enhanced flux of saline water from more oceanic localities to the south destroyed the stratification and allowed for brief oxygen entrainment into the benthic environment. This would have been particularly pronounced during sea-level highstands, which would have made the basin more hydrographically connected to the wider EES and allowed a greater degree of water column ventilation during the winter. The critical piece of evidence used to support this climate/sea-level mediated mechanism for reoxygenation during deposition of the Inoceramenbank, was a high degree of covariation between sedimentological (lamination, silt content) and geochemical (TOC, $\delta^{13}C$, $\delta^{18}O$, pristine/phytane, aryl isoprenoid ratio) variables through the studied section.

7.0 Study aims

In this project, I aim to integrate ichnological (trace fossil), iron speciation, and trace element redox proxies through the LSB, to reconcile the preservation of labile C_{org} with the presence of bioturbating organisms, and of coarse-grained, silt horizons (that imply periods of high bottom water energy not typically associated with black shales). An attempt to evaluate change in sea level (via organic geochemical and palynological analysis) through the LSB will also be made since the model of Fe_{HR} enrichment due to remobilisation of Fe-enriched sediments from proximal settings requires at least a minor transgression. Moreover, evidence for a transgression during the emplacement of the LSB (if indeed present), needs to be reconciled with the trace element data of McArthur *et al.* (2008) and McArthur (2019), implying hydrological restriction. Finally, a combined redox proxy approach is required to better constrain potential pathways for Fe_{HR} enrichment, including trace element, pyrite framboid, and biomarker data. The framboid distribution of the LSB has previously been studied (Wignall & Newton, 1998; Agbi *et al.*, 2015): Wignall & Newton (1998) documented two distinct "populations" of framboid diameters, implying frequent changes in the redox regime. It is, however, also likely that the larger framboid populations are associated with coarser lithologies from the LSB; previous framboid studies on the LSB have not evaluated changes in the framboid distribution against stratigraphic height on a cm-mm scale, and the present study aims to address this.

I address these outstanding questions by employing a high-resolution (≥1 samples per cm) multiproxy geochemical approach. I suggest that poor constraints on palaeoenvironmental changes through the LSB and shell pavements result from low sampling resolution (this is especially true for previous pyrite framboid and biomarker studies). My study combines classic descriptive sedimentology and Fe-redox geochemistry, with TOC/Total S, pyrite framboid and trace element proxies. My study also includes complementary Rock-Eval pyrolysis, palynological, biomarker and compound-specific isotopic (CSIA) analyses. This will better constrain the nature of the organic matter preserved, the relation of organic matter preservation to oxygen depletion/productivity, the impact of oxygen depletion on the marine community, and the relation of all these changes (or lack thereof) to climate change. I also propose that episodic shifts to a dysoxic-oxic state (from an anoxic state) during the deposition of the upper Grey Shale, and Mulgrave Shale Members, were the principal palaeoenvironmental mechanism responsible for the formation of the shell pavements of the Cleveland Basin. Further, I propose that the Inoceramenbank – a shell-rich band in the Posidonia Shale of the SW German basin (Röhl *et al.*, 2001) – is a probable analogue for the shell pavements of the Cleveland Basin. I will employ a similar technique to that of Röhl *et al.* (2001) in my study of the thin shell pavements of the Cleveland Basin, utilising the same proxy suite as I will use for the LSB.

This is the most extensive, high-resolution study of Lower Jurassic black shales to date and reaches the limit of sampling resolution that can be attained without using, e.g., XRF scanning equipment.

8.0 Geological setting

The lower Toarcian succession in the Cleveland Basin consists of 105 m of laminated and massive mudstone, with frequent calcareous concretions (Hesselbo & Jenkyns, 1995; Simms *et al.*, 2004; Powell, 2010), and is coeval with the Lower Jurassic mudstones of the Southwest German Basin (Röhl *et al.*, 2001). The upper Pliensbachian to lower Toarcian Cleveland Ironstone Formation conformably underlies the Whitby Mudstone Formation, and consists of mudstones and bands of sideritic oolite, which have been described as showing orbital cyclicity (van Buchem *et al.*, 1992). The lower Toarcian Grey Shales Member overlies the Cleveland Ironstone Formation (Fig. 1. 1), and consists mostly of structureless, intensely bioturbated shales, deposited under oxic conditions. Overlying the Grey Shales Member is the Mulgrave Shale Member (a.k.a. the Jet Rock), which (along with most the uppermost two beds of the Grey Shale Member – bed32 and part of bed 31) is laminated and organic carbon-rich (TOC up to 12 wt.%; French *et al.*, 2014). The lower Toarcian Grey Shales and Jet Rock form a fining-upward cycle terminating at the base of the overlying Alum shale (Thibault *et al.*, 2018), and were deposited during a major transgression (Hallam, 1997; Hesselbo, 2008). Enrichment in δ^{98}Mo, and the presence of isorenieratane (Pearce *et al.*,2008; French *et al.*, 2014) imply that photic zone euxinia (PZE) was at least periodically attained within the Mulgrave Shale Member. The Grey Shales and Jet Rock encompass the *Dactylioceras tenuicostatum*, and the lower part of the *Harpoceras serpentinum* ammonite zones. These zones are further subdivided, with the most anoxic facies of the Jet Rock belonging to the *Cleviceras exaratum* subzone. Bed-by-bed descriptions of these formations are available in Howarth (1955), Howarth (1962) and Howarth (1973), and the bed numbers from these works are adopted here. The LSB was first described by Chowns (1968), who suggested that the Sulphur Band (LSB being a later term for the same unit, introduced by Newton, 2001) represents the basal, transgressive unit within the *D. tenuicostatum* zone. The LSB was also observed to become increasingly ferruginous to the northwest of the Cleveland Basin, where the upper Lias oversteps the underlying main seam of the Cleveland Ironstone Formation (for example, at Upleatham Mine; Chowns, 1968). Here, the black shale facies laterally grades into a highly pyritised oolitic ironstone, from which the vernacular term "Sulphur Band" was first derived. This difference has led some workers to criticise grouping these two deposits under the same term (Howard, 1985). Regardless, the wide distribution (at least throughout the Cleveland Basin), and relatively constant thickness of the LSB is of great chronostratigraphic

importance, and has led many workers to suggest a lateral equivalence between the LSB, and the Tafelfleins/Seegrasschiefer, of the Posidonia Shale of Southern Germany (Little, 1995; Newton, 2001). However, direct comparison is hindered by the presence of two other thin black shale units within the Grey Shale member, for a total of three (only two thin black shales occur in the Southwest German Basin). These additional units occur 1.45 m (0.53 m thick), and 5.09 m (0.10 m thick) above the upper boundary of the Cleveland Ironstone Formation (beds 2 and 19a of Howarth (1973), respectively). Newton (2001) later designated these the "Middle" and "Upper Sulphur Band", based on their sedimentological similarity to the LSB. McArthur *et al.* (2008) asserted the presence of a fourth Sulphur Band 8.41 m above the boundary with the Cleveland Ironstone Formation (0.05 m thick; bed 26). However, this relies on a redefinition of a "Sulphur Band" as simply any unit in the Grey Shale Member with high pyrite content and is not adopted here. This is because many concretion horizons, which bear little palaeoenvironmental affinity to the Sulphur Bands, also show elevated pyrite levels due to the presence of "knotted" pyrite nodules (Howarth, 1973). TOC for the LSB reaches up to 5.89 wt.% (Littler *et al.*, 2010), which stands in contrast to a baseline TOC level for the Grey Shale Member, not exceeding 1.5-2.0 wt.% (McArthur *et al.*, 2008; Salem, 2013, p.76). The LSB is also distinguished from most Lower Jurassic black shale units by the presence of Hummocky-Cross-Stratification (HCS) in its lower part (Howard, 1984), and a high density of trace fossils in its upper part (*Chondrites* and *Rhizocorallium*; Wignall, 1994, p.92; Little, 1995). The Sulphur Bands are mostly devoid of body fossils, except rare *Dactylioceras* fragments and *P. dubius* (in the Middle Sulphur Band; Newton, 2001).

The LSB, and the shell pavements of the Whitby Mudstone Formation are exposed at many points along the Yorkshire coast, but I decided to collect the samples for this project from Hawsker Bottoms (Chapter 2, Fig. 2.5). This locality was chosen for sample collection, because it is closer to the depocenter of the basin than more proximal sites (e.g. Kettleness and Upleatham mine), as implied by the more bituminous lithofacies of the LSB, and the lack of sedimentary structures indicating reworking in marginal settings (e.g. pyritised chamosite ooids; Chowns, 1968). The processes that are recorded in the LSB at this locality, are therefore less likely to be impacted with interfering processes from marginal settings (e.g. sulphate depletion).

9.0 Palaeoproxies

This project utilises 13 palaeontological, 4 pyrite framboid, 54 inorganic geochemical, 31 organic geochemical, and 6 isotopic geochemical proxies, both for high-resolution redox reconstruction, and in constraining the mechanisms responsible for redox change. What follows is a concise review of

these proxies, starting with the redox-sensitive proxies, and then discussing other proxies of palaeoenvironmental utility.

9.1 Redox

Three of the main methods I will employ when evaluating redox change through the intervals of interest will be an assessment of their sedimentary structures (types present, size, frequency, mineral content. etc.), macrofossil content (species present, abundance, size, etc.), and quantification of the extent of bioturbation. All of these factors taken in combination (as described in 1.4) help to define the Oxygen Restricted Biofacies of a particular bed, and correlating this with a wide variety of geochemical proxies will provide invaluable insight into the biogeochemical processes in operation at each of these stages of oxygen restriction.

It should be noted that the method of bioturbation assessment I will employ (described in Chapter 2, section 2.0) is only an estimate of the true bioturbation intensity, since I will be working with sections cut perpendicular to bedding and evaluating the proportion of this cut surface that is bioturbated. This does not account for the fact that burrows are three-dimensional structures, and a measure of the unit volume, rather than the unit cross-sectional area, that is bioturbated, would be an accurate measure of bioturbation intensity. This method can be carried out either by preparing a large series of thin sections through the sample volume (and scanning these), or by use of XCT scanning (which produces a series of 2D orthoslices). In either case, a 3D model is built from the 2D slice data, and the volume of features of interest is measured. In order to carry out a clean XCT scan, however, the sample cannot be very dense (i.e. large), and ideally needs to be cylindrical to avoid beam-hardening effects (example in Bam *et al.*, 2016 – their Fig.4). Given that the sample blocks to be used in this project (see Chapter 2, section 2.0) are very large and dense, and have an uneven, non-cylindrical shape, I have decided not to employ this method, and instead, employ a wider range of geochemical proxies, which I predict will add greater precision to redox state reconstruction (one of the main aims of this project).

9.1.1 Planktonic responses to dysoxia/anoxia

Dinoflagellates are a group of (mostly) autotrophic protists, whose first appearance dates to, at least, the mid-Triassic (MacRae *et al.*, 1996). They are widely used as a palaeoecological and biostratigraphic tool. In the Lower Jurassic, dinoflagellates became increasingly diverse and

widespread, with diversification being driven by a long-term eustatic sea level rise (van de Schootbrugge *et al.*, 2005).

Dinoflagellates reproduce during the motile (planktonic), haploid stage of their life cycle (illustrated in Fig. 15), with two dinoflagellates fusing to form a motile, diploid cell. At the next stage in the life cycle, the dinoflagellate grows, developing a theca and two flagella, before becoming non-motile and sinking to the sediment/water interface. The encystment stage begins, with the theca being shed, and the dormant cyst lying in the sediment for days to years. During this time, the first meiotic division of the cell occurs, and when the hibernation stage is over, these are excysted, and meiosis continues, producing the motile haploid forms again. The abandoned cyst may then become preserved in the fossil record. In modern environments, the dormant stage of the dinoflagellate life cycle occurs during the winter, with excystment coinciding with the spring bloom (Armstrong & Brasier, 2005).

Given that dinoflagellate encystment requires that the benthic environment contains sufficient oxygen for the encased cells to germinate (Anderson *et al.*, 1987), the presence of dinoflagellate cysts in marine sediments can be used as a micropalaeontological proxy for bottom-water oxygenation: It can be argued that if anoxia persisted at the sediment/water interface for a period exceeding the upper limit of cyst survival, the dinoflagellate life-cycle would be interrupted, with no new cysts being produced until bottom water redox improved (a "dinocyst blackout"). However, viable dinoflagellate cysts are often found in organic matter-rich sulphidic sediments (Anderson *et al.*, 1982), and dinoflagellate "red tides" are commonly associated with eutrophic conditions in modern dysoxic environments (Pitcher & Jacinto, 2019). Therefore, it is more likely that prolonged bottom-water oxygen depletion impacts the diversity of dinoflagellate cysts preserved in the resulting black shale (with specific dinoflagellate genera being hit particularly hard), and not necessarily their overall dominance of the phytoplankton community (Pross, 2001). Another important factor to consider is that dinoflagellate dominance is a function of more environmental parameters than just bottom water redox state. Temperature, salinity, and nutrient loading are all known to strongly influence dinoflagellate ecology, depending upon the genera in question (Tyson, 1995, pp. 285 – 298). In the PETM, for example, the genus *Apectodinium* becomes more dominant in palynological assemblages from shallow marine settings (Sluijs & Brinkhuis, 2009). This was driven mainly by temperature, however, the eutrophication of the marine environment and the lowering of salinity due to enhanced runoff during the PETM, also influenced the spread of *Apectodinium* sp.

Prasinophytes are a group of non-cellulosic, green flagellate algae, with most species being holoplanktonic (although some show rhythmic settling behaviour; Griffin & Aken, 1993). Given that prasinophytes inhabit the photic zone of the water column, along with dinoflagellates, the two phytoplankton groups are brought into competition. This results in changes in the plankton community composition, since the two groups do not compete for the same nutrient resources at the

same rates: dinoflagellates are better competitors for dissolved nitrate (NO_3^-) than prasinophytes, but prasinophytes vastly outcompete dinoflagellates for dissolved ammonium (NH_4^+; Litchman *et al.*, 2006). Therefore, it can be predicted that prasinophytes (while not wholly excluded from NH_4^+ -free waters), will dominate the phytoplankton community when dissolved NH_4^+ becomes abundant. Such is the case under "nitrogenous" conditions, where increased rates of dissimilatory NO_3^- reduction, and ammonification of organic matter-hosted nitrogen (both observed in modern OMZs; Lam & Kuypers, 2011), lead to a higher dissolved NH_4^+ inventory. Nitrogenous conditions are associated with dysoxic to suboxic marine conditions, i.e., where dissolved oxygen is depleted (below 2.0 mL/L; Tyson & Pearson, 1991), but not to the point of anoxia (no oxygen; Quan *et al.*, 2008).

Despite the apparent resilience of dinoflagellates as a whole (irrespective of specific genera) to marine oxygen depletion, there is much empirical evidence from the geological record indicating that during periods of black shale deposition, the dinoflagellate cyst content of the palynological assemblage can drop dramatically, even to zero. For example, Bonis *et al.* (2010) noted a drop in the relative contribution of dinocysts, to the palynological assemblage of the sediments at St. Audrie's Bay (Somerset, UK; A boundary section for the Tr/J), of ~90% (although this was driven principally by a single species – *Rhaetogonyaulax rhaetica*). They also noted a subsequent sharp increase in the abundance of prasinophytes, together with acritarchs - an operationally defined group consisting of organic-walled microfossils of unknown (possibly algal) affinity. In the lower Toarcian, a sharp drop in the abundance of the dinoflagellate *Luehndea spinosa* has been documented in the Lusitanian Basin (Portugal; Correia *et al.*, 2017). This was coeval with the lower boundary of the *Hildaites levisoni* zone, and the base of the Carbon Isotope Excursion (CIE) associated with the T-OAE. *Mancodinium semitabulatum* also disappeared from the assemblage, but this species gradually declined in abundance through the *Dactylioceras polymorphum* zone. In the Cleveland Basin, an absence of dinoflagellate cysts has also been observed, starting at the base of the T-OAE CIE, and persisting

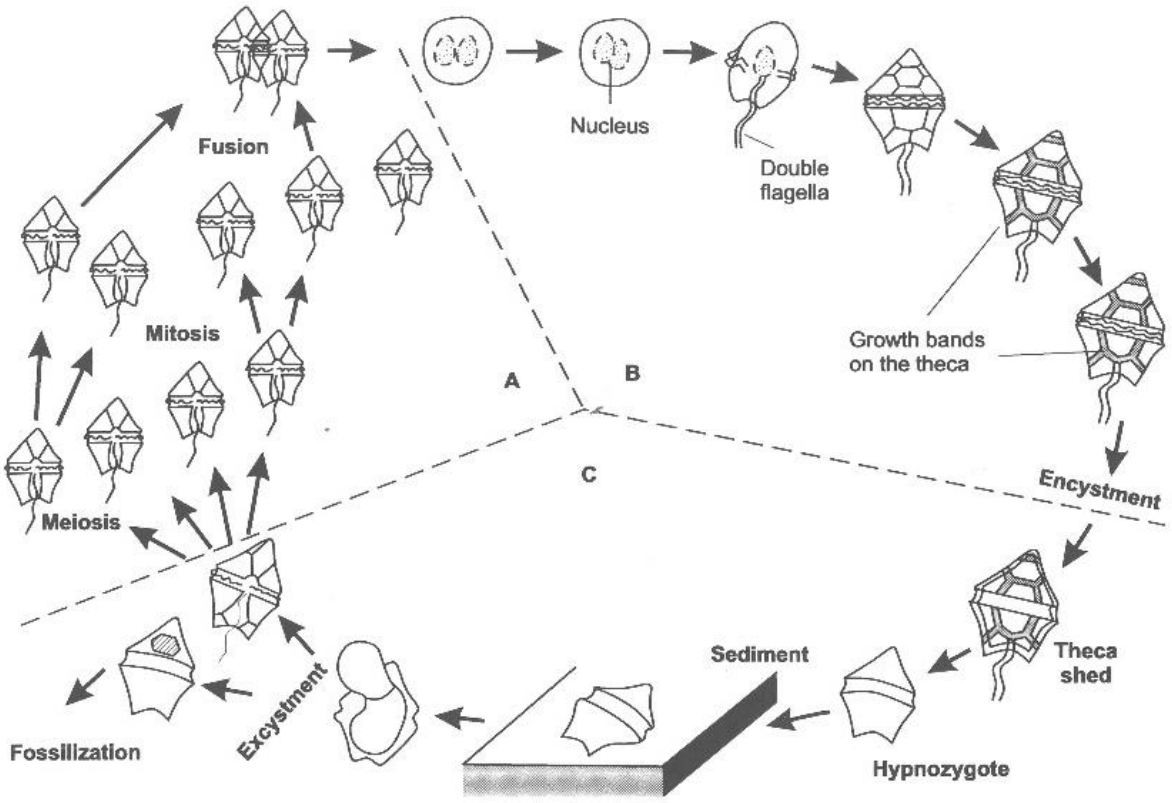

Figure 1.5. The life cycle of a meroplanktonic dinoflagellate (taken from Armstrong & Brasier, 2005). Note that if the benthic environment becomes inhospitable during the hibernation stage, the dormant dinoflagellate might be killed before excystment – in which case the life cycle would be interrupted.

through the succession until the mid *Harpoceras serpentinum* zone (Slater *et al.*, 2019 – but compare with Hesselbo & Jenkyns, 1995 for the biozones omitted from their figures). This was accompanied by a considerable increase in the dominance of sphaeromorph acritarchs, and, for a brief interval, the occurrence of the prasinophyte genus *Tasmanites*. While many of these trends in dinoflagellate predominance are driven by the disappearance of one or two species (that made up the majority of the assemblage to start with), the good correlation of these trends with geochemical data from the same sections indicating a marked decrease in oxygen (e.g. Jaraula *et al.*, 2013; Thibault *et al.*, 2018), still supports the use of dinoflagellate count as a complementary redox proxy. However, the possibility of the resilience of some dinoflagellate species to oxygen depletion, the influence of other paleoenvironmental factors known to effect dinoflagellate populations, and of time averaging in the samples used to derive palynological proxy records should be accounted for.

9.1.2 Pyrite Framboids

When free sulphide generated by sulphate reduction reacts with highly reactive Fe, a monosulphide is formed, which then reacts with partly oxidised sulphur species to form Fe_3S_4 (greigite). This mineral is ferrimagnetic, and the particles are attracted together into spherical aggregations (called framboids due to their resemblance to raspberries; Wilkin *et al.* 1996; 1997). The greigite is converted into pyrite in the presence of free sulphide and mildly oxidised sulphur species. When formed in the sediment, the size these framboids attain is limited by the availability of the reactants, and the range of the magnetic attraction of the greigite microcrystals. However, if these framboids form in the water column, they sink as soon as they reach 6µm in diameter (Muramoto *et al.*, 1991), since greigite is a very dense mineral. A greater amount of pyrite framboids are generated under these conditions, (in the water column), and if the oxic-euxinic chemocline extends high enough into the water column, partially oxidised sulphur species can be precluded from even reaching the sediment, preventing framboids from being formed here (and hence growing to large sizes; Wilkin *et al.*, 1996). Therefore, the distribution of the sizes of pyrite framboids in sediments accumulating beneath a euxinic water column is much narrower (and with a lower mean), than those accumulating under dysoxic/oxic water columns where pyrite formation was limited to the sediment. This proxy has been calibrated against a wide range of modern environments (Wilkin *et al.*, 1996), and has previously been applied (at low resolution) to the thin black shales of the Kimmeridge Clay and the LSB (Wignall & Newton, 1998).

9.1.3 Carbon, Sulphur, and Rock-Eval Pyrolysis

In the absence of oxygen, the microbiota of the water column can become dominated by bacteria that utilise the sulphate reduction respiratory pathway in place of oxygenic respiration. These bacteria produce aqueous sulphide as a by-product. As described in 1.8.1.2, this leads to the water column precipitation of greigite, which is later converted to pyrite. As such, the amount of pyrite generated is limited either by the amount of organic carbon remineralised, the level of available reactive Fe, or the level of sulphate (reduced to sulphide; Berner, 1970). Total organic carbon (TOC), and pyrite-hosted sulphur are also usually positively correlated in marine sediments –especially under varying degrees of oxygen limitation (Raiswell & Berner, 1985; Algeo & Maynard, 2004) – however, the cause of this relationship is still an active area of research. Deviations from this trend are usually characteristic of highly sulphate-limited environments such as rivers. It can therefore be inferred that a high pyrite content of the sediment, especially when correlated with a high TOC content, implies oxygen limitation occurred in the overlying water column whilst the sediments were being deposited.

However, for sulphate reduction to occur, organic carbon has to be of a bioavailable, labile form, that can easily be remineralised and thereby deplete oxygen levels. Non-bioavailable, recalcitrant organic matter is often associated with organic macerals such as wood particles or dinosporin. While this cannot be metabolised easily, it can make up a large proportion of the sediment C_{org} (for example, in proximal settings; Tyson, 1995 and references therein). Analysis for TOC via total combustion cannot distinguish between these two types of carbon, so to evaluate the extent to which the organic carbon content of the sediment could influence pyrite formation, a different method is needed. Rock-Eval pyrolysis can discriminate between easily and poorly combustible sedimentary C_{org} by applying a ramped heating program to a powdered sediment sample in an inert atmosphere. By analysing the CO_2 and CO content of the gases generated through the analysis, the quantities of labile, and recalcitrant C_{org} present in the sample can be calculated (Hazra *et al.*, 2019).

9.1.4 The Fe-speciation proxies

Previous workers on the LSB have used the iron speciation proxies, the most up-to-date versions of which are described by Poulton (2021). Essentially, these proxies rely on the fact that under sulphidic conditions, easily reducible Fe (oxyhydr)oxides (that would otherwise make a minor contribution to the local sediment Fe content; Raiswell & Canfield, 2012) are subjected to reductive dissolution below the chemocline (via the reduction of surface-complexed sulphides, and the release of Fe^{2+} cations; Poulton *et al.*, 2004), leading to syngenetic pyrite formation in the euxinic water column. This leads to an increase in the ratio of pyrite-hosted Fe (Fe_{Py}) compared to the sum total of highly reactive Fe-species (Fe_{HR}). Meanwhile, under anoxic (but not euxinic) conditions, Fe_{HR} can be enriched by precipitation of Fe-carbonates (Fe_{Carb}), Fe (oxyhydr)oxides (Fe_{Ox}), and (occasionally) magnetite (Fe_{Mag}), although the exact mechanisms of many of these enrichment pathways are active areas of research. Fe_{HR} enrichment can be further quantified by the ratio of Fe_{HR} compared with total Fe (Fe_T), which can be used to distinguish euxinic from anoxic ferruginous (i.e. reactive Fe-rich) environments (Poulton & Canfield, 2011). In these settings, the delivery flux of Fe_{HR} outweighs that of sulphide, and if the former outweighs the latter by a factor of at least 2 (the ratio of Fe to S in pyrite), the entire sulphide inventory is sequestered in pyrite, with excess Fe_{HR} being left to accumulate (Raiswell & Canfield, 2012). One possible mechanism for Fe_{HR} enrichment in the sediments under these conditions (of high Fe_{HR} activity but low sulphide activity) is the phototropic oxidation of ferrous

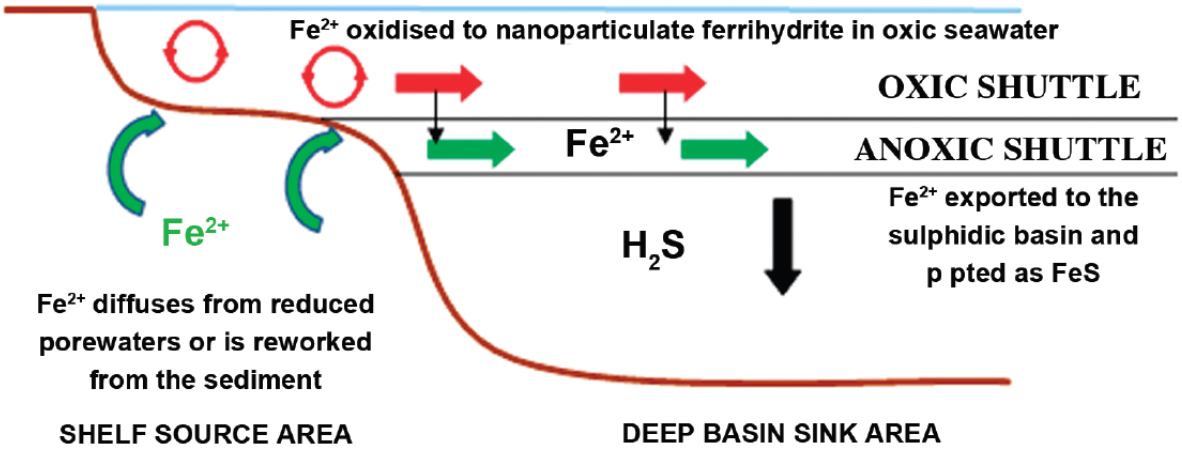

Figure 1.6. A schematic of the shelf-to-basin shuttle (taken from Raiswell & Canfield, 2012). Transport of nanoparticulate ferrihydrite (a highly reactive Fe-bearing mineral phase) under oxic conditions is shown by the red arrows, the aqueous Fe^{2+} shelf flux is shown by the green arrows, and the precipitation of insoluble Fe sulphides is shown by the black arrow.

iron by green sulphur bacteria – a process observed in the ferruginous Lake Matano (Sulawesi, Indonesia; Crowe *et al.*, 2008). The overall pathway of highly reactive Fe species being transported from the basin margins to the depocenter, where drawdown by sulphide then occurs, has been termed the "iron shuttle", or the "shelf-to-basin shuttle" (Illustrated in Fig. 16; Wijsman *et al.*, 2001; Raiswell & Anderson, 2005; Lyons & Severmann, 2006). The iron shuttle may additionally be augmented by a flux of aqueous Fe^{2+} species from anoxic porewaters, directly into the anoxic water column. Inner-shore environments frequently act as a trap for Fe_{HR} supplied by rivers (particularly those with high rates of chemical weathering in the catchment system; Poulton & Raiswell, 2002), and therefore, an increase in the initial amount of Fe_{HR} transported from the basin margins can also raise Fe levels in the distal basin. It is for this reason thatthe normalisation of He_{HR} to Fe_T is essential. It is also important to stress that the aforementioned Fe mineral "pools" are operationally defined by their ease of extraction by various reagents (Poulton & Canfield, 2005), and, therefore, should not necessarily be taken as diagnostic for the enrichment of any given Fe mineral phase. Finally, due to the diagenetic remobilisation of Fe during clay mineral formation, and masking by rapid changes in sedimentation rate, there is no distinct threshold value of the Fe_{HR}/Fe_T, and Fe_{Py}/Fe_{HR} ratios that can be used to distinguish distinct redox regimes. Instead, each proxy has an equivocal zone - 0.22-0.38 for Fe_{HR}/Fe_T, and 0.6-0.8 for Fe_{Py}/Fe_{HR} - that separates unequivocally oxic and anoxic, and ferruginous and euxinic values, respectively (Anderson & Raiswell, 2004; Poulton & Canfield, 2011; Poulton, 2021).

9.1.5 Trace element enrichment

Some metals that are present in trace amounts in seawater are reduced into insoluble states under anoxic conditions and precipitate in marine sediments (Brumsack 2006; Tribovillard *et al.*, 2006). Under euxinic conditions, some trace elements are also incorporated into the crystal lattice of syngenetic pyrite, and are therefore enriched in the sediment. These include As, Co, Cu, Ni, Pb and Zn (Huerta-Diaz and Morse, 1992).

Mo, U and V enrichments are characteristic of euxinic depositional settings, and their co-occurrence is particularly diagnostic (Tribovillard *et al.*, 2006). Mo is readily incorporated into Fe and Mn oxyhydroxides (Adelson *et al.*, 2001; Algeo & Maynard, 2004) and, as such, is drawn down in settings with a strong Fe shuttle. However, Mo is also very strongly scavenged by organic matter that has been sulphurised in a euxinic water column, and the generation of this material has been likened to a geochemical switch that initiates quantitative Mo drawdown (Helz *et al.* 1996). U^{6+} is present in oxic seawater as uranyl ions, and becomes reduced to insoluble U^{4+} under the same conditions that induce Fe reduction, although its biogeochemistry is independent from that of Fe or sulphide (Algeo and Maynard, 2004; McManus *et al.*, 2005). However, U can be easily remobilised from anoxic sediments subjected to episodic reoxygenation, and through bioturbation (Zheng *et al.*, 2002; McManus *et al.*, 2005). V drawdown is strongly mediated by absorption onto Fe and Mn oxides, and incorporation into Fe sulphides has also been reported (Wehrli & Stumm, 1989; Wanty & Goldhaber, 1992).

When Mn is reduced from Mn^{3+} or Mn^{4+} to Mn^{2+}, it becomes soluble, so Mn loss from sediments is often characteristic of oxygen-depleted environments (Klinkhammer & Bender, 1980; Calvert & Pedersen, 1993; Huckriede & Meischner, 1996). For example, in Loch Etive (Scotland, UK), dissolved Mn increased to over 0.5 µM when dissolved oxygen dropped below 40 µM in April 1999 (Overnell *et al.*, 2002). However, if the environment is highly restricted, Mn^{2+} can also become incorporated into carbonates during early diagenesis (Jenkyns *et al.*, 1991; Maynard, 2010).

Other trace elements like Co, Cu, Ni and Zn are relatively enriched in organic matter and can therefore be used as crude proxies for productivity (Saito *et al.*, 2002; Algeo and Maynard, 2004; Naimo *et al.*, 2005). However, these elements are also all readily incorporated into syngenetic pyrite (Huerta-Diaz and Morse, 1992; Tribovillard *et al.*, 2006), and so resolving the relative influence of productivity verses sulphide generation on their enrichments is often not straightforward, especially in settings with high primary production, and free sulphide.

Many of these elements are also supplied from detrital sources. To rule out this competing influence, it is common to normalise the concentrations of redox-sensitive trace elements to detrital, redox-

insensitive elements such as Al and Ti (Calvert & Pedersen, 2007). However, it is important to note that comparing different normalised proxies can introduce spurious correlations (Van der Weijden, 2002). In this work I intend, therefore, to limit the use of Al-normalised data to determine the relative enrichment of major and trace elements compared to a standard shale value, sans the effect of detrital influence (a valid use of Al normalisation).

Depletion of aqueous Mo in restricted anoxic settings leads to a secular decrease in the ratio of Mo to TOC (the reservoir effect; Algeo and Lyons, 2006), and therefore, Mo/TOC is a proxy for basinal restriction in some circumstances. Normalisation to TOC does, however, assume a TOC dominated by marine organic matter – if there is a mixed source, the Mo/TOC ratio attained will underestimate the true value.

9.1.6 Organic geochemical redox proxies

The ratio of Pristane/Phytane preserved in marine sediments is partly a function of redox changes: Both compounds can be derived from the cleavage of phytol, which is derived from chlorophyll, or bacteriochlorophyll (Brooks *et al.*, 1969; Powell & McKirdy, 1973). Under reducing (low oxygen) conditions, the phytyl side chain of chlorophyll is cleaved, and the resulting phytol is subsequently reduced to phytane via dihydrophytol. However, under oxidising conditions, phytol is instead oxidised to phytenic acid, which undergoes decarboxylation to yield pristene, and then reduction to pristane (Peters *et al.*, 2005). Dihydrophytol, however, is also produced by the breakdown of the cell walls of archaea, which tend to colonise anoxic marine environments (Chappe *et al.*, 1982). Despite its sensitivity to redox change, many other factors influence the pristane/phytane ratio, and complementary redox proxies are widely considered essential when presenting pristane/phytane data (Peters *et al.*, 2005). For example, Methyltrimethyltridecylchromans – which often occur in marine sediments and are believed to derive from eubacteria and archaea – can also generate pristene during early diagenesis (Li *et al.*, 1995). Variations in source input (particularly excess input from higher plant material), high thermal maturity (Koopmans, 1999), and possible co-elution with other aliphatic compounds during GCMS (Peters *et al.*, 2005) have also been documented.

Bacteriohopanol (along with other C_{35} hopanes) is common in prokaryotes (see 1.3), and during diagenesis under oxic conditions, is oxidised to a C_{32} carboxylic acid, followed by decarboxylation to a C_{31} compound. The decarboxylation step is, however, limited under suboxic to dysoxic conditions,

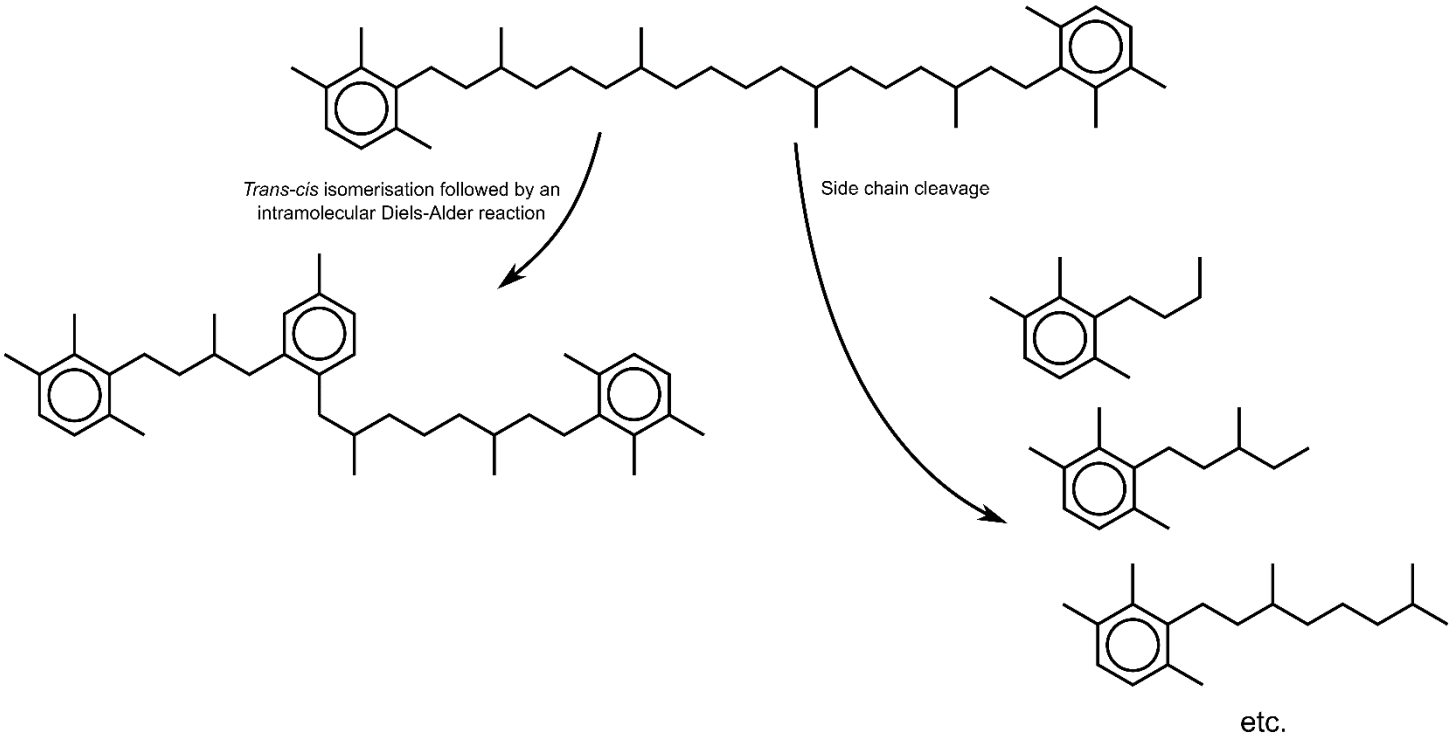

Figure 1.7. Bond-line formulae of Isorenieratane and some of its catagenetic breakdown products. During early diagenesis, isorenieratane can undergo *trans-cis* isomerisation followed by an intramolecular Diers-Alder reaction to form a biphenylic derivative (shown above; Koopmans *et al.*, 1996). The isoprenoid side chain can also be cleaved at multiple points to form aryl isoprenoids (Schwark & Frimmel, 2004). Structures shown are adapted from Koopmans *et al.* (1996).

resulting in more of the C_{32} acid being preserved and less of the C_{31} product being generated (Peters *et al.*, 2005). Under anoxic conditions, the oxidation step is also limited, and more of the original C_{35} hopane is preserved (Peters & Moldowan, 1991). Thus, the percentage contribution of C_{35} homohopane to the pool of $C_{31\text{-}35}$ homohopanes (i.e. the homohopane index) is a proxy for reducing conditions in the sediment. The frequent co-occurrence of high homohopane indices with elevated HIvalues seems to support this. However, the proxy can also be influenced by increased thermal maturity, through processes such as the cleavage of Sulphur-bound C_{35} hopanes (Köster *et al.*, 1997). If excess C_{35} hopanes are released in this way, additional C_{31} homologs are produced, resulting in an apparently oxic signal in the resulting C_{35}-homohopane index. For this reason, like with pristine/phytane, the homohopane index must be used as part of a multiproxy study when determining palaeoredox through organic geochemistry.

Certain strains of brown-coloured green sulphur bacteria (Chlorobiaceae) produce the carotenoid biomarker isorenieratene (Summons & Powell, 1987). These bacteria require both light, and the presence of free sulphide in the water column in order to metabolise organic matter via the reverse

tricarboxylic acid cycle (Sirevåg *et al.*, 1977). When they die, the cell walls of these bacteria are buried in marine sediment, and begin to break down. The isorenieratene is then catagenetically converted to isorenieratane (Koopmans *et al.*, 1996). Therefore, the presence of isorenieratane in a black shale strongly implies that PZE was present (at some point) in the water column during its formation. However, Isorenieratane can also be produced by some sponges (Yamaguchi, 1958; Liaaen-Jensen *et al.*, 1982) and Actinomycetales (Krügel *et al.*, 1999). This group of bacteria is common in both terrestrial and marine environments, and their contribution to sedimentary isorenieratane throughout the geological record is poorly constrained. In addition, the presence of isorenieratane does not by itself indicate that free sulphide existed in the water column – only that Chlorobiaceae were present. They could have been planktonic, or mat-forming, in which case any euxinia is restricted to the sediment-water interface. Isorenieratane has been detected in the upper Grey Shale, and Mulgrave Shale Members of the Whitby Mudstone Formation (beds 31 to 41; French *et al.*, 2014), along with Chlorobactane (produced by green-pigmented *Chlorobiaceae*; Grice & Eiserbeck, 2014) and Okenane (produced exclusively by the *Chromatiaceae* – a family of purple sulphur bacteria; Brocks & Schaeffer, 2008). These data imply that during the T-OAE, euxinia extended into the upper 12 m of the water column, and that the water column was (at least at the points where carotenoids were detected - which are separated from each other by a stratigraphic distance of 0.3-2.0 m) highly redox stratified. It is also possible, however, that the Okenane detected within the black shales of the Mulgrave Shale member was derived from a mat-forming bacterium on the (photic zone) sediment/water interface, especially since modern water-column Okenane production is highly spatiotemporally limited. Wavy lamination within the Mulgrave Shale Member (O'Brien 1990) implies that this is also a potential source for the carotenoid biomarkers as planktonic sulphur-reducers. However, the wavy lamination could also be the remnants of shell pavements that have otherwise been destroyed by compaction. Furthermore, assuming the derivation of carotenoids from an in-situ benthic microbial mat imposes an upper limit on the depth of the water column of, at most, 12 m. This is around 17 times the limit of photosynthesis in clear, oligotrophic waters (200 m). It is highly unlikely that water depth in the Cleveland Basin was persistently shallower than 12 m throughout the deposition of the Mulgrave Shale member, especially given the evidence for a transgression through this interval (Hesselbo 2008; Thibault *et al.*, 2018) – a phenomenon also observed in time-equivalent successions across Europe (for example in Poland; Hesselbo & Pieńkowski, 2011).

The Aryl Isoprenoid Ratio (AIR) proxy was first developed by Schwark & Frimmel (2004), who applied it to the Lower Toarcian-aged black shales of the Southwest German Basin: Given that a major source of Isorenieratane is the post-mortem breakdown of the cell walls of *Chlorobiaceae*, a greater contribution of *Chlorobiaceae*-derived biomass to the organic matter assemblage would lead to higher levels of isorenieratane. Assuming no change in the preservation potential of the sediment

during its accumulation, increases in the contribution of this biomass can be tentatively linked to enhanced productivity of *Chlorobiaceae* (possibly related to enhanced nutrient availability or stratification). The longer the conditions favourable to enhanced *Chlorobiaceae* biomass production last, the more of the resulting sediments contain high levels of isorenieratane. Since Isorenieratane can become cleaved into short chain aryl isoprenoids during catagenesis (illustrated in Fig. 17; Koopmans *et al.*, 1996), intervals with a greater starting proportion of isorenieratane would (by wt.%), be less degraded into aryl isoprenoids than intervals where the starting concentration is lower. In other words, the proportion of the aryl isoprenoids that have been fully broken down is lower in intervals characterised by more persistent isorenieratane production (i.e. more persistent PZE), than in intervals characterised by less persistent isorenieratane production. This does, however, assume that the degradation process remains constant throughout the accumulation of the sediment pile, and that none of the molecular distributions are effected by mineral-matrix interactions.

Phenanthrenes are a class of polycyclic aromatic hydrocarbons (PAHs) based on three fused benzene rings. Some phenanthrenes have been correlated with the occurrence of secohopanoids and their derivatives in oil shales, implying some influence of bacterial degradation of organic matter on their formation (Killops, 1991). PAHs (especially phenanthrenes) are also derived from fossil fuel combustion, and their abundance and geographic distribution have been used to track air quality in modern urban settings (Lehndorff & Schwark, 2004; 2009). This can be done since PAHs are scavenged by epicuticular waxes on the surface of pine needles. Phenanthrene is also enriched relative to other PAHs in weathered, terrestrially derived, sedimentary organic matter (e.g. macrofossil wood; Marynowski *et al.*, 2011). This is because more labile PAHs such as benzopyrene and perylene are extensively broken down with increasing thermal maturity, via processes such as the formation, and cyclisation of phenyl derivatives. Phenanthrene concentration is also a factor in the methylphenanthrene index (MPI-1) for thermal maturation: the lower the phenanthrene concentration, the higher the thermal maturity (Bishop & Abbott, 1995). MPI-1 scales linearly with vitrinite reflectivity (R_0) up to 1.35%, after which the correlation turns negative (Radke & Welte, 1983). However, this relationship only holds within one organic matter kerogen type (typically type III). Both R_0 and MPI-1 also increase in sedimentary C_{org} exposed to dyke intrusion (Bishop & Abbott, 1995). While phenanthrene (being a PAH) in the sedimentary C_{org} record has been attributed to wildfires, the competing influence of bacterial degradation has hampered its utility as a direct proxy (Jiang *et al.*, 1998). The degradation pathway of phenanthrene is unknown, although sulphate reduction is likely to play a role (Coates *et al.*, 1996).

Dibenzothiophene is a sulphur-containing aromatic compound, composed of two benzene rings bonded to a central thiophene ring. The ratio of dibenzothiophene to phenanthrene, when combined with the pristane/phytane ratio is a powerful tool for distinguishing the depositional environment of petroleum source rocks (Huges *et al.*, 1995). This is because while the concentration of

dibenzothiophene increases in more carbonate-rich settings, the concentration of phenanthrene varies independently and can be used as a normalisation factor. Dibenzothiophene, and its alkylated analogues (e.g. methydibenzothiophenes – MDBTs), are also key markers for sedimentary C_{org} exposed to highly sulphidic conditions (e.g. below a frequently, to periodically euxinic water column; van Kaam-Peters & Sinninghe Damsté, 1997; van Kaam-Peters *et al.*, 1998).

9.2 Other proxies used

9.2.1 Palynomorph hydrodynamics and palynofacies

Between their source and site of deposition, palynodebris behave like clastic particles and can be used to reconstruct paleocurrent processes within sedimentary successions (Tyson, 1995, and references therein). This is a powerful tool in palaeoenvironmental analysis, and can be used to assess the relative distance to land and bottom water energy (Wallace *et al.*, 1982; Syvitski *et al.*,1990). For example, Muller (1959) showed how both pollen and leaf cuticle debris becomes more frequent in deltaic sediments closer to the mouth of the Orinoco river, and Heusser & Balsam (1977) found that the pollen concentration in marine sediment cores was highly sensitive both to riverine flux, and the composition of the plant community on the nearby continent.

Based on his palynological work on the Piper and Kimmeridge Clay Formations, Tyson (1989) devised a phytoclast-AOM-palynomorph ternary diagram for palynofacies discrimination. He noted how the ternary diagram had a remarkable ability to distinguish between 10 distinct palynofacies and derived key transport pathways through this diagram, originating from the phytoclast pole. This approach has since been widely adopted in the literature (e.g. Rodrigues *et al.*, 2020; Bang *et al.*, 2022).

9.2.2 Terrestrial plant community shifts

Shifts in climate, and consequently, shifts in the ambient temperature, moisture and nutrient budget of terrestrial ecosystems exert a profound effect on the structure of higher plant communities (e.g. Feeley *et al.*, 2020). These shifts are also accompanied by a change in the assemblage of spores and pollen in the environment, and, if preserved in depositional settings, this can be used as a palaeoproxy for ecological change in the terrestrial environment. Some distinct groups of pollen/spore producers are

also particularly diagnostic for specific environmental changes. For example, fern spikes are often detected in palynological assemblages that post-date mass extinctions, such as the K/Pg (Vajda *et al.*, 2001).

Bryophytes, lycophytes and ferns, all reproduce by releasing male and female (haploid) spores into the environment. If water is present, then the male spore releases a sperm cell, which fertilises the female gametophyte (released from the female spore under wet conditions), leading to the growth of a (diploid) sporophyte, and subsequently, an adult plant (Armstrong & Brasier, 2005). Key to this life cycle is the presence of liquid water during the haploid stage, and so bryophytes, lycophytes and ferns are limited to wet environments, or, at the very least, environments which become wet at predictable times. In these environments, the plants may adapt by producing thicker-walled spores that can lie dormant until wet conditions return (e.g. in bracken; Conway, 1949)

Conifers belong to the gymnosperms, produce bisaccate pollen, and have a different life-cycle than bryophytes, lycophytes and ferns (one that does not require the presence of liquid water). The male haploid pollen grain is produced in male cones, and is equipped with two air-filled sacs (hence bisaccate), that allow it to be carried off the male cone by the wind. It then settles on a female (haploid) cone, leading to fertilisation, and the production of a seed, which later falls out of the mature cone and germinates. While cycads are also gymnosperms (that do not require liquid water for the dispersal of sex cells) and also produce bisaccate pollen, their life cycle is somewhat different (not in the least because the sporophyte is dioecious; Jones, 1993).

Significant shifts in the terrestrial plant community are commonly associated with mass extinctions, and provide invaluable information on palaeoenvironmental changes in terrestrial environments concomitant with those in proximal marine settings. In the Qubuerga and Kangshare formations of Southern Tibet, for example, a major turnover in the terrestrial plant community concomitant with the P/Tr (distinguished by a strong negative $\delta^{13}C_{org}$ excursion of -4‰; Shen *et al.*, 2006) is indicated by a sharp decline in bisaccate pollen producers, followed by a peak in the abundance of trilete spores (produced by quillwort and spike moss disaster taxa; Liu *et al.*, 2020). This further implies that the interval was characterised by an abrupt shift in climate, from cool and dry, to warm and humid.

In addition to evaluating changes in the plankton community through the T-OAE in the Cleveland Basin, Slater *et al.* (2019) also reconstructed change in the terrestrial plant community for the same interval. The number and diversity of higher plant genera suffered sharp declines concomitant with the CIE.The hotter, more seasonal climate (inferred from the co-occurrence of dry-adapted flora, and geochemical evidence for enhanced runoff; Cohen *et al.*, 2004) also led to a growth in the dominance of Cerebropollenites producers (an unknown gymnosperm genus possibly related to the extant *Tsuga*; Shang & Zavada, 2003), and of Cheirolepidaceae, at the expense of bisaccate pollen producers and ferns. The post-CIE terrestrial environment was also palynologically distinct from the pre-CIE

environment, even though the marine plankton community had recovered (i.e. the terrestrial impact of the climate shift concomitant with the T-OAE was long-lasting). These results provide further evidence for a major disruption of the global carbon cycle during/immediately preceding the T-OAE. However, no such study has been carried out for the LSB.

9.2.3 Detrital element ratios

Since Zr is a relatively dense element, mineral grains containing it (such as Zirconium and Titanite; Siefert & Kramer, 2003; Deer *et al.*, 2013) tend to settle out in the coarse sediment fraction (Pedersen *et al.*, 1992). Zr/Al and Zr/Rb ratios are therefore sensitive to the relative contribution of continentally derived silt (along with Si/Al; Schnieder *et al.*, 1997; Govin *et al.*, 2012; Thibault *et al.*, 2018), and can be used as rough indicators for palaeoshoreline distance. Likewise, Rb is more concentrated relative to K in micas, and vice versa for feldspars: the greater radius of the Rb^+ ion compared with the K^+ ion means it is less easily accommodated within the framework silicate structure, and accumulates in mineral phases such as micas, that are typical of late stage magmas(Heier & Adams, 1963; Lange *et al.*, 1966). The ratio of K/Rb is therefore also correlated with grain size (since micas tend to be more associated with the fine sediment fraction) and has been used frequently as a grain size proxy in lieu of Al or Ti data (Matthewson *et al.*, 1995; Dypvik & Harris, 2001). The K/Al and Rb/Al ratios are sensitive to the clay mineral composition of the sediment, with cation-depleted clay minerals such as kaolinite having lower values than more cation-rich minerals such as montmorillonite. They are, therefore, not a proxy for palaeoshoreline distance, but can be used to infer concomitant climatic conditions in the source region of the analysed sediment (Pastouret *et al.*, 1978; Schneider *et al.*, 1997; Calvert & Pedersen, 2007; März *et al.*, 2010, 2011).

9.2.4 Biomarker proxies for plankton community structure

Both prokaryotes (e.g. algae) and eukaryotes (e.g. bacteria) can dominate phytoplankton communities, and the relative contributions of both domains to the phytoplankton can be assessed by measuring the concentrations of hopanes and steranes within a total lipid extraction (TLE). While eukaryotes frequently utilise steroids (the precursor to steranes) in the lipid membranes of their cells, prokaryotes prefer to use hopanoids (the precursor to hopanes; summonslab.com, 2022). Changes in the proportions of these two classes of molecules have been tied to episodes of significant restructuring of

phytoplankton communities, with prokaryotes outcompeting eukaryotes under hostile (low redox, high sulphide) conditions (Kasprak *et al.*, 2015)

Different steroids can also be linked to different algal groups; therefore, the concentrations of the resulting steranes in the TLE can be taken as a crude proxy for the predominance of that group in the palaeoenvironment. C_{27} steranes are derived from C_{27} sterols (e.g. cholesterol), which are produced by marine zooplankton (after grazing on C_{28} and C_{29} steroid producers; Huang & Meinschein, 1979), although they are also strongly associated with Rhodophyte algae, Glaucocystophyta (Kodner *et al.*, 2008), and some (such as epicholestanol) have been observed to be produced by anaerobic microbes in seasonally stratified lakes (Mermoud *et al.*, 1985). They are absent from leaf wax cuticle (Rieley *et al.*, 1991). C_{28} steranes are strongly associated with green algae such as prasinophytes (Huang & Meinschein, 1979; Schwark & Empt, 2008), although these can also produce high amounts of C_{29} steranes (Kodner *et al.*, 2008). C_{28} steranes are also associated with a wider range of phytoplankton groups, the appearance of which has led to a general increase in the C_{28}/ C_{29} (sterane) ratio of oils through geological time (Grantham & Wakefield, 1988). C_{29} steranes reflect the input of terrestrially-derived organic matter – since they are produced by higher plants – and alongside C_{27} steranes, exert the most significant control on the sterane composition of sediments (Huang & Meinschein, 1979; Czochanska *et al.*, 1988; Rieley *et al.*, 1991; Dahl *et al.*, 1994). They are, however, also produced by the classes Charophyceae and Ulvophyceae (Kodener *et al.*, 2008), and high amounts of C_{29} sterane are often found in rocks older than the Devonian (e.g. in Precambrian crude oils from Oman; Grantham, 1986) – probably derived from an algae in these instances. C_{29} sterane is also more resistant to biodegradation than shorter chain steranes, and so can come to predominate in recalcitrant organic matter (Peters *et al.*, 2005). Pelagophyceae – a class of marine chromophyte algae – are the only organisms (apart from the foraminifer *Allogromia laticollaris*; Grabenstatter *et al.*, 2013) able to synthesise 24(E)-24-propylidene-cholesterol (Giner & Djerassi, 1991; Rohrssen *et al.*, 2015). This is a precursor to C_{30} sterane, and so the concentration of C_{30} steranes broadly tracks the occurrence of Palagophyceae. Indeed, the first occurrence of C_{30} sterane in the geological record is in agreement with the age of radiation of the Palagophyceae as predicted by molecular genetics (Brown & Sorhannus, 2010). The above discussion demonstrates that while downcore trends in the contributions of different steranes can be of great palaeoenvironmental utility, a given sterane can rarely ever be taken as a direct proxy for the dominance of any given organism since it is often produced by many. The association of C_{27} steranes with marine organic matter, and of C_{29} steranes with terrigenous organic matter can, however, be tested by correlation with the terrestrial/aquatic ratio for the same samples (see Chapter 5, section 2.1.2; French *et al.*, 2019; Kong *et al.*, 2020).

9.2.5 Biomarker proxies for thermal maturity

During early diagenesis, the methyl group at the 17 position of 17α-22,29,30-trisnorhopane (Tm) can be moved to the 18 position, resulting in the formation of 18α-22,29,30-trisnorhopane (Ts – a neohopane; Seifert & Moldowan, 1978). The demethylation/methylation of Tm to Ts is enhanced by increased heat, and the activation energy for the reaction is lowered by the presence of clay minerals (Peters *et al.*, 2005). This transformation, therefore, takes place exclusively during diagenesis and never in living organisms. The ratio Ts/(Ts+Tm) is, therefore, widely utilised as a thermal maturity proxy.

9.2.6 Biomarker proxies for palaeoshoreline distance

n-alkanes are commonly produced both by marine algae and higher plants. However, the requirement for hydrophobicity of epicuticular leaf wax in higher plants means that the *n*-alkanes they produce are typically long ($C_{17\text{-}35}$; Jeffree, 2006). Marine algae do not possess leaves, so no such barrier is required to maintain equilibrium between water uptake and loss. Therefore, most *n*-alkanes produced by these organisms are comparatively shorter (most commonly nC_{17}; Giger *et al.*, 1980). Bourbonniere & Meyers (1996) used these principles to derive the terrigenous/aquatic ratio (otherwise referred to as the terrestrial-aquatic ratio – TAR), to determine the relative contributions of *n*-alkanes, derived from these two pools, to the sediments of Lake Erie. TAR is defined as:

$$\mathrm{TAR} = \frac{(n\mathrm{C}_{27} + n\mathrm{C}_{29} + n\mathrm{C}_{31})}{(n\mathrm{C}_{15} + n\mathrm{C}_{17} + n\mathrm{C}_{19})}$$

where the terms in the numerator and denominator are the relative abundances of $C_{27\text{-}31}$ *n*-alkanes, and $C_{15\text{-}19}$ *n*-alkanes, respectively. This ratio has since been applied to the deeper geological record and a rise in the TAR can be attributed to an increase in the relative contribution of leaf wax-derived *n*-alkanes, either as a consequence of closer shoreline distance (e.g. Song *et al.*, 2014), or an enhanced flux of terrestrially-derived organic matter (e.g. Adegoke *et al.*, 2015; Mathews *et al.*, 2020).

9.2.7 Compound-specific isotopic analysis

$\delta^{13}C$ excursions have long been used to tie palaeoenvironmental marker horizons (black shales in particular), to global carbon cycle perturbations. The T-OAE, for example, is associated with a

prominent negative $\delta^{13}C$ excursion in bulk organic carbon ($\delta^{13}C_{org}$) of -5 to -6‰, lasting 0.5 to 1.5 Myr (Thibault *et al.*, 2018). When first discovered in Tethyan systems in Southern Europe (Jenkyns, 1988) the negative CIE was attributed to the localised upwelling of ^{12}C depleted waters (Küspert, 1982; see also Sælen *et al.*, 1996; Wignall *et al.*, 2005). In a classic study of the Whitby Mudstone Formation, and of the upper Bagå Formation (south-western Bornholm, Denmark), Hesselbo *et al.* (2000), found concomitant negative $\delta^{13}C$ excursions in both bulk TOC, and macrofossil wood particles (Jet, in the Whitby Mudstone Formation), strongly implying a wider carbon-cycle influence on the T-OAE CIE. While it is now widely recognised that the T-OAE CIE was partly forced by a perturbation in the global carbon cycle, the ultimate source of the injected ^{12}C remains a matter of debate, with suggestions ranging from methane hydrates (Hesselbo *et al.*, 2000; Kemp *et al.*, 2005; Izumi *et al.*, 2018), to thermogenic methane produced by Karoo-Ferrar volcanism (McElwain *et al.*, 2005; Svensen *et al.*, 2007), to permafrost destabilisation at the close of a tentative Pliensbachian Icehouse (Ruebsam *et al.*, 2019; 2020a).

While analysing organic carbon-rich sedimentary rocks for their $\delta^{13}C_{org}$ value is straightforward, interpreting the causal factors behind $\delta^{13}C_{org}$ excursions is often complicated by multiple palaeoenvironmental processes, and the final signature recorded in organic matter (and carbonate, to an extent) might not necessarily be the direct reflection of a perturbation to the global carbon cycle (van de Schootbrugge *et al.*, 2013). In the case of the T-OAE CIE, Küspert (1982) explained the pronounced negative $\delta^{13}C_{org}$ excursion in the Posidonia Shale as being the result of prolonged water column stratification: as ^{12}C depleted organic matter – originally fixed by marine phytoplankton – is exported below the chemocline, the lack of oxygen leads to its accumulation (rather than remineralisation), and this drives the $\delta^{13}C$ signature of the sub-chemocline water mass more negative. When this water mass upwells, the fresh supply of ^{12}C to the surface layer can also drive $\delta^{13}C_{carb}$ more negative, since calcification does not fractionate $\delta^{13}C$ to nearly the same extent as carbon fixation. The T-OAE CIE in marine organic matter, combined with a concomitant (muted) CIE in carbonate, could simply indicate a period of high stratification on a local scale, combined with episodic upwelling.

In addition, marine extinctions associated with the T-OAE not only show diachroneity between Tethyan and Boreal localities, but pre-date the onset of the T-OAE CIE ($\delta^{13}C_{org}$; evident, for example, in the Cleveland Basin; Wignall *et al.*, 2005). This further implies that the $\delta^{13}C_{org}$ excursion was not in sync with the environmental kill mechanisms responsible for the extinctions, and that local processes often affected the final preserved signal.

The presence of multiple carbon pools within the depositional environment, each bearing a distinct $\delta^{13}C$ signature, is another factor worth considering. If the C_{org} content of a black shale is derived solely from marine matter, then the $\delta^{13}C_{org}$ signal would be equivalent (notwithstanding any effects in the circulation regime of the basin) to that of the primary marine carbon fixers. However, organic

matter derived from different (e.g. terrestrial) sources, was often in sync with a different $\delta^{13}C$ reservoir at the time it formed. If, therefore, plant material makes a significant contribution to the sediment C_{org}, the resulting $\delta^{13}C_{org}$ signature would be shifted away from the value of marine organic . This is compounded by the fact that terrestrial plants fractionate ^{12}C to a greater degree than marine organisms (-20 – -37‰ as opposed to -18 – -25‰; Popp *et al.*, 1998; Hayes, 2001; Kohn, 2010). However, this difference in fractionation was smaller prior to the Neogene, and the reasons for this are currently poorly understood (although the evolutionary rise of C4 plants, and a long-term decline in atmospheric pCO_2 over the Cenozoic are possible contributory factors; Tyson, 1995, pp. 414 – 415).

Resolving the influence of earth-system scale carbon-cycle changes on a system subject to the frequent addition of depleted carbon, and/or the presence of multiple carbon pools can be difficult. However,an assessment of exogenic carbon cycle perturbation can still be achieved by separating the carbon pool into marine, and terrestrially derived fractions, and targeting the $\delta^{13}C$ analysis to these independent fractions. Hesselbo *et al.* (2000), demonstrated that the T-OAE CIE in marine organic matter was accompanied by a negative CIE in contemporaneous macrofossil wood particles, indicating that the event was accompanied by the injection of isotopically light carbon into the earth surface system. While it has been argued that the diagenesis of wood particles in sediment dominated by marine C_{org} can alter their isotopic signature (Küspert, 1982), it is likely that the excursion truly tracks a change in atmospheric $\delta^{13}C$, since the trend of Hesselbo *et al.* (2000) is corroborated by compound-specific isotopic analysis (CSIA; French et al., 2014): C_{27}, C_{28} and C_{29} *n*-alkanes are derived mostly from terrestrial plants, being a significant component of epicuticular leaf wax. The plant initially sequestered the carbon used in the growth of epicuticular wax via C3 photosynthesis. It can be assumed, therefore, that the $\delta^{13}C$ signal of leaf wax cuticles derived from these plants was in sync with the $\delta^{13}C$ signal of the atmosphere in which the plant grew. If the leaf wax is subsequently lost from the plant, and accumulates in a distal sedimentary environment, this can provide an archive of ^{12}C sequestration in the contemporaneous terrestrial environment. However, there are competing factors that can influence this signal. For example, under persistently arid, or fluctuating wet/arid conditions, the $\delta^{13}C$ of C3 plant tissues is positively shifted from the atmospheric value. This is due to a decrease in stomatal conductance, depressing the ratio of the plant's internal pCO_2 to ambient (i.e. external) pCO_2 (Schubert & Jahren, 2012; Cernusak *et al.*, 2013). Therefore, a negative isotopic shift in the $\delta^{13}C$ of plant tissues could be interpreted as the result of a secular shift to a wetter climate, at constant atmospheric pCO_2 (Kohn, 2010).

During the early Toarcian, the Cleveland Basin was situated in a humid climate belt (Rees *et al.*, 2000; Ruebsam *et al.*, 2020a), and as Schubert & Jahren (2012) have demonstrated, the $\delta^{13}C$ of C3 plants grown under persistently humid conditions is a function of changes in pCO_2 of the ambient air. Furthermore, the effect of atmospheric pCO_2 on plant $\delta^{13}C$ is more pronounced in gymnosperms than

in angiosperms and animals, and of greater magnitude than the effect of precipitation change (Hare *et al.*, 2018). Given that angiosperms were absent in the Toarcian, and the assumption that the contribution of animal-derived *n*-alkanes to the fraction is low, $\delta^{13}C$ of long-chain *n*-alkanes in the sample can be taken as roughly equivalent to the $\delta^{13}C$ of gymnosperm-derived organic carbon. In other words, changes in $\delta^{13}C$ of long-chain *n*-alkanes are a function of atmospheric ^{12}C content, and the level of aridity of the terrestrial environment.

French *et al.* (2014), applied this approach to the black shales of the Mulgrave Shale Member, and found excursions in the $\delta^{13}C$ of $C_{27\text{-}29}$ *n*-alkanes of around -4‰ (concomitant with excursions of similar magnitude in short-chain, marine-derived *n*-alkanes). This not only corroborated the macrofossil wood data of Hesselbo *et al.* (2000; wrt. exogenic carbon cycle perturbation), but the onset of the $\delta^{13}C$ excursion in *n*- $C_{27\text{-}29}$ occurred within bed 31 (Howarth, 1962; 1973) – at about the same stratigraphic level of the main pulse in marine extinctions, as described by Wignall *et al.* (2005).

Littler *et al.* (2010), reported two $\delta^{13}C_{org}$ excursions similar to the main T-OAE CIE in the upper *P. spinatum*, and lower *D. tenuicostatum* zones, with a magnitude of ~-2.5‰, to -28.5‰. Limited $\delta^{13}C_{wood}$ data corroborated the observed trend. The first of these excursions shows a broad decrease starting in the middle of bed 42 of the Cleveland Ironstone Formation, approaching a sharp minimum in the LSB, before sharply returning to a background signal in the overlying bed. The second excursion spans the MSB, and shows two distinct peaks at its base and top respectively, with an intermediate 'saddle' in-between. Conspicuously, there is no $\delta^{13}C_{org}$ excursion co-incident with the USB – sampling resolution was, however, lower in this interval. By comparison of the $\delta^{13}C_{org}$ profile to a similar dataset from Peniche (Portugal; Hesselbo *et al.*, 2007), it was suggested that the excursions were caused by an event that affected at least the western EES, and that the excursion might serve as a stratigraphic marker for the Pl-To boundary. Possible causes of the invoked carbon cycle were discussed. The suggested causes were identical to those suggested by Kemp *et al.* (2005) and Svensen *et al.* (2007) for the T-OAE CIE, and this was justified based on the stratigraphical proximity of the excursions. This CIE was later detected in the Amellago section, in the High Atlas Rift Basin of Morocco (Bodin *et al.*, 2010), leading those authors to suggest time-equivalence of the CIE to the Pl-To, and that the event was marked by local bottom water deoxygenation. However, unlike the main T-OAE CIE, a compound-specific isotopic analysis of the $\delta^{13}C$ record through the LSB has not yet been resolved. I aim to carry out such an analysis (Chapter 5), and test whether the $\delta^{13}C_{org}$ excursion of Littler *et al.* (2010) can be attributed to local water mass changes, a carbon cycle perturbation, or, perhaps, both processes working in concert.

Chapter 2 – Methods (sample collection, preparation and analysis)

1.0 Sample collection

On 03/2019, six blocks of the LSB, and a block encompassing a *Bositra radiata* pavement (bed 32 of Howarth, 1955, 1962, 1973), were collected from a wave-cut platform at Hawsker Bottoms (6.28 km to the SW of Whitby; sampling locations 54°27'13.27"N, 0°32'3.38"W and 54°27'20.59"N, 0°32'20.12"W, respectively; see Figs. 2.1 – 2.5). On 08/2020, Dr. Crispin Little collected additional samples from two *Pseudomytiloides dubius* pavements (beds 34 and 41), at 54° 27' 24.33"N, 0° 32' 20.41" W and 54° 27' 27.53"N, 0° 32' 24.91"W.

2.0 Sample preparation

Five of the six blocks (coded LSB1 to LSB6) of the LSB were used in this project, since together they span the width of the LSB, and some of the underlying sediments of the Cleveland Ironstone Formation (Fig. 2.6; LSB4 did not encompass enough stratigraphic height to be useful). These were subsequently cut perpendicular to bedding using a circular blade rock saw at the University of Leeds. The fresh, bedding-perpendicular surfaces were then scanned using an office scanner (with a ruler for scale), and 600 dpi .jpg images inspected for bioturbation.

Figure 2.1. Cliff exposure of the Grey Shales Formation, and the lower part of the Mulgrave Shale Member (towards the top). LSB samples were collected just to the south of the location of the two figures on the left.

Figure 2.2. Sampling locality for the LSB. At thispoint,the cliff meets a wave cut platform formed from bed 42 (Howarth, 1955). The LSB is exposed at the foot of the cliff.

Figure 2.3. A view of the wave cut platform from ~15m to the south of the sampling locality. The platform is formed from the upper part of the Cleveland Ironstone Formation.

Figure 2.4. LSB samples wrapped in aluminum foil immediately after collection.

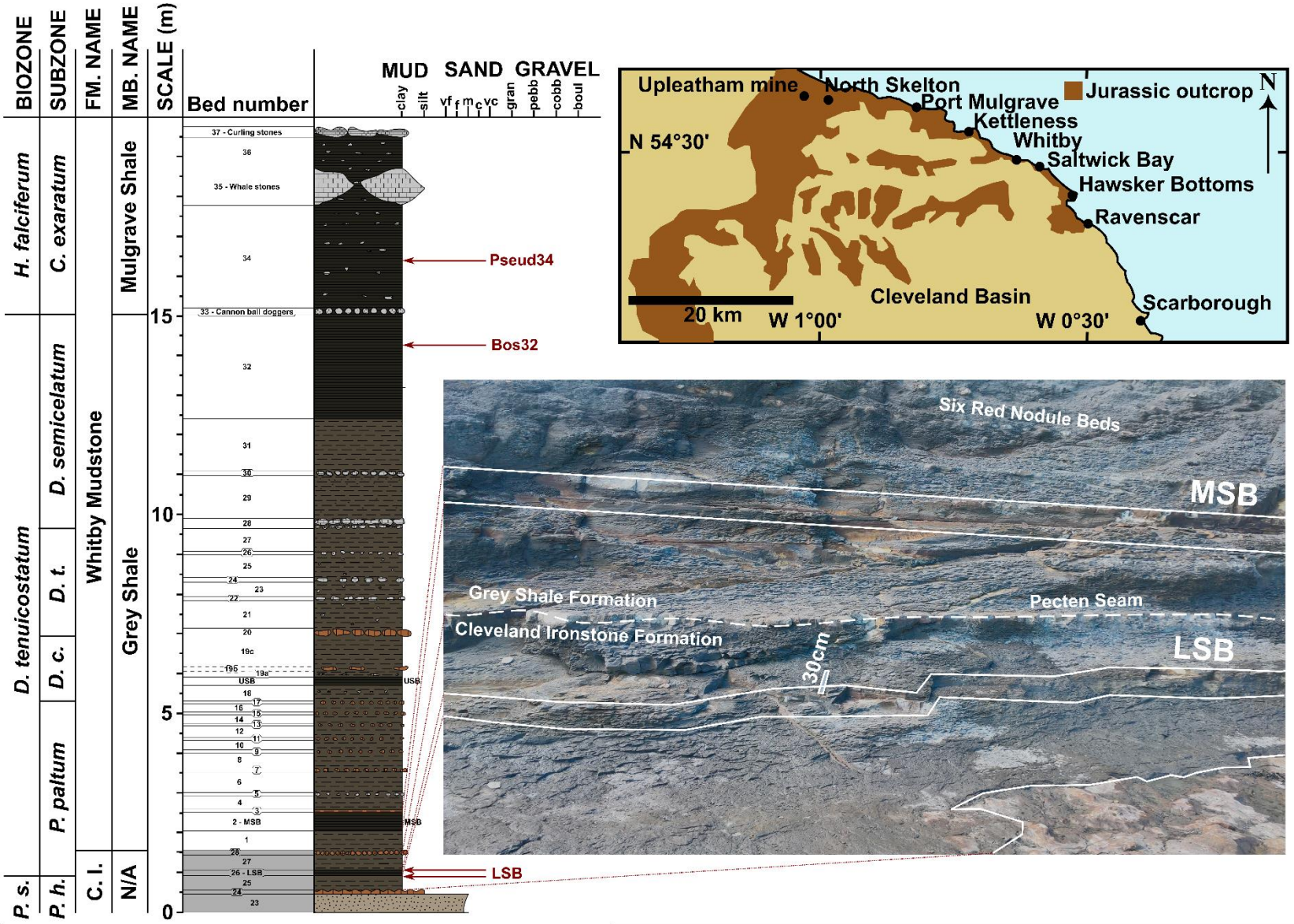

Figure 2.5. Map of the study area, with a photo of the sampling locality (54°27'13.27''N, 0°32'3.38''W), and a graphic log of the lower Toarcian mudstones. The LSB and Middle Sulphur Band (MSB) are highlighted in the figure (along with other stratigraphically important features), and their corresponding positions on the log are indicated. Map adapted from Caswell *et al.* (2009). Abbreviations of ammonite biozone names: *P.hwskrn - Pleuroceras haswskerense; D.Clvlndcm - Dactylioceras clevelandicum; D.tstatm – Dactylioceras tenuicostatum*. Abbreviations of formation names: Clv. Inst. - Cleveland Ironstone Formation.

Fig. 2.6 shows a photomosaic of the scanned images of the LSB, oriented such that their stratigraphic heights are in agreement. Zero datum is indicated by the red line. Note that all stratigraphic height figures mentioned hereafter were measured relative to this line, with measurements taken lower in the stratigraphy being negative with respect to zero datum (these heights have negative values). For all downcore plots of the LSB shown hereafter, this figure is simplified into the photomosaic shown to the right, with enhanced contrast to allow the sedimentary structures to be better discerned. Fig. 2.6 shows scans of the four most extensively sampled blocks, properly oriented with respect to the stratigraphy. Trace fossils, and the surrounding matrix, were manually segmented from the scans in CorelDraw, and total area of each burrow type was measured from the segmented image using Fiji ImageJ (example in Fig. 2.7). Scan images of the shell pavement bedding plane surfaces were also generated using this method, and these are shown in Figs. 2.8 – 2.10. Unlike the LSB samples, bedding-perpendicular scans of the pavements could not be made, due to the thin profile of the samples. I do not, however, consider this to be a major drawback, since bedding-perpendicular thin sections were still made, and for all of the shell pavement samples, the rock texture was finely laminated, with no (macro)bioturbation present (ORB1-4; see chapter 1, section 1.4).

The maximum lengths (umbone to shell edge) of shells in the scanned images were also measured in Fiji ImageJ (with reference to a ruler). Only shells with a visible umbone and shell edge were measured. When possible, the maximum width between each shell was also measured using the same method (albeit from shell edge to shell edge). The data obtained via this method are presented in Appendix 3.

3.0 Optical microscopy and SEM analysis

Six uncovered thin sections (35 μm thick) from the LSB samples, two from the *B. radiata* pavement and *P. dubius* pavement from bed 34, and one from the *P. dubius* pavement from bed 41, were prepared for optical mineralogy and framboid analysis. The portions of the LSB blocks taken for slide preparation are shown by the yellow boxes in Fig. 2.12. The slide material was extracted from the samples with a Dremel 8100 with a diamond-coated cutting wheel attachment, prior to lapping down to 35 μm thickness with circular-blade, water-lubricated saws, sanding

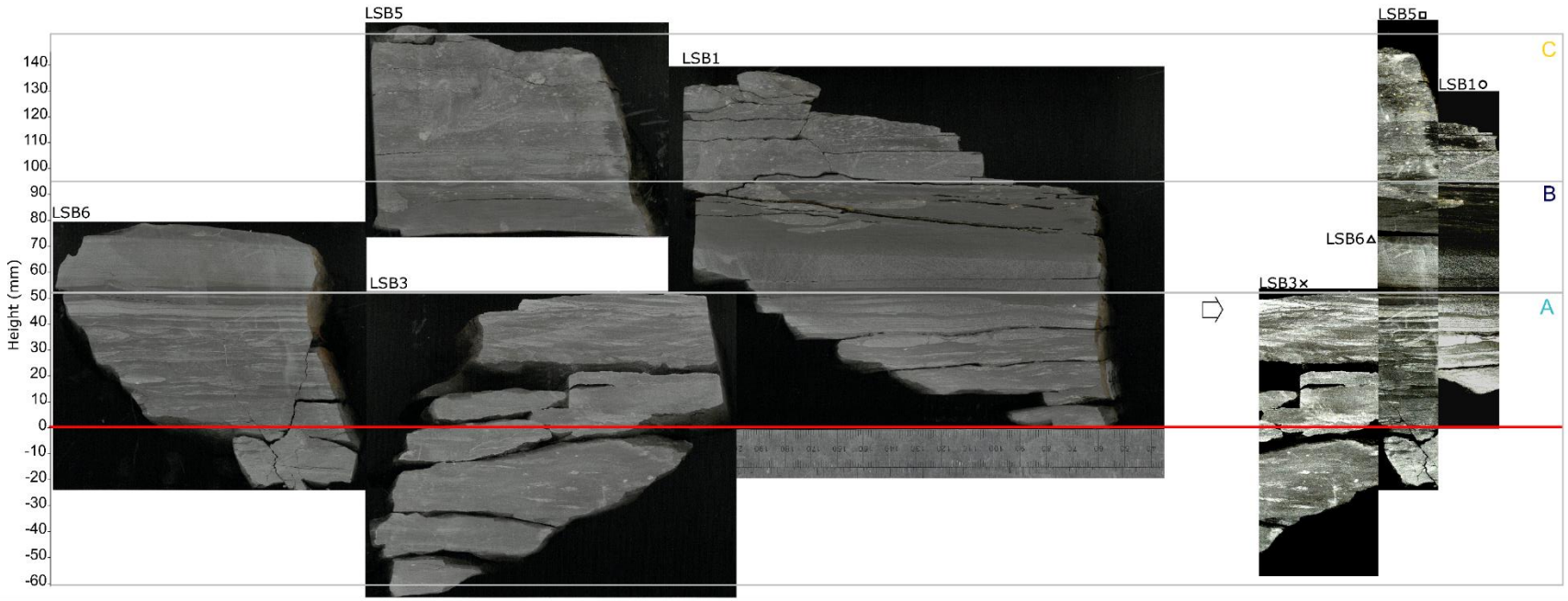

Figure 2.6. Scans of the blocks of the LSB taken from Hawsker Bottoms. The blocks are properly oriented with respect to stratigraphy, with the red line indicating zero datum (the base of the block coded LSB1). The contrast-enhanced photomosaic on the right is included in all up-section plots.

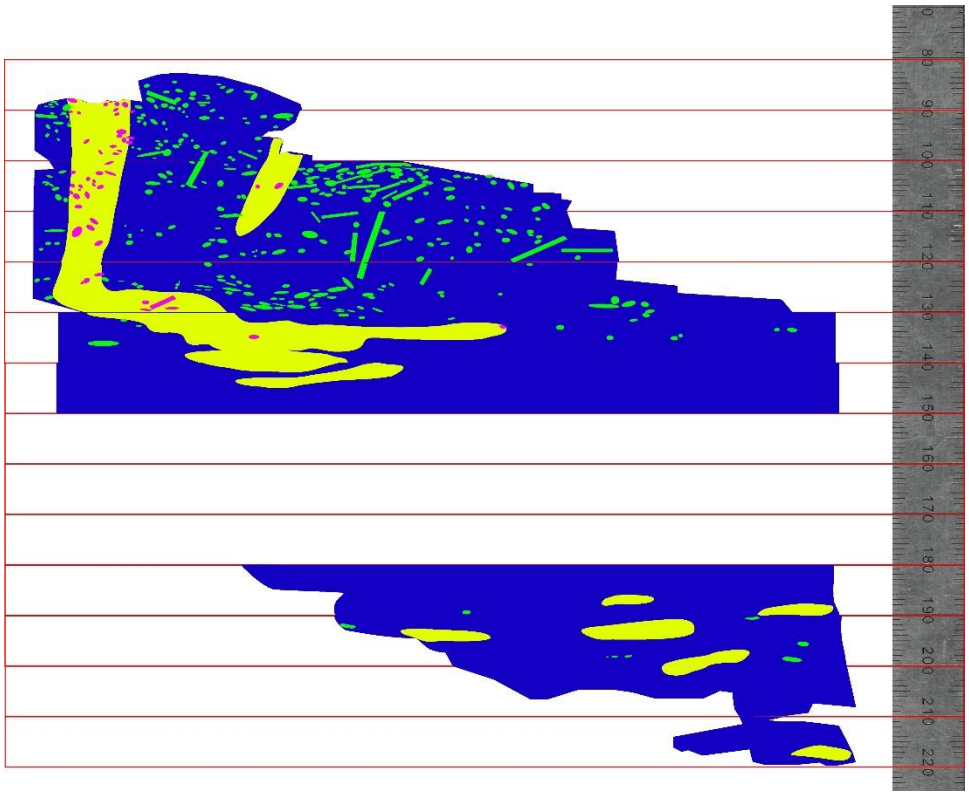

Figure 2.7. Example of a manually segmented image of bioturbation in the LSB (block LSB1 shown). Blue – matrix; Yellow – *Rhizocorallium/Planolites*; Green – *Chondrites*; Purple – *Chondrites* penetrating *Rhizocorallium*. Note that no bioturbation was found between 4–7 cm in this sample, as so here, no segmentation was required.

plates, and aluminium oxide powder. The slides were then mounted on glass slides using Epo-Tek resin, and allowed to dry prior to storage. The slides were coated with graphite prior to back-scattered scanning electron microscopy using a Tescan VEGA3 XM Scanning Electron Microscope (SEM) with a colour filtered CL system – at the Leeds electron microscopy and spectroscopy centre (LEMAS), in the School of Earth and Environment (SEE), at the University of Leeds. When counting framboids, I started from the bottom left corner of each slide, and then collected 20 pictures from a left-to right transect, parallel to bedding, with a width of view of 100 – 300 µm. I determined that 20 pictures captured enough framboids for accurate measurement of mean and standard deviation of framboid diameter (≫100 framboids). After each line of 20 images was taken, I moved back to the far left, and moved up 5 mm, to repeat the same data collection for a point 5 mm higher in the stratigraphy. Theoretically, a much higher resolution

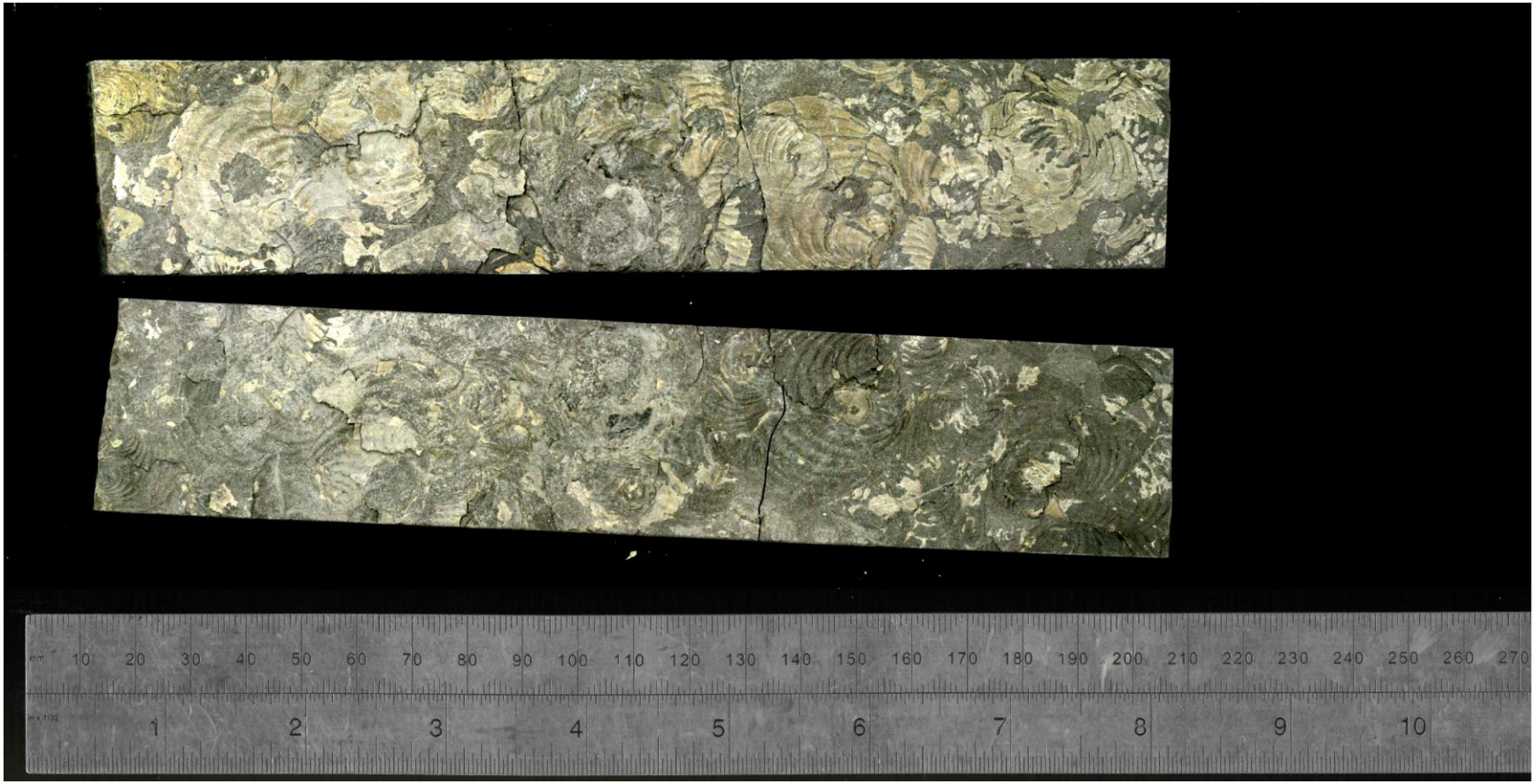

Figure 2.8. Contrast-enhanced photo of *B. radiata* pavement from Bed 32. The total exposed area is approximately 72 cm^2.

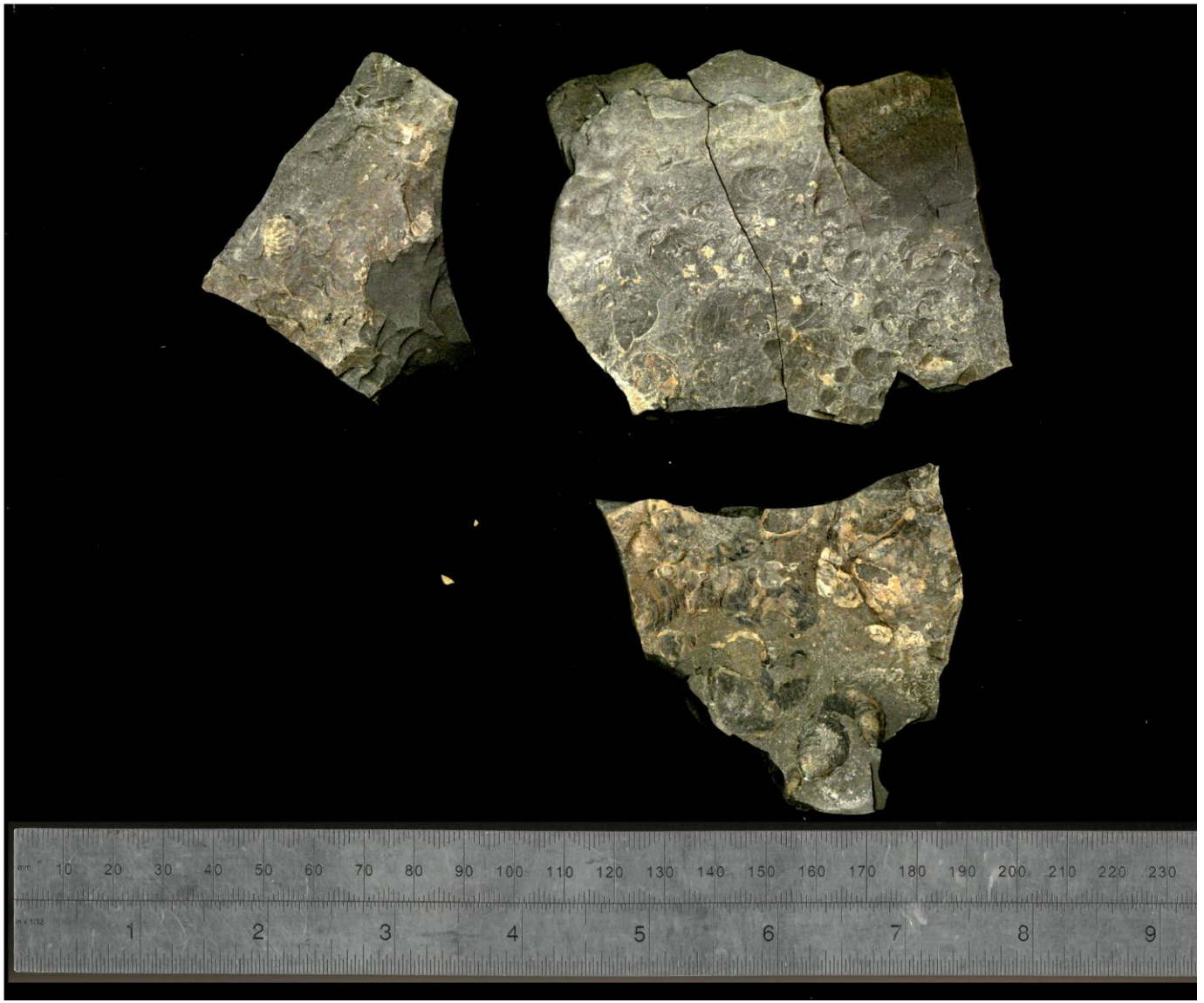

Figure 2.9. Contrast-enhanced photo of *P.dubius* pavement from bed 34. These samples are more fragmented, and contain less material than Bos32 and Pseud41, and as such I did not generate palynological and biomarker samples from this pavement.

Figure 2.10. Contrast-enhanced photos of *P.dubius* pavement from bed 41. Note the sparser coverage of the pavement surface by shells. While one side of this pavement was marked with a permanent marker (to keep track of way up), the marked area of the pavement surface was not sampled.

Figure 2.10. continued

study can be achieved (to a minimum of the chosen width of view – 100-300 μm), but 5 mm was chosen so that the framboid and inorganic geochemical data points were at the same resolution. Ten lines were measured from LSB6.0s and LSB6.1s, and 5 lines were measured from LSB5.0s. Three lines were also measured from each shell pavement (on the pavement, and 2 mm above and below). Framboid diameters were measured from the images taken during SEM microscopy, using Fiji ImageJ. Full-colour photomicrographs (300 dpi) of key features of the LSB and shell pavements were also taken, using a camera-mounted desk microscope.

4.0 Powder sampling

To generate the powdered sample needed for the geochemical analysis of the samples (specifically total combustion, Fe-speciation, bulk pyrite extraction, total digest, and Rock-Eval pyrolysis), a Dremel 8100 with a 2 mm wide (although wider 3.5 mm drill bits were often used) diamond-tipped bit was drawn along a fresh surface, on LSB1, 3, 5 and 6, in straight, bedding-parallel lines, with an interval of ~0.5 cm (and along *Rhizocorallium* trace fossils from LSB1 and LSB2; Figs. 2.6-7). For the shell pavements, samples were taken from the pavement surface (using the side of the drill bit), and bedding-parallel lines 2 mm above and below the pavement were also sampled. Given the discrete, stratigraphically constrained nature of the pavements, and the fact that the enclosing sediments have been very well-characterised geochemically (Pearce *et al.*, 2008; McArthur *et al.*, 2008; French *et al.*, 2014; Thibault *et al.*, 2018), it was determined that three samples from each pavement (directly below, concomitant, and directly above) was sufficient to capture all of the noteworthy variability across the shell pavement. Fig. 2.11 shows an example of a sampled block of the LSB, whereas Fig. 2.12 shows the locations of each sample, and Fig. 2.13 shows the locations of each of the *Rhizocorallium* samples. Powder weights required for the various analyses are presented in Table 2.1. The resulting powder from the drill lines was transferred using clean paper to a glass vial for inorganic geochemical analysis, and aluminium foil for organic geochemical analysis. For some areas of the samples, avoiding the fine, and highly abundant *Chondrites* trace fossils was essentially impossible. The powders generated from these sections are therefore highly suspected to be bearing a mixed signal of matrix and trace fossil chemistry. Drilling at finer width and spacing generates a higher detail proxy record, however, greater depth is required to yield enough sample for the geochemical analyses (required sample weights presented in Table 2.1), and therefore, there is a risk of drilling

Figure 2.11. LSB3 being sampled for high-resolution (sample spacing ~0.5 cm) geochemical analysis, with a Dremal 8100. An example of the glass vials used for powder storage is also included.

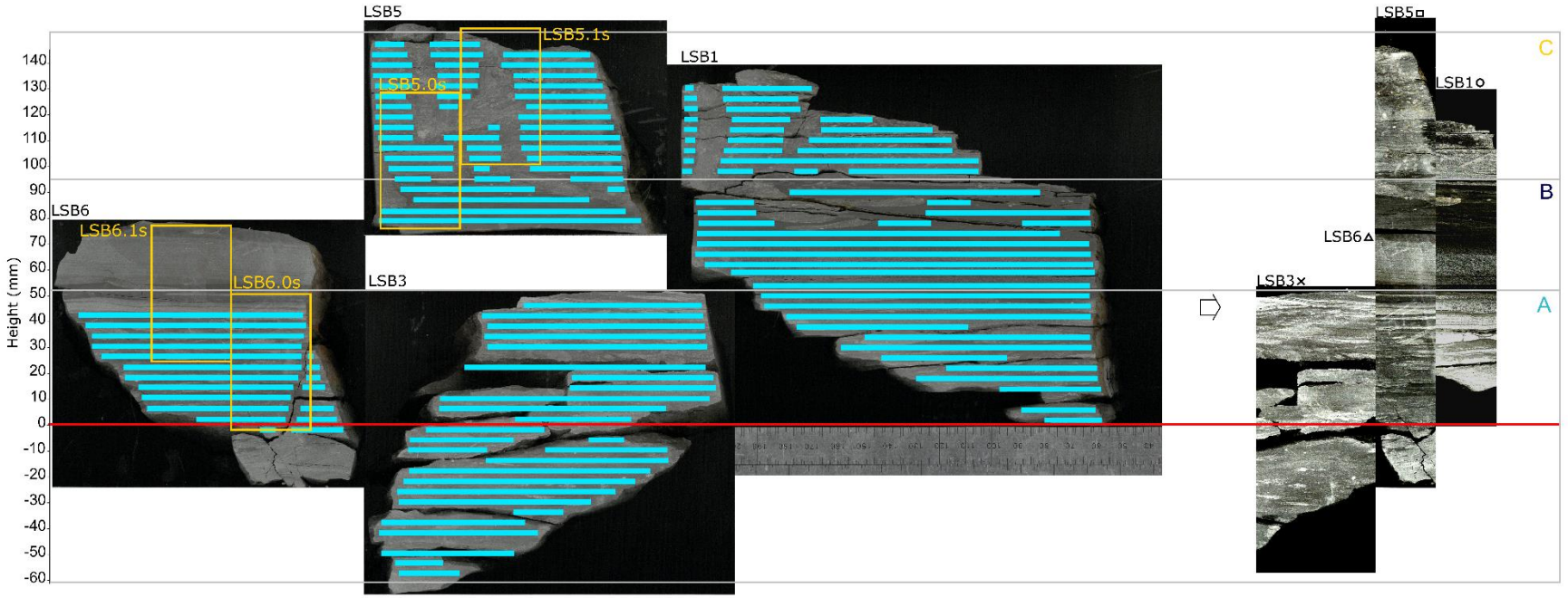

Figure 2.12. Scans of block of the LSB, oriented such that their stratigraphic heights are in agreement (as in Fig. 2.6), with the locations of the high-resolution geochemical samples indicated with blue lines (sample codes omitted for clarity). The locations of the uncovered thin sections (and their codes) are also included.

Figure 2.13. Scans of LSB1 and LSB2, with the locations of the geochemical samples of the *Rhizocorallium* burrows indicated with orange lines (sample codes included).

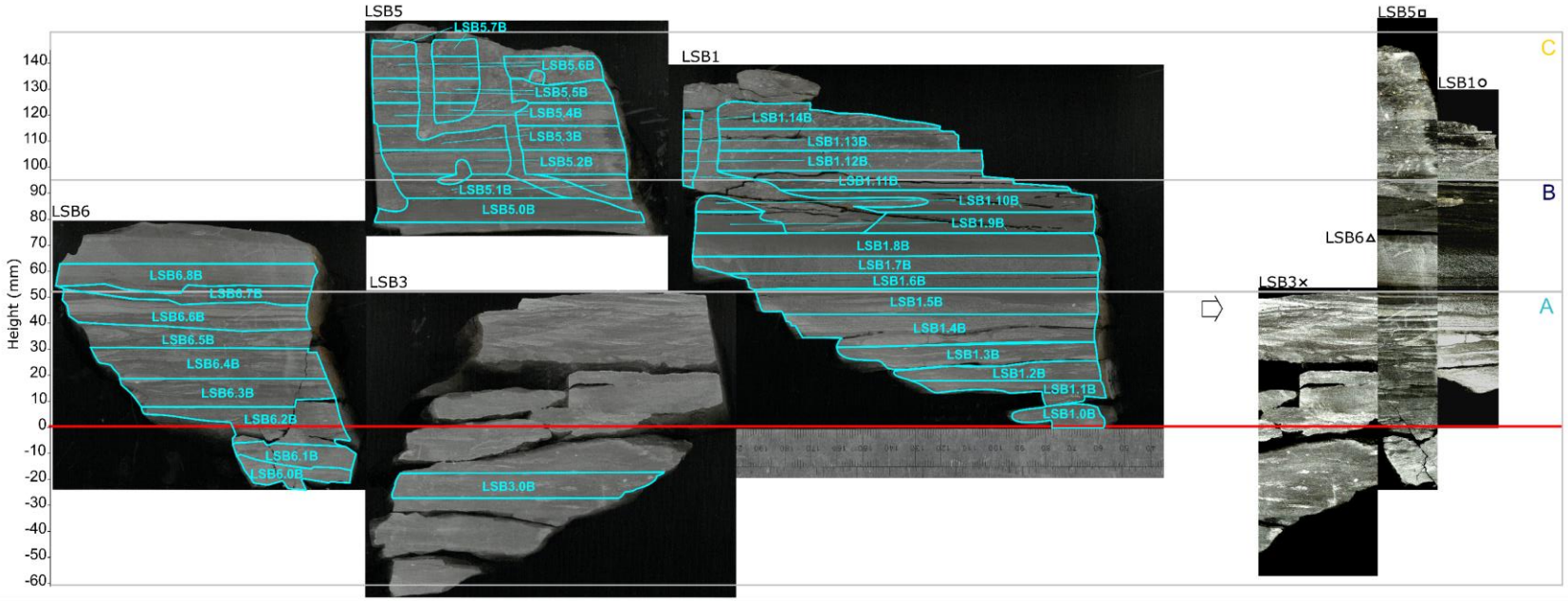

Figure 2.14. Scans of block of the LSB taken from Hawsker Bottoms, oriented such that their stratigraphic heights are in agreement (as in Fig. 2.6), with the locations – and corresponding sample codes – of the TLE samples indicated with blue boxes.

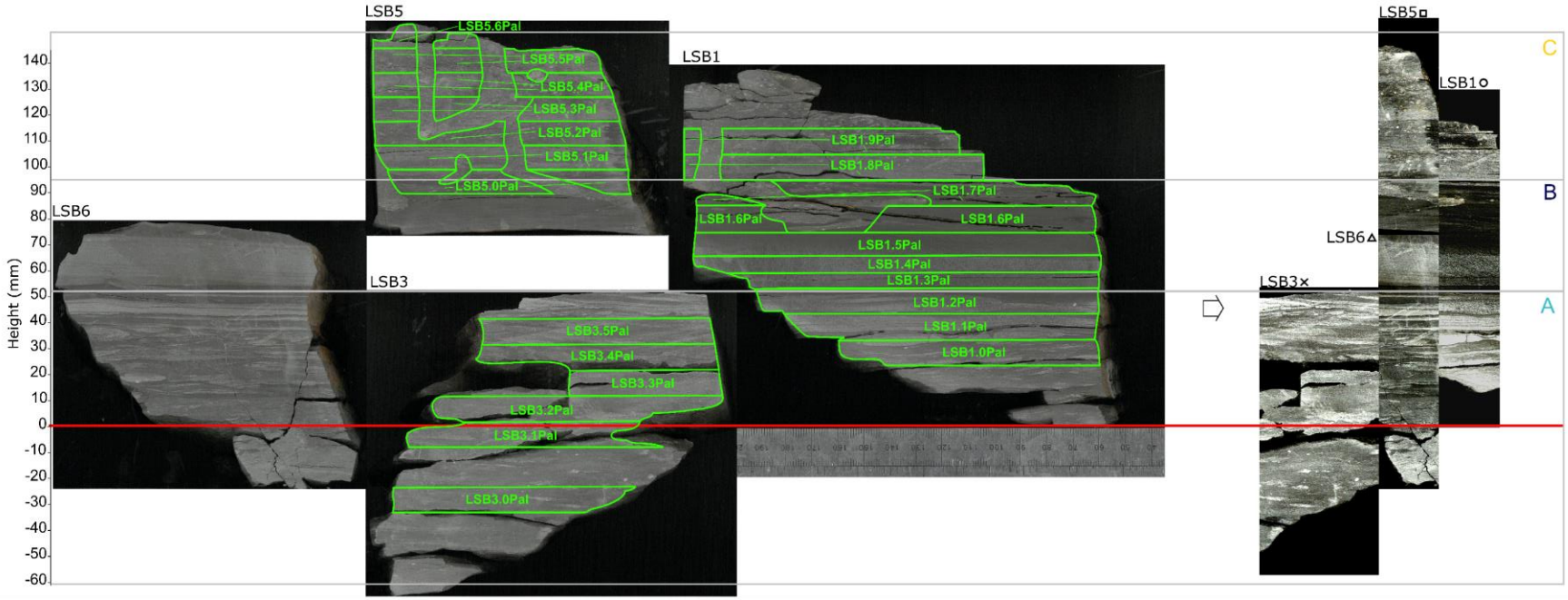

Figure 2.15. Scans of block of the LSB taken from Hawsker Bottoms, oriented such that their stratigraphic heights are in agreement (as in Fig. 2.6), with the locations – and corresponding sample codes – of the palynology samples indicated with green boxes.

into an unseen trace fossil – leading to an averaged geochemical proxy signal, and hence, inaccurate results. At wider spacing and line width, a greater volume of sample can be generated from a given depth, and large trace fossils can more easily be avoided. However, for greater line widths and spacing, resolution of the resulting geochemical records decreases. A line width of 2 mm, with a spacing of 4 mm was used, to strike a fair balance between resolution, accuracy, and sample volume. The LSB samples were coded according to what block of the LSB they were taken from, and then numbered from zero, with zero being the lowest stratigraphically and the highest number being the highest (e.g. LSB1.17 – the 18th sample from the block coded LSB1). The shell pavement samples were coded according to the characteristic genus of the pavement, the bed number, and were numbered from one, with one being the lowest – stratigraphically – and three being the highest (e.g. Pseud34.3 – the 3rd sample [+2 mm] from the *P. dubius* pavement from bed 34).

Given the variable TOC content of the samples (0.185-8.36 wt.%), the sampling procedure employed for the total combustion, Fe-speciation, bulk pyrite extraction, total digest, and Rock-Eval pyrolysis analyses, could not be used for the total lipid extract (TLE) analysis. For an efficient TLE, at least 6.67g of sample (TOC 3.0 wt.%) is needed (Table 2.1). This placed a constraint on the vertical resolution of the required samples of about 1 cm, although due to extensive fracturing in some of the sample blocks, smaller samples were sometimes taken. Rather than running a straight bit along the rock surface, a diamond-coated cutting wheel was instead attached to the Dremel, and ~1 cm wide tiles of rock extracted. The locations of these tiles with respect to the LSB blocks is shown in Fig. 2.14. These were then crushed into a fine powder by hand in a mortar and pestle. In the case of the shell pavements, the higher required sample weight meant that only Bos32 and Pseud41 could be sampled (Pseud34 was too small to be accurately sampled). The greater sample weight also affected the vertical resolution of the biomarker samples – 1 cm thick tiles were taken 5 mm below, and 5 mm above the shell pavement. The sample concomitant with the shell pavement itself could be generated the same way as for the high-resolution analyses, although more of the pavement surfaces needed to be powdered. To minimise contamination from organic matter, all the sampling implements were cleaned thoroughly with a 2:1 mix of dichloromethane (DCM) and methanol. The resulting powders were then transferred, using aluminium foil, to glass vials that had been sterilised by baking at 450^{o}C overnight. These samples were then coded in the same manner as the thinly-spaced samples, but with the suffix “B” (for biomarker; e.g. LSB6.2B – the 3rd biomarker sample from the block coded LSB6, and Bos32.2B – the 2nd biomarker sample from the *B.radiata* pavement in bed 32).

5.0 Palynofacies analysis

In an identical manner to the sampling for the TLE, ~1 cm thick tiles of sample were collected from the LSB and shell pavements, but were then crushed into pea-sized fragments (see Fig. 2.15 for the locations of these tiles with respect to the LSB blocks). This was achieved by wrapping the tile in aluminium foil and hammering until sufficiently crushed. Again, Pseud34 contained insufficient material, and only Bos32 and Pseud41 were sampled (at 5 mm-scale resolution). These samples were then coded in the same manner as the geochemical samples, but with the suffix "Pal" (for palynology; e.g. LSB5.5Pal – the 6th palynology sample from the block coded LSB5, and Pseud41.1Pal – the 1st palynology sample from the *P.dubius* pavement from bed 41). The samples were then transferred to clean glass vials, and shipped to the headquarters of the British Geological Survey (BGS) – at Keyworth, near Nottingham, UK – for palynological preparation.Carbonate and silicate removal of the samples was then carried out by Max Page at BGS. This involved testing the reactivity of the samples with a few drops of 37% hydrochloric acid (HCl), which was very weak for the majority of the samples.

Analysis technique	**Typical weights required for analysis**
Plynolological preparation	20g
TOC and total S via combustion in LECO furnace	1.3 g (1.0g decarbonated + 0.3g original)
Sequential Fe extraction	0.07 – 0.1g
Bulk pyrite extraction	0.1g
Total digest	0.10 – 0.12g
Rock-Eval pyrolysis	0.7g
Total lipid extraction (TLE)	6.67g (at 3.0 wt.% TOC)

Table 2.1 Required sample weights for the analyses techniques employed in this project. Note how palynological perpetration and total lipid extraction require about an order of magnitude more sample than the other (mostly inorganic) geochemical techniques.

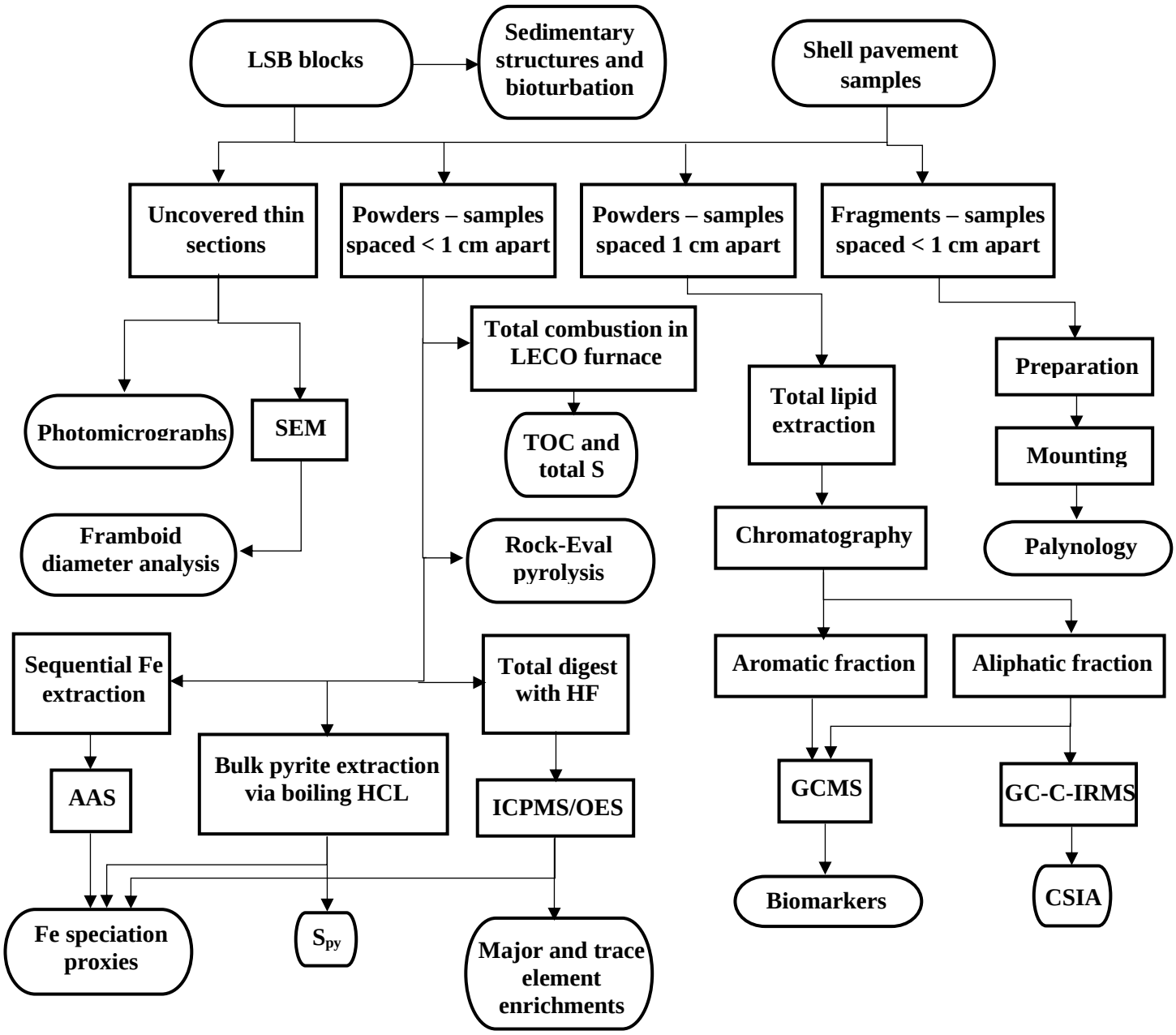

Figure 2.16. Flowchart detailing how samples were treated, what analysis methods were used, and what proxies were derived from the samples during the project.

For all samples that showed a reaction, 50 mL of RO water, plus 20 mL of 37% HCl was added, and the reaction flask was then swirled 3 to 4 times with 1 hour intervals, before being left overnight. This was repeated until further reaction ceased. After dilution, settling, and supernatant decantation of all samples, Max Page then added enough 40% hydrofluoric acid (HF; with full PPE and safety precautions in place) to cover the samples to a depth of 5-6 cm. The samples were

left to react with the HF for two days, and were swirled twice daily. After this, the supernatant was carefully decanted onto sodium carbonate (Na_2CO_3), and the sample was then diluted and allowed to settle. This process was repeated until no further reaction with the Na_2CO_3 occurred. The samples were then stored in RO water until I arrived at BGS Keyworth to perform the remaining steps of the preparation. I then filtered the samples (suspensions of organic matter at this point) using 10µm nylon mesh and an excess of RO water. Following filtration, the organic material was then transferred to glass vials, which are stored at the BGS HQ. A small amount of each sample was then pipetted onto glass slides, along with 2-3 drops of polyvinyl alcohol for decoagulation (thoroughly stirred prior to application), and allowed to dry overnight. The following day, cover slips were mounted to the slides using Elvacite resin. The slides were then labelled appropriately and were shipped to SEE for optical microscopy.

6.0 Geochemical analyses

A wide variety of geochemical procedures was applied to the samples, and a flowchart presenting these is shown in Fig. 2.16. For all geochemical procedures except the TLE, intra-sample variability was checked by analysing LSB1.17, LSB3.22, LSB5.1, or Bos32.1 in triplicate.

6.1 TOC via total combustion in a LECO furnace

Finely powered samples (weighing approximately 1.0g each) were decarbonated with an excess of 10% HCl for 24 hours prior to being rinsed 4-5 times with deionised water. The wet samples were then dried in an oven at 60^{o}C for 48 hours. After reweighing of samples to quantify mass loss, ~0.3 g of each was transferred to ceramic crucibles and combusted in a LECO SC-144DR Carbon/Sulphur analyser at the Cohen Laboratories, in SEE, at the University of Leeds, and %C was measured. Unless otherwise stated, I carried out all the analyses in this project, and where I did not carry out the analysis, I will mention the name of the person who did. Additional finely powdered samples were combusted via the LECO, without first being decarbonated, in order to evaluate %C (total) and %S. TOC was then calculated by multiplying %C from the decarbonated run with the appropriate mass loss coefficient. In addition to the three repeats, a standard derived

from Brush Creek Shale (USGS SBC-1) was included in the runs. High C soil and ZnS calibration standards (part numbers 502-814 and 502-085, respectively), were also included (~0.05, 0.1, 0.2, 0.3, and 0.4g). Ninety-five percent confidence intervals were 2.0 – 2.95 wt.%, and 0.95 – 6 wt.% for TOC and TIC (respectively) via LECO, with Total C and TIC deviating from the Bush Creek standard (SBC-1) by 0.29 – 0.86 wt.%, and 0.14 – 0.15 wt%, respectively (Appendix 3).

6.2 Fe-Speciation

Reactive Fe was extracted (at the University of Leeds Cohen Laboratories) using a version of the Poulton & Canfield (2005) sequential procedure modified for ancient sediments. Fe_{Carb} was extracted from finely powdered samples with a 1M Na-acetate solution, buffered at pH=4.5 with acetic acid: 10 mL of this solution was added to 15mL polypropylene centrifuge tubes, which were already filled with 70-100 mg of the finely powdered sample. Samples were run in batches of 40 at a time, including three repeats of a selected sample, a blank, and a standard derived from the Whitby mudstone (characterisation by Alcott *et al.*, 2020). After 10 mL of the Na-acetate solution was added to the centrifuge tubes, they were placed on a shaker table set at 100rpm and 50^{o}C, for 48 hr. The samples were briefly taken off the shaker table at +6 hr and +24 hr, to vent any evolved CO_2. After 48 hr, the samples were centrifuged at 4000 rpm for 4 min, with 5 mL of the resulting supernatant being retained. A 0.5 mL measure of the supernatant was then added to 9.5 mL of MilliQ water, resulting in a x20 dilution of each sample (including repeats, standards, and blanks), prior to analysis. The remaining undiluted supernatant still in the centrifuge tube was safely disposed of, and any lingering drops carefully knocked out. The above extraction was then repeated with a freshly prepared Na-dithionite (50 g/L) / 0.25 M acetic acid / 0.2 M tri-Na-citrate solution (targeting Fe_{Ox}). This time the samples were shaken at 100 rpm, at room temperature, for 2 hr. Finally (a day later), 10 mL a 0.2 M ammonium oxalate / 0.17 M oxalic acid solution was added to the centrifuge tubes (targeting Fe_{Mag}), prior to placement on the shaker table at 100 rpm, and room temperature, for 6 hr. Six matrix-matched standards of each of the 3 extracting solutions with 0, 1, 3, 5, 7, and 10 ppm of Fe added (1000 ppm $Fe(NO_3)^3$ in 0.5 M NO_3 stock), were also prepared prior to analysis. Analysis of the x20 diluted samples was performed on a Thermo Scientific iCE^{TM} 3300 AAS Atomic Absorption Spectrometer (AAS) at the University of Leeds Cohen Laboratories. The previously prepared standard solutions were included in the runs,

for calibration. Any sample registering >11 ppm Fe was discarded, and the original supernatant diluted twice to yield a x400 solution, which was later analysed instead. Ninety-five percent confidence intervals were 0.09 – 0.22 for Fe_{HR}/Fe_T, and 0.01 – 0.05 for Fe_{Py}/Fe_{HR}, with Fe_{Carb}, Fe_{Ox}, Fe_{Mag} and Fe_T deviating from the Whitby Mudstone standard by 0.002 – 0.1 wt.%, 0.001 – 0.01 wt.%, 0.03 – 2.3 wt.%, and 0.07 – 0.11 wt.%, respectively (Appendix 3).

Fe_{Py}, meanwhile, was extracted via reduction with acidified Chromous (II) chloride (after Canfield *et al.*, 1986). At least 0.1 g of the sample was added to a 100 mL, three-necked reaction bulb fitted to a reflux condenser, circulated with a 10°C solution of 20% propylene glycol. A nitrogen gas line was also fed into the reaction bulb to purge oxygen, and the remaining fitting was stoppered off. All fittings were well-coated in high temperature grease to ensure an airtight seal. The exit end of the reflux condenser was fitted to a syringe placed in a test tube filled ~2/3 full with a $1ML^{-1}$ solution of silver nitrate ($AgNO_3$). Twelve such setups were run in parallel (in a fume hood), with up to 12 samples being processed in each run. Since this is a bulk extraction methodology, no calibration standard was required. ~8mL of 50% HCl was added to the reaction bulb and was quickly stoppered off, prior to steadily heating the reaction bulb, in order to drive off any acid-volatile-sulphide (AVS) present in the sample into the $AgNO_3$ trap. In no run was any AVS detected. If a silver chloride precipitate (milky white in colour) was detected in any of the traps, the sample was discarded (to be repeated later), and the reflux column thoroughly washed with deionised water (after turning off the heat). The sample was allowed to reflux with hot 50% HCl for 10 minutes. Then, ~15 mL of a 3.37 M solution of Chromous(II) chloride in 50% HCl was added to the reaction bulb. Again, the stoppered inlet was quickly opened and then closed to do this. For the majority of the samples, a significant volume of silver sulphide (Ag_2S) precipitate appeared in the traps. A $1ML^{-1}$ $AgNO_3$ solution was added in 5 mL increments to the trap if the solution turned dark, to ensure $AgNO_3$ was constantly in excess. Once the solution was clear, the sample was left to reflux with acidified Chromous(II) chloride for 45 min – 1 hr. After this, the traps were disconnected, the heat was turned off, and the reaction bulbs allowed to cool to room temperature prior to disassembly. The solutions containing the Ag_2S precipitate were then passed through a vacuum-filter onto pre-weighed 45 µm fibreglass filters, and thoroughly rinsed with MilliQ water. After being left for 24-72 hr (or until completely dry), the filters were re-weighed and the mass difference recorded. The original pyrite content of the samples was then calculated stoichiometrically from these values. The Ag_2S precipitate was then carefully transferred to glass vials for storage. The 95% confidence interval of S_{py} was 0.6 – 1.9 wt.%.

6.3 Total digest for major and trace elements

Trace element proxies for sediment accumulation rate (e.g. Zr/Rb; Schneider *et al.*, 1997; Thibault *et al.*, 2018) aid greatly in testing the proposed formation mechanisms in Chapter 1, Section 7.0, and so I subjected the LSB samples to a total digest followed by ICPMS/OES analysis. This was chosen in preference to x-ray fluorescence (XRF) of sample pellets, due to the lower cost, and increased accuracy of concentration values (at the expense of the inability to quantify Si). The finely powdered sample was added to ceramic crucibles (100-120 mg), and ashed overnight in a Carbolite® AAF ashing furnace (t = 550^{o}C, ramp = 10 min, dwell = 8 hr), to remove organic and volatile components. The contents of the ceramic crucibles were then transferred into Teflon pots with 5x1mL washes of concentrated 69% nitric acid. 2mL of concentrated, 40% HF was then carefully added to each pot, with full PPE and safety precautions in place. Three to four drops of 70% perchloric acid were added to each pot, before they were left on a hotplate set at 70^{o}C, overnight in a sealed fumehood with scrubbers on. The next day, the dried samples were reconstituted with 2mL of 50g/L boric acid, before being returned to the hotplate, and again, left at 70^{o}C overnight. The dried samples were then reconstituted with another 5x1 mL washes of concentrated 69% nitric acid and heated until fully dissolved. Nitric acid – as opposed to hydrochloric – was chosen for the reconstitution, since the former leads to an interference effect with P (which I did not intend to measure), while the latter leads to an interference effect with V (which I did intend to measure). The samples were then each made up to 100mL, with MQ water, in small volumetric flasks. A 13-15 mL aliquot of this solution was retained for analysis. Four mL of the solution was diluted with 5.9 mL of MQ in 15 mL centrifuge tubes, with 0.1 mL of a 100 ppm Y, 200 ppb Rh internal standard added to each. Major and trace element extracts were analysed on a Thermo Scientific iCAPQc ICP-MS, by Steven Reid, at the University of Leeds Cohen Laboratories. (see Appendix 2 for detailed methodologies – document prepared by Stephen Reid). Ninety-five percent confidence intervals were 0.5 – 0.9 wt.% for Al, 0.2 – 1.6 ppm/wt.% for Cu, and 0.0007 – 0.008 ppm/wt.% for Cd (full list in Appendix 3), with deviations from the Bush Creek standard ranging between 0.0002 wt.%/wt.% (K), and 6.3 ppm/wt.% (Zn; Appendix 3).

6.4 Rock-Eval pyrolysis

0.7g of each powdered sample was transferred to a glass vial and analysed using a Rock-Eval6 analyser configured in standard mode (pyrolysis and oxidation as a serial procedure) at BGS in 02/2020, by Dr. Christopher Vane. Samples (60.5 mg /dry wt) were isothermally heated at 300ºC (hold for 3 min) to release free hydrocarbons and then heated from 300 to 650ºC (hold for 3 min) at 25ºC/min to crack non-volatile organic matter (kerogen) in an inert atmosphere of N_2. The residual carbon was then oxidized from 300ºC to 850ºC at 20ºC/min. Hydrocarbons released during the two stage pyrolysis were measured using a flame ionization detector (FID) and CO and CO_2 measured using an IR cell. The instrument performance was checked against the accepted values of the Institut Français du Pétrole (IFP) standard (IFP 160 000, S/N15-081840). Ninety-five percent confidence intervals were 14.8 – 18 for HI, 1.3 – 1.5 for OI, 0.79 – 2.1 °C for T_{max}, and 0.02 – 0.07 wt.% for Inorganic C, with these proxies deviating from the IFP standard by 9 – 10, 1, 2 – 40°C, and 0.13 – 0.14 wt.%, respectively (Appendix 3).

6.5 Biomarker and isotopic analyses

The powdered samples intended for the TLE were shipped to professor Lorenz Schwark at the Christian-Albrecht University of Kiel (Germany). Extraction was carried out using a Büchi Speed Extractor E914 pressurized solvent extractor, with a 93:7 mix of DCM and methanol, at 75ºC and at a pressure of 50 bar. Bitumen extracts were separated in an LCTECH automated SPE system into aliphatic, aromatic, and polar fractions via silica gel-column chromatography (6 mL SPE column, 2.8 g Silica 60, 25–40 μm). Aliphatic hydrocarbons were eluted with n-hexane. Aromatic hydrocarbons were eluted using a 3:2 v/v mixture of n-hexane and DCM. Polar compounds were eluted with a 1:1 v/v mixture of DCM and methanol. Activated copper turnings were added to the aliphatic hydrocarbon fraction for the removal of elemental sulphur. The aliphatic fraction was spiked with two internal standards; A 0.1 mg/g extract of D50 tetracosane (for quantification of acyclic compounds such as n-alkanes and isoprenoids), and a 0.025 mg/g extract of D4 cholestane (for quantification of cyclic compounds such as hopanes and steranes). Similarly, the aromatic fraction was spiked with an internal standard – a 0.1 mg/g extract of D12 pyrene (for quantification of carotenoids and other aromatic biomarkers).

Gas chromatograph mass spectrometry (GCMS) analysis of the aliphatic fraction was carried out on an Agilent 7890 gas chromatograph (GC) coupled to a Chromtech Evolution mass spectrometer (MS), by Lorenz Schwark. The GC was fitted with a DB-1MS capillary column (Agilent DB1-HT; 30 m length, 0.25 mm inner diameter, 0.25 μm film thickness), and helium was used as the carrier gas (flow rate of 1.2 mL/min). Aliphatic hydrocarbons were constituted to a concentration of 1 mg/mL, and 1μL was injected by a COMBI PAL liquid autosampler into a split/splitless injector operated in splitless mode at a temperature of 310 °C. The GC oven-temperature program used was: a 5-minute isothermal hold at 70°C, followed by a 10°C/min increase to 140 °C, then a 3 °C/min increase to 325 °C, and finally a 15-minuite isothermal hold at 325 °C. The MS was operated in EI mode with an ionization energy of 70 eV and a scanning range from m/z = 50 to m/z = 600. The ion source was maintained at 300 °C and the transfer line at 320 °C. The quadrupole mass spectrometer was operating in full scan mode in the 50 – 750 m/z range at an energy of 70 eV. GCMS analysis of the aromatic fraction was carried out on an Agilent 7890 GC coupled to an Agilent 5977 quadrupole MS, by Lorenz Schwark. The GC was fitted with a DB-5 capillary column (30 m length, 0.25 mm inner diameter, 0.25 μm film thickness), and helium was used as the carrier gas (flow rate of 1.2 mL/min). Samples were injected splitless at 300 °C. The GC oven-temperature program used was: a 5-minuite isothermal hold at 70 °C, followed by a 10 °C/min increase to 120 °C, then a 3 °C/min increase to 325 °C, and finally a 12-minuite isothermal hold at 325 °C. Integration of peak areas from the resulting chromatograms was carried out both by myself (using the Agilent Chemstation software), and by Lorenz Schwark (using the Agilent Masshunter software), for verification of compound identifications and peak area data.

Following the TLE, the aliphatic fraction was shipped to the National Environmental Isotope Facility (NEIF; Bristol, UK) for compound-specific isotopic analysis via gas chromatography combustion isotope ratio mass spectrometry (GC-C-IRMS). The GC-C-IRMS analysis was conducted using an Agilent Industries 7890A gas chromatograph coupled to an IsoPrime 100 mass spectrometer by Helen Whelton and Ian Bull (at NEIF). Samples were introduced via a split/splitless injector in splitless mode (purge time 2, purge flow 15) onto a 50 m × 0.32 mm fused silica capillary column coated with a HP-1 stationary phase (100% polysiloxane, Agilent, 0.17 μm). The GC oven temperature program was set to hold at 50 °C for 2 min, followed by a gradient increase to 300 °C at 5 °C min^{-1} followed by an isothermal hold for 10 min. Helium was used as a carrier gas and maintained at a constant flow of 2 mL min^{-1}. The combustion chamber was maintained at 850°C, and consisted of a quartz tube packed with copper oxide pellets. An external FAME standard mixture (C_{11}, C_{13}, C_{16}, C_{21}, and C_{23}), of known isotopic composition was

included in the runs. $\delta^{13}C$ values are determined from the $^{12}C/^{13}C$ data, as compared with the Vienna Pee Dee Belemnite (VPDB) and calibrated against a CO_2 reference gas of known isotopic composition. Instrument error was ± 0.3 ‰. Data processing was carried out using Ion Vantage software (version 1.6.1.0 IsoPrime).

Chapter 3 - High-resolution inorganic redox proxy, and Rock-Eval analysis of the Lower Sulphur Band

1.0 Aims

This chapter aims to integrate ichnological (trace fossil), iron speciation, and trace element redox proxies through the LSB, to reconcile the preservation of labile C_{org} with the presence of bioturbating organisms, and of horizons of silty to fine-grained material (that imply periods of high bottom water energy not typically associated with black shales). Additionally, a combined redox proxy approach is required to better constrain potential pathways for Fe_{HR} enrichment, including trace element, pyrite framboid, and biomarker data. The framboid distribution of the LSB has previously been studied (Wignall & Newton, 1998; Agbi *et al.*, 2015): Wignall & Newton (1998) documented two distinct "populations" of framboid diameters, implying a frequent changes in the redox regime. It is, however, also likely that the larger framboid populations are associated with coarser lithologies from the LSB; previous framboid studies on the LSB have not evaluated changes in the framboid distribution against stratigraphic height on a cm-mm scale, and the present study aims to address this. Here, I address these outstanding questions by employing the high resolution (>1 samples per cm) multiproxy geochemical approach detailed in Chapter 2. This is the most extensive, high-resolution study of a Lower Jurassic black shale to date and reaches the limit of sampling resolution that can be attained without the use of, e.g., XRF scanning equipment.

2.0 Results

2.1 Lithofacies

Investigation of the LSB in hand specimen revealed three distinct Lithofacies, which were stratigraphically ordered, and are hereafter termed Lithofacies A, B and C (with A being the lowest stratigraphically, and C the highest). Points on cross plots of geochemical data are colour coded with respect to which of these Lithofacies they were taken from (A – teal, B – dark blue, C – yellow). The base of the block of the LSB coded "LSB1" was taken as zero datum. Lithofacies A extends from -66 mm to 52 mm and is characterised by the presence of sedimentary structures indicative of sediment reworking. In the lower 66 mm of this lithofacies, bioturbation exceeds 75%, with relict primary depositional structures visible (see Chapter 2, Fig. 2.6).

Between -10 and 20 mm, bioturbation begins to decline (see 2.2), and this allows for the preservation of ripple-scale sedimentary structures akin to hummocky cross-stratification, that would have otherwise been destroyed. The hummocks are on average ~22 mm long, by ~3 mm deep. The hummocks have sharp bases, and sometimes contain thin (on average ~38 μm) organic laminae, particularly at the top (Fig. 3.1). Towards the top of Lithofacies A (at ~40 mm), the hummocks give way to wavy, silty units, with a lateral extent of 5-10 mm, and sharp, erosional bases. The thicknesses of these show considerable lateral variability across the LSB, ranging from 7.7 mm in LSB1, to 1.2 mm in LSB3. LSB6 and LSB3 also show a organic-rich 'parting', 4 mm wide at ~48 mm. Thinner organic-rich partings occur intermittently in these units, with thicknesses of 40 μm to 1.72 mm. Viewing the silty units under cross-polarised light (Fig. 3.8) reveals that the sediment is texturally mature, composed of subangular, well-sorted, very fine quartz grains (~90%), with minor muscovite (5%), plagioclase feldspar (3%), and glauconite (~1%), without significant contribution from lithic fragments. This is consistent with a continental sediment source (Dickinson, 1988).

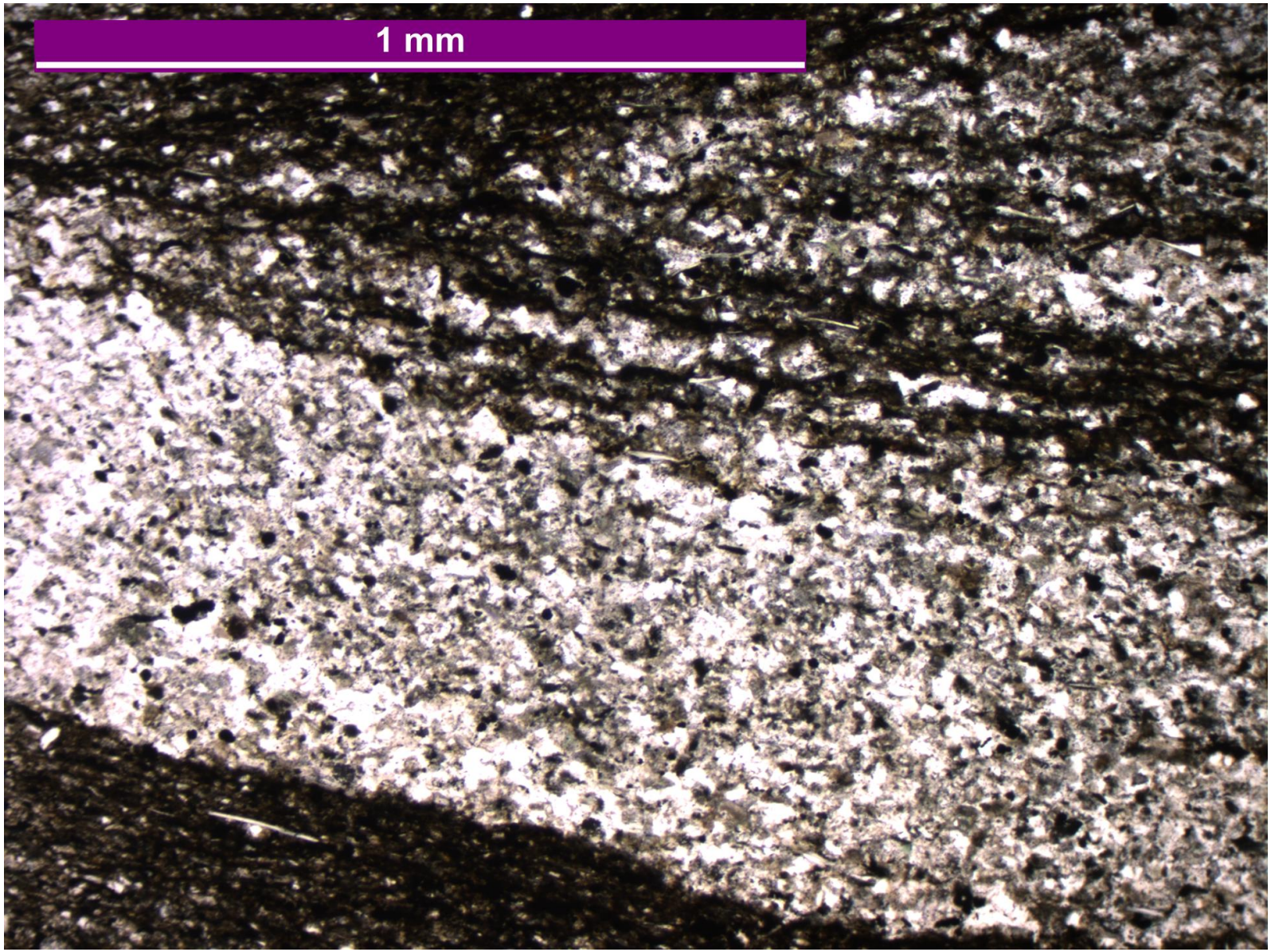

Figure 3.1. Photomicrograph of Hummocky Cross-Stratification from Lithofacies A. From slide number LSB6.0s (see Chapter 2, Fig. 2.12). Note the presence of thin C_{org}-containing laminae near the top of the predominantly silty bedform.

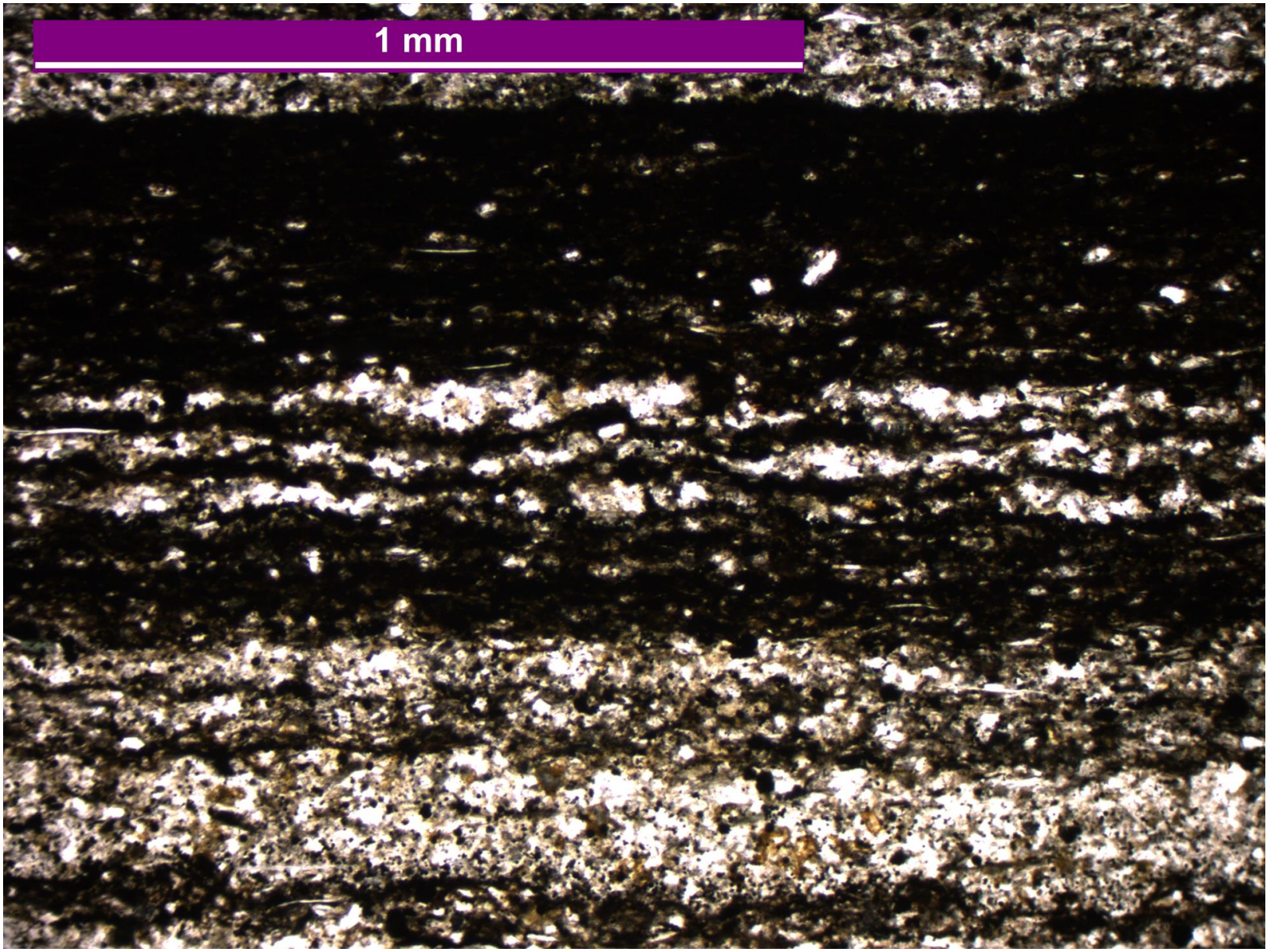

Figure 3.2. Photomicrograph of thin silty laminae in the uppermost, TOC-rich part of Lithofacies A. From slide number LSB6.0s (see Chapter 2, Fig. 2.12).

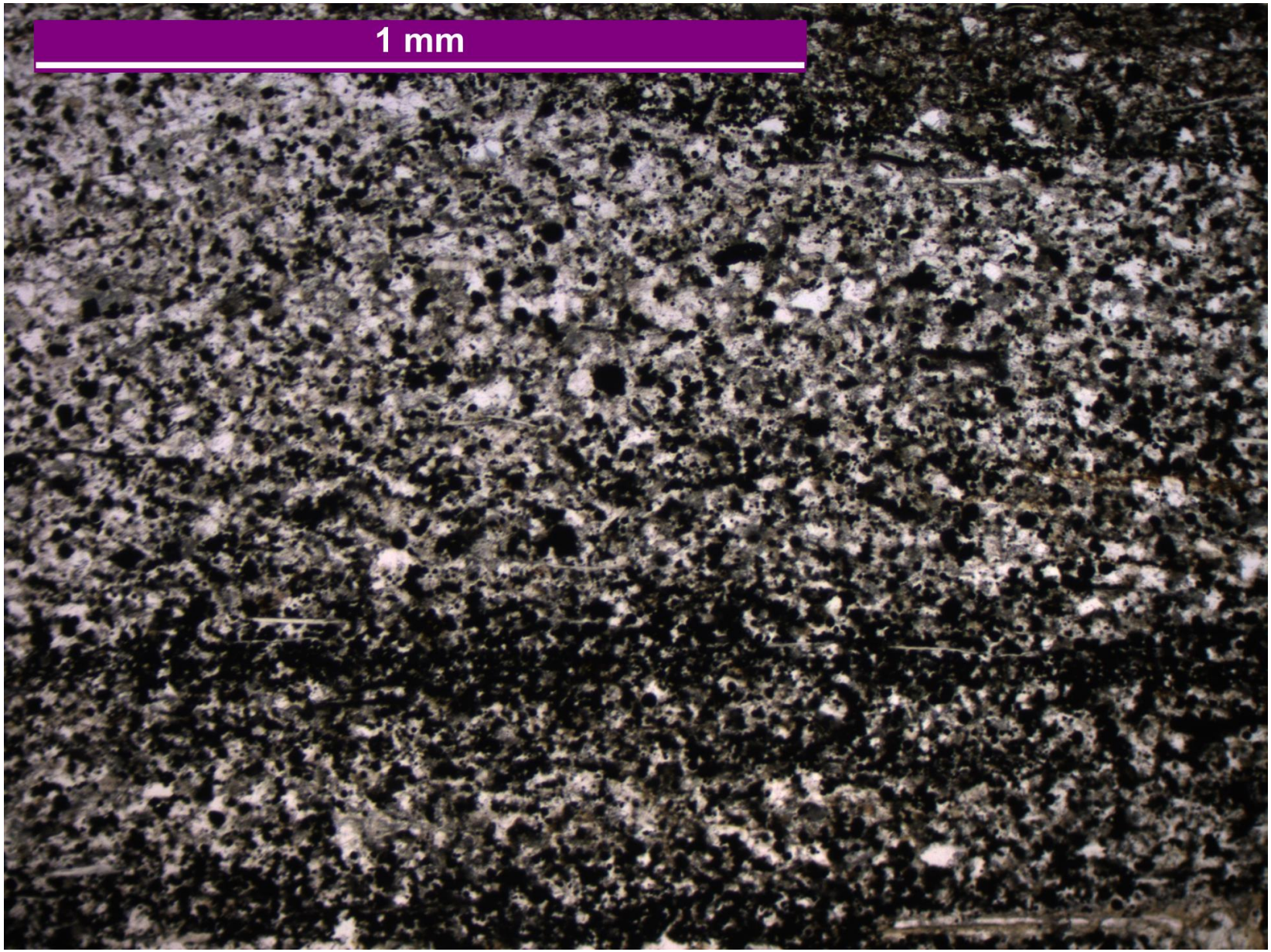

Figure 3.3. Photomicrograph of the large silty lens in the lower part of Lithofacies B, containing "lags" of pyrite framboids (small dark spots). From slide number LSB6.1s (see Chapter 2, Fig. 2.12).

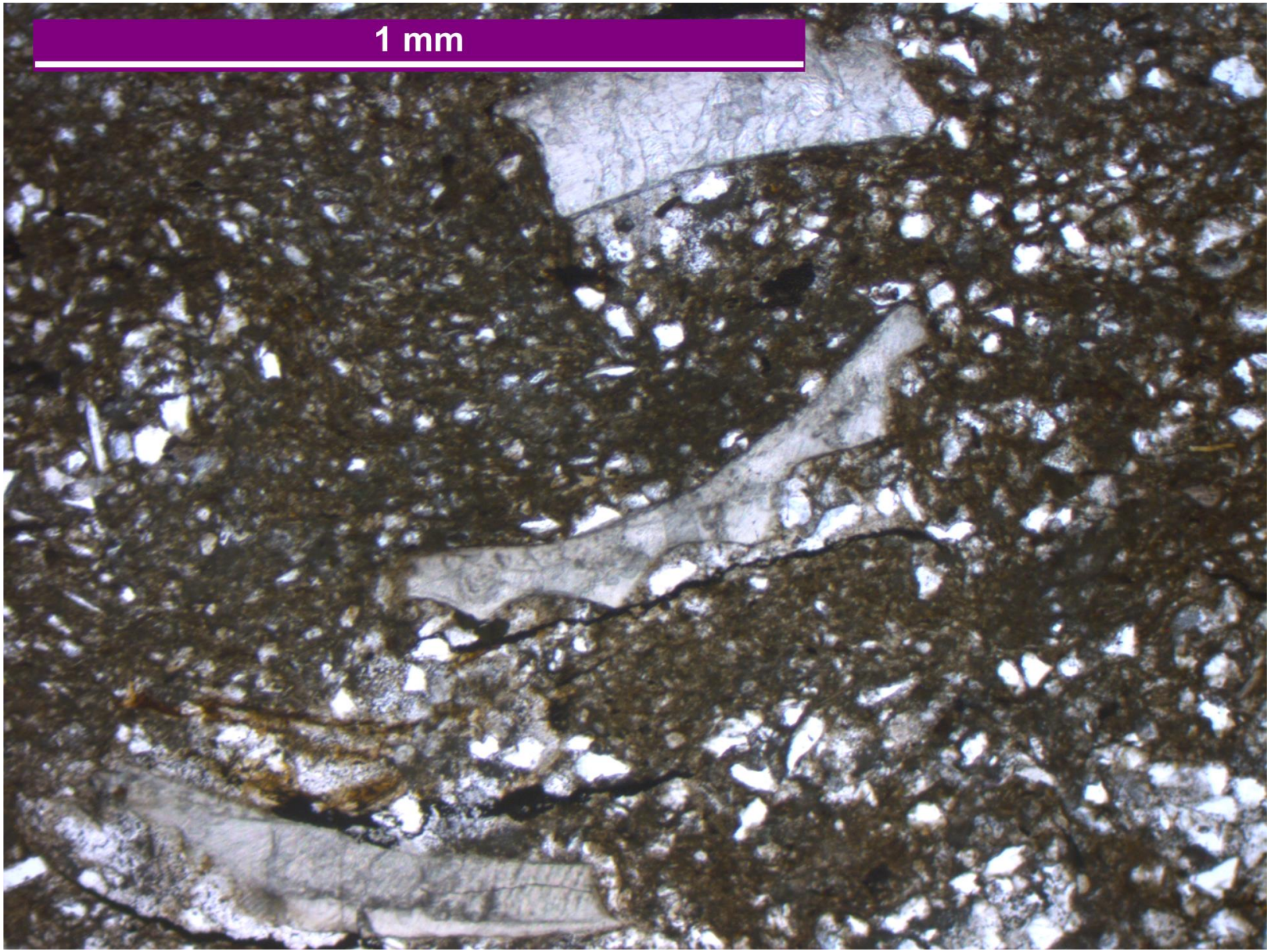

Figure 3.4. Photomicrograph of shell fragments included in the burrow fill of a *Rhizocorallium* trace from Lithofacies C. From slide number LSB5.0s (see Chapter 2, Fig. 2.12).

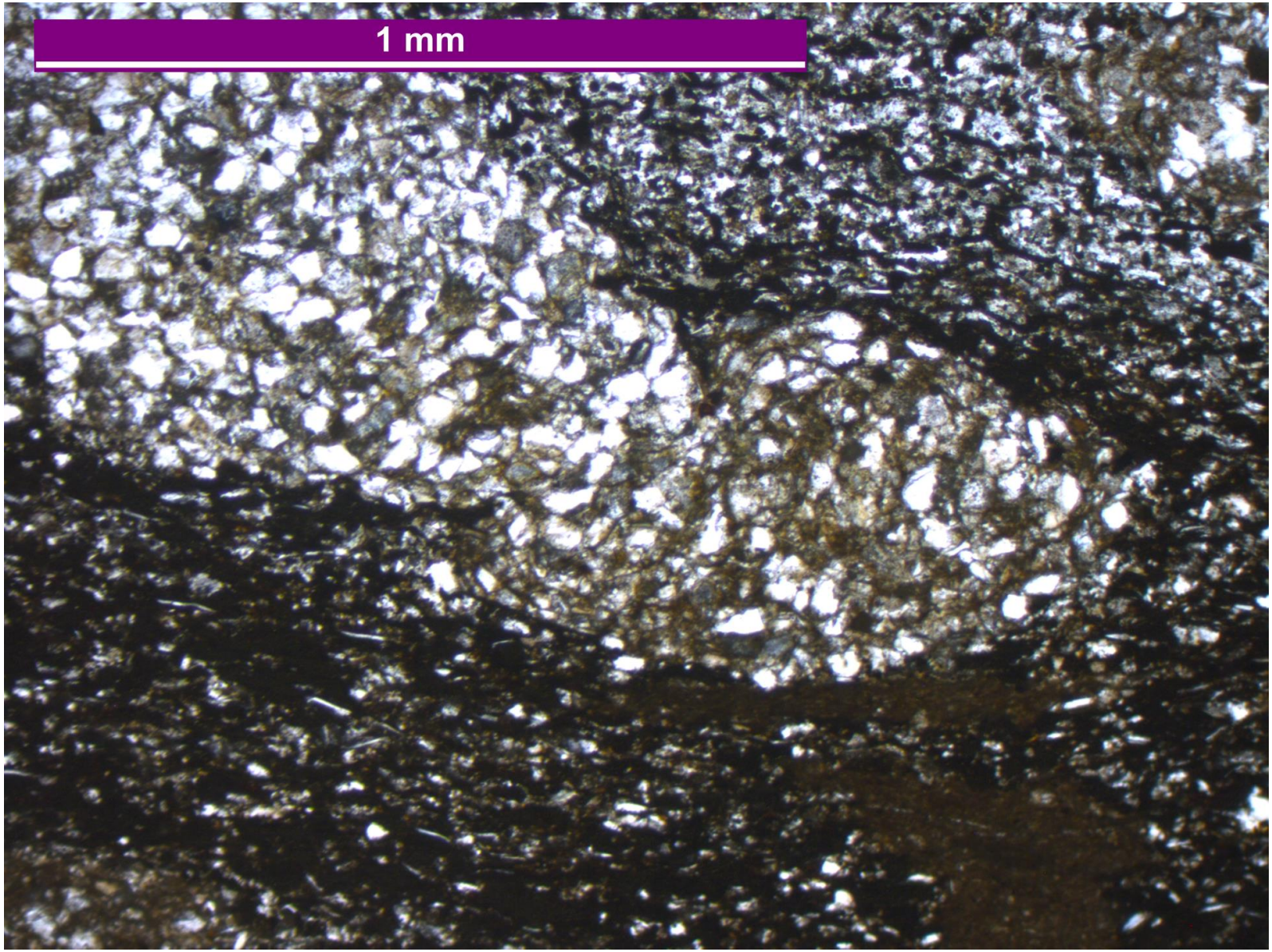

Figure 3.5. Photomicrograph of one *Chondrites* traces cutting across another, indicating the presence of at least two generations of burrowing. From slide number LSB5.0s (see Chapter 2, Fig. 2.12).

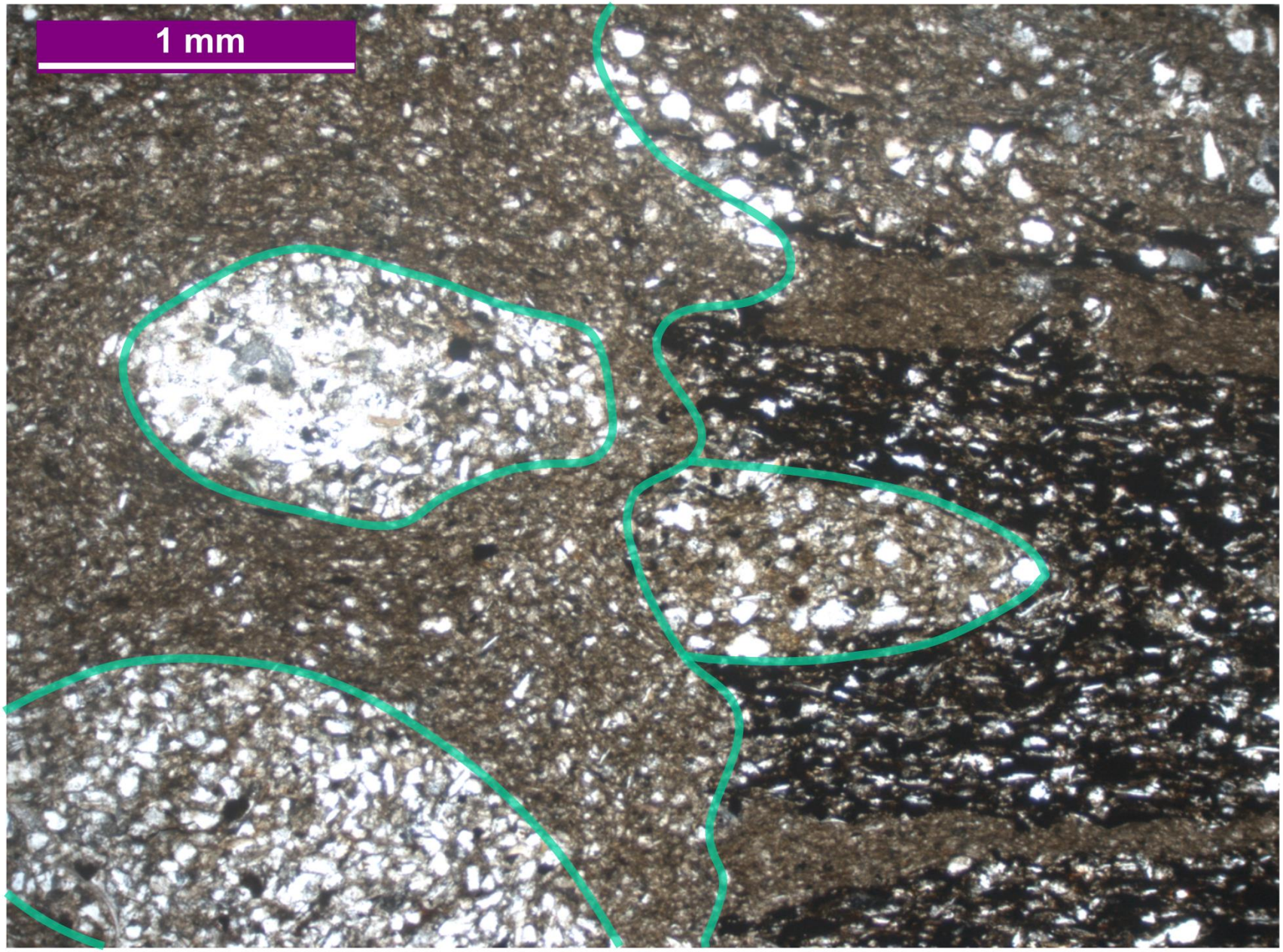

Figure 3.6. Photomicrographs of a *Rhizocorallium* burrow cutting across a *Chondrites* burrow, which is in turn, overprinted with a later generation of *Chondrites*. From slide number LSB5.0s (see Chapter 2, Fig. 2.12). Burrows are highlighted with the pistachio green lines.

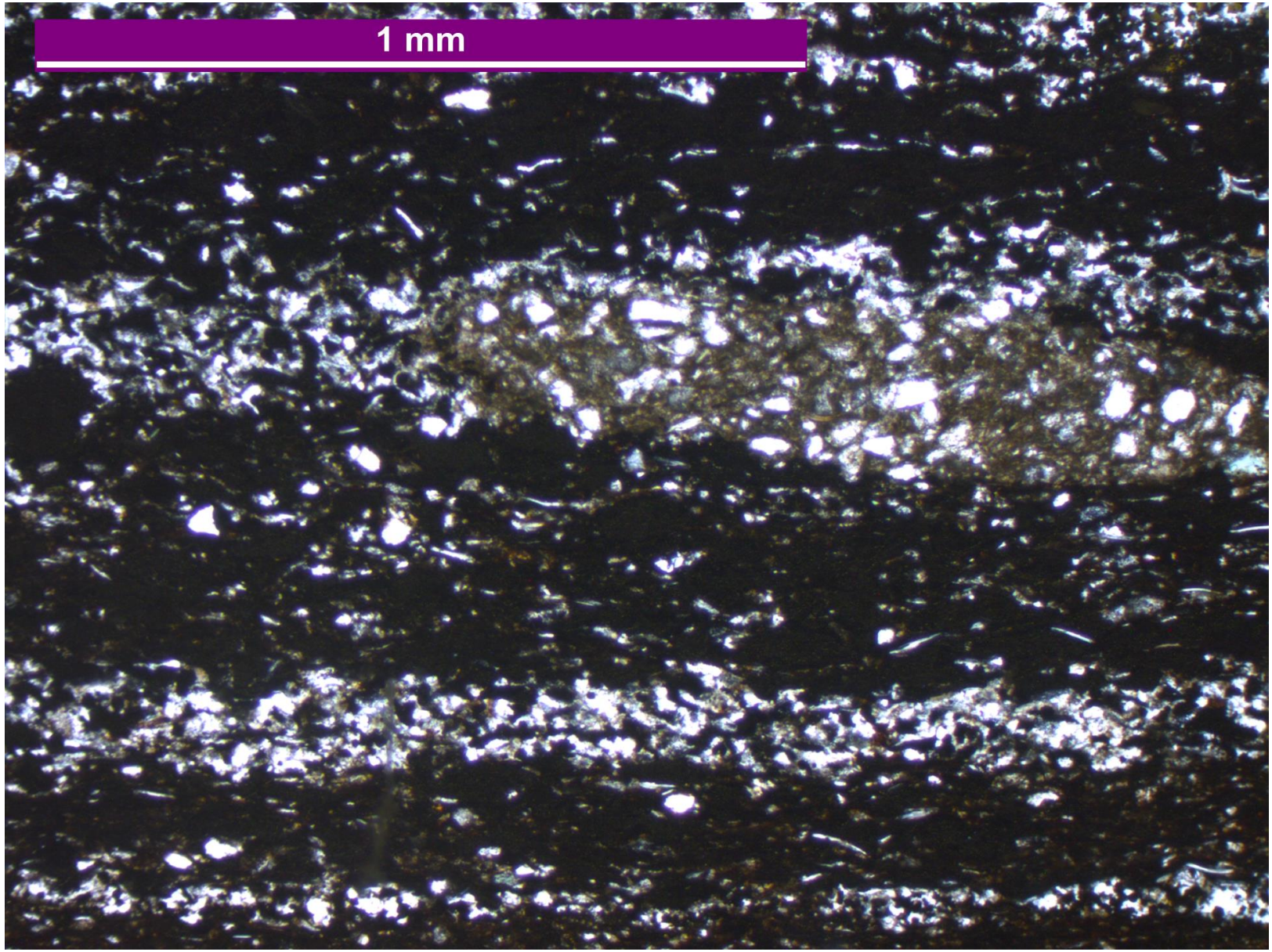

Figure 3.7. Photomicrograph of a *Chondrites* burrow in the lowest part of lithofacies C, enclosed by sediment composed of large blebs of organic matter (this point corresponds with the highest production index (PI; see section 2.6) value of the section – see Fig. 3.19). From slide number LSB5.0s (see Chapter 2, Fig. 2.12).

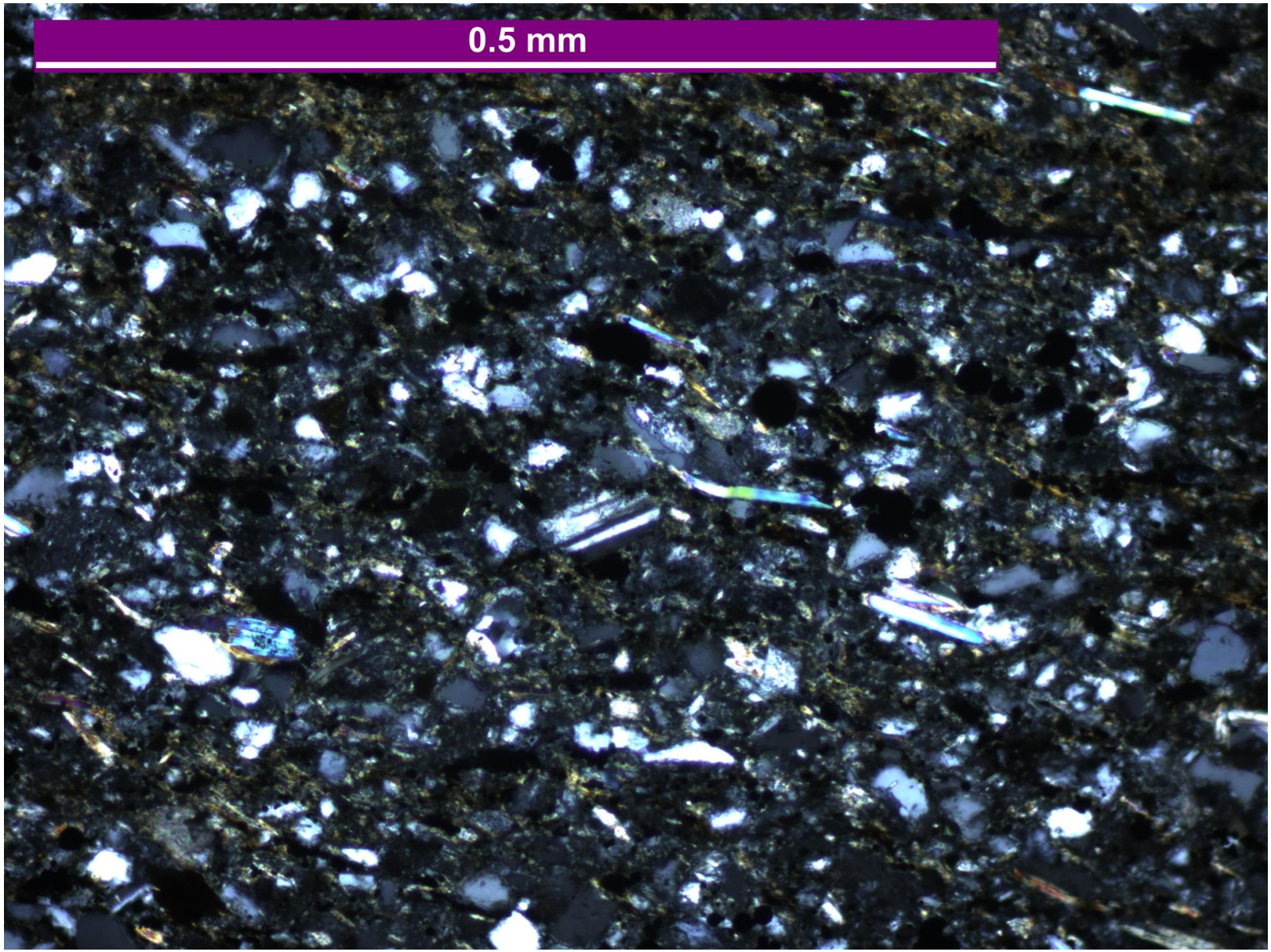

Figure 3.8. Photomicrograph of the mineralogy of a siliciclastic bleb from Lithofacies A, consisting mostly of quartz, with some minor plagioclase and mica (cross-polorised light). From slide number LSB6.0s (see Chapter 2, Fig. 2.12).

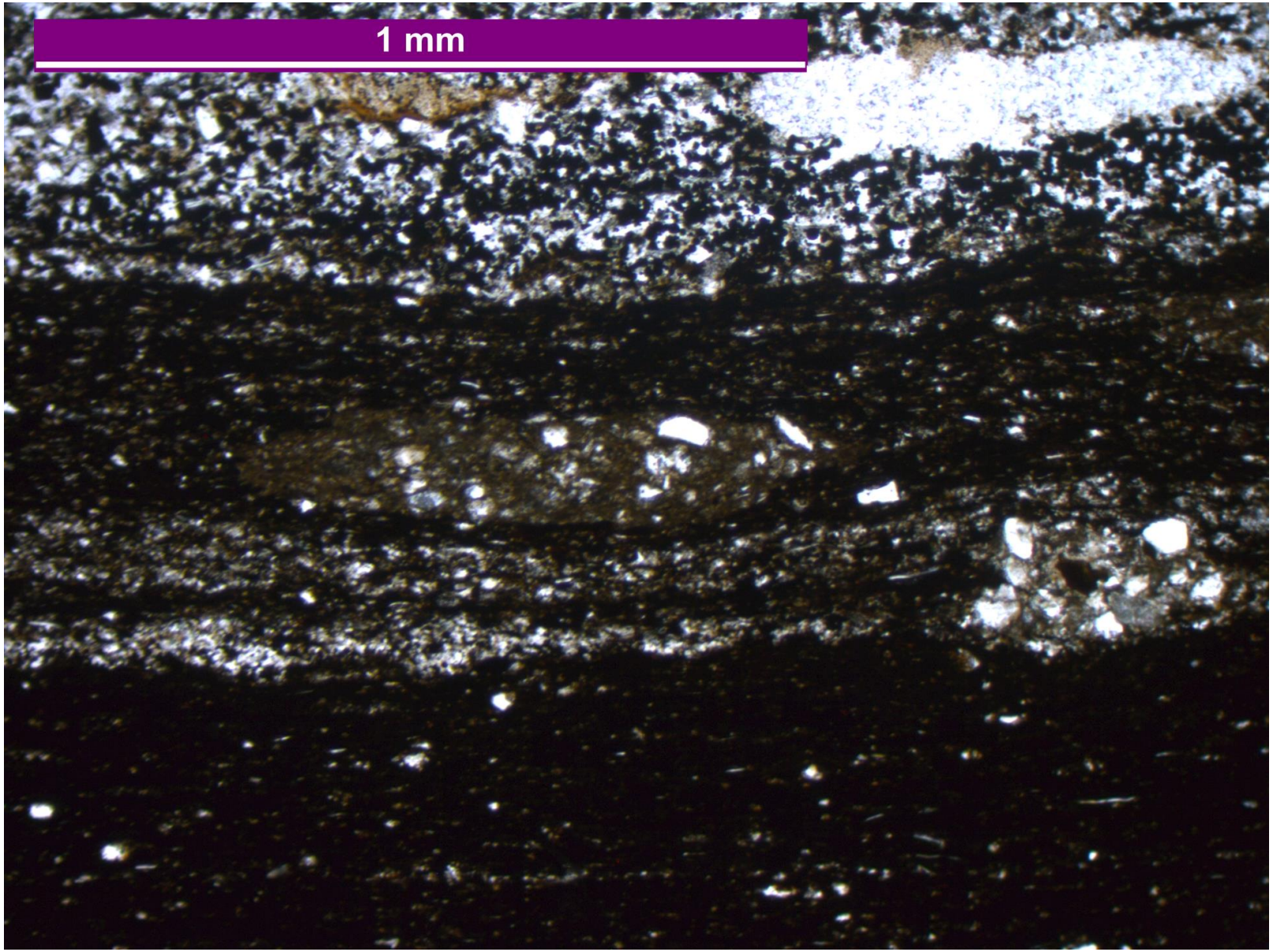

Figure 3.9. Photomicrograph of *Chondrites* penetrating both organic-rich sediment, and siliciclastic sediment (note the presence of organic matter in the former, and the lack of framboids in the latter). From slide number LSB5.0s (see Chapter 2, Fig. 2.12).

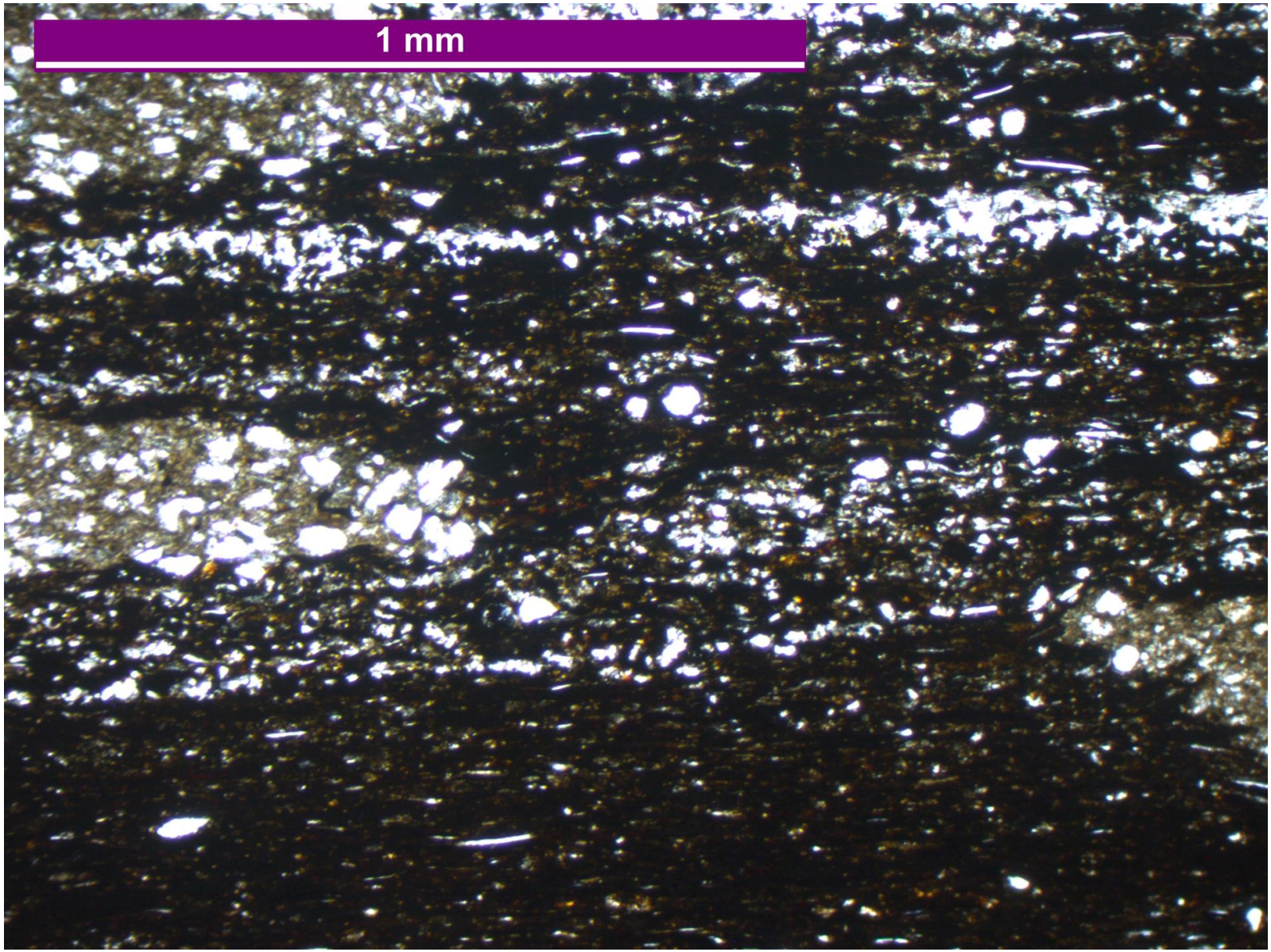

Figure 3.10. Photomicrograph of *Chondrites* burrows penetrating the organic-rich sediments of Lithofacies B – this is from near the top of the lithofacies, where some mm-scale siliciclastic laminae are preserved. From slide number LSB5.0s (see Chapter 2, Fig. 2.12).

At 52 mm, the complex sedimentary architecture of Lithofacies A abruptly gives way to the organic-rich, laminated, Lithofacies B. This interval extends from 52 mm to 94 mm and is devoid of primary bioturbation – the only traces present penetrate from the more intensely bioturbated Lithofacies C above (see 2.2). The lamination is a result of platy clay mineral and organic matter deposition, with no rhythmic lamination present. In thin section, the organic matter is visible as elongate, platy blebs 14.4 μm wide by 79.3 μm long (see Fig. 3.10), with minor (<5%) siliciclastic grains. At 60 mm, this Lithofacies is abruptly cut by a silty lens, with a sharp, erosional base. Like in the preceding Lithofacies, the thickness of this lens varies (from 13 mm in LSB1, to 18 mm in LSB6), but unlike its older counterparts, displays few, if any, organic-rich partings (no thicker than 0.68 mm when present). It also contains abundant pyrite framboids that sometimes form dense accumulations (composing up to ~50% of the sediment; see photomicrograph in Fig. 3.3) ~200 μm thick. In the uppermost 2 mm of this Lithofacies (as bioturbation intensity begins to recover), very thin (0.27 – 0.50 mm thick) silty laminae are visible (Fig. 3.2). They are continuous across both LSB1 and LSB5, and their thicknesses show very little lateral variability (although they are anastomosing). Between these thin laminae, the organic matter forms large (139 μm) anisotropic blebs in thin section (Fig. 3.7).

Lithofacies C extends from 94 mm to 145 mm and is characterised by its abundance of *Chondrites* traces (further discussed in 3.2). In between the traces, some primary depositional structures are present: the matrix remains organic-rich, with two further silty units observed at 103 mm (9.34 – 13.1 mm thick), and at 120 mm (4.98 – 5.31 mm thick). These contain frequent, very thin (less than 0.21 mm thick) organic-rich partings. Above 130 mm, the sheer intensity of bioturbation makes investigation of depositional features difficult, but some patches of organic-rich sediment are still visible, particularly in thin section.

2.2 Bioturbation and macrofossils

Trace fossils identified in the LSB (*Chrondrites*, *Rhizocorallium, Zoophycos and Planolites*) are either clearly visible as light silty patches against the dark rock matrix (Figs. 2.6; 3.5, 3.6; 3.9; 3.10), or discernable only by disruption of the sedimentary fabric. Table 3.1 shows the disgnostic criteria used to identify the various trace fossils, along with their distribution throughout Lithofacies A, B and C. The *Chondrites* traces are limited almost exclusively to the upper 5 cm of

Trace fossil	Diagnostic criteria	Distribution through LSB
Chondrites	A high density of thin, circular to semicircular burrows, that form a branching network in three dimensions	High density in Lithofacies C, with possible occurrences in Lithofacies A.
Rhizocorallium	A wide, equilibrichnia–style burrow, with a sharp turn (as opposed to the straight equilibrichnia–style burrow of *Diplocraterion.*	Frequent in Lithofacies C, penetrating down into Lithofacies B.
Zoophycos	An inclined burrow, with a layered internal texture. Forms a spiraling conical structure in three dimensions.	Rare occurrences restricted to Lithofacies A.
Planolites	An isolated thin, circular to semicircular burrow.	Rare occurrences restricted to Lithofacies A.

Table 3.1. Diagnostic criteria and distribution of trace fossils identified in the LSB.

the LSB and are the defining feature of Lithofacies C. *Rhizocorallium* penetrates further down the section than *Chondrites* (down to 84 mm; Fig. 3.16), but never reaches the abundance that *Chondrites* shows in the upper 5 cm (up to ~30.8%). The *Chondrites* burrows are on average 1.5 mm in diameter, with the *Rhizocorallium* burrows showing an average diameter of 8 mm. The *Chondrites* burrows are not circular in cross-section when viewed end-on, indicating that post-depositional compaction has taken place. The average horizontal width of the *Chondrites* burrows is 1.5 mm, and the average vertical width is 0.75 mm.

In the lower 60 mm of the sampled interval (i.e. the lower part of Lithofacies A), bioturbation of the sediment varies between 71% and 94% (Fig. 3.16). Occasional *Zoophycos*, isolated *Planolites*, and possible *Chondrites* are preserved within this interval. However, between 0 mm and 20 mm, total bioturbation intensity drops from 80% to around 10%. Bioturbation intensity continues to

Figure 3.11. A fossiliferous assemblage from the very top of Lithofacies C ca. 145 mm. Ribbed shell indicated by the white arrow is a small *Pseudopecten*.

Figure 3.12. A small external mould of *P. dubius* (10 mm in diameter), from 52 mm. This is near the top of Lithofacies A. The sediment here is characterised by a lack of bioturbation, and the preservation of HCS.

Figure 3.13. Three *P. dubius* fossils from Lithofacies A (-58 mm), with little compaction discernible.

Figure 3.14. Two belemnite rostra found at 145 mm (upper part of lithofacies C).

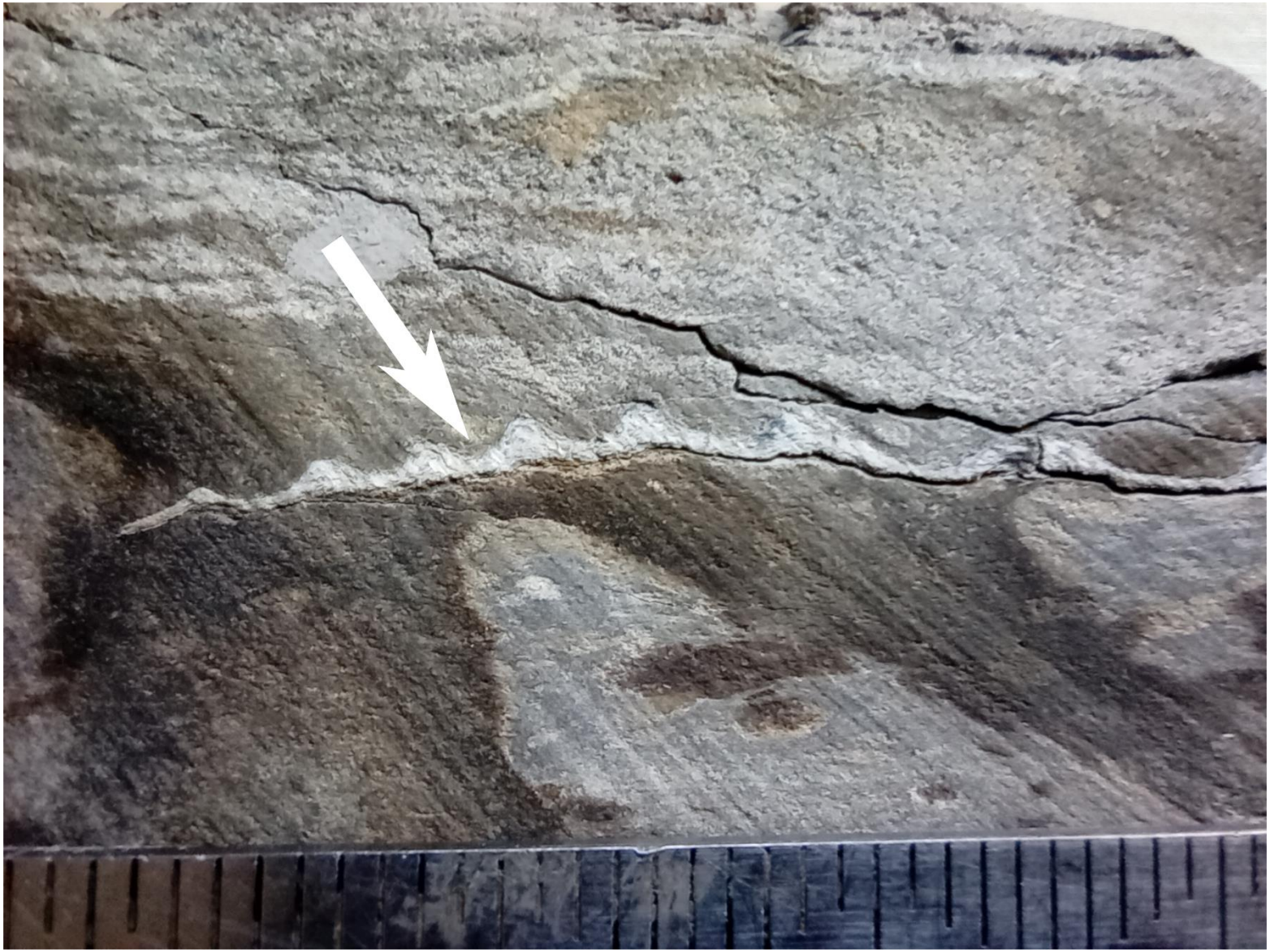

Figure 3.15. *Pseudopecten* sp. Shell fragment in lithofacies C. The shelly assebledge shown in Fig. 3.11 is just out of frame (at the top of the image).

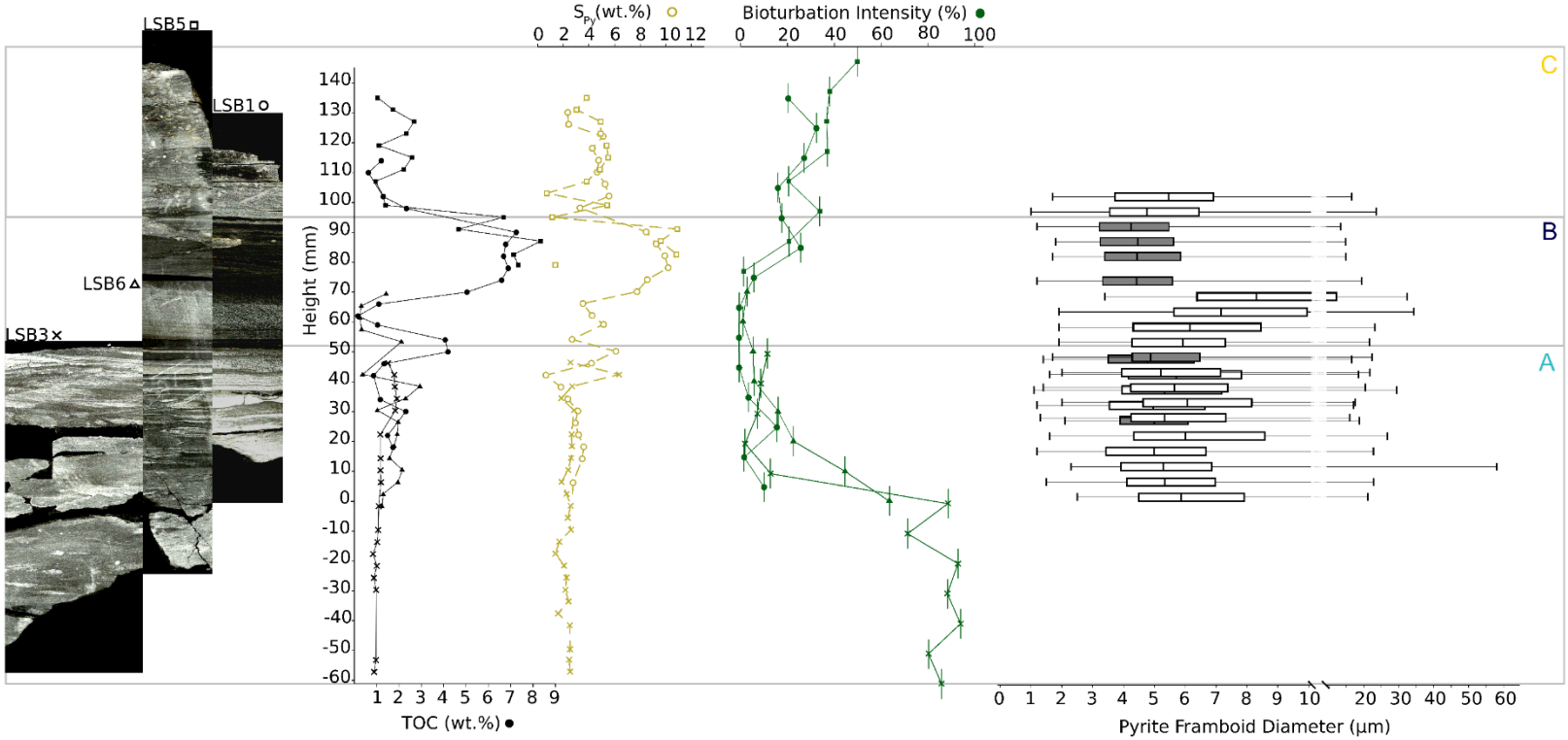

Figure 3.16. TOC, pyrite Sulphur (S_{py}; included in all plots but see 4.3), bioturbation intensity (by percentage cross-sectional area; see 2.1 & Fig. 3), and box-and-whisker plots of pyrite framboid diameters (arranged by stratigraphic height) of the LSB. A photomosaic of scanned photos of the LSB (enhanced contrast and with block codes) is also included. Circles indicate data taken from LSB1, crosses from LSB3, squares from LSB5, and triangles from LSB6. The vertical bars on the bioturbation plot indicate that the data point is an average over 10.0 mm. Dark boxes indicate pyrite framboid data that plot to the left of the euxinic/oxic-anoxic boundary in the Wilkins plot (Fig. 3.19). Lithofacies A, B and C are indicated by the large grey boxes, with colour-coded letters corresponding with the colours of the data points in Figs. 3.4, 3.8, 3.12, 3.21, 3.22, 3.23 and 3.25

gently decline, reaching a minimum of 0-3% at ~60 mm. Essentially all bioturbation in this interval is composed of *Rhizocorallium* traces. From ~65 mm to the top of the section (i.e. from the middle of Lithofacies B, through Lithofacies C), bioturbation intensity increases precipitously (at an average of 6% per cm), to a maximum of 50%. This is driven predominantly by *Chondrites*, although *Rhizocorallium* traces are present within this interval as well. Slight deviations from the upward trend are seen at 104 mm, and at 134 mm (both by ~20%). These decreases correspond with the two silty horizons. The occasional interpenetration of *Chondrites* traces (Fig. 3.5) indicates at least two generations of burrowing. *Chondrites* traces are also found penetrating *Rhizocorallium* traces (Fig. 3.6). Traces within this interval are generally light grey in colour, although some brown staining is visible in some of the burrows.

An isolated *Pseudomytiloides dubius* fossil, 1.0 cm in maximum shell length, was found at 52 mm (Fig. 3.12). Three other *P. dubius* fossils 1.2 cm, 1.1 cm and 0.4 cm in maximum shell length were also found at -58 mm (Fig. 3.13). No other macrofossils were found until 143 mm, where the fabric becomes dominated by shell fragments, and small *Pseudopecten* (Fig. 3.11). Two belemnite rostra (Fig. 3.14), and a large shell fragment (probably belonging to *Pseudopecten* sp.), were also found at this interval (Fig. 3.15).

2.3 Pyrite framboids

The most common pyrite framboids in the LSB are composed of uniformly sized microcrysts, closely packed into spherical aggregations, with rarer examples of less densely packed aggregations ("Type 1" and "Type 2" framboids of Wignall & Newton [1998], respectively; Fig. 3.17; proportions of each type were not measured). Occasionally, poly-framboids (usually aggregations of Type 1 framboids) are observed (e.g. Fig. 3.18, SEM photomicrograph 4).

Euhedral, non-framboidal pyrite crysts ~0.5-10 μm in diameter were also found, sometimes forming irregular, framboid-sized accumulations. The pyrite framboids are often composed of these euhedral microcrysts (Fig. 3.18, SEM photomicrograph 1). It is assumed that these framboids were diagenetically recrystallised, and their diameters are therefore not included in the plots. The silty intervals often contain large grains of heavy minerals, sometimes with euhedral form (see Fig. 3.18, SEM photomicrograph 2). Small (<10 μm) framboids and euhedral

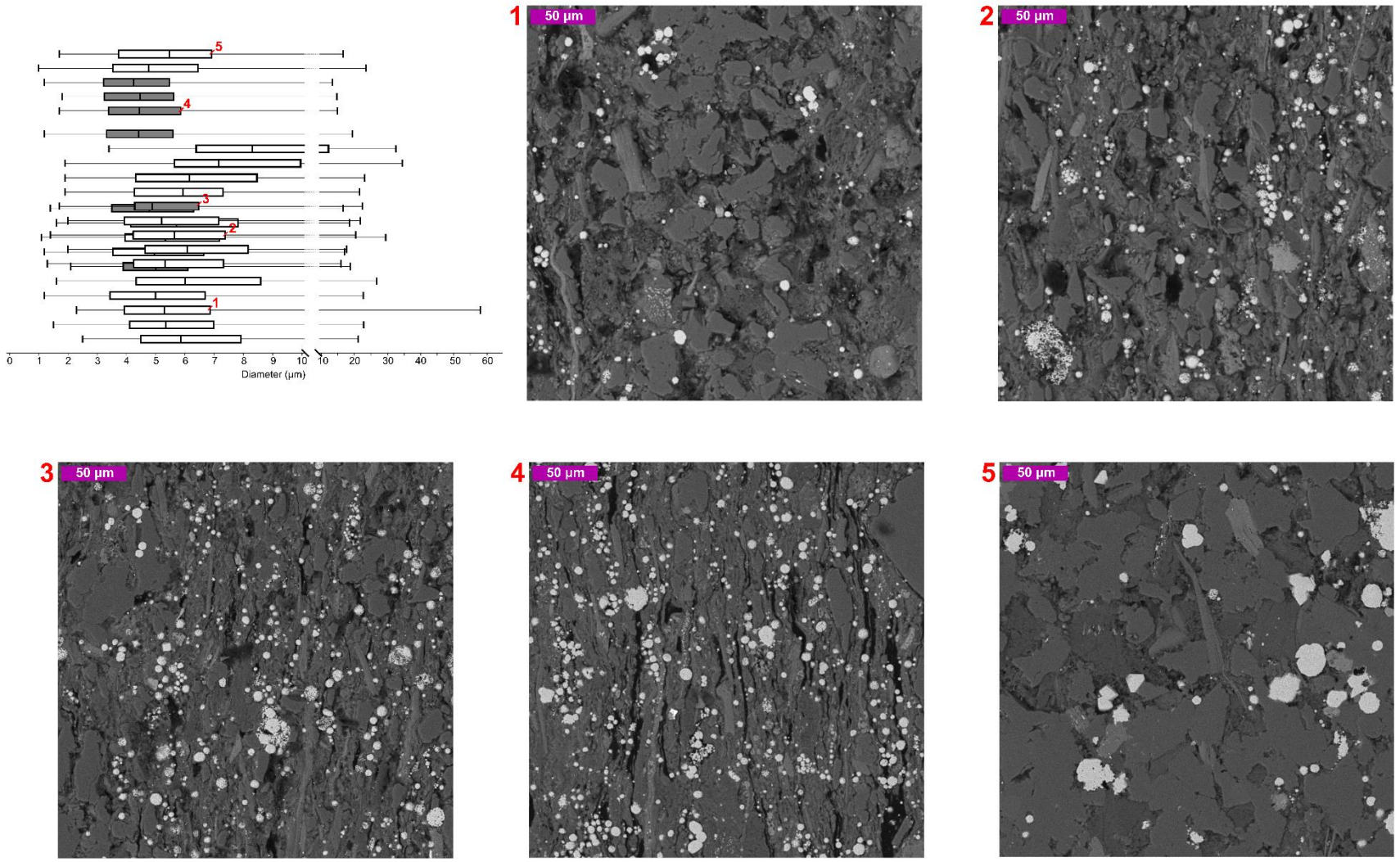

Figure 3.17. SEM photomicrographs of the LSB, with positions in the plot of pyrite framboid diameters from Fig. 3.16 indicated. Younging in all images is right to left. Photomicrograph 1 is stratigraphically lowest, and photomicrograph 5 is stratigraphically highest. Framboids and other heavy minerals are much brighter than the surrounding, less dense matrix. From slide numbers LSB6.0s, LSB6.1s and LSB5.0s (see Chapter 2, Fig. 2.12)

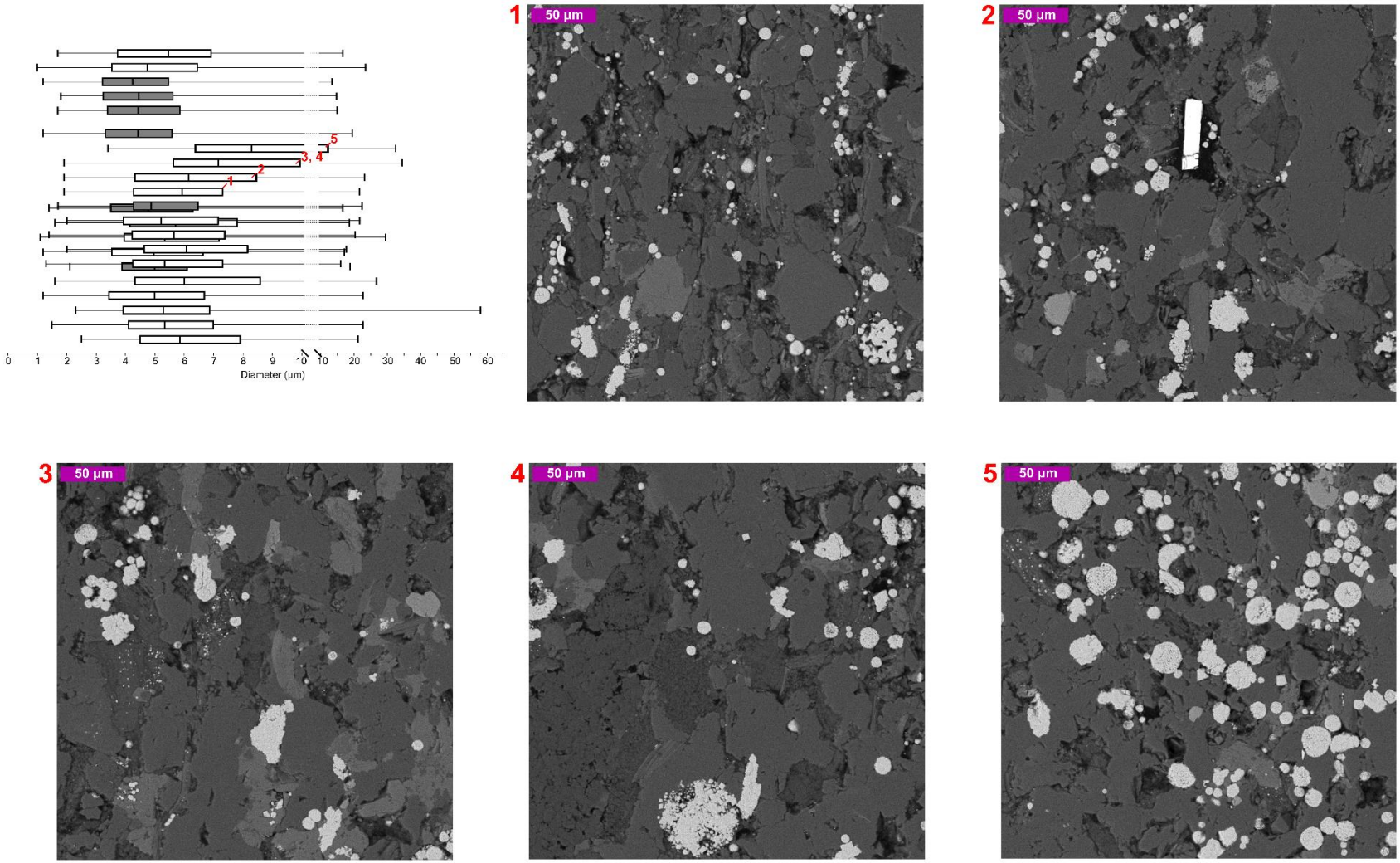

Figure 3.18. SEM photomicrographs from the large siliciclastic lens, with stratigraphic position indicated as in Fig. 3.17. Younging in all images is right to left. Photomicrograph 1 is stratigraphically lowest, and photomicrograph 5 is stratigraphically highest. From slide number LSB6.1s (see Chapter 2, Fig. 2.12)

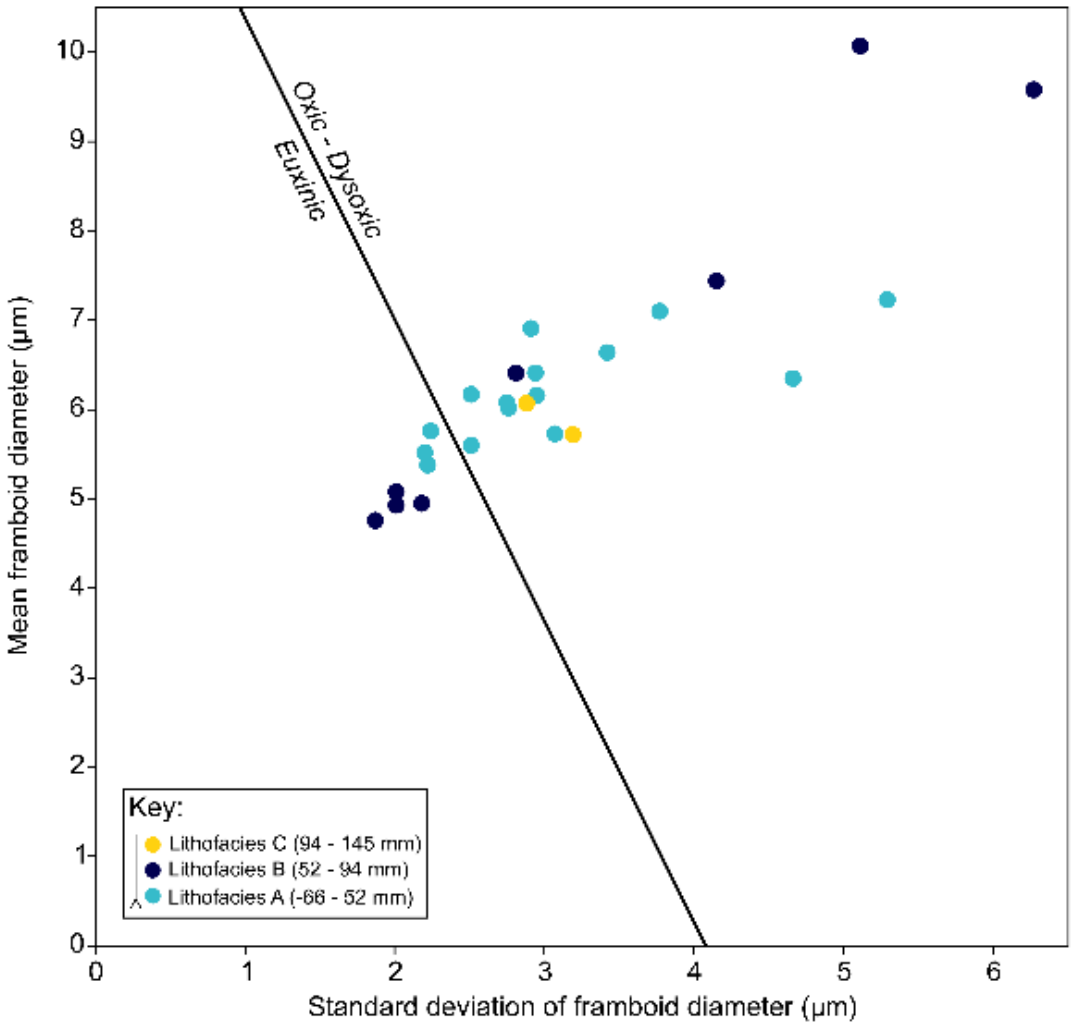

Figure 3.19. Wilkins plot comparing the mean and standard deviation of framboid diameters through the LSB. The regression line (after Wilkin *et al.*, 1996) separates conditions characterised by the growth of pyrite framboids in the sediment (on the right), and in a sulphidic water column (on the left).

microcrysts sometimes occur in lags and irregular accumulations of a variety of sizes especially in the lower part of the silty lens at 62 mm (Fig. 3.3). No siderite rhombs overgrowing pyrite framboids are found in the LSB – this contrasts with evidence of such overgrowth in the LSB from Kettleness, 14.7 km to the NW of Hawsker Bottoms (Newton, 2001). In the lower, intensely bioturbated part of Lithofacies A, pyrite framboids are infrequent, and show a wide

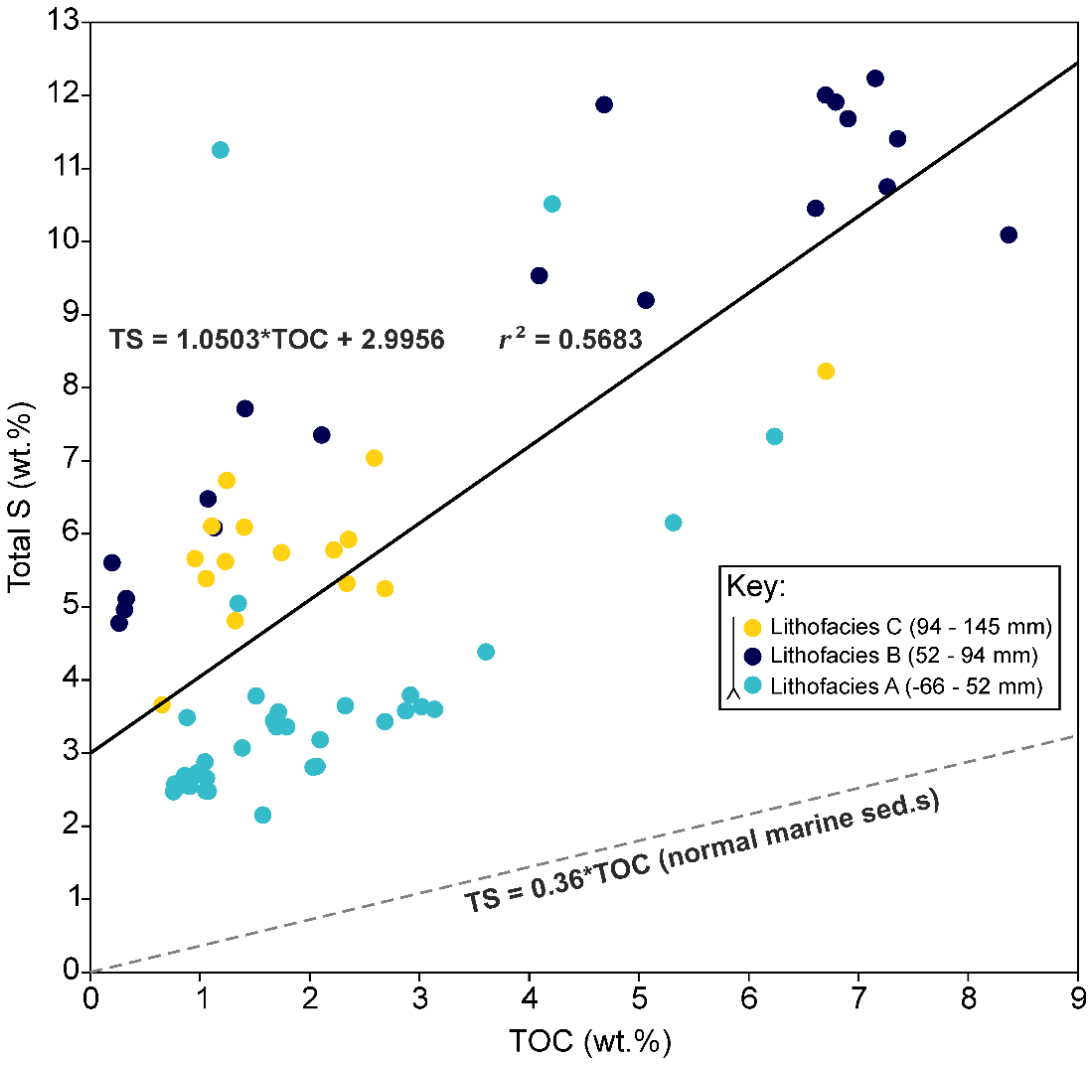

Figure 3.20. Cross-plot of TOC and TS, with least-squares regression line displayed (and corresponding R^2). Normal marine regression line is taken from Berner (1984).

range of sizes (median 5.29 – 5.86 μm). In the upper part of Lithofacies A (characterised by HCS and silty units) the distribution of pyrite framboid diameters varies more widely, with the median size ranging from 4.79 – 6.10 μm (Fig. 3.16). Three samples from this interval plot in the euxinic field of the Wilkins plot (Fig. 3.19) – these are within the thin, organic-rich partings between the HCS and silty lenses (the latter showing comparatively higher median and maximum framboid diameters). The 13 – 18 mm wide silty lens at the base of Lithofacies B shows a coarsening-upward trend in pyrite framboid diameters (Figs. 3.16 and

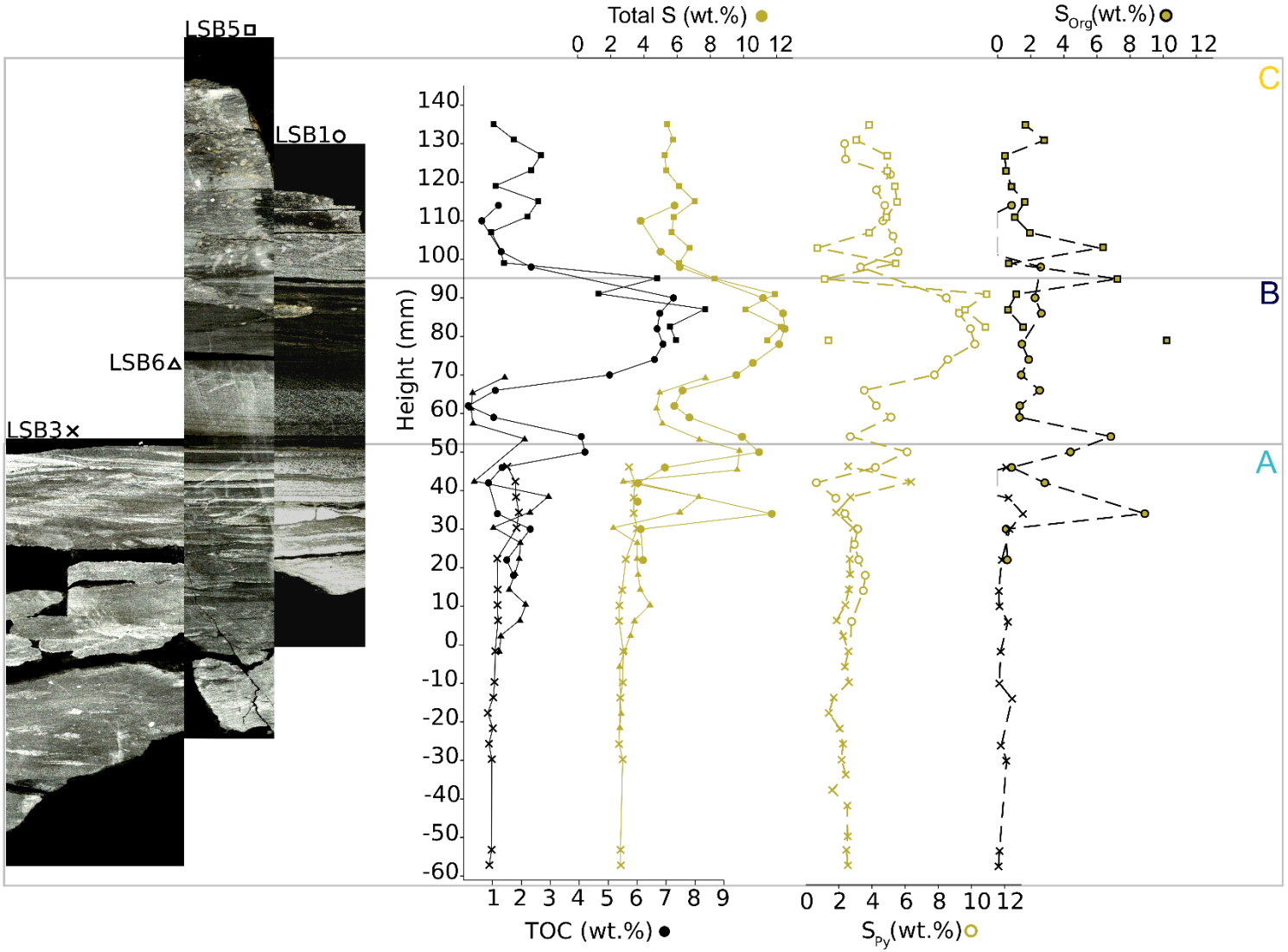

Figure 3.21. S_{py} and organic-matter hosted sulphur S_{org} of the LSB, with TOC and total S included. S_{org} is defined as the difference between Total S and S_{py} (but see 4.3 for a critique of this method).

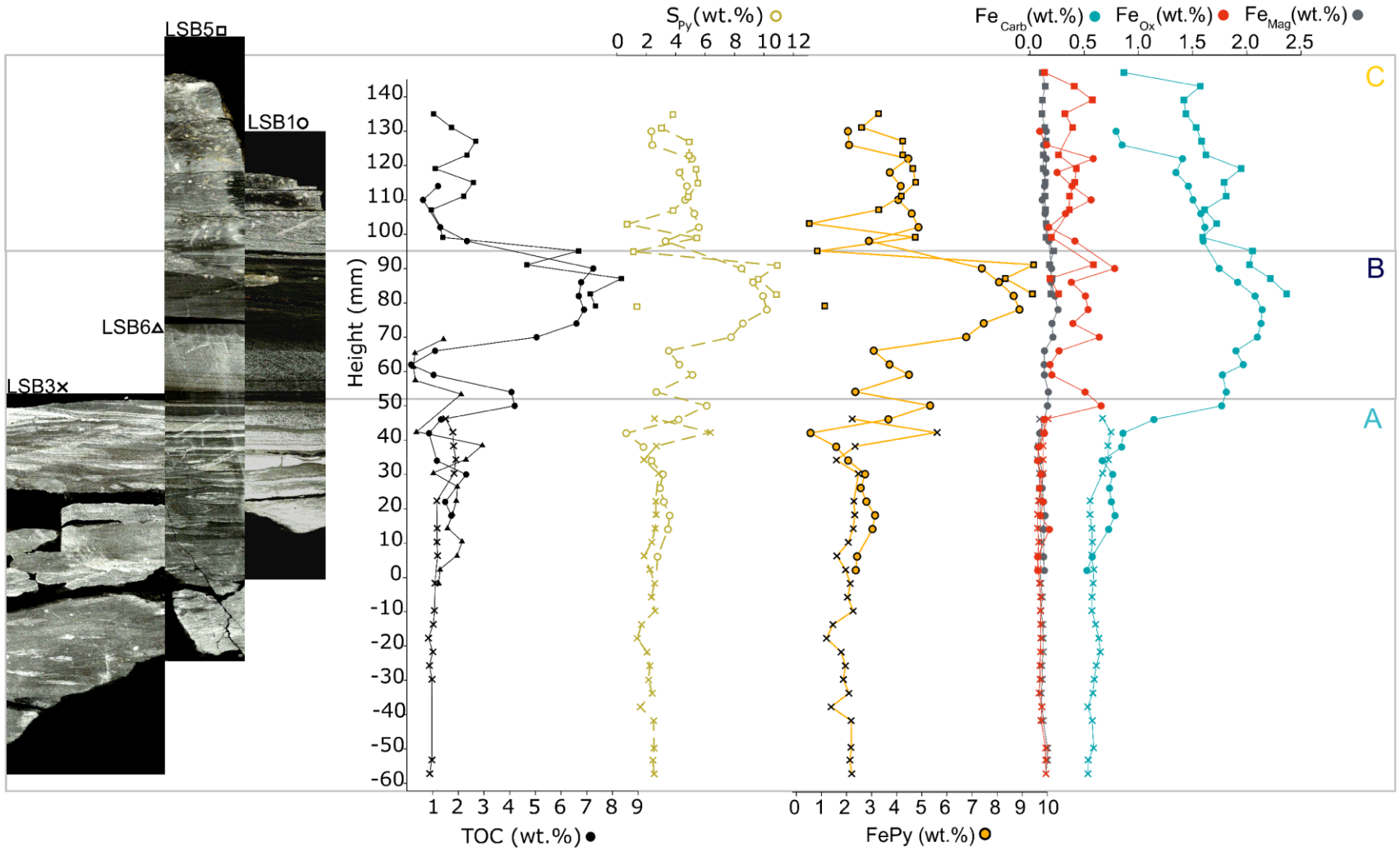

Figure 3.22. Fe_{Py}, Fe_{Carb}, Fe_{Ox}, and Fe_{Mag} of the LSB. These operationally defined reactive Fe pools roughly correspond with Fe-carbonate phases, Fe (oxyhydr)oxides, and magnetite, respectively (see Chapter 1, section 9.1.4).

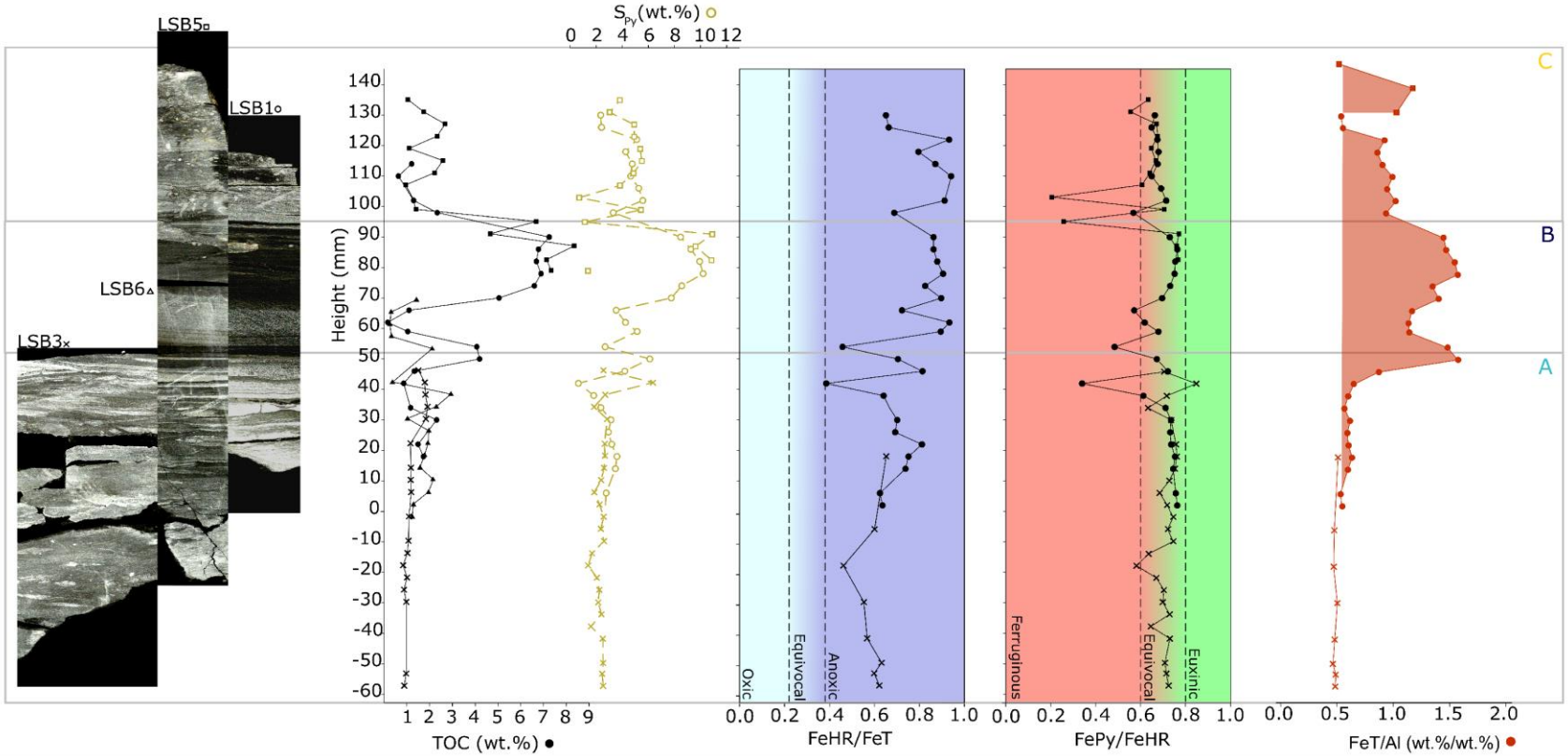

Figure 3.23. Fe_{HR}/Fe_T , Fe_{Py}/Fe_{HR} and Fe_T/Al of the LSB. Recall that Fe_{HR}/Fe_T is the proportion of sedimentray Fe that is highly reactive towards sulphide (Chapter 1, section 9.1.4), and Fe_{Py}/Fe_{HR} is the proportion of this Fe that is in pyrite. Thresholds for the Oxic-Equivocal-Anoxic, and Ferruginous-Equivocal-Anoxic fields of Anderson & Raiswell (2004), Poulton & Canfield (2011) and Poulton (2021), indicated with dashed vertical lines, and background colour. Shaded areas indicate enrichment relative to the standard shale value of Wedepohl (1971; 2004).

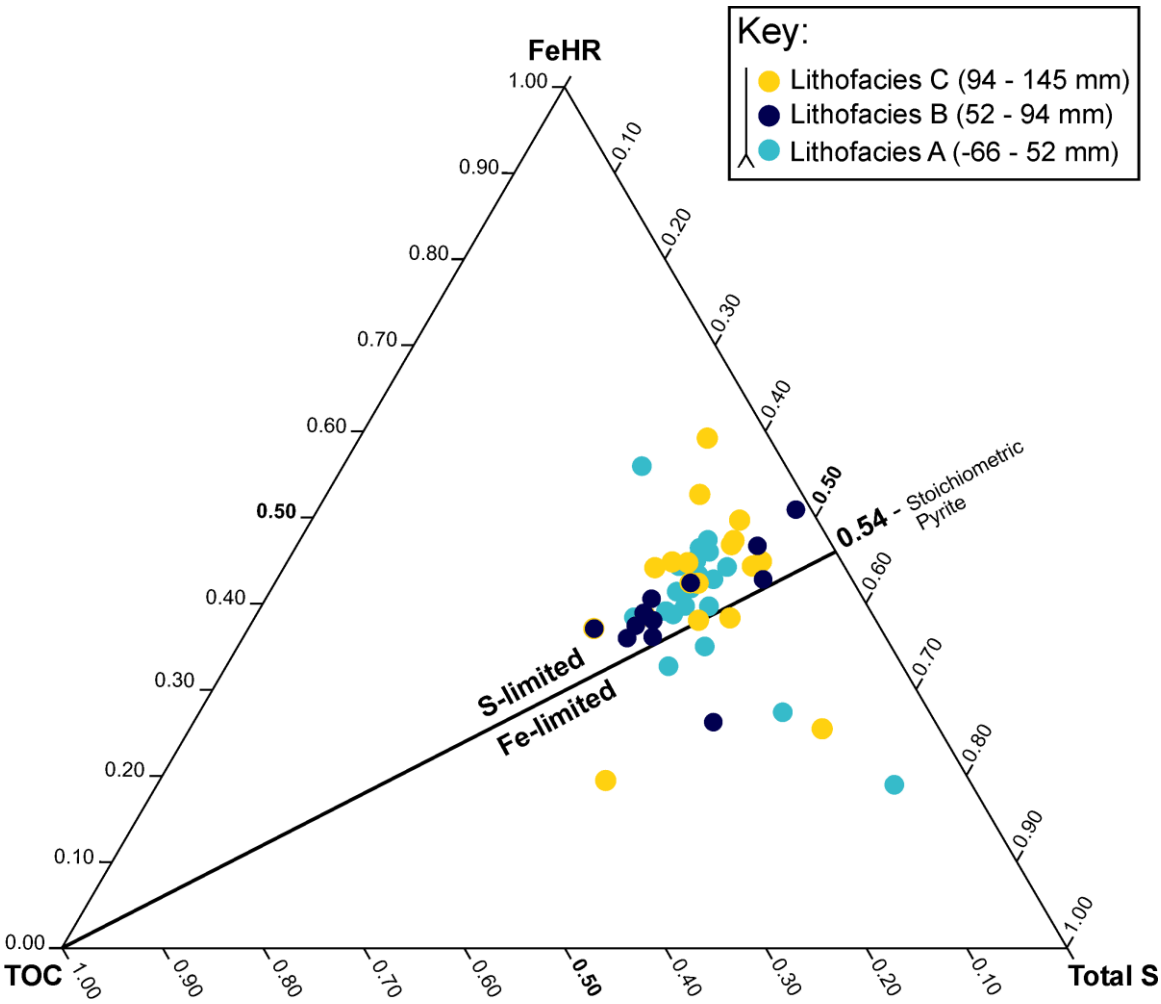

Figure 3.24. Ternary plot comparing TOC, TS and Fe_{HR} for the LSB, with the regression line for stoichiometric pyrite indicated. Note that in the S-limited zone, S is assumed to be derived from sulphate reduction in anoxic sediments (see text).

3.18), with the median diameter increasing from 5.95 µm at the base, to 8.34 µm at the top. The 1st and 3rd quartiles of framboid width also increase through this interval from 4.27 µm to 6.38 µm, and from 7.30 µm to 12.1 µm, respectively (i.e. the interquartile range of framboid diameters increase from 3.03 µm to 5.73 µm). At 73 mm, the median framboid diameter sharply drops to ~4 µm, and remains relativity constant for the rest of Lithofacies B. All four samples that record this trend plot in the euxinic field of the Wilkins plot (Fig. 3.19). In the lower part of Lithofacies C, the median framboid diameter begins to increase, up to 5.56 µm at 102 mm (Fig. 3.16).

2.4 Sulphur-iron systematics

Total S (TS, as determined by combustion) mostly varies as a function of TOC, excepting slight lateral heterogeneity in the upper part of Lithofacies A, and a smoother excursion in the upper part of Lithofacies B (Fig. 3.16).

The S_{py} trend broadly tracks both TOC and TS. S_{py} remains at a background level of 2.62 wt.% up to 42.0 mm, where it reaches 6.33 wt.%. S_{py} then varies between 0.65 – 6.33 wt.% until 70.0 mm, where it increases to 7.77 wt.%, giving a "stepped" appearance to the S_{py} profile (Fig. 3.21). After reaching a maximum of 10.7 wt.% at 91.0 mm – in Lithofacies B – S_{py} abruptly drops at 94.0 mm (the upper boundary of Lithofacies B), varying between 0.64 – 5.41 wt.% for the rest of the section.

Organic-matter hosted Sulphur (S_{org}) can be defined as the difference between Total S and S_{py} (Tribovillard *et al.*, 2019; but see 4.3). For most of the LSB, S_{org} values are constant, and at background level (around 0.34 wt.%; Fig. 3.21). However, significant deviations from this trend occur between 30-60 mm, and again between 90-110 mm. In both intervals, a bimodal peak in S_{org} occurs, reaching a maximum value of 8.88 wt.% at 34 mm, and 7.15 wt.% at 94 mm. The first of these intervals of S_{org} enrichment occurs in the upper part of Lithofacies A, where HCS is present and undisturbed by bioturbation, and where TOC ranges between 0.881 – 6.71 wt.%. The second of the S_{org} enrichment intervals occurs at the base of Lithofacies C, where TOC abruptly drops from 7.35 wt.% to 1.52 wt.%, and *Chondrites* traces start to become more predominant.

Below 42 mm, all reactive Fe pools show stable, relatively low values (Fe_{Carb} 0.61 wt.%, Fe_{Ox} 0.11 wt.%, and Fe_{Mag} 0.11 wt.%; Fig. 3.22), with no significant changes in enrichment. At 50 mm, Fe_{Carb} shows a sharp increase to 1.77 wt.%, before gradually increasing to a maximum of 2.37 wt.% at 82.5 mm (in Lithofacies B). Fe_{Carb} remains > 1.40 wt.% until 122 mm (in Lithofacies C), where it begins to decline. The height and magnitude of this decline varies between different blocks of the LSB, with Fe_{Carb} declining by 0.56 wt.% at 126.0 mm (LSB1), and by 0.70 wt.% at 147 mm (LSB5). In addition to the sharp enrichment in Fe_{Carb} at 50.0 mm, the Fe_{Ox} baseline is elevated from 0.11 wt.% to 0.09 – 0.78 wt.% at this point. This higher baseline of Fe_{Ox} is maintained for the rest of the section. Fe_{Mag} is never significantly enriched above the initial background value. Fe_{Py} is derived from S_{py} by a stoichiometric calculation, and therefore follows the same trend, but with all values multiplied by a factor of ~0.87.

The Fe_{HR}/Fe_T profile varies between 0.39 – 0.94 for the entire section (Fig. 3.23). There is a gentle upward trend in the data from 0.46 at -18 mm, to a maximum of 0.94 at 110 mm, but only one data point (LSB1.9 at 42 mm) plots near the equivocal field. In addition, Fe_{Py}/Fe_{HR} varies between 0.58 – 0.77 for most of the section, reaching 0.77 in the interval of maximum Fe_{Py}. However, between 38 – 59 mm, and 94 – 107 mm, the Fe_{Py}/Fe_{HR} value varies more widely (between 0.21 – 0.84), and distinctly lower than the baseline value for the section.

The trend for Fe_T/Al sharply increases at 50 mm, tripling from a background value of ~0.59 wt.%/wt.% to 1.57 wt.%/wt.% (Fig. 3.23). Fe_T/Al then stays relatively constant through Lithofacies B, excepting a small decrease of 0.33 wt.%/wt.% coeval with the large silty lens. After a drop of 0.45 wt.%/wt.% at 94 mm, values vary between 0.53 – 1.17 wt.%/wt.% for the rest of the section.

Pyrite formation in the LSB was predominantly S-limited, with most of the data plotting above the compositional Fe-S ratio of stoichiometric pyrite (Fig. 3.24). The points plotting below this line roughly correspond with the interval of Fe limitation in the upper part of Lithofacies A.

2.5 Major and trace elements

Aluminium content does not show extreme variation through the LSB (Fig. 3.25), with values ranging between 5.67 – 10.8 wt.%. The only prominent increase is found between 62 – 74 mm, coeval with a large silty lens in the lower part of Lithofacies B. The same trend is reflected in Ti, and I therefore consider Al-snormalisation of element contents valid for this section.

Major and trace element profiles tend to follow one of three patterns – either elevated levels in pyrite-rich intervals (As, Cd, Co, Cu, Fe, Mo, Zn), or background levels outside of the silty lenses - where they show either depletion (Cr, K, Rb, V) or enrichment (Ba, Ca; Figs. 3.26 – 3.29). Mn/Al is also enriched within the LSB and shows a smooth increase from background values of 34.0 ppm/wt.% (starting at 14 mm), up to a maximum of 137 ppm/wt.% at 64 mm (within the silty lens; Fig. 3.14). The trend then gradually decreases to 79.7 ppm/wt.% at 98 mm, before briefly increasing again (to 114 ppm/wt.% at 110 mm), and then decreasing at the top of the section to 42.1 ppm/wt.%. In addition, Ni/Al is enriched to a strangely high degree, reaching a

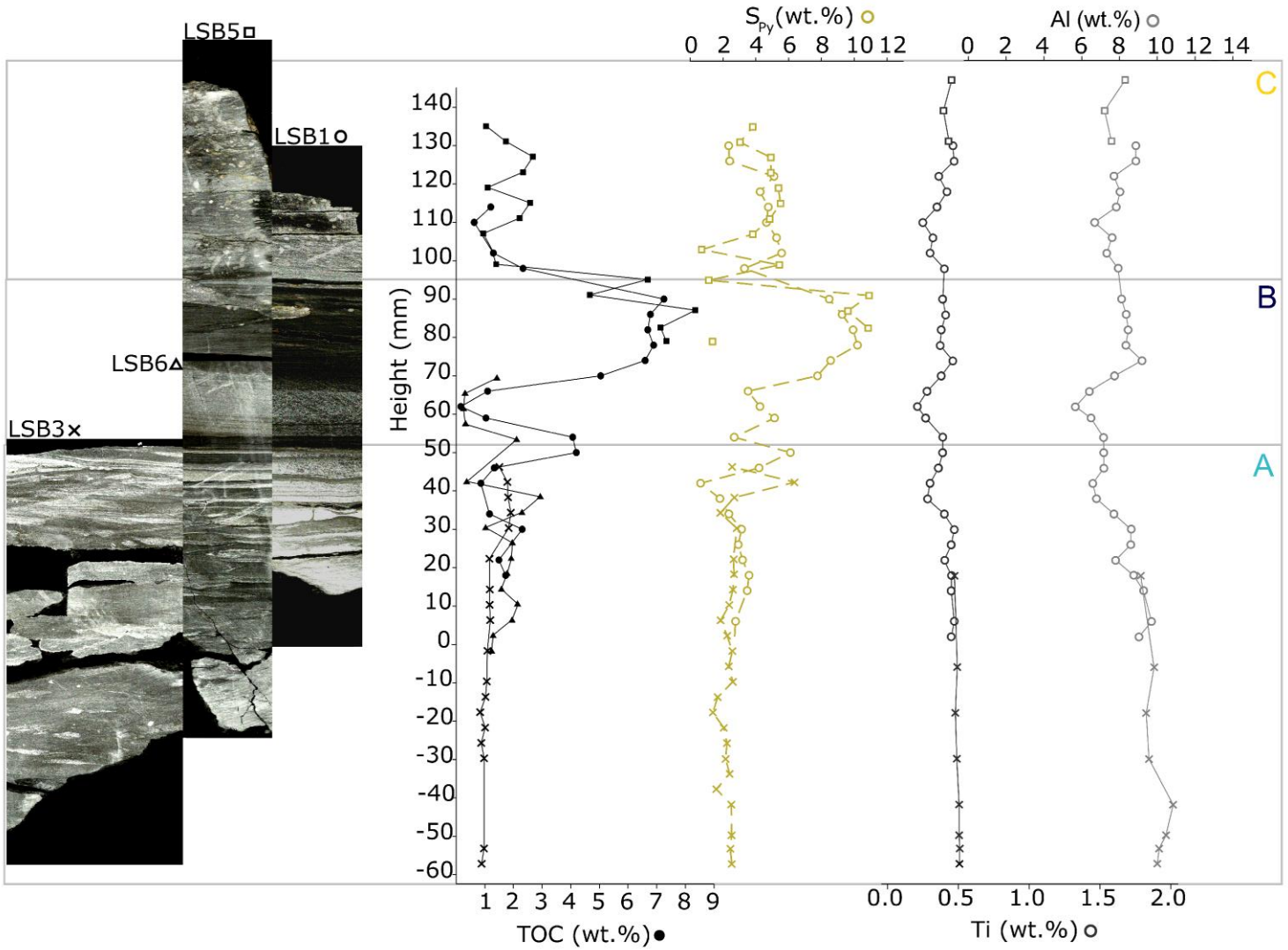

Figure 3.25. Plot of Ti (wt.%) and Al (wt.%) for the LSB. Note that neither shows enrichment relative to the standard shale values of Wedepohl (1971; 2004). Given the reletivley muted variability of Al, I decided to use its concentration as a normalization factor.

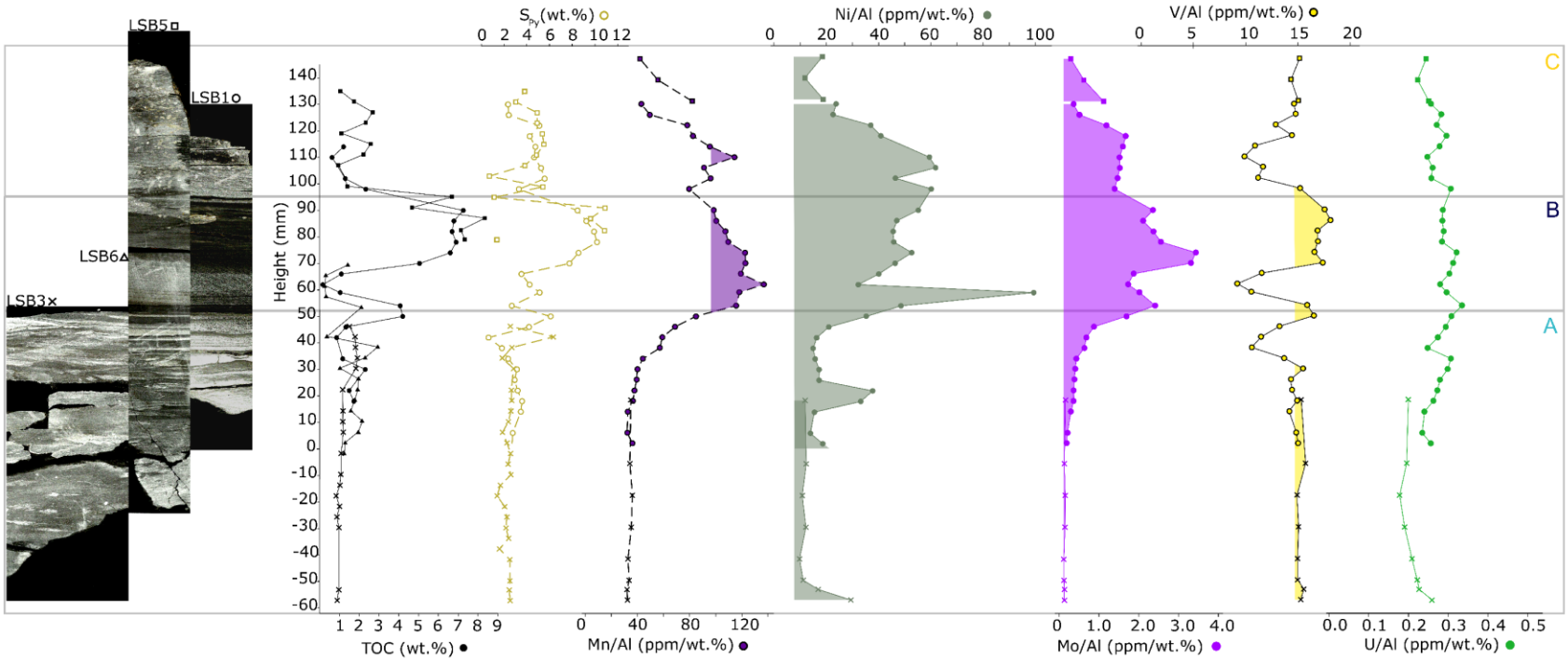

Figure 3.26. Plot of Mn/Al, Ni/Al, Mo/Al, V/Al and U/Al for the LSB (all in ppm/wt.%). As in Fig.3.23, shaded areas indicate enrichment relative to the standard shale value of Wedepohl (1971; 2004).

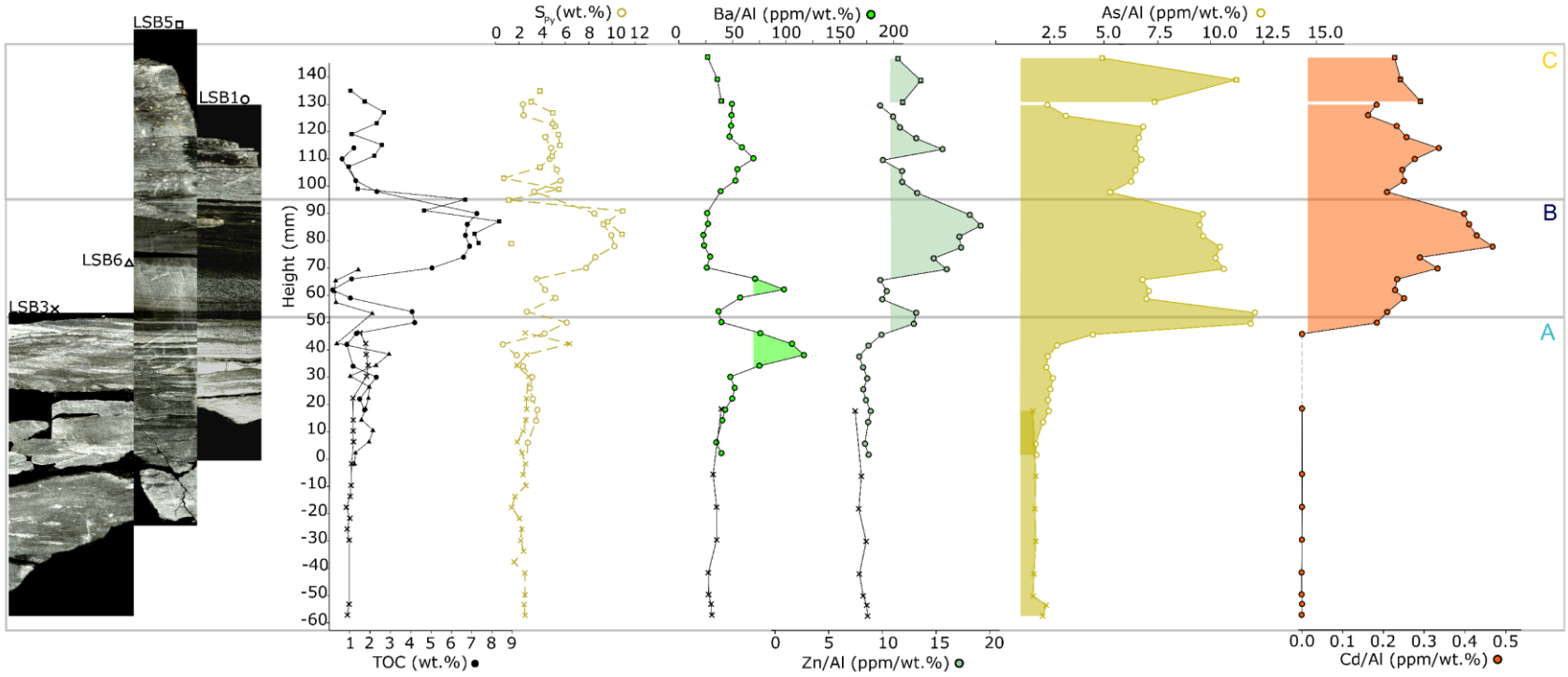

Figure 3.27. Plot of Ba/Al, Zn/Al, As/Al and Cd/Al for the LSB (all in ppm/wt.%). Dotted grey line indicates values are below the detection limit. As in Fig.3.23, shaded areas indicate enrichment relative to the standard shale value of Wedepohl (1971; 2004).

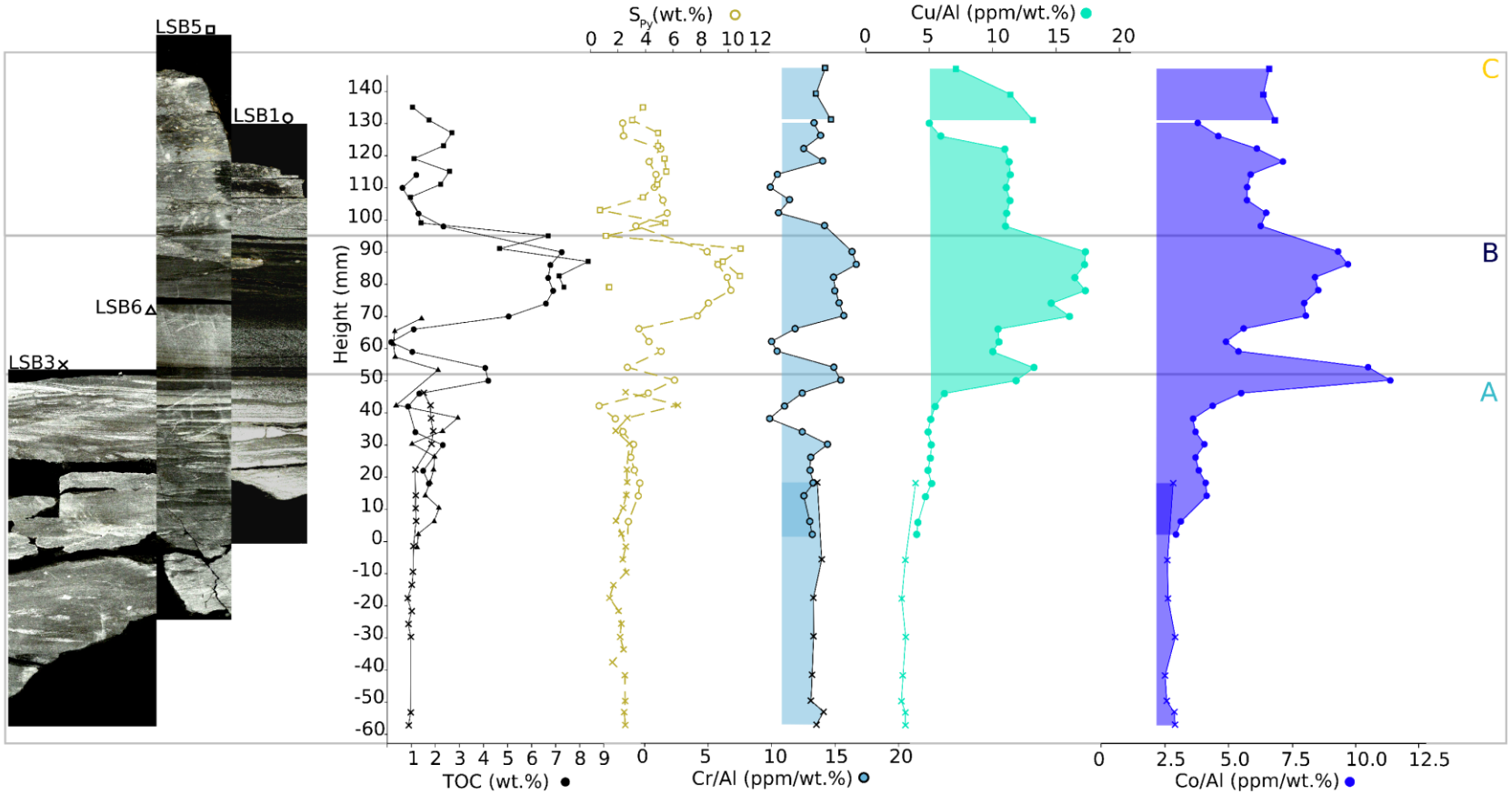

Figure 3.28. Plot of Cr/Al, Cu/Aland Co/Al for the LSB (all in ppm/wt.%). As in Fig.3.23, shaded areas indicate enrichment relative to the standard shale value of Wedepohl (1971; 2004).

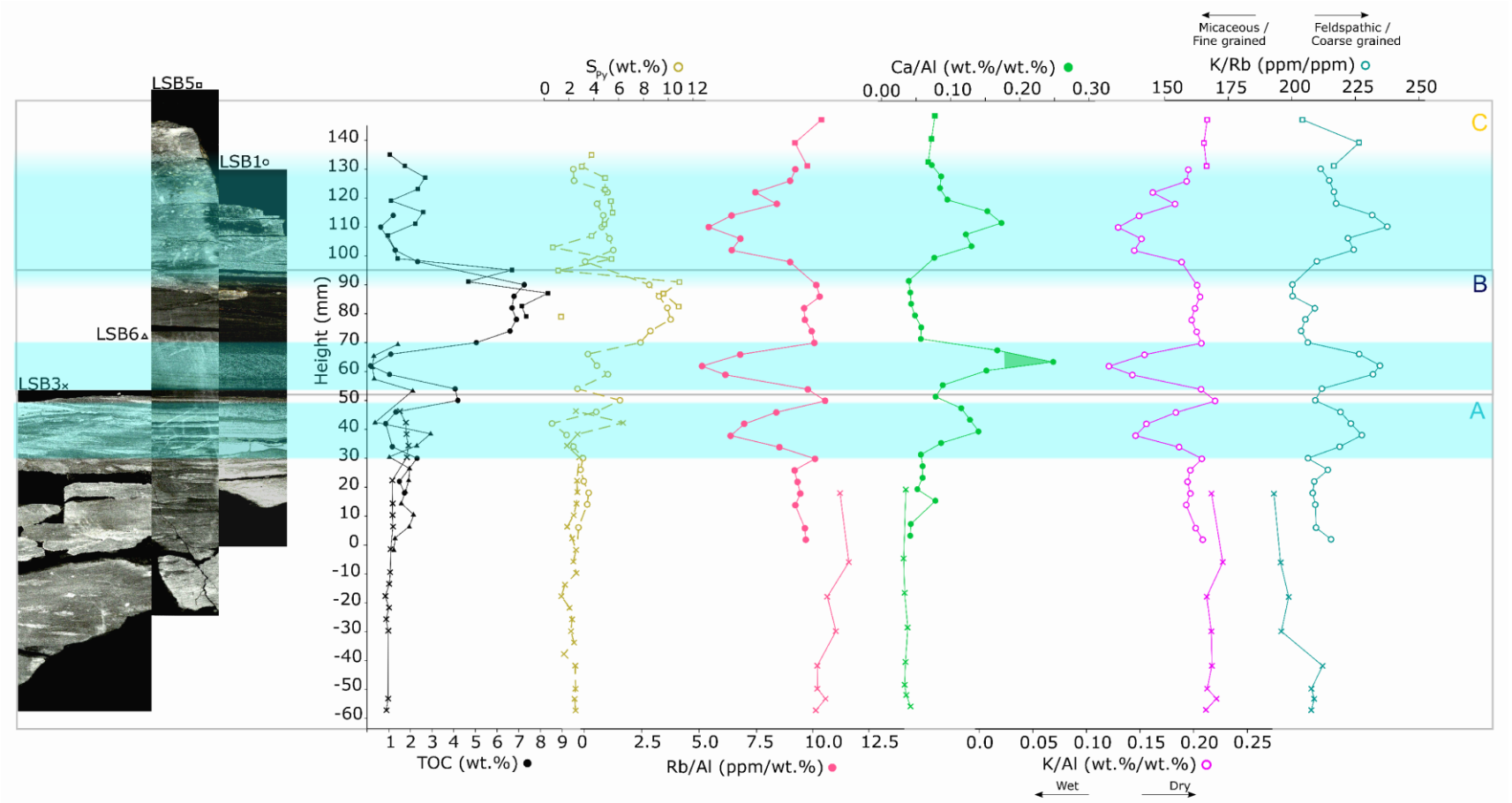

Figure 3.29. Plot of Rb/Al (ppm/wt.%), Ca/Al (wt.%/wt.%), K/Al (wt.%/wt.%) and K/Rb (ppm/ppm) for the LSB. Inferred humid "pulses" are indicated by blue shading, along with interpretations of the K/Al and K/Rb traces. Note that Ca does not indicate a greater occurrence of carbonates in this section, since TIC is low for the entire LSB (see section 2.6 and data in Appendix 2).

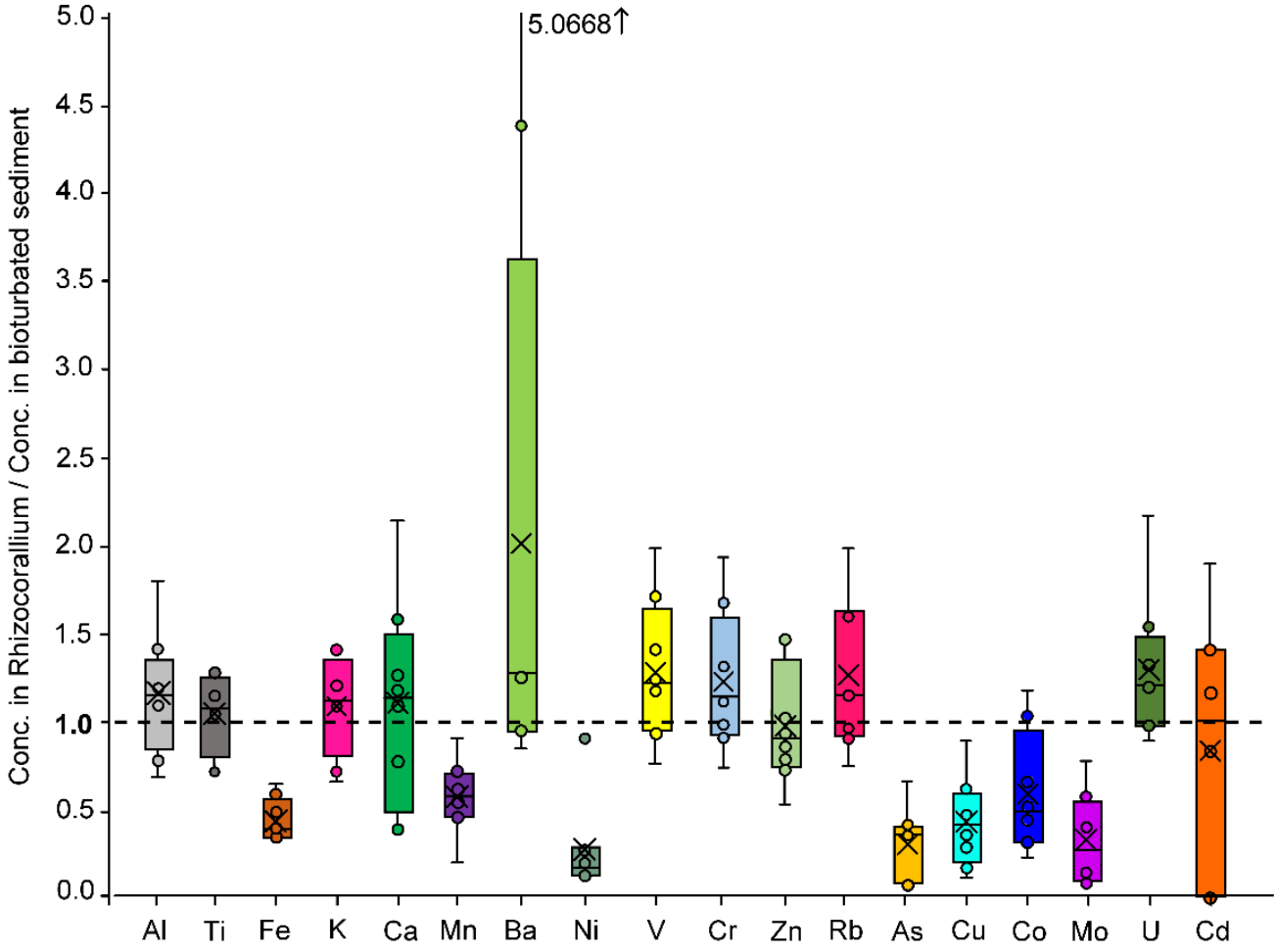

Figure 3.30. Box and whisker plots of the concentration of selected elements in the *Rhizocorallium* burrows, relative to the concentration in the TOC-rich, unbioturbated sediment of Lithofacies B. Crosses represent the mean for each element, and circles data points. The value of 1.0 is indicated, i.e., points below the line indicate depletion, and points above indicate enrichment. Note that the fourth quartile for Ba is off the chart (also the case in Fig. 3.31), and so it is indicated in text.

maximum of 99.5 ppm/wt.% at 59 mm, but also never falling below 22.4 ppm/wt.% between 50 – 130 mm (Fig. 3.26). Mo/Al gradually increases from a background value of 0.14 ppm/wt.%, from 2 mm to 74 mm, where it reaches a maximum of 3.43 ppm/wt.% (excepting a small negative inflection in the silty lens) it then gradually declines to 0.29 ppm/wt.% at the top of the

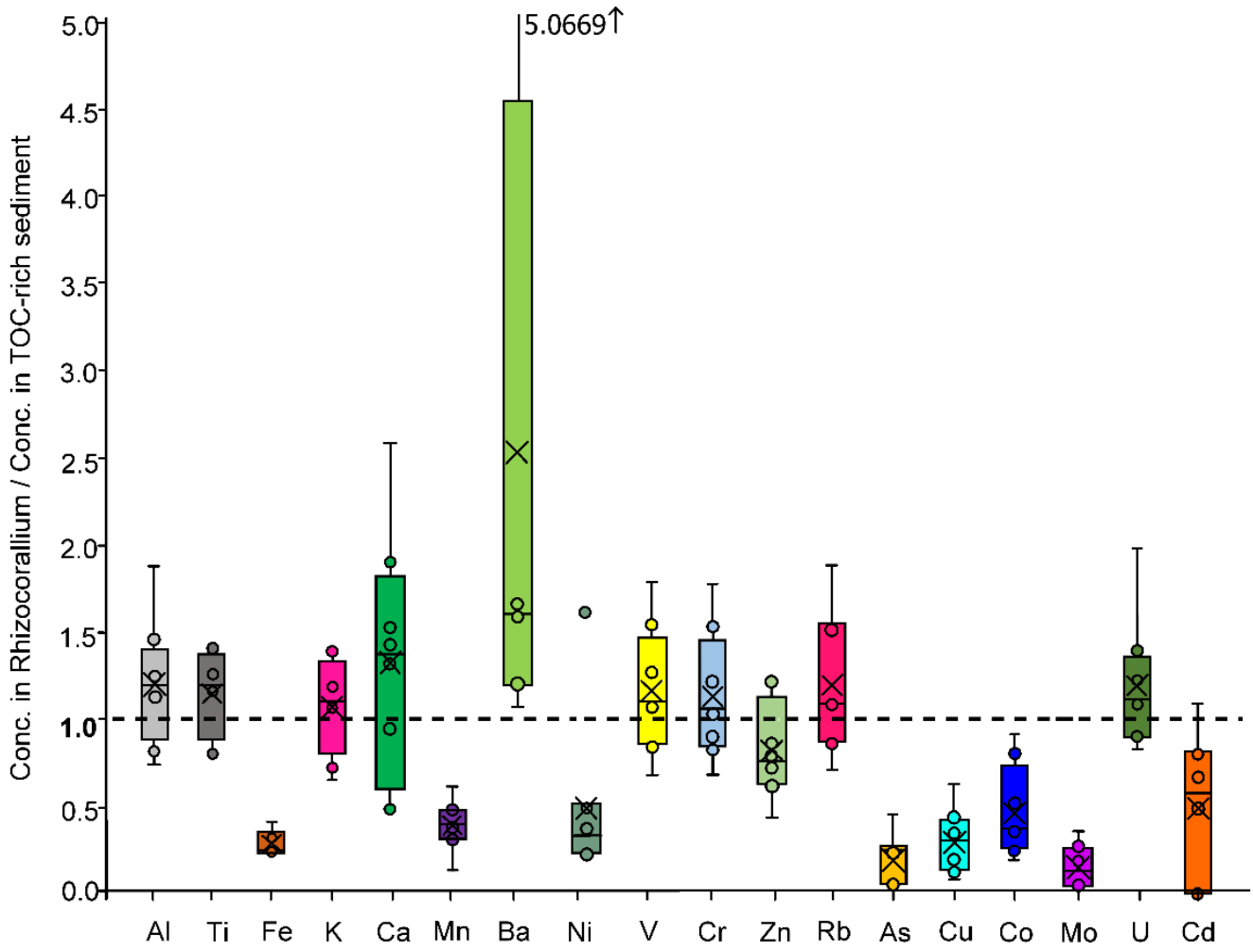

Figure 3.31. Box and whisker plots of the concentration of selected elements in the *Rhizocorallium* burrows, relative to the concentration in the bioturbated sediment of Lithofacies C. As in Fig. 3.30, crosses represent the mean for each element, and circles data points. The value of 1.0 is indicated, i.e., points below the line indicate depletion, and points above indicate enrichment. Note that – as in Fig. 3.30 – the fourth quartile for Ba is off the chart, and so it is indicated in text.

section (Fig. 3.26). Note that here I do not apply the Mo/TOC proxy, since the provenance of the organic matter within the LSB is most likely of a mixed origin (see 3.10), and therefore the Mo/TOC trend could not be indicative of the quantitative drawdown of Mo associated with highly

restricted settings (McArthur *et al.*, 2008). U/Al is depleted within the LSB and shows muted variability between 0.18 – 0.34 ppm/wt.% (Fig. 3.26).

In contrast to the redox-sensitive metals, K/Al stays roughly constant (0.20 – 2.22 wt.%/wt.%; Fig. 3.29) outside of three intervals: between 30 – 48 mm, K/Al is depleted by 0.06 wt.%/wt.%, as well as between 53 – 70 mm (0.09 wt.%/wt.%), and between 94 – 132 mm (0.05 wt.%/wt.%). Ca/Al is anti-correlated with this trend, with background values of 0.03 – 0.08 wt.%/wt.%, and three peaks in enrichment (up to 0.25 wt.%/wt.%) exactly coinciding with the negative peaks in K/Al, and silty lenses within the LSB (Fig. 3.29). Mg/Al remains essentially constant throughout the LSB (varying between 0.09 – 0.12 wt.%/wt.%), implying only a minor contribution of $CaCO_3$ to the sediment geochemistry (see Appendix 3).

K/Rb shows peaks concomitant with troughs in K/Al and Rb/Al, ranging between 21.4 – 28.4 in size (Fig. 3.29). The second peak in K/Rb, likewise, shows exact correspondence with the large silty lens at the base of Lithofacies B. The *Rhizocorallium* traces show enrichment in Ba/Al and depletion in redox-sensitive elements (particularly As/Al; Fig. 3.27), more-or-less regardless as to whether the burrow elemental composition is normalised to that the of the TOC rich sediment of Lithofacies B, or the sediment of Lithofacies C. Detrital elements such as K/Al are mostly unaffected.

2.6 Organic geochemistry

From -60 mm to 0 mm, TOC varies between 0.77 – 0.95 wt.% (Fig. 3.16), with no significant fluctuations. Between 0 and 62 mm, the TOC profile shows considerable lateral variability, but nonetheless, an increase in TOC relative to the underlying sediments is discernable (between 0.881 – 6.71 wt.%, with a mean of 2.21 wt.%). All sampled sections of the LSB indicate that between 60 – 64 mm, TOC values drop to near zero (lower than between -60 mm to 0 mm). This sharp drop is concomitant with the silty lens of Lithofacies B. Immediately after this negative shift, TOC levels rise sharply (by ~7.38 wt.%) and remain between 4.67 – 8.36 wt.% for the rest of Lithofacies B. At 94 mm, the TOC value drops sharply, almost to background levels. Two further positive TOC excursions are recorded, with peaks at 115 mm and 127 mm. These are 12 mm and 16 mm wide, respectively, and reach peak values of 2.58 wt.% and 2.68 wt.%, respectively. These roughly correlate with more organic-rich horizons in Lithofacies C (barely visible through the thorough chondrites bioturbation).

The TOC profile generated from rock eval pyrolysis closely mirrors that generated through total combustion (Fig. 3.32), although for values >1.5 wt.%, TOC via rock eval underestimates TOC via total combustion (Fig. 3.33). It is hereafter assumed that the TOC through total combustion better reflects the true TOC: highly recalcitrant C_{org} might have escaped combustion in the rock eval process, the HCl decarbonation preceding the LECO analysis might have opened pores and caged moites, and the IR cell of the rock eval might have been oversaturated by high levels of CO_2 from the combustion.

HI values broadly track TOC, reaching values of up to 391 mgHC/gTOC in the upper part of Lithofacies B (Fig. 3.32). Two points (at -38 mm and -2 mm) deviate from this trend, showing slight increases of HI (236 mgHC/gTOC and 230 mgHC/gTOC, respectively), with a negligible increase in TOC. The pyrograms at show bimodal S2 peaks at these points. Bimodal peaks are also detected at 59 mm, and 106 mm.

OI is for the most part an anticorrelate of HI, with values ranging between 9.0 – 16 mgCO_2/gTOC (Fig. 3.32), apart from sharp peaks at 62 mm (83 mgCO_2/gTOC), 110 mm (65 mgCO_2/gTOC), and at -38 mm (33 mgCO_2/gTOC) and -2 mm (46 mgCO_2/gTOC). The latter two peaks are concomitant with the small peaks in HI, from samples with bimodal S2 peaks. The highest peaks in OI (and the lowest peaks in HI) correspond with intervals that are higher in silty content, and that show deficits in K/Al, and enrichments in K/Rb (Fig. 3.29).

T_{max} remains reletivley constant for the lower 106 mm of the studied section (between 433 – 442ºC), before abruptly dropping at 50 mm to 427ºC (Fig. 3.32). It then gradually recovers, reaching 438ºC at the top of the studied section. This sudden drop is 2 mm below the point where HCS disappears, ~40 mm above the point where bioturbation rapidly drops and is roughly coeval with reactive Fe (in the Fe_{Carb} pool), and Mn enrichment.

PI is relatively constant though the studied section (around 0.1), with a single, sharp peak at 102 mm (0.23), followed by steady decay to background values over an interval of 20 mm (Fig. 3.32). This peak corresponds with the base of the sharp drop in TOC, the increase in the density of *Chondrites*, and the occurrence of the thick, anisotropic blebs described in section 2.1 (Figs. 3.7 and 3.16).

Inorganic C shows a broad peak through the studied section, from a background of between 0.1-0.2 wt.%, reaching a maximum of 0.54 wt.% at 79 mm (Fig. 3.32). This increase is largely concomitant with TOC (apart from in the silty intervals where it does not show sharp drops like TOC does), S_{py}, and reactive Fe and Mn enrichment (Figs. 3.16; 3.21; 3.23; 3.26).

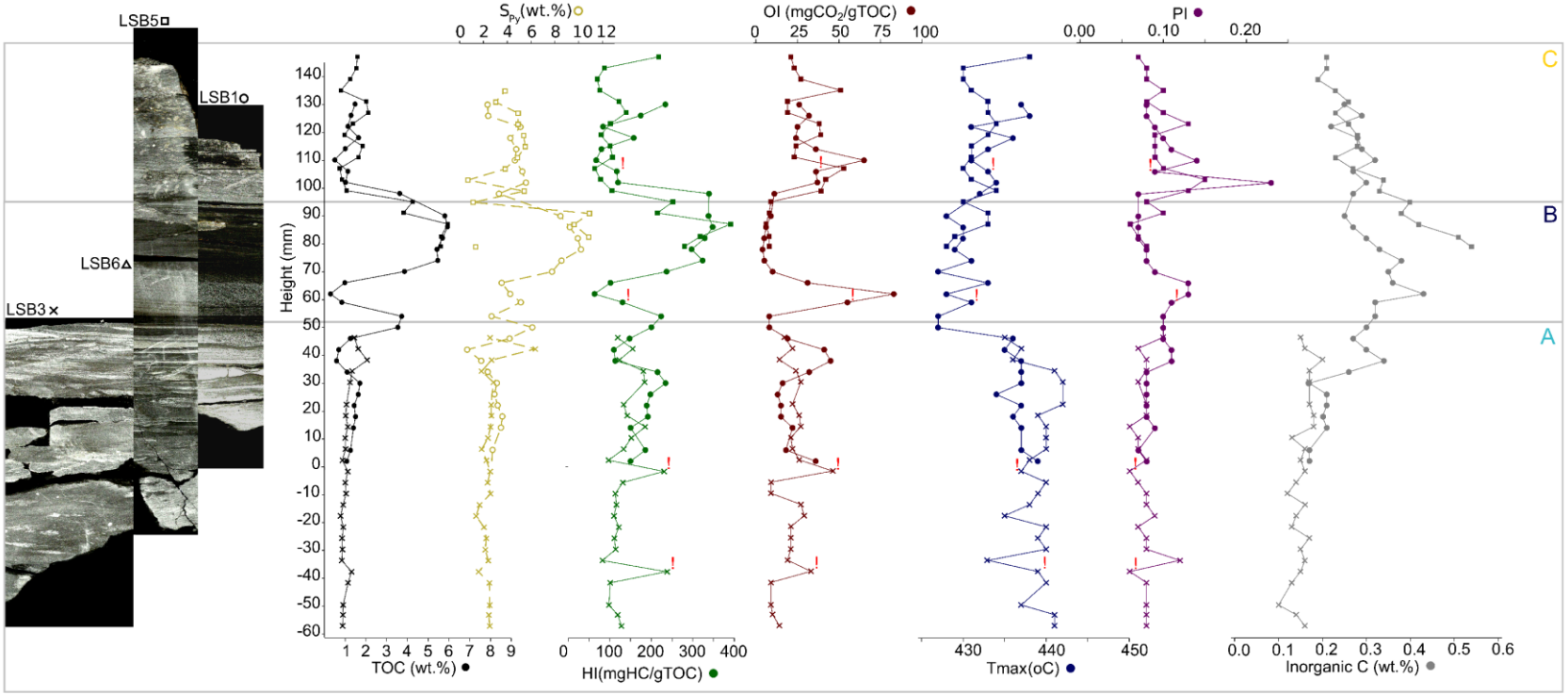

Figure 3.32. TOC (from Rock-Eval), total Sulphur (LECO), and the Rock-Eval parameters HI (mgHC/gTOC), OI ($mgCO_2$/gTOC), T_{max} (^oC), PI and Inorganic C (wt.%) of the LSB. Samples with bimodal S2 peaks are indicated with red exclamation points.

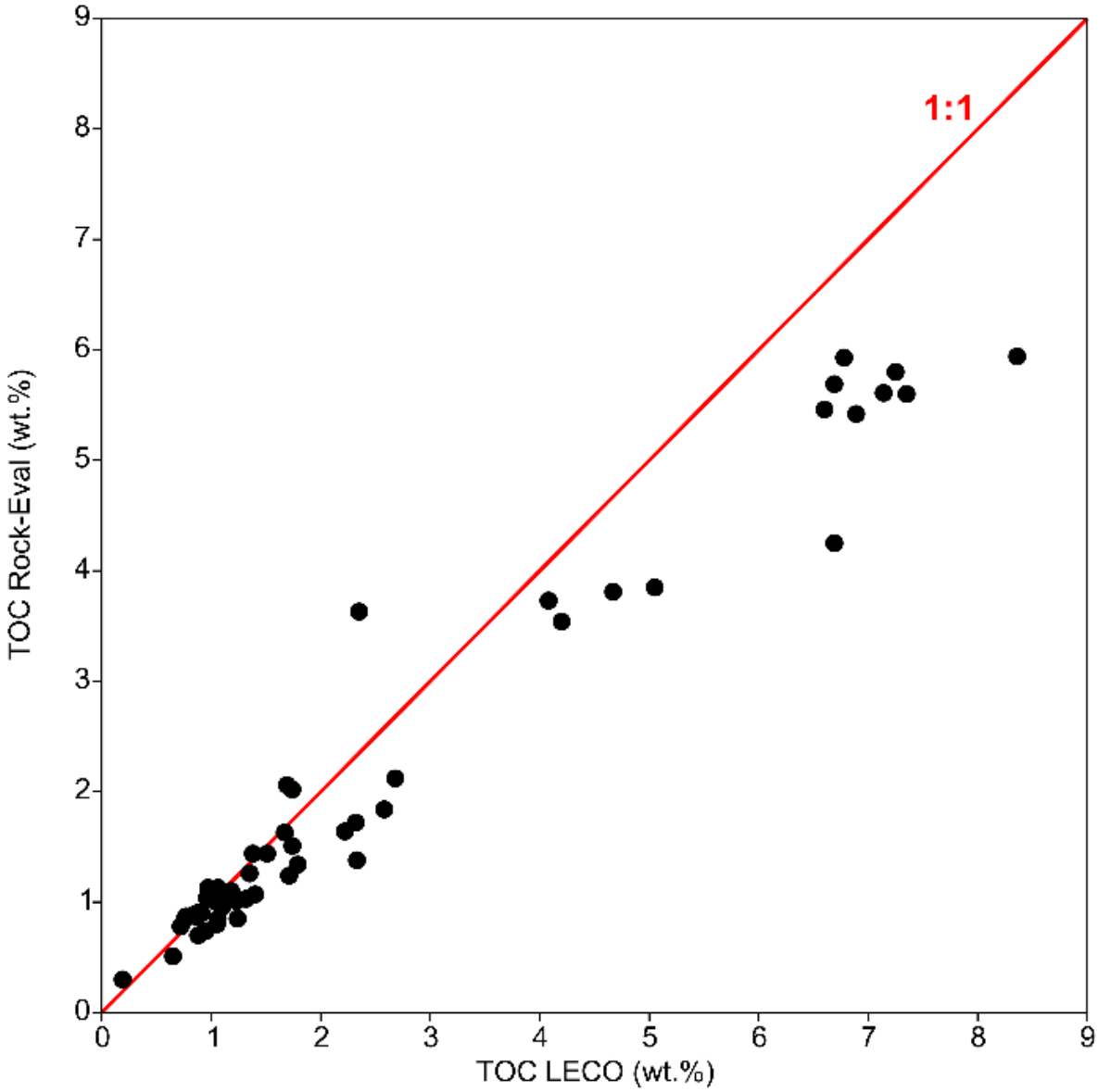

Figure 3.33. Cross plot comparing TOC measurements via LECO with TOC measurements via Rock-Eval. The red line indicates an idealised 1:1 correspondence. Beyond approximately 2 wt.%, the TOC measurements via Rock-Eval pyrolysis drift away from the TOC measurements of the same samples via total combustion in a LECO furnace.

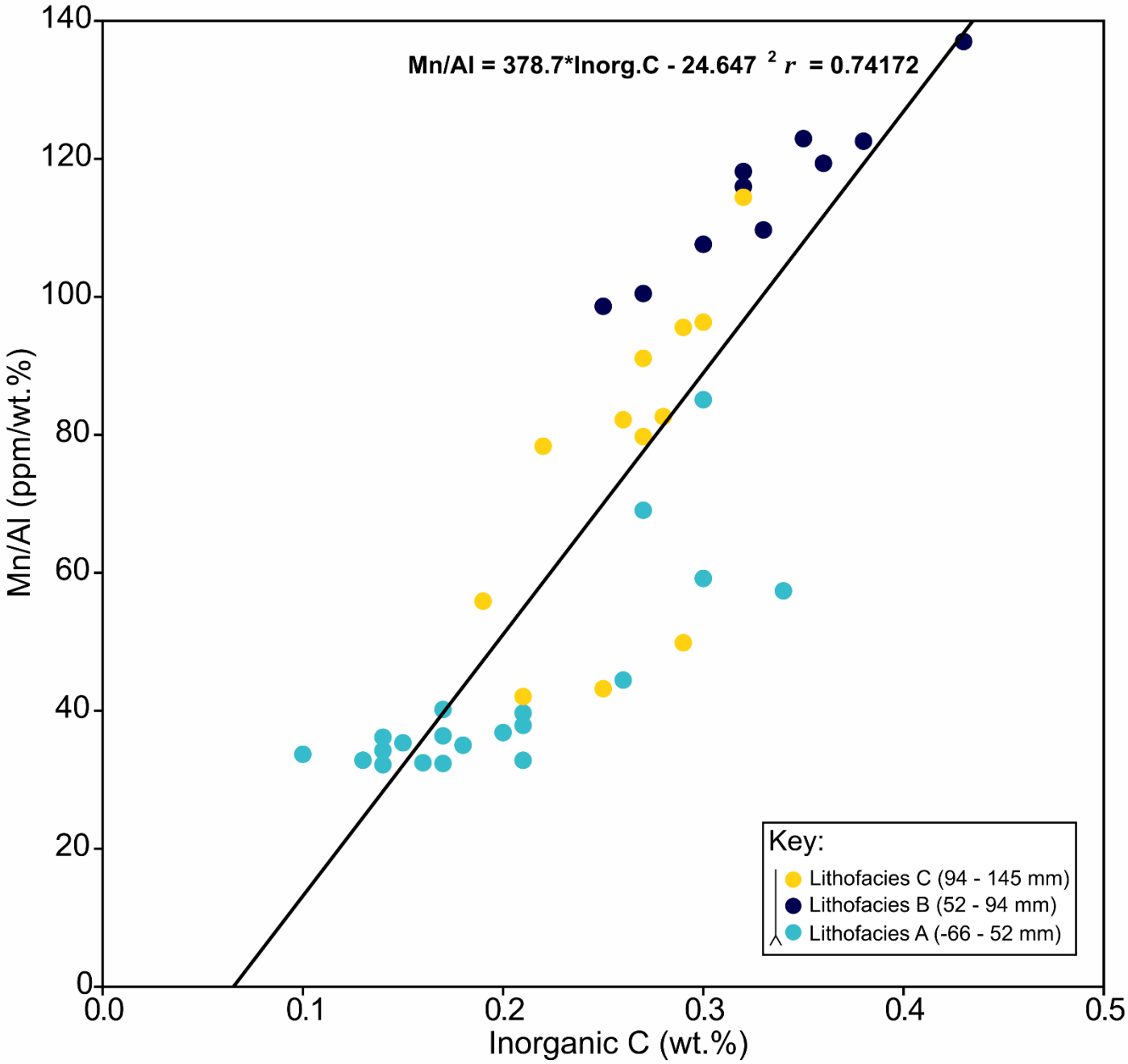

Figure 3.34. Cross-plot of Inorganic C (from Rock-Eval) and Mn/Al(ppm/wt.%), with least-squares regression line displayed (and corresponding R^2). Note that the regression line has a negative y-axis intercept, implying that at 0 ppm/wt.% Mn/Al, some carbonate should be present.

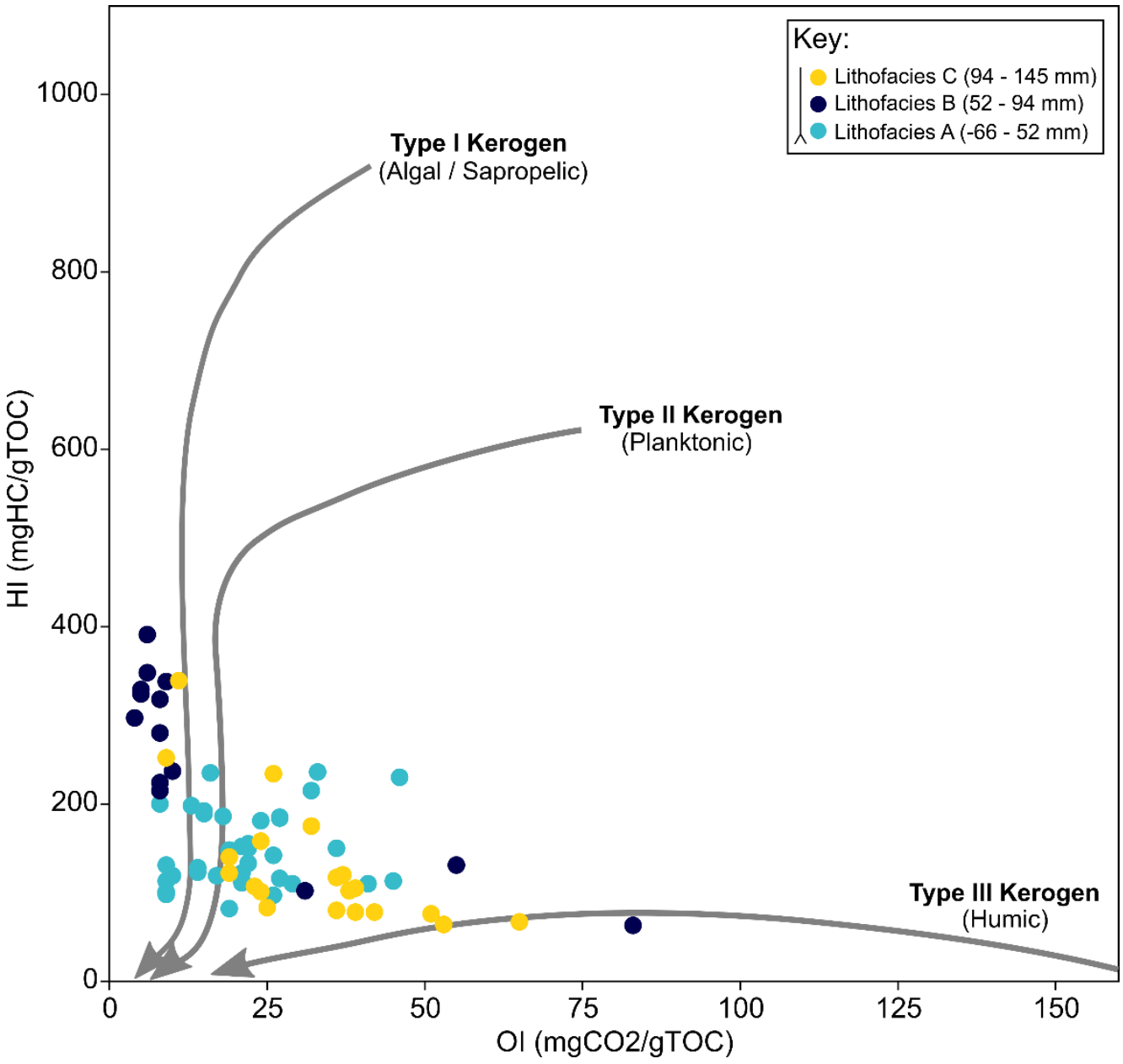

Figure 3.35. Van-Krevelen-style plot of OI vs. HI for the LSB. Note the relatively wide spread of the data points, which intersect the evolution trends of all kerogen types.

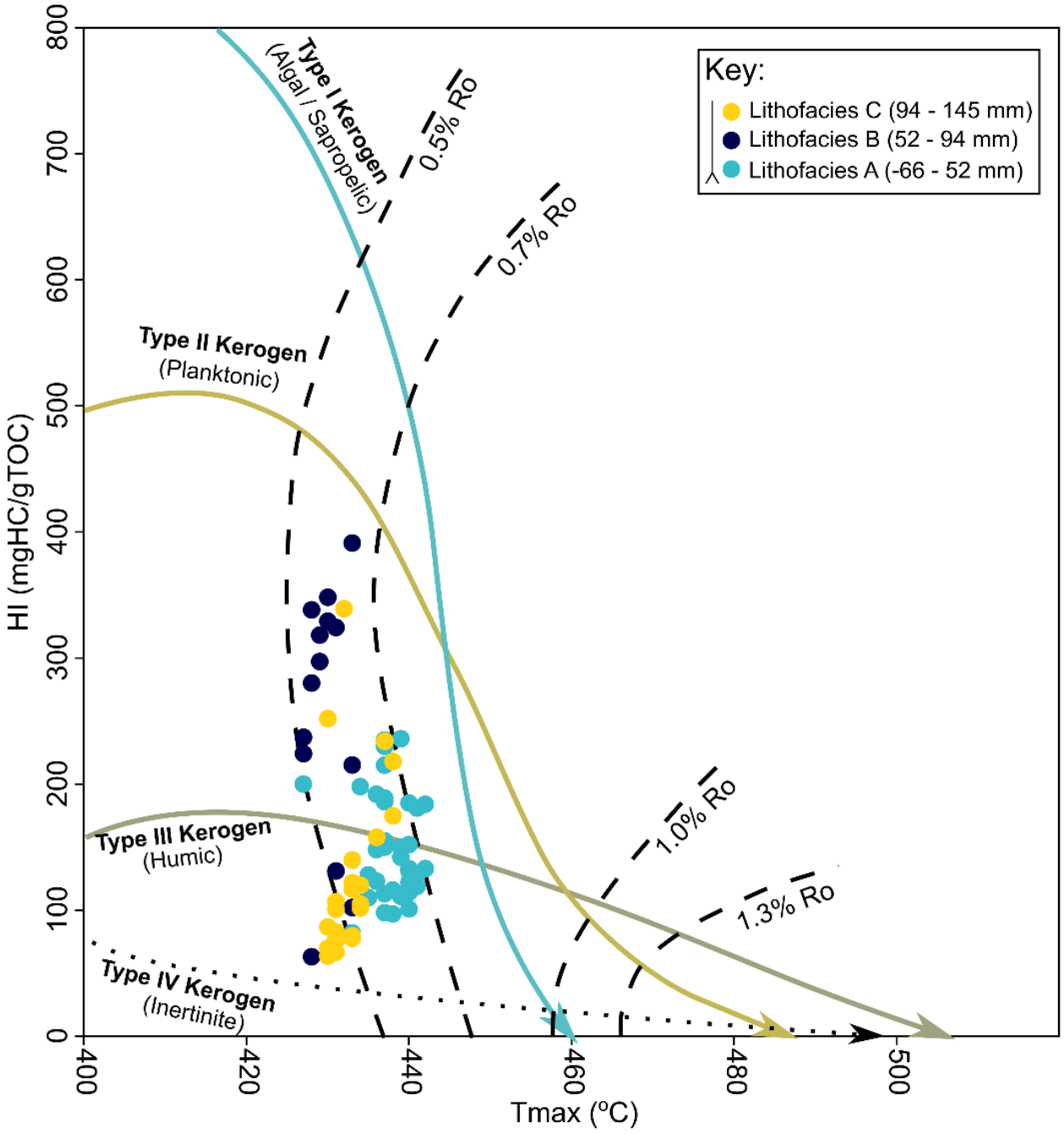

Figure 3.36. HI vs. T_{max}, with kerogen evolution trends from Cornford *et al.* (1998). Note the restriction of the data points to R_0 values between 0.5 – 0.7%.

An OI HI cross plot (Fig. 3.35) shows that the samples from the LSB generally cluster between OI = 12-55, and HI = 100-250. However, several outliers occur, with one group of low OI and high HI values (O1 = 12, HI = 200 – 400), and another of high OI and low HI values (OI = 50-80, HI = 100).

3.0 Interpretations

My study of the LSB encompasses a total of 211 mm of stratigraphic height. This interval includes the entirety of the LSB, but also includes 61 mm of sediments from the underlying bed 25 of the Cleveland Ironstone series (Howarth, 1973). Little, if any, sediment from the overlying bed 27 was sampled. The sediments here had poor consolidation due to exposure to air and were, therefore difficult to sample using the petrol-driven rock saw – they broke apart before they could be collected. I also decided not to attempt to sample this interval with a hammer and chisel, since it would have been difficult to obtain a precise stratigraphic control on the location of any collected samples within bed 27. Sampling using the petrol-driven rock saw also meant that only the upper 61 mm of bed 25 could be sampled, with lower sediments being too deep for the rock saw to reach. The sampling methodology employed allowed me to extract the entire 150 mm of the LSB itself, and sample the resulting blocks (in a lab environment) at cub-cm scale resolution. However, alternate methods should have been employed to capture proxy variability over a wider stratigraphic range. In other words, my sampling methodology prioritised resolution over completeness. As a consequence of these practical limitations of the sampling methodology, it is possible that some key variability in the paleoenvironmental proxies of interest has been missed. This might be the case for the Fe speciation proxies, which (as discussed in sections 3.3 and 3.9) show lower variability than initially expected. However, as also discussed in sections 3.3 and 3.9, there are alternative explanations for the low variability in Fe_{HR}/Fe_T and Fe_{Py}/Fe_{HR}, that have important implications, not only for the interpretation of the palaeoenvironment of the LSB, but for the study of bioturbated black shale sequences in general.

3.1 Sedimentology

The absence of HCS above 40 mm (Chapter 2; Fig. 2.6) implies a change in bottom water energy occurred at this point. Since HCS is typically produced by bidirectional waves with a period of 9.4-10.5 seconds (Dumas *et al.*, 2005), it is also possible that its disappearance indicates the movement of the fair-weather wave base above the sediment-water interface. The erosion of fine material necessary for the formation of the scour marks observed in Lithofacies A also means that small-scale hiatuses are created. While both features can be attributed to a transgression through the LSB, a water depth increase cannot be directly inferred from the disappearance of HCS, and sea level changes cannot be directly inferred without an investigation of time-equivalent deposits from the basin margins (i.e. to determine whether the LSB oversteps underlying Ironstones in the Cleveland Ironstone Formation). Near North Skelton, and at Upleatham Mine (two such marginal settings), the LSB contains pyritised ooids that where probably reworked from the underlying main seam of the Cleveland Ironstone Formation. Chowns (1968) suggested that this was due to reworking of the Cleveland Ironstone Formation during a marine transgression, and subsequent incorporation into the LSB. It is, therefore, possible that the disappearance of HCS at ~40 mm was due to greater water depth, but complementary proxies for the distance of the environment from the palaeo-shoreline (e.g. palynofacies), are needed to test this (see chapters 4 and 5).

3.2 Palaeontology

Up to 0 mm, bottom water oxygen levels were sufficient to sustain actively bioturbating organisms (ORB 4/5; Wignall, 1994; Fig. 3.37). The *Pseudomytiloides dubius* individuals occasionally observed in Lithofacies A (Figs. 3.12 – 3.13) would have required a relatively stable bottom water redox state, at least for the geologically brief interval of time they were alive (years to decades; Röhl *et al.*, 2001; Caswell & Coe, 2013). In the modern deep marine dysoxic environment off southern Baja California, bivalves have been found capable of tolerating oxygen

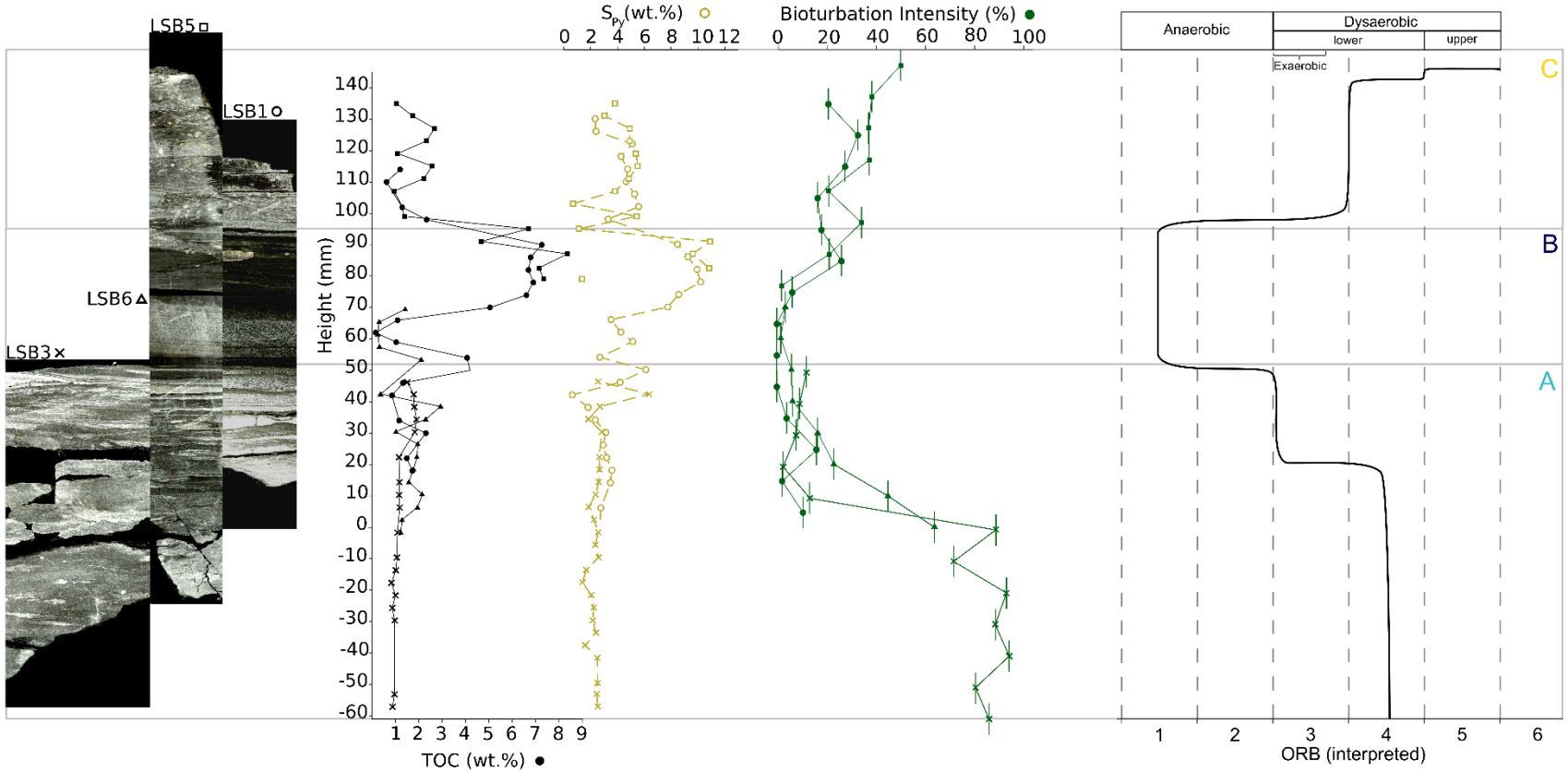

Figure 3.37. Interpreted up-sectionplot of ORB for the LSB. The bioturbation plot is also included. Note how jumps in the ORB correspond with major changes in bioturbation intensity.

concentration as low as 0.05 mL/L (*Jupiteria callimene*; Hendrickx *et al.*, 2016). *P. dubius* might have been able to tolerate similar redox conditions. Additionally, the presence of fodichnical (feeding) traces *(Zoophycos* and *Planolites*) in the interval below 0-20 mm implies oxygen levels were high enough to support active burrowing and feeding behaviour, which is typically reduced at oxygen levels below 0.5 mL/L (Tyson & Pearson, 1991; Hagerman, 1998; Thomas *et al.*, 2019). These palaeoecological constraints mean that for the lower 112 mm of the section, the dysoxic/anoxic redoxcline was below the sediment-water interface most of the time, however the redoxcline may have occasionally risen into the water column (see 3.6). For the lower 60 mm of the section, any dysoxia present was either not frequent, nor intense enough to exclude shallow infaunal organisms. Over time, however (up to 52 mm), dysoxic episodes increased in frequency and/or severity, progressively excluding the shallow infauna. Conditions at the sediment-water interface became barely hospitable to epifaunal *P. dubius* (ORB 3), until even this species became excluded, with the establishment of a very frequently anoxic regime above 52 mm (ORB 1/2).

The decline in bioturbation at 0-20 mm, ~30 mm below the rise in TOC (Fig. 3.16) implies bottom waters became less hospitable before significant organic carbon (C_{org}) preservation occurred, but the enrichment in TOC can be tied to a reduction in oxygen availability (see section 3.3). To reconcile this, I suggest that the brief interval between 20-52 mm represents a period where the oxic-anoxic redox boundary fluctuated rapidly across the sediment-water interface (Kauffman, 1978). The brief, highly frequent periods of anoxia would have "sterilised" the benthic environment (Tyson & Pearson, 1991; Newton, 2001), but the intervening brief oxic episodes would have allowed for the re-oxidation of any labile C_{org} that had accumulated. Given that HCS does not disappear until 40 mm, the interval between 20-40 mm could therefore be representative of the original texture of the upper Cleaveland Ironstone Formation, prior to bioturbation.

As bottom water oxygen levels began to improve (starting during the deposition of Lithofacies C), bioturbating organisms began to colonise the substrate (Fig. 3.37). The preference of *Chondrites* for the TOC rich sediments could be indicative of sulphide-farming behaviour (Baucon *et al.*, 2020). This is seen in modern thyasirid bivalves, which are known to colonise a wide range of modern reducing environments (although they are also found in entirely oxic settings; Dando & Southward, 1986; Dubilier *et al.*, 2008). Although no thyasirids have been found in the section, the niche for sulphide farming is nonetheless present, and so it is possible that an unidentified organism carried out the same behaviour from ~94 mm upwards. However, the *Chondrites* trace-maker could have just been a deposit feeder adapted to dysaerobic

conditions, and was targeting the organic matter rich sediments with its burrowing behaviour. The relative depth of the *Rhizocorallium* traces implies they were formed after 140 mm (and penetrated down from above), but clearly before at least one of the generations of *Chondrites*, since some of these interpenetrate the *Rhizocorallium* traces (Fig. 3.6). This implies that from 94 mm, bottom water redox conditions returned to a state capable of supporting a low diversity benthic community (ORB 4; Fig. 3.37). *Chondrites* is often observed in black shale successions and is widely interpreted as a marker for low diversity dysaerobic communities, developed under relatively stable bottom water dysoxia (Wignall, 1994). Incidentally, bioturbation caused by thyasirid bivalves frequently occurs in modern low diversity sediment ichnofabrics (Dando & Southward, 1986). The appearance of *Rhizocorallium* implies further improvement of bottom water conditions (ORB 5), with the appearance of a shelly fossil assemblage at 145 mm (Fig. 3.11) indicating a return to normal bottom-water conditions (ORB 6/Oxic).

3.3 Sulphur and iron

The difference between total S and S_{py} , taken at face value, implies the presence of other S-bearing phases in the samples. Since fresh surfaces were selected for geochemical samples, and no lithological evidence for evaporitic processes was found, it is was assumed that any S in the LSB not associated with pyrite was associated with sulphurised organic matter (Tribovillard *et al.* 2019). The high levels of S_{py} between 30-110 mm (Fig. 3.21) indicates sulphide generation was occurring in this interval; however, between 30-60 mm and 90-110 mm, High levels of S_{org} (difference between total S by combustion, and S_{py}) also occur (Fig. 3.21). The lack of correlation between Mo/Al and S_{org} (compare Figs. 3.21 and 3.26) could indicate that S-bearing organic matter was not transported from the basin margins (sensu Tribovillard *et al.*, 2019), and that S_{org} levels were a function mainly of authigenic C_{org}-mediated S sequestration (Vandenbroucke & Largeau, 2007). However, the values of the S_{org} trend at these points are much higher than would be expected if the sulphur were indeed hosted in organic matter, and not in sulphur-bearing evaporite minerals (which are indeed absent from the section). At LSB1.7, for example, TOC is 1.18 wt.%, and "S_{org}" is 8.89 wt.% (Fig. 3.21), implying the presence of a sedimentary organic compound that is 88.2 atom% sulphur, and only 11.7 atom% carbon. No such compounds exist in nature. It is, therefore, likely that the total S data is corrupted at these points, possibly from using contaminated ceramic sample boats during TOC and total S analysis on the LECO (note these are

not the same ceramic crucibles used during the total digest for major and trace elements, i.e. the contamination only affects the total S dataset). It is unlikely that the S_{py} data is an underestimate of true pyrite sulphur, since S_{py} was evaluated by reflux with boiling HCl, and it is very likely that this method libeated all pyrite sulphur in the samples. The "S_{org}" data will, therefore, not be discussed any further, and it is for this reason that all downcore plots are compared with TOC and S_{py} (as opposed to total S).

The silty lenses preserved within Lithofacies B and C stand in contrast to the C_{org}-rich mudstone that makes up the rest of these lithofacies and imply episodes of high bottom-water energy. They are difficult to attribute to episodes of shoaling, since HCS does not return to the LSB after 40 mm (Chapter 2, Fig. 2.6). The intervals are also accompanied by peaks in OI (Fig. 3.32), implying brief re-oxidation of labile C_{org}. Furthermore, the framboid lags, and coarsening-upward trend within the large silty lens at 60 mm (Figs. 3.3 and 3.16) imply that this interval was associated with reworking of previously deposited sulphidic sediments. Decreases in K/Al, Rb/Al, and concomitant increases in K/Rb (Fig. 3.29) are also observed in the silty intervals, and S_{py} is suppressed relative to the higher levels attained in the C_{org}-rich units (Fig. 3.16). Given the lack of conclusive evidence for significant freshwater input, and of any change in seawater sulphate concentration, pyrite formation within the LSB can reasonably be assumed to be limited either by the presence of Fe_{HR} or of laible C_{org} (and the sulphide generated by its degradation in anoxic sediments). The low TOC values within the silty intervals (Fig. 3.16) imply that relatively little sulphide was generated here. Outside of these intervals, where Fe_{HR} was abundant, sulphide, as generated by the anaerobic decay of organic matter, was the limiting factor on pyrite formation. This is indicated by the positive correlation between Total S and TOC for the section (Fig. 3.20).

The Fe_{HR}/Fe_T data (Fig. 3.23) shows values persistently higher than 0.4 for the entire section (even in the silty intervals), which implies a persistent operation of the shelf-to basin shuttle (and, apparently, persistent bottom-water anoxia). The Fe_{Py}/Fe_{HR} trend lies almost entirely in the equivocal field throughout the LSB, and Fe_{Py} makes up the largest part of Fe_{HR} throughout the section (Fig. 3.22). It is therefore, probable, that one of the predominant mechanisms for the enrichment of Fe_{HR}/Fe_T was capture of nanoparticulate Fe (oxyhydr)oxides by free sulphide (i.e. under euxinic conditions). However, given the relatively low concentration of Mo below 40 mm (Fig. 3.26), whatever euxinia occurred during the deposition of Lithofacies A was likely episodic, although common enough for the sequestration of a large amount of Sulphur in syngenetic pyrite (enough to raise S_{py} to around 2%; Fig. 3.16).

Persistently anoxic (and commonly euxinic) bottom-water conditions during the deposition of Lithofacies A, also conflicts with the presence of bioturbation (Fig. 3.16), and of in situ benthic fauna (all of which require at least minimal oxygen levels to survive; Figs. 3.12 and 3.13; Diaz & Rosenburg, 2008), as well as the lack of small framboid size populations in the lower part of Lithofacies A (Fig. 3.16). As alluded to in 4.2, I cannot rule out the possibility of fluctuations in redox state giving an apparently anoxic signal when sampled at a rate of 1 sample per 0.5 cm, especially in Lithofacies A. This alone could reconcile the presence of the *Pseudomytiloides dubius* fossils and the high Fe_{HR}/Fe_T values: the shells only need years to decades to grow (see 3.2), whilst an estimate for the duration of the LSB of around 10 Kyr *et al.* implies that the sampling intervals are on the order of centuries in duration. Additionally, the high bioturbation levels in the lower part of Lithofacies A have the potential to shomogenise redox proxy signals (Poulton, 2021). In non-bioturbated successions, very high resolution (up to 0.2 mm with core scanning XRF) can deconvolve time averaged redox signals (Dahl *et al.*, 2019). In Lithofacies A, however, the intense bioturbation, and the high lateral variability of the fabric precludes this analysis from effectively resolving the redox proxy signal. The Fe_{HR}/Fe_T and Fe_{Py}/Fe_{HR} records for Lithofacies C might also have been impacted by the presence of bioturbation; however, since the trace-metal content of the *Rhizocorallium* burrows is still distinct from that of the Lithofacies C samples (Fig. 3.31), it is speculated that the effect on the overall Fe speciation interpretation is small (see below). In other words, the bioturbation occurring in the lower part of the LSB (-62 - 52 mm), was far more pervasive than that which occurred in the upper part (94 – 145 mm). The *Chondirites* trace makers alone evidently did not disturb the sediment profile enough to rehomogenise the Fe_{HR}/Fe_T signal, whereas the *Zoophycos* and *Planolites* trace-makers did. This further implies that the biofacies associated with Lithofacies A was capable of sustaining more energetically demmanding modes of life than that associated with Lithofacies C, and that through the LSB, the benthic environment became less habitable, becoming uninhabitable to all benthos in Lithofacies B. Taken together, these lines of evidence imply that the LSB contains a record of frequently changing redox state in the Cleveland Basin, rather than (necessarily) a record of persistent oxygen depletion of varying severity. The frequency of anoxic events was sufficiently low in Lithofacies A as to not exclude bioturbating organisms entirely, but nonetheless frequent enough to facilitate the drawdown of Fe_{HR}. The absence of bioturbation in Lithofacies B (together with higher Fe_{HR}/Fe_T and Mo enrichment), implies that an increase in the frequency of anoxic events occurred prior to the emplacement of this lithofacies. I will discuss this further in section 3.11.

Enrichment of Fe_{HR} was also a nearly persistent characteristic of the Cleveland Basin during the deposition of the LSB, as indicated by the fact that pyrite growth was mainly sulphide-limited (Fig. 3.24). Continental runoff is a possible means for the delivery of a high Fe_{HR} flux, since the generally hot, humid climate of the Lower Jurassic (Rees *et al.*, 2000) could have facilitated the development of laterite profiles on the surrounding hinterlands (although no remnants of these soils have been found in the British Jurassic). The occurrence of high continental weathering rates in the British Lower Jurassic is supported by the presence of detrital Fe-rich chlorite in the coeval Llanbedr core (Mochras, Cardigan Bay basin; Xu *et al.*, 2018). However analysis of the $\delta^{18}O$ of belemnites from the Cleveland Basin (Korte & Hesselbo, 2011; Korte *et al.*, 2015) imply that surface water temperatures around the time of the Pl-To were between 15 – 25°C (cooler than that typically seen in climates associated with laterite formation).

The dominance of small framboids between 70-94 mm (Figs. 3.16 and 3.19) indicates that this interval (in Lithofacies B) was euxinic (at least in bottom waters). While pyrite framboid frequency per unit area was not quantified, Figs. 3.17 and 3.18 clearly show how Lithofacies B also contains a greater number of framboids than the underlying Lithofacies A. The majority of these framboids are less than 5 μm in diameter (section 2.3), and so the decrease in mean framboid diameter in Lithofacies B can be attributed to an expansion of bottom water euxinia. It is unlikely that the framboids outside of this interval were exclusively produced in the water column under euxinic conditions, and then grew to larger sizes in the sediment: under euxinic conditions, pyrite framboids form near the chemocline (where some oxidised sulphur species are present) before sinking to the sediment, where they cannot grow any larger due to a sudden lack of oxidised sulphur species. It is, however, possible that some resumed growth of pyrite framboids occurred if the chemocline fluctuated between the sediment and the water column frequently enough, since this could have introduced fresh oxidised sulphur species into the sediment porewater environment.While the deposition of buoyant plumes associated with turbidity currents takes weeks to months (Stow & Wetzel, 1990), and framboids ~5 μm in diameter take only ~3 days to form (Rickard, 2019), the sheer number found in Lithofacies B implies that it is very unlikely to be a turbidity deposit.

3.4 Detrital element ratios

The changes in detrital element ratios (Fig. 3.29) within the silty intervals could additionally imply a change in continental weathering regime, resulting in a shift in the clay mineral assemblage of the LSB. Under more humid climatic conditions, cations such as K and Rb are more effectively leached by chemical weathering, leading to the generation of kaolinite clay profiles on the hinterlands, as opposed to more cation-enriched clays such as montmorillonite. The fluvially-derived siliciclastic component of the LSB, therefore, might reflect this change in the clay mineral assemblage (Calvert & Pedersen, 2007; März *et al.*, 2010, 2011). More humid climatic conditions are also associated with episodic mega-monsoons over the European Epicontinental Seaway (EES) – events accompanied by storms, which would raise bottom-water energy levels for brief intervals of time. These intervals might have also induced transportation of shelfal sediments to the basin, which could account for the subtle grading in some of the silty units, as well as the framboid lags (Fig. 3.3). Mega-monsoons over the EES have been invoked to explain the development of anoxic conditions in the Posidonia Shale, due to enhanced nutrient flux and salinity stratification (Röhl *et al.*, 2001). This does not, however, preclude the possibility of episodes of bottom water re-oxygenation against a predominantly anoxic background. Similar structures in a prodelta succession from the Cenomanian-aged Dunvegan Formation (Alberta, Canada), and from an early Ordovician mudstone in Newfoundland, have been attributed to fluid mud remobilisation associated with storm winds (Plint, 2013; Harazim & McIlroy, 2015).

It should be noted, however, that in and of themselves, these excursions cannot be tied to a shift in the clay mineral assemblage without a complementary crystallographic analysis (which was not carried out in this study). The SEM work carried out was also focused on determining pyrite framboid diameter, and no observations on the structure of clay minerals were made. However, there is sufficient precedent from similar studies of Toarcian mudrock successions from the British Isles (Thibault *et al.*, 2018; Hollaar *et al.*, 2023) to support the correlation of the intervals of K/Al depletion and K/Rb enrichment (at least tentatively) with sediment changes related to hydrodynamics. There is also independent proxy evidence from the LSB (in the form of palynology and biomarker distributions; Chapters 4 and 5) from which to argue the occurrence of humid climate episodes concomitant with the intervals of depleted K/Al and enriched K/Rb.

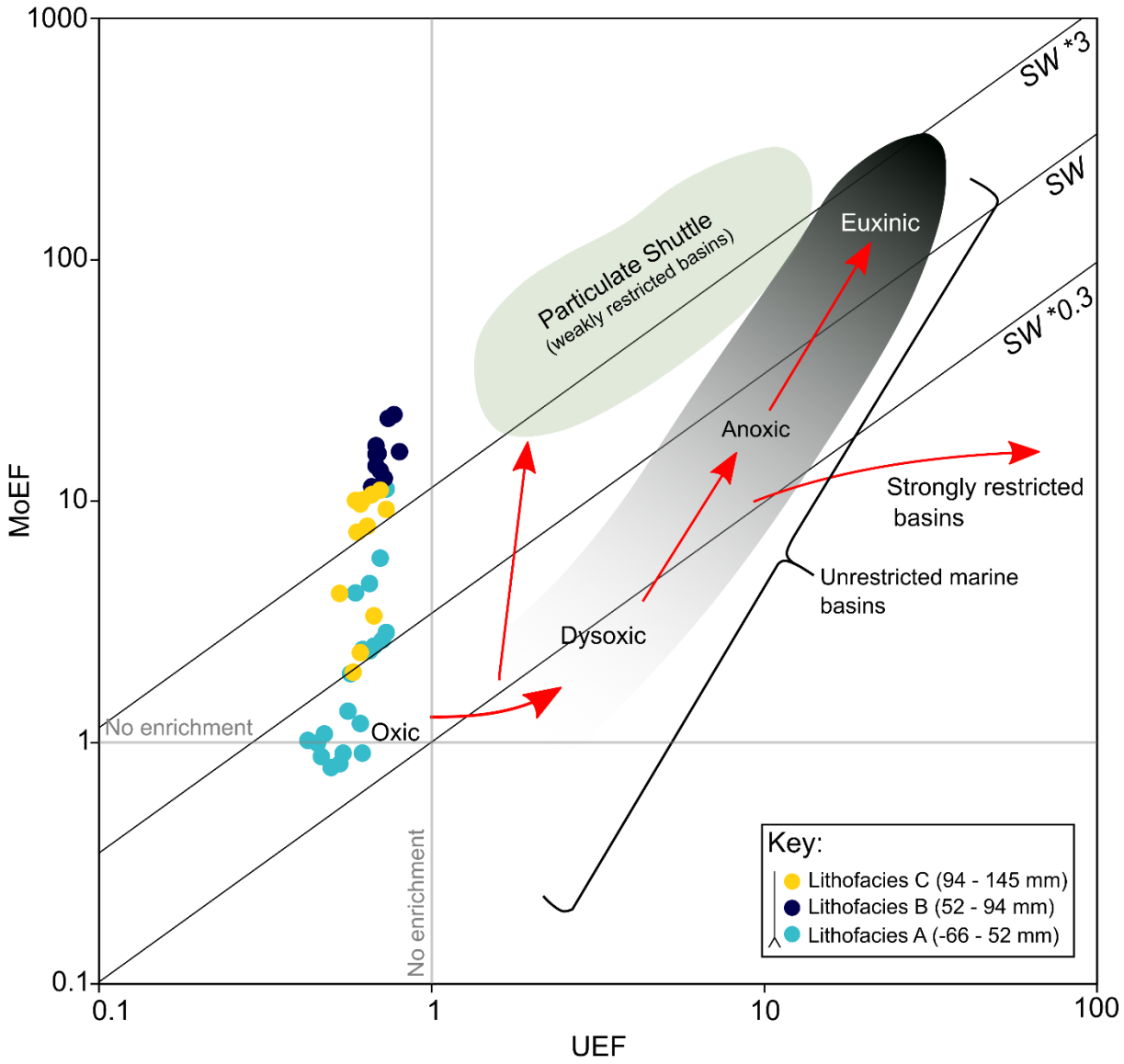

Figure 3.38. Uranium enrichment factor **(**UEF) vs. Molybdenum enrichment factor (MoEF) plot for the LSB. Trendlines and annotations adapted from Algeo & Tribovillard (2009).

3.5 Manganese

Enrichment of Mn/Al (Fig. 3.26) implies that the depositional system was highly restricted. Mn^{2+} is liberated from sediments under anoxic conditions (Klinkhammer & Bender, 1980; Calvert & Pedersen, 1993; Huckriede & Meischner, 1996). Due to being trapped in the basin by redox cycling at the anoxic/oxic interface, aqueous Mn^{2+} was incorporated into carbonate phases

generated by microbially-mediated C_{org} degradation during early diagenesis (Fig. 3.34; Calvert and Pedersen, 1996). Rhodochrosite is likely to be the carbonate mineral phase hosting Mn in the LSB (Jenkyns *et al.*, 1991; Maynard, 2010), given the presence of Na-acetate extractable Fe (Section 2.4), and the fact that appreciable quantities of siderite have been detected in the LSB at Kettleness (a more marginal depositional environment than Hawsker Bottoms; Newton, 2001). Siderite and Rhodochrosite lie at opposite ends of a solid solution, and it is reasonable to suggest that a high proportion of the sedimentary Mn content of the LSB became incorporated into diagenetic siderite. Mn can also become incorporated into carbonate phases such as Kutnohorite and as a replacement after Ca in calcite (Deer *et al.*, 2013). The low Mg content of the LSB (Appendix 2), however, implies that dolomatisation was not pervasive in this unit (i.e. Kutnohorite content is probably low), and no major carbonate clasts (mineral or biogenic) were observed in thin section. An XRD analysis would be required to conclusively determine the mineral host of Mn within the LSB, but regardless of the specific mineral host, the positive correlation between Mn/Al and Inorganic C (from Rock Eval; Fig. 3.34) supports the presence of a Mn-containing carbonate mineral phase within the LSB. In addition, the high basinal restriction and low oxygen levels (when below 5 μM) might have resulted in direct water column precipitation of $MnCO_3$ (Wittkop *et al.*, 2020). However, relatively low levels of pelagic carbonate were introduced to the sedimentary environment (see TIC data in Appendix 3, as well as Fig. 3.32), and so if carbonate saturation was indeed elevated in sub-chemoclinal waters, the required dissolved inorganic carbon would have been supplied either through sulphate reduction, or possibly by an elevated shelf flux (e.g. Dekov *et al.*, 2020). In any case, the presence of Mn-bearing carbonate phases is supported by my combined trace element and Rock-Eval analysis, and furthermore, the presence of strong redoxcline is supported by the small framboid size distribution found in Lithofacies B (Figs. 3.16 and 3.19). Mn flux to the sediments could therefore have been particularly high when the sediment-water interface intersected with a fluctuating redox boundary.

3.6 Molybdenum

Mo/Al closely tracks Mn/Al (Fig. 3.26), implying delivery to the sediment primarily through capture by Mn oxyhydroxides (Tribovillard *et al.*, 2006), and by sulphides/sulphurised OM during the brief interval of euxinia in Lithofacies B. Mo is therefore likely to be hosted either in syngenetic pyrite, or within authigenic Mn mineral phases (Algeo & Maynard, 2004; Algeo & Tribovillard, 2009). The Mo enrichment implies anoxic conditions were developed in bottom waters (particularly in Lithofacies B), but the values are depleted relative to those from persistently euxinic environments such as the Black Sea (maximum Molybdenum enrichment factor – MoEF = 22.8, as opposed to MoEF ~50; Algeo & Tribovillard 2009 and references therein; Fig. 3.38). Given that the Cleveland Basin was highly restricted (as indicated by Mn enrichment), if sulphide-mediated drawdown of Mo took place, the level of Mo enrichment by this pathway was likely intrinsically limited (Algeo & Lyons, 2006). Similarly, in their work on the Mo geochemistry of the Toarcian sediments of the Cleveland Basin, McArthur *et al.* (2008) argued that their value of the Mo/TOC regression curve (rsMo/TOC) in the Sulphur Bands (rsMo/TOC = 17 ppm/wt.%) was indicative of a small reservoir of Mo. They argued that this could have been due to either a limited Mo inventory within a moderately restricted basin, or oceanic Mo depletion (i.e. a non-restricted setting with access to the Tethyan realm). They further argued that since the rsMo/TOC values were correlated with geochemical proxies for oxygen depletion (such as DOP-T and δ^{98}Mo), and since assuming an oceanic drawdown of Mo during the T-OAE necessitates an unrealistically high average Mo value of lower Toarcian black shales, McArthur *et al.* (2008) conclude that the Cleveland Basin was restricted. Furthermore, it was argued that increased Mo enrichment, at relatively constant TOC was indicative of an expansion of a euxinic water mass (i.e. chemocline shoaling), encompassing a larger Mo inventory, which was then drawn down. So even if bottom waters were euxinic during the deposition of the LSB, the height of the anoxic-euxinic chemocline within the water column could have affected the amount of Mo drawn down, in addition to the basin reservoir effect. To test the relative influence of these two factors, further proxy constraints on the height of the anoxic-euxinic chemocline (e.g. the biomarker isorenieratane), are needed. A further study by McArthur (2019), found that the Sulphur Bands were also enriched in Mn and Cd (notwithstanding occasional dilution by the high pyrite content). On the basis of CoEF x MnEF, it was concluded that both the Sulphur Bands, and the overlying Mulgrave Shale Member, were deposited under restricted conditions. The emerging picture of a restricted Cleveland Basin has recently led to the assertion that the

Cleveland Basin was partly freshwater/brackish, based on poorly constrained B/Ga and S/TOC data (Ramirez & Algeo, 2020a; see also comment by Hesselbo *et al.* (2020), and reply by Ramirez & Algeo, (2020b)).

The assertion that a limited Mo inventory in the Cleveland Basin was due to high basinal restriction has, however, been challenged. Based on assessment of detrital element ratios, Thibault *et al.* (2018) have argued that a broad transgression occurred during the deposition of the Whitby Mudstone Formation, and that Mo drawdown occurs on a much larger scale during OAEs. In addition, the sluggish oceanic currents across the EES would have also afforded many opportunities for the depletion of the Mo inventory of water masses moving into the Cleveland Basin from the Tethyan realm (Baroni *et al.*, 2018). While the hydrographic regime concomitant with the deposition of the Mulgrave Shale Member remains a matter of debate, the LSB is nonetheless associated with both a lower sea level than the overlying Mulgrave Shale Member (Thibault *et al.*, 2018), and a short-lived regressive-transgressive couplet near the Pliensbachian-Toarcian boundary (Wignall & Bond, 2008). Therefore, the co-occurrence of oxygen depletion with (short-lived) high basinal restriction remains plausible (at least for this unit), although an independent analysis of sea level is needed to test this (see Chapter 5).

3.7 Other trace elements

Low U levels (Figs. 3.26 and 3.38) could be indicative of either a highly restricted system (a limited aqueous U inventory), or possible re-oxygenation of bottom waters leading to the reoxidation of authigenic U hosted in carbonates (e.g. Zheng *et al.*, 2002; Tribovillard *et al.*, 2006). Re-oxygenation, however, is difficult to reconcile with the persistently high levels of Fe_{Py} through the section (Fig. 3.23), little evidence of pyrite framboid recrystallisation, and the lack of bioturbation within Lithofacies B (Fig. 3.16). Despite this, the re-oxidation of U by bioturbation is still a viable depletion pathway for the bioturbated portions of Lithofacies A and C (just as with Fe). A MoEF vs UEF cross-plot (Fig. 3.38) implies that the system was dominated by a particulate shuttle, due to the trend observed (albeit shifted left due to the uniform U depletion). This further indicates Mn cycling was present at the oxic-anoxic redox boundary, and that Mo was incorporated into authigenic Mn mineral phases (Algeo & Tribovillard, 2009).

Some of the highest trace element enrichments encountered in the LSB are for elements that associate very readily with Fe and Mn (oxyhydr)oxides, such as As (Fig. 3.27; Tribovillard, 2020), Cu (Fig. 3.28; Fernex *et al.*, 1992), Ni (Fig. 3.26; Peacock & Sherman, 2007), and Mo (Fig. 3.26; Bertine & Turekian, 1973; Brumsack, 2006; Tribovillard *et al.*, 2006;). Alongside the high values of Fe_{HR}/Fe_T (particularly in Lithofacies B; Fig. 3.23), and the very low U content (Fig. 3.26), this implies a strong operation of the Fe shuttle in the basin. A large flux of (potentially hinterland-derived) highly reactive iron might have been in operation, moving from a proximal shelf environment to the basin depocentre. When the expansion of anoxic conditions brought the anoxic/euxinic chemocline into contact with this flux, colloidal Fe_{HR} was then reduced into FeS, which was then converted to Fe_3S_4 (Wignall & Newton, 1998). This then sank out of the water column. Many of these trace elements were subsequently reduced in the euxinic environment (closer to the sediment/water interface), and incorporated into syngenetic pyrite when the level of Fe_{HR} was high (Tribovillard *et al.*, 2006). The strong Fe shuttle may also have been accompanied by a Mn shuttle - Large amounts of Mn oxides (primarily hosted in particle coatings; Tribovillard *et al.*, 2006) would have been titrated during episodes of chemocline expansion, raising the dissolved Mn inventory of sub-chemoclinal waters. This dissolved Mn^{2+} would have then been confined to be basin by strong Mn cycling at the chemocline. Precipitation of Mn-oxides above the oxic-anoxic chemocline would have additionally acted as a sink for Co, Cu, Mo, Ni and Zn. The high Ni enrichment (Fig. 3.26) was possibly due to incorporation into sulphides, although high values of Ni/Al in Lithofacies C (up to 62.0 ppm/wt.%), where pyrite levels are in decline, remains enigmatic.

3.8 Burrow enrichments/depletions

The relative element enrichments of the *Rhizocorallium* burrows (Fig. 3.30) implies that they resulted mostly in a remobilisation of redox-sensitive elements. This was due to exposure of sulpidic sediments to oxygenated water circulating in the newly opened burrows, leading to the local oxidation of pyrite. The lack of significant changes in detrital element ratios implies simple mechanical reworking of the local sediment, rather than replacement. The slight increase in Zr relative to the host sediment could have been enriched due to transport of resuspended sediment by traction and saltation: reworked sediment from intense bioturbation becomes funnelled into the burrows by turbulent flow at the sediment-water interface (Fustic *et al.*, 2021). Ba is highly enriched in the *Rhizocorallium* burrows (both when normalised to local sediment and high TOC

sediment; Figs. 3.30 and 3.31), and may partly reflect substitution of the K^+ ion for the Ba^{2+} ion in the alkali feldspars – a common component of the silty lithologies of the LSB. However, given the low Ba content of the surrounding sediments (Fig. 3.27), the elevated Ba signatures may be nothing more than normalisation artefacts.

The distinct difference in elemental composition between the burrows, and the sediments they penetrate implies that the sediment samples from Lithofacies C (notwithstanding minor contribution from *Chondrites* traces), are still broadly representative of the original signal. However, due to the small size, and indistinct boundaries of the traces preserved in Lithofacies A, a similar analysis could not be carried out. It is, therefore, impossible to rule out the possibility of a mixed geochemical signal for this interval. Indeed, the presence of Fe_{HR}/Fe_T values apparently inconsistent with the macropalaeontological evidence indicating habitable bottom water conditions (Figs. 3.16 and 3.23; see section 3.2), strongly implies that this is the case.

3.9 Implications for use of the Fe-speciation proxies

The difficulty in resolving accurate geochemical redox proxy records for the bioturbated sediment of Lithofacies A, should serve as a warning that sampling of bioturbated sediments for geochemical analysis should be carried out with care, to minimise the chance of drawing erroneous palaeoenvironmental interpretations. Given the high Fe_{Py}/Fe_{HR} values associated with this interval (Fig. 3.23), despite the relatively low Fe_T/Al values (around 0.5 wt.%), it is probable that redox conditions frequently fluctuated from fully oxic, to fully euxinic. Additionally, Fe_T/Al values may have initially been much higher in Lithofacies A, with excess Fe_{HR} becoming remobilised into the water column, during early diagenesis under an anoxic ferruginous water column (Poulton & Canfield, 2011, Poulton 2021). This process has been invoked to explain low Fe_T/Al values associated with Devonian-aged black shales in Western Canada (Li *5*, 2022), and requires rapidly fluctuating redox conditions. If this process indeed operated during the deposition of the LSB, then given a sample spacing of 0.5 cm (and that the 15 cm-thick LSB represents 10 kyr of sedimentation; Chapter 1, section 6.0), the frequency of these fluctuations would be, at most, on the order of centuries. Bioturbation associated with high Fe_{HR}/Fe_T and Fe_{Py}/Fe_{HR} can also be found in the Rhaetian-Hettangian aged sediments of the Bristol Channel basin (He *et al.*, 2022), and again, is likely indicative of benthic colonisation during brief oxic intervals, with a duration of insufficient length to be captured by the sample resolution of the iron proxies. These

observations in no way undermine the utility of the Fe_{HR}/Fe_T and Fe_{Py}/Fe_{HR} proxies, which have been well calibrated over a wide range of modern environments, and have time and again accurately resolved palaeoredox state in multiproxy studies of palaeoenvironments ranging from the Precambrian to the Quaternary (Raiswell & Canfield, 1998; Wisjman *et al.*, 2001; März *et al.*, 2008; Poulton *et al.*, 2010; Raiswell *et al.*, 2018; Poulton, 2021). Rather, they demonstrate the remarkable variability of redox state in black shale sequences, beyond those traditionally assumed. These deposits are likely characterised by frequent redox shifts, allowing for the short-lived recolonisation of the benthic environment, especially by dysoxia-tolerant animals. In modern environments, dysoxia/anoxia occur over a wide range of spatial and temporal scales (Rabalais *et al*, 2010), and show annual growth/reduction in many shallow marine settings (mediated by factors such as enhanced nutrient loading during the spring bloom; Tyson & Pearson, 1991; Li *et al.*, 2016). This fine redox variability can be preserved in laminated sediments, and even resolved with high-resolution XRF (Dahl *et al.*, 2019); however, the high level of bioturbation in Lithofacies A means that such mm-scale variations cannot be resolved here. Even in modern nearshore settings with high sediment accumulation rates, sediments typically spend on the order of 10-100 yr in the mixed layer, and so sedimentary signals that take place on a shorter timescale than this (with the exception of short-lived, non-steady state events such as storm deposits) are unlikely to be preserved intact in bioturbated sediments (Wheatcroft & Drake, 2003).

3.10 Rock-Eval pyrolysis

Given that redox proxies (e.g. Fe_{Py}, Mo/Al, and framboid diameter; Figs. 3.16; 3.22; 3.26) correlate with TOC (positively in the case of Fe_{Py} and Mo/Al and negatively in the case of framboid diameter), and that the redox proxies reach low values along with TOC, I interpret increased TOC to be a consequence of enhanced preservation: as sub-chemoclinal waters expanded during the deposition of the LSB (as implied by the peak in Mn/Al; Fig. 3.26), C_{org} accumulating in the Cleveland Basin depocentre was more protected from oxidation. Exceptions to this are the brief periods of higher bottom-water energy, marked by the silty units, where anticorrelation in the HI and OI trends (Fig. 3.35) implies that previously deposited organic matter was oxidised, consistent with bottom-water oxygenation. This is not to say that episodes of enhanced productivity did not occur, or even that (if present) they did not further accelerate oxygen consumption. The isolated nature of the basin, and subsequent long deep-water renewal

times (Baroni *et al.*, 2018), however, mean that invoking high productivity levels is not required. Furthermore, invoking productivity enhancement carries an additional burden of proof, and therefore requires additional proxy evidence to validate/disprove. In Chapters 4 and 5, I employ palynological and biomarker proxies to further investigate these questions.

A large proportion of the organic matter preserved in the LSB is marine in origin (HI values of up to 318 mgHC/gTOC; Fig. 3.32), however, bimodal S2 peaks imply the presence of two intermixing organic matter pools (Newell *et al.*, 2016). One of these could have been derived from an algal source, and another from a humic source. This is also implied by the HI and OI data. While the relatively close clustering of the data points on the HI vs OI plot (Fig. 3.35), approaching the origin, is typical of ancient organic rich sediments that have undergone slight thermal maturation, the clustering also implies the organic matter is most likely a mixture of algal and humic material. It is possible that some organic matter is derived from a planktonic source (particularly in Lithofacies A), however, the data points at the base of the Type II kerogen evolution line could just as easily represent a mixture of highly matured type I and type III kerogen. It has, however, been noted by Cornford *et al.* (1998) that Fe_{Carb} rich samples might give false OI signals due to thermal decomposition of siderite during Rock-Eval analysis. The authors recommend that in these cases, HI vs T_{max} plots (e.g. Fig. 3.36) are to be preferred over HI vs OI plots, when discussing kerogen properties of the section under investigation. A plot of HI vs T_{max} also shows how my data do not fit along any single kerogen-type trend (Fig. 3.36), and that the sediments of the LSB have been subjected to a moderate degree of thermal maturation (R_0 between 0.5-0.7%). To further discriminate the relative influence of these carbon pools, a palynological analysis is required (Chapter 4). Rock-Eval pyrolysis only provides information on the bulk organic properties of the sediment, although the presence of prominent S2 and S3 peaks can be tentatively attributed to the presence of both marine, and terrestrially-derived organic matter (Carrie *et al.*, 2012).

The T_{max} versus HI plot (Fig. 3.36) shows how the samples do not fall along any of the defined trends for kerogen types I-III, further implying a mixed signal. The spread of points also falls between R_0 values of 0.5% and 0.7%, indicating that the samples have been thermally matured. Some of the samples (mostly from Lithofacies A) show T_{max} values exceeding 435ºC (Fig. 3.32), plotting in the oil generation window on the T_{max}/HI plot. Any future study on the organic geochemistry of the LSB should therefore account for the probable migration of short-chain compounds within the pore space (see Chapter 5).

3.11 Model for LSB formation

The Cleveland Basin was highly restricted, and small changes in continental weathering regime, temperature, organic carbon export, etc., greatly affected the redox state (like the modern Danish Straits; see Chapter 1, section 1.0). It should be noted, however, that during the early Jurassic the Cleveland Basin was probably more restricted than the Danish Straits (as implied by the small Mo inventory of the basin; McArthur *et al.*, 2008; Baroni *et al.*, 2018) and was situated in a winter-wet temperate climate as opposed to a cool temperate climate (Rees *et al.*, 2000; Ruebsam *et al.*, 2020a).

As recorded in the lower 112 mm of the section (Fig. 3.39), many episodic fluctuations into a dysoxic to anoxic state occurred, as implied Fe_{HR}/Fe_T ratios exceeding 0.38. However, oxic intervals were sufficiently long to allow for recolonisation of the benthic environment. The high levels of bioturbation effectively homogenised redox signals in the lower 100 mm of the section (see 3.9), and so establishing the lengths, durations, and the frequency of these alternate redox states is very difficult.

Above 10 mm, redox conditions might have fluctuated at a higher rate (Fig. 3.40), which precluded most epifaunal benthic organisms, and all large infauna (although the possibility of meiofauna continuing to create microbioturbation during periods of intense dysoxia remains Savrda & Bottjer 1991, Tyson & Pearson, 1991; Levin, 2002; Schieber & Wilson, 2021). The only organisms that remained were either tolerant towards prolonged dysoxia (but not anoxia), or had reproduction and growth rates sufficiently high that they could become established during the increasingly brief oxic spells. The exclusion of bioturbating infauna resulted in the preservation of the original sediment fabric.

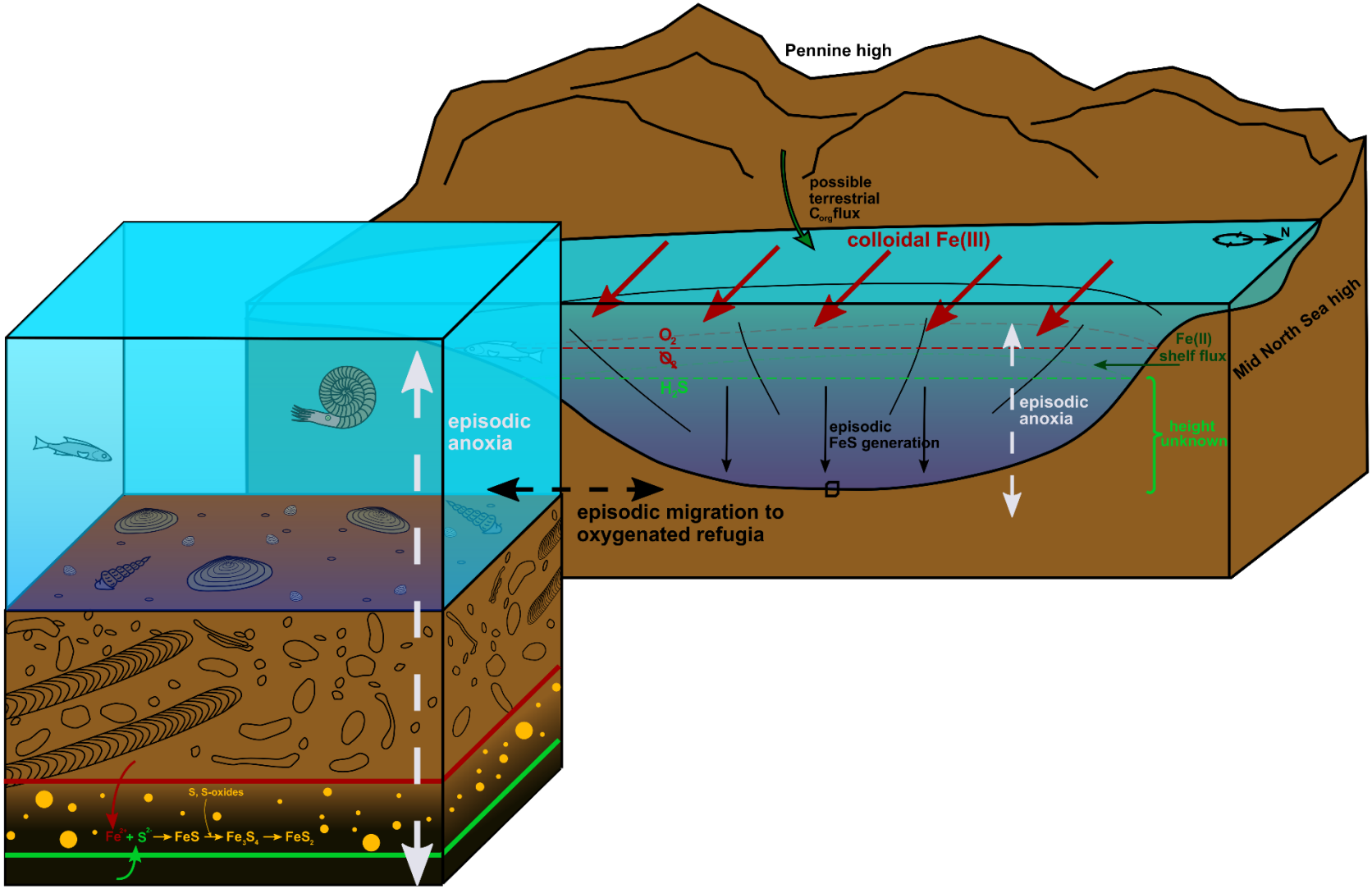

Figure 3.39. Geological reconstruction of the Cleveland Basin during the deposition of the lower part of the LSB (-60 – 10 mm – Lithofacies A). Periods of dysoxia/anoxia were episodic, allowing for the development of a low diversity benthic community, which included active burrowers. Pyrite framboids (orange circles), could only form below the sediment-water interface, where both oxygen and free sulphide

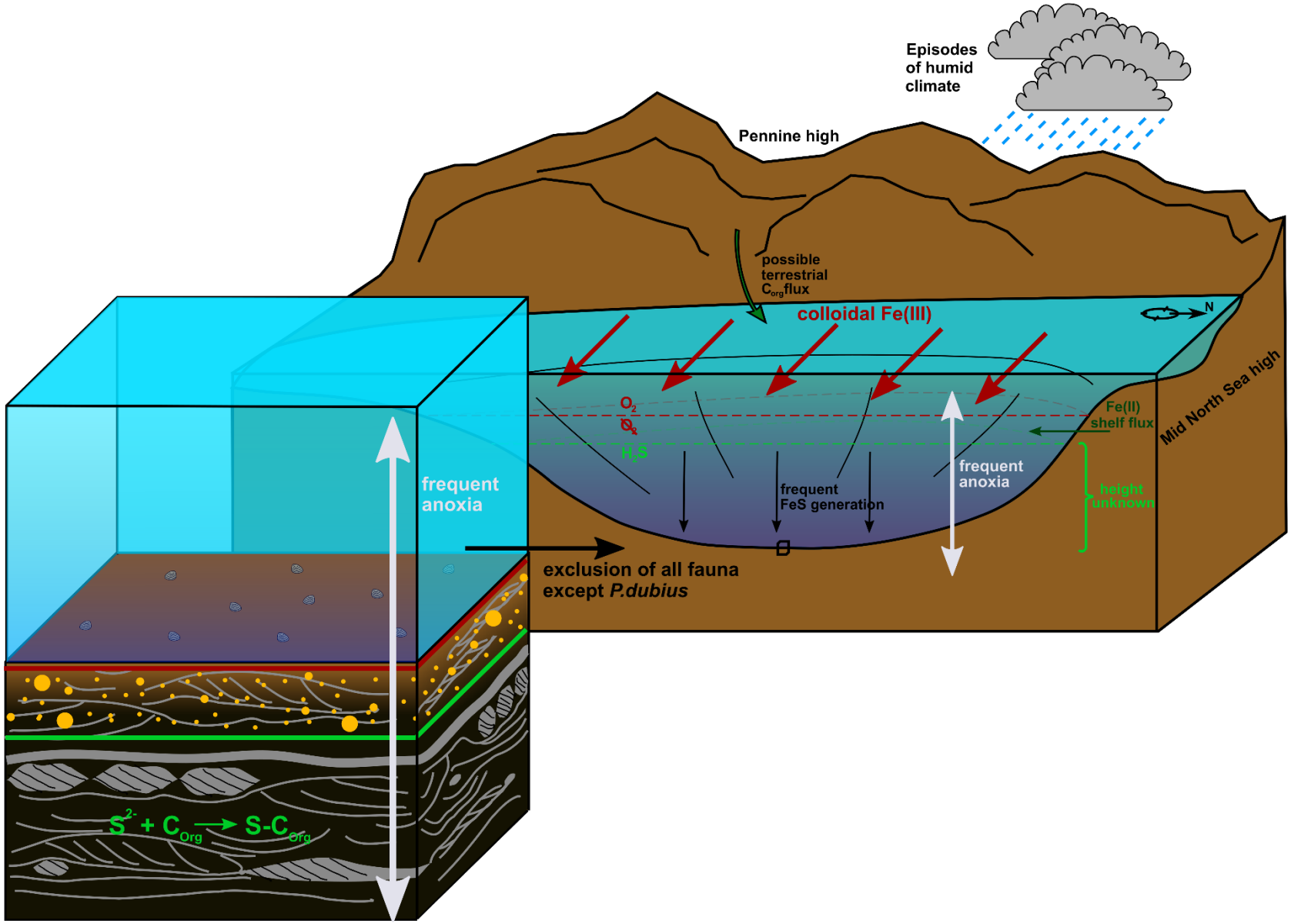

Figure 3.40. Geological reconstruction of the Cleveland Basin during the deposition of the interval between 10 – 52 mm (Lithofacies B). periods of dysoxia/anoxia become increasingly frequent, precluding burrowing behaviours, and most benthic organisms (except *P. dubius*). HCS (grey blebs) is preserved due to the lack of bioturbation, and the increased sulphide content initiates organic matter sulphurisation.

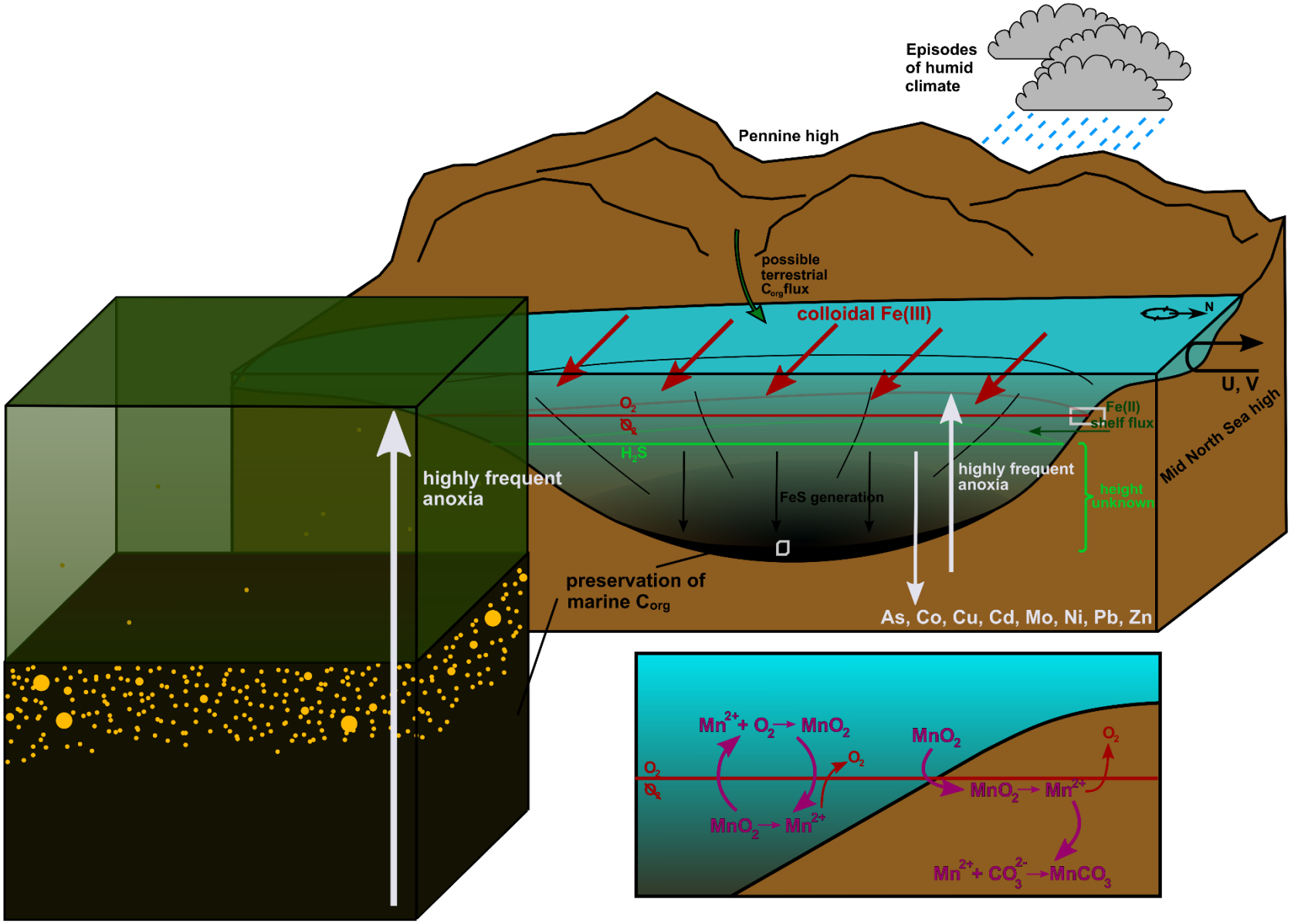

Figure 3.41. Geological reconstruction of the Cleveland Basin during the deposition of the interval charcaterised by highly frequent anoxia (between 52 – 94 mm, Lithofacies B), and the accumulation of labile C_{org}. This interval is also characterised by the formation of pyrite framboids in the water column (euxinia), intense Mn cycling at the chemocline (panel in bottom right), and the sequestration of trace elements in syngenetic pyrite.

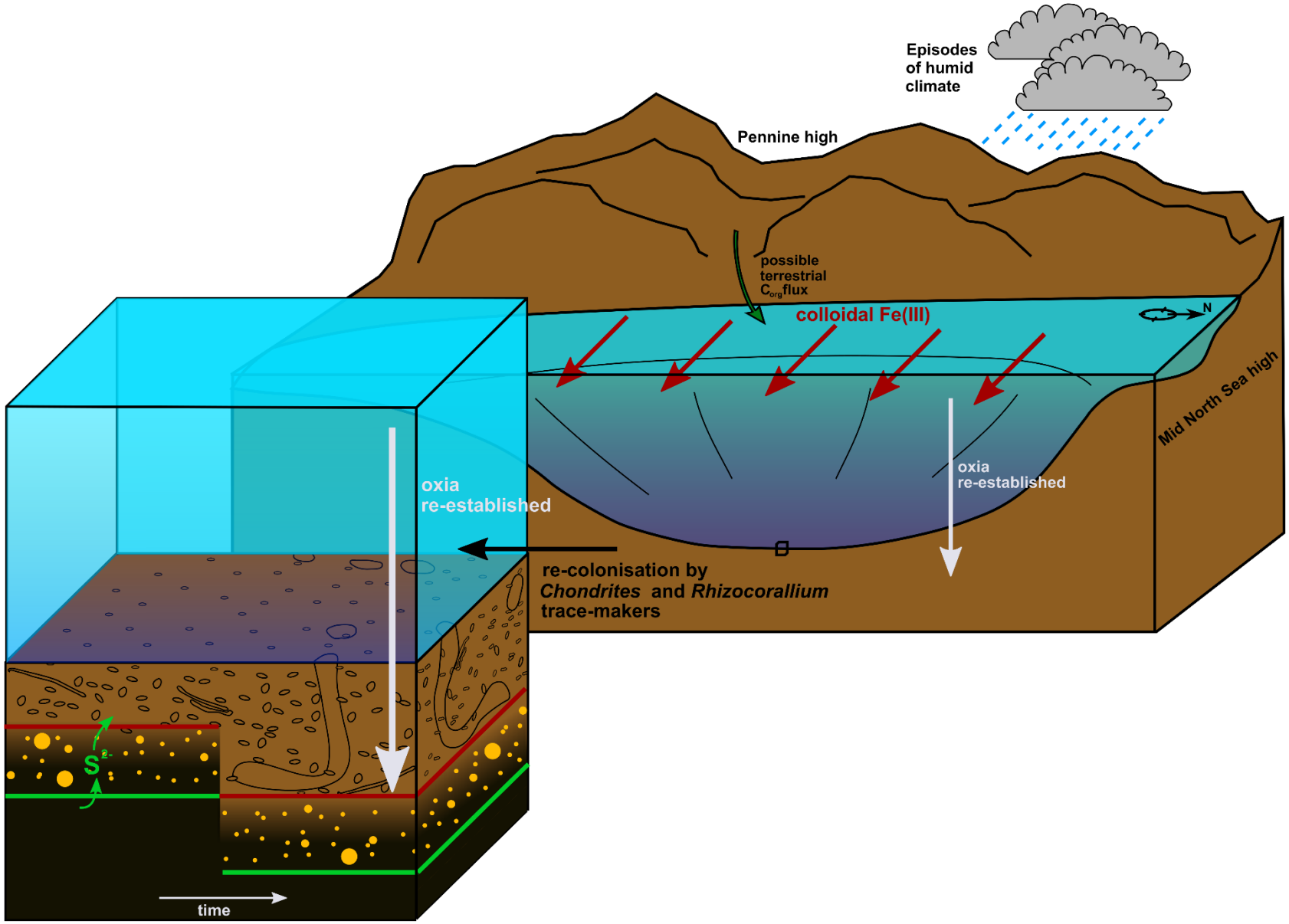

Figure 3.42. Geological reconstruction of the Cleveland Basin during the deposition of the sediments above 94 mm (Lithofacies C). Dysoxic/anoxic periods become far less frequent/severe, allowing for a phased recovery of the benthic community. *Chondrites* trace makers first colonise the sediment (left of reconstruction), with *Rhizocorallium* trace-makers arriving later (right of reconstruction).

Above 52 mm, the crossing of some environmental threshold shifted the system into a very frequently anoxic, redox-stratified state (Fig. 3.41), which allowed laible C_{org} to become buried in the basin depocentere, forming the LSB. The production of sulphide by the anaerobic decay of organic matter, and possibly by sulphate reduction in the water column, led to the generation of large quantities of sygenetic pyrite, leading, eventually, to the characteristically high sulphur content of the LSB.

Above 94 mm, the redox state of the basin gradually shifted into a dysoxic-oxic state (Fig. 3.42), with levels of pyrite formation decreasing, and (presumably) with column stratification becoming increasingly weak. The improvement in bottom-water conditions allowed for colonisation of the sediment by a dysoxia-tolerant animal(s). This trace maker(s) created burrow networks (possibly for the purpose of sulphide farming), and in so doing produced *Chondrites* trace fossils. Sometime after this, with continued bottom water oxygenation, a *Rhizocorallium* producer appeared, and gradually, organisms with more energetically demanding life modes re-joined the benthic community.

4.0 Discussion

4.1 Comparison with the black shales of the Whitby Mudstone Formation

The LSB pre-dates the Mulgrave Shale Member, occurring in the *Protogrammoceras paltum* subzone, rather than the *Cleviceras exaratum* subzone (Howarth, 1973; Hesselbo & Jenkyns, 1995; Simms *et al.*, 2004). This demonstrates that the Cleveland Basin became highly susceptible to the development of dysoxia (or anoxia), due to hydrographic restriction, at least 1.7 Myr before the carbon cycle perturbation at the T-OAE (based on the biozone durations of Page, 1995, 2004). Indeed, moderate oxygen restriction was likely an episodic occurrence in the Cleveland Basin as early as the Hettangian (Atkinson *et al.*, 2020). The high level of basinal restriction is likely to have limited the supply of oxygen from the Tethys Ocean. However, my work implies that significant oxygen depletion could only occur in this setting when an additional condition is met – one that results in a system shift in the oxygenation regime, accompanied by chemocline expansion and stabilisation. The causal mechanism behind this cannot be inferred from the data presented here, however, insofar as similar conditions existed during the later *C. exaratum*

subzone (McArthur *et al.*, 2008), and in the south-west German basin (Posidonia Shale; Röhl *et al.*, 2001), enhanced nutrient flux may have played a role. A shift to a more humid, monsoonal climate during the deposition of the LSB may also be a symptom of higher northern-hemisphere temperatures during a disturbance of the global carbon cycle. Evidence for a negative $\delta^{13}C_{Org}$ excursion in the LSB (Littler *et al.*, 2010) could reflect this, and so an investigation of the $\delta^{13}C_{Terrestrial}$ trend (e.g. French *et al.*, 2014) in the LSB would be worthwhile. $\delta^{13}C_{Org}$ excursions coeval with (or at least near to) the Pl-To are by no means limited to the Cleveland Basin, with similar excursions observed in Peniche, Portugal (Hesselbo *et al.*, 2007), and to varying degrees across north-western Europe (van de Shootbrugge *et al.*, 2013). It is possible that these CIEs are related to brief periods of volcanic activity (on the basis of Hg/TOC spikes; Them *et al.*, 2019 – their fig. 5), and, additionally, some workers have suggested a connection with permafrost destabilisation during the close of the Pliensbachian icehouse (Ruebsam *et al.*, 2019; 2020a).

4.2 Comparison with the other Toarcian black shales

Trace element enrichment and pyrite framboid distributions indicative of anoxia, concomitant with sedimentological evidence for high bottom water energy, have also been documented from the Toarcian-aged black shales of the Dutch Central Graben (Trabucho-Alexandre *et al.*, 2012). Like in the LSB, organic matter accumulation was accompanied by frequent erosion and reworking of the sediment, probably by storm activity.

Thin black shales in the lowermost Toarcian are seen in other sedimentary basins, notably the Posidonia Shale of southern Germany. However, the carbon isotope excursions associated with these basins often show inconsistencies between sites, and are not present at all in more Tethyan, and Pacific localities (van de Schootbrugge *et al.*, 2013 – their fig. 8). This points to some short-lived climatic event in the lowermost Toarcian, that induced a brief period of chemocline expansion in more northerly EES localities – environments with redox states that were far more sensitive than the Tethys to small changes in climate, due to the weakening of an anticlockwise gyre by the rough bathymetry of the EES (Baroni *et al.*, 2018).

4.3 Comparison with the Kimmeridge Clay

The LSB shares some features in common with the thin black shales of the Kimmeridge Clay, notably the presence of erosive sedimentary structures (Oschmann, 1988; Atar, 2020), and relatively depleted levels of U and V (Tribovillard *et al.*, 1994). Both black shales also reflect the combined influence of the local marine environment, and interannual climate variability on redox state. In the Kimmeridge clay, magnetic susceptibility cycles of around 0.5 – 1 cycles per meter have been documented, and related to Milankovitch-driven climate variability (specifically to obliquity and precession cycles; Weedon *et al.*, 1999). In the lower Jurassic, $\delta^{13}C_{org}$ records also show Milankovitch cyclicity, albeit at frequencies of 0.2 – 0.3 cycles per meter. While some workers have argued that these correspond with obliquity (due to the purported presence of large hiatuses in the *D. Tenuicostatum* zone; Boulila & Hinnov, 2017), others contend that they reflect 100 kyr short eccentricity cycles (at least before the T-OAE CIE; Suan *et al.*, 2008; Huang & Hesselbo, 2014; Ait-Itto *et al.*, 2018). These disagreements have led to widely differing estimates for the length of the T-OAE CIE, a debate which has been exacerbated by a lack of formalised agreement on the initiation and termination of the CIE (see Thibault *et al.*, 2018 for a discussion).

Despite their similarities, the LSB is much thinner than many of the black shales of the Kimmeridge clay (with the Blackstone Band being around 6 times thicker; Strahan, 1898). The Blackstone Band is also renowned for its extremely high TOC content (reaching 50 wt.%;), which is around 6 times the highest value found in the LSB. I depositional environments of these two black shales are also markedly different, with the Kimmeridge Clay being deposited in a wide shelfal environment, characterised by seasonally-controlled currents (Oschmann, 1988). Intervals of organic matter enrichment in the Kimmeridge Clay have been attributed to increases in primary production; however, this played a far less important role in C_{org} enrichment of sediments in the Cleveland Basin. TOC and $\delta^{13}C_{org}$ are positively correlated in the Kimmeridge Clay, but negatively correlated within the Mulgrave Shale Member of the Cleveland Basin (Sælen *et al.*, 2000). This implies that, during the deposition of this unit, isotopically light carbon was primarily supplied through new production, with disruption of the chemocline (and resulting phytoplankton blooms) being relatively rare. In the Kimmeridge Clay, by contrast, frequent overturning led to depletion of sub-chemoclinal ^{12}C, and resulted in a more positive $\delta^{13}C_{org}$. As of yet, it is unknown whether the marine carbon-cycle processes associated with the deposition of the Mulgrave Shale Member (as described by Sælen *et al.*, 2000), also applied during the deposition of the LSB; however, given the high level of basinal restriction, this seems likely. An

isotopic analysis capable of targeting the influence of upwelling and stratification on the carbon isotope signature of marine organic matter could better constrain the record of these processes through the LSB, and aid in comparison between the black shales of the *C. exaratum* subzone, and from other successions such as the Kimmeridge Clay. I shall present the findings of such a study in Chapter 5.

4.4 Possible influence of interannual climate variability on the LSB

The LSB corresponds with a negative $\delta^{13}C_{org}$ excursion of -2.5‰ (Littler *et al.*, 2010). Similar excursions in the lower *D. tenuicostaum* zone (and the contemporaneous *D. polymorphum* zone; Page, 2004; Wignall *et al.*, 2005) occur in many European lower Jurassic successions, and capture a 100 kyr short eccentricity signal (Thibault *et al.*, 2018; Ruebsam *et al.*, 2019). However, not all localities contain three thin black shales concomitant with the negative $\delta^{13}C_{org}$ excursions, and not all thin black shales in *D. tenuicostatum* or *H. polymorphum* zones are necessarily accompanied by a distinct negative $\delta^{13}C$ excursion. The Upper Sulphur Band (in the Cleveland Basin), for example, occurs between beds 18 and 19a, in the *D. clevelandicum* subzone (Howarth, 1973), and is not accompanied by a corresponding $\delta^{13}C_{org}$ excursion (Kemp *et al.*, 2005; Littler *et al.*, 2010; Thibault *et al.*, 2018). Additionally, no prominent negative $\delta^{13}C$ excursions occur in the *D. tenuicostatum* subzone (which, in the Cleveland Bain, encompasses beds 20 – 27 of Howarth, 1973) in any European lower Toarcian succession, despite the occurrence of ~1.5 100 kyr cycles within the $\delta^{13}C_{org}$ record (van de Schootbrugge *et al.*, 2013; Ruebsam *et al.*, 2019). This implies that while Milankovitch-driven climate variability during the upper Pliensbachian and lower Toarcian (prior to the T-OAE) could have contributed to oxygen depletion in shallow marine settings (especially highly restricted ones), an additional climatic influence (i.e. volcanogenic CO_2) was probably necessary to trigger black shale preservation. However, assuming an entirely volcanogenic source for the injection of isotopically light carbon during the Toarcian leads to unrealistically high pCO_2 estimates (Ruebsam *et al.*, 2020a), and while Hg/TOC anomalies have been detected in thin black shales from the Pl-To (Percival *et al.*, 2015), the attribution of Hg enrichment in TOC to volcanogenic deposition been questioned (Them *et al.*, 2019). A similar distribution of negative $\delta^{13}C$ excursions could have also been generated through the stepwise collapse of climate-sensitive methane reservoirs at the end of the Pliensbachian and towards the T-OAE (Ruebsam *et al.*, 2019). A compound-specific isotopic analysis capable of evaluating the

signature of a carbon pool(s) in sync with the atmosphere during this event (i.e. a record isolated from any competing influences from marine dynamics) could not only link oxygen depletion with coeval carbon cycle perturbation, but could provide powerful constraints on the source of isotopically depleted carbon, and its dynamics in the lower Jurassic earth system.

5.0 Conclusions

- The crossing of a (possibly climate-influenced) redox threshold at the top of the Cleveland Ironstone Formation resulted in increasingly frequent periods of bottom-water dysoxia/anoxia in the Cleveland Basin, which resulted in the reductive dissolution of reactive Fe, and its subsequent incorporation into syngenetic pyrite. The frequent strong redox stratification in this hydrographically restricted environment also led to an elevated sedimentary Mn content. Through the deposition of the LSB, anoxia frequency increased to the point where benthic organisms were excluded. The resulting lack of bioturbation allowed for the preservation of the sediment fabric, characterised first by hummocky cross-stratification, and then by C_{org}-rich laminae.

- High levels of bioturbation homogenised redox proxy signals (especially Fe_{HR}/Fe_T) in the lower part of the LSB, resulting in a mixed geochemical signal. This does not undermine the utility of the iron-speciation proxies, but instead indicates that the bioturbated black shale facies represented a period of rapidly fluctuating redox, the Fe_{HR}/Fe_T signal of which has since been time-averaged. I recommend that future studies on redox variability in bioturbated black shales employ a multiproxy ichnological, and Fe-redox geochemical approach, and bear in mind that in intensely bioturbated sediments, Fe_{HR}/Fe_T is less a function of anoxia, and more a function of the frequency of anoxia.

- The redox chemistry in the Cleveland Basin was metastable for most of the Lower Jurassic, with environmental perturbations at the Pl-To and the T-OAE triggering shifts into a regime dominated by very frequent anoxia.

Chapter 4 – Palynology and Palynofacies of the Lower Sulphur Band.

1.0 Study aims

In Chapter 3, I speculated that the organic carbon content of the LSB is a mixture of marine and terrestrially derived macerals. If this is true, then a study of the organic microfossil component of the LSB could resolve a wider range of palaeoenvironmental processes than those offered by inorganic geochemistry alone (e.g. palaeocurrent, plankton community structure, the terrestrial environment etc.), and such a study is the aim of this Chapter.

This aim is achieved through a palynological preparation of samples extracted from the LSB sample blocks (Chapter 2, section 5.0). I suggest that the assemblage of land-derived palynomorphs will be able to constrain palaeoenvironmental changes in the terrestrial environment concomitant with redox shifts in the Cleveland Basin. The composition of the planktonic community, and the occurrence of carbon burial can additionally provide independent records of the water column redox state, complementary to the inorganic geochemical data presented in Chapter 3. I anticipate that the proxies mentioned above will, when taken together, resolve environmental processes such as sea level rise/fall and climate change- processes which have the potential to impact (either solely or in concert) the water column redox state of the Cleveland Basin.

I will also attempt to evaluate change in sea level through the LSB, since the model of Fe_{HR} enrichment due to remobilisation of Fe-enriched sediments from proximal settings, requires at least a minor transgression. Moreover, evidence for a transgression during the emplacement of the LSB (if indeed present), needs to be reconciled with the trace element data of McArthur *et al.* (2008) and McArthur (2019), implying hydrological restriction.

2.0 Results

It is important to stress at the outset that the data presented here should be viewed with a small degree of caution, since the palynomorph count employed in each sample was 300, and this deviates from many count numbers utilised in the literature, as a count of 500 is recommended by Tyson (1995), and Slater *et al.*. (2019) counted 500-632. At the time of the analysis I assumed that beyond 300 counts, additional identifications would not greatly shift the results due to the effect of the law of large numbers. Any palynofacies components making up less than 5% of the total count will have a standard deviation of greater than 25% (Traverse, 2007, p. 664). However, I do not believe that the uncertainties associated with this selected count number significantly affect the accuracy of the conclusions I have drawn, since the absolute changes in per cent occurrence between data points that are not statistically significant are (in the worst case) limited to 56%. For example, each point contained between 0 and 9 bryophyte spores, with a mean count of 1.96, or 0.65% of a palynoclast count of 300. According to Traverse (Traverse, 2007, p. 664), this percentage value will have a standard deviation of 80% (i.e. a 95% confidence interval of 160% assuming repeated counts are normally distributed). Therefore, the mean value for bryophyte spore count, with 95% confidence, is 0.65 +/- 1.05%, or about 2 +/- 3 spores. An uncertainty of 5 spores (2+3) is 56% of the variability (0 to 9) in bryophyte spore count throughout the samples, which could mean that no change between two given samples of less than five spores (or 1.7% of the total palynoclast count) is statistically significant (at least at 95% confidence). However, bryophyte spores are the least common variety of palynoclast under consideration in this study, and for a more dominant palynoclast (e.g. phytoclasts), the associated uncertainty is much lower for a total palynoclast count of 300. For example, each point contained between 47 and 145 phytoclasts, with a mean count of 90.6, or 30.2% of the total palynoclast count. This has a standard deviation of 8.5%, or a 95% confidence interval of 17% (Traverse, 2007, p. 664). The mean phytoclast count, with 95% confidence, is, therefore 30.2 +/- 5.13%, or 90.6 +/- 15.4 phytoclasts. An uncertainty of 31 phytoclasts (2×15.4) is approximately 21% of the variability, which is less than half of the equivalent figure for bryophyte spores. Statistically significant (95% confidence) change between any two phytoclast occurrence data points, therefore, must exceed 31 phytoclasts (or 10.3% of the total palynoclast count). The lower than literature-recommended number selected for the palynofacies count also allowed more time to be given to the complementary biomarker analysis (Chapter 5), which also generated a wide range of very palaeoenvironmentaly informative proxy records. Any issues could, however, easily be addressed by a re-analysis of the slides (stored in the School of Earth and Environment at the University of Leeds), utilising a higher palynomorph count, more in line with the recommendation of Tyson (1995), but I do not anticipate that the results of such a recount would be significantly different.

2.1 Palynology and Palynofacies

The amorphous, palynomorph, and phytoclast kerogen groups have all been identified within the LSB, although no conclusive zoomorphs (e.g. foraminiferal test linings), were found. Photomicrographs of representative macerals are shown in Figs. 4.1 - 4.6. AOM dominates the majority of the samples, and as such, follows a similar trend to TOC (Fig. 4.7), ranging from a minimum of 21.3% at -3 mm (in Lithofacies A), to a maximum of 64.7% at 80.3 mm (in Lithofacies B; Appendix 3). However, phytoclasts (predominantly degraded leaf wax cuticle), make up a large proportion of the palynofacies throughout the LSB as well: they range from a minimum of 19.3% at 48.5 mm (Lithofacies A), to a maximum of 48.3% at 139 mm (Lithofacies C).

Dinoflagellates, acritarchs and prasinophyte algae all make a varied, but small contribution to the palynofacies (Fig. 4.7), with dinoflagellates being the most common (1.0-12.0%, with an average of 4.0%), and prasinophytes being the least common (0.0-6.7%, with an average of 1.5%) of the marine palynomorphs. The abundance of dinoflagellates shows a decrease around the top of Lithofacies A (to a minimum of 1.0%), with the abundance of acritarchs showing a corresponding increase (to a maximum of 7.3%), and with the abundance of prasinophytes remaining relatively constant (around 1.5%, excepting at -28 mm where it reaches 6.7%). When normalising the abundance of these groups to the abundance of marine palynomophs (Fig. 4.8), this turnover in the planktonic community becomes more pronounced. The predominance of dinoflagellates shows a precipitous decline from a maximum of 77.2% (of marine plankton) at 28.5 mm, to a minimum of 10.0% at 99.0 mm (but, never declining 0.00%). The dinoflagellate genera *Nanoceratopsis* sp. and *Mancodinium* sp. drive the majority of this decline (Fig. 4.9), with the dominance of *Liasidum* sp. remaining relatively constant throughout.

The relative proportions of *Nanoceratopsis* sp. and *Mancodinium* sp., however, varies widely through the section, from maxima of 85.7% and 68.6%, respectively, to minima of 0.0%. Again, the acritarchs increase in abundance as the dinoflagellates decrease, making up 73.3% of the marine plankton assemblage (their highest value in the LSB) when dinoflagellate abundance is at its lowest. Apart from at –28.5 mm, prasinophytes do not make up more than 34.5% of the marine plankton content of the LSB, but broadly speaking, increases in prasinophyte abundance, and the abundance of articarchs are concomitant.

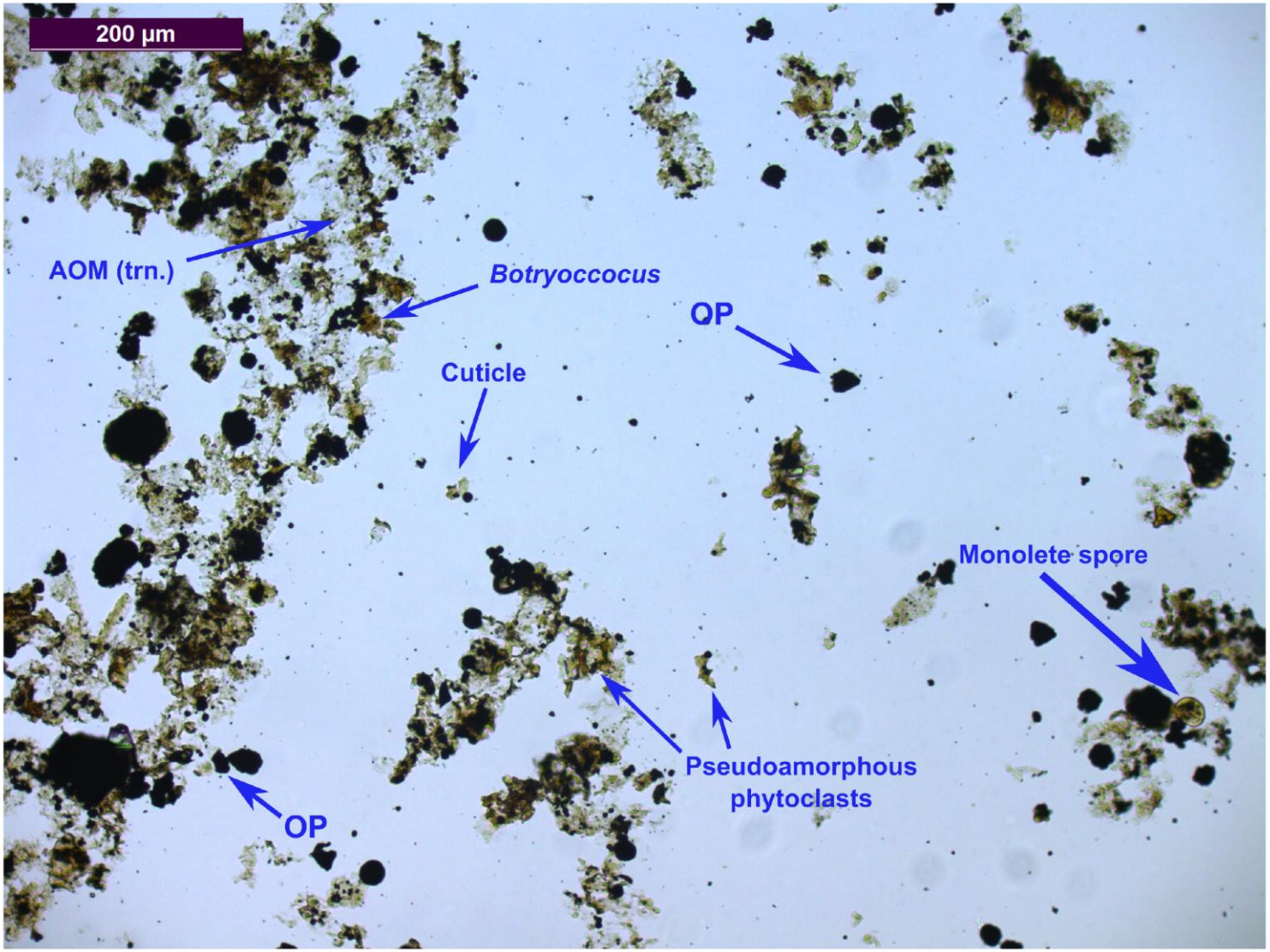

Figure 4.1. Representative photomicrograph of the kerogen assemblage of the LSB (LSB1.1 Pal, height= 38.5 mm, Lithofacies A) with translucent (trn.) AOM, opaque phytoclasts (OP), pseudoamorphous phytoclats, leaf cuticle, *Botryococcus*, and a monolete spore.

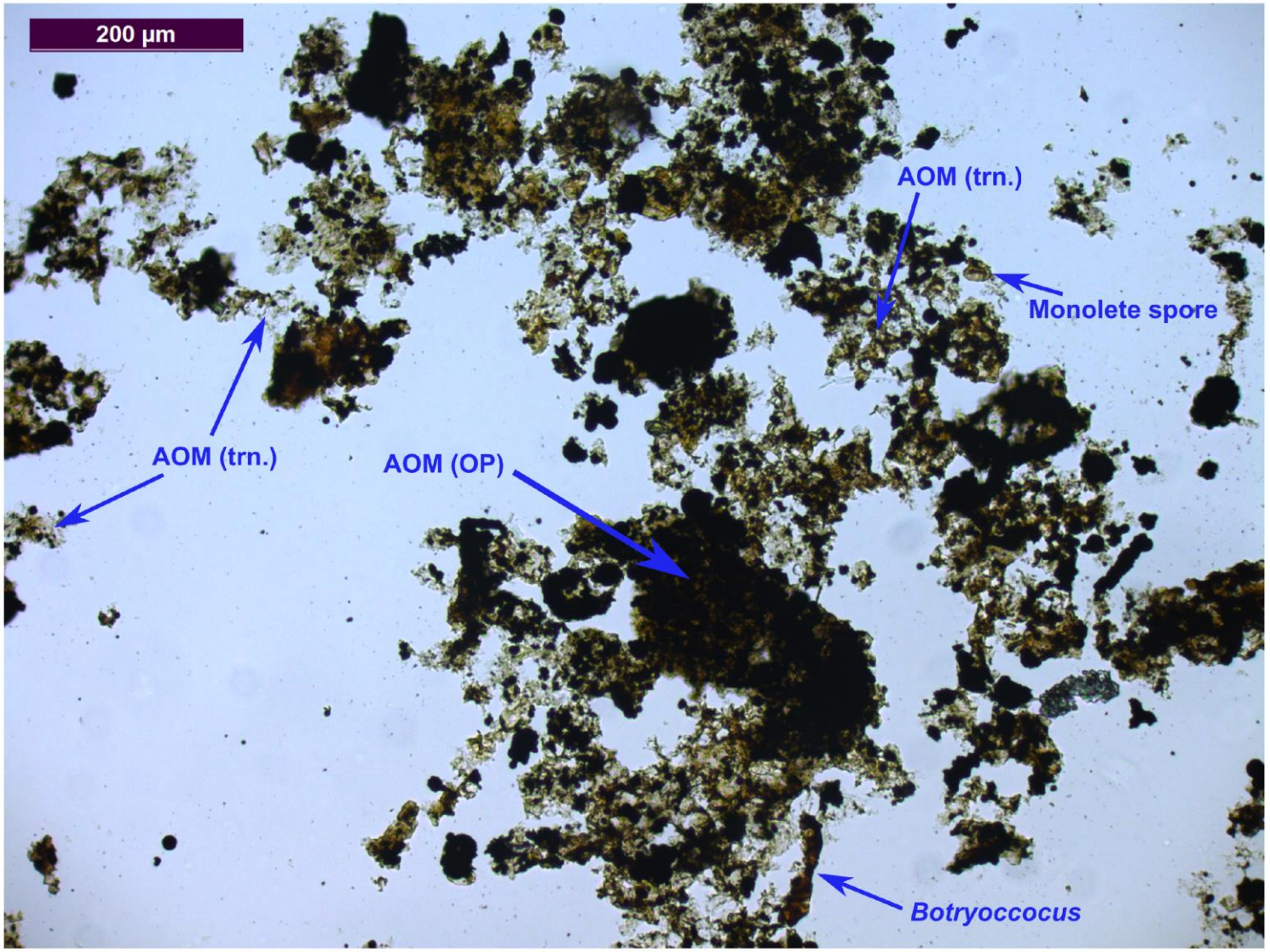

Figure 4.2. Kerogen assemblage of LSB1.3 Pal (height= 56.8 mm, Lithofacies B) with translucent AOM, opaque (OP) AOM, *Botryococcus*, and a monolete spore.

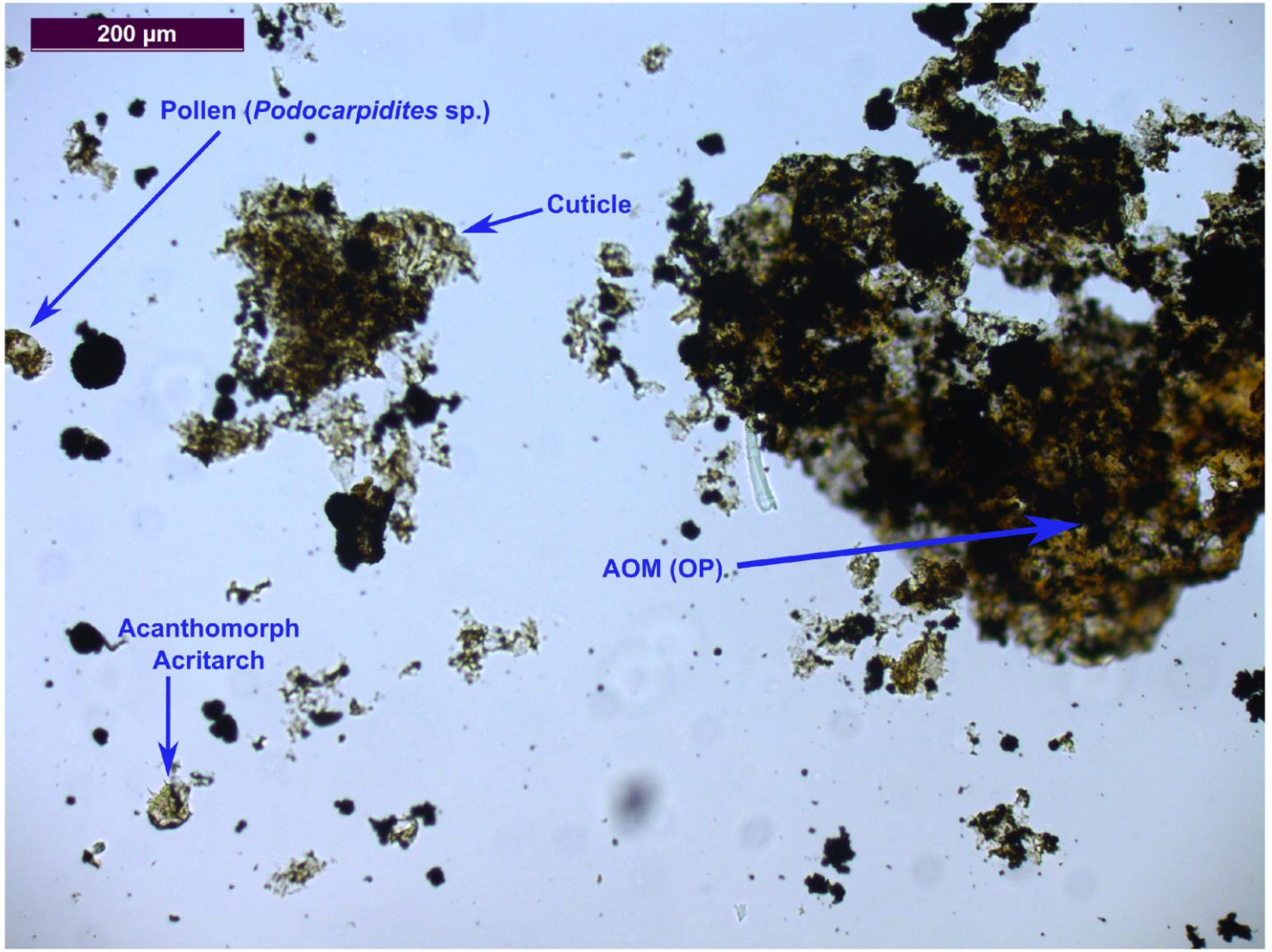

Figure 4.3. Kerogen assemblage of LSB1.8 Pal (height= 99.0 mm, Lithofacies C) with opaque AOM, leaf cuticle, pollen (*Podocarpidites* sp.), and an acanthomorph acritarch.

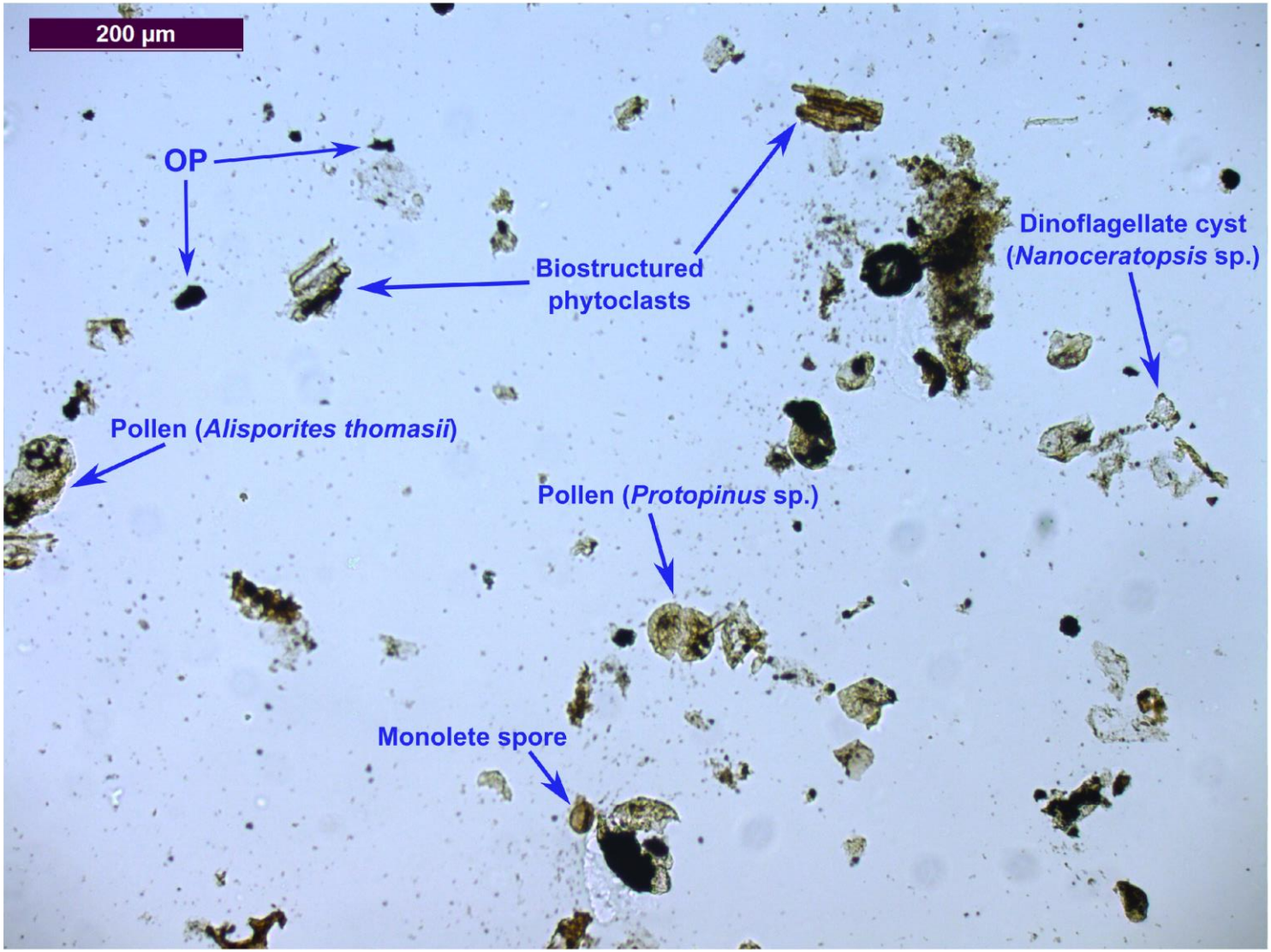

Figure 4.4. Kerogen assemblage of LSB3.1 Pal (height= -3.00 mm, Lithofacies A) with opaque phytoclasts, biostructured phytoclasts, pollen (*Alisporites thomasii* and *Protopinus* sp.), a dinoflagellate cyst (*Nanoceratopsis* sp.), and a monolete spore.

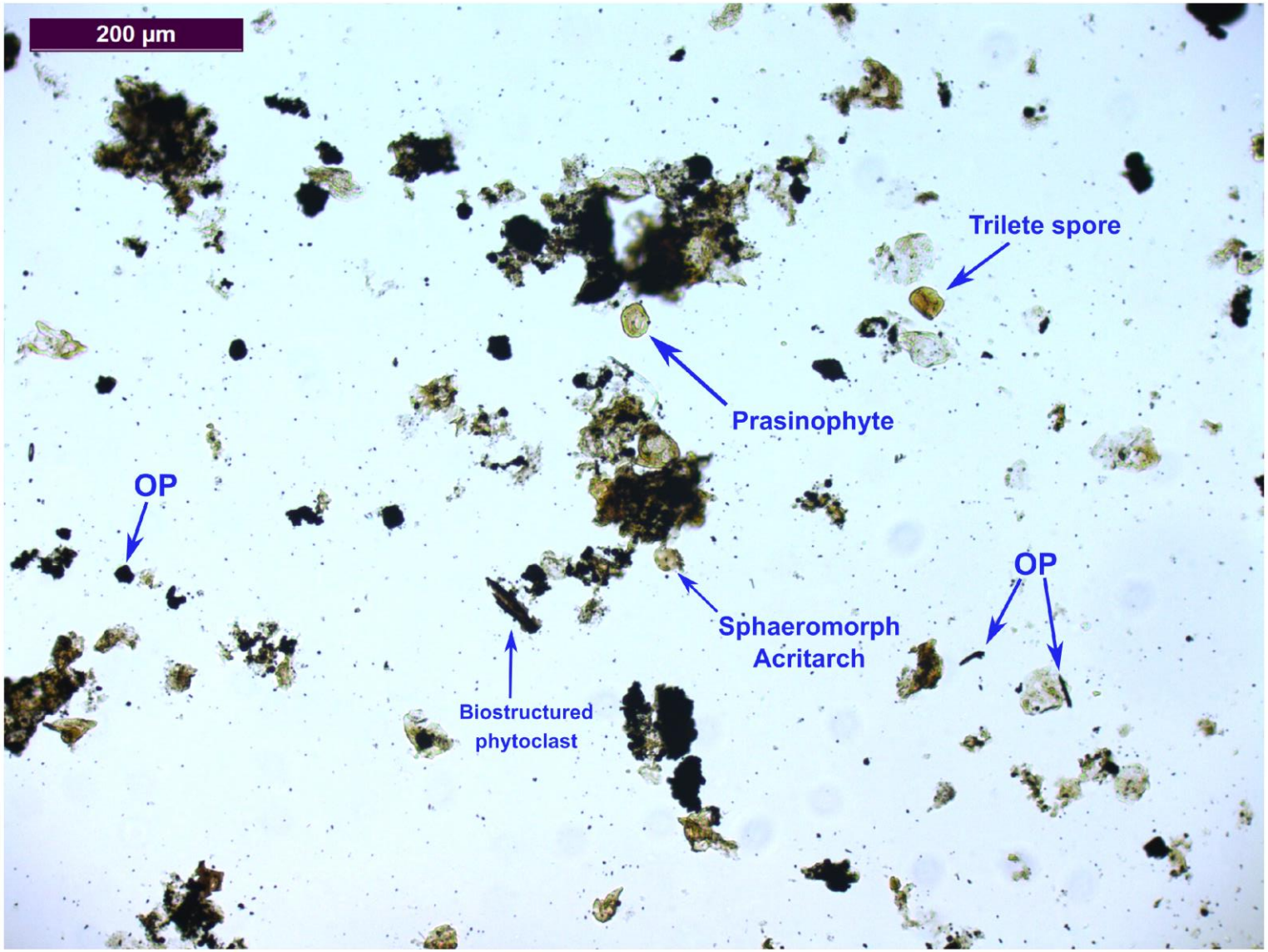

Figure 4.5. Kerogen assemblage of LSB5.5 Pal (height= 139 mm, Lithofacies C) with opaque phytoclasts, a biostructured phytoclast, a prasinophte, a sphaeromorph acritarch and a trilete spore.

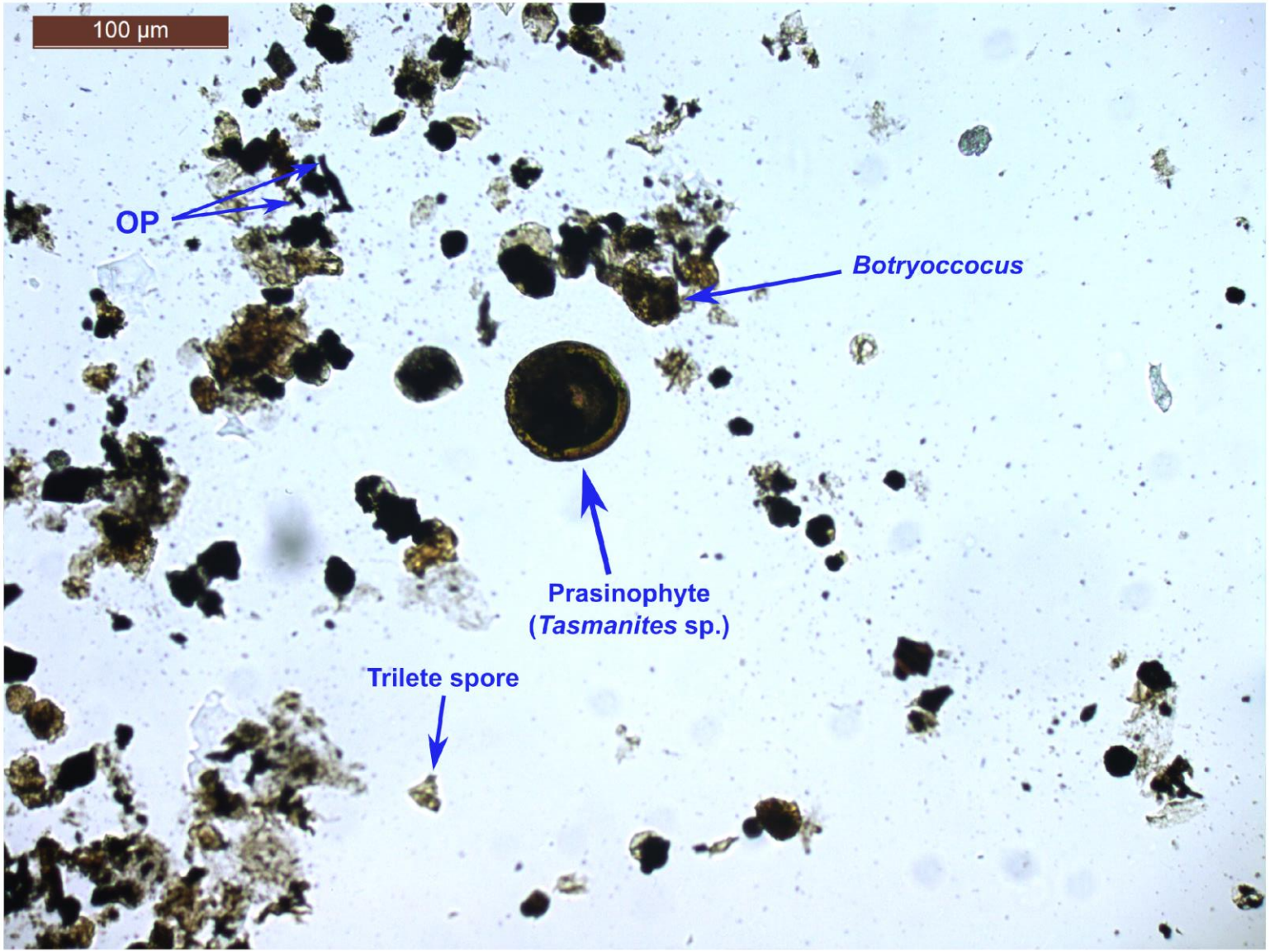

Figure 4.6. Kerogen assemblage of LSB3.0 Pal (height= -28 mm, Lithofacies A) with a well-preserved prasinophyte (*Tasmanites* sp.), opaque phytoclats, *Botryoccocus*, and a trilete spore

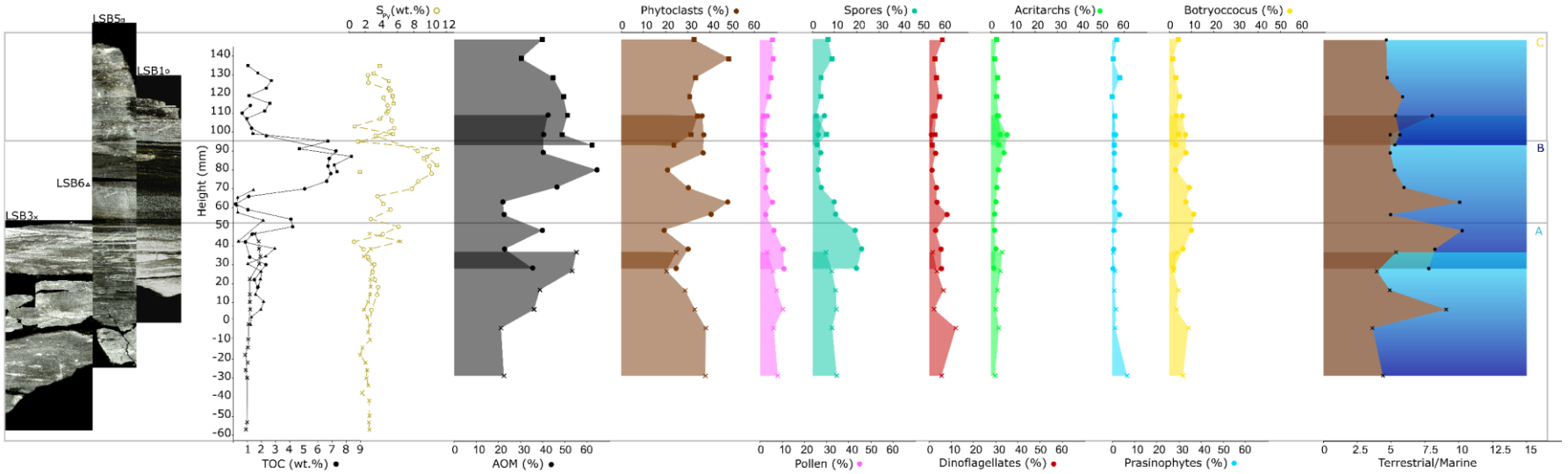

Figure 4.7. Plot of TOC and S_{py} (repeated on all downcore plots, as in Chapter 3), compared with the abundance of various palynofacies components through the LSB. These are; AOM, phytoclasts, pollen, spores, dinoflagellates, acritarchs, prasinophytes, and botryoccocus. A plot of the terrestrial marine ratio (see Appendix 3 for quantification) is also included. As in Chapter 3, a contrast-enhanced photomosaic of scans of the LSB is included. Circles indicate data taken from LSB1, crosses from LSB3, squares from LSB5, and triangles from LSB6.

Both spores and pollen contribute to palynofacies, but spores are more dominant throughout (average of 8.2% compared to 5.1% for pollen). Both reach higher abundance in the upper part of Lithofacies A (up to 22.0% and 10.7%, respectively), compared with the overlying Lithofacies B (down to 1.7% and 1.3%, respectively). Fig. 4.10 visualises the up-section variability in the terrestrial floral assemblage of the LSB. Assemblages are dominated by ferns (average 28.1%), *Chasmatosporites* (15.2%), *Cycadopites* (11.1%), and bisaccate pollen producers (16.5%), with *Classpolis*, *Cerebropollenites*, *Perinopollenites*, *Araucariacites* and *Callialasporites* producers being relatively rare (averages 2.3%, 1.8%, 5.2%, 2.8% and 0.9%, respectively). The contributions of most of the floral groups delineated in Fig. 4.10 show relatively little variability for most of the LSB, apart from at 56.8 mm, 99.0 mm, 7.00 mm and 27.0 mm. At 56.8 mm and 99.0 mm, ferns (and to a lesser extent bryophytes and lycophytes) make up a relatively higher proportion of the assemblage, with the abundances of *Chasmatosporites* and bisaccate producers showing coeval decreases. At these points, ferns, lycophytes and bryophytes together make up over 50% of the terrestrial assemblage. Point increases in the abundance of bisaccate producers (and to a lesser extent *Cycadopites* producers) also occur at 7.00 mm and 27.0 mm, with *Chasmatosporites*, *Classpollis* and *Cerebropollenites* producers showing corresponding decreases.

Although insufficient numbers of terrestrial palynomorphs have been identified to quantify diversity properly, a steady decline in the number of identified genera of terrestrial palynomorphs can be discerned, falling from 25 at 28.5 mm, to a minimum of 7 between 99.0 mm and 109 mm (Fig. 4.10). At this point, a gradual recovery then starts, with the number of identified genera reaching 17 at 139 mm.

Botryoccocus also makes up a significant proportion of the palynofacies, reaching as high as 11.0% at 56.8 mm (Lithofacies B; Fig. 4.7). Its abundance shows two broad peaks – one centered at the basal part of Lithofacies B (peak of 11.0% at 56.8 mm), and the other in Lithofacies A (peak of 8.7% at –3 mm) – superimposed on a broadly constant trend of 5.3%. The lowest value (1.7%) occurs at 139 mm, in the upper part of Lithofacies C.

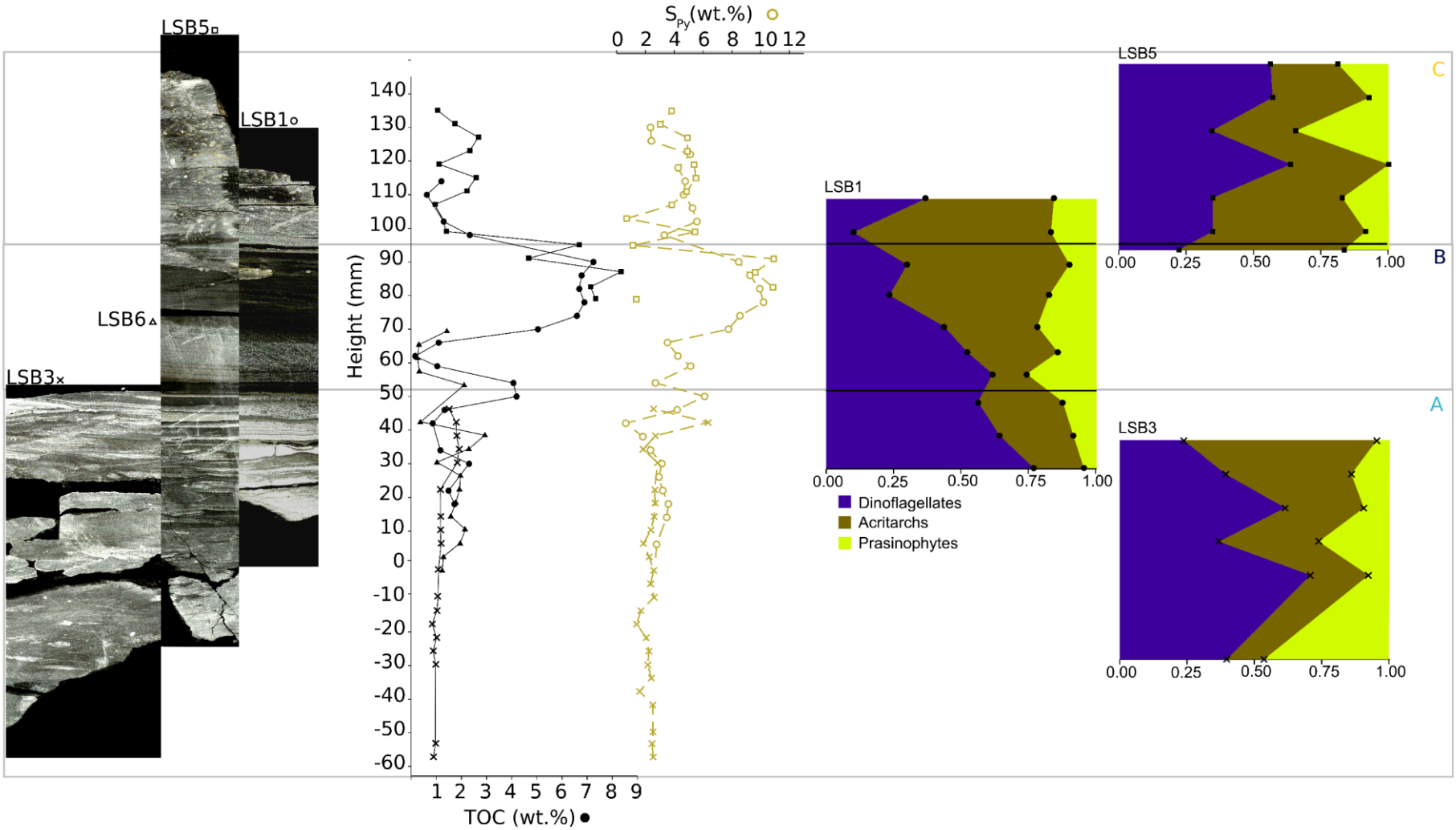

Figure 4.8. Plot of the percentage contribution of dinoflagellates, acritarchs and prasinophytes to the phytoplankton community (here defined as dinoflagellates + acritarchs + prasinophytes) through the LSB. The three different plots correspond to the three different LSB blocks from which palynological samples were prepared, and are labelled accordingly.

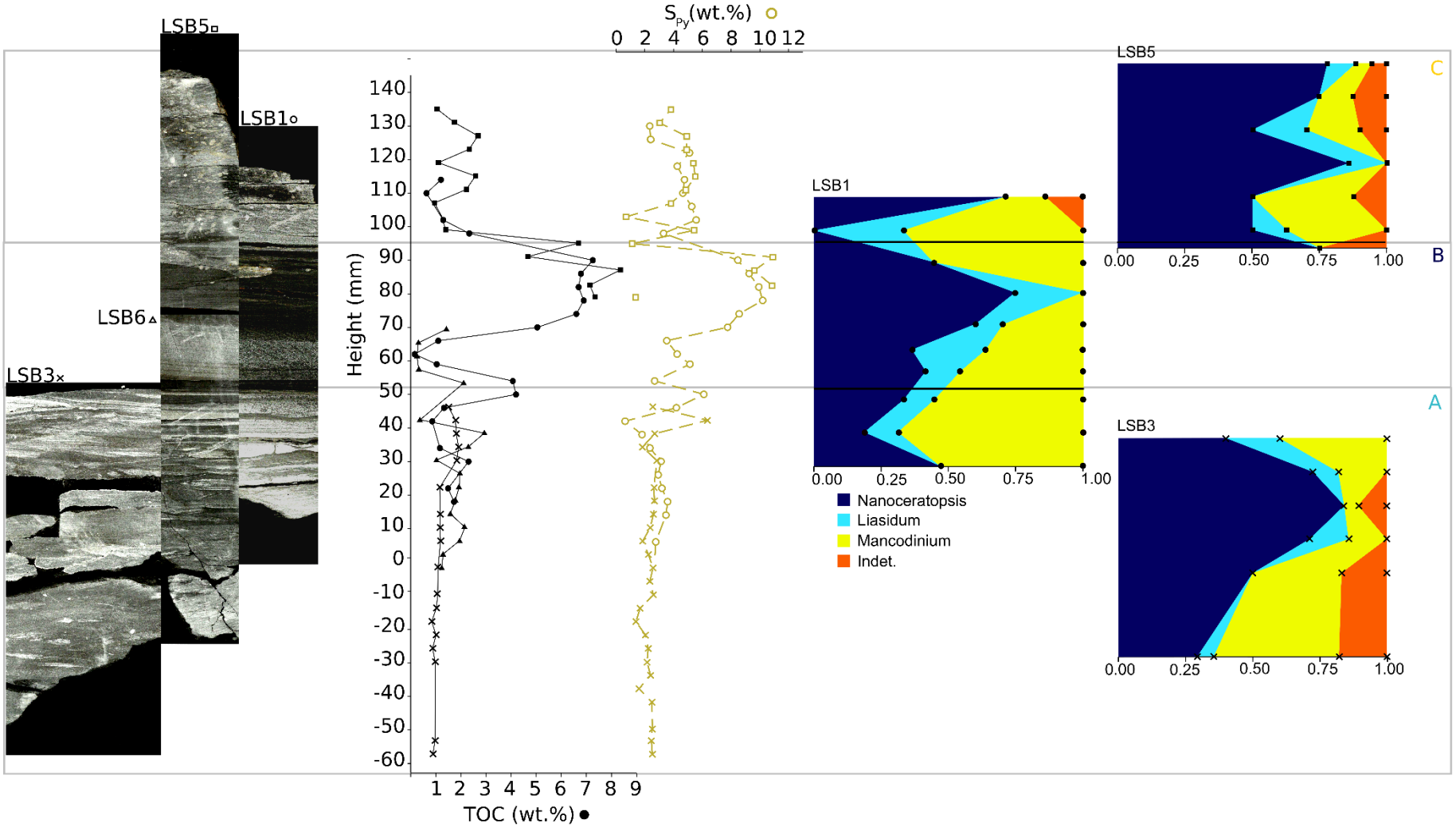

Figure 4.9. Plot of the percentage contribution of *Nanoceratopsis* sp., *Liasidum* sp., *Mancodinium* sp. and indeterminate dinoflagellate cysts to the dinoflagellate assemblage through the LSB. As in Fig. 4.8, the three different plots correspond to the three different LSB blocks.

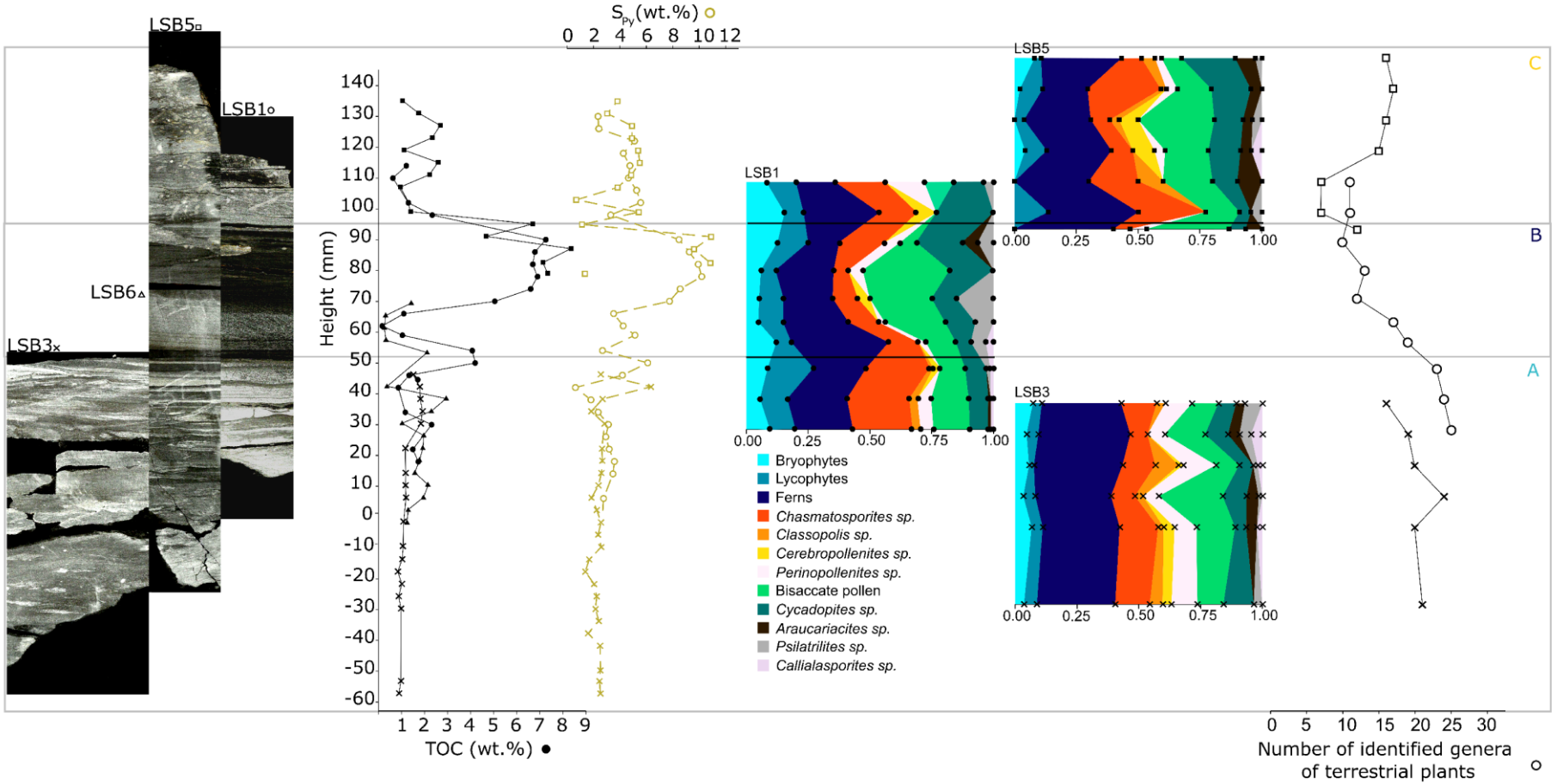

Figure 4.10. The contribution of a range of terrestrially-derived spores and pollen (grouped by genus with the exceptions of bryophytes, lycophytes, ferns and bisaccate producers) to the total spore + pollen count through the LSB. As in Fig.4.8, different plots correspond to different sample blocks. A downcore plot of the number of identified genera (excluding spores and pollen of unknown genus) is also included.

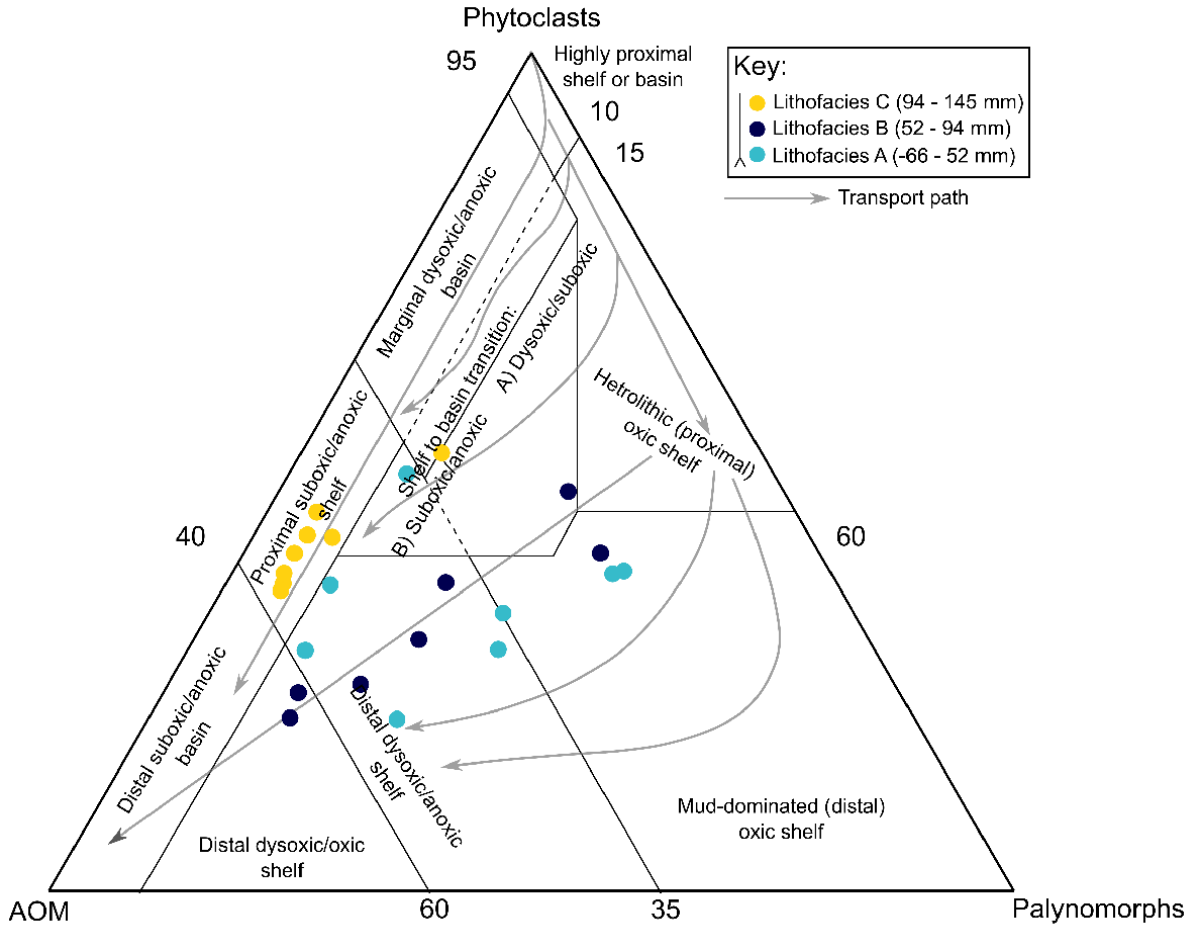

Figure 4.11. Ternary plot of phytoclasts, AOM and palynomorphs (spores + pollen + dinoflagellates + acritarchs + prasinophytes + botryoccocus), after Tyson (1989).

3.0 Interpretations

3.1 Palaeoenvironment via Palynofacies

Unsurprisingly, for a shallow marine section through which HI grows in proportion with TOC (Chapter 3, section 3.5), AOM is both the largest constituent of the sedimentary organic matter, and is most enriched in the bituminous layer of Lithofacies B (characterised by high pyrite and Mo content). The frequent anoxia associated with this interval, and lower bottom-water energy, clearly allowed for a high degree of carbon burial.

Lithofacies A, by contrast, was subject to episodes of higher bottom water energy, as indicated by the presence of hummocky cross-stratification (HCS; Chapter 3, section 3.1), and AOM content is generally lower in the palynofacies samples taken from this interval. Spores are also particularly common in the interval characterised by HCS, forming up to 22.0% of the assemblage (an apparent peak is located at 38.5 mm). In modern depositional settings, spores generally do not travel as far as bisaccate pollen. This is both due to the closer association of spore producers with damp environments typically found around rivers (see Chapter 1, section 9.2.2), and (more importantly) to the greater density of spores as compared with bisaccate pollen (Tyson, 1995, p. 265). More energetic currents might have been able to transport these heavy spores further into the basin depocentre (see section 3.2.0). However, the apparent peak in spore concentration does not match well with the large silty lens at the base of Lithofacies B, where there is good independent evidence for an increased fluvial flux (Chapters 3 and 5). This lens is, instead, characterised by an increase in terrigenous palynomorphs generally (compared with marine palynomorphs), and phytoclasts particularly (mostly as cuticle, see Appendix 3).

Botryococcus makes a small contribution to the palynofacies, but shows a muted peak at 56.8 mm. This can be crudely correlated with an increase in the terrestrial/marine palynomorph ratio, and with the silty lens at 62 mm. So it can be tentatively argued that the increased fluvial flux at this point delivered a greater quantity of *Botryococcus* into the distal marine environment. While Botryococcaceae are exclusively non-marine, freshwater algae (Tyson, 1995, p.312), fragments can be transported a considerable distance, and often make up a minor percentage of marginal (Piaseki, 1986; Robert & Yapaudjian, 1990; Hudson *et al.* 1995) and even shallow marine sediments (Williams, 1992). Andrews & Walton (1990) found occasional spikes in *Botryoccocus* dominance (of up to 43%) in a Bathonian-aged sequence of fossil oyster-dominated lagoons from the Isle of Skye (Scotland, UK), and tied these with episodic increases in fluvial flux. Bearing the above in mind, there is no need to invoke a greater freshwater content of the basin overall (contra Ramirez & Algeo 2020) to explain the presence of *Botryococcus* – its occurrence was primarily controlled by fluvial flux into the marine basin.

While the absolute abundance of dinoflagellates is relatively minor compared to many of the other macerals identified, they decline in Lithofacies B. This decline is controlled primarily by the declining habitability of the benthic environment (see 4.2.1), limiting the opportunities for successful encystment, and killing any dormant cysts before excystment. However, the abundance of dinoflagellate cysts does vary by 3.3 – 11% within Lithofacies A, and in this interval (characterised by HCS), hydrodynamics probably exerts a greater control on cyst abundance. The presence of HCS in this interval indicated that the sediments were deposited above the storm wave base, and so it is likely that the dinoflagellate cysts (which share a hydrodynamic equivalence with fine silt and clay;

Tyson, 1995, p. 285) were swept into seed beds – areas of the seafloor rich in dinoflagellate cysts, with a spatial distribution governed by the hydrodynamic equivalence of the cysts to fine silt (e.g. White & Lewis, 1982). This concentration effect might have also been balanced by a lower rate of dinoflagellate cyst production due to the closer distance to land (see Chapter 5, section 3.2; Wall *et al.* 1977, p.162; Tyson, 1989), and possibly by lower rates of primary production (see Chapter 5, section 3.4). Brief episodes of high dinoflagellate production might have also led to the local saturation of the sediment, and hence a decoupling from the sediment grain size distribution (Lewis, 1988). The fluctuating redox state of Lithofacies A might have also controlled the abundance of dinocysts, albeit to a lesser extent than in Lithofacies B, due to the lower frequency of anoxic episodes. All of these factors, in combination, could explain the variable dinocyst content of Lithofacies A, and the lower variability in Lithofacies B is mainly due to the lower benthic redox state. The greater shoreline distance and generally lower bottom water energy might have also played a role.

The ternary diagram in Fig. 4.11 shows that the majority of the data points from Lithofacies A and B, broadly cluster around the "distal dysoxic/anoxic shelf" field, which is consistent with a large (albeit hydrographically restricted) marine basin, with the depocenter located under a water column prone to oxygen depletion. However, many of the data points lie along a transport path line, which originates from the hetrolithic proximal shelf field. Many of these data points are located within the HSC structures of Lithofacies A, and the silty layer in the lower part of Lithofacies B, both characterised by a distinctly coarser lithology than the black shale of Lithofacies B (Chapter 3). The transport path was originally defined by Tyson (1989), and represents a redirection of material from a less direct shelf-to-basin path, capturing a more phytoclast-dominated palynodebris from the shelf and transporting it into the basin depocenter. Tyson (1989) suggested that this pathway might indicate an increase in the influence of turbiditic or storm-generated depositional processes. Given that the large silty lens in this section (in particular) is associated with geochemical indicators interpreted to represent humid climatic conditions (such as low K/Al and Rb/Al ratios Chapter 3), I argue that enhanced storm activity and resulting episodes of shelf-to-basin transport likely took place here. This also means that some of the dinoflagellate cysts recovered from the generally anoxic Lithofacies B high have been transported into the basin depocentre from more proximal settings that remained oxic during this time. However, few sedimentary structures indicate this, apart from the large silty lens at 62.00 mm.

Fig. 4.11 also shows how most of the data points from the bioturbated Lithofacies C clump in the field associated with sediment deposited on a "proximal suboxic/anoxic shelf". This is somewhat puzzling, given that the *n*-alkane terrestrial-aquatic ratio decreases up section, implying a greater distance from the palaeo-shoreline (see Chapter 5, section 3.2). However, it is also likely that the main palynomorph groups contributing to this clustering (phytoclasts) were transported onto the shelf from a more proximal setting. This is supported by the presence of thin silty horizons in Lithofacies C, and

occasional decreases in the K/Al and Rb/Al ratios (Chapter 3, section 3.4). The "proximal suboxic/anoxic shelf" field also lies at the termination of a phytoclast transport path. Tyson (1989) originally defined this transport path based on data from a fault scarp fan facies, in the Late Jurassic Toni-Thelma oil field (North Sea). In this scenario, phycoclast material delivered to the palynofacies by lateral transport, combined with a high degree of AOM preservation under suboxic/anoxic conditions, vastly dilutes the contribution from other palynomorphs. In my studied section, woody phytoclast debris was likewise added directly into a distal AOM-dominated setting by turbidite-style bottom currents. In other words, small fluvial pulses into the basin might have continued to occur even after the deposition of Lithofacies B. The record of these fluvial pulses is more subtle than that of the large pulse at 62.00 mm, which implies either that the humid climatic shifts were less intense, or that a secular increase in shoreline distance (and sea level, water mass connection, etc.) meant that any nutrient pulse didn not result in a shift to a frequently anoxic state (see Chapter 5, section 4.1), and that the fluvial flux left less of a record in this more distal setting.

3.2 Biological community structure through the LSB

3.2.0 Phytoplankton

While the dominance of dinoflagellates within the phytoplankton community declines through the LSB (concomitant with increases in pyrite and Mo), it never reaches zero (the nadir is 10.0%). This implies that while the declining redox state of the basin negatively affected the dinoflagellate population (probably by interfering with the cyst-forming stage of the life cycle), it did not decline enough to eliminate it. This could either be due to a low intensity of oxygen depletion (i.e. conditions were persistently dysoxic, but not anoxic), or periods of anoxia interspaced by oxia. Given the wealth of proxy evidence in this interval for anoxia and euxinia, it can be inferred that the second of these options is most probable. Essentially, while dinoflagellates were precluded from reproducing via cyst formation during the anoxic periods (which negatively affected their population size), the oxic periods, while short, were long enough for the surviving dinoflagellates to carry out the encystment stage of their life cycle. Therefore, the decline in dinoflagellate dominance (like the Fe_{HR}/Fe_T proxy discussed in Chapter 3) tracks the frequency of oxia, rather than the absolute oxygen level of the basin. The feasibility of at least some periods of bottom-water oxia and consequent dinoflagellate encystment is especially likely, considering that for the samples used for my palynological preparation, 1cm of stratigraphic height (probably representing centuries of sedimentation) was averaged together. Alternatively, the presence of a small number of dinoflagellate cycts in the C_{org}-rich sediments could imply that the frequent anoxia coeval with the deposition of these sediments was

restricted to the basin interior, with marginal environments remaining oxic. Intermittent episodes of shelf-to-basin transport could have, therefore, remobilised cysts formed I these settings and redeposited them in the C_{org}-rich sediments of the basin interior, under frequently anoxic conditions. This mechanism would, however, imply that the highest dinoflagellate cyst content of the sediment would be encountered in the interval characterised by the most energetic shelf-to-basin transport. This is the silty lens at 62 mm, and it is not characterised by an increase in the number of dinoflagellate cysts (Fig. 4.7). While this lens does not contain a high organic matter content in general, dinosporin is a very resistant material (Bogus *et al.*, 2014), and could have probably survived redeposition in the silty lens if shelf-to-baisn transport was indeed the primary delivery mechanism of palynomorphs into the basin.

The decline in dinoflagellate dominance of the phytoplankton community was also driven by both *Nanoceratopisis* sp. and *Mancodinium* sp., implying that both genera were equally affected by declining oxygen levels. However, *Nanoceratopsis* sp. makes a relative recovery in the middle of Lithofacies B (up to 75% of the dinoflagellate assemblage at 80.3 mm), while the *Mancodinium* sp. makes up a larger proportion of the community at 38.5 mm and 99 mm. This could mean that *Nanoceratopsis* sp. was better adapted to exploit the brief oxic recoveries within the core of the LSB (bracketed by more intense anoxia and euxinia) than *Mancodinium* sp. In other words, *Nanoceratopsis* was a more opportunistic genus than *Mancodinium*, which was better suited to exploit oxic spells bracketed by less severe oxygen depletion.

Acritarchs took up most of the empty niche space left by the dinoflagellates. This implies that whatever organisms produced the acritarch palynomorphs were meroplanktonic, and that a decline in the habitability of the benthic environment (and lower water column) would not markedly affect their reproduction. These organisms, therefore, possessed a competitive advantage over dinoflagellates (particularly during the deposition of Lithofacies B), which relied on the increasingly rare oxic events to maintain their population size.

While prasinophytes make a constant, but minor contribution to the phytoplankton community throughout, their dominance does reach a local peak at -28 mm. As mentioned in Chapter 1 section 9.1.1, prasinophytes are uniquely adapted to nitrogenous conditions (high levels of dissolved NH^{4+}). Therefore, this brief peak in their population could be indicative of more frequent nitrogenous conditions at this time – conditions typically associated with a dysoxic, rather than anoxic water column (Quan *et al.*, 2008). This could mean that the lowest 60 mm of the LSB correspond to the beginning of the decline in the redox state of the basin, with the episodes of oxygen depletion being relatively weak (only depleting oxygen to the level of dysoxia, as opposed to full anoxia). The low TOC level of these sediments compared with the rest of the LSB seems to support this. However, a

study of the $\delta^{15}N$ signature of this interval would be needed to directly asses the presence or absence of nitrogenous conditions.

3.2.1 Terrestrial environment

Throughout the studied section, the relative proportions of different terrigenous palynomorph producers do not vary much, indicating that, for most of the LSB, no marked change occurred in the terrestrial environment. However, there are two distinct exceptions to this trend – moderate increases in the dominance of bryophytes, lycophytes and ferns (and corresponding declines in the dominance of most of the other identified plant groups) at 56.8 mm and 99 mm. What is particularly noteworthy is that these peaks match up with the negative peaks in K/Al and Rb/Al described in Chapter 3 (sections 3.4 and 4.4), and with positive peaks in the terrestrial-aquatic ratio (Chapter 5, sections 2.1.1 and 3.2). This corroborates the hypothesis – formed in Chapter 3 – that the silty lenses of the LSB (particularly the large lens at 62.00 mm) indicate periods of enhanced fluvial flux to the Cleveland Basin (and the cation leaching of clay profiles in the surrounding hinterland), initiated by an episode of relatively humid climate. Bryophytes, lycophytes and ferns are all moisture-loving plants (Chapter 1; 9.2.2), and under a relatively humid climate, it is probable that a greater niche space opened up for these plant groups. During the intervening drier periods, the moisture-loving plants then lost their temporary competitive advantage, and the ecospace became filled by dry-adapted bisaccate producers, cycads, and *Chasmatosoprites* instead. Interestingly, no peaks in the dominance of *Perinopollenites* sp. are seen concomitant with the peaks in moss/fern dominance, even though this genus is adapted to wetter climatic conditions (Stukins *et al.*, 2013).

No marked peak in the abundance of *Cerebropollenites* was observed. Increased prevalence of this genus has been associated with the T-OAE (Koppelhus & Dam, 2003) and Tr/J (Belcher *et al.*, 2010), suggesting an association with hyperthermal events. The absence of such a peak in the LSB implies that the ambient temperature in the terrestrial environment did not rise greatly, and possibly that the episodes of enhanced fluvial flux were due to an increase in climatic humidity, but not temperature. This situation – local to the Cleveland Basin – seems difficult to reconcile with wider evidence for a slight increase in global temperatures at this time: a compilation of $\delta^{18}O$ measurements of belemnites from across Europe implies the presence of a negative shift of around 1.0 ‰ occurred around the Pl-To (Dera *et al.*, 2011; Ruebsam *et al.*, 2019). Additionally, a recent TEX86 analysis of Pliensbachian-Toarcian sediments from two localities in the Tethyan realm implies that the Pl-To was accompanied by a temperature rise as of as much as 5°C (at least in these localities; Ruebsam *et al.*, 2020b). In contrast, $\delta^{18}O$ analysis of belemnites ($\delta^{18}O_{bel}$) from the Cleveland Basin (Hesselbo & Korte, 2011;

Korte *et al.*, 2015) shows that SSTs did not change appreciably from the late Pliensbachian event through to the T-OAE (varying between 5 – 20°C). This dataset, however, does not sample the LSB itself, with the two closest $\delta^{18}O_{bel}$ values being 16 cm below, and 45 cm above the LSB. This either implies a period of climatic stasis on the order of 100 kyr across the Pl-To, or that this dataset is of insufficient resolution to capture short-term (ca. 10 kyr) variability. It is also possible that the rise SST that characterised the Pl-To in the Tethyan realm was simply not expressed in the northern EES. A palaeontological study of the T-OAE indicates that it was anoxia, rather than temperature, that was the primary kill mechanism for extinctions in the northern EES, (Wignall *et al.*, 2005), and it is probable that this applied to the Pl-To as well. Future work in the LSB employing $\delta^{18}O_{bel}$, or possibly TEX86 (Ruebsam *et al.*, 2020b) would be needed to better assess temperature change through this interval (see Chapter 5, section 4.1).

Bisaccate producers are slightly better represented in the terrestrial community in Lithofacies B, which could indicate a shift to a wetter terrestrial environment (Slater *et al.* 2019). However, bisaccate pollen is very susceptible to transportation (e.g. Tyson, 1989), with grains from the modern genus *Pinus* remaining afloat for several weeks to a year (Hopkins, 1950; Traverse 2007) – although some modern bisaccae pollen grains, such as *Abies* sp. do not remain afloat for this long (Mudie, 1982). The higher bisaccate content of the LSB with respect to the Toarian CIE interval is also in line with the observation of Slater *et al.* (2019) that bisaccate producers were more prevalent around the Cleveland Basin during the Pliensbachian.

The gradual decline in the number of higher plant genera through the LSB could be related to a longer-term stress on the terrestrial environment – possibly forced by a global-scale carbon cycle disruption. Alternatively, the decline in the number of plant genera could be only apparent, and related to an increased distance of the depositional environment from the palaeo-shoreline: as the pollen and spore content of the sample decreases, then the number of plant genera that can be identified will also decrease. Indeed, the palynomorph count through the LSB was insufficient to quantify diversity (i.e. the Simpson D-1 index; Slater *et al.*, 2019), so separating the magnitude of these two competing influences is difficult. However, a longer count of the palynofacies slides could easily test this.

4.0 Discussion

The shift in the composition of the phytoplankton community described in 2.1, provides further evidence in favour of a secular decline in the habitability of the benthic environment of the Cleveland Basin through the deposition of the LSB, mediated by an increase in the frequency of anoxia. However, a complete "blackout" of dinocysts from the palynological assemblage was not observed. This contrasts with the data of Slater *et al.* (2019), who documented a steep decline in the occurrence of dinoflagellate cysts in the Mulgrave Shale member of the Cleveland Basin, frequently reaching 0.0%. During these periods, the plankton community became dominated by sphaeromorph acritarchs, which were interpreted as representing a period of algal dominance of the marine community (this is corroborated by a positive shift in the sterane/hopane ratio through the same interval; French *et al.*, 2014). However, the lowest dinoflagellate count I report is 3 – from an interval 50 – 150 times shorter than the Toarcian CIE (see Chapter 1, section 6.0). This implies that the duration of exposure of the benthic marine environment to frequent anoxia exerts a control on the decline of dinocyst formation: a period of several millennia (approximate duration of Lithofacies B) is sufficient to reduce dinoflagellate dominance by about 70%. A longer duration of exposure to episodes of benthic anoxia is required to drive out dinoflagellates completely. Other palaeoenvironmental variables are also known to influence temporal variability in dinocyst counts, and so it is also possible that while declining oxygen levels made the Cleveland Basin less hospitable to dinoflagellates, no compounding stresses from temperature or salinity changes were present (see Chapter 1, section 9.1.1) The occurrence of infrequent dinoflagellate cysts in the core of the LSB also corroborates (along with the infrequent occurrence of *P. dubius*) the occurrence of brief reoxygenation episodes in these intervals. However, since dinoflagellates only require days to years (less than a decade) of oxia for cyst formation and germination (Armstrong & Brasier, 2005), the presence of dinoflagellate cysts is not incompatible with evidence for a generally anoxic environment.

Unlike purported dinocyst blackouts such as at the Tr/J (Bonis *et al.*, 2010), the decline in dinoflagellate dominance of the phytoplankton community driven here is driven by two genera (as opposed to one species), which both made relatively important contributions to the community before the decline in benthic habitability. In other words, the decline in the frequency of periods of oxia in the Cleveland Basin affected the life cycles of all the dinoflagellate genera. It could be argued that the dinoflagellate community of the Cleveland Basin was, as a whole, less well adapted to a decline in benthic redox state than the dinoflagellate community of the Upper Triassic Lilstock Formation (Bonis *et al.*, 2010). However, the low dinoflagellate count of my slides makes this claim rather speculative.

Unlike the Mulgrave Shale Member, the land plant sporomorph assemblage of the LSB does not indicate a board shift towards a hotter climate, but rather, a generally stable climate punctuated by episodes of enhanced humidity. No large increases in the dominance of genera typically associated with high temperatures are seen, and most wet climate-adapted genera become increasingly dominant within the terrestrial community at 56.8 mm and 99 mm. The palynological record of the terrestrial environment through the LSB, therefore, corroborates inorganic (Chapter 3) and organic (Chapter 5) geochemical evidence for brief episodes of a more humid climate during the deposition of the LSB. While climatic humidity can be influenced by geographically localised factors (such as orogeny), it can also be influenced by global climate change. While it has been postulated (based primarily on shifts $\delta^{18}O_{bel}$ data) that a magmatic plume emplaced a thermal dome in the North Sea around this time (Korte & Hesselbo, 2011; Korte *et al.*, 2015), there is little evidence for any uplift in the region of the Cleveland Basin, that could have led to a disruption of precipitation patterns. Furthermore, it is probable that the Pl-To boundary (to which the LSB is likely concomitant, being the basal unit within the *D. tenuicostatum* zone and accompanied by a negative $\delta^{13}C_{org}$ excursion; Hesselbo & Jenkyns, 1995; Simms, 2004; Littler *et al.*, 2010; Powell, 2010) was characterised by a short period of global warming, possibly due to enhanced activity of the Karoo-Ferrar LIP (Ruebsam *et al.*, 2019). However, attributing the fluvial pulses recorded in the LSB to any change in global climate requires additional proxy evidence (I present such a study in Chapter 5), and needs to be reconciled with the apparent absence of floral markers for a hyperthermal event. It is also likely, given the high hydrographic restriction of the Cleveland Basin at this time (Chapter 3), that a fluvial pulse would have raised the nutrient loading of the basin, and induced local salinity stratification. Both these factors would have made the basin more suspectable to episodes of eutrophication, and therefore, the fluvial pulses may have played a causal role in the change in basin redox. I also test this hypothesis in Chapter 5.

Shelf-to-basin transport was a major control on palynomorph transport, since increases in the proportions of phytoclasts (and, to a small extent, *Botryococcus*) are linked to the emplacement of silty lenses, and the position of the samples within phytoclast-AOM-palynomorph ternary space could easily be controlled by the palynofacies transport paths of Tyson (1989). These palynodebris components are strongly associated with terrigenous settings, and in order to be preserved in significant quantities in the basin depocentere, they require lateral transport from marginal settings (via the basin shelf). What is interesting is that although episodes of shelf-to-basin transport were a common feature of the LSB, these do not seem to have disrupted the redox regime to a great extent: the large silty lens at 62 mm contains reworked (but not re-oxidised) pyrite framboids (Chapter 3; section 3.1), and is not associated with a relative recovery in the dominance of dinoflagellates (Fig. 4.8). I shall further examine the possibility of shelf-to-basin transport under anoxic conditions in Chapter 5.

The slight shift in the spore and pollen content of the LSB (at around 52 mm) could be indicative of a shift to a more distal environment. However, both spores and pollen have well-documented hydrodynamic equivalence to silt (Tyson, 1995, p. 261). The apparent shift could therefore merely indicate dilution of the silty component of the sediment by clay at the boundary between lithofacies A and B – although this is also a distinctive feature of deeper water facies. Ultimately, distance to the palaeoshoreline is better constrained by different sets of proxy data presented in my work, such as the terrestrial/aquatic ratio (Chapter 5).

5.0 Conclusions

- Dinoflagellate dominance of the phytoplankton community within the Cleveland Basin was negatively impacted by the increased frequency of bottom water anoxia during the deposition of the LSB. However, it is possible that brief periods of bottom water reoxygenation (lasting at least weeks to years) permitted a limited degree of dinoflagellate cyst formation even during the interval characterised by the most frequent anoxia. The vacant ecospace left by the dinoflagellates was reoccupied mainly by acritarchs.

- The terrestrial environment around the Cleveland Basin was generally warm and dry during the deposition of the LSB, but was intermittently more humid. These conditions favoured the growth of wet-adapted bryophytes, lycophytes and ferns. Episodes of humid climate were strongly linked with enhanced fluvial flux (which may have played a causal role in oxygen depletion), and were possibly related to global climatic perturbation at the Pl-To boundary. These assertions, however, need to be tested against additional suites of (organic geochemical and isotopic) proxy data.

- Shelf-to-basin transport was a common feature of the LSB, and shelf-to-basin transport was a major pathway for the delivery of palynomorphs (especially phytoclasts) to the basin depocentre. The shelf-to-basin transport episodes also do not appear to have significantly affected the redox state of the basin.

- The palynological data presented here cannot conclusively demonstrate a general increase in palaeoshoreline distance through the LSB, due to the dominance of shelf-to-basin transport, and hydrodynamic equivalence effects.

Chapter 5 – An organic geochemical and isotopic study of the Lower Sulphur Band

1.0 Study aims

In Chapter 3, the progressive decline in the habitability of the benthic environment of the Cleveland Basin, and the enhanced preservation of TOC, pyrite and trace elements in the LSB, was attributed to the increased frequency of anoxic/euxinic chemocline expansion episodes in a restricted basin. Little could, however, be concluded about the causal environmental mechanisms behind chemocline expansion, or those responsible for its frequency. In Chapter 4, section 5.0, it was additionally speculated that there was a causal link between enhanced delivery of nutrients (supplied by episodes of enhanced fluvial flux), and the development of more frequently eutrophic conditions in the basin. In Chapter 3, section 4.3, I determined that euxinia was present during the deposition of the LSB (especially in Lithofacies B), but could not determine how far up the water column it extended: although Mo/Al was enriched up to 3.43 ppm/wt.%, it was difficult to tell whether the amount of Mo drawdown was limited by the size of the Mo inventory, or the extent of euxinia. Finally, the possibility of a link between climatic and basinal redox state changes, and global climate disruption at the Pl-To, was raised (Chapter 1, section 9.3; Chapter 3, section 5.0), and I suggested that an isotopic analysis could be used to test this hypothesis (Chapter 3, section 4.6). In this Chapter, I will present the results of an organic geochemical (biomarker) study, and a compound-specific isotopic study of the LSB. I will also discuss whether or not the data support either a nutrient enhancement model for basinal redox disruption, the expansion of euxinic conditions into the photic zone during the deposition of Lithofacies B, or a link between the paleoenvironmental changes observed, and the wider climatic conditions of the Pl-To.

2.0 Results

2.1 Organic geochemistry and biomarkers

2.1.1 *n*-Alkanes

I have identified chain *n*-alkanes from *n*-C_{12} to *n*-C_{40}, in the LSB, along with pristane and phytane (see Fig. 5.3 for a representative chromatogram). *n*-alkane content follows a very similar trend to TOC (ranging between 10 – 154 mg/g), implying *n*-alkanes make a relatively constant contribution to sediment TOC. Pristane (pr) and phytane (phy) show similar trends, with pristane content between 1 – 35 mg/g and phytane content between 0 – 13 mg/g.. pr/*n*-C_{17} and phy/*n*-C_{18} gently increase through Lithofacies A, rising by 1.33 and 0.903, respectively. In Lithofacies B, both trends reverse, and reach a minimum at 84 mm. After peaking briefly at the base of Lithofacies C, both trends finally begin to decline, reaching 1.99 and 0.838 at 145 mm, respectively. A pr/*n*-C_{17} vs phy/*n*-C_{18} cross plot (Fig. 5.4) shows that the LSB has undergone a small degree of thermal maturation, and has a mixed organic matter source, corroborating the conclusions drawn from my Rock-Eval data (Chapter 3, section 4.10). Pr/phy gently declines through the section, reaching a minimum of 1.59 at 63 mm before gently recovering (Fig. 5.2). The terrestrial/aquatic ratio (TAR) gently declines from 0.666 at -22 mm, reaching a minimum of 0.217 at 94 mm, before recovering to 0.44 at 145 mm. This trend, however, is interrupted by two prominent positive single-point excursions at 62 mm and 102 mm, the first of which corresponds with the 13 – 18 mm thick silty layer, and one of the prominent troughs in K/Al described in Chapter 3, section 3.4.

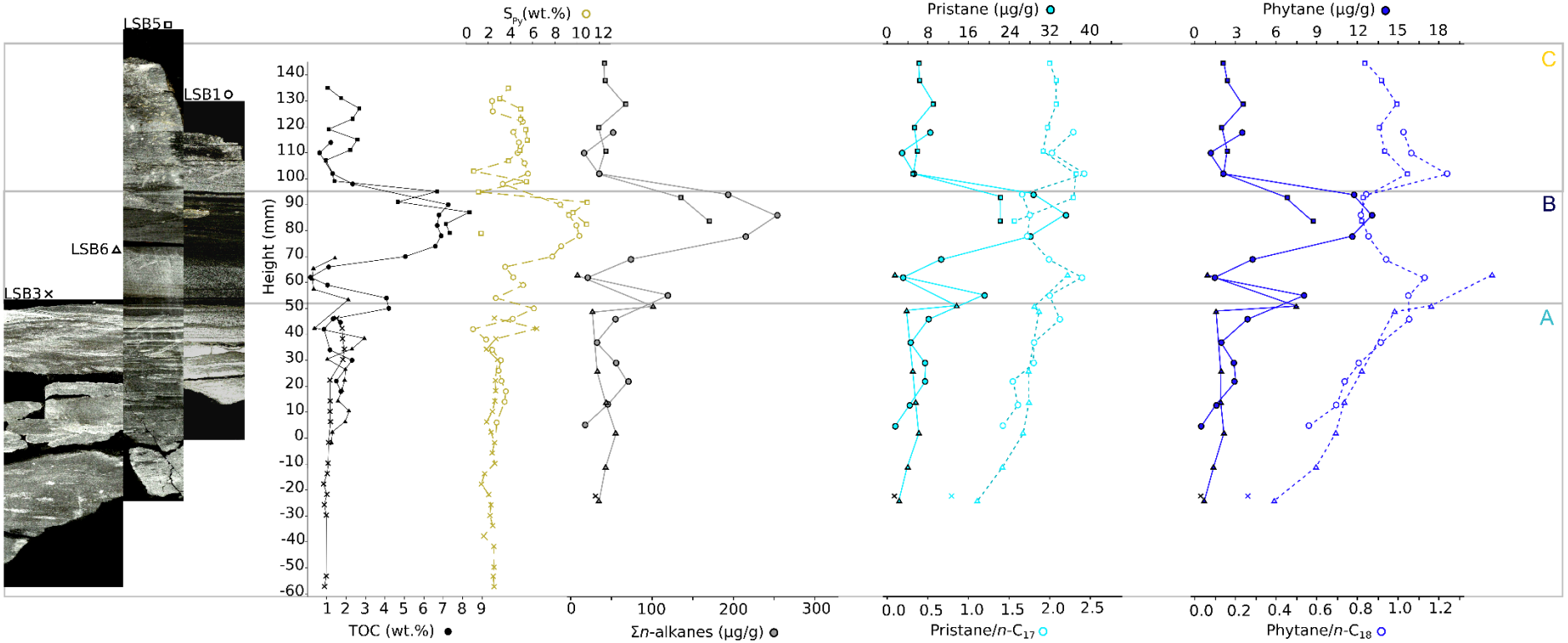

Figure 5.1. TOC, pyrite Sulphur (S_{py}; included in all plots, as in Chapters 3 and 4), Σ *n*-alkanes, pristane (alongside pristane/*n*-C_{17}) and phytane (alongside phytane/*n*-C_{18}) of the LSB.. As in Chapters 3 and 4, a photomosaic of scanned photos of the LSB (enhanced contrast and with block codes) is also included. Circles indicate data taken from LSB1, crosses from LSB3, squares from LSB5, and triangles from LSB6. Lithofacies A, B and C are indicated by the large grey boxes, with colour-coded letters corresponding with the colours of the data points in Figs. 5.4, 5.9, 5.14, 5.20 and 5.21.

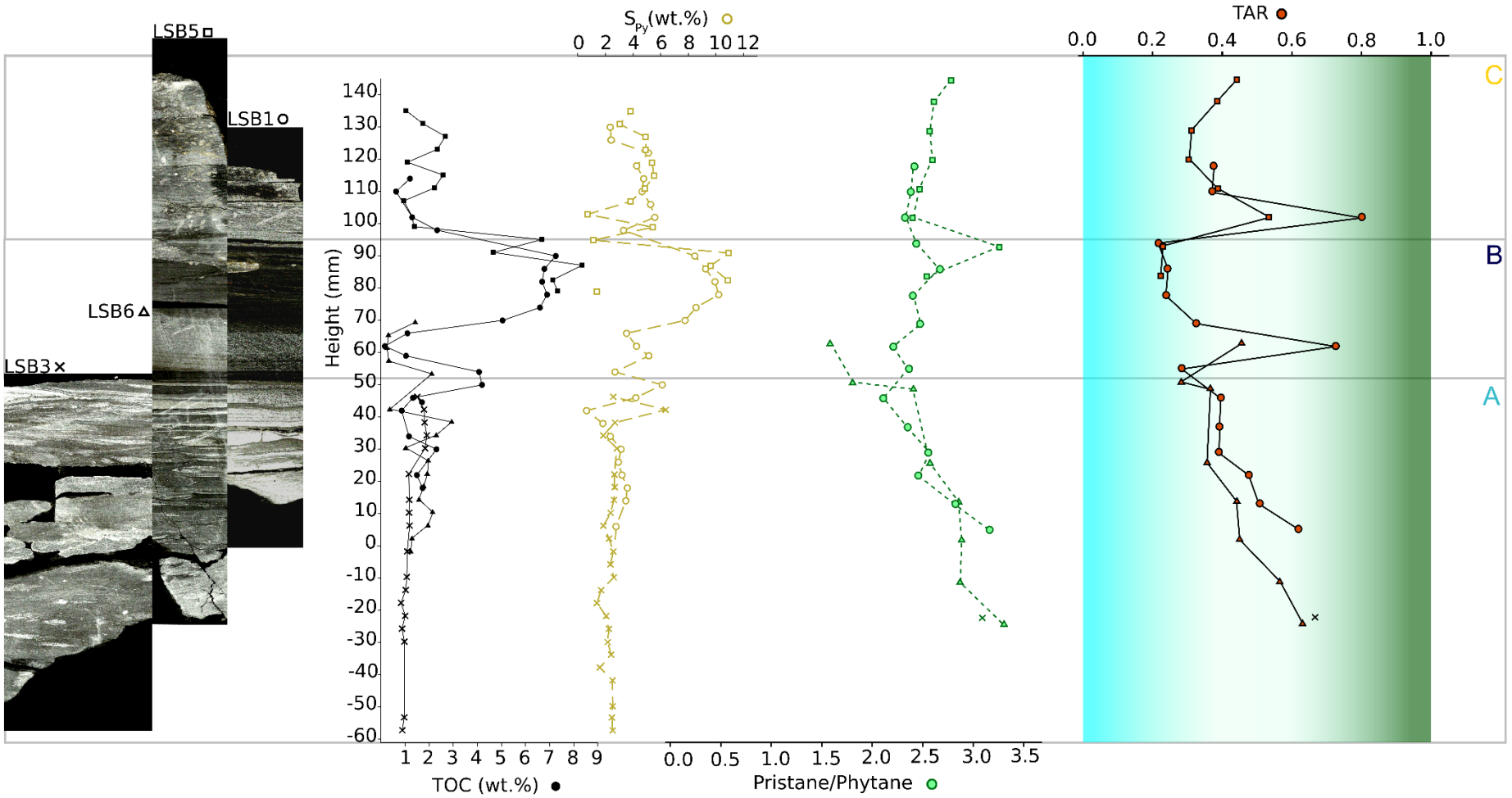

Figure 5.2. Pr/phy, and the terrestrial/aquatic ratio (TAR; definition in Chapter 1, section 9.2.6) of the LSB. Note the presence of two sharp peaks in the the TAR, one of which is concomitant with the large silty lens at 62mm.

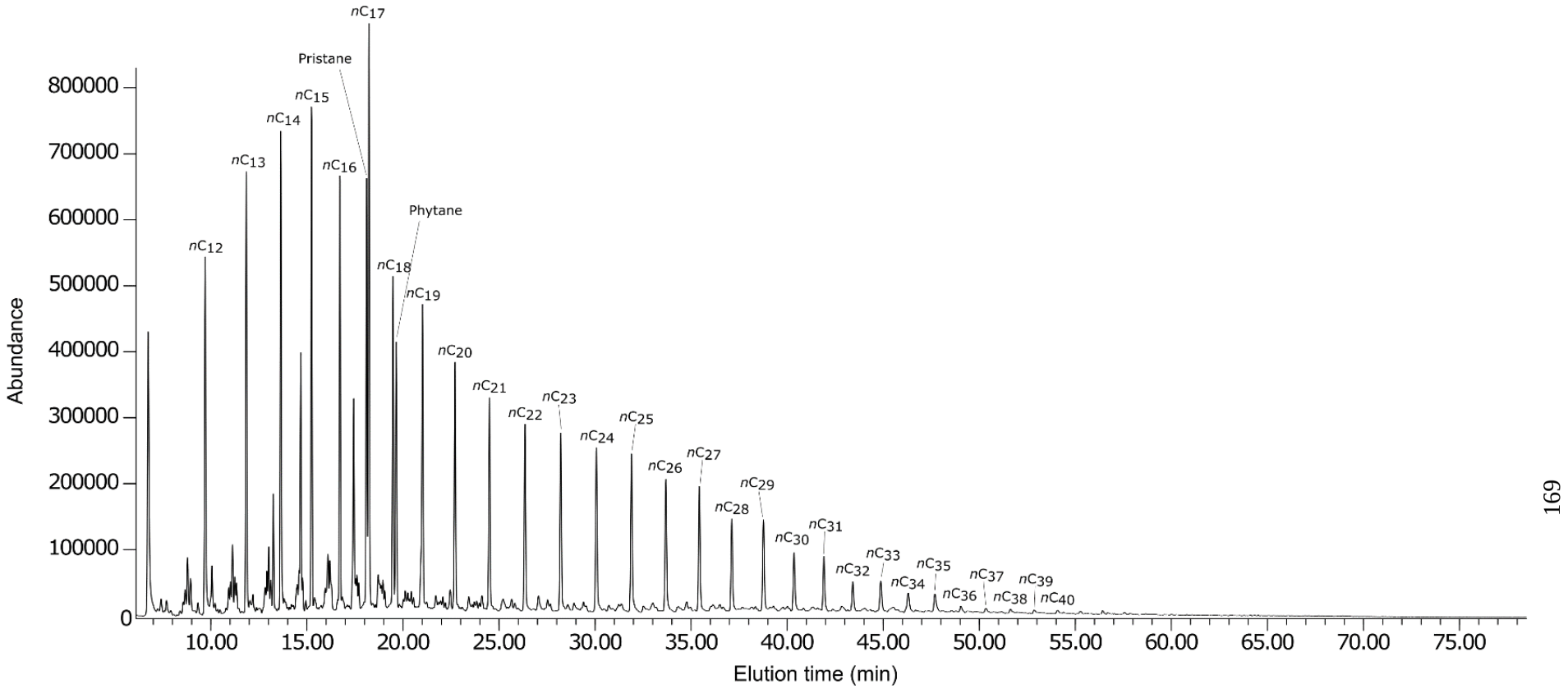

Figure 5.3. Gas Chromstograph (GC) trace of a representative aliphatic fraction derived from the LSB (LSB1.8B), with m/z= 85. Peaks attributed to *n*-alkanes and branched isoprenoids are labelled.

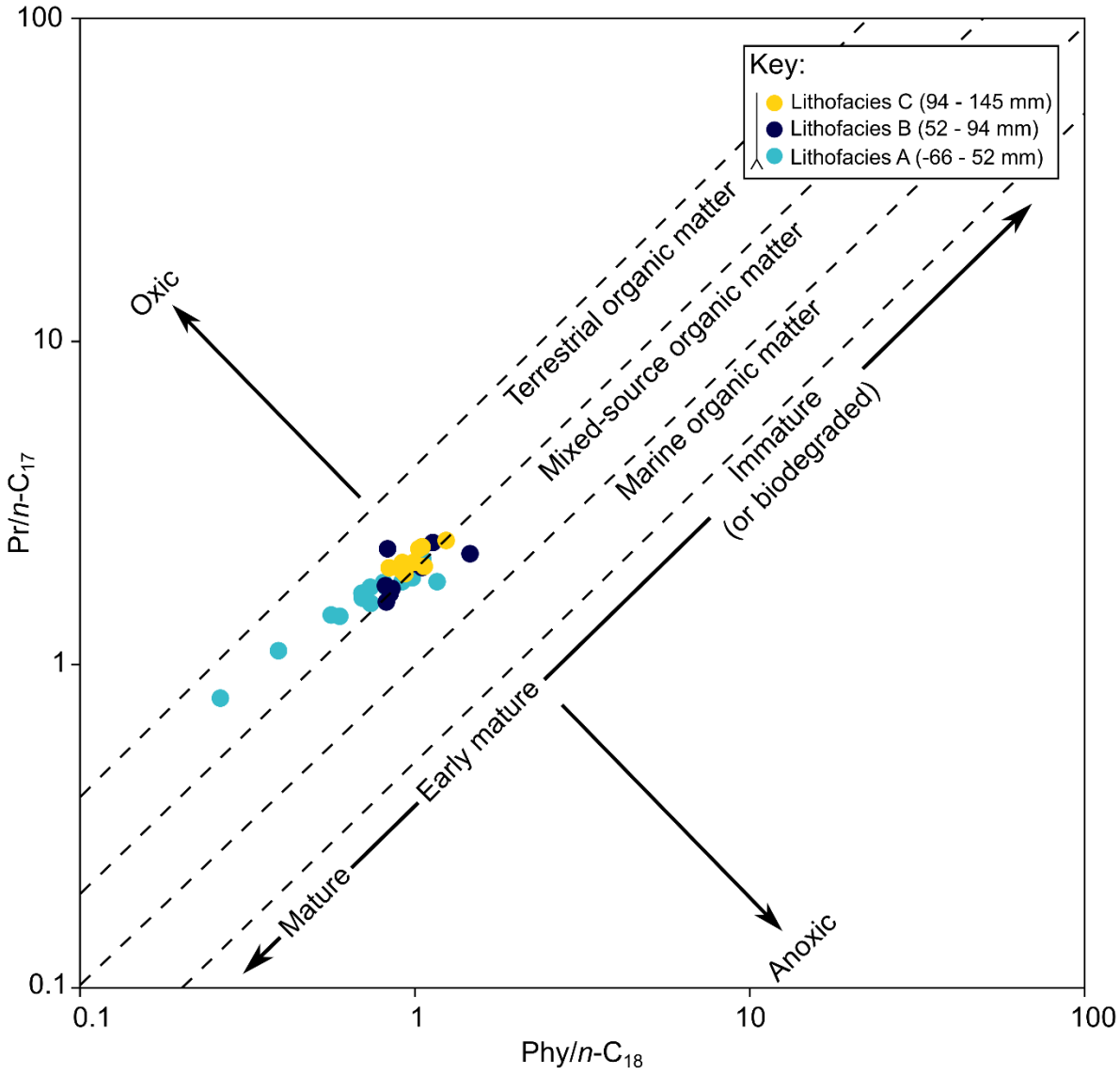

Figure 5.4. Cross plot of phytane/*n*-C_{18} versus pristane/*n*-C_{17}, with trends for various organic matter assemblages, and the influence of redox and thermal maturity (adapted from Peters *et al.*, 1999). Note the close match of the data to the trend for mixed-source organic matter, corroborating the evidence from Rock-Eval pyrolysis for a mixed organic matter pool (Chapter 3, section 4.10).

2.1.2 Hopanes and steranes

Both hopanes and steranes contribute to the organic matter assemblage of the LSB, with hopanes being much more abundant than steranes (see Figs. 5.7 and 5.8 for representative chromatograms).

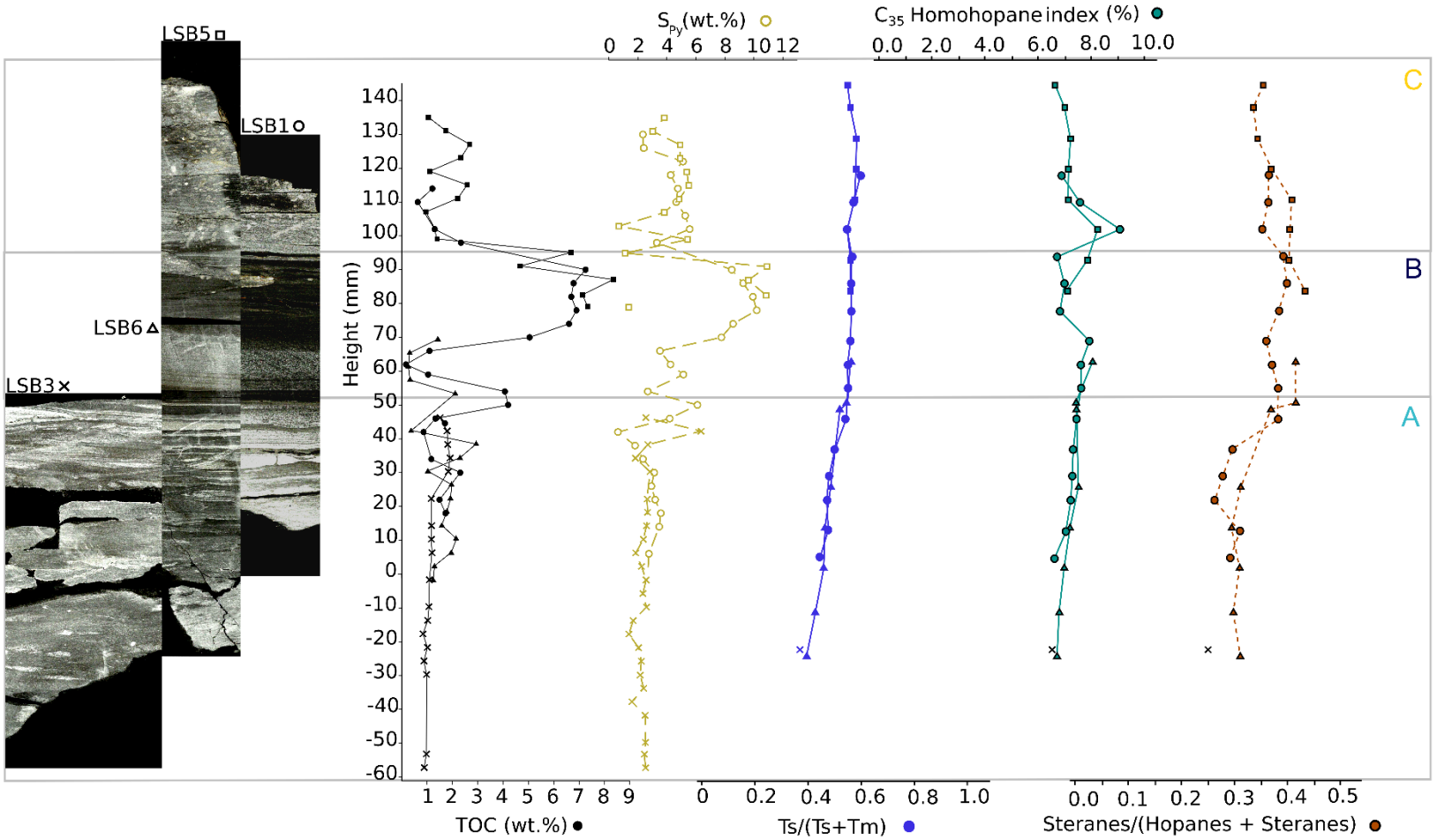

Figure 5.5. Ts/(Ts+Tm), C_{35} homohopane index, and Steranes/(Steranes + hopanes) of the LSB. Note the lack of a pronounced positive excursion in the C_{35} homohopane index in Lithofacies B, and the shift of 0.08 in the steranes/(steranes+hopanes) ratio at 46 mm (see text for a discussion).

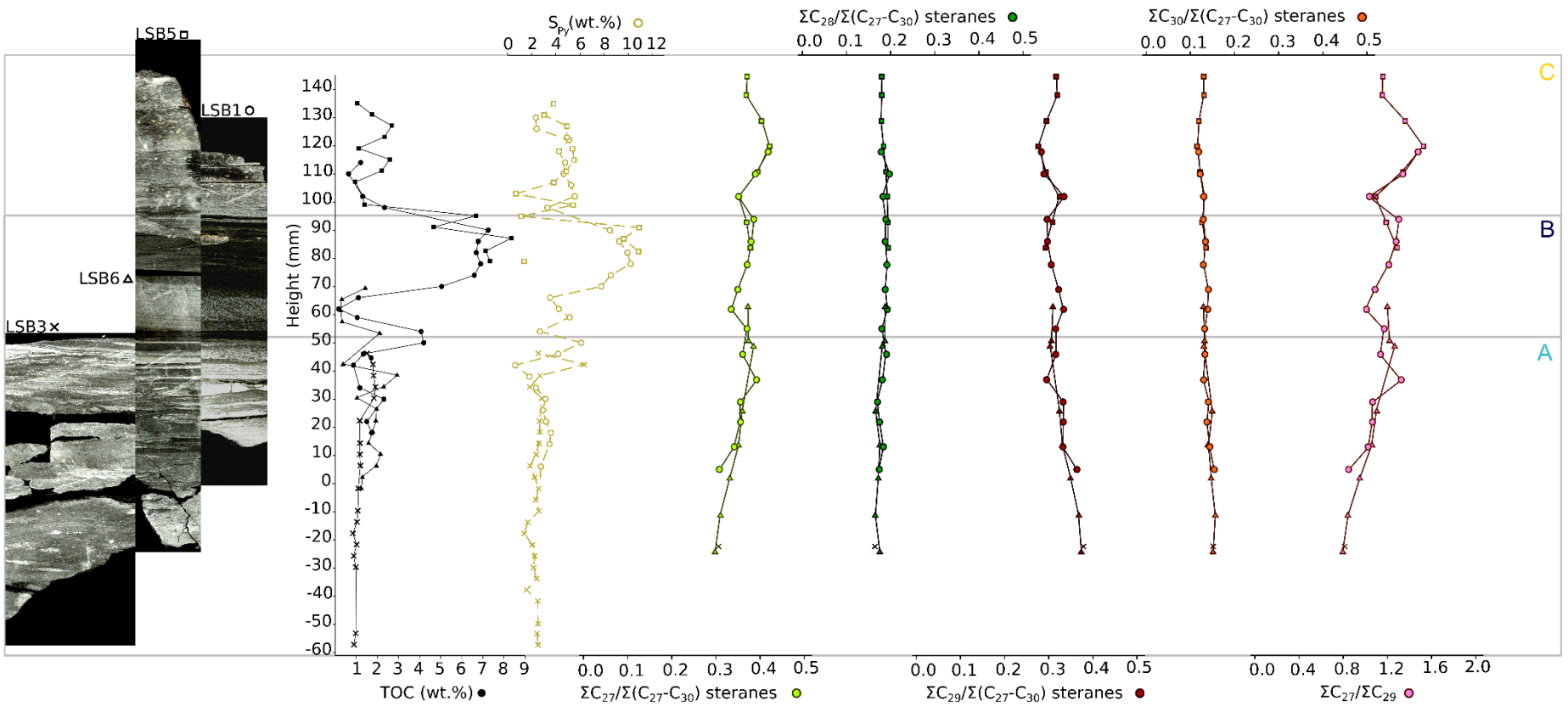

Figure 5.6. $\Sigma C_{27}/\Sigma(C_{27\text{-}C30})$ sterane, $\Sigma C_{28}/\Sigma(C_{27\text{-}C30})$ sterane, $\Sigma C_{29}/\Sigma(C_{27\text{-}C30})$ sterane, and $\Sigma C_{30}/\Sigma(C_{27\text{-}C30})$ sterane of the LSB. $\Sigma C_{27}/\Sigma C_{29}$ is also shown, to visualise relative change in these steranes sans the closed-sum effect. Note the presence of two slight decreases in this ratio at 62 mm and 102 mm (see text for a discussion).

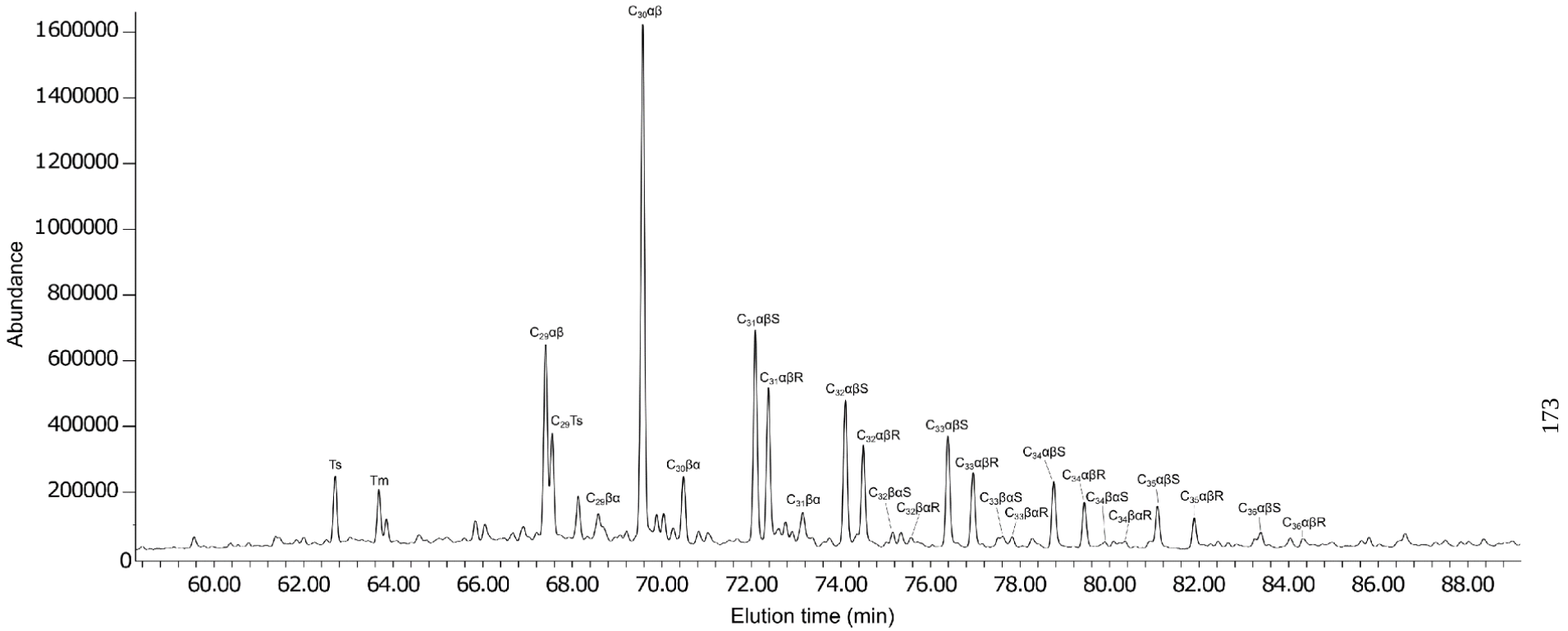

Figure 5.7. GC trace of a representative aliphatic fraction derived from the LSB (LSB1.8B), with m/z=191. Peaks attributed to hopanes are labelled.

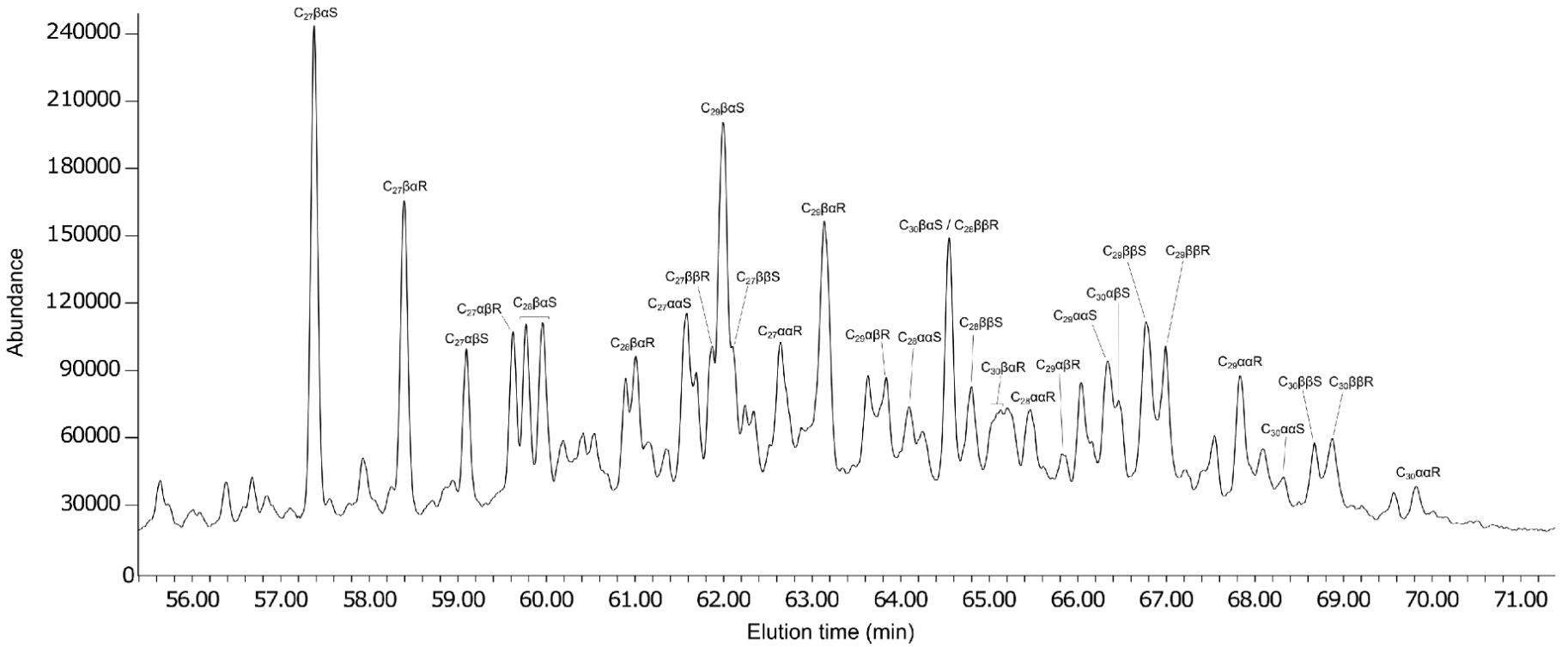

Figure 5.8. GC trace of a representative aliphatic fraction derived from the LSB (LSB1.8B), with m/z=217. Peaks attributed to steranes are labelled.

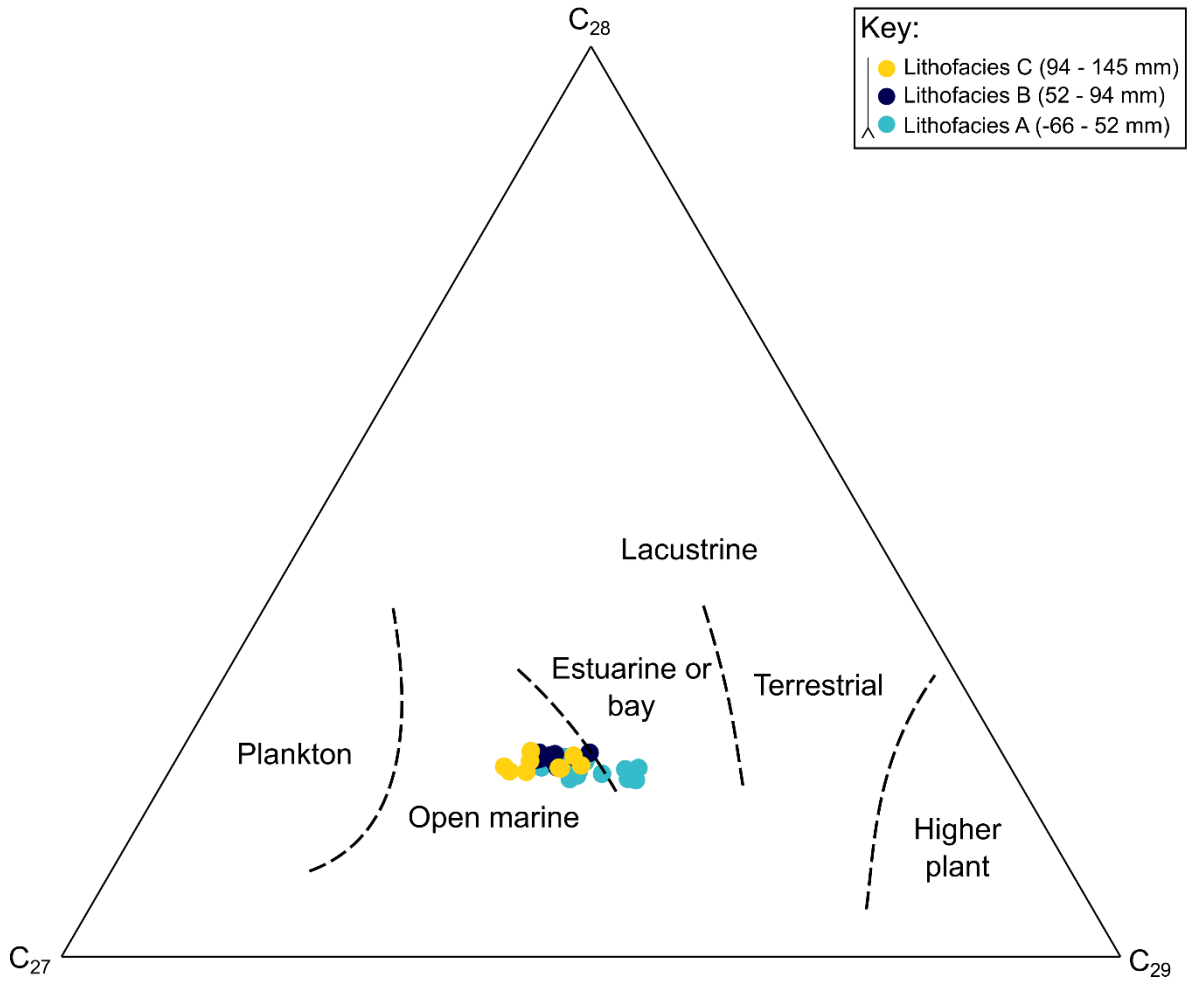

Figure 5.9. Ternary plot comparing the relative contributions of C_{27}, C_{28} and C_{29} steranes (after Huang & Meinschein, 1979). Given that the relative contribution of C_{28} does not very much, and the contributions of C_{27} and C_{29} are roughly anticorrelated, the spread of data is very constrained (on the boundary between the open marine, and estuarine fields). However, a slight up-section trend into the open marine field can be discerned.

The C_{35} homohopane index follows a similar trend to pr/*n*-C_{17} and phy/*n*-C_{18} (albeit muted and slightly offset vertically): it rises from 6.52% at -22 mm, to 6.62% at 145 mm, with a negative inflection of ~1.5% between 69-102 mm (corresponding with TOC values of over 5.0 wt.%). The negative inflection is also followed by a brief positive inflection of up to 9.07%.

At 46 mm there is a slight shift in the relative contribution of steranes to the assemblage: the steranes/(steranes+hopanes) ratio jumps from 0.296 to 0.382. Otherwise, the trend in this ratio is more or less constant.

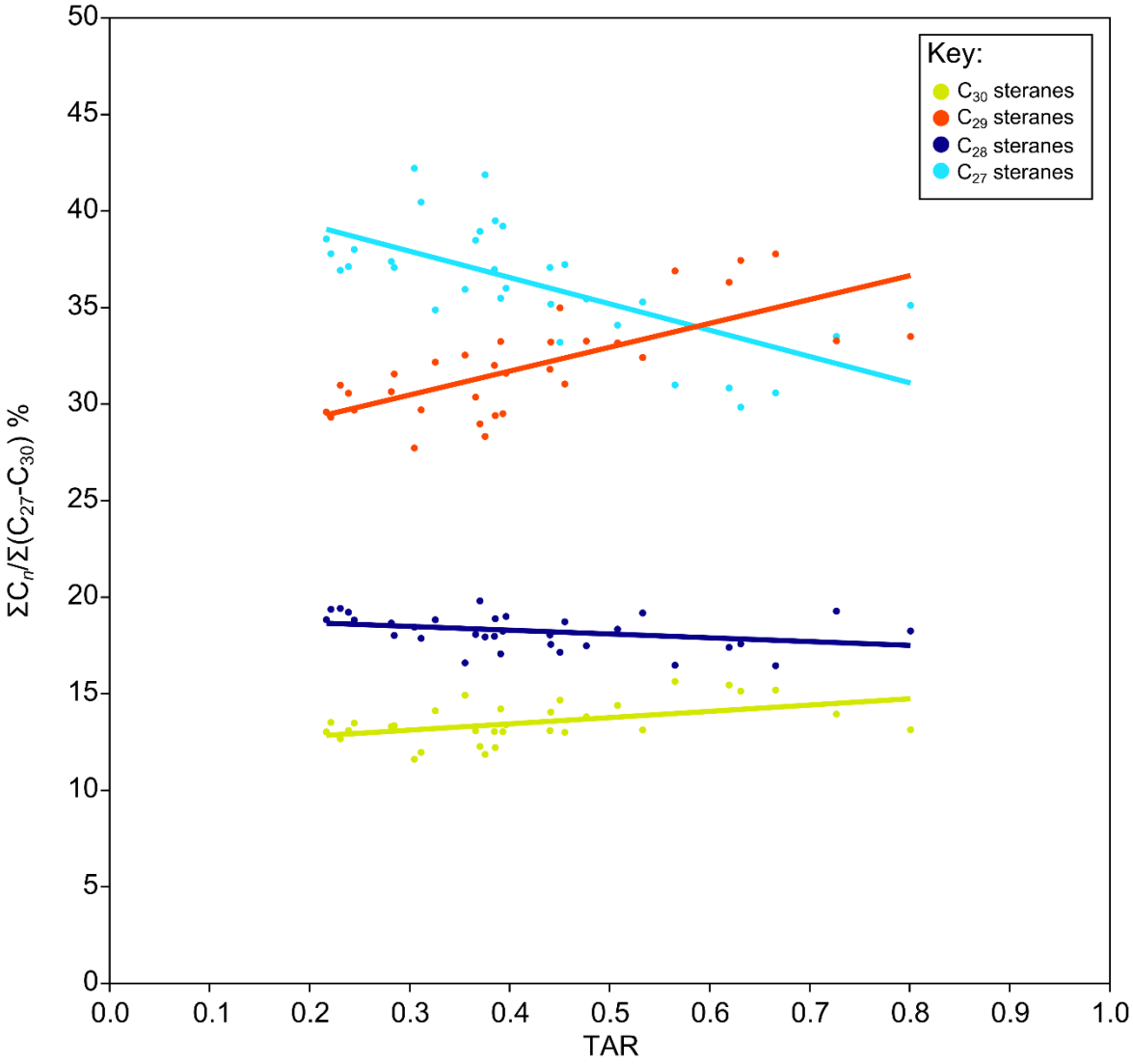

Figure 5.10. Correlation of the proportions of *n*-C_{27-30} regular steranes with TAR. Positive correlations imply an association of the sterane with terrigenous organic matter, and negative correlations imply an association with marine matter (see 3.2).

The Ts/(Ts+Tm) ratio is essentially constant for the section, showing only a slight rise from 0.369 at -22 mm, to 0.547 at 145 mm. This trend also shows no appreciable deviation with differing lithologies (e.g., no deviation in the silty layer at 62 mm, nor in the TOC-rich upper part of Lithofacies B).

Of the C_{27-30} regular steranes, only C_{27} and C_{29} show appreciable variability (Fig. 5.6), and their trends are essentially anticorrelated: $\Sigma C_{27}/\Sigma(C_{27-C30})$ rises from 0.306 at -22 mm to 0.371 at 145 mm, while $\Sigma C_{29}/\Sigma(C_{27-C30})$ falls from 0.378 at -22 mm to 0.318 at 145 mm. To circumvent the closed sum effect, I have also plotted $\Sigma C_{27}/\Sigma C_{29}$, and this follows a similar trend to $\Sigma C_{27}/\Sigma(C_{27-C30})$. A C_{27-29} sterane ternary plot shows that the LSB lies in the open marine marine-estuarine/bay fields (Fig. 5.9), and therefore,

that the total lipid extract (TLE) contains contributions from both planktonic and higher plant sources (in agreement with my *n*-alkane and palynological data). When plotted against TAR (Fig. 5.10), $\Sigma C_{27}/\Sigma(C_{27\text{-}30})$ shows a negative correlation (-13.7, $R^2 = 0.45$), and $\Sigma C_{29}/\Sigma(C_{27\text{-}C30})$ shows a positive correlation (12.5, $R^2 = 0.52$).

2.1.3 Isorenieratane and aryl isoprenoids

Isorenieratane is present in the LSB (consistent with the unpublished findings of Salem, 2013), however, the section contains a substantial amount of diagenetically rearranged carotenoids and aryl isoprenoids, as well as biphenylic isorenieratane (Fig. 5.13). In Lithofacies A, the concentration of isorenieratane rises sharply at 2mm to 0.07µg/g , and varies between 0.01 – 0.09 µg/g below 62 mm (although there is also variability between sample blocks). At 62 mm (in the lower part of Lithofacies B), there is a brief drop in the concentration of isorenieratane (down to 0.01 µg/g), but this is followed by a rise up to a maximum of 0.16 µg/g at 86 mm (mirroring the trend of TOC and S_{py}). At 86 mm, isorenieratane content drops to 0.03 µg/g, and then gradually declines through Lithofacies C (not exceeding 0.01 µg/g). . Biphenylic isorenieratane follows a very similar trend, but shows lower values than isorenieratane.

In Lithofacies A, the AIR (Chapter 1, section 9.1.6) decreases from 4.50 at -24 mm, to 3.73 at 51 mm then (like the K/Al and Rb/Al proxies discussed in Chapter 3, section 3.4), shows a negative peak down to 1.52 at 62 mm – in the silty layer in the lower part of Lithofacies B, and corresponding with the large peak in biphenylic isorenieratane (Fig. 5.12). The AIR then recovers to a maximum of 4.62 at 94 mm, before showing another negative peak in the lower part of Lithofacies C (2.30 at 102 mm). Finally, the AIR gradually recovers again, reaching 4.32 at 145 mm. The AIR and pr/phy do not show significant correlation (Fig. 5.14), which, together with the elevated pr/phy values for the section, further indicates the strong influence of terrestrially derived organic matter.

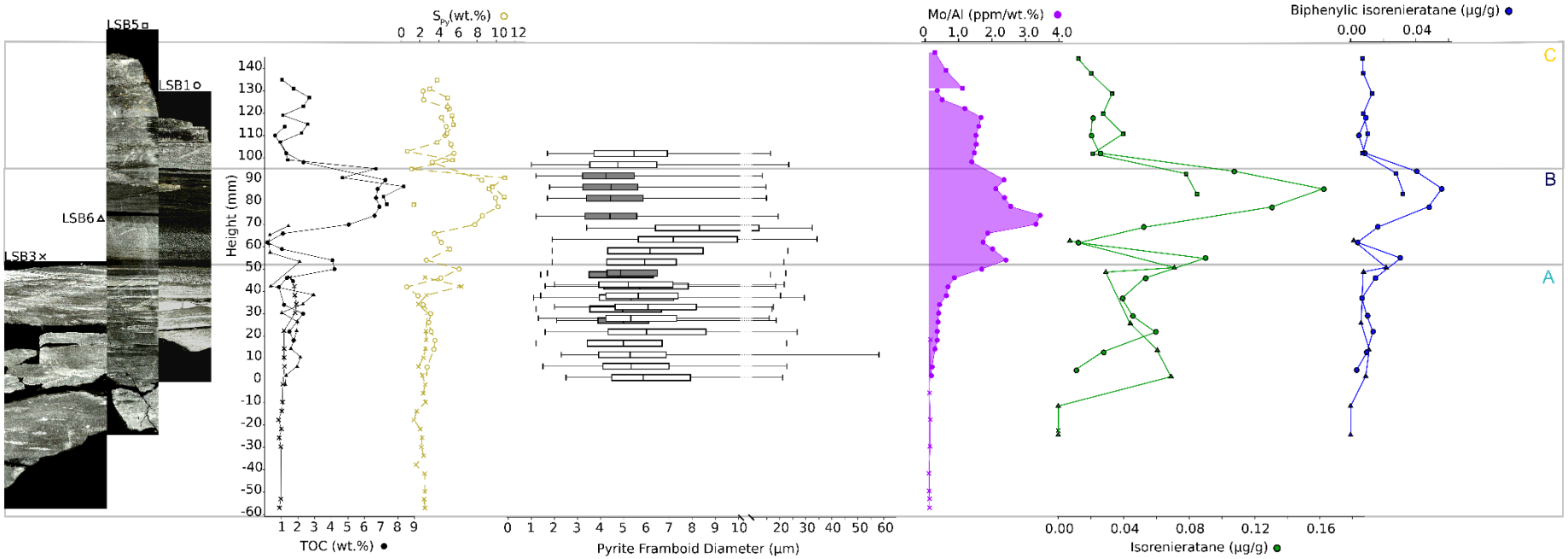

Figure 5.11. Isorenieratane and biphenylic isorenieratane content of the LSB. The carotenoids are plotted against pyrite framboid diameter and Mo/Al (Chapter 3, sections 3.1.1 and 3.4), to form a comparison of different proxies sensitive to euxinia.

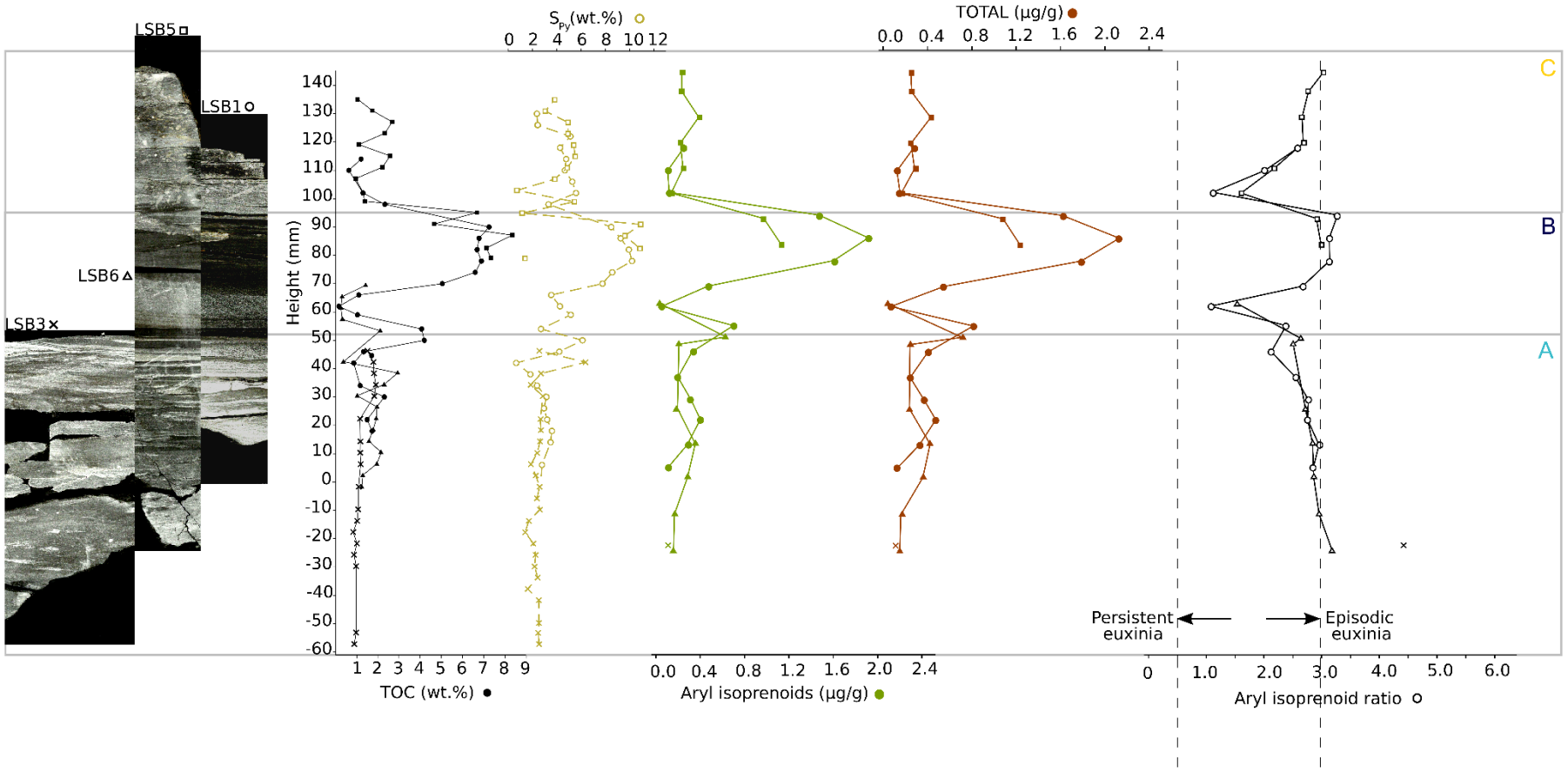

Figure 5.12. Aryl isoprenoid content, total aryl isoprenoid, Isorenieratane and biphenylic isorenieratene content (TOTAL), and aryl isoprenoid ratio(AIR) of the LSB.

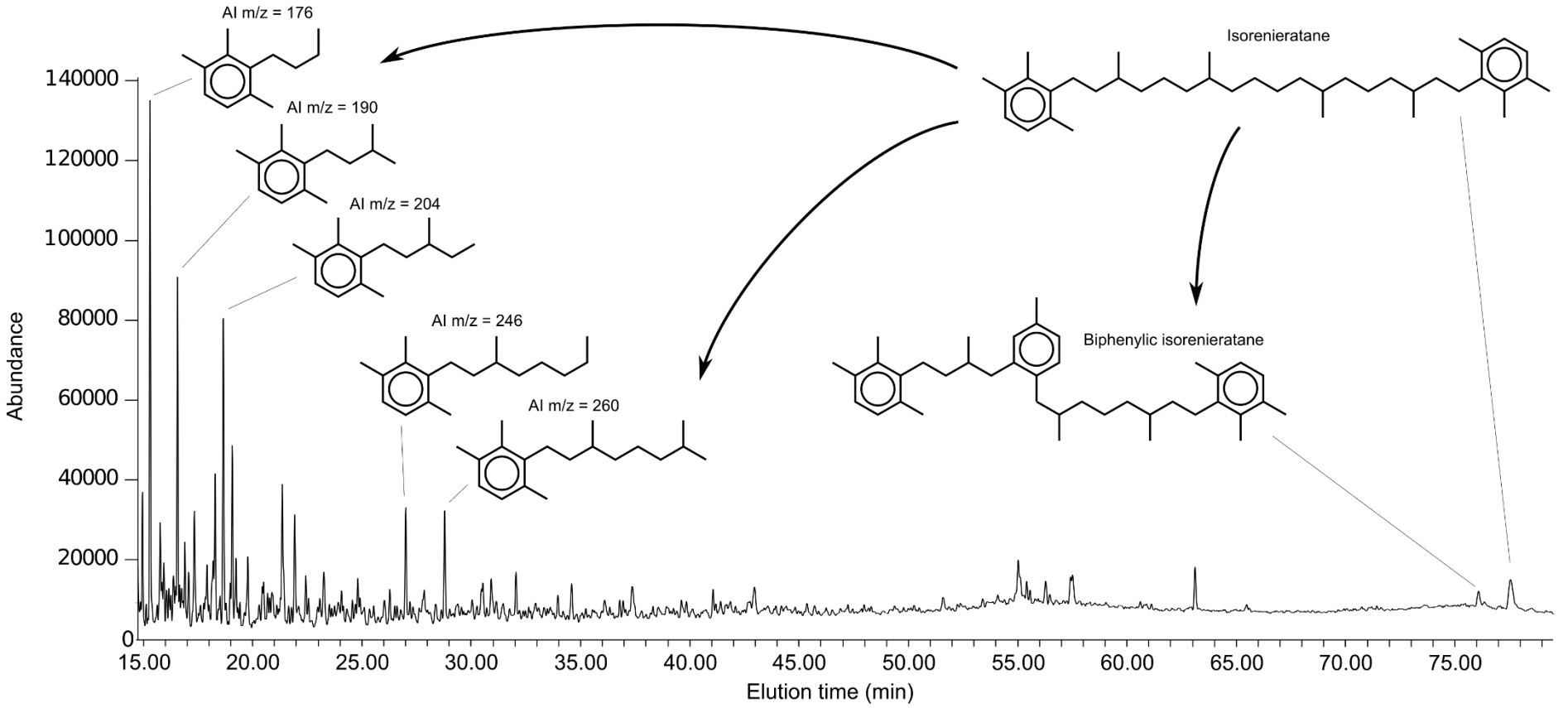

Figure 5.13. GC trace of a representative aromatic fraction derived from the LSB (LSB1.8B), with m/z=133. Peaks attributed to isorenieratane, and its catagenetic breakdown products are labelled, and bond-line formulae are also included.

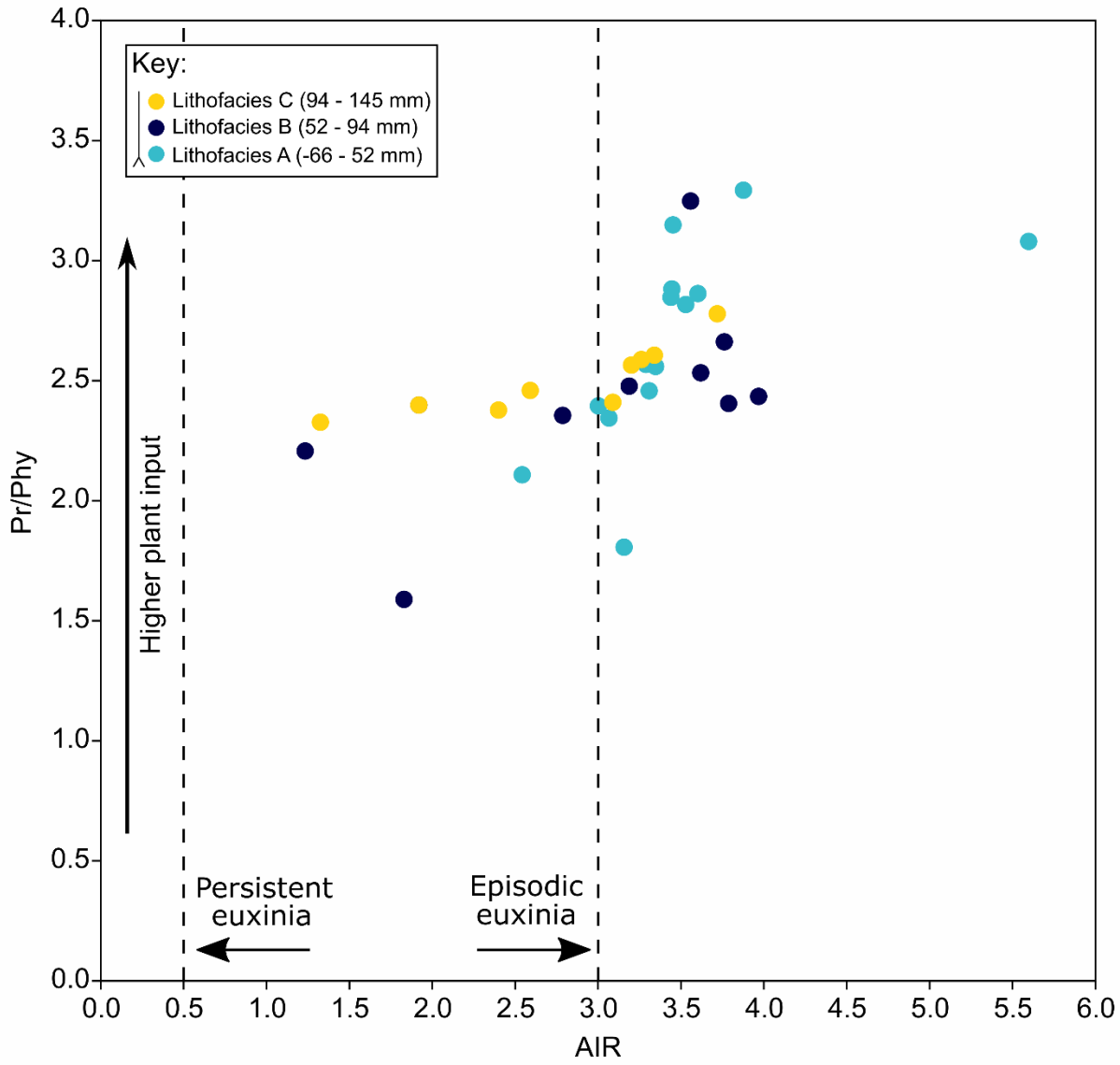

Figure 5.14. Pr/phy plotted against AIR for the LSB. The values display little correlation, and pr/phy is generally high, possibly indicating an input of excess plant material (chlorophyll being a source of phytol).

2.1.4 Other aromatics

Phenanthrene, Σ-methylphenanthrenes, retene, dibenzothiophene, and Σ-methyldibenzothiophenes are all present within the LSB, and show nearly identical downcore trends (Figs. 5.15 and 5.16). All the trends appear to show enrichment in Lithofacies B, along with increased S_{py} content.

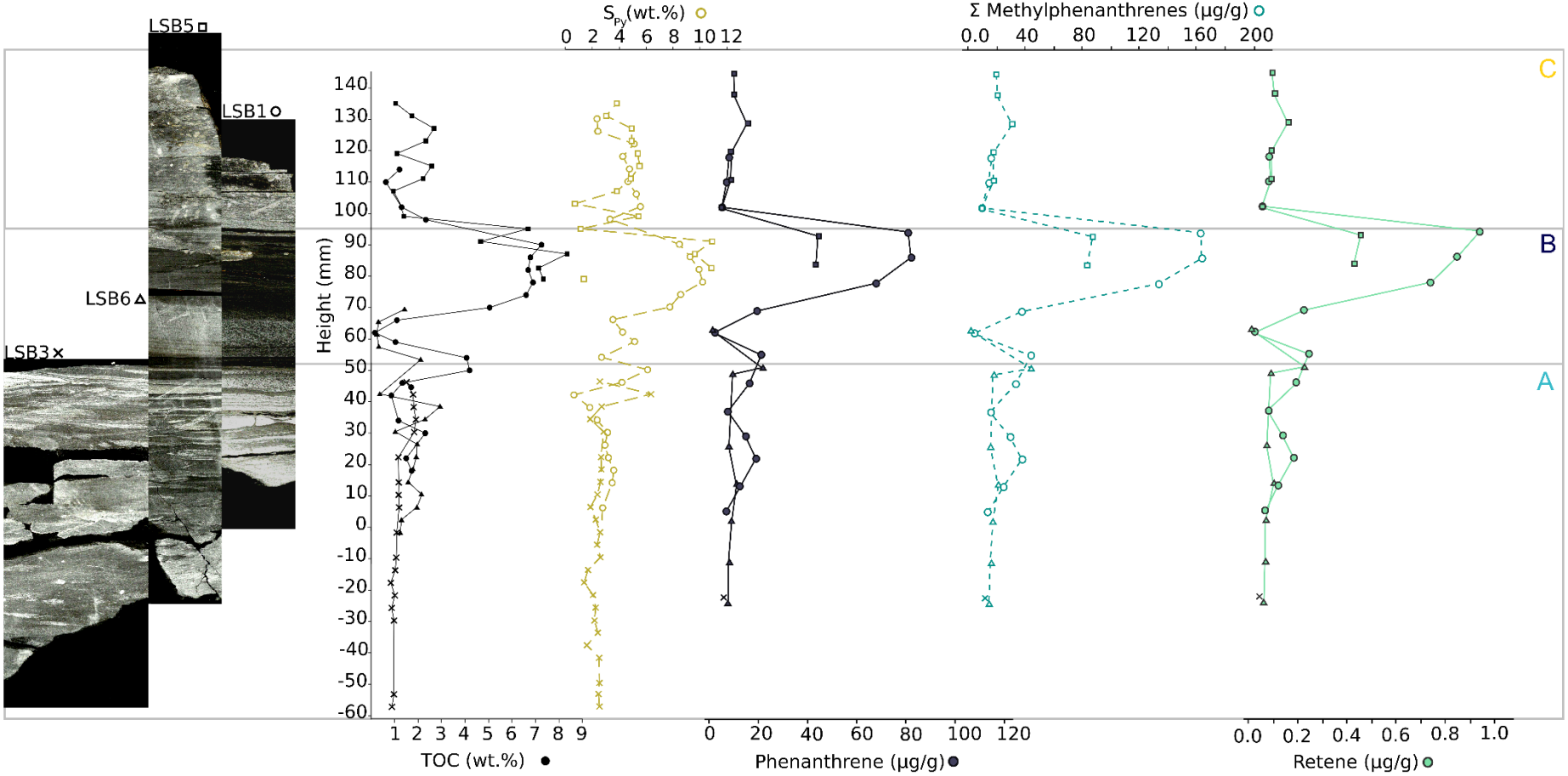

Figure 5.15. Phenanthrene, Σ-methylphenanthrenes, Retene, Dibenzothiophene, Σ-methyldibenzothiophenes, and phenanthrene/dibenzothiophene of the LSB.

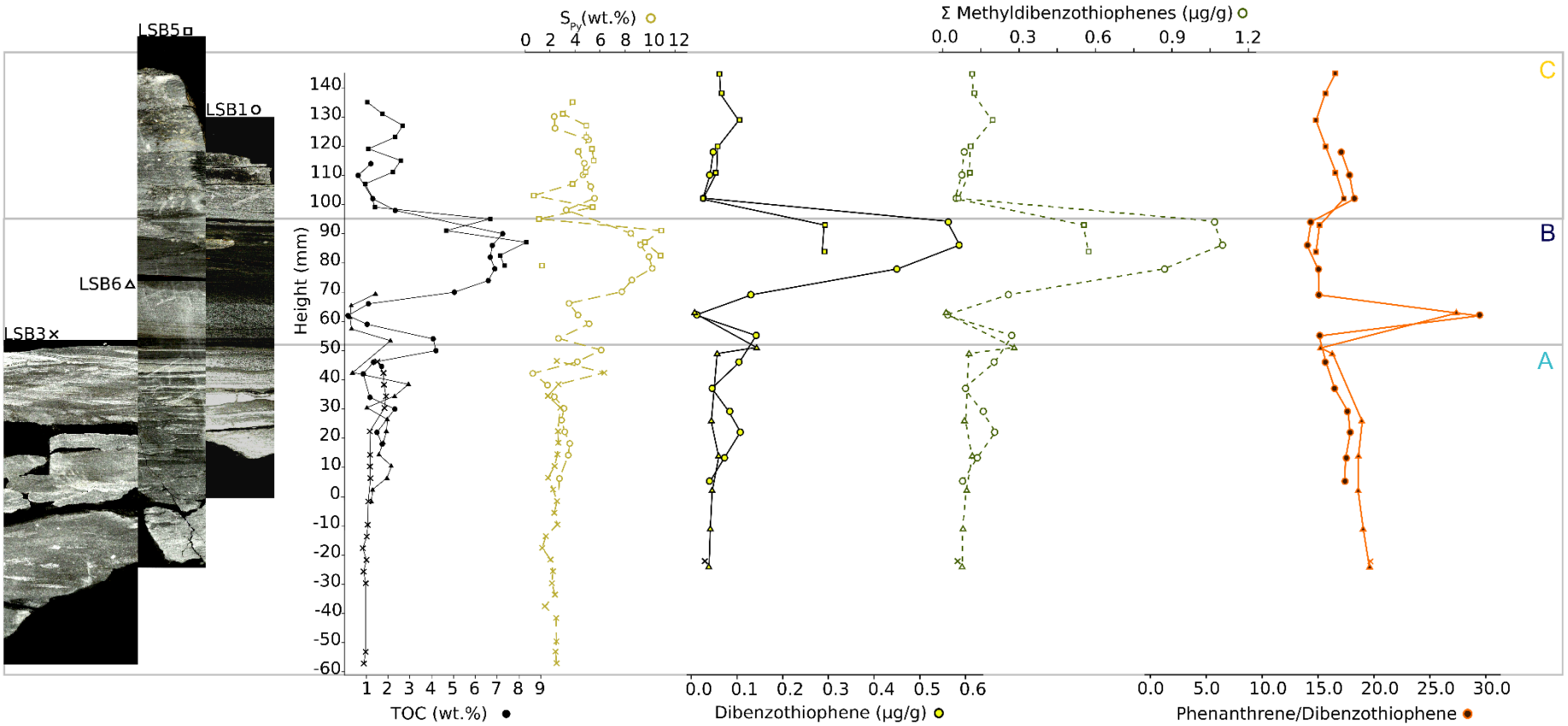

Figure 5.16. Phenanthrene, Σ-methylphenanthrenes, Retene, Dibenzothiophene, Σ-methyldibenzothiophenes, and phenanthrene/dibenzothiophene of the LSB.

By contrast, the Phenanthrene/Dibenzothiophene ratio varies less, and shows a gentle decrease through Lithofacies B (from 17.6 at 29 mm to 14.4 at 94 mm), and then a recovery towards 16.6 at the top of Lithofacies C. The exception to this trend is at 62 mm, where the ratio shows a large positive spike up to 29.3.

2.2 Compound-specific isotopic analysis (CSIA)

The compound-specific carbon isotopic trends, both in marine (*n*-C_{17-19}; Fig. 5.17) and terrestrial (*n*-$C_{27-29;}$ Fig. 5.18) fractions, are frequently in conflict with one another, with no unequivocal positive or negative excursion evident over the studied interval. While a negative peak is observed in the terrestrial fractions in LSB1 during Lithofacies B (minima of -35.7‰, -35.0‰ and -35.6‰ in *n*-C_{27}, *n*-C_{28} and *n*-C_{29}, respectively), comparable values are also found in LSB3 during Lithofacies A (*n*-C_{27}, = -37.2‰ to -32.3‰, *n*-C_{28} = -36.5‰ to -32.4‰, and *n*-C_{29} = -36.0‰ to -32.3‰) and in LSB5 during Lithofacies C (*n*-C_{27}, = -36.8‰ to -31.7‰, *n*-C_{28} = -36.1‰ to -31.8‰, and *n*-C_{29} = -35.6‰ to -31.9‰). The marine fractions show even less agreement, with an apparent negative point excursion at 94 mm in *n*-C_{17} and *n*-C_{19} (-38.4‰ and -37.4‰, respectively), but not *n*-C_{18}. The *n*-C_{17} and *n*-C_{18} values from LSB6 also appear to be negatively shifted from the concomitant trend of LSB1, but the *n*-C_{19} values are in near-perfect agreement. Regardless of the variability in the CSIA trends, they all show consistently negative $\delta^{13}C$ values, with the heaviest isotopic signature residing in *n*-C_{27} (-31.7‰ at 102 mm) The lowest $\delta^{13}C$ value of the interval is in *n*-C_{17} (-39.4‰ at 129 mm).

3.0 Interpretations

I have decided to plot key biomarkers normalised to sample weight, rather than TOC. Despite the frequent use of TOC normalisation in the organic geochemical literature, when applied to my dataset, the biomarkers often show widely exaggerated values at intervals characterised by low TOC. Isorenieratane, for instance, reaches 6.5 µg/gTOC in the silty lens when normalised to TOC, and shows apparently muted values in the interval of Lithofacies B characterised by small framboid diameters (Figs. 3.16; 5.19). I argue that the composition of TOC in the LSB is too complex to allow for a straightforward normalisation – it is composed of both marine, and terrestrially-derived organic matter (Chapter 3, section 3.10; Chapter 4, section 3.1; this Chapter, section 3.2), as opposed to entirely marine organic matter (a situation where TOC normalisation is, arguably, valid). A consequence of sediment normalisation, however, is that the trends of many biomarkers of interest closely follow that of TOC (e.g. Fig. 5.19). This could mean that the decline in redox state responsible

for enhanced organic matter preservation was also the case of the enrichment of these biomarkers. However, it is difficult to discriminate the effect of an enhanced TOC delivery flux on biomarker content at a given redox state. It is likely that with some of the biomarkers evaluated here, both enhanced formation under low redox, and enhanced delivery flux in TOC acted in concert (e.g. with isorenieratane). However, in the case of biomarkers such as dibenzothiophene, which is exclusively produced in the geosphere (Hughes *et al.*, 1995; Peters *et al.*, 2005, p.32), it is safe to say that an increase, with sediment normalisation, reflects enhanced production of the biomarker, rather than simply enhancement of the biological pump.

3.1 Migration of biomarkers

While I interpret the up-section variability in the contractions of *n*-alkanes, pristane, phytane, and isorenieratane to be of palaeoenvironmental significance (3.2 and 3.3), it is important to bear in mind that the LSB has been subjected to a moderate degree of thermal maturation (R_0 = 0.5-0.7%; Chapter 3, section 3.5), and as shown in Fig. 5.20, Lithofacies A is partly in the early oil generation window. The section is also heterolithic, with coarser silty layers punctuating C_{org}-rich shale. Therefore, it is probable that the observed trends in *n*-alkanes, pristane, phytane, and isorenieratane are (at least to an extent) the result of post-depositional migration of these compounds within the sediment pore space. The degree to which organic compounds are expelled from kerogen (and thus enter the pore-space of proximal high porosity sediments) can be modelled by polymer solution theory. When the temperature rises sufficiently high to overcome the van der Waals forces holding the organic molecule in the kerogen, the molecule can be expelled (Ritter, 2003). The affinity a given molecule has for retention in the kerogen vs expulsion is captured by the Hildebrand solubility parameter δ, where higher values of δ indicate greater affinity of kerogen. While aromatic and cyclic hydrocarbons have δ values typically between 8-11, *n*-alkanes and branched isoprenoids have δ values between 6-7. All this is to say that it is likely that some degree of migration of *n*-alkanes, took place within the pore space of the LSB during early diagenesis, especially in Lithofacies A. The silty layer at 62 mm might also contain higher levels of remobilised *n*-alkanes than the surrounding lithologies – the coarser sediment has greater pore space, allowing for expelled compounds to accumulate. It is, however, unlikely that these changes will greatly affect the final palaeoenvironmental interpretation, since the thermal maturity is not very advanced. Additionally, the δ values of pristane and *n*-C_{17}, and of phytane and *n*-C_{18} are very similar. Therefore, the pr/*n*-C_{17} and phy/*n*-C_{18} ratios are unaffected by migration out of the kerogen, since both the numerator, and denominator in these terms, are affected to about the same degree.

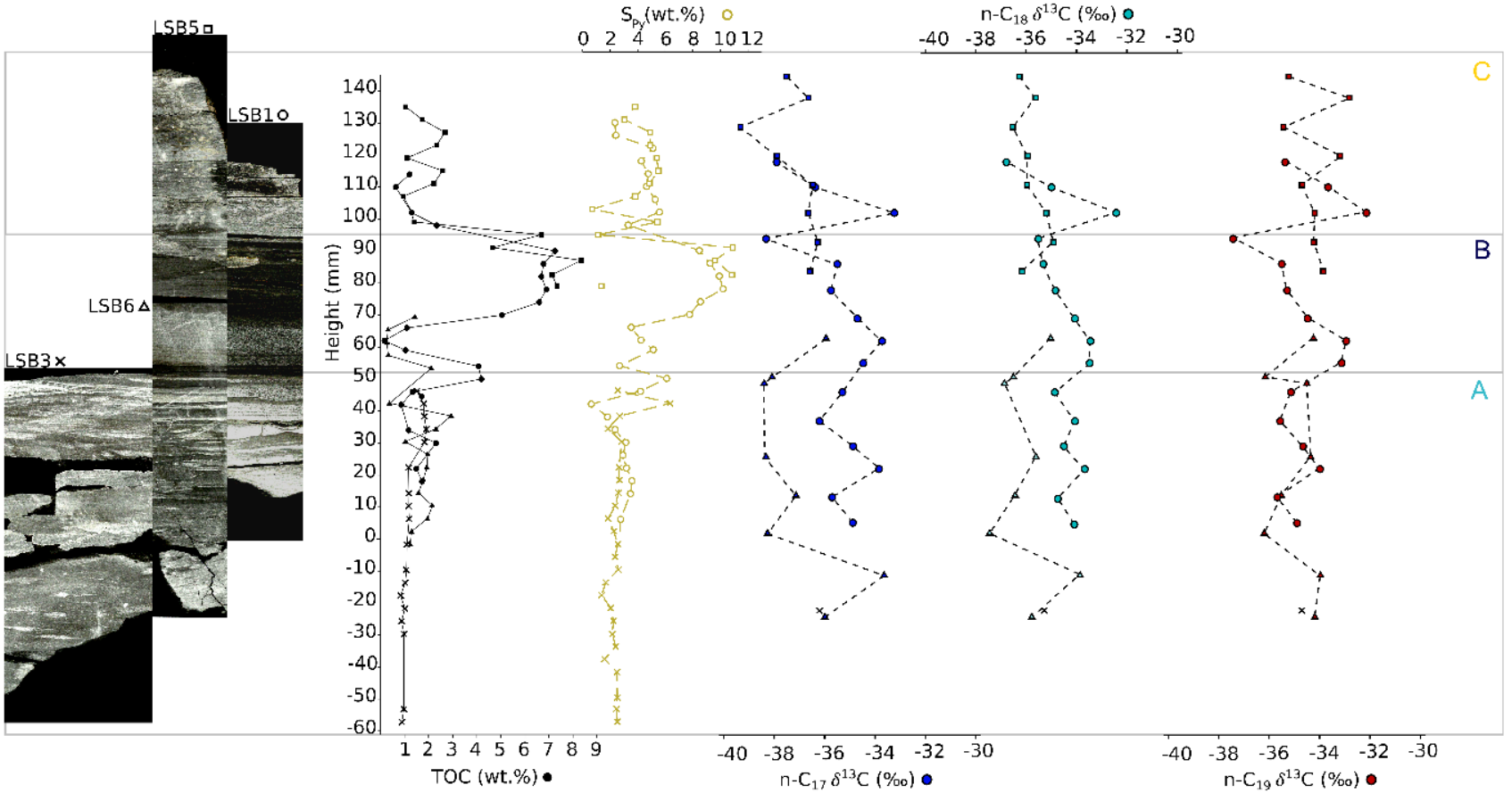

Figure 5.17. δ^{13}C of *n*-C_{17}, *n*-C_{18} and *n*-C_{19} , through the LSB.

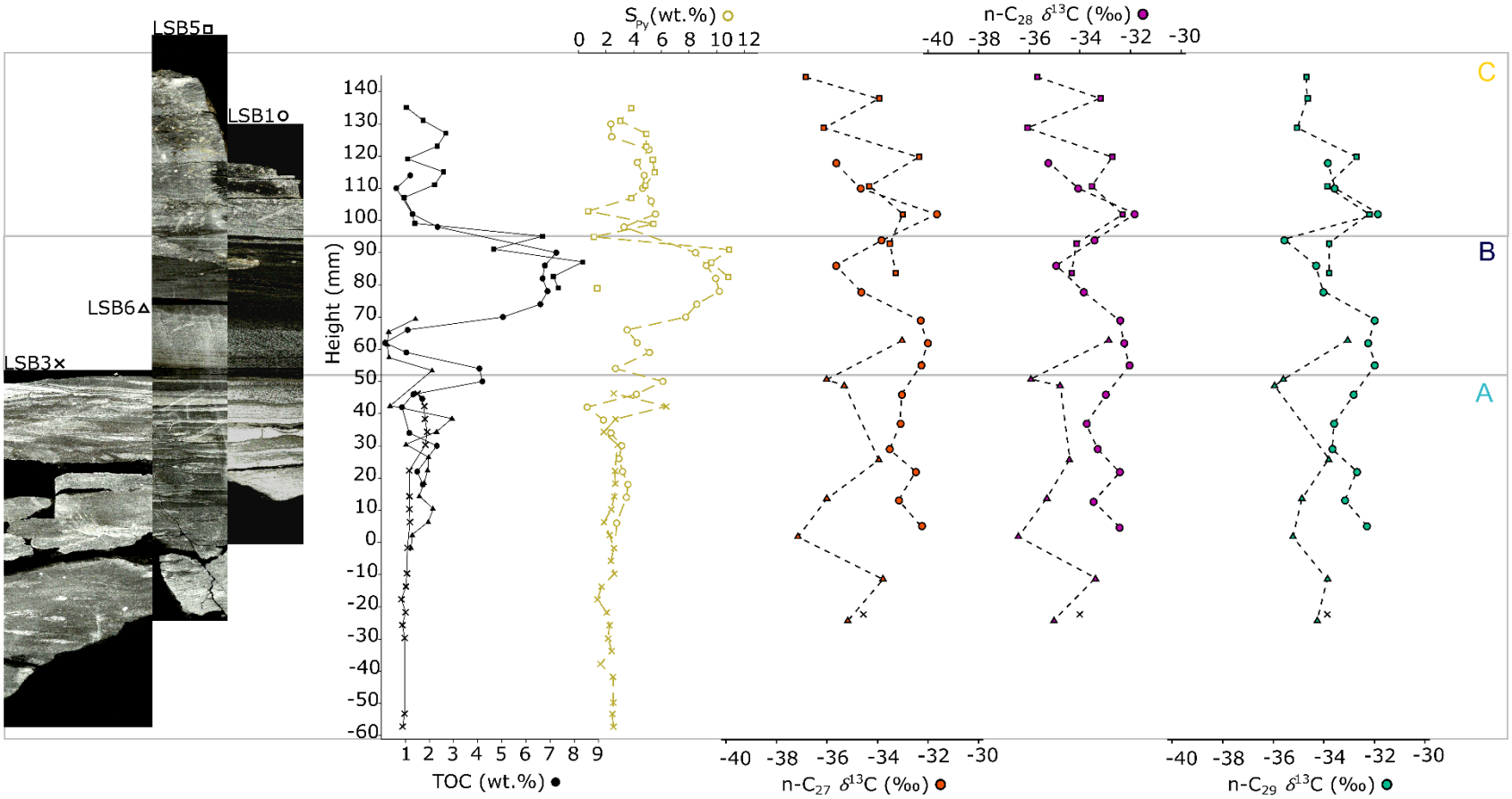

Figure 5.18. $\delta^{13}C$ of *n*-C_{27}, *n*-C_{28} and *n*-C_{29} , through the LSB.

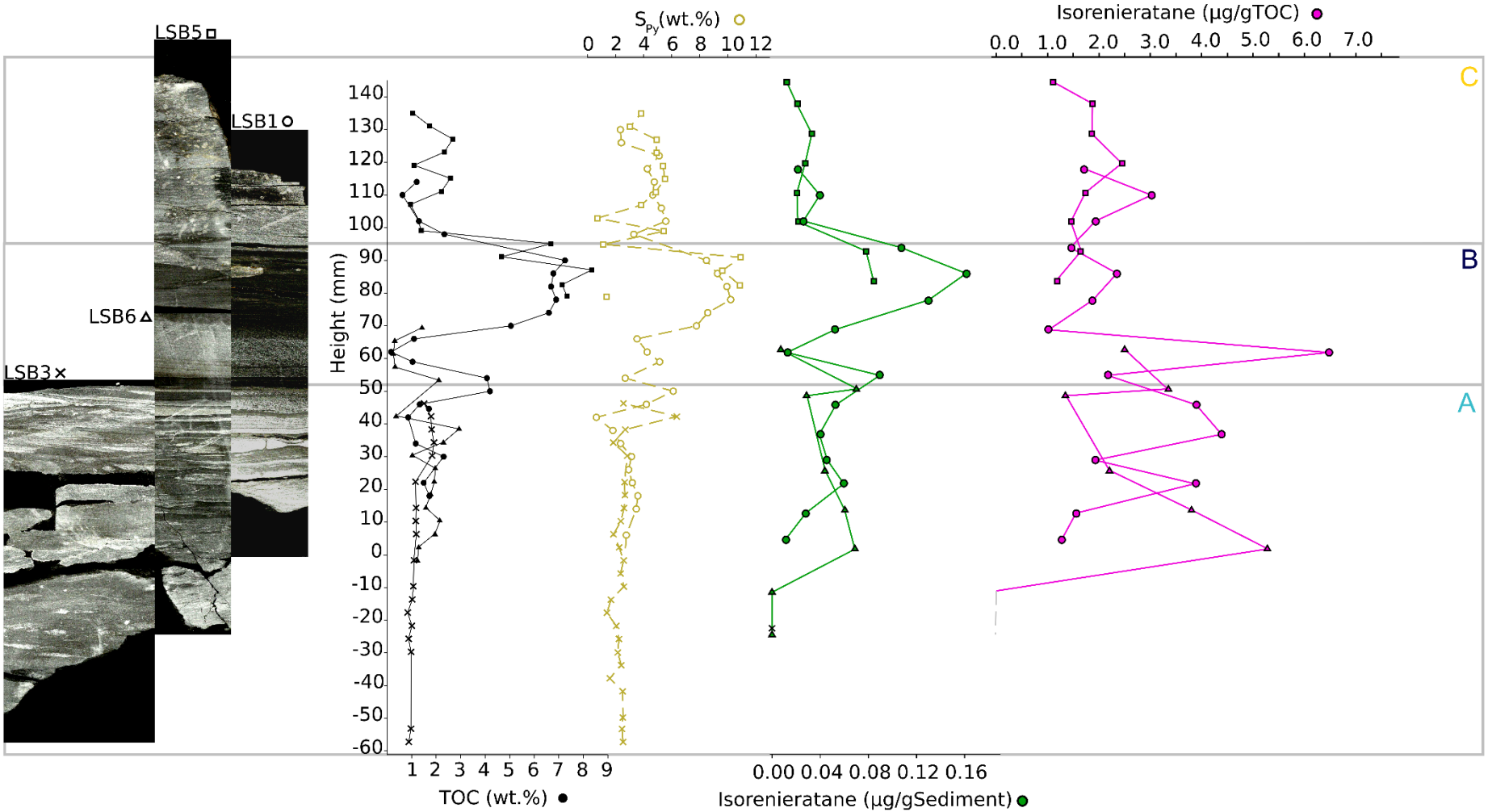

Figure 5.19. Isorenieratane as expressed in µg/g sediment (green) compared with isorenieratane as expressed in µg/gTOC (pink). Note how sediment normalization produces a plot similar to that of TOC, while normalization to TOC results in a plot with greatly exaggerated values in TOC lean lithologies (see text for a fuller discussion).

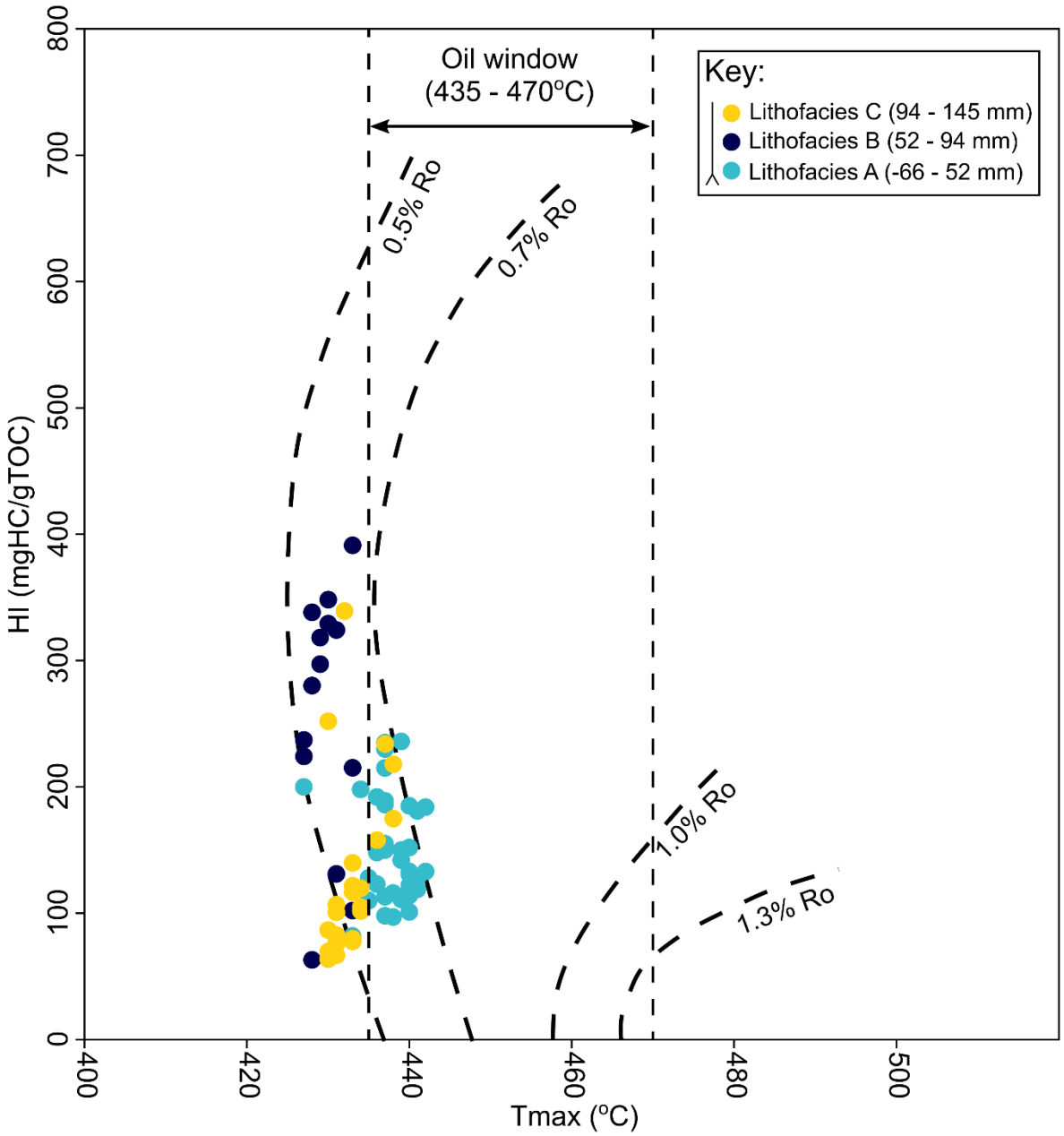

Figure 5.20. HI vs T_{max}, (see Chapter 3, section 3.5) with vitrinite reflectivity equivalence (R_0) and the oil generation window indicated.

3.2 Palaeoshoreline distance

It was speculated in Chapters 1, 3 and 4, that a key palaeoenvironmental parameter controlling redox dynamics during the deposition of the LSB, was sea level. During lowstands, reduced hydrodynamic contact with the wider EES would both increase water residence time within restricted basins, and reduce the dissolved oxygen content (leaving the system vulnerable to a shift into a frequently anoxic state). During highstands, this effect was reversed due to enhanced hydrodynamic connectivity, which

allowed ventilation of isolated basins by ocean currents. The difficulty with testing this model is that the data presented in this study was collected from a single site (near the basin depocenter), and no similar high-resolution work on time-equivalent sections from the basin margins has been carried out. Here, a transgression would be indicated by features such as stratigraphic overstep, or reworking of older lithologies. However, a relative sea-level change can still be implied with the use of some proxy for the relative distance of the depositional setting to land. For the LSB, I argue that the TAR makes the strongest case for a change in this parameter. The TAR gently decreases through the section, excluding two sharp, positive peaks at 62 and 102 mm. This implies that, over time, the environment became increasingly distal, with terrigenous *n*-alkanes making up less of the sediment C_{org}. The sharp positive peaks are exceptions to this general trend, and correspond perfectly with the fluvial pulses described in Chapter 3, section 4.4. I argue, therefore, that at these points, an increased flux of terrigenous material entered the basin, and the higher bottom-water energy also allowed this material to be transported further away from the basin margins. In other words, the TAR records the combined influence of sea level and climate on the sedimentary organic matter composition. It is also important to stress that the TAR is not TOC normalised, so these negative peaks cannot simply reflect episodes of dilution (or lack thereof) by other organic matter components.

While pristane and phytane are often interpreted in the context of redox change, the presence of pristane can also provide information on the relative contribution of terrestrially-derived C_{org}. Both of these isoprenoids are derived from the cleavage of the phytyl side-chain of chlorophyll (a major component of terrestrial phytoclasts, especially leaves). Under oxic conditions, an increased flux of this material from the hinterland would lead to an increase in pristane, but not phytane (which does not typically survive long-distance transportation, due to oxidation of the precursor phytol to phytenic acid, and subsequent decarboxylation to pristane; Peters *et al.*, 2005, p. 499). It is, therefore, unusual to see both pristane and phytane, together making such high contributions to sediment C_{org}. There is no evidence for reoxygenation of the bottom water during deposition of Lithofacies B. It is therefore reasonable to suggest that while shelf-to-basin transport of organic material occurred during the deposition of Lithofacies B, its strength was insufficient to entrain enough oxygen into the benthic environment to facilitate the oxidation of phytol. Phytol was, therefore, protected from conversion into pristane during transport. If the flux of terrestrial organic matter accompanying these episodes of shelf-to-basin transport also had a high initial phytol content, and if these episodes were especially rapid, this mechanism can explain the high phytane content of the silty layer. The high levels of pristane could indicate that the shelf-to-basin transport event also reworked previously deposited pristane from more persistently oxic, marginal settings.

The relative contributions of marine and terrestrial carbon pools were also the main controls on the sterane distributions recovered from the LSB. Only C_{27} and C_{29} regular steranes show significant

variability (Fig. 5.6), and these are negatively, and positively (respectively) correlated with the TAR (Fig. 5.10). The $\Sigma C_{27}/\Sigma C_{29}$ regular sterane ratio also shows muted negative peaks roughly concomitant with the strong peaks in the TAR. This is in line with the widely reported association of C_{27} regular steranes with marine zooplankton and Rhodophyceae, and of C_{29} regular steranes with terrestrial organic matter (Huang & Meinschein, 1979; Czochanska *et al.*, 1988; Rieley *et al.*, 1991; Dahl *et al.*, 1994; Kodner *et al.*, 2008). The slight shift of the sterane data towards the marine field in $C_{27\text{-}29}$ regular sterane ternary space (Fig. 5.9) also corroborates the interpretation made based on the TAR – that palaeoshoreline distance increased through the deposition of the LSB.

C_{29} regular steranes are also associated with Charophyceae and Ulvophyceae, and the increase in the relative contribution of these steranes has been tied to shifts in redox-sensitive algal production (Kasprak *et al.*, 2015). The slight increases in C_{29} regular sterane abundance at 37 and 120 mm, could therefore, also be a function of enhanced productivity of green algae. While the nutrient stimulation of the surface layer (that I propose was present during the deposition of the silty layers; see section 4.1) could very well have favoured the proliferation of green algae, it is difficult to separate the relative influence of this proliferation from the effect of enhanced terrestrial organic matter flux on the C_{29} sterane content of the LSB.

No variation is observed in the contribution of C_{28} steranes to the LSB (in contrast to sediments deposited during the end Triassic extinction; Kasprak *et al.*, 2015). While prasinophytes (one of the main producers of C_{28} steranes), are nonetheless present (Chapter 4, section 2.1), their absolute contribution to the palynofacies, and the sterane distribution of the LSB is relatively low (although their relative contribution to the phytoplankton assemblage varies markedly).

3.3 Euxinia

Although partly degraded during catagenesis into aryl isoprenoids, and a biphenylic derivative (see Chapter 1, section 9.1.6), the presence of isorenieratane in the LSB corroborates (along with small framboid diameters and the enrichment in Mo; Chapter 3, sections 3.1.1 and 3.4) the occurrence of euxinia, and the presence of free sulphide in the photic zone of the water column. While isorenieratane can also be produced by mat-forming Chlorobiaceae (Beatty *et al.*, 2005; Bühring *et al.*, 2011), no lithological evidence of this (i.e. wavy lamination; O'Brien *et al.*, 1990) was found in hand specimen, or thin section of the LSB. Some mat-derived isorenieratane may have been delivered into the basin depocenter during storms (see Chapter 6, section 3.4 for a fuller discussion), however, it is tentatively assumed that the amount of isorenieratane supplied by this pathway is lower compared to that produced by Chlorobiaceae blooms within the water column.

The trend in the concentration of isorenieratane through the LSB mirrors that of TOC, S_{py} and Mo/Al (and is approximately inverse with that of mean framboid diameter, Figs 3.16; 3.26). This indicates that the euxinia that characterised the upper part of Lithofacies A, and most of Lithofacies B did indeed extend into the photic zone, and that free sulphide availability was the limiting factor on planktonic Chlorobiaceae production.However, it is possible that the primary productivity of Chlorobiaceae was controlled by more factors than just the presence of free sulphide. As discussed in Chapter 3, section 4.5, this interval of the LSB was likely characterised by strong stratification (as implied by strong Mn cycling). If this was the case, then it is possible that bioavailable nutrients were locked below the chemocline, only being returned to the photic zone by infrequent episodes of upwelling. Sælen *et al.* (1996) invoked such a mechanism to explain the low $\delta^{13}C$ values of the black shales of the Mulgrave Shale Member, with upwelling episodes returning isotopically depleted carbon to the surface layer. If present during deposition of the LSB, upwelling episodes would have returned euxinic water masses to the photic zone during the deposition of Lithofacies B – the frequency of which could have also been a limiting factor on Chlorobiaceae production. Recent work has shown that the modern Benguela Upwelling System – known for high productivity levels and the occasional upwelling of sulphidic water masses - can support booms of (isorenieratane-producing) brown-pigmented green sulphur bacteria (Ma *et al.*, 2021). Alternatively, there could have been some limitation on light penetration during the deposition of the LSB (since Chlorobiaceae require fluorescent light intensities of at least 5 – 10 $\mu mol \cdot m^{-2} \cdot s^{-1}$, and no more than 200 $\mu mol \cdot m^{-2} \cdot s^{-1}$; Overmann, 2006), and this could well have been the case during the emplacement of the large silty lens at 62 mm.

While the lithology of the LSB indicates that episodes of storm activity occurred, it was likely at its most intense in the silty lens at 62 mm. It is, therefore, probable that the temporary decrease in Chlorobiacae production during this brief interval was related to reduced light penetration in a turbid water column, despite the presence of sufficient sulphide – S_{py} and Mo/Al values do not show significant depletion during the silty lens (Fig. 3.26), and sedimentary features such as the silty lens are often diagnostic of infrequent, strong storms. Alternatively, the episode of shelf-to-basin transport responsible for the formation of the silty lens could have raised the oxygen content of the photic zone for a geologically brief period. However, the silty lens also contains reworked pyrite framboids (Chapter 3, section 2.1), and its location directly below the most organic-rich interval of the LSB (characterised by the most intense oxygen depletion), implies its emplacement lead (ultimately) to a depletion of the basinal oxygen inventory (see section 4.1). However, the low isorenieratane content per gram of sediment in the silty lens could also be related to dilution of the sample by the high silt content. While this is a potential consequence of sediment normalisation, TOC normalisation would yield unrealistically high (for a low TOC sediment) isorenieratane concentration values in the silty lens (see section 3.0).

The positive shift in the steranes/steranes+hopanes ratio at 46 mm (Fig. 5.5) implies that algal production increased at this point. It is also possible that a general shift towards greater levels of primary production occurred here, although the shift pre-dates the emplacement of the silty layer (and therefore, the interval of enhanced nutrient flux). Enrichment of Zn/Al and Cu/Al in Lithofacies B could be interpreted as tracking an increase in productivity (Saito *et al.*, 2002; Algeo and Maynard, 2004; Naimo *et al.*, 2005), but the enrichment of both metals is also controlled by syngenetic pyrite formation (which was intense in the LSB; Chapter 3, section 4.3; Huerta-Diaz and Morse, 1992; Tribovillard *et al.*, 2006). A better evaluation could, however, be attempted through the use of sequential P extraction, which can be used to evaluate changes in the organic matter and Fe oxide-associated P content of the LSB – a proxy for the extent of P utilisation following episodes of upwelling of sub-chemocline waters (März *et al.*, 2008). $\delta^{114}Cd_{Org}$ is also negatively shifted by biological uptake of ^{110}Cd, and hence (assuming no change in authigenic sulphide precipitation), a negative shift in the $\delta^{114}Cd$ signature of the LSB could be indicative of higher primary productivity (although the validity of this method is still an active area of research; Sweere *et al.*, 2020; Bryan *et al.*, 2021). Thermal or salinity stratification could be further evaluated by a targeted $\delta^{18}O$ and $\delta^{13}C$ analysis of belemnite rostra through the LSB (as in Sælen *et al.*, 1996).

The presence of isorenieratane in Lithofacies A, like the Fe speciation data, strongly implies that the environment was subjected to episodes of severe oxygen depletion (to the point of euxinia), despite the high bioturbation levels seen in this interval. During these periods, the anoxic/oxic chemocline rose above the sediment-water interface, and resulted in infrequent blooms of chlorobiaceae in the water column. However, the wide framboid diameter distribution, and limited (essentially background) Mo content of the sediments argue against the presence of a large volume of aqueous sulphide in the water column. It is possible, therefore, that the euxinic episodes were short-lived enough that any euxinia signal in these proxies became time-averaged by intense bioturbation during intervening episodes of bottom-water oxia.

The positive point excursions in TAR (i.e. fluvial pulses), are also coeval with negative excursions in the AIR, against a relatively constant background. Taken at face value, this implies that the silty lenses were associated with longer-lasting episodes of photic zone euxinia, compared with the sediments of Lithofacies A, and the TOC-rich Lithofacies B. While it is possible that nutrient stimulation of surface waters during the emplacement of the silty layer (see section 4.0) led to prolonged episodes of Chlorobiaceae production (with coeval strong fluxes of Chlorobiaceae-derived organic matter to the sediment), this layer is associated with reverse grading (Fig. 3.16). It is more than likely that under these relatively energetic conditions, any short-chain aryl isoprenoids that comprised the sediment were selectively winnowed away, leaving behind only the long-chain aryl

isoprenoids. A straightforward interpretation of the AIR does require the assumption that the preservation conditions of sedimentary organic matter remained constant (Schwark & Frimmel, 2004), and the dynamic nature of sediment deposition in the LSB, therefore, complicates the interpretation of the AIR. Additionally, the AIR shows values associated with episodic euxinia (Fig. 5.12) in the interval characterised by the highest levels of isorenieratane. This further implies that the interval was characterised by strong stratification, with the majority of Chlorobiaceae production occurring in sporadic episodes of water column overturning.

3.4 Redox

Since the Cleveland Basin was hydrographically isolated from the wider EES – and the resupply of aqueous oxygen therefore limited – an enhanced biological pump could have drastically reduced the dissolved oxygen inventory of the basin, and, therefore, could have been the key factor in triggering the system-shift of the basin (see section 4.1). This is implied by the close juxtaposition of a silty lens with an interval of C_{org}-rich sediment (implying an enhanced fluvial flux and nutrient stimulation; see section 4.0), and by the shift in the steranes/steranes+hopanes ratio at 46 mm – a typical organic geochemical marker of enhanced algal productivity.

The pr/phy ratio is somewhat elevated throughout the section (compared to typical marine shale values) due to the addition of excess phytol from terrestrial organic matter (Figs. 5.4 and 5.14). This means that the widely accepted threshold values for distinguishing anoxic and dysoxic/suboxic environments (Huges *et al.*, 1995), cannot be applied here. However, the ratio shows a gentle decrease in the middle of the LSB, further strengthening the case for a decline in the average redox state. C_{35} homohopanes are present within the LSB, indicating reduced oxidation of the bacteriohopanetetrol precursor (consistent with a periodically anoxic environment; Peters & Moldowan, 1991). However, the lack of significant increase in the C_{35} homohopane index within Lithofacies B implies that the fixation of hopanoids in the kerogen through sulphurisation of the side chain was greatly reduced (Köster *et al.*, 1997). This further implies that most free sulphide was incorporated into pyrite before significant organic matter sulphurisation could occur. Curiously, the presence of dibenzothiophene within the LSB (see 3.6) indicates that organic matter sulphurisation did occur, although the content of dibenzothiophene, and methyldibenzothiophenes is not correlated with that of C_{35} hopanes (Fig. 5.21). The dominant pathway for dibenzothiophene formation in marine sediments is unknown, but

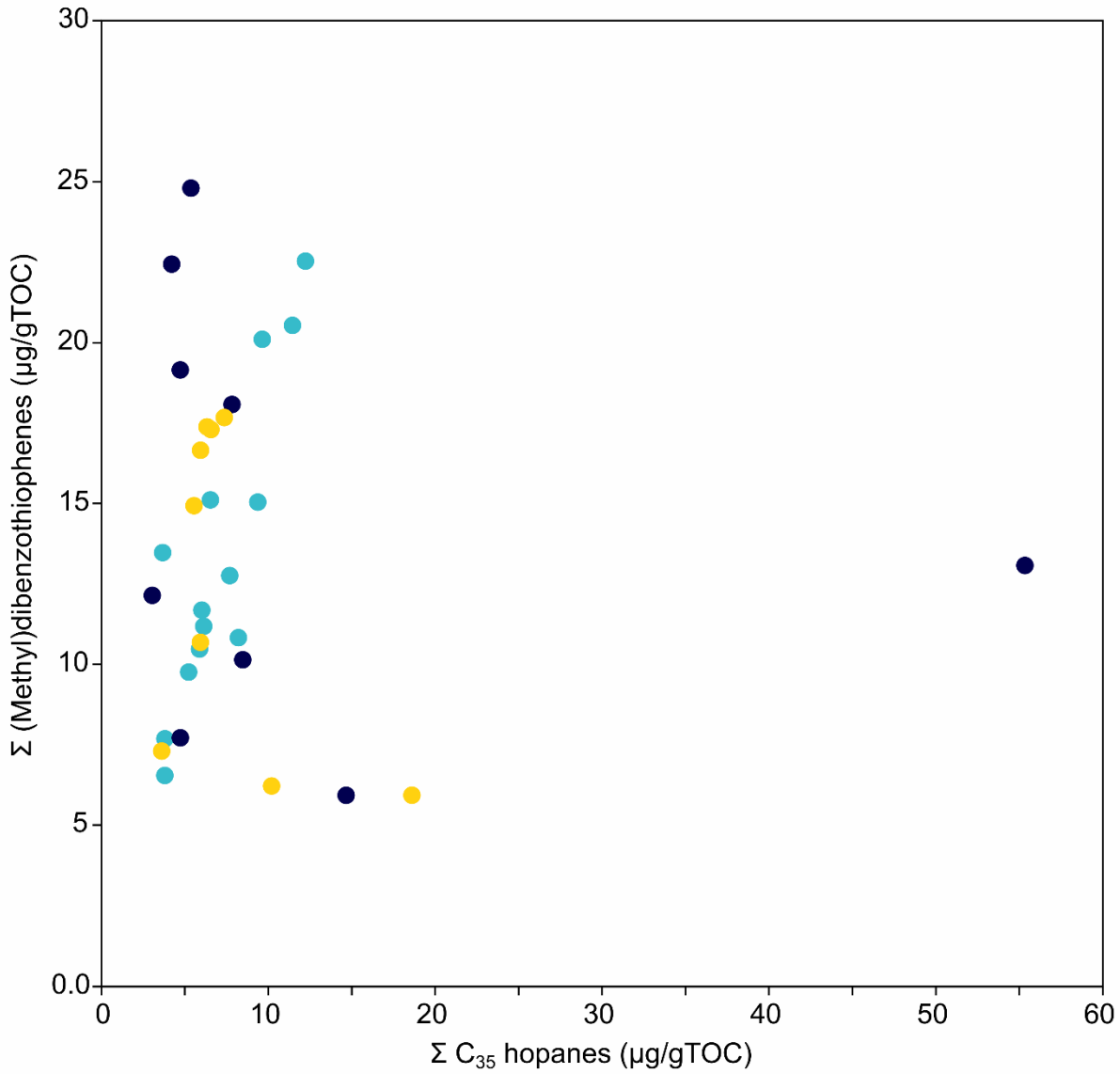

Figure 5.21. Concentration of C_{35} hopanes through the LSB, compared with that of dibenzothiophene and methyldibenzothiopnehes (grouped together as Σ(methyl)dibenzothiophenes.

one possibility is that biphenyl is catalytically sulphurised in the presence of elemental sulphur, on the surface of carbonaceous particles (Asif *et al.*, 2009). The high levels of dibenzothiophene, concomitant with relatively low C_{35} homohopane index values, imply that this sulphurisation pathway (if present) was a more active process than the sulphurisation of hopanoid side chains. The presence of biphenyls in marine sediments has been linked with the biodegradation of carotenoids (Grice *et al.*, 1996) and the oxic degradation of PAHs hosted in plant-derived resins (Sun & Püttmann, 2001). Of these two processes, the biodegradation of carotenoids is a more likely source of biphenyl within the LSB, since carotenoids are abundant, and there is no evidence for extensive oxidation of the organic matter post-deposition (the presence of biphenyl in the German Kupferschiefer was attributed to this, Sun & Püttmann, 2001). However, it could be argued that a slight positive correlation between C_{35}

hopanes and (Methyl)dibenzothiophenes is evident in Lithofacies A (Fig. 5.21), which would mean that the sulphurisation of biphenyl became a dominant process only after 52 mm. This would require either an increase in the availability of elemental sulphur or biphenyls.

3.5 Organic matter sulphurisation

The presence of dibenzothiophene, methyldibenzothiophenes, and the depression of the phenanthrene/dibenzothiophene ratio in the LSB, indicate the post-depositional sulphuristation of organic matter within the LSB. Dibenzothiophene is exclusively produced during diagenesis, and is believed to be particularly characteristic of reactive Fe-limited sulphidic conditions (Hughes *et al.*, 1995; Peters *et al.*, 2005, p.32). While highly reactive Fe is abundant in this section (Chapter 3, section 3.3), the presence of dibenzothiophene indicates that the sulphide concentration (especially in sediment porewaters), often exceeded the reactive Fe supply. The trends observed are completely different to that of the "S_{org}" trend presented in Chapter 3, section 3.3, and further invalidate its utility in this study.

Although not detected in this analysis, it is also possible that other S-bearing organic phases were present, and separated from the TLE into the polar fraction during the SPE. An analysis of this fraction may better quantify the occurrence of isoprenoid polysulphides, which can be formed via successive sulphurisation of phytol (de Graaf *et al.*, 1992). It is possible that the enhanced Mo/Al level of Lithofacies B was, in part, due to sequestration by sulphurised organic matter species (although the efficiency of this pathway of Mo sequestration has been questioned; Helz *et al.*, 1996; Tribovillard *et al.*, 2004; Helz & Vorlicek, 2019).

The ratio of phenanthrene/dibenzothiophene shows a very distinct positive spike at 62 mm, implying that organic matter sulphuristation was greatly reduced here. This is not especially surprising given that the interval was very TOC lean, and therefore, unlikely to generate any significant quantity of aqueous sulphide during diagenesis. However, the reworked pyrite framboids within this silty layer imply that the shelf-to-basin transport responsible for its formation did not entrain much oxygen into the marine environment (see section 3.2). Since there is also evidence for a fluvial pulse at this point, the high phenanthrene/dibenzothiophene ratio might in part be driven by sulphate limitation (i.e., the influence of low-salinity waters), independently from redox change. However, the pr/phy ratio does not nearly meet the threshold associated with true brackish environments (pr/phy = 3.0; Hughes *et al.*, 1995), and the majority of the section displays clear palaeontological (marine bivalves and belemnites) and geochemical (sulphide-rich) evidence for being deposited in a shallow marine environment. The transgression invoked in section 3.2 might also partly explain the gentle downward

trend in phenanthrene/dibenzothiophene through the section, due to the loss of sulphate limitation via the predominance of marine waters.

3.6 Retene and phenanthrene

The trend in the enrichment of retene in the LSB does not differ markedly from that of the phenanthrenes and dibenzothiophenes, and does not perfectly mirror the dominance of bisaccate producers in the terrestrial plant community (Chapter 4, section 2.1): bisaccate producers make a small, but persistent contribution terrestrial plant sporemorph assemblages during the deposition of Lithofacies A, before proliferating at the expense of *Chasmatosporites* sp. in Lithofacies B. Retene, however, only shows elevated concentrations in the TOC-rich part of Lithofacies B (along with phenanthrenes and dibenzothiophenes), which implies that it was produced primarily in the sediment during early diagenesis.

Since the content of retene and phenanthrenes within the LSB broadly track that of dibenzothiophenes (exclusive geosphere compounds), it is unlikely that they are indicative of any change in the frequency and severity of wildfires through the section. The increased occurrence of wildfire-derived charcoal concomitant with the termination of the TOAE CIE has been interpreted as a marker for enhanced atmospheric pO_2 levels, which might have been instrumental in the termination of the TOAE (Baker *et al.*, 2017). Retene and a range of other PAHs have also been recovered from Toarcian-aged coals in Poland (Rybicki *et al.*, 2016), which implies that they could be used to track the severity of wildfires through this stage of the Lower Jurassic. While retene is elevated within Lithofacies B, it is not accompanied by any supporting proxy evidence for wildfire activity, such as increased opaque phytoclast content (Appendix 2), and I, therefore, suspect its increased content in Lithofacies B reflects the diagenetic breakdown of aromatic compounds. The phenanthrene detected within the LSB is likely to be microbial in origin, and produced by the degradation of aromatic 8,14-secohopanoids (Killops 1991).

3.7 Carbon cycling via Compound-Specific Isotopic Analysis (CSIA)

While a clear negative excursion is not evident in the CSIA data, the $\delta^{13}C$ values of both short and long-chain *n*-alkanes are lower than the values of both bulk TOC and *n*-alkanes in the upper Grey Shale and Mulgrave Shale Members (which have been attributed to exogenic carbon cycle perturbation; French *et al.*, 2014). The long-chain CSIA data points are also consistently lower than concomitant $\delta^{13}C_{org}$ data (Littler *et al.*, 2010) by 3.33 – 10.6 ‰ (Fig. 5.22). This is of great

palaeoenvironmental significance, and implies that during the deposition of the LSB, both marine and terrestrial carbon pools were isotopically depleted. The low $\delta^{13}C$ signatures of marine *n*-alkane pools (lower than bulk $\delta^{13}C$) strongly imply that the primary producers in the Cleveland Basin acquired their carbon from an isotopically depleted reservoir. If the environment was strongly stratified (as suggested by the Mn/Al data; Chapter 3, section 3.5), then primary producers in the photic zone would have acquired the carbon needed to synthesise short-chain (C_{17-19}) *n*-alkanes from highly isotopically depleted carbon recycled from below the chemocline by episodic upwelling. Such a mechanism has been invoked to explain the prominent negative $\delta^{13}C_{org}$ excursion in the *C. exaratum* subzone (Sælen *et al.*, 1996). However, the concomitant $\delta^{13}C$ signatures of terrestrial *n*-alkane pools in the LSB are also consistently isotopically depleted with respect to bulk $\delta^{13}C$ (by 3.33 – 10.6 ‰), which indicates that terrestrial primary producers incorporated depleted carbon as well. A decline in the $\delta^{13}C$ signature of *n*-alkanes derived from leaf wax cuticle could also reflect a shift to a more humid climate at constant pCO_2 levels (Kohn, 2010), but humid climate shifts in the geological past a frequently associated with high pCO_2 levels (e.g. the Carnian pluvial event; Dal Corso *et al.*, 2012) – in which case a decline in the $\delta^{13}C$ of leaf wax cuticle reflects the influence of two linked palaeoenvironmental changes. Additionally, as argued by Hesselbo *et al.* (2000), the presence of prominent, concomitant $\delta^{13}C$ excursions in marine and terrestrial carbon reservoirs is highly unlikely to be coincidental, given the network of interactions between the atmosphere and terrestrial and marine ecosystems in the surface carbon cycle. The isotopically light carbon in the *n*-alkanes from the LSB, therefore, is likely to have been added to the earth surface system through either the dissociation of a climate-sensitive methane reservoir (Kemp *et al.*, 2005; Ruebsam *et al.*, 2019; 2020a), or possibly through volcanic activity (Svensen *et al.*, 2007).

The fact that large jumps in the up-section $\delta^{13}C$ trends were not observed is probably to the low stratigraphic coverage of my study. It is possible that if my sampling interval extended further down into bed 25, or further up into bed 27 of the Cleveland Ironstone series, different $\delta^{13}C$ values could have been encountered. As discussed in Chapter 3, section 3.0, the chosen sampling methodology prioritised resolution over completeness, and while highly detailed up-section plots of the specific isotopic signatures of palaeoenvironmentaly important carbon pools have been evaluated, it is difficult to place them in a wider stratigraphic context. The CSIA dataset presented here would be greatly improved by the inclusion of as little as 1-2 samples from the upper part of bed 25, or the lower part of bed 27, even at the expense of some resolution in these beds. At the very least, it is probable that such an analysis would help to better align the dataset with the bulk $\delta^{13}C$ study of Littler *et al.* (2010) – attempted in Fig.5.22.

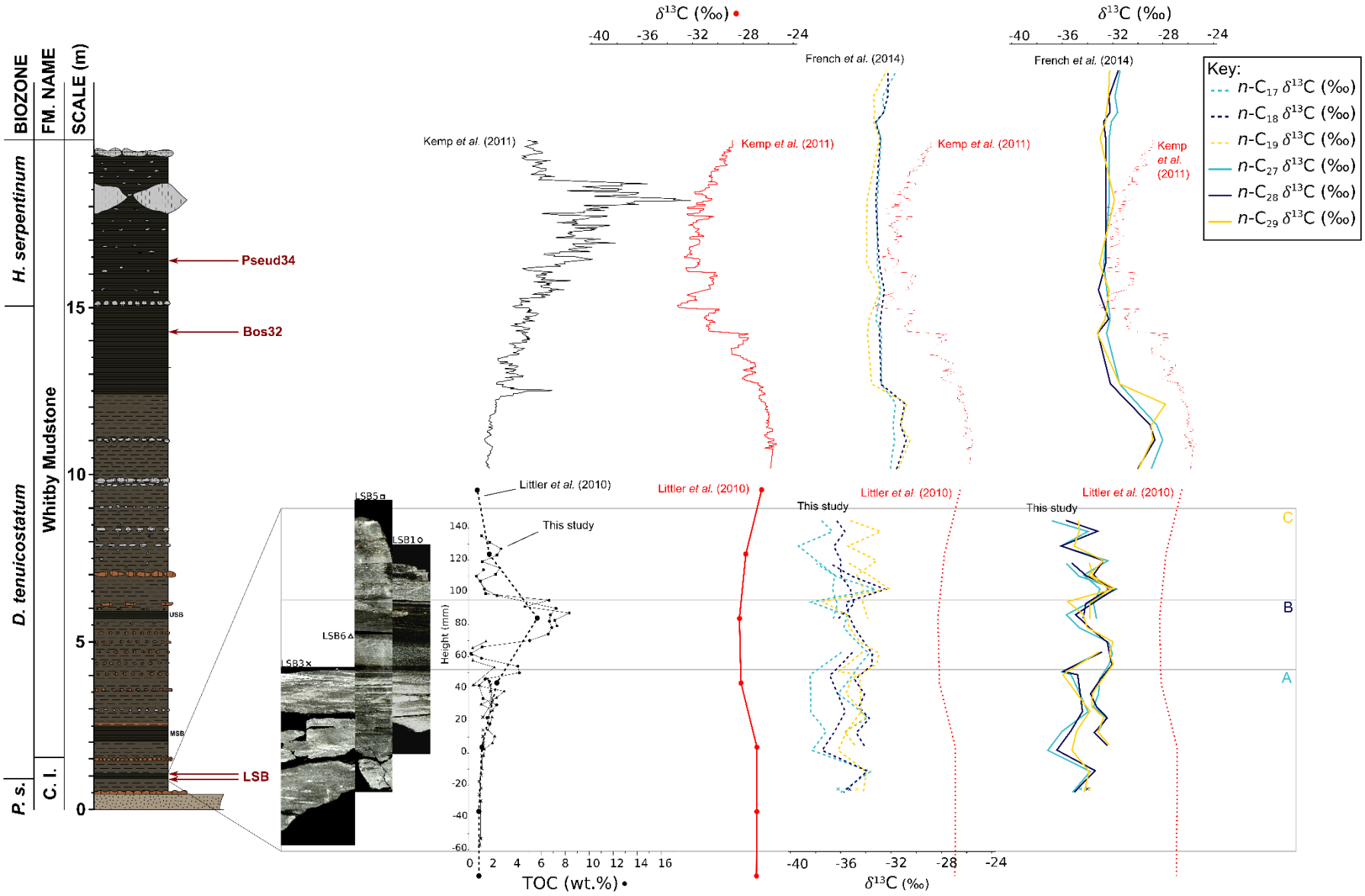

Figure 5.22. My CSIA dataset compared with published bulk and compound-specific isotopic studies of the Cleveland Basin. Two bulk isotopic datasets are plotted in red – one for the LSB (Littler *et al.*, 2010), and one for the *C. exaratum* subzone (Kemp *et al.*, 2011). The corresponding TOC values for these samples are also plotted (superimposed in my TOC dataset in the LSB). My CSIA plots are compared with the bulk d13C trends, as well as the CSIA plots of French *et al.* (2014) – short chain CSIA plots are dashed, and long chain CSIA plots are solid lines. Note that the lower part of the diagram encompasses the LSB (and is centimeter scale), while the upper part of the plot encompasses the *C.exaratum* subzone (and is meter scale). A simplified stratigraphic column is also included on the far left.

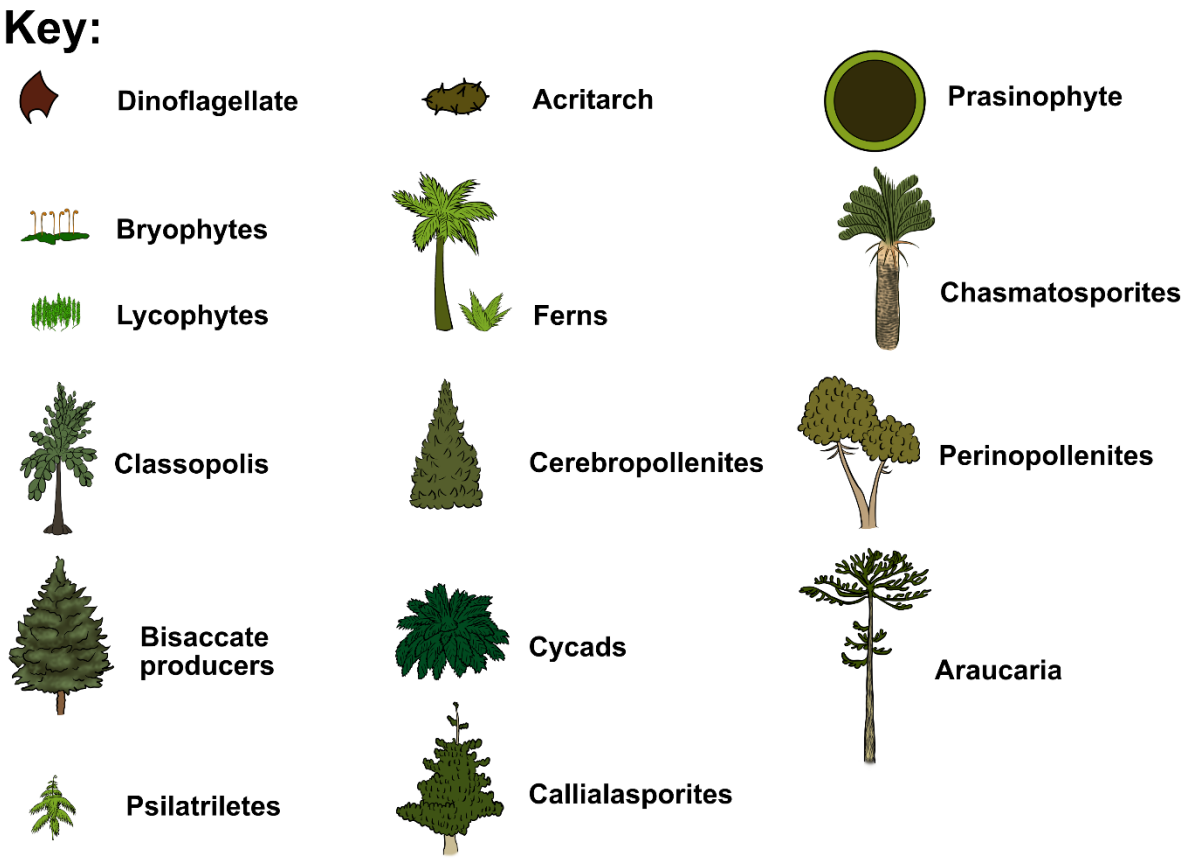

Figure 5.23. Key for phytoplankton and terrestrial plant illustrations used in Figs. 5.23 – 5.26.

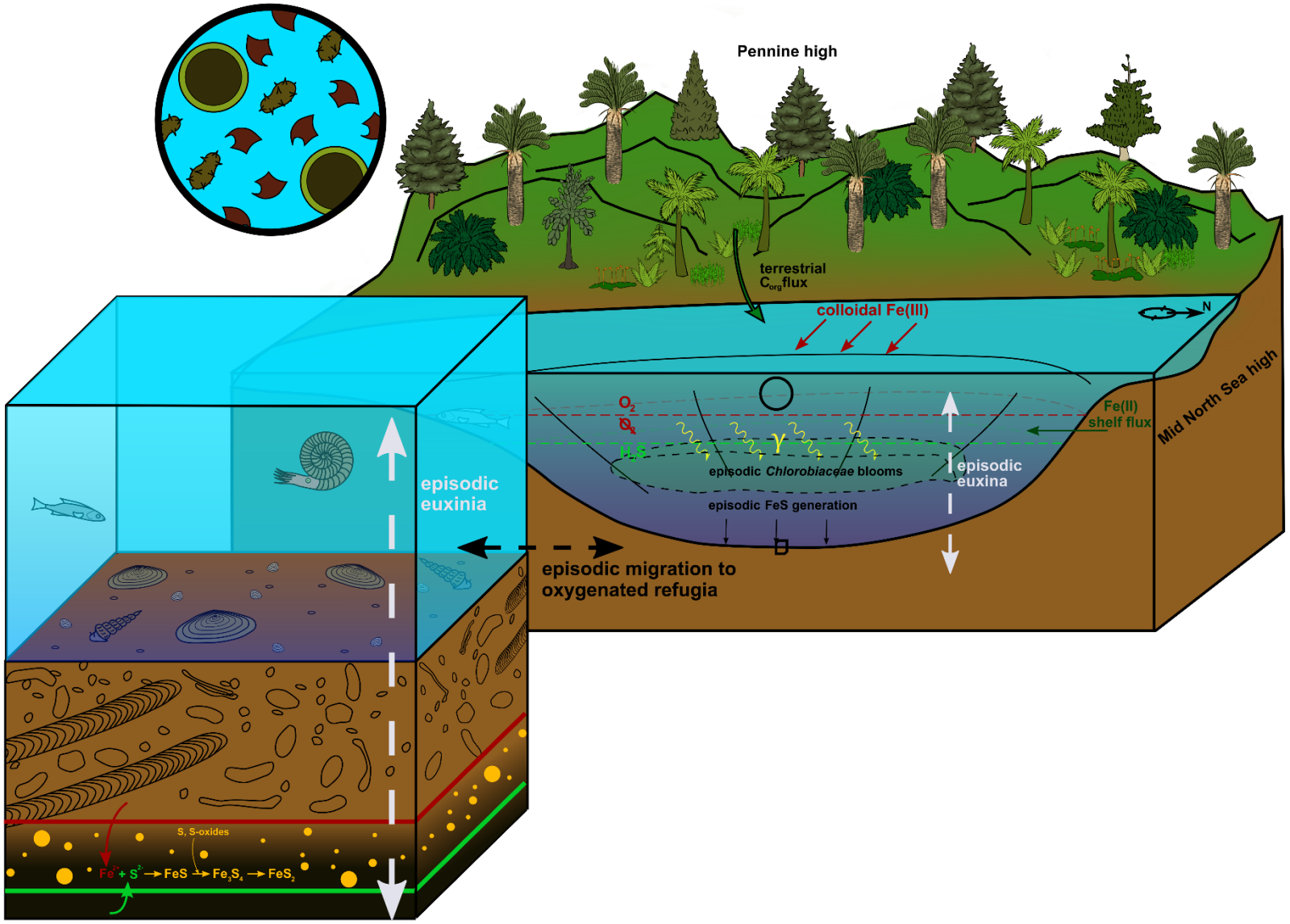

Figure 5.24. Geological reconstruction of the lower part of the LSB (-60 - 52 mm, Lithofacies A), with reconstructions of the marine phytoplankton, and terrestrial floral communities. Frequent dysoxia and episodic anoxia/euxinia results in a phytoplankton community dominated by dinoflagallates and prasinophytes, while the warm, slightly humid climate favors a terrestrial plant community characterized by ferns, Chasmatosporites and bisaccate pollen producers. Episodes of photic zone euxinia also lead to a moderate level of chlorobiaceae production, but are not frequent enough to significantly impact the benthic community.

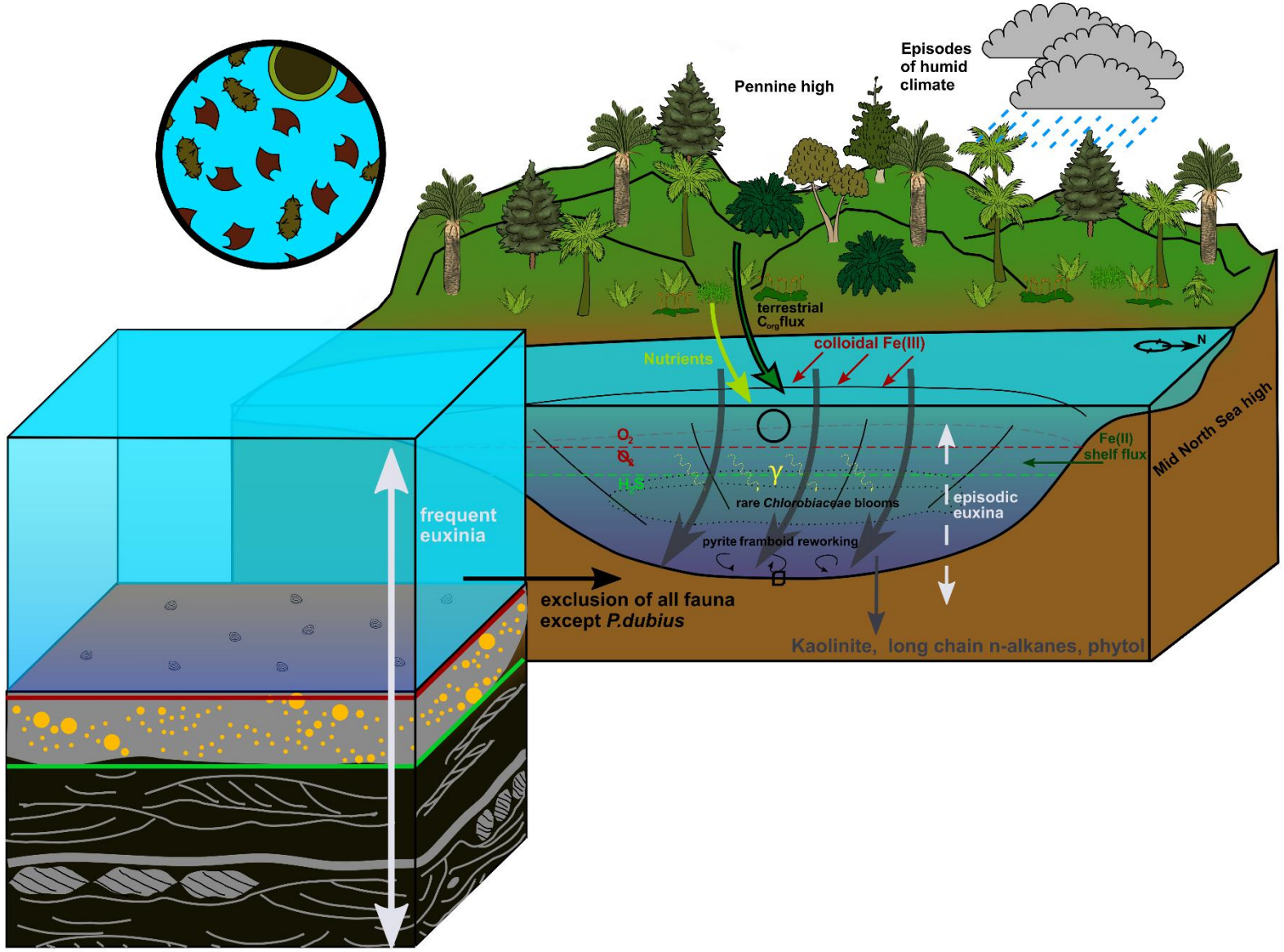

Figure 5.25. Geological reconstruction of the LSB from 52 – 66 mm (Lithofacies B). An episode of pronounced humidity results in a greater fluvial flux into the Cleveland Basin from the surrounding hinterlands, enhancing the nutrient loading of the basin, and delivering kaolinite clay, and a higher proportion of recalcitrant C_{org} to the basin. Episodes of shelf-to-basin transport result in the deposition of a large silty layer, and reworking of pyrite framboids. The higher nutrient loading results in frequent chlorobiaceae blooms, and the more frequent episodes of anoxia/euxinia preclude all macrobenthos apart from *P.dubius*. Prasinophytes make up less of the phytoplankton community, and the terrestrial pant community becomes dominated by bryophytes, lycophytes and ferns.

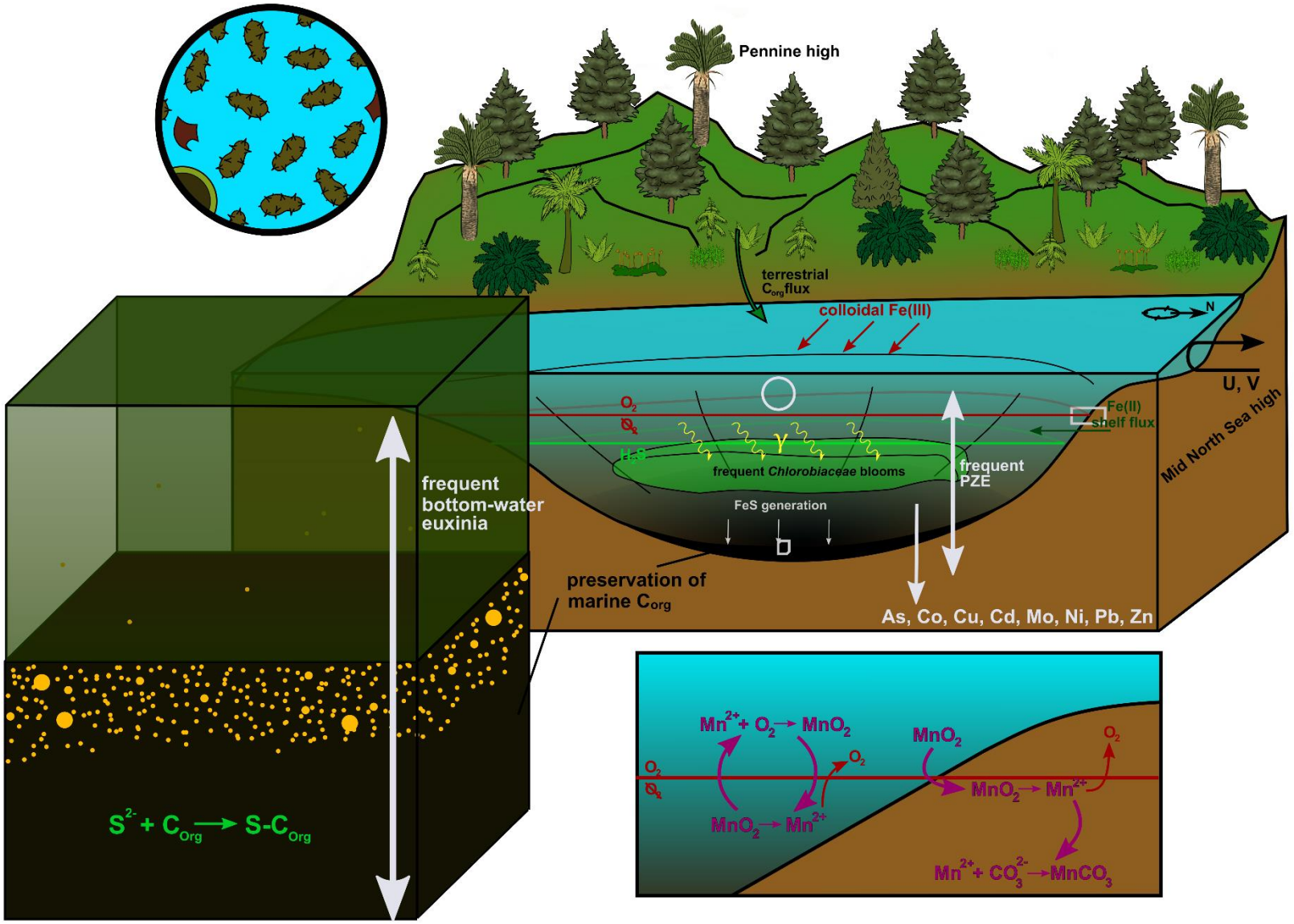

Figure 5.26. Geological reconstruction of the LSB from 66 - 94 mm (Lithofacies B). While a drier climate favors a land plant community dominated by bisaccate producers, the Cleveland Basin has shifted into a state characterised by highly frequent anoxia. A strong chemocline results in prominent Mn cycling (Chapter 3, section 4.5), and the frequently anoxic/euxinic conditions result in the sequestration of labile C_{org} and of trace elements within syngenetic pyrite. The highly stressed marine phytoplankton community is dominated by acritarchs, while strongly stratified conditions, with infrequent upwelling of euxinic water masses, support episodic chlorobiaceae blooms.

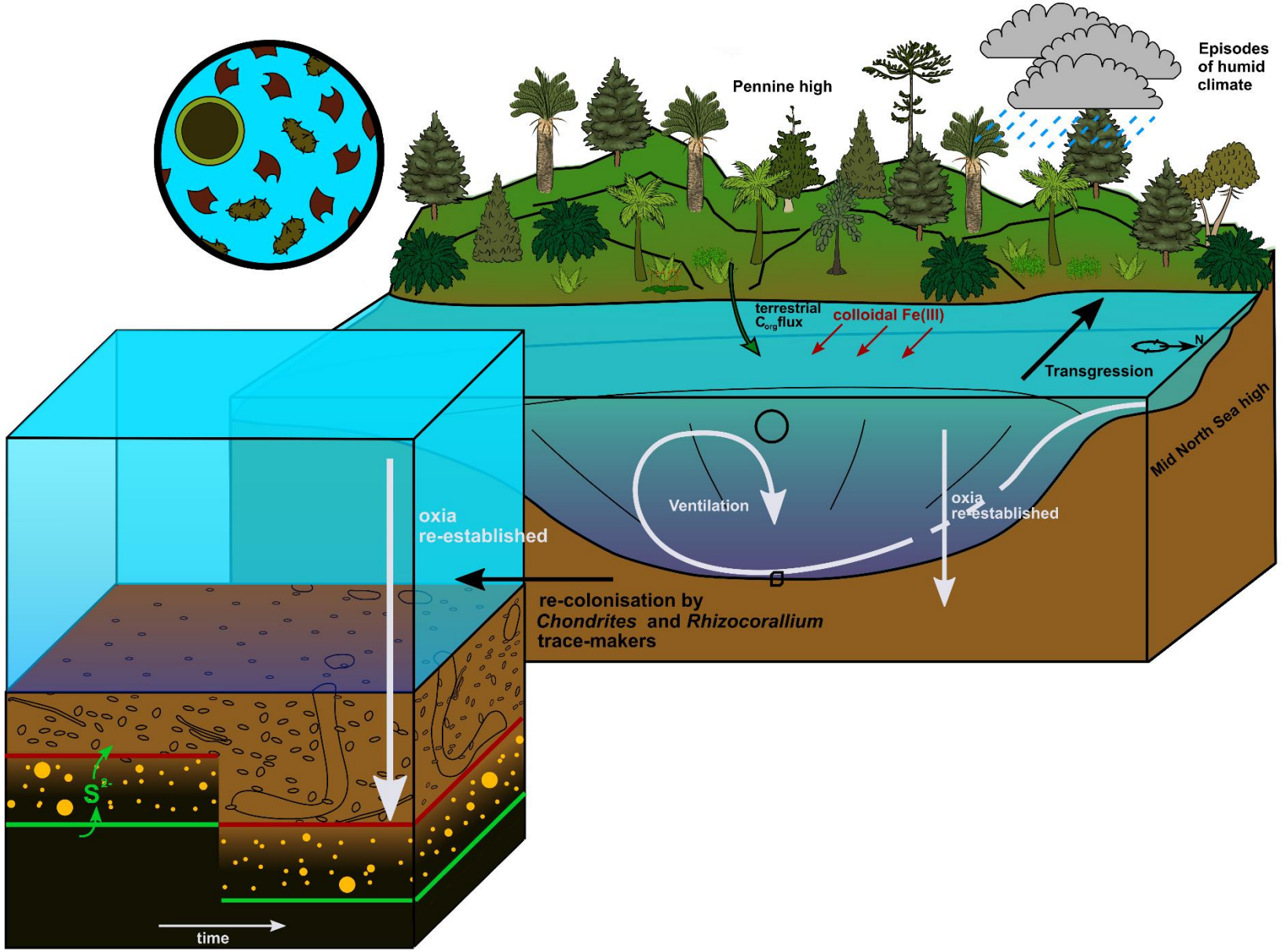

Figure 5.27. Geological reconstruction of the LSB from 94 - 145 mm (Lithofacies C). A transgression, possibly forced by deglaciation at the close of the Pliensbachian iceahouse (see text), results in ventilation of the water column in the Cleveland Basin. This results in the gradual recovery of the benthic community, with *Chondrites*-producing pioneers being followed by *Rhizocorallium* producers. Dinoflagellates begin to dominate the phytoplankton community, and chlorobiaceae production ceases. The intermittently humid climate leads to a land plant community composed of ferns, cycads and bisaccate producers.

4.0 Discussion

4.1 Implications for model of formation of the LSB

My comprehensive investigation into the redox chemistry of the LSB, both via inorganic and organic geochemical analysis, reveals that the enhanced frequency of anoxia concomitant with the deposition of the LSB was initiated due to an episode of enhanced nutrient flux into a restricted basin. The large silty layer at 62 mm (concomitant with frequent episodes of high Chlorobiaceae biomass production), immediately precedes the deposition of large amounts of organic matter in Lithofacies B, and it is therefore reasonable to suggest a genetic relationship here. The more hydrographically restricted a basin becomes, the longer the residence time of water within it. Assuming no change in removal fluxes, any increase in nutrient flux into the basin would raise the baseline nutrient concentration in the water mass. Moreover, enhanced freshwater fluxes into proximal marine environments frequently lead to short, sharp spells of stratification (e.g. Ærtebjerg *et al.*, 2003). An enhanced nutrient flux into a hydrographically restricted marine setting, therefore, raises the probability for periods of enhanced eutrophication, either directly (through nutrient loading), or during episodes of upwelling in a stratified setting (which return nutrient-rich waters to the photic zone). While enhanced primary production (irrespective of oxygen depletion) is poorly correlated with organic carbon accumulation in the modern ocean (Tyson, 1995, p.34), these environments are typically open marine upwelling zones, so any oxygen consumed by remineralisation of excess production would be replaced by ocean currents. In restricted environments, the ability of ocean currents to replenish aqueous oxygen supply is greatly reduced. Therefore, the effect of an increase in primary productivity on the marine oxygen budget (and, as a consequence, organic matter preservation), is much more pronounced. Indeed, sediments from restricted environments tend to have TOC values five to six times higher than those deposited in more oxic settings (Raiswell *et al.*, 1988). The *n*-alkane and regular sterane data presented here imply that a transgression was the primary mechanism responsible for the recovery of the redox state of the Cleveland Basin after the deposition of the LSB. A higher sea level would have probably (assuming no tectonically controlled change in basin architecture) improved the hydrographic connection of the Cleveland Basin to the wider EES, and would therefore have favoured the ventilation of the basin through the circulation of oxic marine waters. This would also explain why the fluvial fluxes that occurred during the deposition of Lithofacies C did not lead to a decline in basin redox like they did in Lithofacies B. The enhanced connectivity of the basin meant that any oxygen consumed in the remineralisation of an enhanced organic matter flux (due to enhanced new production under eutrophic conditions in the photic zone) would be replaced. This model for the development, and disappearance of, frequently anoxic conditions within the LSB is summarised in the series of geological reconstructions presented in Figs. 5.24 – 5.27 (A key for the illustrations used is

presented in Fig. 5.23). The geological reconstructions also illustrate the changes in the marine phytoplankton and land plant assemblages described in Chapter 4 (sections 3.2.1).

While an enhanced fluvial flux would have greatly enhanced stratification towards the basin margins, it is unlikely that this led to the prolonged stratification of the basin during the deposition of Lithofacies B (as indicated by, for example, Mn/Al enrichment; Chapter 3, section 3.5). Salinity stratification is typically only developed where a significant flux of freshwater enters a saline water body (e.g., in estuaries), and is, therefore, inherently spatially limited. Higher sea-surface temperatures in the Cleveland Basin, over a prolonged period of time (thousands of years) are more likely to have been the cause of sustained water column stratification. While existing $\delta^{18}O_{bel}$ datasets from the Pl-To of the Cleveland basin do not indicate any major changes in SST (Korte & Hesselbo, 2011; Korte *et al.*, 2015), it is likely that these datasets do not capture sufficiently high-resolution variability in SST across the LSB to rule out a short, sharp temperature rise. Belemnites are occasionally found in the LSB, and a $\delta^{18}O$ analysis targeting these belemnites will provide a better constraint on temperature change through the LSB. It is also possible that an organic geochemical proxy for palaeotemperature, such as TEX86 (Ruebsam *et al.*, 2020b) could be evaluated through this interval. A palaeotemperature record with much greater vertical resolution could be reconstructed this way (since it is a bulk sediment analysis).

Ultimately, I argue it is probable that the LSB marks a regional expression of global climatic disruption at the Pl-To, given the evidence I have presented for enhanced fluvial fluxes during episodes of wetter climate. The Palaeocene-Eocene Thermal Maximum (PETM) was another interval of global climatic perturbation, and was in many ways analogous to the Pl-To: both events are marked by carbon isotope excursions of similar magnitude (and shape), and by atmospheric carbon injection of high rate, and short duration (Clapham & Renne, 2019). The PETM was also associated with an enhanced hydrological cycle (Carmichael *et al.*, 2017), and consequent changes in clay mineral assemblages (John *et al.*, 2012). While black shales were not as well developed in the PETM as in the Pl-To, oxygen depletion (sometimes to the point of photic zone euxinia) was nonetheless a widespread phenomenon during this event as well (Schoon *et al.*, 2015). The PETM was marked by a temperature shift of 5 – 8 °C (McInerney & Wing, 2011), and it is believed that a similar excursion in temperature occurred (at least in some localities) during the Pl-To (Ruebsam *et al.*, 2019). However, I have not uncovered any direct evidence for higher temperatures, and indeed, one of the markers for a hotter terrestrial environment (the occurrence of *Cerebropollenites*; Chapter 4, section 3.2.1; Slater *et al.*, 2019) is absent. While it could be argued that this is consistent with a relative stasis in temperature throughout the deposition of the LSB (Korte *et al.*, 2015), it is, again, unlikely that a geologically brief period of water column stratification (such as is observed in the LSB), accompanied by episodes

of enhanced surface runoff under humid climatic conditions, occurred in the absence of a temperature rise.

4.2 Wider implications

The upper Pliensbachian stage of the Lower Jurassic was characterised by significantly cooler global temperatures than the Toarcian, as indicated by the heavier $\delta^{18}O$ of shelly macrofauna recovered from successions of this age, such as the Cleveland Ironstone Formation (Korte & Hesselbo, 2011), and the Rodiles Formation of the Asturian Basin (Northern Spain; Gomez *et al.*, 2016). The occurrence of glendonites (and, occasionally, pseudomorphs after ikaite) in upper Pliensbachian sediments from Germany and Siberia (Suan *et al.*, 2011; Teichert & Luppold, 2013) strongly imply that the high latitudes reached temperatures below 4 °C, and episodes of mantle-upwelling induced uplift in the North Sea are likely to have limited circulation of warm ocean waters to the high latitudes (Korte *et al.*, 2015). Furthermore, recent work has suggested that the CIEs of the Pl-To and the T-OAE were produced by the destabilisation of a climate-sensitive reservoir of ^{13}C depleted carbon, and that it is likely that this reservoir was permafrost developed in the high latitudes of Eurasia during the upper Pliensbachian (Ruebsam *et al.*, 2019; 2020a). If this is the case, then it is probable that the Pl-To event was characterised by a eustatic sea level rise in addition to higher global temperatures. The sea level curve of Hesselbo (2008) – based on the lithological identification of transgressive and regressive systems tracts – shows a brief transgressive-regressive couplet coeval with the uppermost Cleveland Ironstone Formation, and a subsequent high-resolution detrital element analysis has revealed concomitant peaks in Si/Al, Zr/Al and Zr/Rb (Thibault *et al.*, 2018). My model for the recovery of the redox state of the Cleveland Basin after the deposition of the LSB fits well with this emerging picture of sea level rise coeval with the Pl-To. It implies that a brief rise in temperature (that influenced temperature and humidity around the Cleveland Basin) preceded the short transgression observed at the Pl-To boundary in Europe. This temperature rise could have been a symptom of the injection of isotopically depleted carbon into the ocean-atmosphere system. It is also possible that the short, sharp temperature rise could have been a consequence of the intrusion of lavas in the Karoo-Ferrar LIP prior to the main phase of eruption (McElwain *et al.*, 2005). However, the $\delta^{13}C$ signature of the pre-TOAE CIE interval is too light to have been produced by an exclusively volcanic source (the pCO_2 level predicted by volcanogenic $\delta^{13}C$ does not agree with stomata data; Ruebsam *et al.*, 2020a), and Hg/TOC anomalies detected at the Pl-To in the Cleveland Basin (Percival *et al.*, 2015), might be better explained by an influx of terrestrially derived materials (Them *et al.*, 2019). Hg/TOC was not evaluated in my study since the elemental analysis was conducted via a bulk HF digest. Therefore, any Hg would have been liberated as a gaseous phase during the analysis. An elemental analysis via XRF, or flame ionisation detection (FID), could quantify Hg content (as well as Si). However,

although the global warming of the Pl-To might have been ultimately triggered by a small degree of intrusive activity in the Karoo-Ferrar, some workers have argued that the small extent of thermal metamorphism of coals in the Karoo-Ferrar basin (Gröcke *et al.*, 2009) implies that this process was minor compared to the subsequent destabilisation of climate-sensitive methane reservoirs.

Like with the Fe Speciation proxies (Chapter 3, section 4.9), the high degree of bioturbation in Lithofacies A might explain the apparent presence of Isorenieratane in sediments belonging to ORB 3-4 (Chapter 3, section 4.2). This lower part of the LSB was deposited under a widely oscillating redox state, with potentially many episodes of euxinia (and Chlorobiaceae production) occurring in *et al.*an interval that was probably several millennia in duration. However, given that the sediment was intensely bioturbated between these episodes, the organic geochemical record of isorenieratane content became time-averaged, and resulted in an apparent record of PZE concomitant with a lower dysaerobic biological community. An additional factor affecting the apparent high levels of isorenieratane in Lithofacies A (more so than the high values of Fe_{HR}/Fe_T and Fe_{Py}/Fe_{HR}), is the greater degree of time averaging required to generate samples for a TLE: about a centimetre of stratigraphic hight was required (in this case), to generate bitumen extracts of over 10 mg (at TOC = 2 wt.%; Appendix 3). Regrettably, this is the highest resolution that can currently be achieved for biomarker analysis. These two issues mean (as for the inorganic proxies), that in highly bioturbated sediments, inorganic geochemical proxy records should be interpreted as a function of anoxic/euxinic event frequency, rather than absolute redox state. Reworking of isorenieratane has also recently been identified in the lower Jurassic Pre-planorbis beds at Lilstock (Somerset, UK), where a thin interval of intense bioturbation leads to a local enrichment of isorenieratane by nearly three orders of magnitude (Fox *et al.*, 2020, and their supplementary information). As discussed in Chapter 3, section 4.9, a subsequent Fe-redox study of this section by He *et al.* (2022) also yielded Fe_{Py}/Fe_{HR} data indicating euxinic conditions concomitant with the heavily bioturbated interval. Comparison of the data from the LSB, and the pre-planorbis beds makes a strong case against a straightforward application of palaeoredox proxies to bioturbated units, and in favour of an appreciation of the dynamic nature of both the Bristol Channel, and Cleveland Basins.

5.0 Conclusions

- The LSB was formed due to an enhanced flux of nutrients (via an enhanced fluvial flux) into a restricted marine environment, with an enhanced biological pump depleting the oxygen inventory of the basin. This resulted in the preservation of organic matter, and the exclusion of (eventually) all benthic organisms. The oxygen depletion was also accompanied by intense

stratification (probably temperature mediated), which was the limiting factor on primary production during the period of maximum carbon burial.

- The enhanced fluvial fluxes into the Cleveland Basin are probably indicative of periods of greater climatic humidity, due to their association with changes in the clay mineral and palynological assemblages. Analogy with the PETM would suggest that the climatic shifts were due to a disruption to the global carbon cycle.

- During the deposition of the LSB, both marine and terrestrial primary producers obtained their carbon from isotopically depleted reservoirs, indicating the concomitant occurrence of water column stratification, and isotopic depletion in atmospheric carbon. The close association between these two processes strongly implies that the oxygen depletion responsible for the formation of the LSB was the regional expression of a global climate perturbation at the Pl-To.

- Intervals of intense bioturbation have the ability to time average both inorganic, and organic geochemical redox proxy records, leading to the apparently bizarre juxtaposition of anoxic or euxinic geochemical markers with a dysaerobic biofacies. This does not invalidate the use of any of these proxies, but instead implies that (during bioturbated intervals) the values generated through geochemical analysis are a function of anoxia/euxinia frequency, rather than of absolute oxygen levels.

- The preceding three Chapters of this work demonstrate that the LSB is a condensed record of a highly dynamic depositional environment, with anoxia, shelf-to-basin transport, and the marine biological community all playing an active role in the development of its sedimentary architecture. My work is a noteworthy example of black shale deposition under episodically high energy conditions, and serves as a case study of the ability of high-resolution, multproxy analysis to accurately reconstruct the formation of this facies.

Chapter 6 – A multiproxy analysis of thin Shell Pavements from the Whitby Mudstone Formation

1.0 Study aims

In the previous three chapters, I have presented a detailed, multiproxy study of a thin black shale unit from the Lower Jurassic mudrocks of the Cleveland Basin. The Lower Sulphur Band (LSB) is a brief period of highly frequent anoxic events in an otherwise oxic/dysoxic environment. However, it is also possible that the opposite case applies to thin, monospecific shell pavements from the Grey Shale and Mulgrave Shale Members, where the thin-shelled bivalves *Pseudomytiloides dubius* (hereafter *P. dubius*), and *Bositra radiata* (hereafter *B. radiata*), are found in high abundance, in mm-scale interval, often overlapping to the point where they form a distinct layer (often laterally continuous but occasionally containing gaps indicating partial development). A brief period of reoxygenation concomitant with these pavements has not been confirmed by geochemical analysis, and I will apply the same high-resolution analysis used in my study of the LSB to test this. In this chapter I will present the results of the sedimentological, palaeontological, pyrite framboid, Fe redox, major and trace element, and Rock-Eval analyses I have performed on three shell pavements from the Lower Jurassic of the Cleveland Basin, and the results of the palynological, biomarker, and compound-specific isotopic analyses I have performed on two of these pavements. I will then expand upon the implications of my findings for the palaeoenvironment of the Cleveland Basin, and the palaeobiology of paper pectens.

Three thin shell pavements were analysed, and are coded according to the bed from which they were extracted (numbering of Howarth, 1955; 1962; 1973). See Chapter 2, section 4.0 for the sampling methodology.

2.0 Results

2.1 Lithofacies and macrofossils

All three shell pavements are situated within laminated black shales (ORB 1-2 of Wignall & Hallam, 1991), mostly composed of clay-sized particles and sedimentary organic matter, with occasional thin silt laminae 0.5 - 1.5 mm in thickness (Fig. 6.8). Unfortunately, assigning durations to these intervals with an acceptable level of precision is impossible. Applying the age models discussed in Chapter 1, section 6.0 to the shell pavements produces durations on the order of 10 – 100 yr. However, they are all thinner than the mm-scale scour marks that typify the sediments of the Whitby Mudstone Formation (often, in fact, occurring within them; see section 4.1). This means that any duration estimate derived from sampling an interval of this size would fall well within the 95% uncertainty envelopes modelled by Kemp *et al.* (2018 – their Figs. 9 and 10). The stratigraphic heights the shell pavements are summarised in table 6.1.

Bos32 is 1.4 mm in thickness (measured via photomicrograph). The shells that comprise this pavement were likely derived from both *Pseudomytiloides dubius* and *Bositra radiata*: 53.3% of the shells show a prismatic microstructure in thin section (Fig. 6.9), which is a known morphological feature of shells from the family Inoceramidae, to which *P. dubius* belongs (MacLeod & Orr, 1993; Henderson, 2004). The remaining 46.7% of the shells are thinner, and do not show a prismatic microstructure. These shells can therefore be attributed to *B. radiata*, which I identified upon inspection of the pavement in hand specimen. The majority of the shells preserved in this pavement are concave-up (Fig. 6.9). The shells of both *P. dubius* and *B. radiata* have a length of 10 – 33 mm (mean = 21 mm, standard deviation = 8 mm; measured from the bedding place surface – Figs. 6.1 – 6.3; Appendix 3). The shells also overlap, completely covering the bedding plane surface, so no spacing measurements could be made (hence there is no corresponding histogram for this pavement). The pavement is accompanied by a 1.25 mm-thick, normally graded silty lamination. Many of the shells in this pavement are pyritised, and euhedral crystals of diagenetic pyrite are often found encrusting the shells (Figs. 6.9 and 6.16). In addition to Bos32, the sediments enclosing the pavement contain frequent individual shells of *P. dubius* and *B. radiata*, and occasional shell pavements with a lower number of shells than Bos32 (examples in Figs. 6.6

Pavement	*Bed*	*Position in stratigraphy*	*Bivalves present*	*Thickness (µm)*
Pseud41	41	70 cm above the top jet dogger	*P. dubius* only	730
Pseud34	34	10 cm below the central nodule layer in bed 34	*P. dubius* only	580
Bos32	32	69 cm below the cannon ball doggers	*P. dubius* and *B. radiata*	1390

Table 6.1. The locations of each of the studied shell pavements within the stratigraphy of the Whitby Mudstone Formation, along with the faunal composition, and the interpreted duration of each pavement.

and 6.7). These are also associated with thin, normally graded silty laminae, which occasionally contain reworked pyrite framboids (Figs. 6.7 and 6.17).

While the shell pavements were invariably associated with the thin silty laminae, not all laminae were accompanied by a shell pavement (e.g. Fig. 6.8). Another, a partially developed pavement (not analysed geochemically) is preserved within bed 32, with the shells occasionally showing orientation not parallel with the bedding (Fig. 6.10). Many of the shells in this pavement are thicker than in Bos32, and display prismatic microstructure, implying they belonged to *P. dubius*. A subhedral calcareous bioclast is contained within this shell pavement (Fig. 6.11), and is probably derived from an echinoderm (e.g. a crinoid ossicle), since the whole clast goes into extinction simultaneously when observed under XPL.

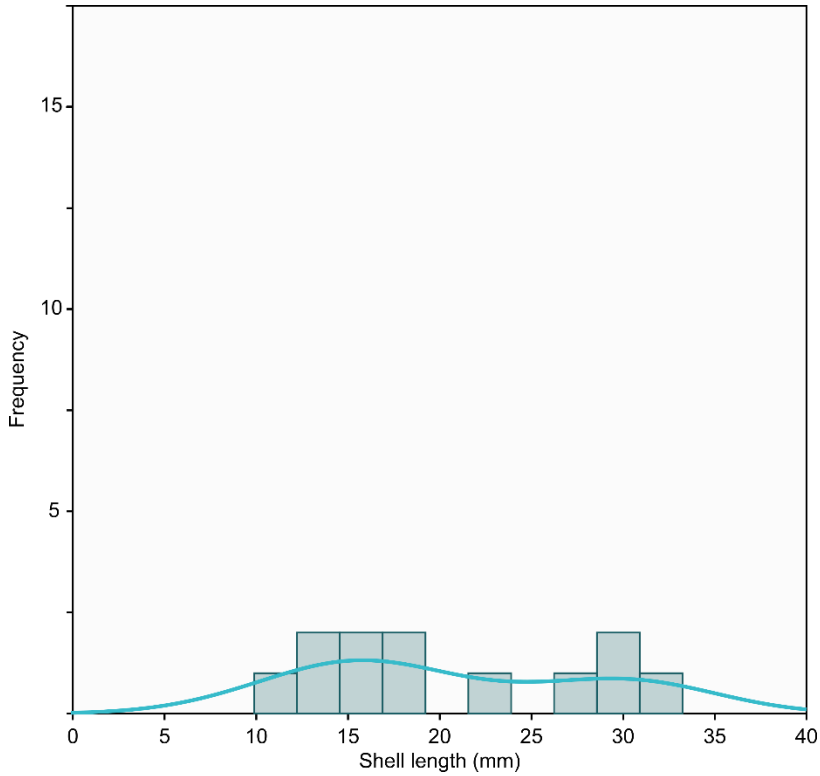

Figure 6.1. Frequency distribution of the lengths of the shells from Bos32 (n = 12). The data for all histograms was collected from the scanned images of the shell pavements (Figs. 2.8 - 2.10). Note that not all of the visible specimens could be measured, since the overlap meant that edges could not be identified.

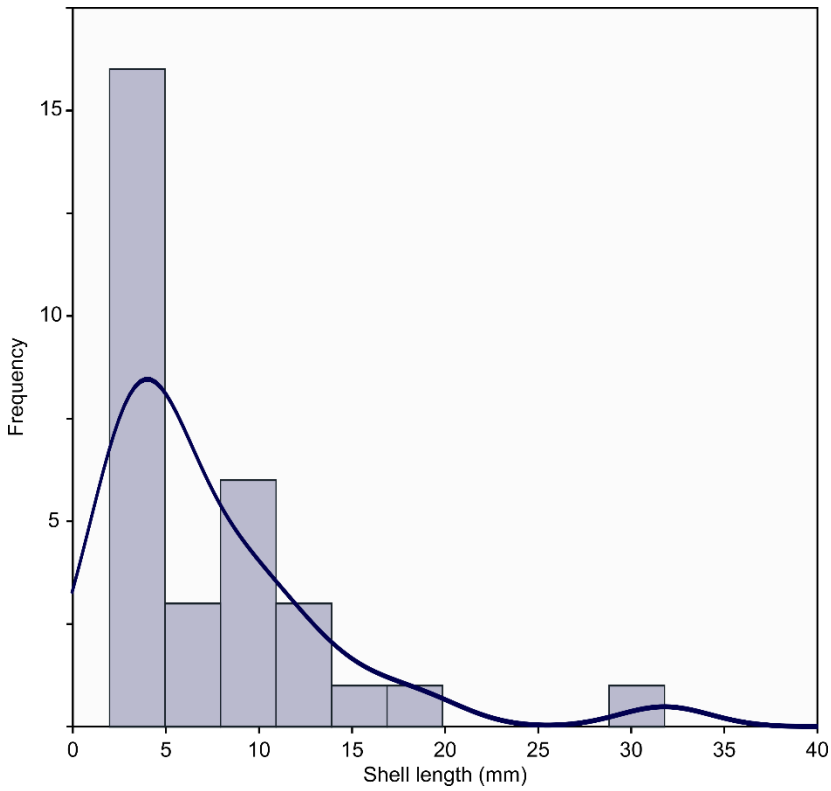

Figure 6.2. Frequency distribution of the lengths of the shells from Pseud34 (n = 31).

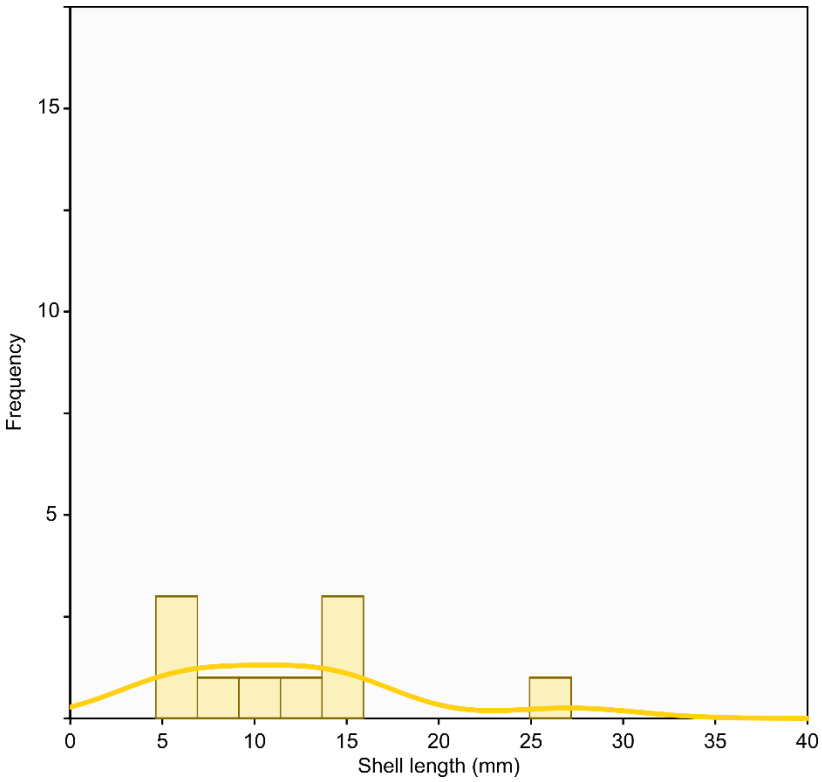

Figure 6.3. Frequency distribution of the lengths of the shells from Pseud41 (n = 8).

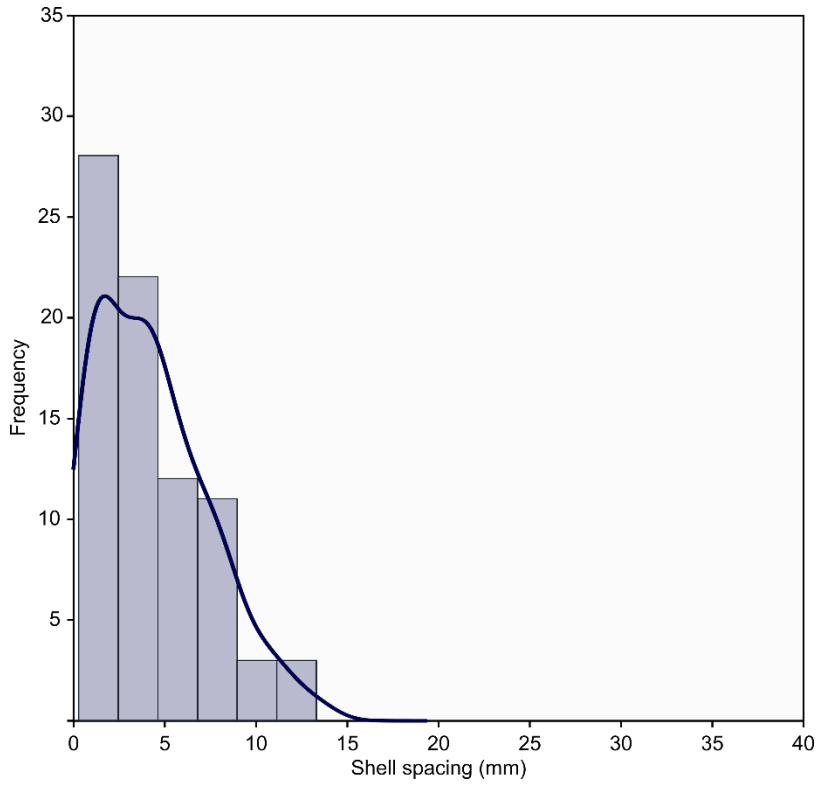

Figure 6.4. Frequency distributions of the spacing of the shells from Pseud34 (n = 79).

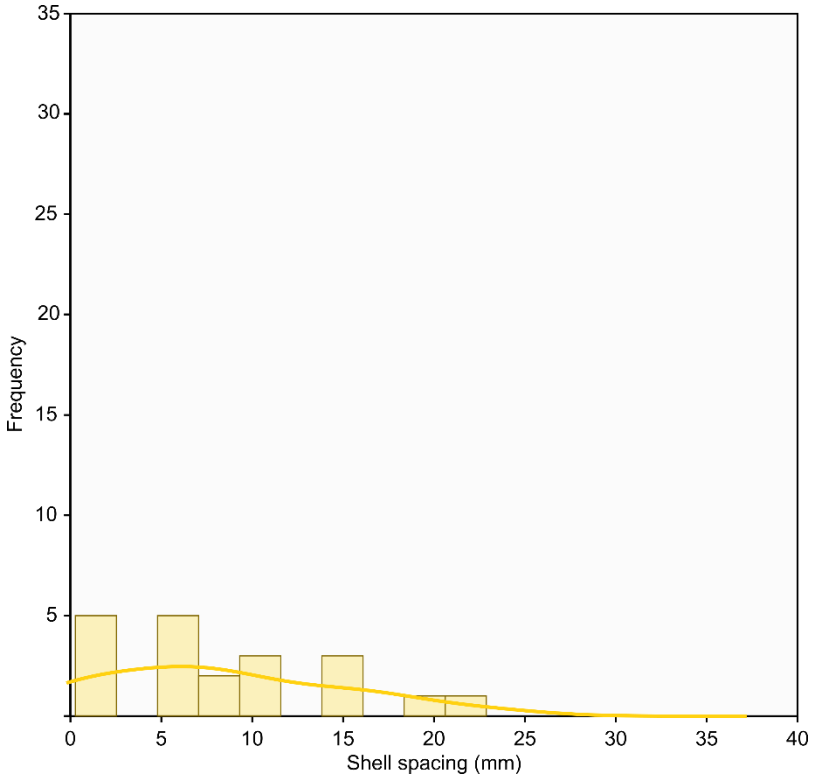

Figure 6.5. Frequency distributions of the spacing of the shells from Pseud41 (n = 20).

Pseud34 is 0.6 mm thick, and it only contains shells with a prismatic microstructure, implying that the pavement was composed entirely of *P. dubius*. In some shells, the outer layer has become recrystallised, with just the inner layer retaining the original prismatic microstructure (Fig. 6.13). Like Bos32, Pseud34 is also associated with a thin, normally graded silty horizon approximately 0.5 mm in thickness (Figs. 6.12 and 6.13). The *P. dubius* shells in Pseud34 are generally smaller than those in Bos32, with a length of 2 – 32 mm (mean = 8 mm, standard deviation = 6 mm; Fig. 6.2; Appendix 3). They are also more widely spaced apart, with some of the bedding plane surface uncovered. The gaps between the shells range between 0 – 13 mm, with a mean of 4 mm and a standard deviation of 3 mm (Fig. 6.4). This pavement also contains a large shell fragment with dark brown colouration implying partial replacement by siderite (Fig. 6.12).

Pseud41 is 0.7 mm thick, and like Pseud34, it is composed entirely of *P. dubius* shells with prismatic microstructure, with no *B. radiata* shells present. The shells have a length between 5 – 27 mm (mean = 12 mm, standard deviation = 7 mm; Fig. 6.3; Appendix 3). The shells are also widely spaced apart, with the gaps between the shells being between 0 – 23 mm (mean = 8 mm, standard deviation = 6 mm; Fig. 6.5; Appendix 3). An elongate phosphatic bioclast (likely a fish scale) was also found in bed 41 (Fig. 6.14), implying the sediments belong to ORB1.

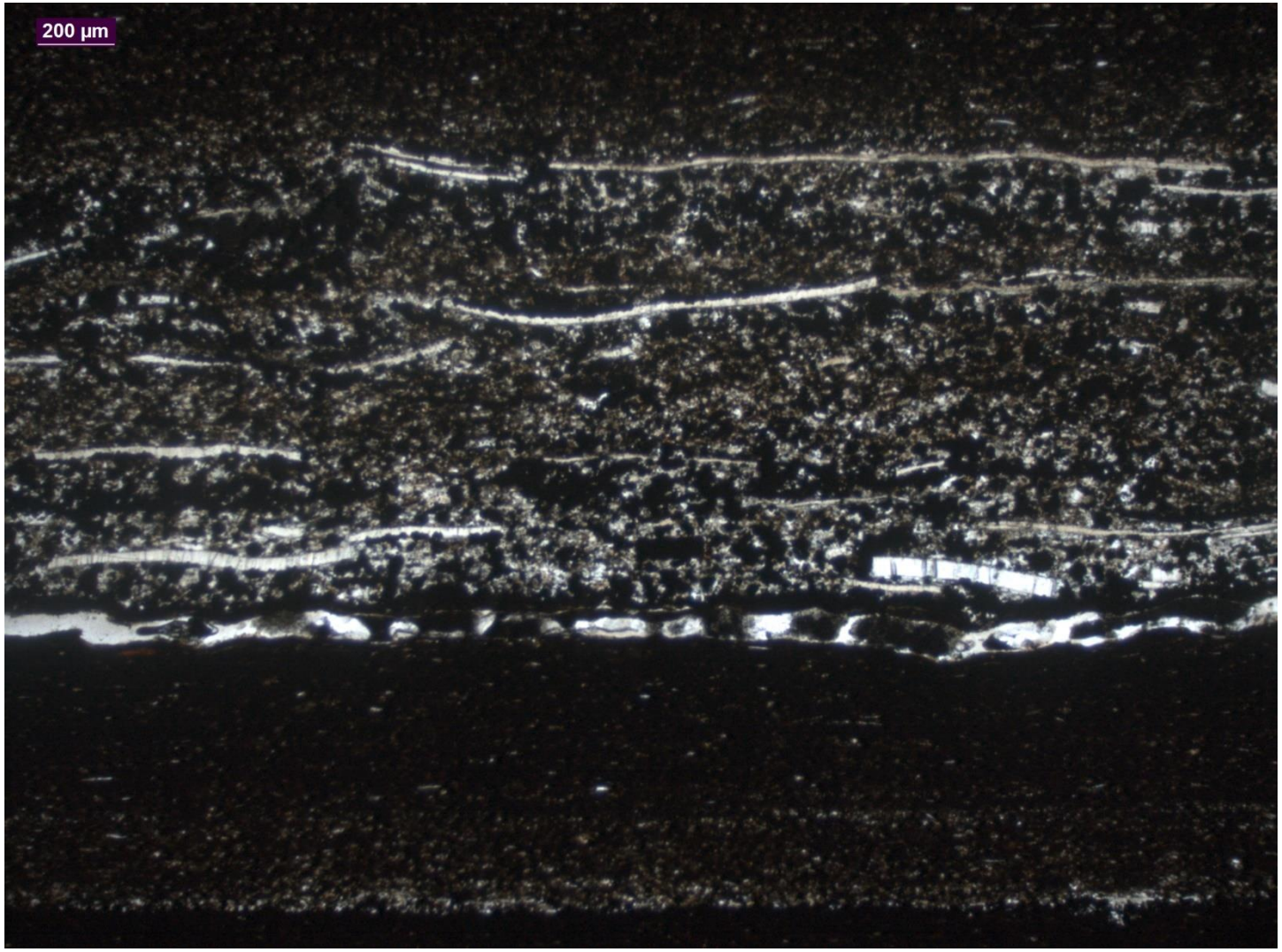

Figure 6.6. A photomicrograph (taken under transmitted, plane polarised light) of another shell pavement from bed 32, also composed of both *P. dubius* and *B. radiata* (prismatic and non-prismatic microstructure observed). Younging is from bottom to top.

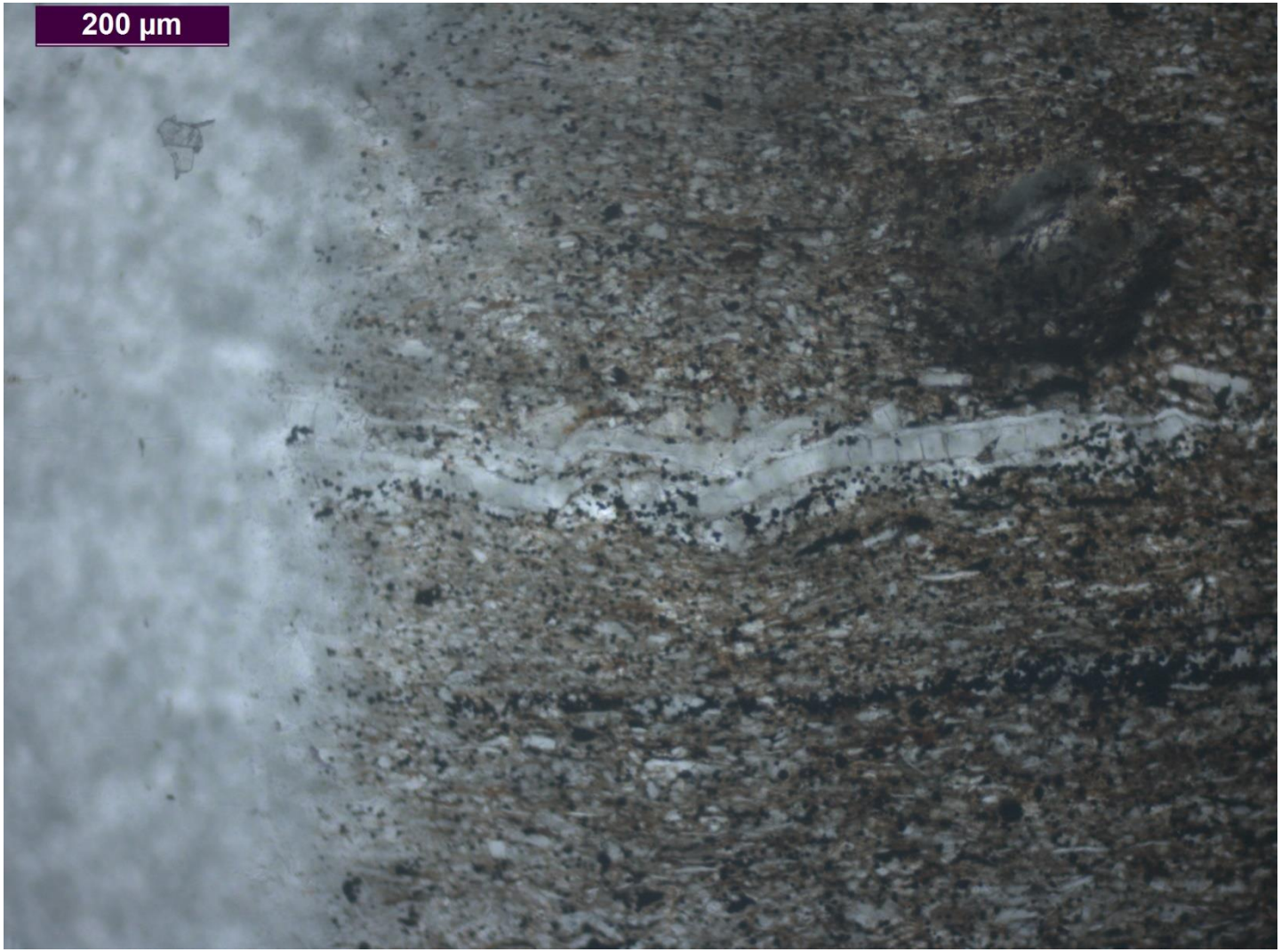

Figure 6.7. A photomicrograph (taken under transmitted, plane polarised light) of a discontinuous pavement of *P. dubius* from bed 32, with reworked pyrite framboids forming a lag at the base of the pavement. Younging is from

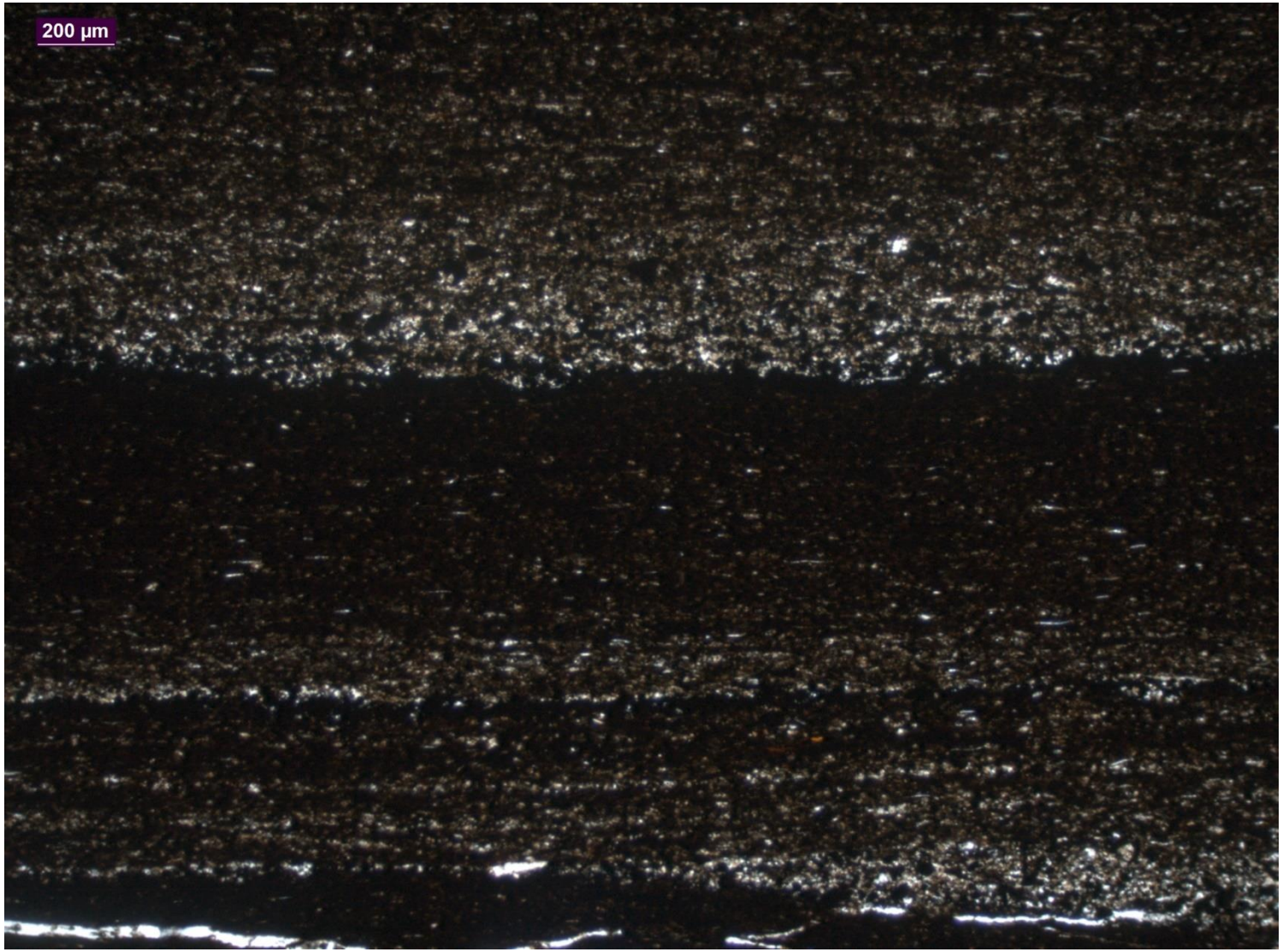

Figure 6.8. A photomicrograph (taken under transmitted, plane polarised light) of silt laminate from bed 32. The bottom lamina is accompanied by occasional shell fragments, but the top is not. Neither is accompanied by a shell pavement (continuous or discontinuous). Younging is from bottom to top.

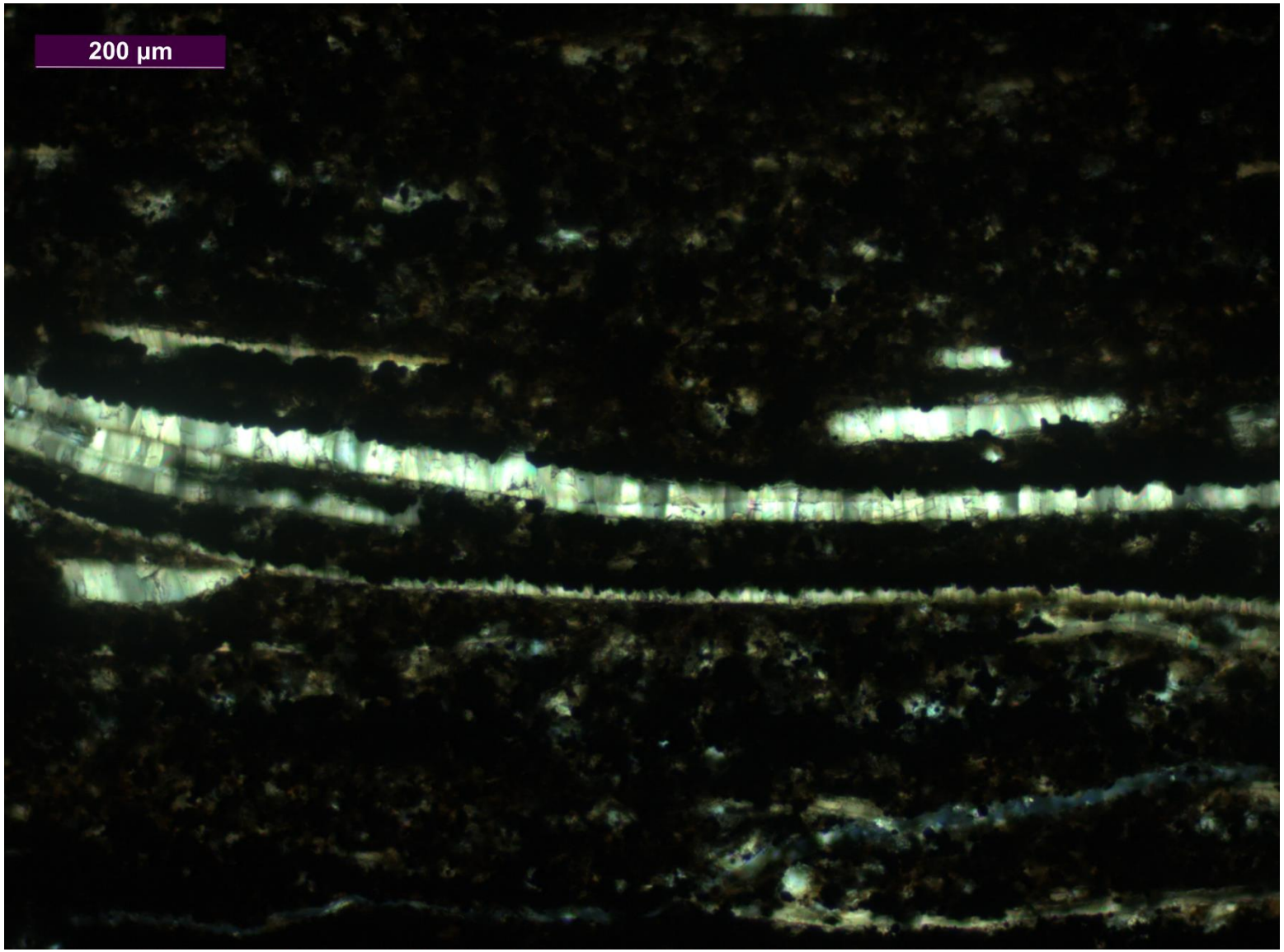

Figure 6.9. A photomicrograph (taken under transmitted, plane polarised light) of the Bos32 pavement, containing shells with both prismatic (*P. dubius*), and non-prismatic (*B. radiata*) microstructure. Younging is from bottom to top.

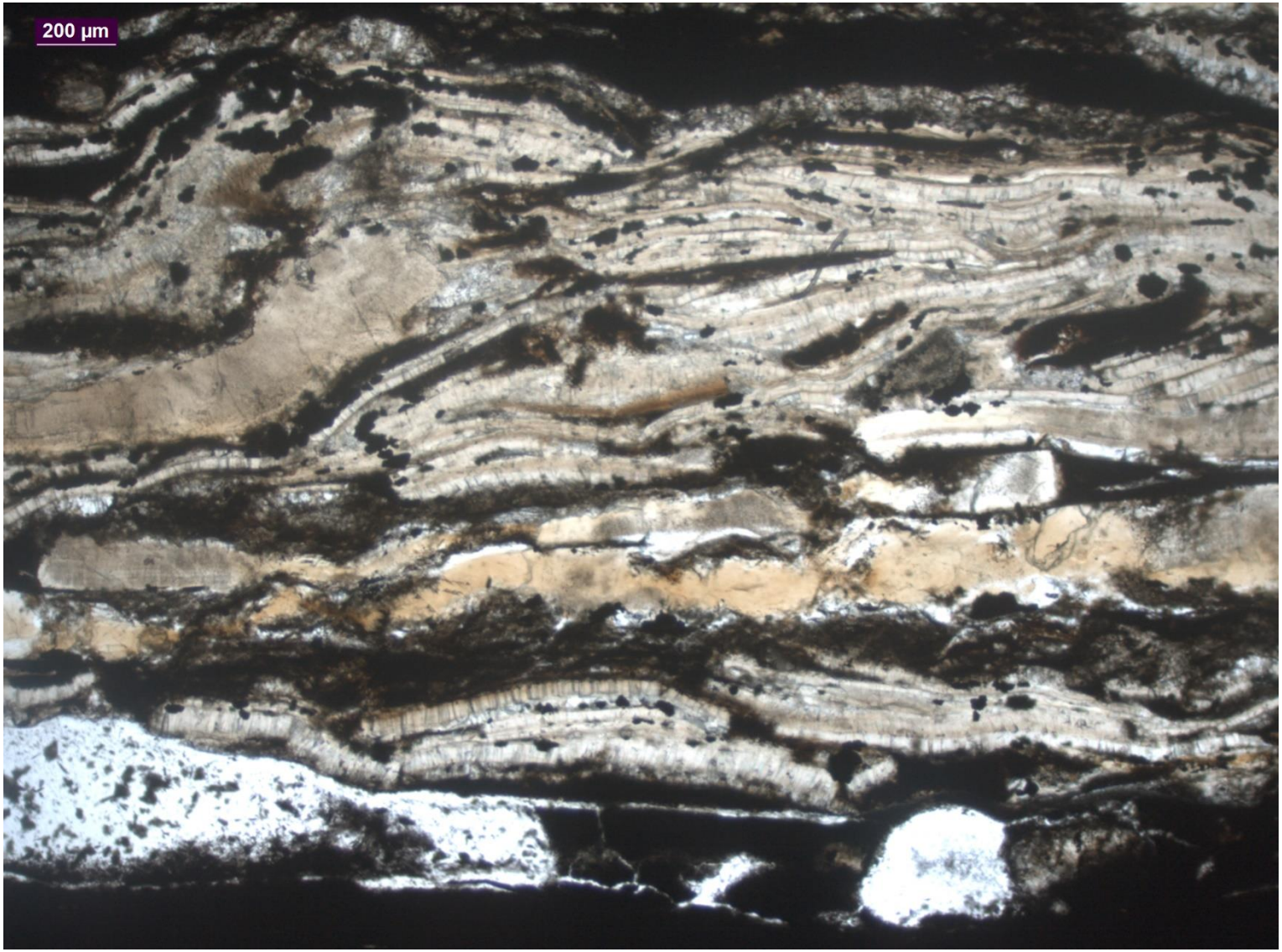

Figure 6.10. A photomicrograph (taken under transmitted, plane polarised light) of a discontinuous pavement from bed 32 - with thicker shells (*P. dubius*). Younging is from bottom to top.

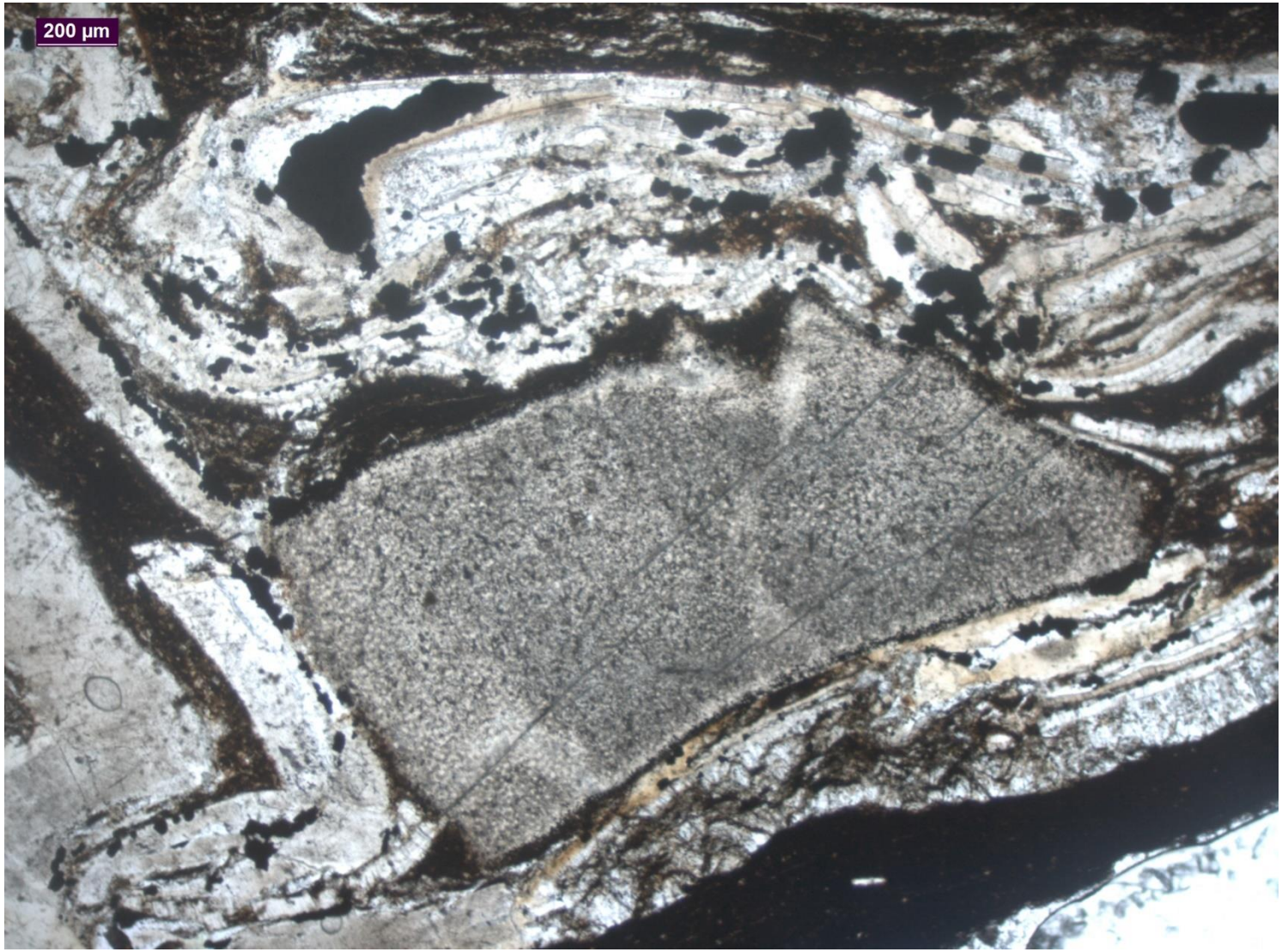

Figure 6.11. Calcareous bioclast (crinoid ossicle) encased within the shell pavement shown in Fig. 6.10. Younging is from bottom to top.

Figure 6.12. A photomicrograph (taken under transmitted, plane polarised light) of a shell fragment from Pseud34 (possible siderite replacement). Younging is from bottom to top.

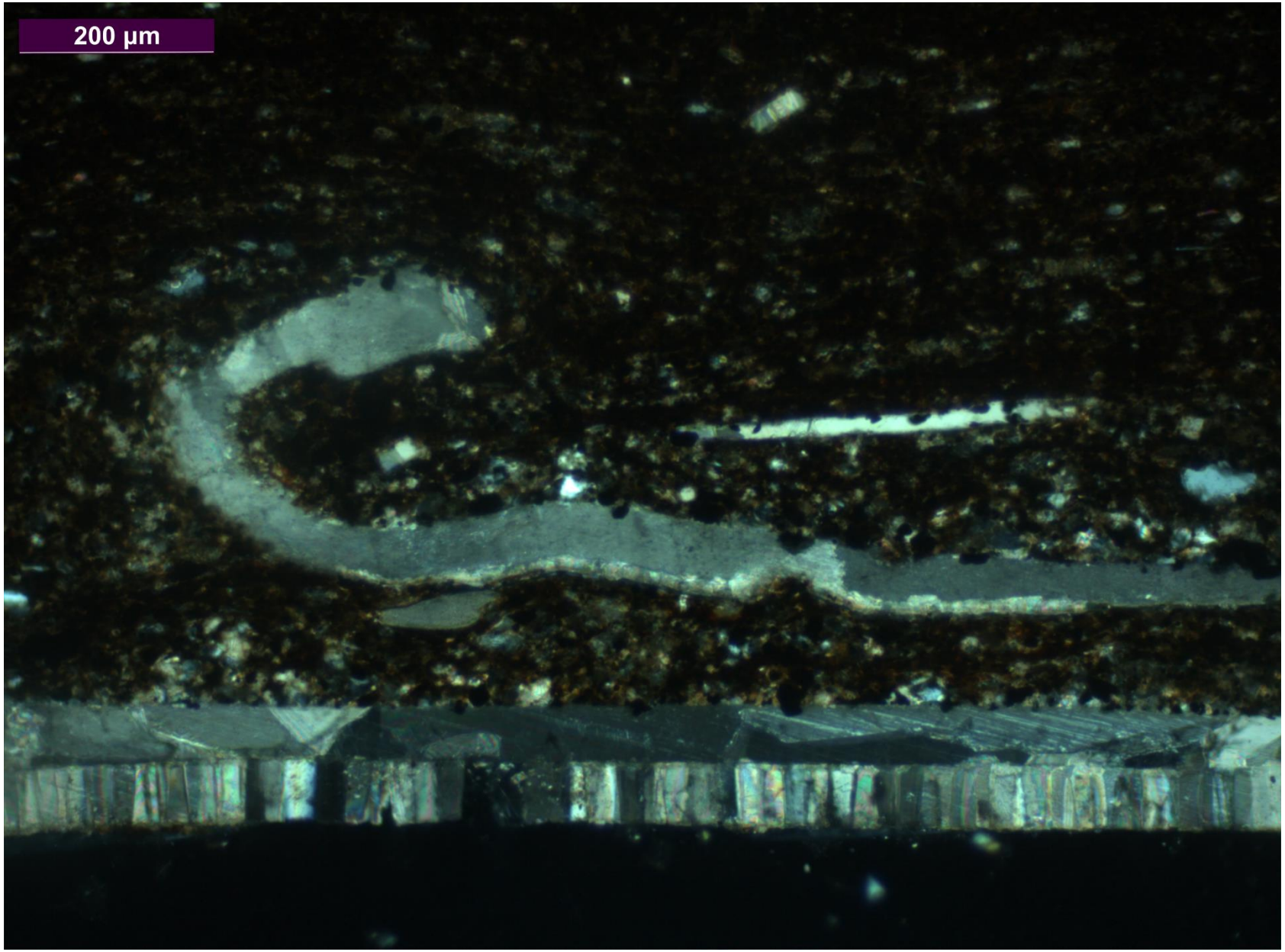

Figure 6.13. A photomicrograph (taken under cross-polarised light) of a cross section through a shell from the Pseud34 pavement, with prismatic microstructure clearly visible. Younging is from bottom to top.

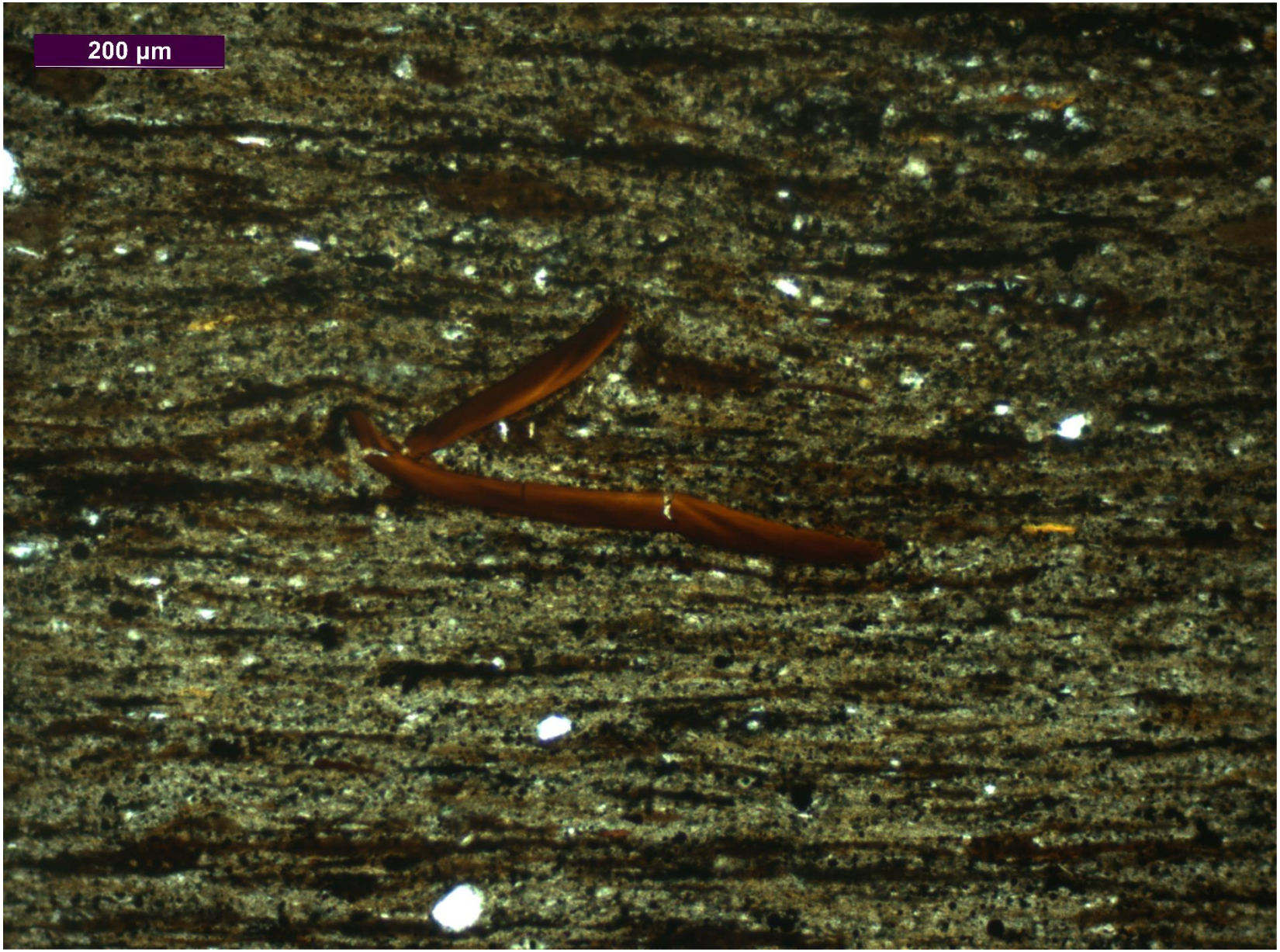

Figure 6.14. A photomicrograph (taken under transmitted, plane polarised light) of an elongate, fractured phosphatic bioclast (probably a fish scale) found in bed 41. Younging is from bottom to top.

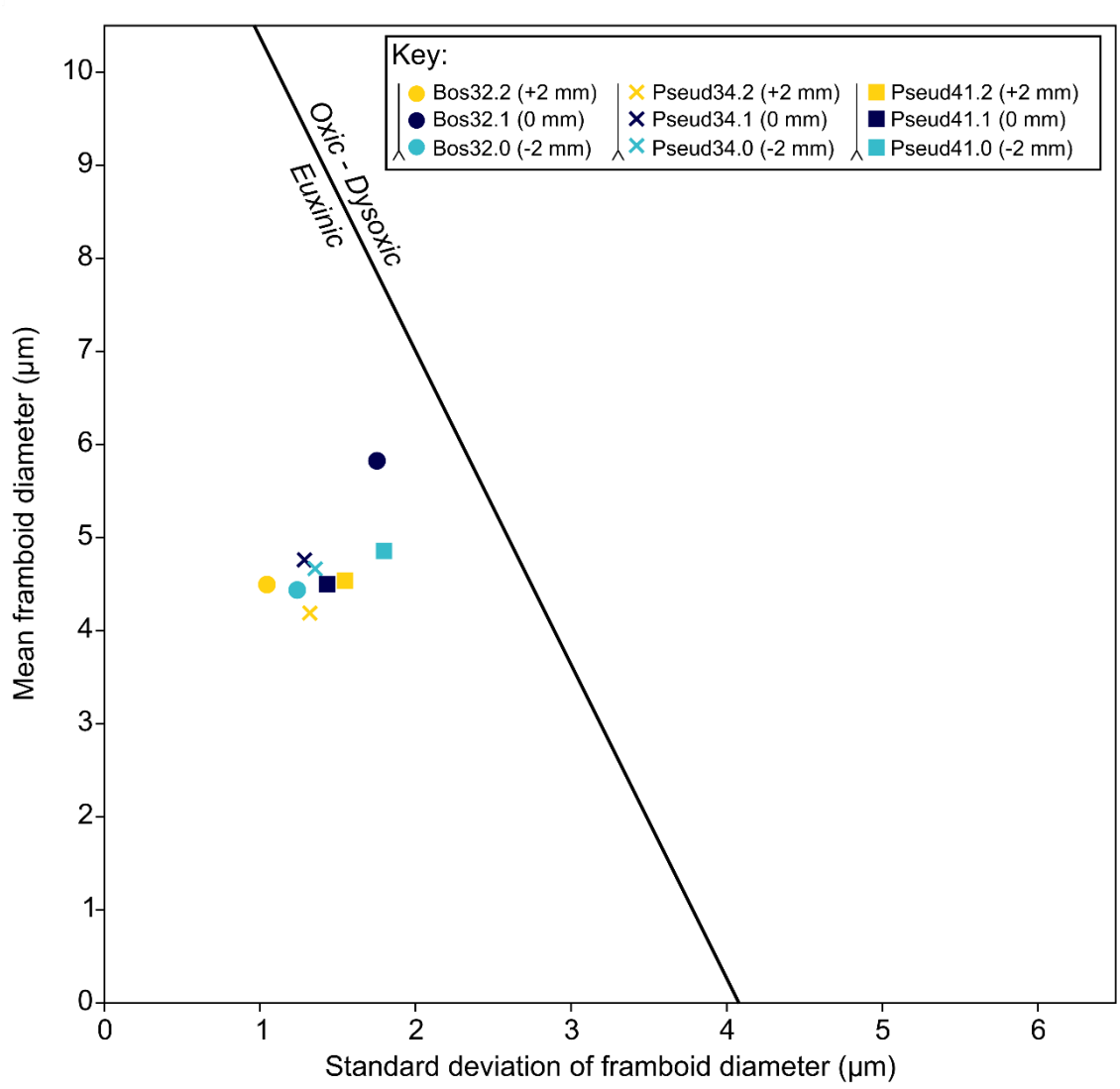

Figure 6.15. Wilkins plot for each of the shell pavements. Note that in this figure, as well as Figs. 6.24, 6.28, 6.48 and 6.50, circles denote samples from Bos32, crosses from Pseud34, and squares from Pseud41. Teal symbols indicate the sample 2 mm below the pavement (depending on the sample resolution), dark blue the sample concomitant with the pavement, and yellow the sample 2/5 mm above the pavement (see younging direction in key).

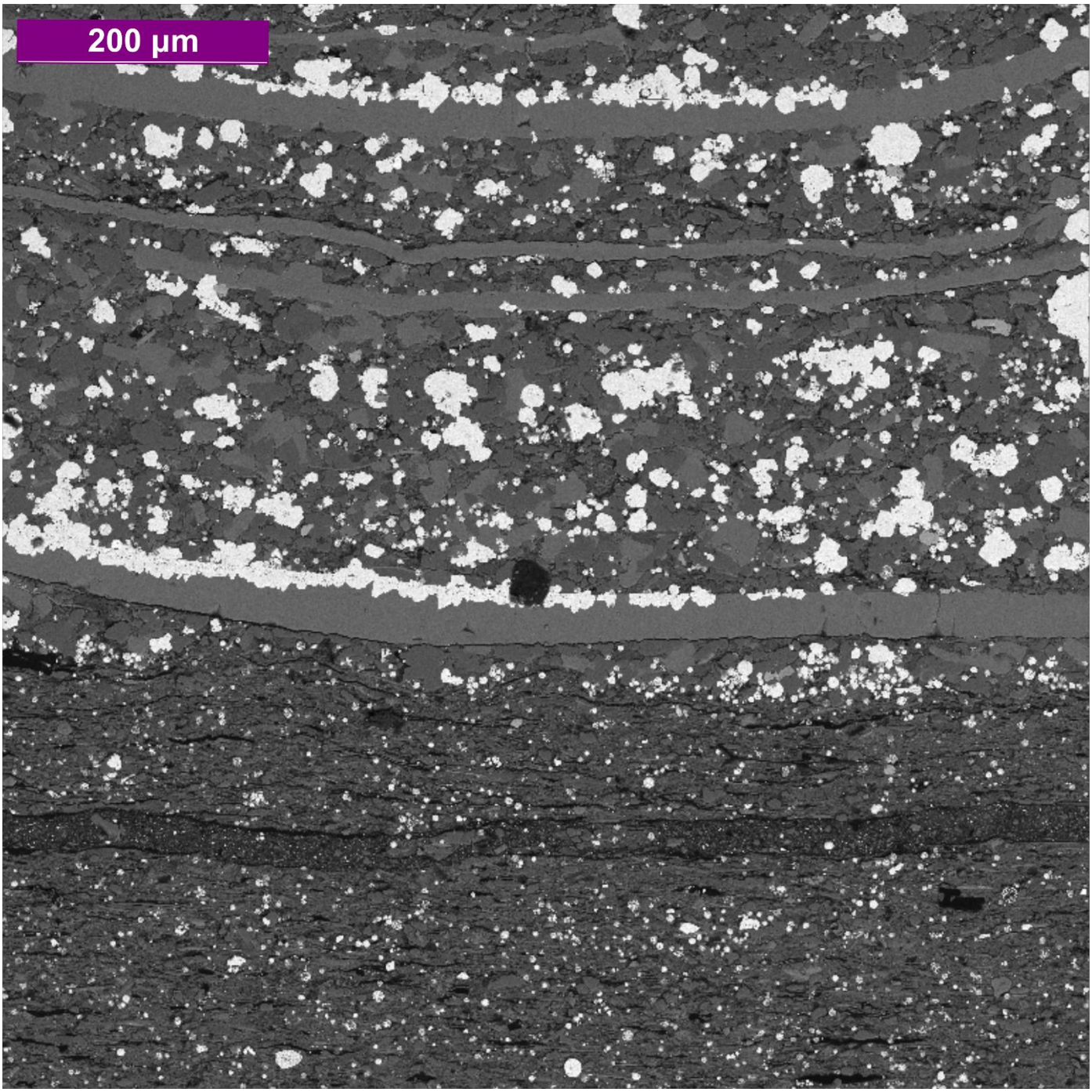

Figure 6.16. Backscattered SEM photomicrograph of Bos32 (younging up), showing the encrustation of euhedral pyrite on the shell surfaces (and partial replacement). Younging is from bottom to top.

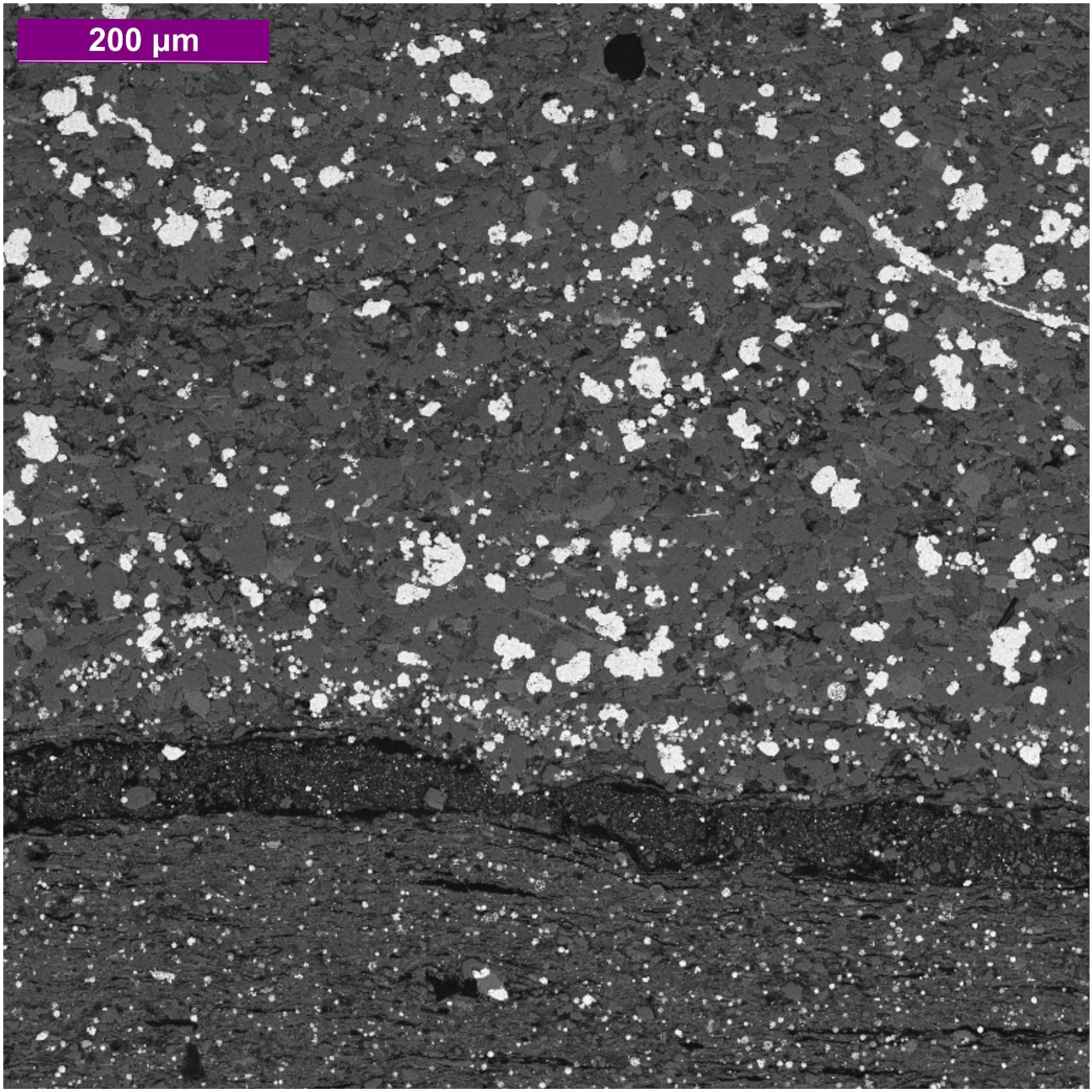

Figure 6.17. Backscattered SEM photomicrograph of a silty lamina from Bos32. Note the presence of a pyrite framboid lag 50 µm in thickness at the base of the lamina, followed by the occurrence of large reworked euhedral pyrite crysts. Younging is from bottom to top.

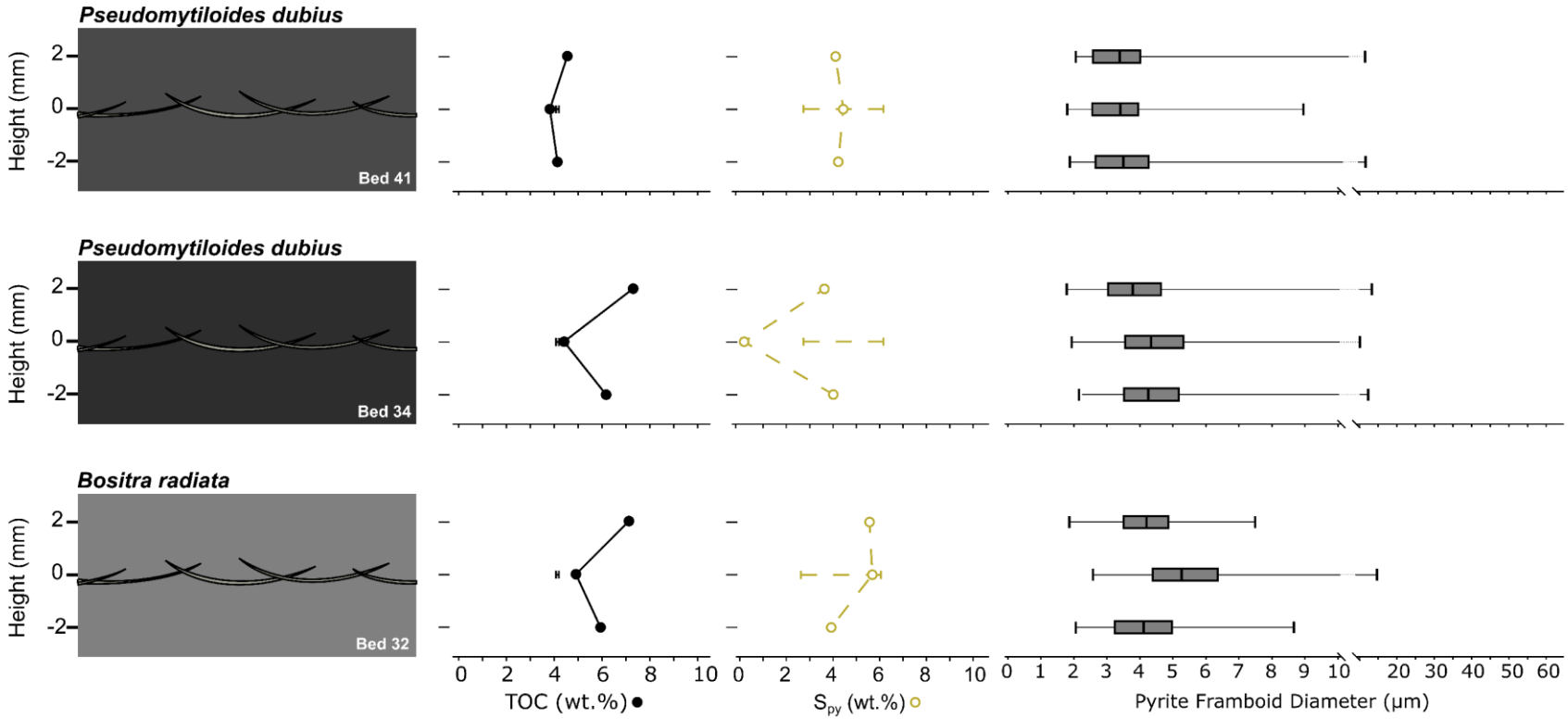

Figure 6.18. TOC, pyrite Sulphur (S_{py}; included in all plots, as in previous chapters), and box-and-whisker plots of pyrite framboid diameters (arranged by stratigraphic height) through each of the shell pavements. Schematics of the shell pavements are also included. Dark boxes indicate pyrite framboid data that plot to the left of the euxinic/oxic-anoxic boundary in the Wilkins plot (Fig. 6.15). Note that in all up-section plots, the horizontal bar ( ) indicates the range of values for the proxy in question recovered from around the individual *P. dubius* fossil from the LSB (i.e. the samples LSB1.11 and LSB1.12 Chapter 3, section 3.2)

2.2 Pyrite framboids

The morphology of the pyrite framboids encountered within the sell pavements is, overall, very similar to those found in the LSB, with both type 1 and (occasional) type 2 framboids observed (Wignall & Newton, 1998).

Euhaedral pyrite crysts were also present, occasionally forming framboids, which (as in Chapter 3, section 3.1.1) were not counted in the framboid diameter analysis (assuming a diagenetic origin). Large euhedral pyrite crysts were especially common in the Bos32 pavement, where they often encrusted the shells (Figs. 6.9 and 6.16). The thin silty laminae also contained euhedral pyrite crysts, as well as generally larger framboids, that sometimes accumulate in lags (Figs. 6.7 and 6.17) – implying transport and redeposition.

Despite the presence of in situ benthic macrofauna, the mean diameter of the pyrite framboids did not significantly increase concomitant with the shell pavements, and all three shell pavements plot within the euxinic field of the Wilkins plot (Fig. 6.15). In fact, Pseud41 is accompanied by a decrease in the maximum framboid diameter (by 2.8 µm; Fig. 6.18), implying a lower redox state. An increase in the mean, maximum and minimum framboid diameters are observed in Bos 32, but only by 1.39 µm, 6.04 µm, and 0.55 µm (respectively). The first and third quartiles of framboid diameter increase in Bos32 (by 1.15 µm and 1.42 µm, respectively) but remain relatively constant in Pseud34 and Pseud41.

2.3 Palynology

Amorphous, phytoclast, sporomorph and palynomorph kerogen groups were identified within the palynological slides prepared from the shell pavements (no zoomorphs were found). Representative photomicrographs are shown in Figs. 6.19 and 6.20.

In Bos32 and Pseud41, AOM dominates the palynofacies, making up no less than 68.3% of the assemblages (Fig. 6.21). The second most common macerals identified in the palynological preparations were phytoclasts, which comprise 15.7 – 22.7% of the palynofacies. Levels of AOM are 28.3 – 47.3% higher in the shell pavements than in the LSB, and the levels of phytoclasts are up to 24.7% lower.

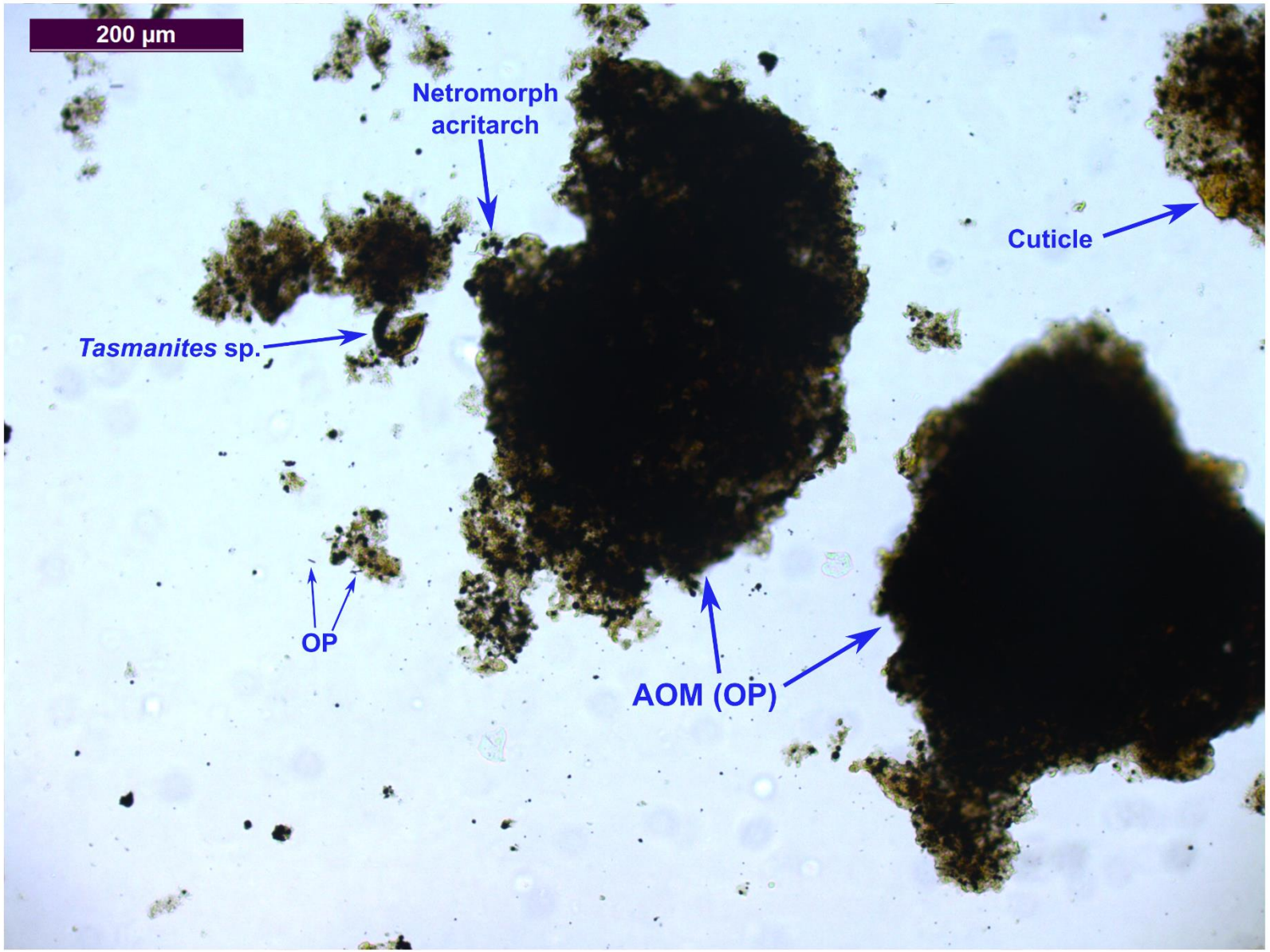

Figure 6.19. Representative photomicrograph of the kerogen assemblage of Bos32.2 (pavement sample), with the prasinophyte *Tasmanites sp.*, a netromorph acritarch, opaque (OP) AOM, leaf cuticle and very small opaque phytoclasts (OP).

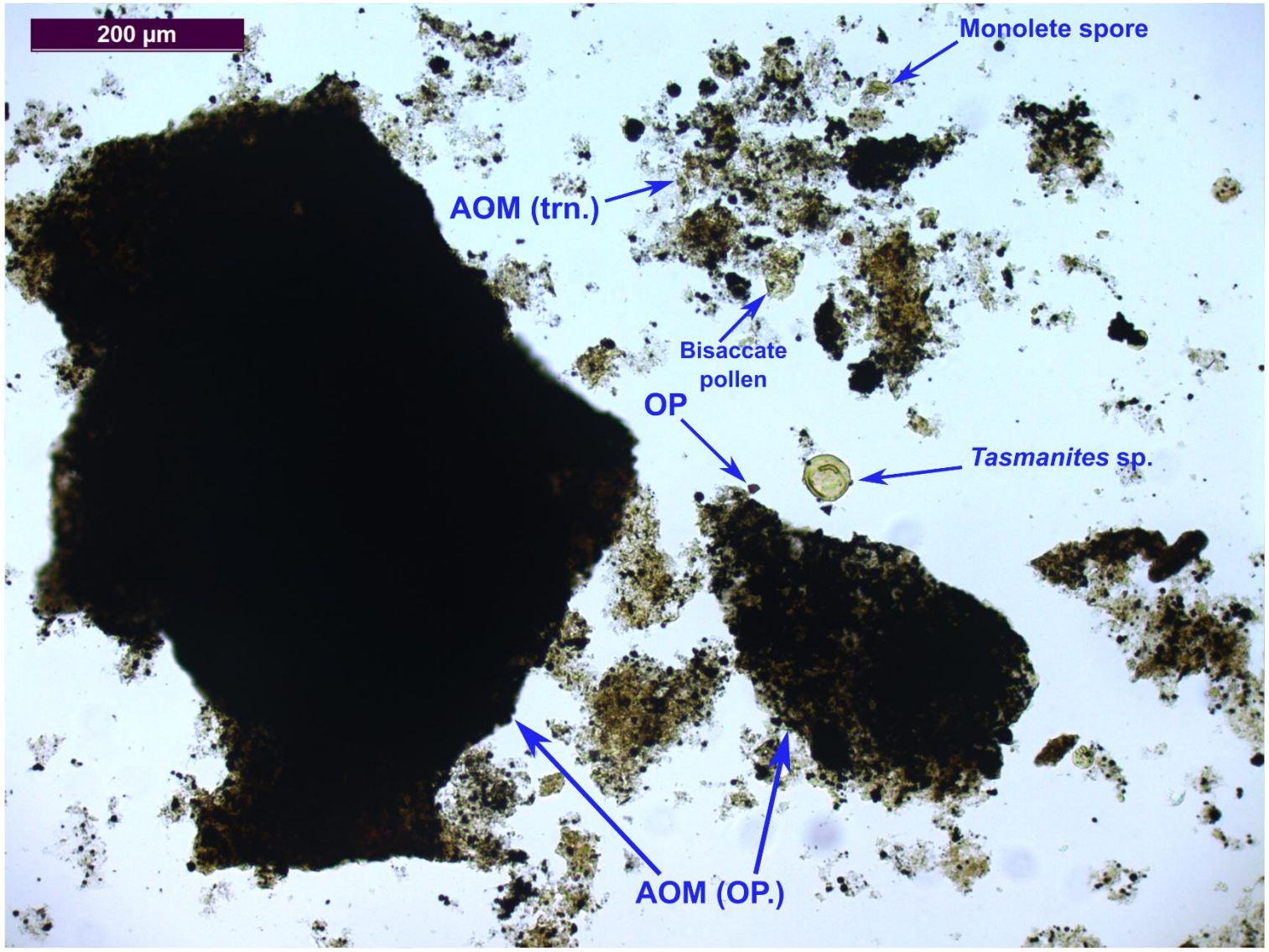

Figure 6.20. Representative photomicrograph of the kerogen assemblage of Pseud41.2 (pavement sample), with tanslucent (trn.) AOM, bisaccate pollen, opaque phytoclasts, opaque AOM, a monolete spore and *Tasmanites* sp.

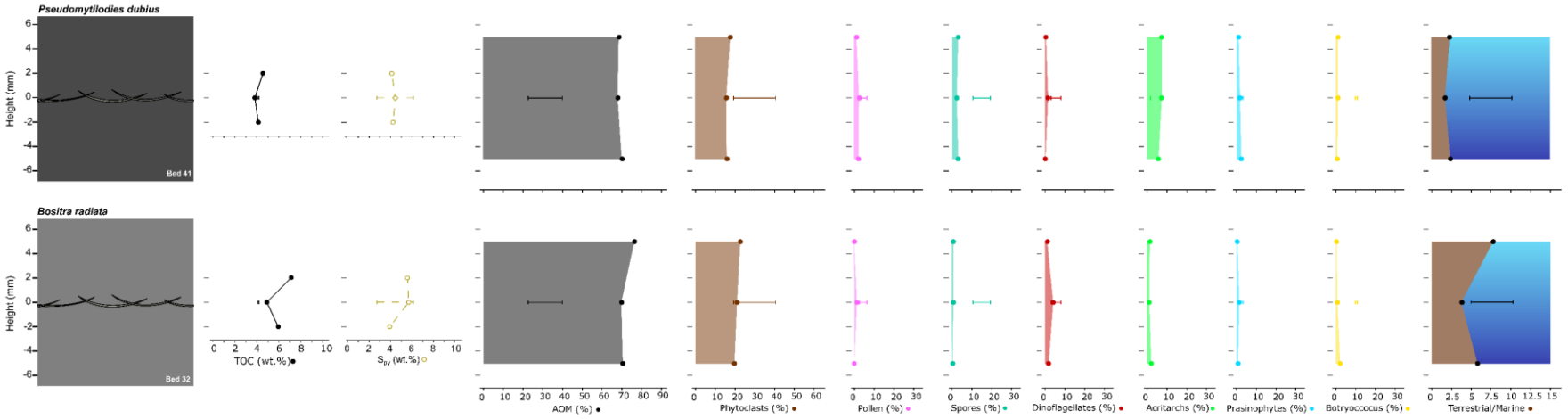

Figure 6.21. Plot of TOC and S_{py}, compared with the abundance of various palynofacies components through through each of the shell pavements. These are; AOM, phytoclasts, pollen, spores, dinoflagellates, acritarchs, prasinophytes, and botryoccocus. A plot of the terrestrial marine ratio (see Appendix 3 for quantification) is also included. Note that in all up-section plots, the horizontal bar (⊢) indicates the range of values for the proxy in question recovered from around the individual *P. dubius* fossil from the LSB (i.e. the samples LSB1.11 and LSB1.12 Chapter 3, section 3.2)

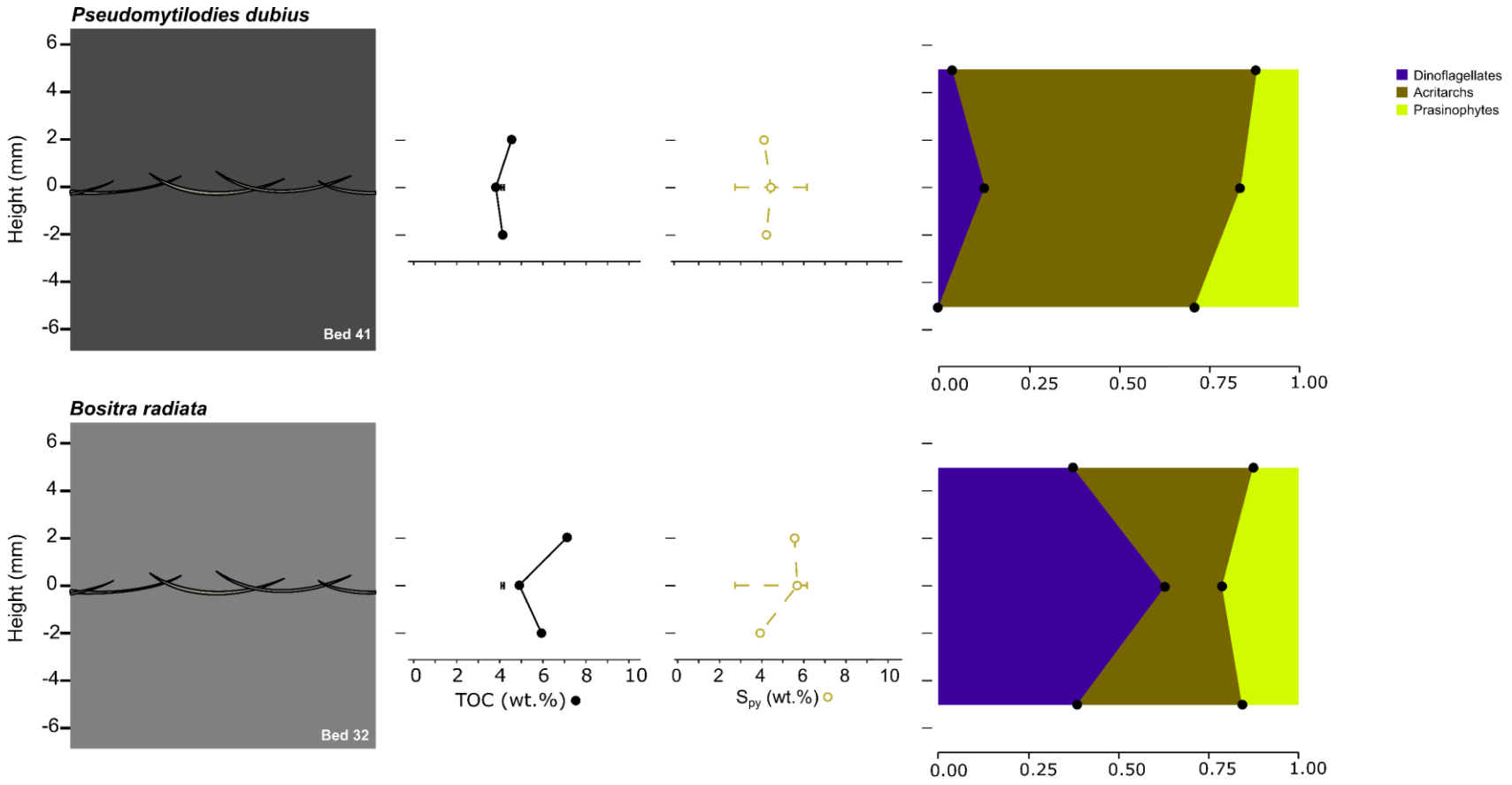

Figure 6.22. Plot of the percentage contribution of dinoflagellates, acritarchs and prasinophytes to the phytoplankton community (defined as dinoflagellates + acritarchs + prasinophytes) through Bos32 and Pseud 41. Note that in all up-section plots, the horizontal bar (⊢) indicates the range of values for the proxy in question recovered from around the individual *P. dubius* fossil from the LSB (i.e. the samples LSB1.11 and LSB1.12 Chapter 3, section 3.2)

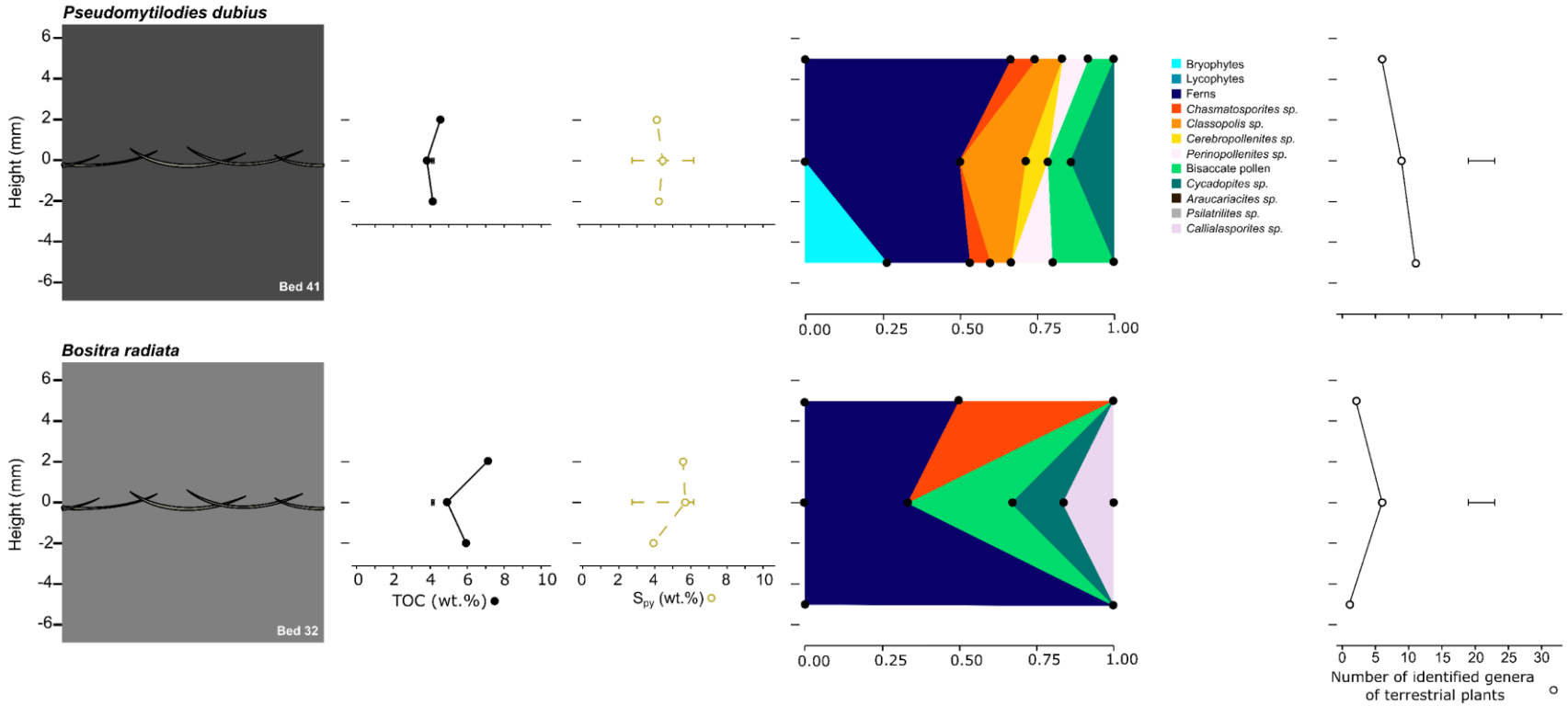

Figure 6.23. The contribution of a range of terrestrially-derived spores and pollen (grouped by genus with the exceptions of bryophytes, lycophytes, ferns and bisaccate producers) to the total spore + pollen count, and a up-section plot of the number of identified genera (excluding spores and pollen of unknown genus) through Bos32 and Pseud 41. Note that in all up-section plots, the horizontal bar ( ) indicates the range of values for the proxy in question recovered from around the individual *P. dubius* fossil from the LSB (i.e. the samples LSB1.11 and LSB1.12 Chapter 3, section 3.2)

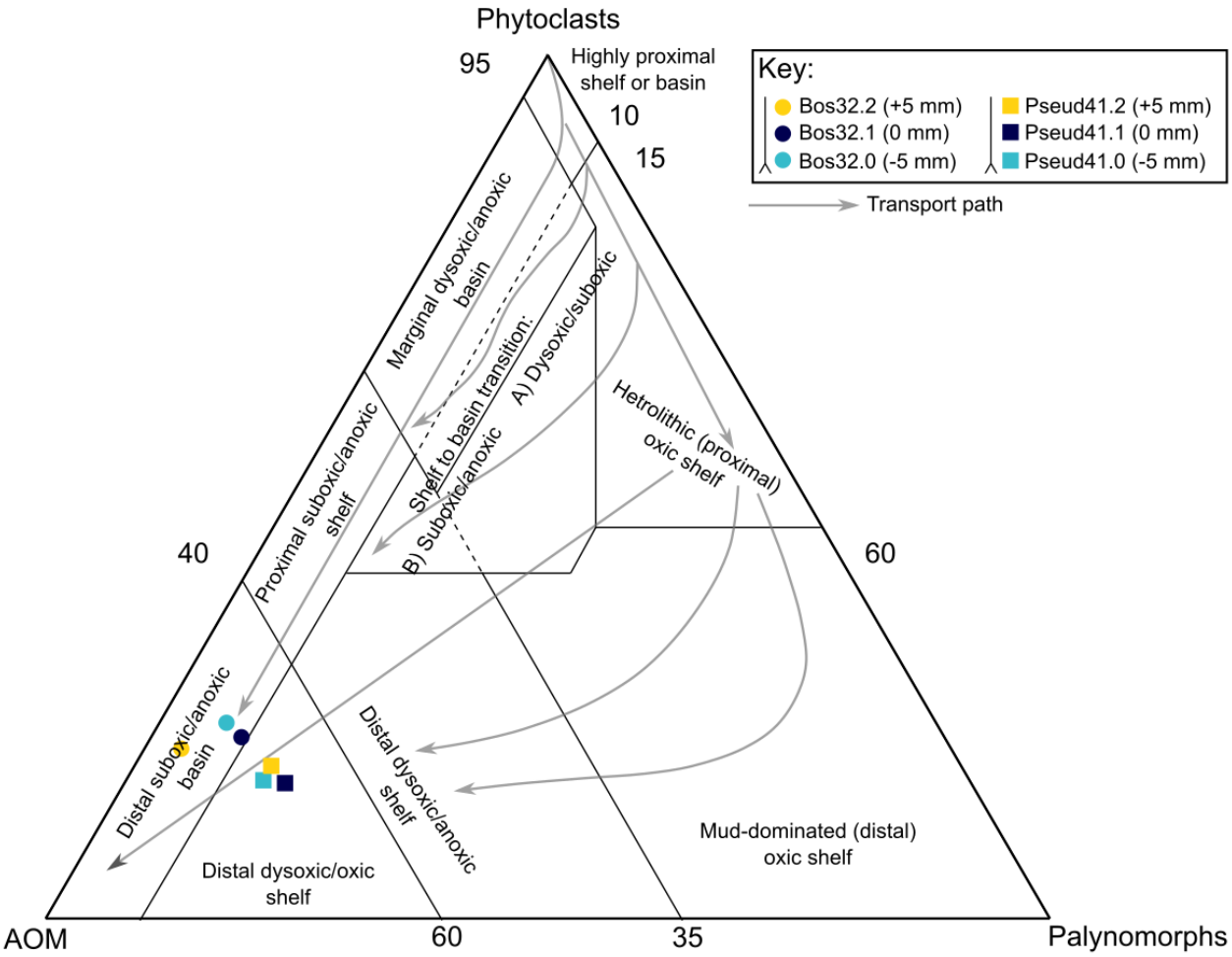

Figure 6.24. Ternary plot of phytoclasts, AOM and palynomorphs (spores + pollen + dinoflagellates + acritarchs + prasinophytes + botryoccocus), after Tyson (1989).

Variability in the remaining palynofacies components is relatively low, with the greatest point increase being in dinoflagellate content concomitant with Bos32 (an increase of 2.33%; Fig. 6.21). Acritarchs are also more common in all three samples from Pseud41 than in Bos32 (by 3.67 – 6.33%). While the terrestrial/marine ratio shows a decrease concomitant with both shell pavements, the decrease is much more pronounced in Bos32 than in Pseud41 (by 2.03 verses 0.64). The abundance values in all pavement samples are roughly comparable with the values from the LSB, except for spores, which are 8.0 – 18.3% less common in the shell pavements than in the LSB. The terrestrial/marine ratio is also lower in both shell pavements than in the LSB (by 1.21 – 8.03), even though the values of Bos32.1 and Bos32.3 are

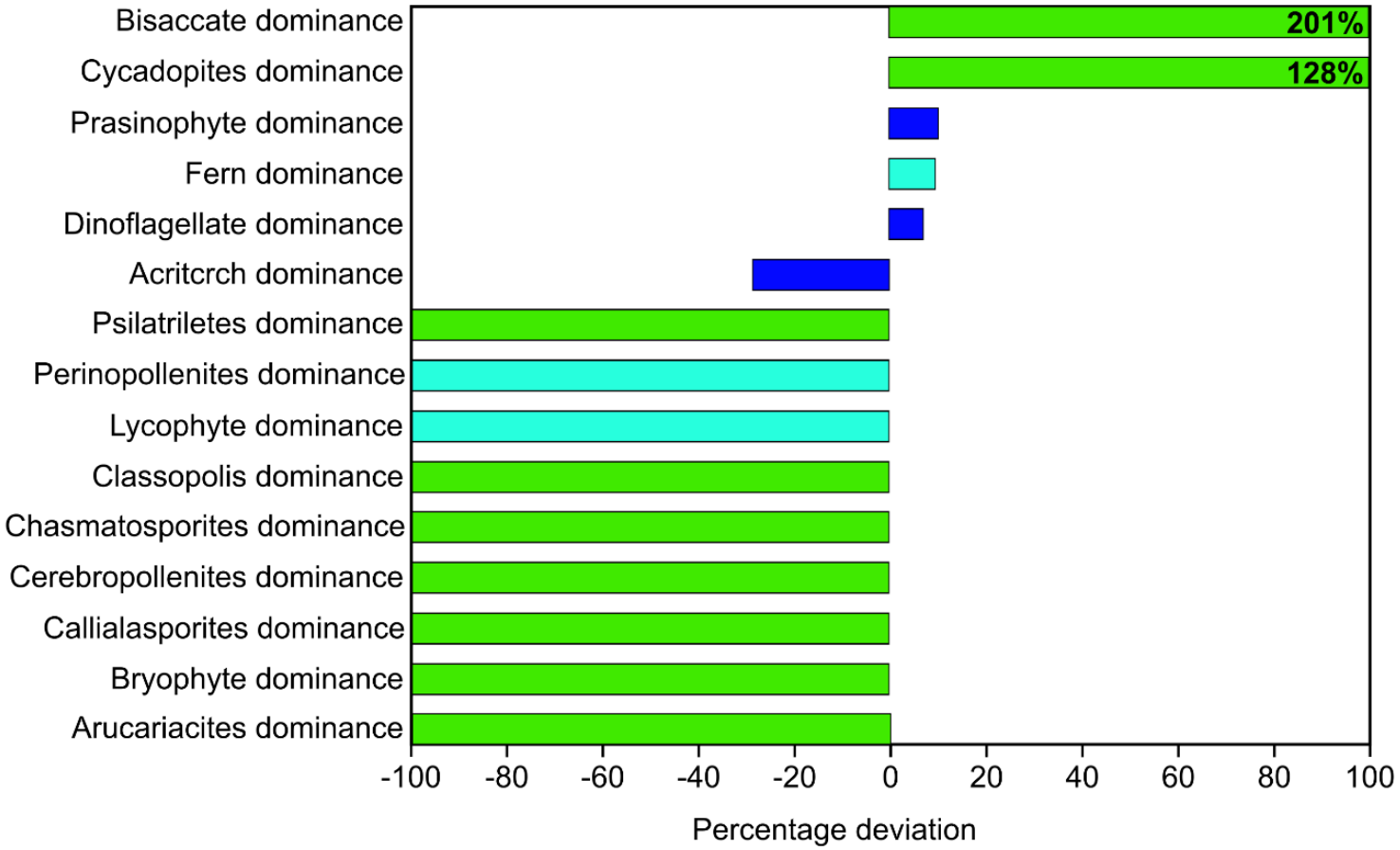

Figure 6.25. Staked chart of the relative deviations of the dominance of various marine (dark blue bars) and terrestrial plant (green and teal bars) genera/groups in Bos32 compared with the LSB. Teal bars indicate plant groups adapted to wet conditions.

roughly comparable with the LSB. Dinoflagellate dominance within the phytoplankton community also increases concomitant with both pavements, and this is also more pronounced in Bos32 than in Pseud41. In most of the palynological samples, the only dinoflagellate genus identified was *Nanoceratopsis* sp. (except in Bos32.2, where one cyst attributed to *Mancodinium* sp. was found). In Bos32, prasinophytes also show a slight increase (at the expense of acritarchs), reaching up to 21.1% dominance. This is not observed in Pseud41.

Ferns make up the largest proportion of the terrestrial community concomitant with both Bos32 and Pseud41, and in Bos32, a distinct drop in dominance occurs on the shell pavement (by 66.7%; Fig. 6.23). The combined dominance of ferns and bryophytes (both being wet-adapted plant types) shows a decrease

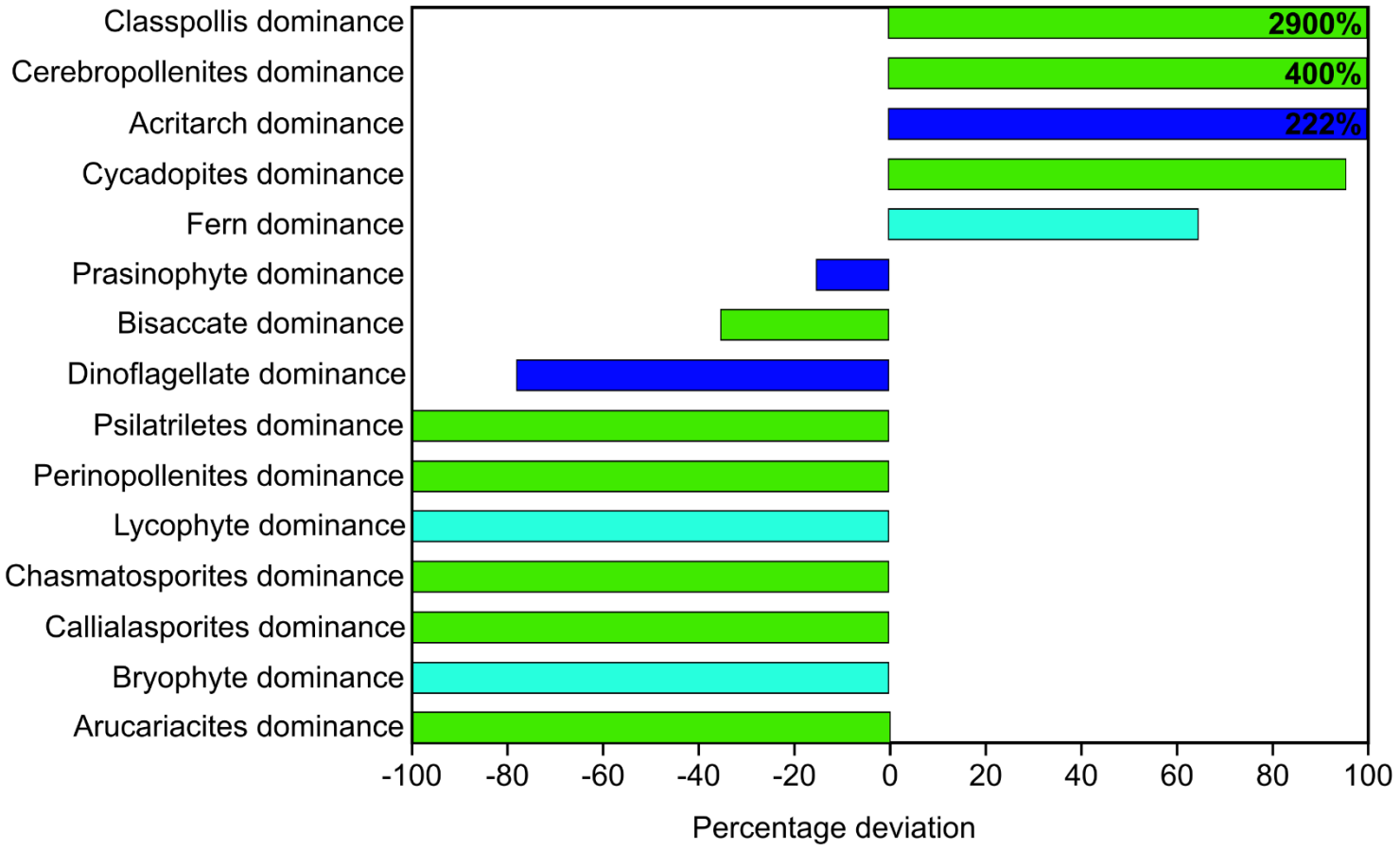

Figure 6.26. Staked chart of the relative deviations of the dominance of various marine (dark blue bars) and terrestrial plant (green and teal bars) genera/groups in Pseud41 compared with the LSB. Teal bars indicate plant groups adapted to wet conditions.

concomitant with the Pseud41 pavement (by 3.33%). Conversely, *Cycadopites* is more dominant in the terrestrial community coeval with both pavements, reaching 16.7% in Bos32, and 14.2% in Pseud41.

One to six land plant genera were identified in Bos32 (Fig. 6.23), whereas 6 – 11 were identified in Pseud41 – both ranges are significantly lower than the values from the LSB (by 8-13). The number of identified genera also increases concomitant with the Bos32 pavement (by 5), but no deviation from a gentle downward trend (from 11 at -2 mm to 6 at +2 mm) is observed concomitant with the Pseud41 pavement. Since graphically representing the differences in plankton and land plant community dominance values between the shell pavements and the LSB is difficult in an up-section plot (using the I-shaped bar), I have plotted stacked bar charts of these values in Figs. 6.25 and 6.26. Prasinophytes and

dinoflagellates were more dominant in the phytoplankton community during the formation of Bos32 than they were in the LSB, and acritarchs were less dominant. During the formation of Pseud41, by contrast, acritarchs were far more dominant, and prasinophytes and dinoflagellates were less dominant. During the formation of both pavements, ferns were more dominant within the terrestrial plant community than they were in the LSB, and bryophytes and lycophytes were less dominant. *Cycadopites* was also more dominant in the terrestrial plant community during the formation of both pavements (compared with the LSB), whereas bisaccate producers were more dominant in Bos32, and *Classpolis* and *Cereborpollenites* were more dominant in Pseud41 (both compared with the LSB). All other plant genera were more dominant within the floral assemblage of the LSB than with the floral assemblages of either pavement.

When plotted on an AOM-Phytoclast-Palynomorph ternary diagram (after Tyson, 1989; Fig. 6.24), all the data points from Bos32 plot in the distal suboxic/anoxic basin field, and all the data points from Pseud41 plot in the distal dysoxic/oxic shelf field. The Bos32 samples also plot at the end of a transport path originating from a highly proximal shelf or basin, while the Pseud41 samples plot close to a transport path from a heterolithic (proximal) oxic shelf.

2.4 Sulphur-iron systematics

Pyrite is the dominant S-bearing phase in most shell pavement samples. However, the S_{py} trend only perfectly follows the total S trend in Pseud41. The sample Bos32.1 contains other S-bearing phases (accounting for 39.7% of the total S value), and so does Pseud34.2 (accounting for 90.6% of the total S value; Fig. 6.27). It is unclear what this secondary sulphur-bearing phase is, since both carbonate (in the form of shell calcite) and sulphurised organic matter species (see section 2.6.5) are present.

Both Bos32 and Pseud41 are associated with relative increases in the S_{py} level, increasing by 1.76 wt.% in the former, and by 0.213 wt.% in the latter. Pseud34, by contrast, shows a relative decrease in S_{py} (by 1.46 wt.%). Compared with the individual *P. dubius* shell recovered from the LSB, Pseud34 is greatly depleted in S_{py}, whereas Bos32 is slightly enriched, and Pseud41 is more-or-less comparable.

A TOC-Fe_{HR}-Total S ternary (Fig. 6.28) shows that in most of the shell pavement samples, pyrite formation was S-limited. The two exceptions, where pyrite formation was Fe limited, are Bos32.1, and Pseud41.2.

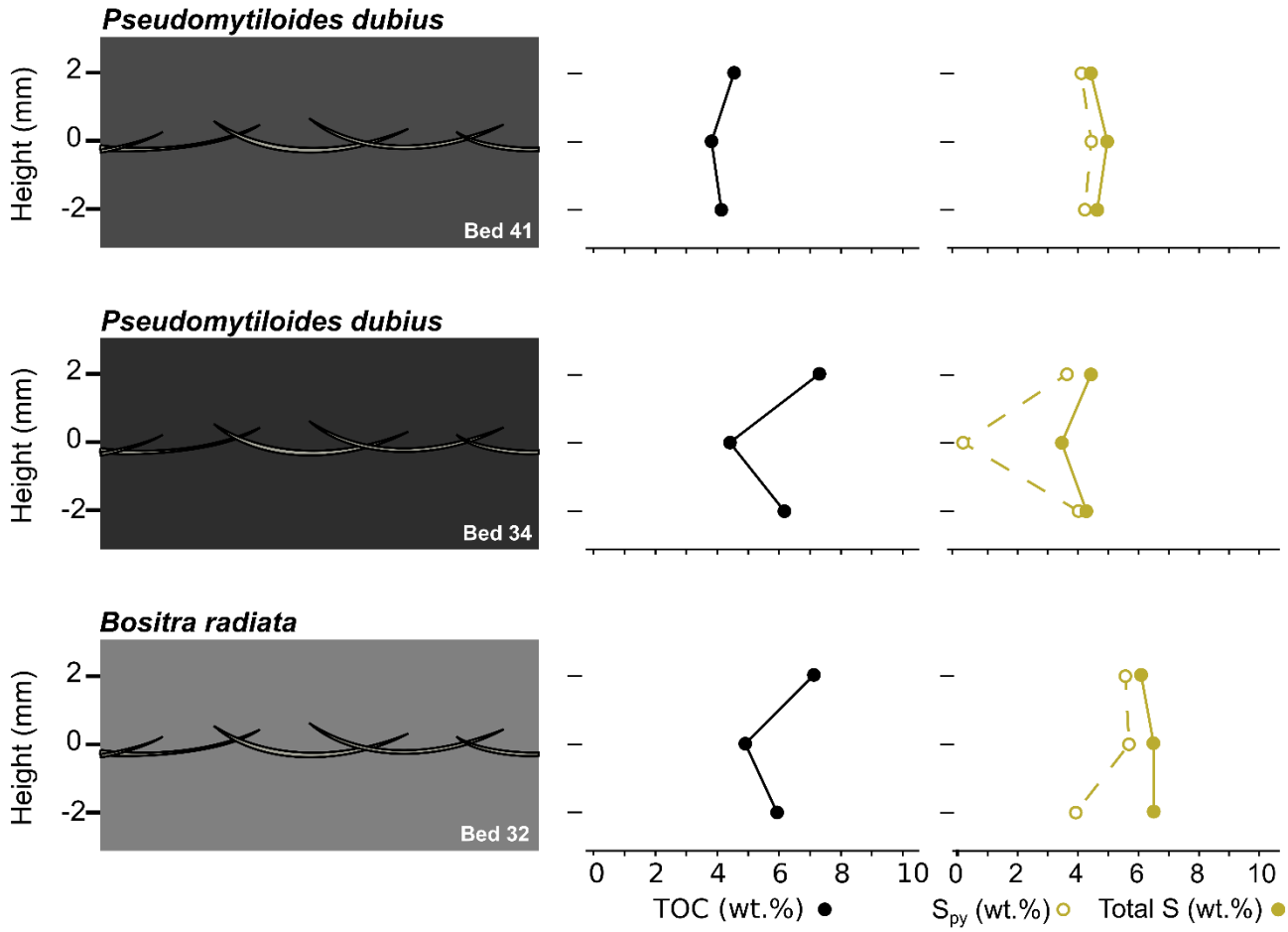

Figure 6.27. Total S and S_{py} for each of the shell pavements plotted together, showing S_{py} is greatly depleted compared with total S in the samples Bos32.1 and Pseud34.2.

Pseud34 and Pasud41 show point decreases in Fe_{HR}/Fe_T, by 0.540 and 0.0680, respectively (Fig. 6.29). However, most values remain in the unequivocally anoxic field, with the data point for Pseud34.2 plotting near the upper boundary of the equivocal field. Furthermore, Bos32 shows a relative increase in Fe_{HR}/Fe_T (by 0.21), with all three data points plotting in the anoxic field. These values are outside the range found for the individual *P. dubius* from the LSB, with Bos32 and Pseud41 having higher Fe_{HR}/Fe_T signatures (0.21 – 0.45, and 0.18 – 0.43, respectively), and Pseud34 having a lower signature (0.08 – 0.32).

Most of the Fe_{Py}/Fe_{HR} data points from the shell pavements plot in or near the equivocal field, with only Pseud34 showing a prominent decrease into the ferruginous field (by 2.95). Bos32 and Pseud34 show

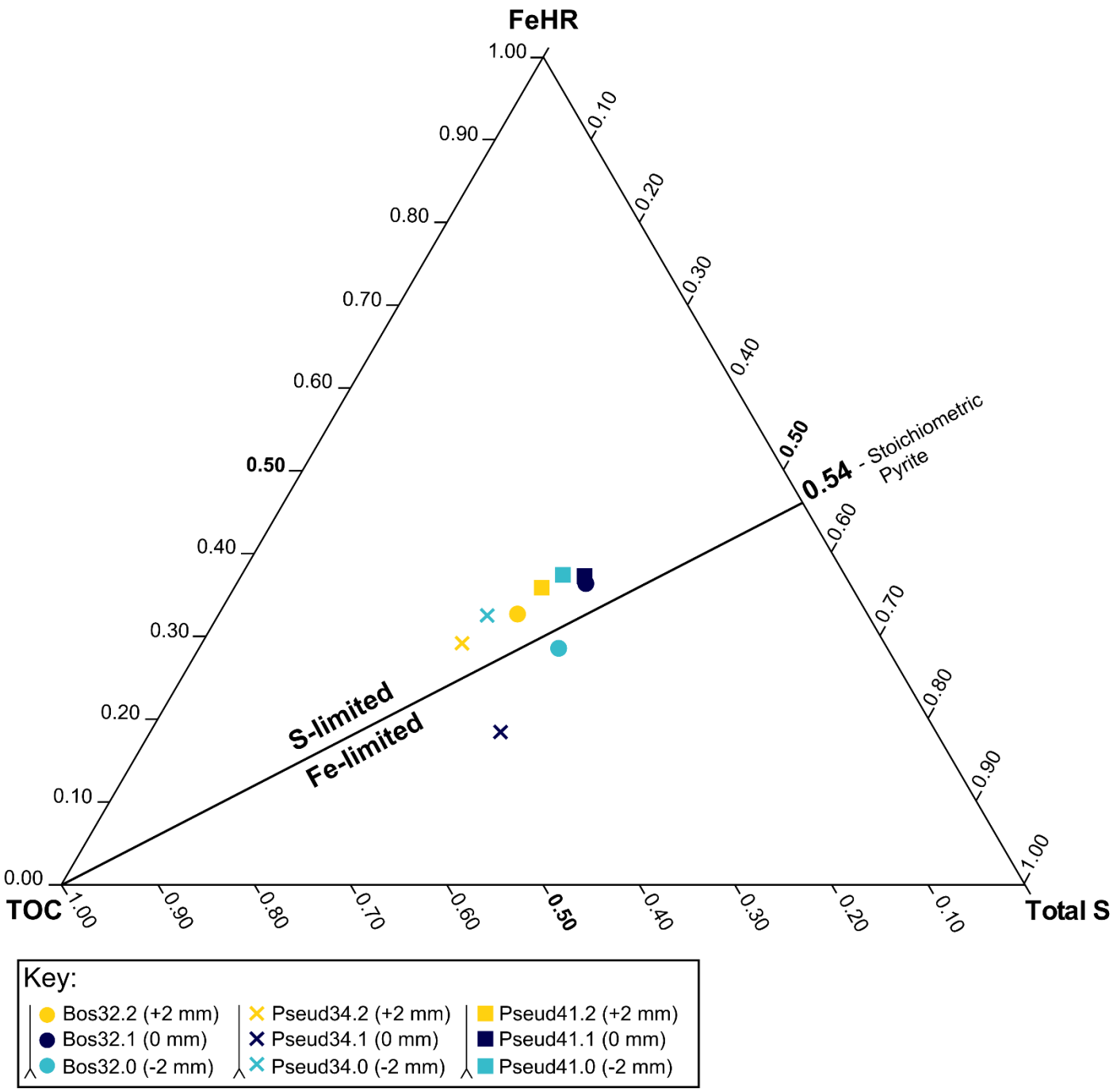

Figure 6.28. Ternary plot comparing TOC, TS and Fe_{HR} for the shell pavement samples, with the regression line for stoichiometric pyrite indicated. Note that in the S-limited zone, S is assumed to be derived from sulphate reduction in anoxic sediments.

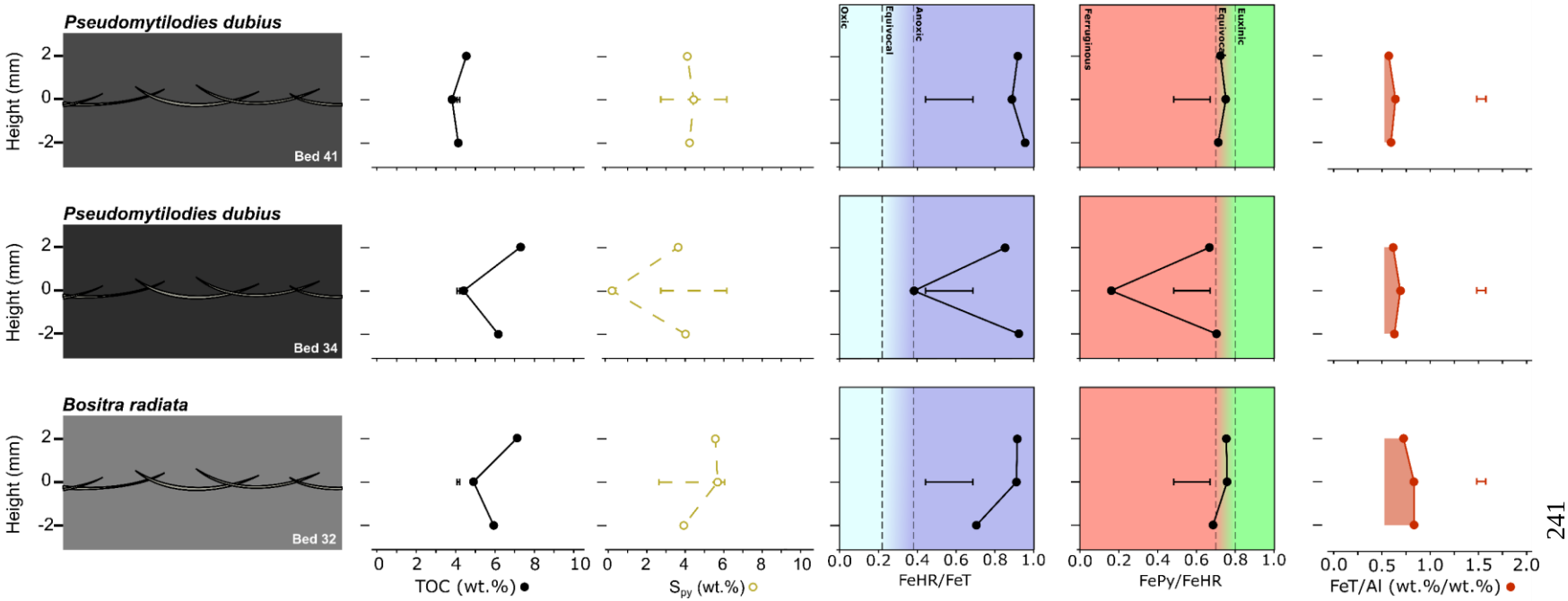

Figure 6.29. Fe_{HR}/Fe_T, Fe_{Py}/Fe_{HR} and Fe_T/Al through each of the shell pavements. Thresholds for the Oxic-Equivocal-Anoxic, and Ferruginous-Equivocal-Anoxic fields of Anderson & Raiswell (2004), Poulton & Canfield (2011) and Poulton (2021), indicated with dashed vertical lines, and background colour. Shaded areas indicate enrichment relative to the standard shale value of Wedepohl (1971; 2004). Note that in all up-section plots, the horizontal bar (⊢⊣) indicates the range of values for the proxy in question recovered from around the individual *P. dubius* fossil from the LSB (i.e. the samples LSB1.11 and LSB1.12 Chapter 3, section 3.2)

minor increases (by 1.54 and 0.185, respectively). As with Fe_{HR}/Fe_T, all the Fe_{Py}/Fe_{HR} values concomitant with the pavements plot outside the range of the LSB *P. dubius* individual, being either elevated (in Bos32 and Pseud41; by 0.09 – 0.27 and 0.08 – 0.27, respectively), or depleted (in Pseud34; by 0.33 – 0.51). All pavements show a slight increase in Fe_T/Al (by a maximum of 0.05wt.%/wt.% in Pseud41), but none reach the enrichment levels encountered in the LSB. All the values taken from the shell pavements are also enriched relative to the standard shale values of Wedepohl (1971; 2004).

2.5 Major and trace elements

To account for the dilution effect of both siliciclastic input (from the silt laminae) and carbonate formation (from the shells) on the redox-sensitive trace element enrichment values, I have normalised these to Al (wt.%), and are also multiplied by a carbonate correction factor (D):

$$\mathrm{D} = \frac{100}{(100 - \ \mathrm{CaCO_3(wt.\%)[TIC])}}$$

where $\mathrm{CaCO_3(wt.\%)[TIC]}$ is the concomitant value of carbonate, defined as the difference between

Total C and TOC. This is assuming that the majority of the carbonate content of the shell pavement samples is supplied from the shells, and that the concentration of authigenic Fe carbonate phases is small by comparison.

Neither Al nor Ti show significant variation concomitant with the shell pavements (Fig. 6.30), except for a slight decrease in Al (by 1.90 wt.%) in Pseud34. Correcting Al wt.% and Ti wt.% for carbonate dilution using D does not affect these trends (Appendix 3).

D*Mn/Al shows a small enrichment concomitant with Bos32 (up to 38.4 ppm/wt.%; Fig. 6.31), and a larger enrichment in Pseud34 (up to 57.8 ppm./wt.%), but no appreciable enrichment or depletion in Pseud41. All samples are depleted in D*Mn/Al relative to the standard shale value by 11.8 – 71.3 ppm/wt.%. While the D*Mn/Al content of Bos32 and Pseud41 are much lower than for the individual *P. dubius* from the LSB (by 50.6 – 90.3 ppm/wt.%), Pseud34 is in about the same range.

There are small increases in the level of D*Mo/Al concomitant with all three of the shell pavements, with the greatest being in Pseud34 (by 0.21 ppm/wt.%; Bos32 shows an increase of 0.06 ppm/wt.%, and Pseud41 an increase of 0.102 ppm/wt.%). All D*Mo/Al values from Pseud41 are higher than the other pavements (by 1.37 ppm/wt.% - 2.26 ppm/wt.%), but all samples are enriched relative to the standard

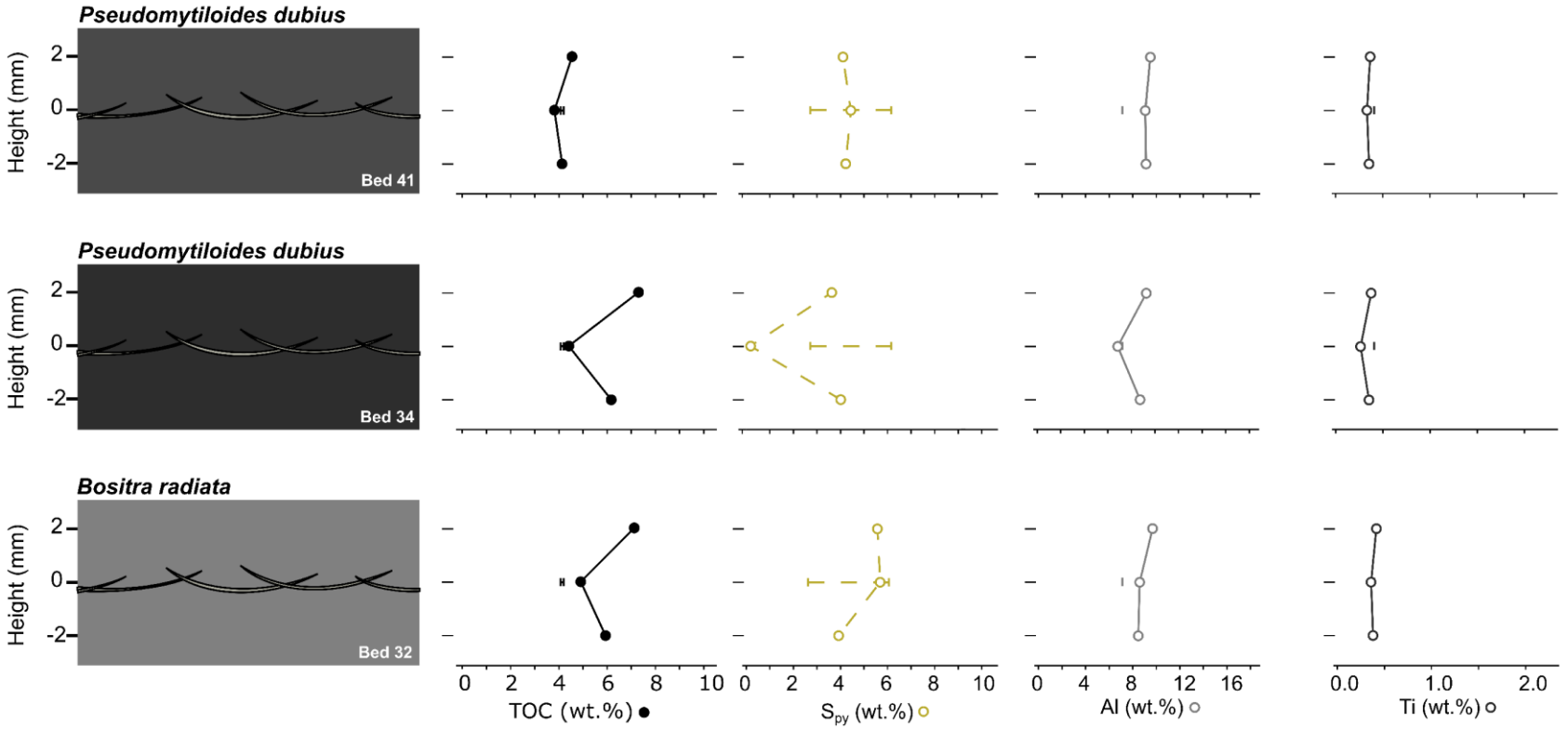

Figure 6.30. Plot of Ti (wt.%) and Al (wt.%) through each of the shell pavements. Note that in all up-section plots, the horizontal bar (▬) indicates the range of values for the proxy in question recovered from around the individual *P. dubius* fossil from the LSB (i.e. the samples LSB1.11 and LSB1.12 Chapter 3, section 3.2)

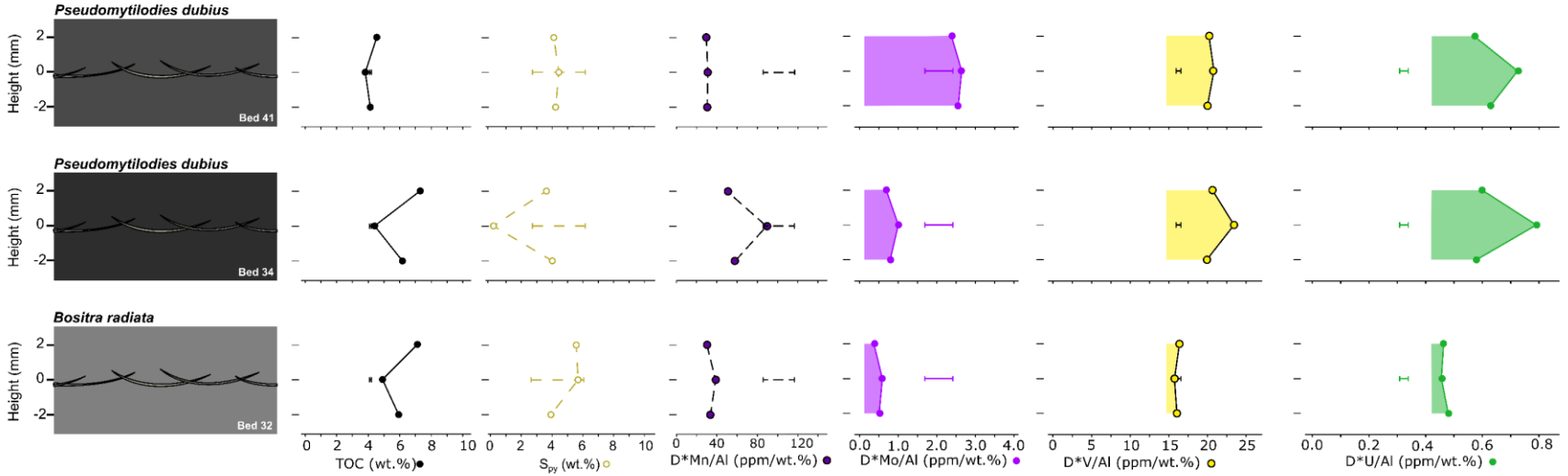

Figure 6.31. Plot of Mn/Al, Mo/Al, V/Al and U/Al through each of the shell pavements. As ig Fig. 6.29, shaded areas indicate enrichment of the plotted trace element relative to the standard shale values of Wedepohl (1971; 2004). Note that in all up-section plots, the horizontal bar (⊢) indicates the range of values for the proxy in question recovered from around the individual *P. dubius* fossil from the LSB (i.e. the samples LSB1.11 and LSB1.12 Chapter 3, section 3.2)

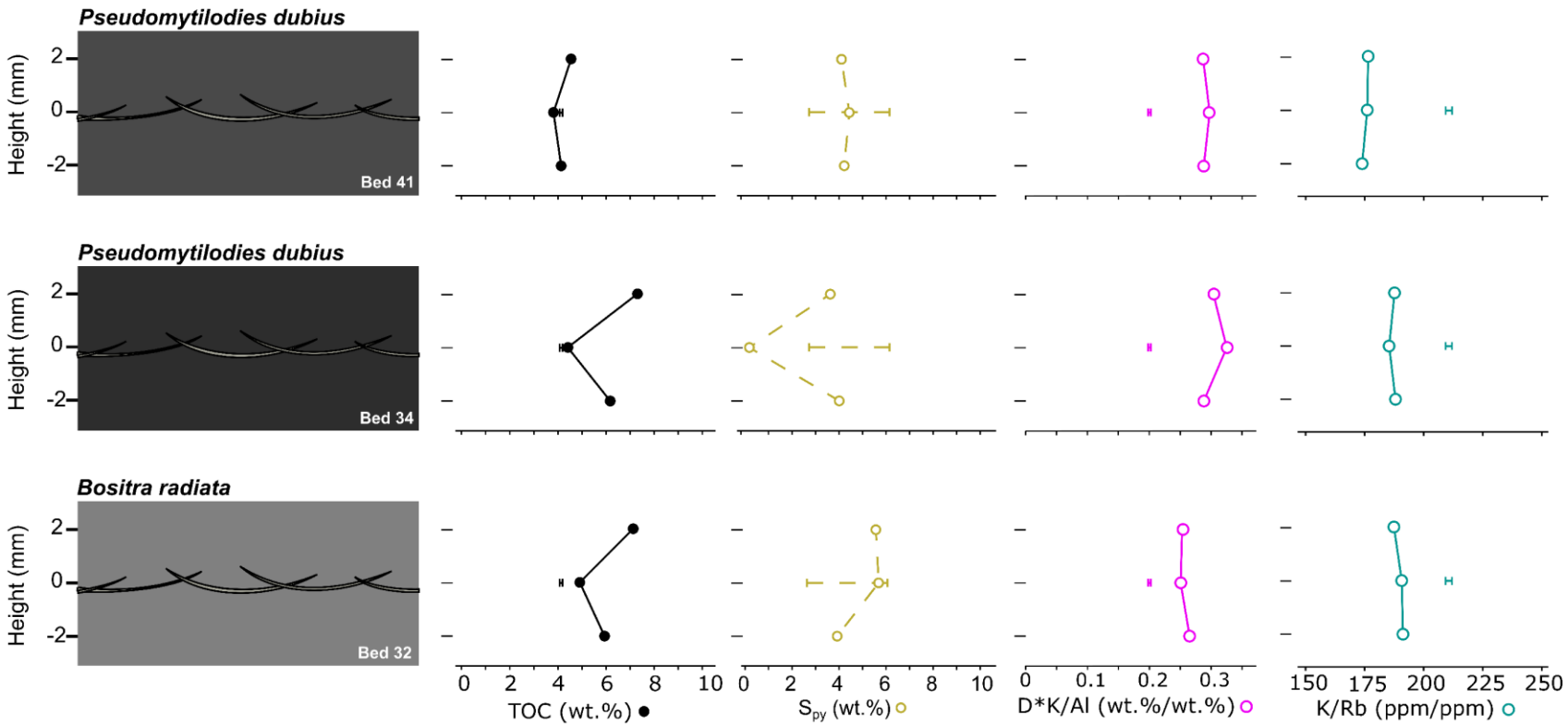

Figure 6.32. Plot of K/Al (wt.%/wt.%) and K/Rb (ppm/ppm) through each of the shell pavements. Note that in all up-section plots, the horizontal bar (⊢) indicates the range of values for the proxy in question recovered from around the individual *P. dubius* fossil from the LSB (i.e. the samples LSB1.11 and LSB1.12 Chapter 3, section 3.2). For some plots (including in this figure), this range can be very small.

shale value (Wedepohl 1971; 2004). Mo enrichment is higher in Pseud41 compared with the LSB (by -0.26 – 0.46 ppm/wt.%), but lower in Bos32 and Pseud34 than with the LSB (1.17 – 1.88 ppm/wt.% in Bos32 and 0.99 – 1.70 ppm/wt.% in Pseud34).

Both D*U/Al and D*V/Al show a slight decrease concomitant with Bos32 (by 0.03 ppm/wt.% and 0.36 ppm/wt.%, respectively), and an increase concomitant with Pseud34 (0.22 ppm/wt.% and 3.52 ppm/wt.%, respectively) and Pseud 41 (0.1 ppm/wt.% and 0.77 ppm/wt.%, respectively). D*U/Al and D*V/Al are also both greatly enriched in the shell pavement samples compared with the LSB (-0.759 ppm/wt.% - 7.55 ppm/wt.% for D*V/Al, and 0.120 ppm/wt.% - 0.485 ppm/wt.% for D*U/Al), except V*/Al in Bos32 (which is roughly comparable).

2.6 Organic geochemistry

All the shell pavements are associated with a point decrease in TOC, although this is to be expected given the dilution effect of the shells (in addition to any change in background TOC). The magnitude of this decrease was the largest for Pseud34 - with TOC decreasing by 1.76 wt.% - even though the coverage of the pavement by shells is less in Pseud34 than in Bos32 (which shows a TOC decrease of 1.03 wt.%; compare with Figs. 2.9 and 6.2). The TOC content concomitant with all three shell pavements is roughly comparable to that of the individual *P. dubius* from the LSB.

2.6.1 Rock-Eval pyrolysis

As discussed in Chapter 3, section 3.5, it is highly suspected that the TOC value obtained by Rock-Eval pyrolysis is an underestimate of the true TOC value, so I will not be relying on the Rock-Eval TOC data in the interpretation. It suffices to say that the trends in TOC via Rock-Eval roughly compare with those in TOC via LECO (see Appendix 3).

HI varies in proportion with TOC in Bos32 and Pseud41, although it shows no considerable variability through Pseud41 (Fig. 6.33). The HI values are also 152 – 307 mgHC/gTOC higher than those reported from the LSB individual.

OI shows no variability concomitant with either Bos32 or Pseud41, but shows a point increase on Pseud34 by 9 $mgCO_2$/gTOC. The values also do not deviate significantly from that of the LSB (by no more than 7 $mgCO_2$/gTOC).

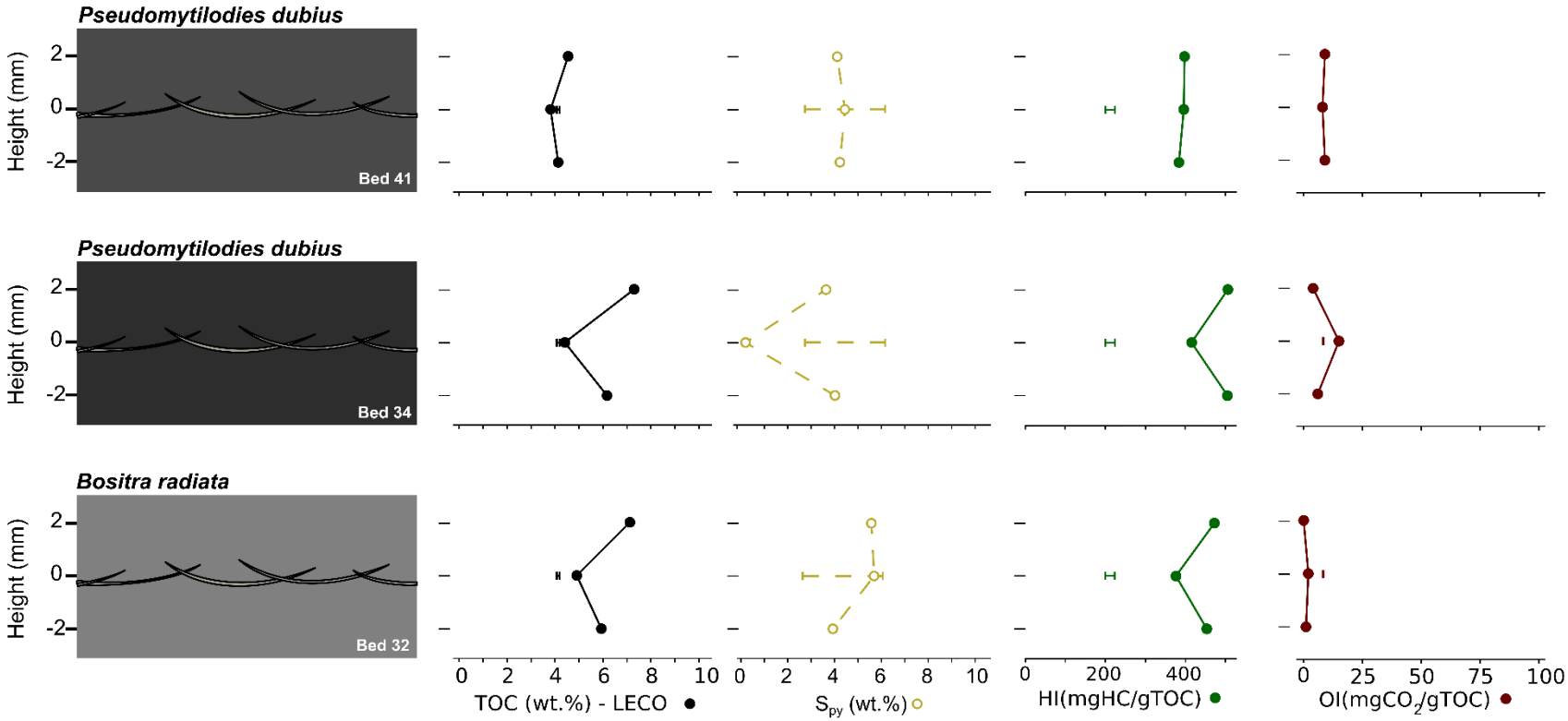

Figure 6.33. TOC (from LECO), S_{py}, and the Rock-Eval parameters HI (mgHC/gTOC) and OI ($mgCO_2$/gTOC) through each of the shell pavements. Note that in all up-section plots, the horizontal bar (⊢) indicates the range of values for the proxy in question recovered from around the individual *P. dubius* fossil from the LSB (i.e. the samples LSB1.11 and LSB1.12 Chapter 3, section 3.2)

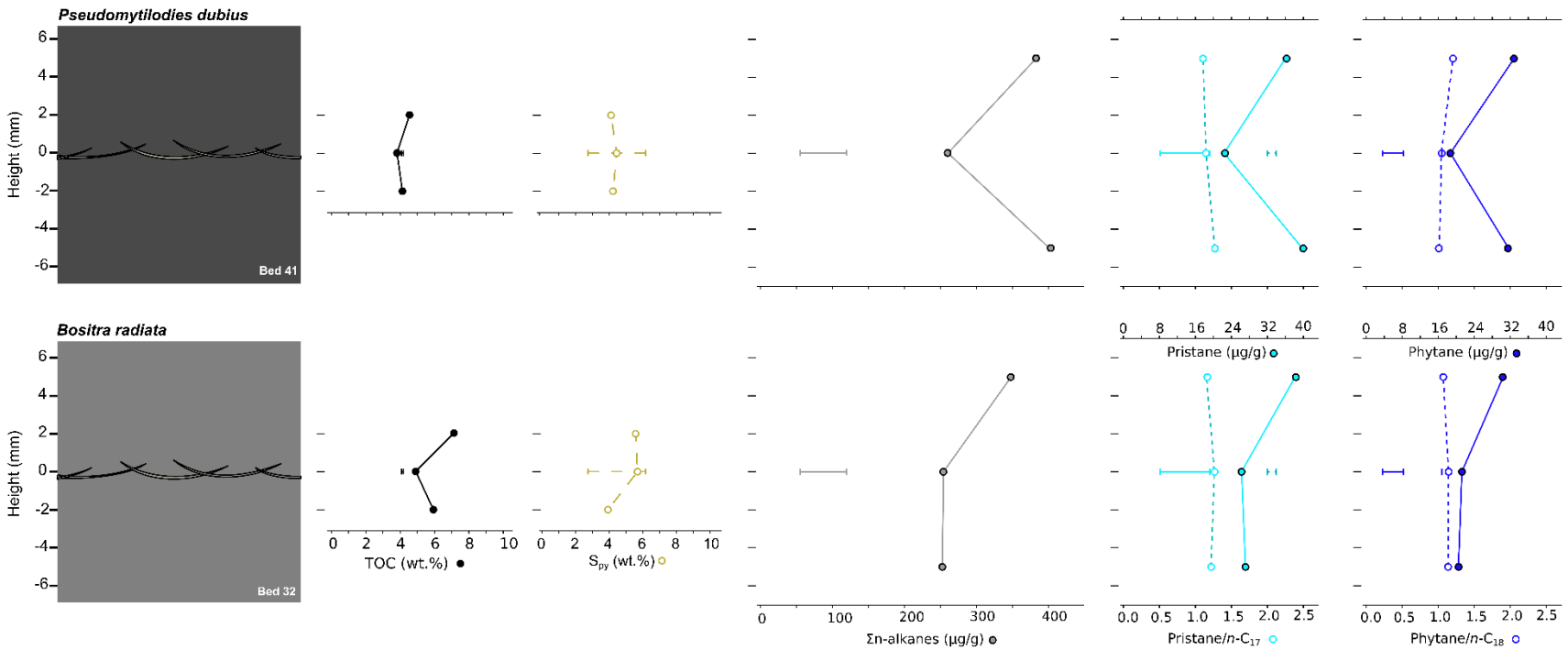

Figure 6.34. TOC, pyrite sulphur, Σ *n*-alkanes, pristane (alongside pristane/*n*-C_{17}) and phytane (alongside phytane/*n*-C_{18}) through Bos32 and Pseud41. Unless otherwise stated, all the biomarkers of interest are normalised to TOC (via LECO; see Chapter 5, section 3.0), to isolate the enrichment of the biomarker independent of TOC.

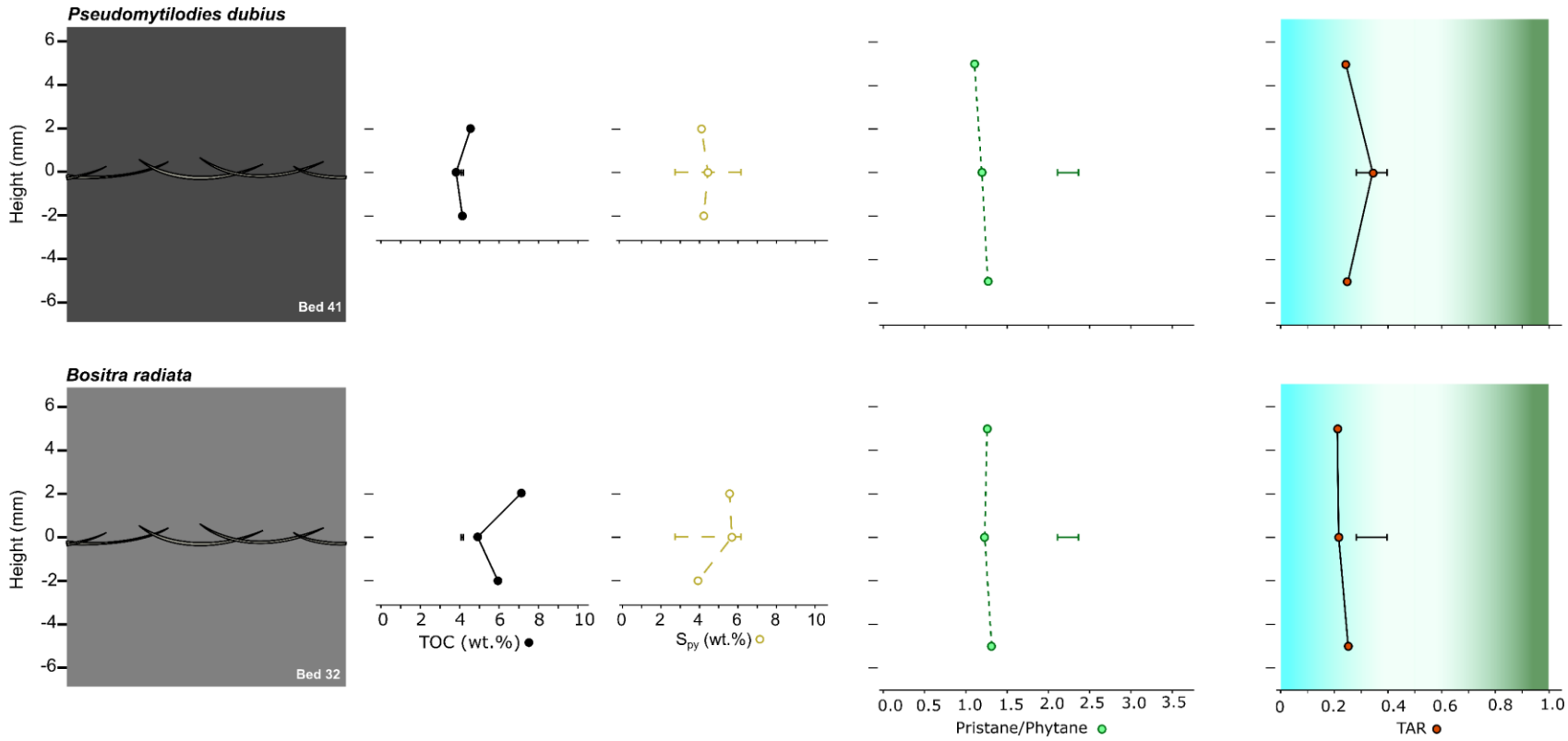

Figure 6.35. Pristane/phytane and the TAR (definition in Chapter 1, section 9.2.6) through Bos32 and Pesud41. Note that in all up-section plots, the horizontal bar (⊢) indicates the range of values for the proxy in question recovered from around the individual *P. dubius* fossil from the LSB (i.e. the samples LSB1.11 and LSB1.12 Chapter 3, section 3.2)

2.6.2 *n*-Alkanes and isoprenoids

As discussed in Chapter 5, section 3.0, I have normalised most biomarker proxy records presented here to local TOC to independently quantify their abundances.

The concentration of *n*-alkanes shows a slight increase in Bos32 (by 0.925 mg/gTOC; Fig. 6.34), and a slight decrease in Pseud41 (by 2.97 mg/gTOC). However, for both pavements, the level is higher than for the individual from the LSB (by 1.00 – 3.02 mg/gTOC).

Pristane and phytane do not show significant variability through Bos32, but both show a decrease coeval with Pseud41 (by 379 µg/gTOC and 270 µg/gTOC, respectively). Neither Pr/*n*-C_{17} or Phy/*n*-C_{18} show significant excursions in either of the shell pavements. Pristane concentrations in the shell pavements are comparable to the individual *P. dubius* from the LSB, but Phytane is enriched by 147 – 295 µg/gTOC. Conversely, Pr/*n*-C_{17} is depleted in the shell pavements compared with the LSB (by 0.74 – 0.98), whereas Phy/*n*-C_{18} is comparable.

Unlike in the LSB, neither pr/phy nor the TAR vary considerably across either shell pavements (Fig. 6.35). Pr/Phy is also lower than for the LSB (by 0.88 – 1.16), and the TAR in Bos32 is slightly depleted compared with the LSB (by 0.07 – 0.18).

2.6.3 Hopanes and steranes

Ts/(Ts+Tm) does not vary through either of the shell pavements, nor does the C_{35} homohopane index (which is higher than for the LSB by 1.65 – 2.56 %; Fig. 6.36). The steranes/(hopanes+sternes) ratio is extremely small in all of the shell pavement samples (i.e. the hopane concentration vastly overwhelms the sterane concentration) and does not display any variability. It is also depleted in both pavements, relative to the LSB value, by 0.38.

The relative contributions of ΣC_{27}, ΣC_{28}, ΣC_{29} and ΣC_{30} to $\Sigma(C_{27\text{-}30})$ do not vary through either Bos32 or Pseud41, and are essentially identical to the values coeval with the individual *P. dubius* from the LSB (Fig. 6.37). Likewise, $\Sigma C_{27}/\Sigma C_{29}$ also does not vary greatly through either pavement, and shows values comparable with the LSB.

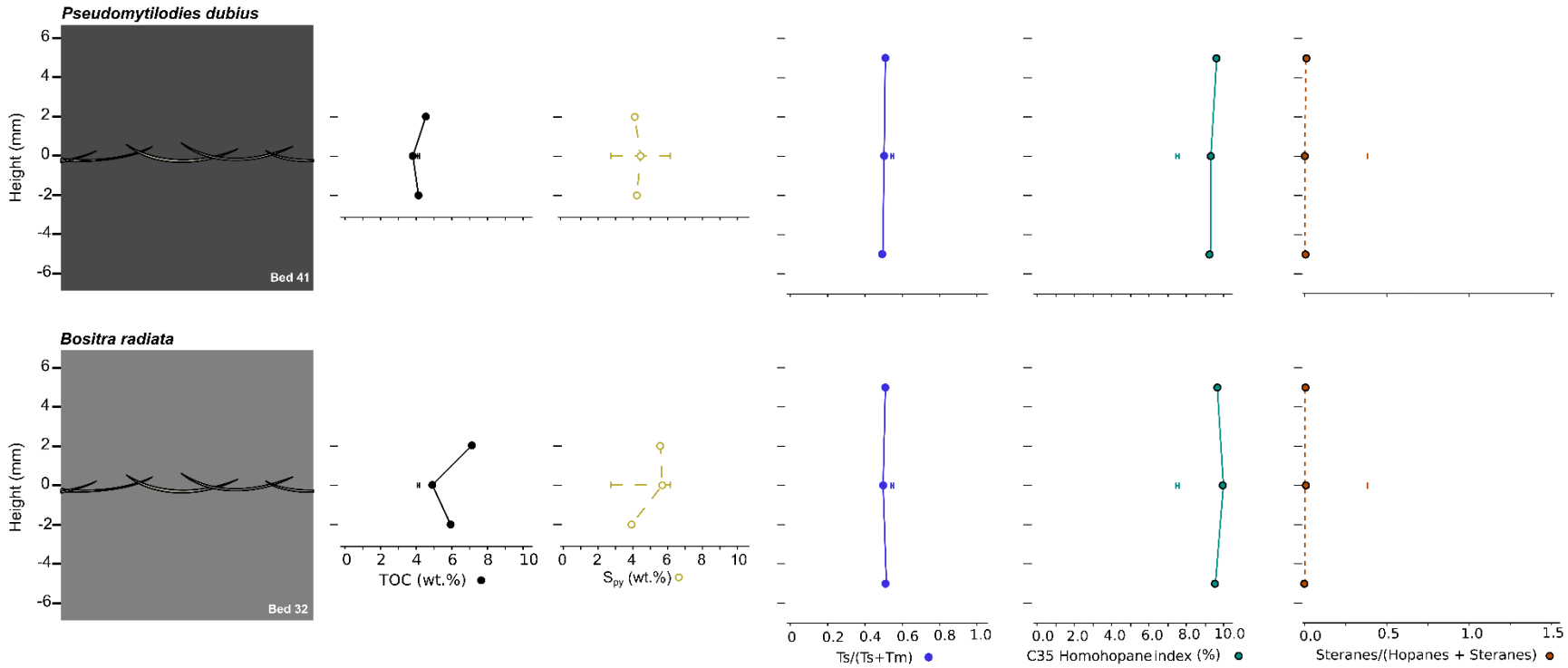

Figure 6.36. Ts/(Ts+Tm), C_{35} homohopane index, and steranes/(steranes + hopanes),through Bos32 and Pseud41. Note that the points that plot away from the axes are in fact the bars used to indicate the range of values for the proxy in question recovered from around the individual *P. dubius* fossil from the LSB (i.e. the samples LSB1.11 and LSB1.12 Chapter 3, section 3.2)

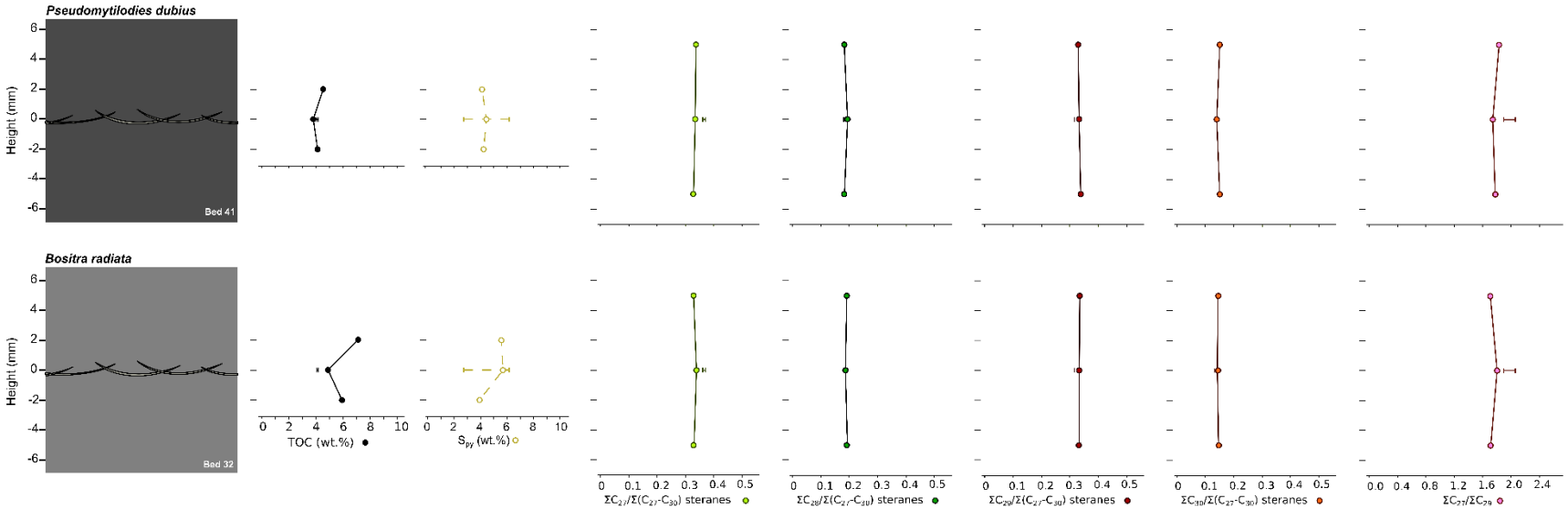

Figure 6.37. Steranes/(Steranes + hopanes), $\Sigma C_{27}/\Sigma(C_{27}\text{-}C_{30})$sterane,$\Sigma C_{28}/\Sigma(C_{27}\text{-}C_{30})$sterane,$\Sigma C_{29}/\Sigma(C_{27}\text{-}C_{30})$sterane, $\Sigma C_{30}/\Sigma(C_{27}\text{-}C_{30})$sterane, and $\Sigma C_{27}/\Sigma C_{29}$ through Bos32 and Pseud41.

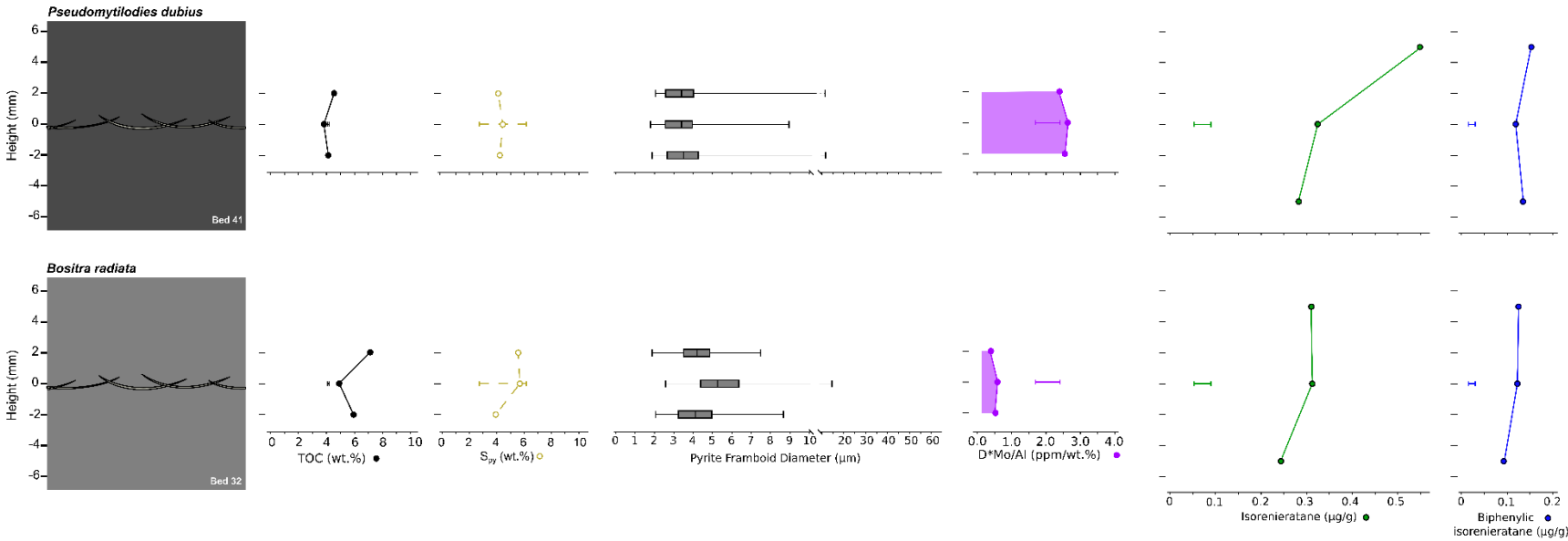

Figure 6.38. Isorenieratane and biphenylic isorenieratane content through Bos32 and Pseud41. The carotenoids are plotted against pyrite framboid diameter and Mo/Al, to form a comparison of different proxies sensitive to euxinia. As in all the up-section plots in this chapter, the horizontal bars (⊢⊣) indicate the range of values for the proxy in question recovered from around the individual *P. dubius* fossil from the LSB (i.e. the samples LSB1.11 and LSB1.12 Chapter 3, section 3.2)

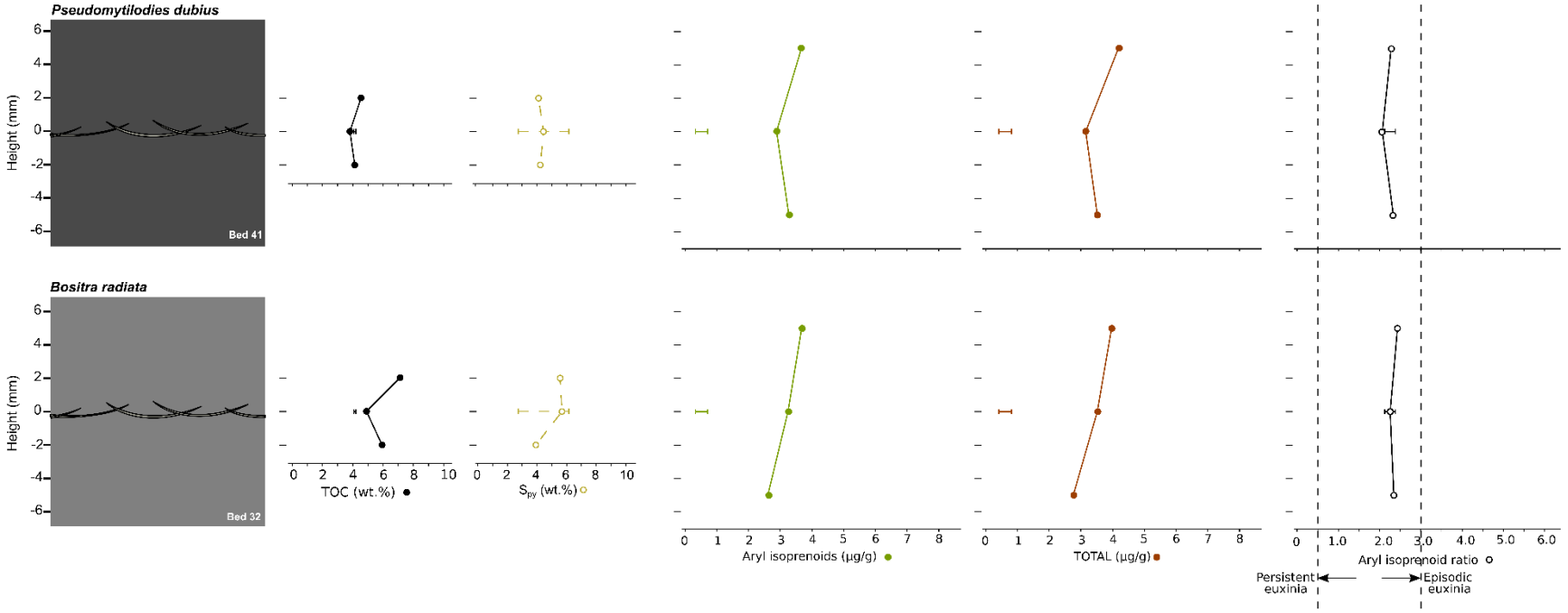

Figure 6.39. Aryl isoprenoid content, total aryl isoprenoid, Isorenieratane and biphenylic isorenieratane content (TOTAL), and AIR through Bos32 and Pseud41.

2.6.4 Isorenieratane and aryl isoprenoids

Both Isorenieratane, and the biphenylic derivative described in Chapter 5, section 2.1.3, were identified within the Bos32 and Pseud41 samples. Both carotenoids were at a higher concentration – in all samples – than in the samples concomitant with the *P. dubius* individual from the LSB (by 1.43 – 6.34 µg/gTOC; Fig. 6.38).

Biphenylic isorenieratane, aryl isoprenoids and total carotenoids+isoprenoids show a relative decrease concomitant with Pseud41 (by 0.16 µg/gTOC, 4.17 µg/gTOC, and 2.67 µg/gTOC), although isorenieratane shows an increase (by 1.67 µg/gTOC). By contrast, both isorenieratane, and biphenylic isorenieratane are relatively enriched in Bos32 (by 2.26 µg/gTOC, and 0.94 µg/gTOC), along with aryl isoprenoids (22.0 µg/gTOC), and total carotenoids+isoprenoids (25.2 µg/gvTOC). Neither pavement is accompanied by a significant change in the AIR (Fig. 6.39), and the values observed are comparable to those from the LSB (and imply somewhat episodic euxinia).

2.6.5 Other aromatics

The trends in Phenanthrene, Σ methylphenanthrenes, retene, dibenzothiophene, and Σ methyldibenzothiophenes all show roughly similar trends through both Bos32 and Pseud41 (Figs. 6.40 and 6.41), with a slight increase in concentration concomitant with the pavement (by 3.47 – 24.8%), that persists into the sediment 5 mm above. Phenanthrene and dibenzothiophene reach similar concentrations to the LSB in both pavements, whereas Σ methylphenanthrenes and Σ methyldibenzothiophenes are more highly concentrated (by 35.2 – 174 µg/gTOC and 13.9 – 28.8 µg/gTOC, respectively). Retene levels are also higher (by 11.8 – 8.19 µg/gTOC) in Pseud41 compared with the LSB, but roughly comparable in Bos32. The Phenanthrene/Dibenzothiophene ratio does not show marked variation through either shell pavements, and is elevated relative to the LSB values by 6.30 – 9.34.

2.7 Compound-specific isotope analysis

The greatest excursion observed in the CSIA data presented here is in $\delta^{13}C$ of *n*-C_{17} from Pseud41 (Fig. 6.42), where there is an increase of 3.0 ‰ coeval with the shell pavement.

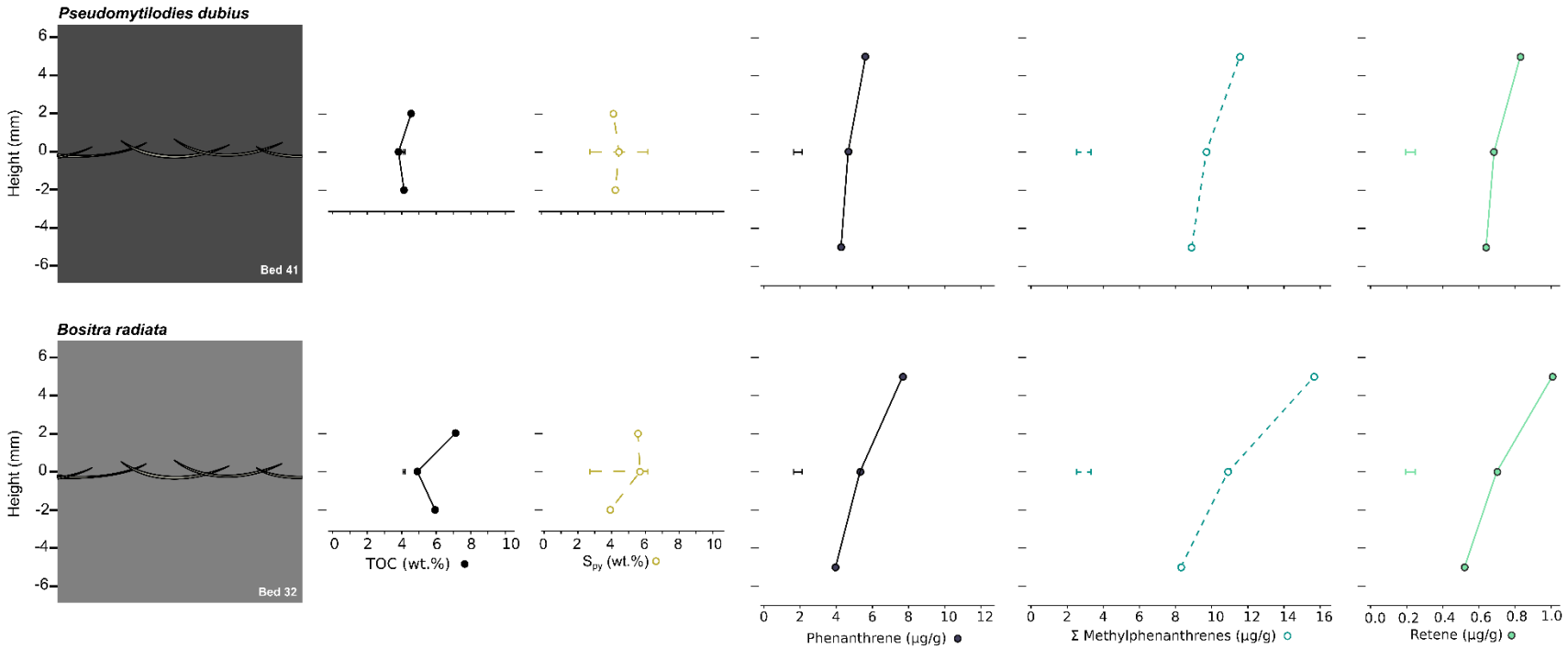

Figure 6.40. Phenanthrene, Σ-methylphenanthrenes, and retene through Bos32 and Pseud41.

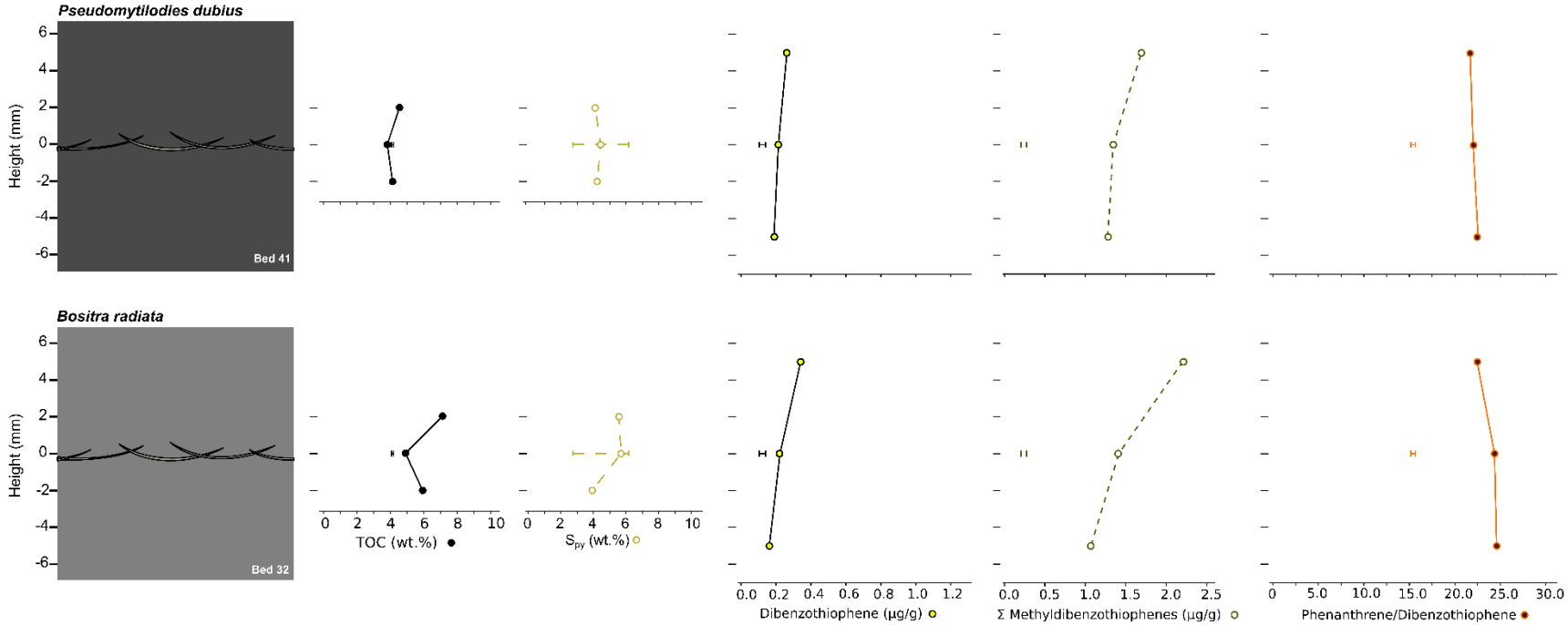

Figure 6.41. Dibenzothiophene, Σ-methyldibenzothiophenes, and phenanthrene/dibenzothiophene through Bos32 and Pseud41.

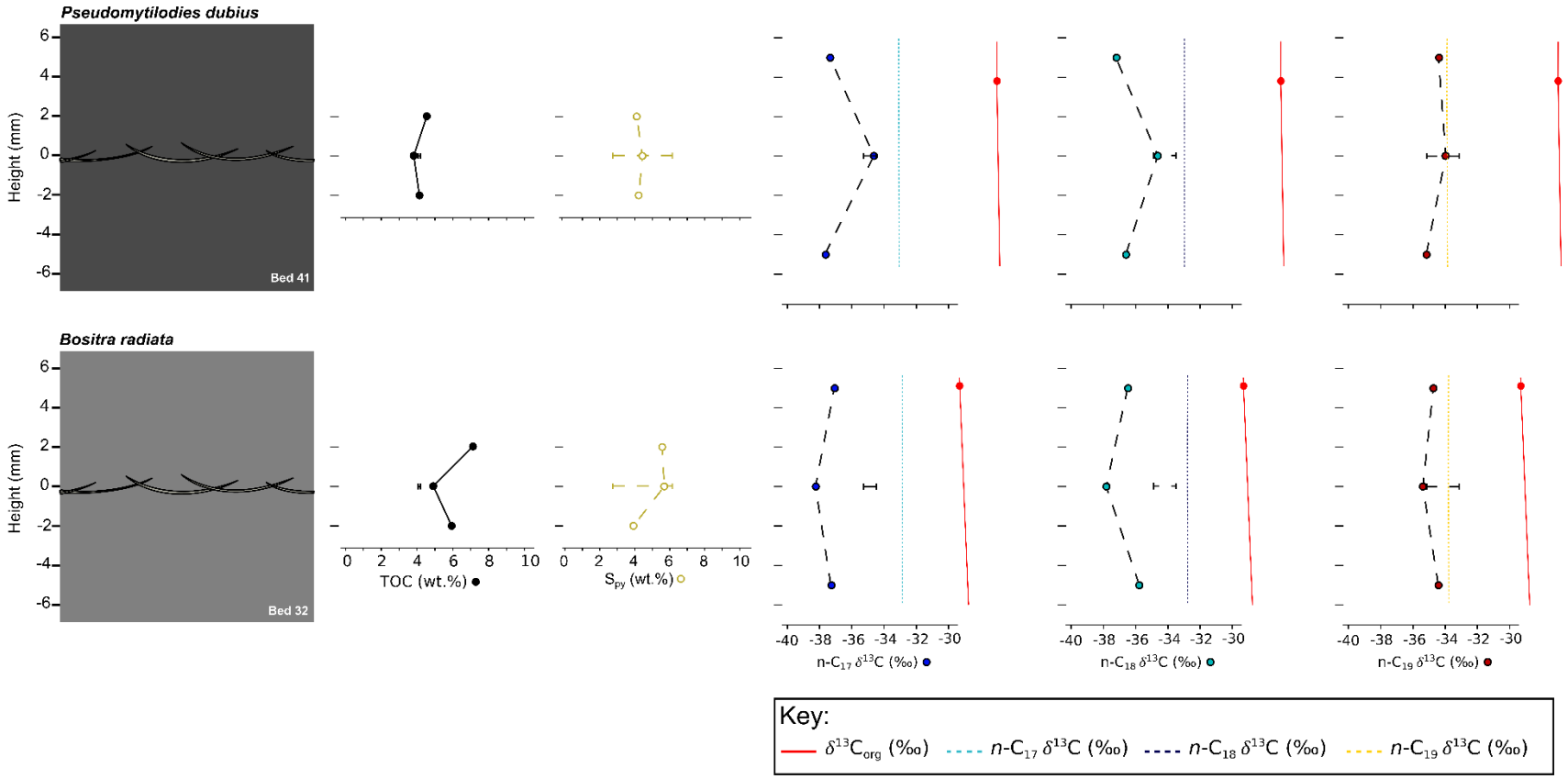

Figure 6.42. $\delta^{13}C$ of *n*-C_{17}, *n*-C_{18} and *n*-C_{19} chain alkanes through Bos32 and Pseud41. The bulk $\delta^{13}C_{org}$ trend of Kemp *et al.* (2011), and the CSIA trends of French *et al.* (2014) are also included, although due to the high stratigraphic resolution – focusing on the shell pavements – most of the data points are not plotted.

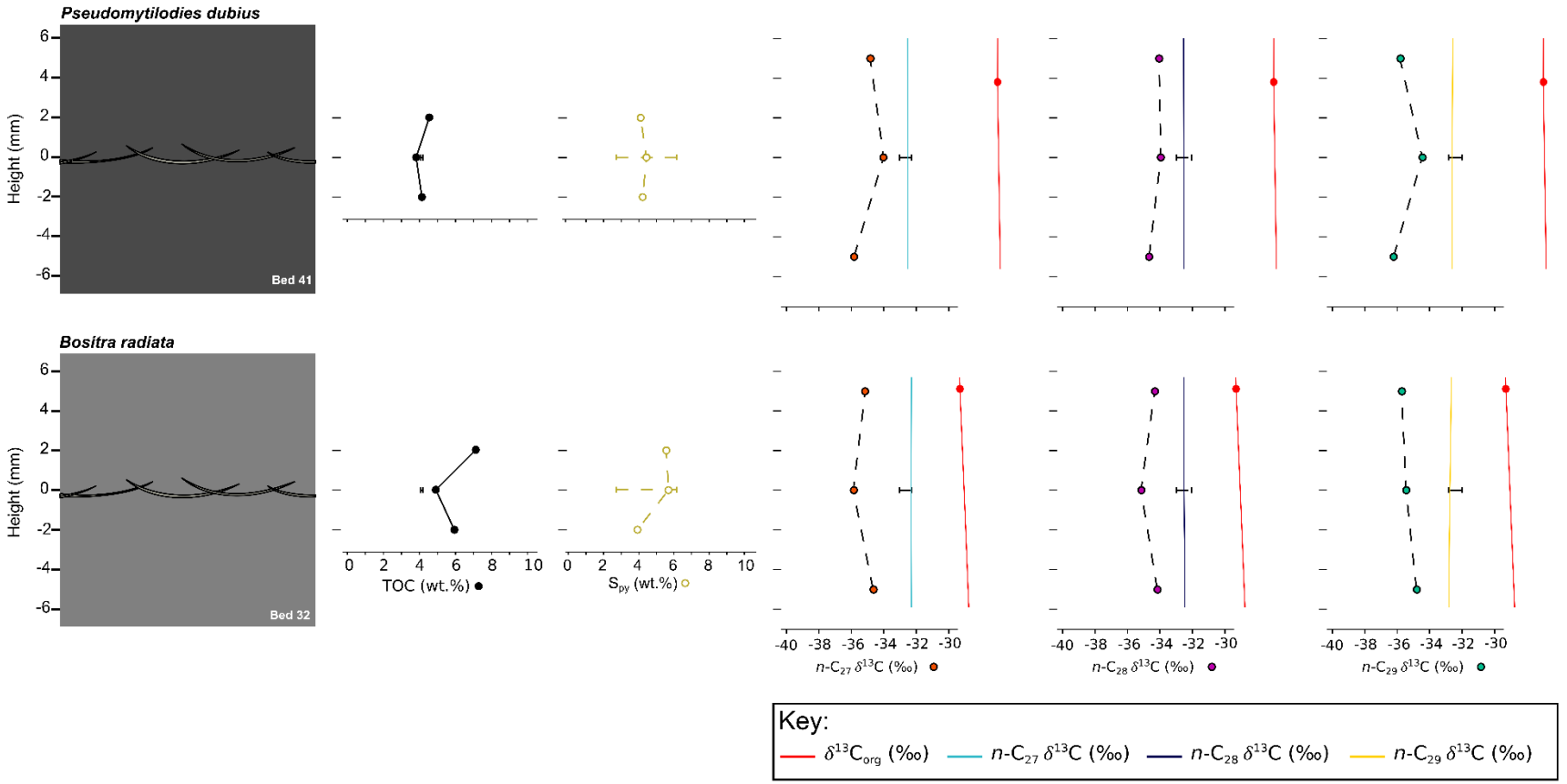

Figure 6.43. $\delta^{13}C$ of *n*-C_{27}, *n*-C_{28} and *n*-C_{29} chain alkanes through Bos32 and Pseud41. As in Fig. 6.42, the bulk $\delta^{13}C_{org}$ trend of Kemp *et al*. (2011), and the CSIA trends of French *et al*. (2014) are also included, although due to the high stratigraphic resolution – focusing on the shell pavements – most of the data points are not plotted.

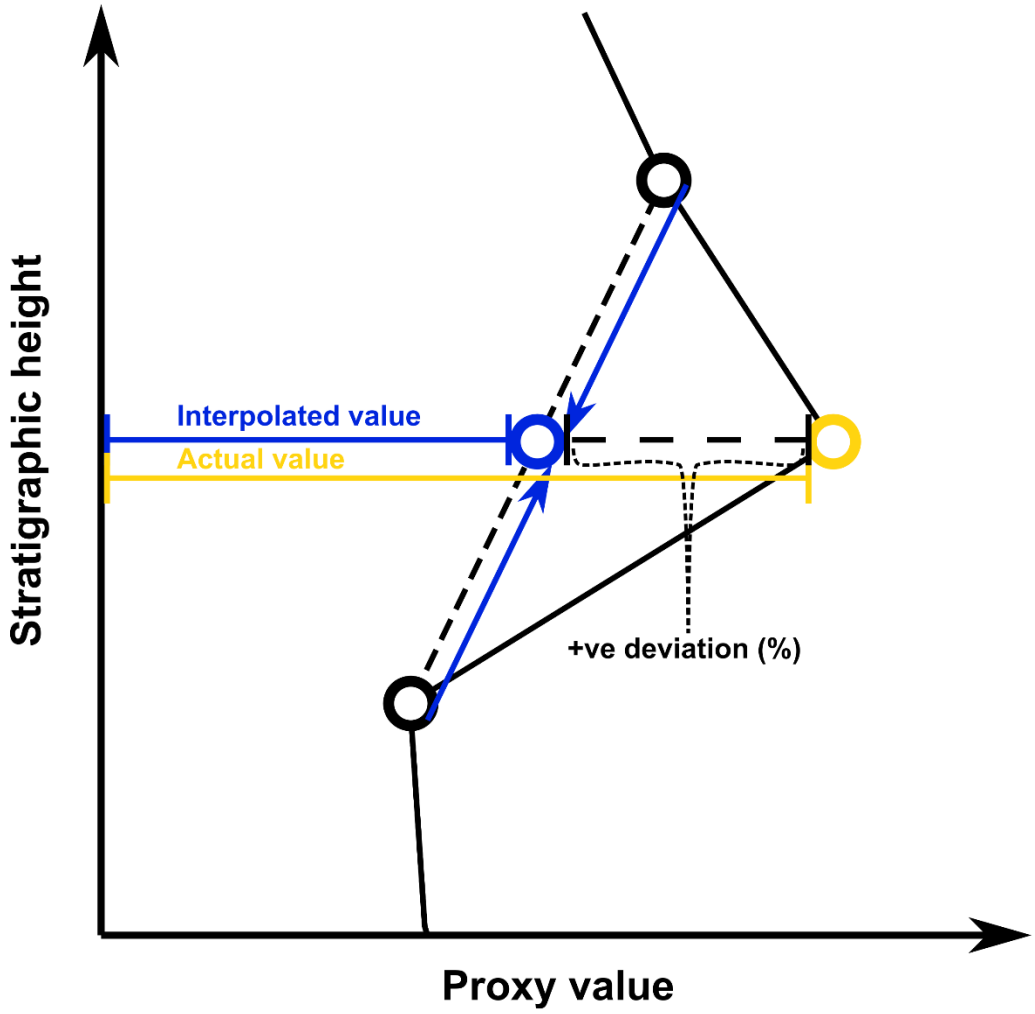

Figure 6.44. A visual representation of the quantification of percentage deviation from interpolated value (presented in Figs. 6.45 - 6.47).

A similar positive excursion is reflected in the concomitant $\delta^{13}C$ of *n*-C_{18} and *n*-C_{19} signatures (+2.6‰ and +1.2‰, respectively). Bos32 is accompanied by negative excursions in $\delta^{13}C$ of *n*-C_{17}, *n*-C_{18} and *n*-C_{19} (of -1.0‰, -2.0‰ and -1.0‰, respectively). The $\delta^{13}C$ of *n*-C_{27}, *n*-C_{28} and *n*-C_{29} trends of Bos32 and Pseud41 are likewise negative and positive (respectively; Fig. 6.43), ranging between -0.6 – -1.2‰ in Bos32, and 0.7 – 1.8‰ in Pseud41. Compared with the individual *P. dubius* shell from the LSB, the isotopic signatures of Bos32 are generally (up to 3.0‰) lower, with the $\delta^{13}C$ of *n*-C_{19} signature just about reaching the lower end of the range of values from the LSB (-34‰). In Pseud41, the values of $\delta^{13}C$ of *n*-C_{17}, *n*-C_{18}, and *n*-C_{19} are comparable to those from the LSB, whereas the $\delta^{13}C$ of *n*-C_{27}, *n*-C_{28}, and *n*-C_{29} signatures are lower (by 0.5 – 1.8‰)

2.8 Different shell pavements compared

Figs. 6.41 – 6.43 show stacked charts of percentage deviations of each measured proxy from the background value (interpolated from the samples directly above and below the pavement), for each of the shell pavements (see Fig. 6.44 for a visual explanation). I have decided to produce these figures, since they take up less space than a large number of up-section plots, while retaining the same information. Carbonate-associated elements (Ba, Ca, Mg, Li and Sr) are generally enriched in the shell pavements (between -0.004 – 1.34 wt.%/wt.% for Mg and Ca, and -0.438 – 41.1 ppm/wt.% for Ba, Li and Sr), even when correcting for carbonate dilution. The redox-sensitive elements (As, Co, Fe, Mn, Mo, Pb, U and V) generally show enrichment (by 0.071 – 0.224 wt.%/wt.% for D*Fe/Al and -0.362 – 31.6 ppm/wt.% for As, Co, Mn, Mo, Pb, U and V). Bos32 is the only pavement that shows relative depletions in As, Co, Pb, U or V (by 0.026 – 0.362 ppm/wt.%, respectively), whereas Pseud34 shows enrichment in all these elements (by 0.215 – 3.52 ppm/wt.%, respectively). Greater enrichment variability is seen in the elements sensitive to both authigenic sulphide formation and organic matter flux (Cd, Cu, Ni, Tl and Zn), ranging between -4.66 – 40.1 ppm/wt.%. Again, Bos32 shows the greatest number of depletions (in Cu, Ni and Tl, by -1.19 – -4.5×10^{-3} ppm/wt.%, respectively), whereas Pseud34 shows enrichments in the same elements (by 1.88×10^{-3} – 11.2 ppm/wt.%, respectively). Finally, the elements sensitive to detrital influence (Cr, K, Rb and Zr) are enriched in Pseud34 (by 0.0377 wt.%/wt.% for K, and 1.7 – 2.26 ppm/wt.% for Cr, Rb and Zr) and Pseud41 (by 9.32×10^{-3} wt.%/wt.% for K, and 0.02 – 0.327 ppm/wt.% for Cr, Rb and Zr), but are all depleted in Bos32 (with the exception of Zr, which is only enriched by 0.021 ppm/wt.%).

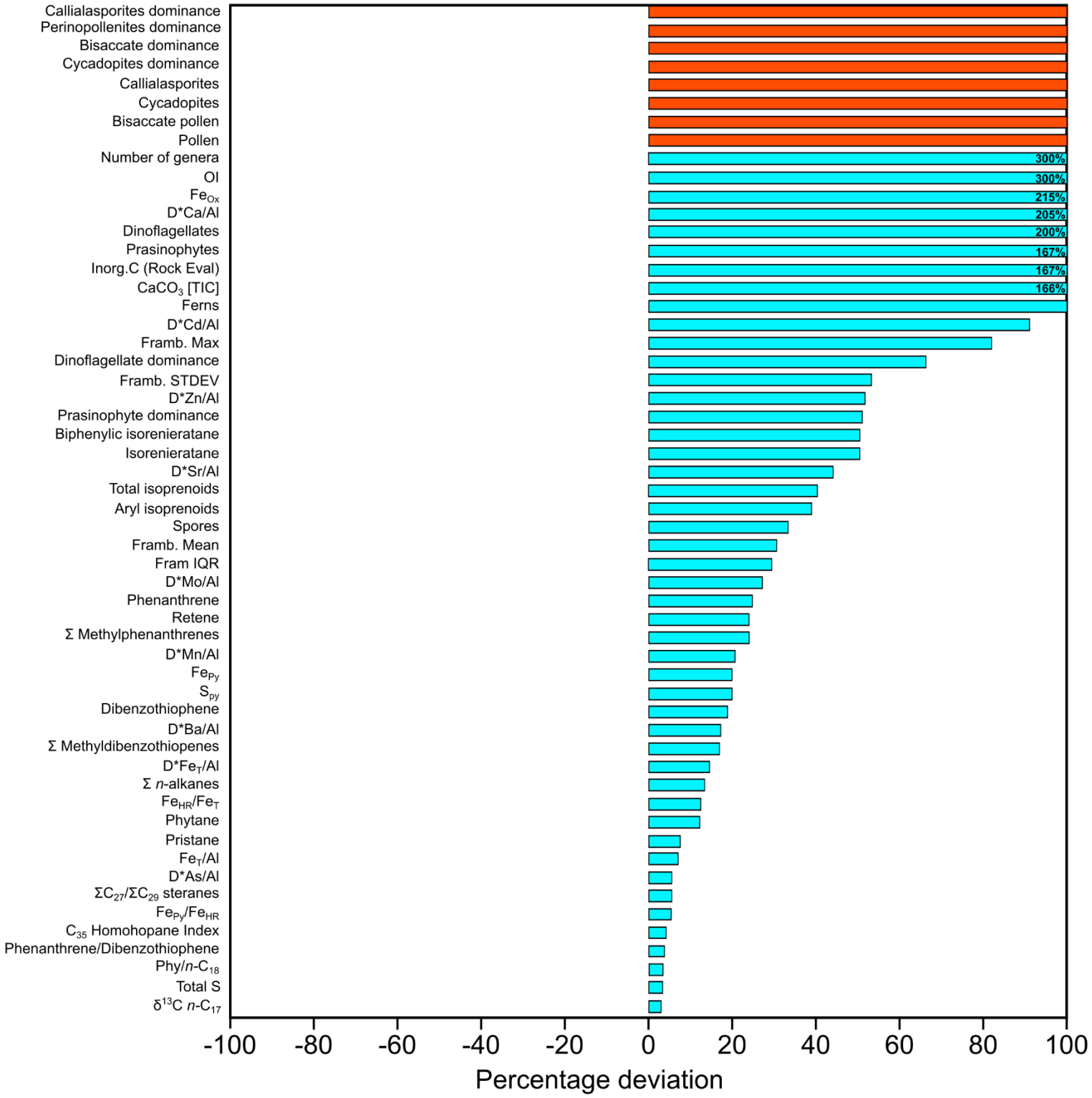

Figure 6.45. Staked chart of the relative deviations of a range of proxies concomitant with the Bos32 pavement. Deviations of >100% are indicated. Red bars indicate a div/0 error in the calculation.

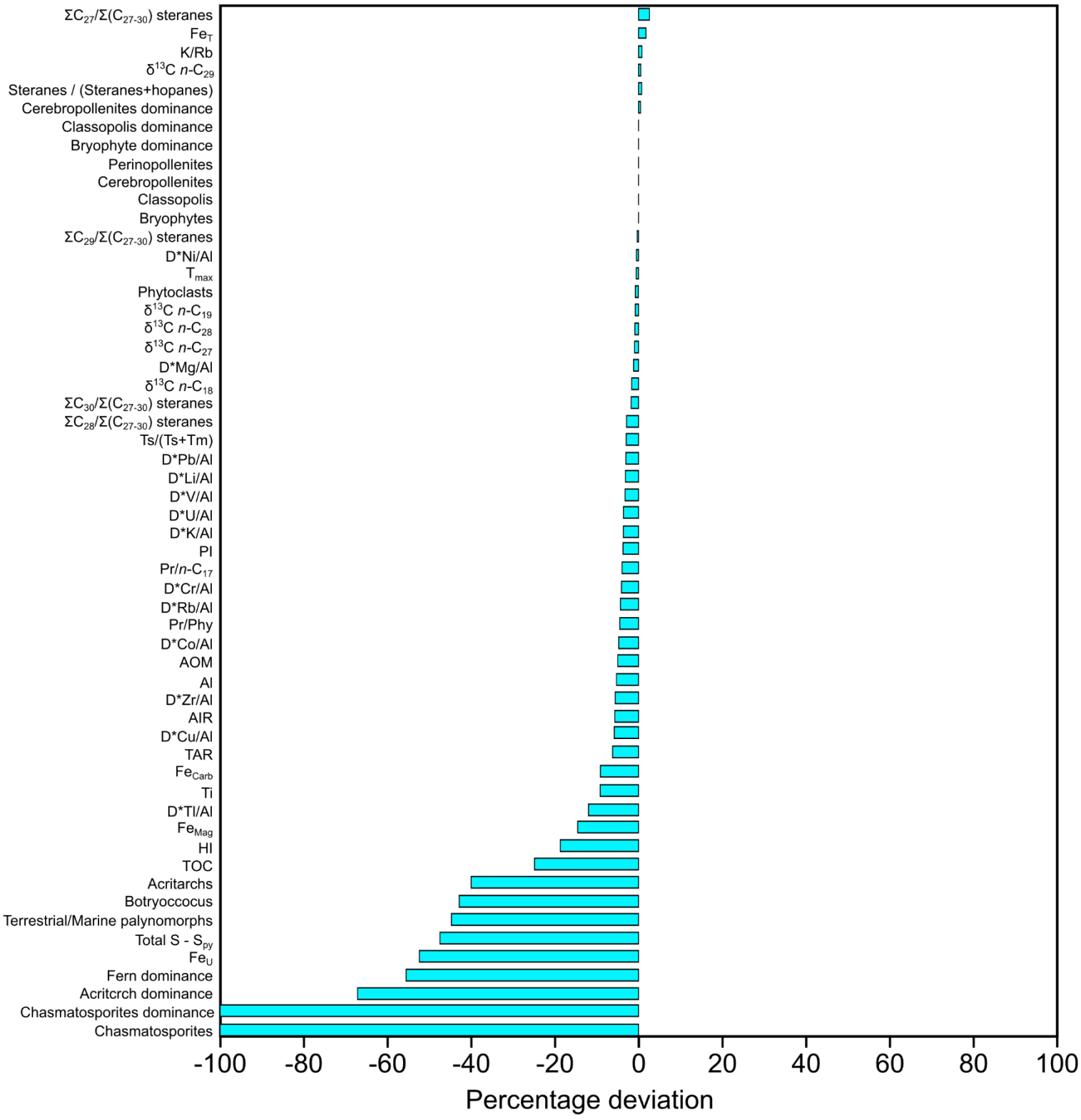

Figure 6.45. continued

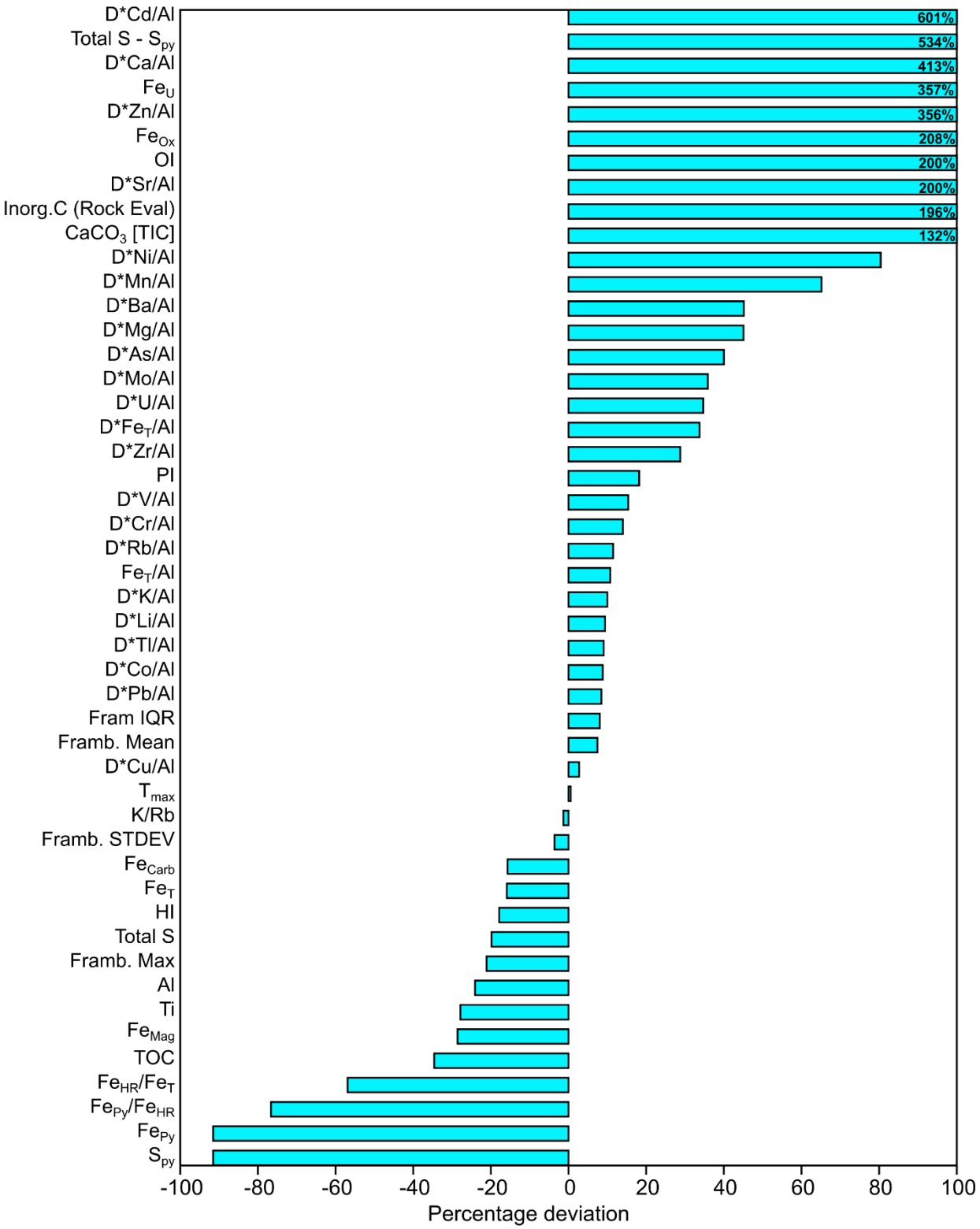

Figure 6.46. Stacked chart of the relative deviations of a range of proxies concomitant with the Pseud34 pavement.

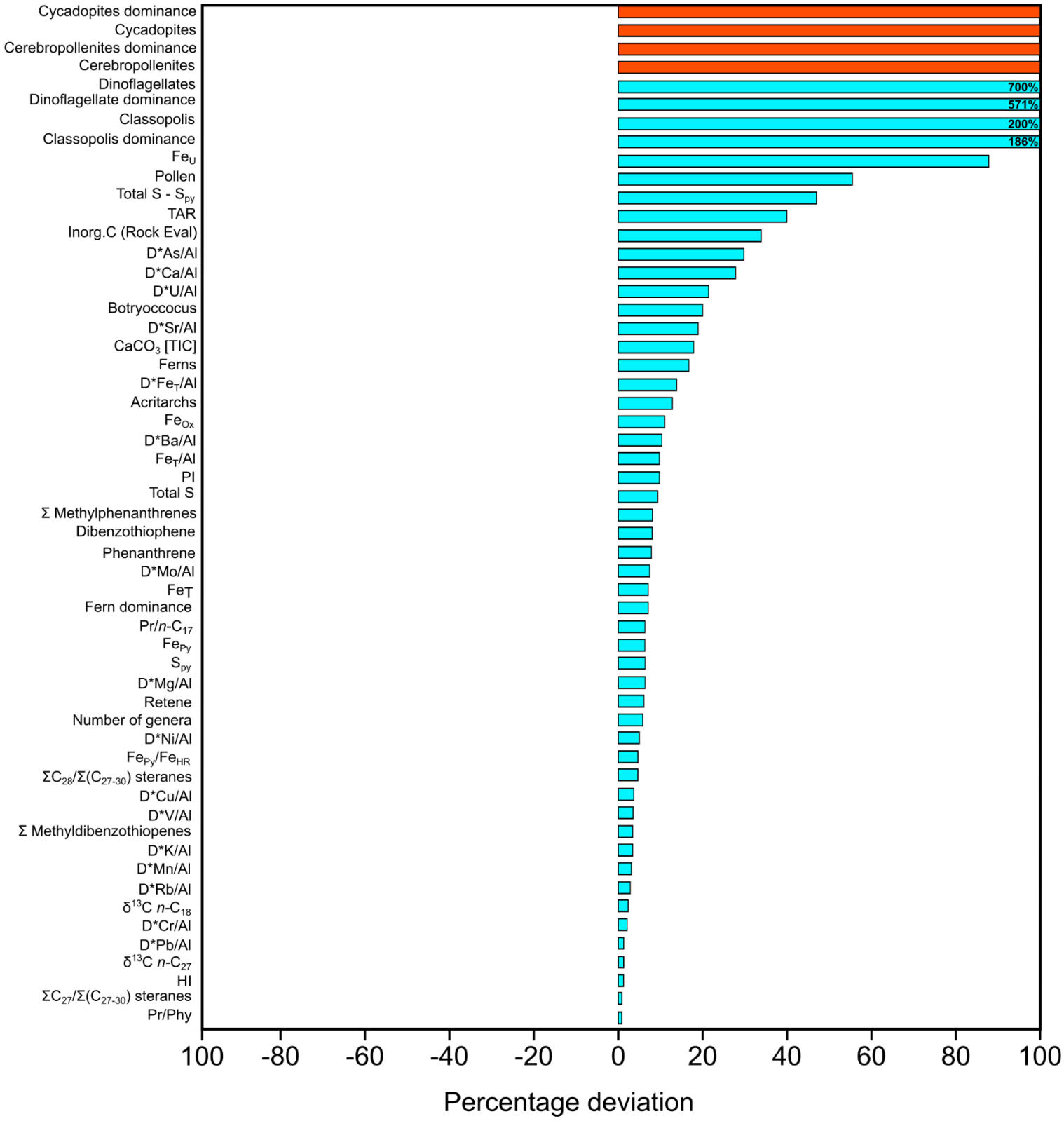

Figure 6.47. Stacked chart of the relative deviations of a range of proxies concomitant with the Pseud41 pavement. Deviations of >100% are indicated. Red bars indicate a div/0 error in the calculation.

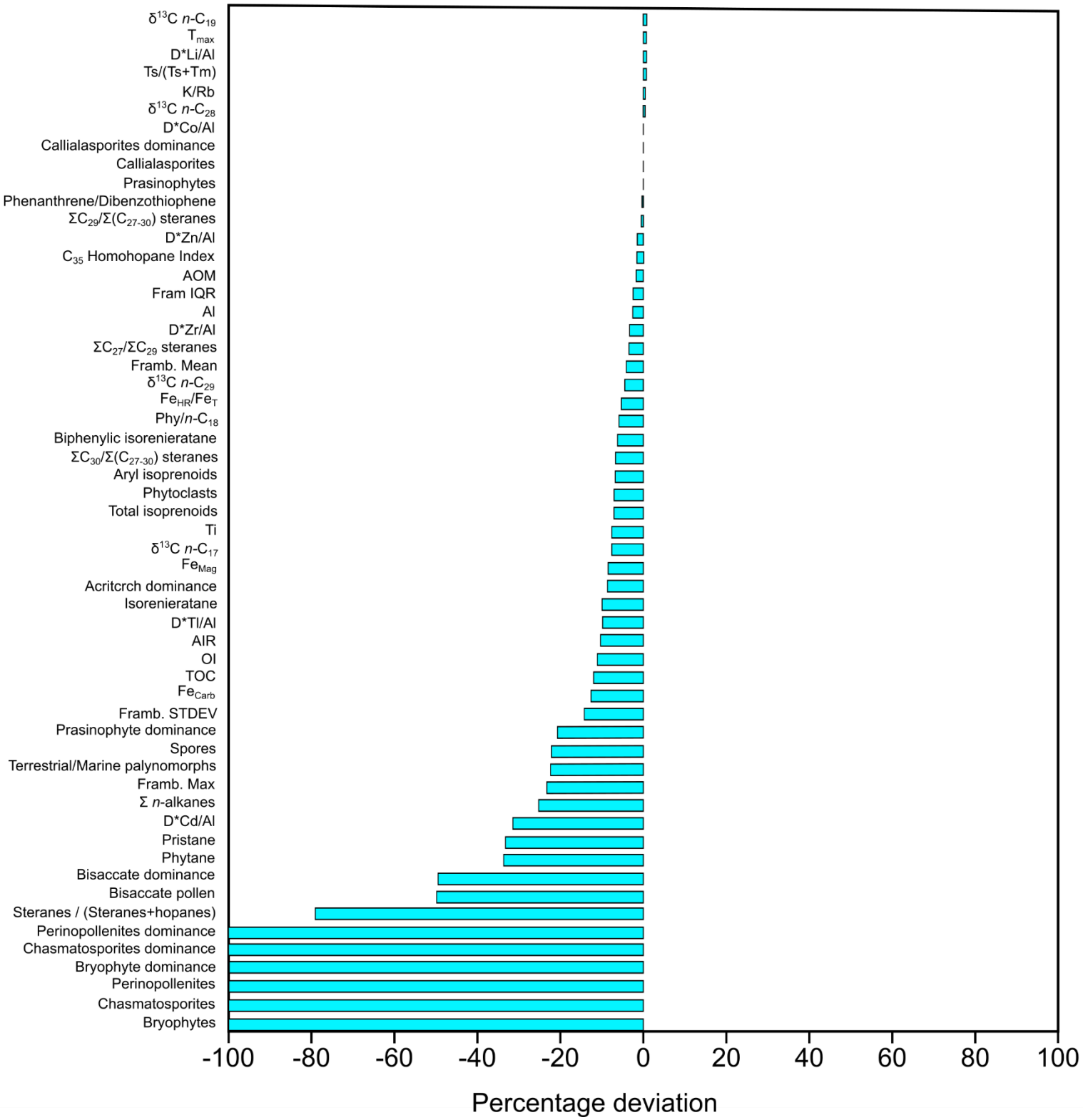

Figure 6.47. continued

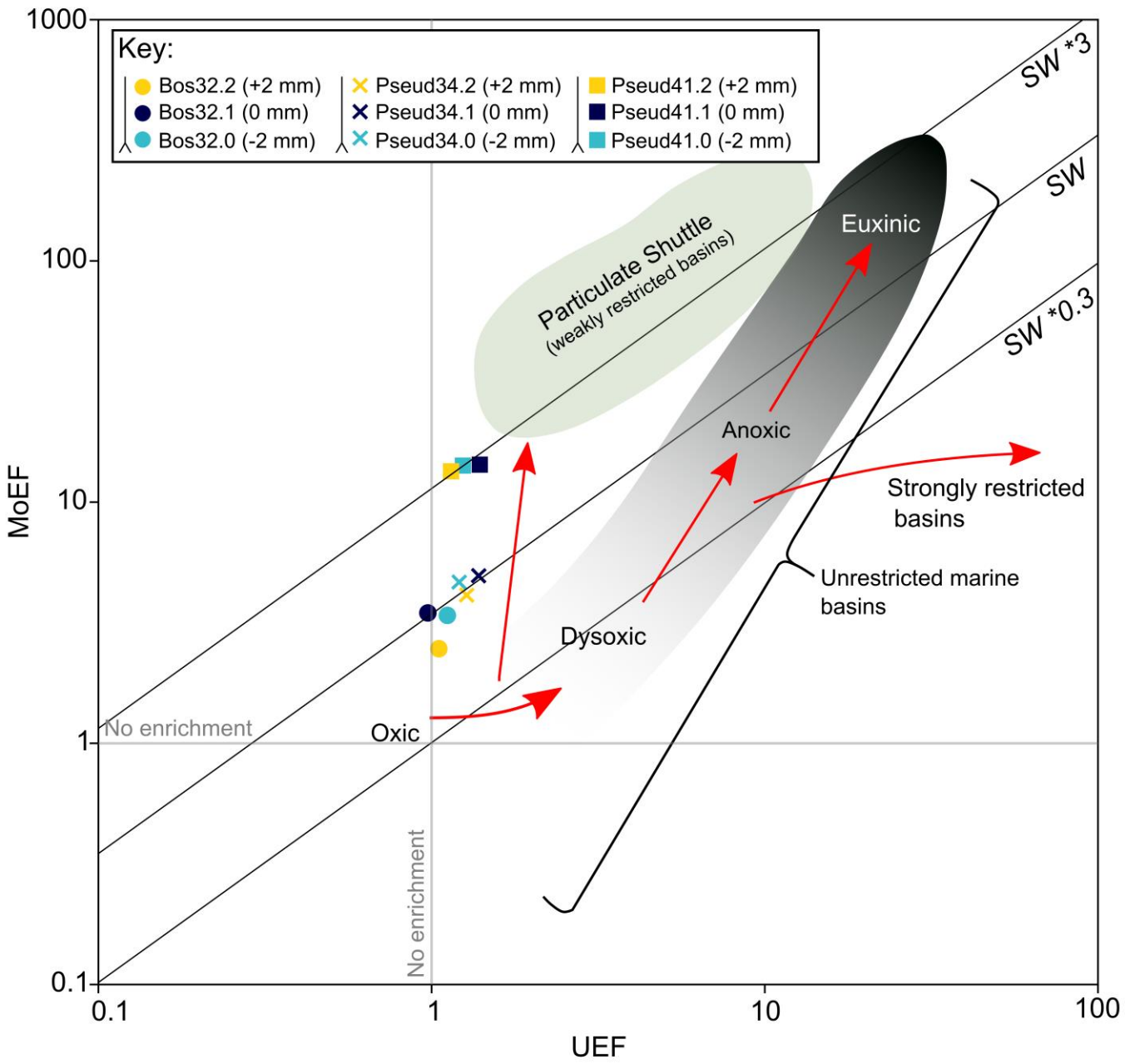

Figure 6.48. UEF vs MoEF plot for the shell pavements. Trendlines and annotations adapted from Algeo & Tribovillard (2009).

3.0 Interpretations

3.1 Statistical significance

In this chapter, I have attempted to evaluate palaeoproxy variability across the shell pavements. However, the sampling method I chose, and the nature of the material, raise concerns over the statistical significance of the findings. The geochemical methods I employed require minimum sample weights for precise analytical results (see Chapter 2, table 2.1). As discussed in Chapter 2 (section 4.0), I adopted a sapling approached that balanced the requirement for highly resolved records against required sample weights, and decided to sample using a 2 mm drill bit, at 2 mm resolution (approximately 5 mm resolution in the LSB). While this approach still permitted the resolution of cm-scale proxy variability within the LSB, few noteworthy lithological changes encompassing less than 2 mm of stratigraphic height were found in that bed. The shell pavements, however, are, on average, 0.9 mm thick (average of the thicknesses presented in Table 6.1). A 2 mm drill bit, therefore, will yield a sample composed mainly of sediments directly adjacent to the pavement (above and below) when drawn along the exposed edge. Despite the mixing of geochemical signals inherent in this sampling methodology, I chose to use a 2 mm drill bit for sampling the shell pavements, since that was the only method available to generate the required sample weights for the inorganic geochemical and pyrolysis analyses. While a thinner drill bit could have generated samples with a smaller amount of contamination from adjacent sediments, the smaller bit diameter would mean that the resulting powder volume would be insufficient for obtaining precise analytical results. Where the sample blocks were fissile enough, I was able to draw the long edge of the drill bit along a greater area of the pavement surface. However, this was not possible for all pavements (due to limited sample material), and the act of drilling along the pavement surface still incorporated a large amount of sediment from below the pavement into the sample. The same effect of signal mixing in the shell pavement geochemical samples also applies to the palynological, biomarker, and CSIA data collected from the shell pavements, and is, in fact, greatly exacerbated in these analyses due to the greater stratigraphic height covered by these samples (Chapter 2, section 4.0). It could even be argued that in these analyses, all three samples essentially cover the background signal of each proxy, with negligible influence from the pavement itself. Ultimately, these problems demonstrate that the shell pavements, due to their width, fall below the minimum stratigraphic resolution that can be precisely analysed via conventional geochemical analysis. Non-destructive analysis techniques such as core-scanning XRF (Dahl *et al.*, 2019) would be more appropriate for the study of lithological variability on this scale. In my study, I chose to employ the same methods of sampling to the LSB and shell pavements, both to test the limits of conventional geochemical

sampling, and in an attempt to evaluate palaeoenvironmental changes across two intervals using directly comparable methods. The frequently low variability, and inconsistent nature of the proxy datasets, however, show that the sampling methods employed for the analysis of the LSB, are ill-suited for the study of the shell pavements. These caveats, however, only apply to the data gathered through the collection of geochemical and palynological samples. Data gathered through descriptive sedimentological, macropalaeontological, and SEM analysis (with the exception of up-section pyrite diameter plots), should, in theory, not be subject to the same limitations.

3.2 Sedimentological and macropalaeontological interpretations

The narrower distribution of shell lengths in Pseud34 compared with the other two pavements indicates that, on average, the individuals composing this pavement were younger, and were probably killed before they could grow to their adult size (59 – 104 mm^2 in area for *P. dubius* and 166 – 298 mm^2 for *B. radiata*; Caswell & Coe, 2013). However, the shell length distribution for this pavement is slightly bimodal (Fig. 6.2), implying a few *P. dubius* survived long enough to reach a size of 30 – 35 mm. It could be the case that, over the length of time marked by the pavement, two generations of *P. dubius* were able to colonise the sediment surface, with the second being composed of many more individuals than the first. Pseud41 shows a similar, if greatly muted, shell length frequency distribution (Fig. 6.3), which also implies that this interval was marked by several generations of colonisation. However, the distribution is wider, implying that the first-generation shells had time to grow to a larger size before the return of anoxic conditions resulted in a mass mortality, ending the growth of the pavement. Bos32 shows both a much wider distribution of shell sizes, and the largest mean shell size of all the pavements (21 mm; Fig. 6.1). There is also no discernible space between the shells, and the pavement is characterised by ubiquitous overlapping (so shell spacing was not measured – compare Figs. 6.1 and 6.2). Bos32, therefore, represents a far more mature pavement than Pseud34 or Pseud41, probably indicating an uninterrupted period of redox amelioration in the benthic environment. Interestingly, a mixed fauna is also only present in this pavement (although out of only three pavements studied in detail). *B. radiata* does not appear to grow on top of *P. dubius* in this pavement (implying no commensalistic relationship), and several pavements formed exclusively by *B. radiata* occur through bed 32 (not studied here), which do not appear to be associated with *P. dubius*. It is, therefore, probably the case that the Bos32 pavement studied here represented conditions favourable to both *P. dubius* and *B. radiata*, and the two species competed for the same resources. *B radiata* pavements, however, are not found in the overlying Mulgrave Shale Member (Little, 1995), which implies that this species was more adversely effected by the deteriorating redox state

of the Cleveland Basin than *P.dubius*. For both Pseud34 and Pseud41, the mean and standard deviation of shell spacing is similar (mean = 4 mm, standard deviation = 3 mm, and mean = 8 mm, standard deviation = 6 mm, respectively). The distributions are also unimodal (Figs. 6.4 and 6.5). A bimodal distribution would be expected if the shells formed 'islands' within the pavement, but the unimodal spacing distributions imply that during each colonisation event, the shells were distributed relatively evenly across the sediment. This means that it is unlikely (although still possible) that the first generation of *P. dubius* acted as growing surfaces for future generations, and instead implies that *P. dubius* individuals of any generation were able to grow on the sediment-water interface. However, when discussing the shell length and spacing data presented here, it is important to bear in mind the relatively limited sample size, with the number of measurements (n in Appendix 3) ranging between 8 – 79. Such a survey of a larger exposed area of shell pavement, on the order of 1-10 m^2 is likely to yield more accurate results (ideally with n > 300 for both shell length and spacing). Figure 6.49 graphically summarises my model for the development of the shell pavements.

3.2.1 The association of shell pavements with silty laminae

The deposition of thin silty laminae and the development of a shell pavement appear closely related, with Bos32 and Pseud34 occurring within silty laminae. These sedimentary structures have been studied in detail by Ghadeer & MacQuaker (2011; 2012), who attributed them to density flows (due to their sharp, erosional bases, and normal grading) and suggested that these were probably triggered by storms. Similar structures have also been found in the Toarcian-aged Nishinakayama Form55ation (Japan), and have been interpreted as indicating fluvial pulses, taking place in a humid climate forced by the injection of isotopically light carbon into the earth's surface environment (Izumi *et al.*, 2018). The tops of most of the studied silty laminae in the Mulgrave Shale Member were homogenised, and the occasional presence of *Chondrites* traces led Ghadeer & MacQuaker (2011) to suggest that the flow events were followed by a brief return of bottom water oxygenation (likening the triplet motif of the sediments to the "lam-scram" textures found in some turbidites). *Chondrites*-bearing sediments are likely to represent extended periods of bottom water dysoxia (Wignall, 1994, p.22), and it is also probable that tops of the silty laminae were homogenised by meiofauna tolerant of low oxygen. In modern dysoxic environments, nematodes can withstand oxygen concentrations as low as 0.2 mL/L (although they are far less numerous than at 4.0 mL/L; Hendelberg & Jensen, 1993), and while their burrows have low preservation potential, the blurring

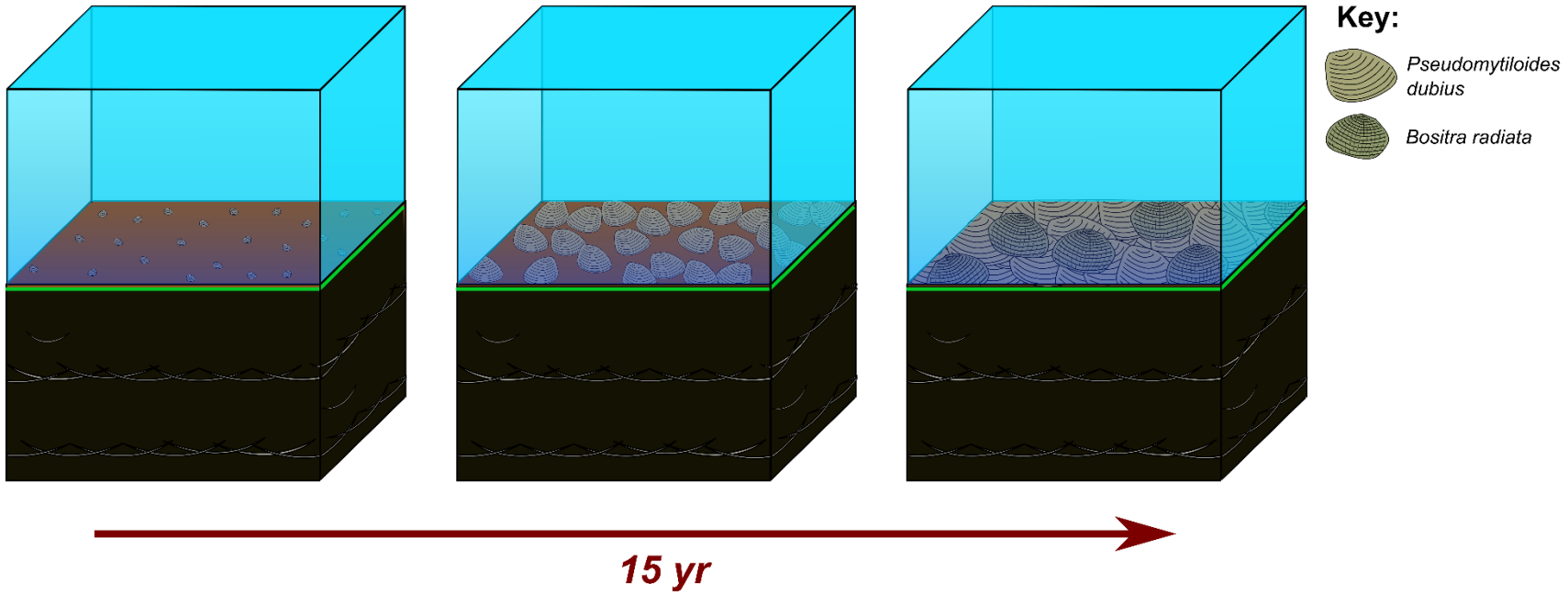

Figure 6.49. Development of a shell pavement. On the left, a return of oxygen levels of between 0.0 – 1.1 mL/L allows a generation of *P. dubius* to colonise the sediment. The oxic/euxinic boundary (represented by the green line) remains fixed just below the sediment-water interface, allowing for benthic colonisation, while excluding bioturbating organisms from the (sulphidic) sediment. In the centre, the bivalves grow to a larger size (possibly enhanced by the availability of prasinophytes), and start to form an interlinked pavement. On the right, a fully interlinked pavement stabilises the sediment surface, allowing for the colonisation of the benthic environment by later generations of *P. dubius* and *B. radiata* (but see text). The growth of a mature pavement takes place over a time period of about 15 years. The subsequent return of anoxia kills the bivalves, with the cycle of frequent anoxia, punctuated by the growth of a pavement, repeating many times.

of initially sharp sedimentological contacts can persist in the geological record (Schieber & Wilson, 2021). However, despite the association of two of the shell pavements with silty horizons, Pseud41 (the least well-developed of the shell pavements) was not associated with a silty lamination, and not all silty laminae found in thin section were accompanied by a shell pavement (Fig. 6.8). It is possible that the small size of the thin sections compared with the lateral extent of the silty laminae, meant that any pavements developed at this point were missed in my analysis. However, if we were to assume bottom water oxygen levels improved during the formation of the silty laminae, then the lack of a pavement would indicate that relatively few spat colonised the sediment. In modern marine invertebrates, the dispersal of spat following a mass spawning can be greatly enhanced by storms, so long as reduced water residence times do not negatively impact the probability of successful fertilisations (Sasaki & Shepherd, 1995; Shanks, 1998). The lack of colonisation could therefore indicate quiet conditions in the basin during reoxygenation.

Another possibility is that even though shelf-to-basin transport occurred intermittently throughout the upper Grey Shale and Mulgrave Shale Members, these events were not necessarily accompanied by improvements in benthic oxygen levels long enough to sustain the formation of a pavement (with the in situ bivalves developing during periods of dysoxia unrelated to shelf-to-basin transport). In Chapter 5, section 3.2, I invoked a similar scenario to explain the coexistence of high pristane and phytane levels in the large silty lens of the LSB. The concentrations of the two isoprenoids also vary in tandem through Bos32 and Pseud41 (Fig. 6.34), implying that the same process exerts a control on their final concentrations in the sediment: in the absence of this anoxic transport pathway, pristane and phytane would be anticorrelated (see Chapter 1, section 9.1.6). While a small amount of co-enrichment of pristane and phytane is observed in Bos32, the opposite (a decrease in the concentration of both isoprenoids) is seen in Pseud41, which is consistent with the lack of lithological evidence for shelf-to-basin transport. The small variations in pristane and phytane coeval with the pavements could indicate that while anoxic transport of phytol precursor occurred, the amount was small, which is consistent with a more distal environment of the Upper Grey Shale and Mulgrave Shale Members compared with the LSB. The presence of small framboids (<5 μm in diameter) within the silty laminae (Fig. 6.17) also argues in favour of anoxic transport, since oxic transport would have re-oxidised pyrite framboids this small (Raiswell *et al.*, 2008).

If the coarser lamina present within Bos32 was indeed deposited under anoxic conditions (as implied by the presence of re-deposited small framboids), then the pavement could not have been directly associated with it. It is still possible, however, that this episode of anoxic transport was immediately preceded by a

shift to extreme dysoxic conditions, with an exaerobic biofacies: the recovery of the redox state of the water would have offered an opportunity for dysoxia-tolerant bivalves to become established, while the persistently sulphidic sediments would have protected small framboids and phytane from reoxidation.

Finally, it is also important to point out that excessive storminess during the formation of the pavements was unlikely in the first place if the climatic variability model I describe in section 4.2 (decadal to centennial-scale episodes of relatively dry climate) held true. Summing all of these arguments together, it becomes apparent that even though shell pavements and silty laminae sometimes occur together, their emplacements are controlled by different paleoenvironmental processes. To better test this, a wider survey of the shell pavements of the Whitby Mudstone Formation, sampling around 100 shell pavements, and comparing with concomitant sedimentary architecture, is required.

3.2.2 Pyrite framboids

While the framboid data from all nine samples (including the three from the pavements themselves) plot in the euxinic field of the Wilkins plot (Fig. 6.15), the mean framboid diameter increases in Bos32 and Pseud34, with the mean and standard deviation of framboid diameter in Bos32 also increasing on the pavement. Only Pseud41 shows a reduction in the mean framboid diameter (by 0.35 μm). A large proportion of these framboids may also be diagenetic: if the shell pavements are characteristic of the exaerobic biofacies of Savrda & Bottjer (1987; 1991), then oxic and sulphidic conditions were closely juxtaposed on the shell pavement. Since the formation of pyrite framboids requires free sulphide, and partially oxidised sulphur species (Chapter 1, section 9.1.2), these conditions are ideal for their growth. The association of some of the shell pavements with shelf-to-basin transport episodes also implies that the pyrite framboids could have been reworked, and the occurrence of pyrite framboid lags towards the base of some of the silty laminae (Fig. 6.17) might indicate this. It should also be noted that due to the more frequently euxinic conditions of the upper Grey Shale and Mulgrave Shale Members, compared with the LSB, small framboids are more common here, and so the same degree of reworking would be likely to generate a more apparently euxinic signature. Despite these potential explanations for small values in the mean and standard deviation of framboid diameter coeval with in situ benthic macrofauna, the possibility of an error in this analysis must also be recognised: the width of view selected during the framboid counting process was around 100 μm, and as can be seen in Figs. 6.16 and 6.17, pyrite granules much larger than six micrometres are visible with the width of view set to 870 μm. While many of these larger pyrite crysts are not, in fact, framboidal (they are predominantly recrystallised), the exclusion of some

large framboid sizes by choice of view width could have introduced a bias into the results, with apparently euxinic values ultimately being generated. During my pyrite framboid analysis of the LSB, I selected a field of view around 300 μm wide, and therefore the data generated during this study is probably more accurate.

3.3 Palynological interpretations

The composition of the phytoplankton community changes significantly across the first and third shell pavements, with dinoflagellates showing a limited recovery during both. Prasinophytes also show a slight recovery concomitant with Bos32, but not Pseud41. One of the key distinguishing features between these two beds is the presence of *B. radiata* alongside *P. dubius* in Bos32, but not in Pseud41, which, as discussed earlier, might indicate a more developed, longer-lived pavement. However, the high degree of sample averaging in the palynological analysis implies that the true change in prasinophyte dominance through the shell pavements cannot be determined from this analysis (section 3.1).

In their analysis of shell pavements of the Whitby Mudstone Formation, Caswell & Coe (2013), discovered a positive correlation between the shell area of *P. dubius*, and the concentration of Mo. These workers suggested that Mo availability limited the growth of N_2-fixing cyanobacteria (based on a culture study by Cole *et al.*, 1993), and that Mo enrichment typifies nitrogenous conditions. Since prasinophytes possess a competitive advantage over other phytoplankton groups under these conditions (see Chapter 1, section 9.1.1), Caswell & Coe (2013) argued that they were common during intervals characterised by Mo enrichment (although no palynological study was performed). They also suggested that due to their high nutritional value, *Tasmanites* (the dominant prasinophyte genus in the Cleveland Basin during the deposition of the Whitby Mudstone Formation) was the preferred food of *P. dubius*. They thus established a causal link between Mo enrichment, nitrogenous conditions, prasinophyte dominance and bivalve size. Therefore, the prediction resulting from this claim is that both Mo enrichment, and increases in the relative contribution of prasinophytes to the phytoplankton community would also characterise the shell pavements characterised by larger bivalve shell sizes. If larger bivalve shell sizes also enhance the probability of pavement formation due to a sediment stabilisation effect, it could further be argued that Mo enrichment, and subsequent prasinophyte proliferation, also typify the formation of a shell pavement (although a high quantity of spat is also required). While my palynological investigation of the shell pavements does suggest a link between bivalve size and prasinophyte dominance (compare Figs. 6.1 and 6.19), and while all the studied pavements show a Mo increase (Fig. 6.31), the pavement characterised by the greatest Mo enrichment (Pseud41) is accompanied by a decline in the dominance of prasinophytes,

rather than an increase (Fig. 6.22). This could mean that despite the Mo enrichment, either nitrogenous conditions were not developed, or another factor was limiting the proliferation of prasinophytes. While Mo is a component of nitrogenase (along with V), the quantity of Mo delivered to the sediment by the preservation of this enzyme is low compared with fluxes such as that of Mn (oxyhydr)oxides or sulphurised organic matter (Tribovillard *et al.*, 2006). An alternative explanation for the lower-than-expected dominance of prasinophytes is that the highly frequent photic zone euxinia prior to the development of Pseud41 could have eliminated all but the hardiest phytoplankton from the basin. Even though the conditions concomitant with Pseud41 were favorable for the proliferation of prasinophytes, the population density was both severely depleted, and demonstrated a hysteresis-like response to a sudden return of favorable conditions. Despite this, both the highest contribution of prasinophytes to the phytoplankton community, and the widest shell lengths, are observed in Bos32, which the Caswell & Coe (2013) model: shell pavements could become established in the absence of prasinophytes, but the added nutritional value of a prasinophyte-containing diet could have enabled *P. dubius* to reach the large size that it did in Bos32, and thereby form a much thicker, and interlinked pavement. Since both Bos32 and Pseud41 show an increase in the dominance of dinoflagellates (which is almost exclusively driven by the genus *Nanoceratopsis*), it is also possible that this was a food source for *P. dubius*, which filter-fed the dinoflagellates out of the water as they attempted to descend to the sediment to form cysts. However, only two shell pavements contained enough material for a palynological study, and it is equally likely that the co-occurrence of dinoflagellate cysts, prasinophytes, and shelly macrofauna, simply reflects improved bottom water redox (i.e. prasinophytes being a direct nutritional source for the bivalves cannot be proved based on this dataset alone). Furthermore, as discussed in section 3.1, the palynological data derived from the shell pavements is almost certainly carries a mixed signal of the pavements, and the sediments above and below them. I strongly suspect (given that dinoflagellates are a common food source for modern bivalves; Wang & Fisher *et al.*, 1996; Etheridge, 2010), that a wider palynological study of *P. dubius*-containing sediments, from both oxic and dysoxic (or frequently anoxic) environments would both confirm this, and better test the prasinophyte predation model of Caswell & Coe (2013).

All of the data points of my palynofacies study of the shell pavement samples plot in either the distal suboxic/anoxic basin, or the distal dysoxic/oxic shelf fields of Tyson's palynofacies ternary diagram (Fig. 6.24; Tyson, 1989). The corresponding palaeoenvironment described in Tyson's 1989 study of the Piper and Kimmeridge Clay formations (Dorset, UK), was a very distal subsiding basin with orbitally paced changes in stratification (Oschmann 1988). The data might, however, also partially indicate the lateral transport of recalcitrant palynomorphs, since the points also plot towards the end of two transport paths in the ternary space. This is in agreement with the presence of thin silty horizons within the sections, which

are likely to have redeposited resistant macerals originating from the terrestrial environment and the basin margins.

The land plant community structure evaluated from my shell pavement palynomorph slides (presented in Fig. 6.23) should be interpreted with caution, since (as demonstrated by the low spore and pollen content, low TAR; and lower Ti content relative to the LSB; Figs. 6.21, 6.30 and 6.35), the palaeoenvironments of both Bos32 and Pseud41 were distal. In addition,. These two issues compound in the shell pavement samples, and as a result, the data compares poorly with previously published palynological data from the same section. Slater *et al.* (2019), found that ferns were 6.88 – 25.2% dominant, and bisaccate producers were 11.5 – 35.3% dominant within the terrestrial plant community, during their "Toarcian-CIE" interval. These figures contrast sharply with mine (compare Appendix 3).

However, the influence of differing hydrodynamic properties of spores and pollen is unlikely to have significantly impacted my analysis. While sporomorphs are hydrodynamically equivalent to fine silt (Muller, 1959), the absolute content of spores and pollen do not vary greatly across either Bos32 or Pseud41 (despite the presence of a silty lamination in the former; Fig. 6.21). This is in agreement with the TAR showing little to no change in the relative contribution of long-chain versus short-chain *n*-alkanes (Fig. 6.35). While the Terrestrial/Aquatic palynomorph ratio does decrease slightly concomitant with Bos32, this is driven mainly by the decrease in AOM in this pavement, which is depleted in coarser lithologies (Tyson, 1995, pp. 249 – 251). Furthermore, sporomorph assemblages from distal localities (notwithstanding the tendency for bisaccate pollen to be overrepresented) tend to be less impacted by hydrodynamic effects compared with proximal settings, and, therefore, are often more representative of the terrestrial community (and can therefore serve as decent palaeoclimate records; Tyson, 1995, pp. 261 – 279 and references therein). High spore counts are also typically found in proximal shelf sediments, with episodes of shelf-to-basin transport delivering a greater quantity of spores to the basin depocenter. However, the silty lamination in Bos32 is not marked by a significant increase in spore content. Slater *et al.* (2019) also determined that the Toarcian transgression (Hesselbo, 2008) did not significantly affect the palynological assemblages recovered from the Cleveland Basin, with the abundance of bisaccate pollen decreasing while the abundance of fern spores remained constant. These workers also demonstrated that the number and terrestrial diversity of land plant genera dropped substantially around the T-OAE CIE, and while my analysis also seems to indicate that the number of identified genera are much lower in the shell pavement samples, compared with the LSB, this decrease is not significantly large to be attributed to true variability – it is more likely to be an artefact of the high degree of sample averaging (section 3.1) .

Furthermore, even if significant, this finding adds to the uncertainty associated with my terrestrial flora reconstructions.

If one were to overlook these issues, my land plant records appear to indicate that the climate of the Cleveland Basin became drier during the deposition of the pavements, as moisture-loving plants (particularly ferns) became far less dominant. The vacant niche space is filled primarily by bisaccate producers and *Cycadopites* sp. It could be argued that this indicates a shift to a drier climate: The dominance of the dry-adapted *Chasmatosporites* and *Classpolis* genera also increases slightly in Pseud41, with a corresponding decline in the wet-adapted *Perinopollenits sp.* (Sutkins *et al.*, 2013; Slater *et al.*, 2019), although this trend is not observed in Bos32, with *Chasmatosporites sp.* increasing in abundance after the shell pavement. This is to be expected if the apparent trends in sporemorph content are not significant, due to sample averaging. Alternatively, the climate might have become more seasonal during the formation of the shell pavements, with frequent shifts between wet and dry conditions (as in the model of Röhl *et al.*, 2001). In their study of the same section, Slater *et al.* (2019) argued that the land plant assemblage was indicative of a highly seasonal terrestrial environment, to which dry-adapted flora was best suited. However, the presence of mixed palynological signals in my study of the shell pavements (section 3.1) renders this interpretation very speculative.

3.4 Inorganic geochemical interpretations

The combination of lower water column sulphide, and high pyrite content, in the Bos32 layer, implies an exaerobic biofacies (low water column sulphide sharply juxtaposed with high sediment sulphide). Given that the presence of in situ *P. dubius* and *B. radiata* in Bos32 indicates that oxygen was present in the benthic marine environment, the relative increase in pyrite concomitant with this pavement (and the corresponding positive shifts in Fe_{HR}/Fe_T and Fe_{Py}/Fe_{HR}; Fig. 6.29) is apparently contradictory. However, as can be seen via SEM microscopy (Fig. 6.16), a proportion, if not the majority of this pyrite is diagenetic. This underscores the importance of understanding the lithology of a geological sample before applying the Fe speciation proxies (while in no way undermining their use as reliable palaeoredox indicators). The Fe-redox proxies are best complemented by an assessment of the concentration of trace elements that are sensitive to the formation of authigenic sulphides, and/or pyrite framboid analysis (Poulton, 2021), to deconvolve the competing influences of syngenetic verses diagenetic pyrite formation (both of which I have applied here). Indeed, Fe_{HR}/Fe_T implies that Pseud34 and Pseud41 were accompanied by a shift to more oxygenated conditions: the lower frequency of anoxia at these points meant that although the Fe shuttle was probably still in operation (and still facilitated the delivery of Mo

and U; Fig. 6.48), its strength was greatly reduced, with less particulate Fe being converted to pyrite (Fig. 6.29).

Moreover, the presence of diagenetic pyrite encrusting shells of in situ *P. dubius* and *B. radiata* further implies that the animals died in situ, and that the proliferation of sulphate reducing bacteria within the bivalve tissues, during decay under anaerobic conditions, created sulphidic microenvironments characterised by rapid pyrite growth. In other words, if the bivalve shells remained in contact with the decaying bivalve tissues, (i.e. if the valves were not transported into the depositional environment from another location), they would have become ensconced within sulphidic porewaters, with the shell surface becoming a site for the nucleation of pyrite crystal growth. This effect is further enhanced if levels of dissolved Fe^{2+} are high, and if the supply of organic matter capable of being metabolised by sulphate reducers is limited to that provided by the decaying bivalve (i.e. the organic content of the surrounding sediment is lowered, as is the case in the coarser laminae; Briggs *et al.*, 1996; Raiswell *et al.*, 2008; Farrell *et al.*, 2009). While the supply of Fe^{2+} to Bos32 was high, the sulphur-limitation on the growth of pyrite within the pavement (Fig. 6.28), combined with the lower level of metabolizable organic matter (occurring within a silty lamination), implies that the in situ decay of bivalve tissues was the limiting factor on pyrite growth. It can therefore be suggested that pyritisation of a shell pavement is taphonomic evidence that the deposit was autochthonous, and that the animals grew in situ, during a brief oxic spell, within a predominantly anoxic environment. A classic example of pyrite growth being enhanced by the presence of metabolisable organic matter is the pyritisation of soft tissues in fossils from the Hunsrück Shale (Germany; Briggs *et al.*, 1996). Here, the high Fe^{2+}, but low pyritisation of the host sediment (C_{org} content limiting the growth of sulphate reducing bacteria), resulted in a residual pool of seawater sulphate in the host sediment. The free Fe^{2+}, and residual sulphate then combined with sulphide generated by anaerobes in the decaying carcases to form pyrite.

Additionally, in a recent study of *Varicorbula gibba* shells from episodically anoxic environments in the northern Adriatic, Tomašových *et al.* (2021), demonstrated how the nucleation of pyrite framboids on the surfaces of articulated bivalve shells, indicates that they were immediately enclosed within an anoxic, Fe^{2+} rich microenvironment post-mortem. The decay of the dead bivalves by sulphate reducing bacteria within the sediment microenvironment, then leads to conditions ideal for (sulphide-limited) pyrite formation. In order to preserve these sulphidic microenvironments, bioturbation needs to be absent, and so Tomašových *et al.* (2021) suggested that an increase in the frequency of pyritised shells through a recent (or geological) sediment archive is indicative of declining habitability of the benthic environment, particularly when pyritisation exceeds 10% of the shelly assemblage. The two samples that plot in the Fe-limited field of the ternary plot (i.e. exceptions to the general trend of s-limitation) are Bos32.1 and

Pseud41.2. It is possible that, at these points, the supply of aqueous sulphide greatly exceeded the supply of highly reactive Fe, and therefore, that the growth of the Bos32 marked a point where aqueous sulphide became scarcer, while Pseud41 marks a point of Fe limitation.

To confirm whether the pyrite preserved within the shell pavements (especially Bos32) originated from diagenetic sulphide, a study of the $\delta^{34}S$ signature of the Ag_2S precipitate generated during my pyrite extraction would be required. In their study of the pyritised soft tissues of the Hunsrück Shale, Briggs *et al.* (1996) found that the pyritisation of soft tissues sequestered the leftover seawater sulphate, resulting in a $\delta^{34}S$ signature more positive than that of the sedimentary pyrite. Therefore, the pyritisation of soft tissues required a diagenetic environment high in aqueous Fe^{2+}, but with relatively low levels of metabolizable organic matter. This technique has also been used to determine the diagenetic history of pyritised lobsters in the Speeton Clay Formation, showing how, in contrast to the Hunsrück Shale, frequent bioturbation of the sediment led to the reoxidation of early diagenetic pyrite, and the formation pyrite with a light $\delta^{34}S$ signature (Poulton *et al.*, 1998). It is possible that a shift to heavier $\delta^{34}S$ values (analogous with the Hunsrück Shale) would be observed in the shell pavements. However, the deposit is orders of magnitude thinner than the fossil beds of the Hunsrück Shale, and surrounded by sediments with very negative $\delta^{34}S$ values (as implied by the high drawdown of ^{32}S from the local seawater by pyrite formation; Newton *et al.*, 2011). My sampling method, however, has yielded inherently mixed geochemical signals (section 3.1). Therefore, a $\delta^{34}S$ analysis of the Ag_2S precipitates (stored in the School of Earth and Environment at the University of Leeds) generated from my S_{py} analysis, would almost certainly yield a mixed signal, and the precipitates are therefore are unfit for this purpose. However, even with appropriately prepared samples, it would be difficult to determine whether ^{32}S in the pavement pyrite was primarily supplied from the decay of the bivalve tissues, or the diffusion of free sulphide from the surrounding sediments.

The small degree of Mn enrichment concomitant with Bos32 and Pseud34 also implies that these shell pavements were associated with brief recoveries in the bottom-water redox state. Mn is soluble in its reduced (2+) state. As such, sediments with appreciable Mn (oxyhydr)oxide content typify either oxic conditions, or environments with a high degree of authigenic Mn^{4+} formation in the sediment (which requires impingement of a strong redoxcline on the sediment-water interface; Chapter 3, section 4.5). The slightly elevated Mn/Al levels concomitant with these shell pavements could indicate Mn reduction (i.e. anoxia) becoming less dominant, compared with the sediments directly above and below. It is also possible that the episodes of Mn enrichment indicate brief periods of enhanced restriction (irrespective of redox change), that resulted in Mn^{2+} that would have otherwise left the basin being incorporated into diagenetic Mn carbonate phases. A similar model was invoked to explain the Mn enrichment in the LSB

(Chapter 3, section 4.5). However, while still hydrographically isolated from the European Epicontinental Seaway (EES), the Cleveland Basin was probably much less restricted during the deposition of the upper Grey Shale and Mulgrave Shale Members, since a transgression occurred over this interval (although the degree of restriction is a matter of debate; McArthur *et al.*, 2008; Thibault *et al.*, 2018; McArthur, 2019). Soluble Mn^{2+} was, therefore, more likely to have left the basin. The fact that Mn is depleted relative to the standard shale values (Wedepohl, 1971; 2004) in my shell pavement samples (in contrast with my LSB samples), therefore, seems to agree with the Mn enrichment occurring under more hydrographically open conditions. Given the co-occurrence of elevated Mn within the shell pavements with the presence of in situ benthic macrofauna, I argue that the primary cause of relative Mn enrichment (if present) was the lack of dissolution of Mn (oxyhydr)oxide phases during a brief period of bottom-water oxia.

The Fe_T/Al values through the shell pavements are probably depleted relative to those of the individual *P. dubius* from the LSB (Fig. 6.29), which is consistent with a lower supply of highly reactive Fe into the (more distal) basin. While the basin depocenter was at least as frequently euxinic as the LSB (lithofacies B), the lack of a strong flux of highly reactive Fe from the reworking of marginal sediments, combined with a less restricted hydrodynamic setting, significantly reduced the strength of the Fe shuttle compared with the LSB: As suggested in Chapter 3, section 4.3 (and as argued by Newton, 2001), the persistent reworking of marginal sediments enriched in reactive Fe phases such as siderite (belonging to the Cleveland Ironstone Formation), could have been a major source of Fe to the Cleveland Basin during the deposition of the LSB. However, reactive Fe could have also been supplied to the basin via a riverine flux, with the Fe originally being derived from the weathering of older rocks around the basin margins. In either case, the higher sea level during the deposition of the Whitby Mudstone Formation, and the more distal nature of the depositional setting, mean that in this formation, the ability of such a flux to supply a high load of highly reactive Fe (that can be titrated by free sulphide when present) is greatly reduced. The lower availability of reworked marginal ironstone material might also account for the lower As and Pb levels of the shell pavement samples, since both of these elements are readily incorporated into Fe(oxyhydr)oxide particles (Lu *et al.*, 2011; Tribovillard, 2020). This would imply that the capture of As and Pb by these Fe-bearing phases (prior to titration by free sulphide) constituted the main flux of these elements into the Cleveland Basin.

There is no evidence for an increased flux of sulphurised organic matter, and the availability of free sulphide during the growth of the shell pavements was greatly reduced. Therefore, the elevated level of Mo in all of the shell pavements is possibly indicative of the incorporation of Mo^{6+} into authigenic Mn (oxyhydr)oxide phases, under extreme dysoxic conditions, at the sediment-water interface (Calvert & Pedersen, 1993). Since euxinia was not persistent, and conditions fluctuated between euxinic, through

anoxic, to dysoxic (resulting in largely equivocal values for the Fe-speciation proxies; Fig. 6.29), the geochemical switch described by Helz *et al.* (1996) was not activated (Erickson and Helz, 2000), and therefore, Fe(oxyhydr)oxides and organic matter might have not played a major role in enhancing Mo levels in the pavements (TOC, in fact, decreases on all of them).

Uranium enrichment occurs within the sediment when U^{6+} ions diffuse into the Fe reduction zone, and are reduced to U^{4+} prior to capture by CO_3^{2-} (Klinkhammer & Palmer, 1991). High sedimentation rates, or sudden changes in sedimentation rate, are known to disrupt this process, with the redox boundary being pushed further down into the sediment (Crusius & Thompson, 2000), and so the depletion in U observed in Bos32 is consistent with shelf-to-basin transport. However, U is enriched in Pseud34 and Pseud41, which, again, is likely due to sample averaging. Small enrichments in U could indicate a lack of shelf-to-basin transport, or possibly enhanced scavenging by organometallic complexes under higher carbon burial rates (Klinkhammer & Palmer, 1991; Wignall, 1994, pp. 45-48; McManus *et al.*, 2005). Alternatively, reoxidation of the might remobilise U and Mo from authigenic phases and result in their re-precipitation (Crusius *et al.*, 1996; Morford *et al.*, 2001). Vanadium frequently associates with Fe and Mn (oxyhydr)oxide particulates (Calvert & Piper, 1984), but the small enrichments seen in Pseud34 and Pseud41 cannot be attributed to paleoenvironmental change with any accuracy, due to V/Al being a mixed geochemical signal (section 3.1). If it were significant, V enrichment could reflect an enhanced Fe-shuttle, or precipitation of Mn oxides at the sediment-water interface. U and V are also more enriched in the shell pavement samples overall, compared with the LSB, which again highlights how the environment was more hydrodynamically open then at the termination of the Pliensbachian (Chapter 3, section 4.7).

It is also probable that many of the trace elements I evaluated that are easily incorporated into sulphides (As, Cd, Cu, Mo, Ni, Pb, U and Zn) are enriched in diagenetic pyrite formed post-deposition, and, therefore, do not reflect sulphidic conditions in the water column. Upward-migrating aqueous As (liberated from Fe (oxyhydr)oxides during suboxic diagenesis) is known to reprecipitate during sediment reworking (Sullivan & Aller, 1996). Cd is also readily re-precipitated in the event of a sudden deepening of the sedimentary oxic/anoxic chemocline, which often occurs when a turbidite is emplaced on top of organic-rich sediments (Rosenthal *et al.*, 1995). A rapidly fluctuating Mn redoxcline can potentially concentrate Mo in surficial sediments (Adelson *et al.*, 2001). Ni and Zn are both liberated from organometallic complexes during the decay of organic matter (Calvert & Pederson, 1993; Tribovillard *et al.*, 2006) and might have become adsorbed onto Fe-Mn (oxyhydr)oxide particles during a brief oxic spell (Fernex *et al.*, 1992; Peacock & Sherman, 2007). However, the proxy records of all of these trace elements within the shell pavements are mixed signals, and so while there is good lithological evidence

(in Bos32, for example; Fig. 6.16) in favour of diagenetic sulphide precipitation, the extent to which this resulted in trace element redistribution cannot be assessed.

In Chapter 3, section 4.4, I interpreted variations in the K/Al and Rb/Al ratios through the LSB as reflecting variations in the clay mineral assemblage, with intervals of low K/Al and Rb/Al corresponding with the input of cation-depleted clays, formed under humid climatic conditions. However, the shifts in K/Al in the shell pavements are negligible (by 9.3×10^{-3} – 0.04 wt.%/wt.%), and do not occur in all three pavements, with Bos32 showing a negative excursion. This could indicate that the depositional environment was sufficiently distal that the effect of a shift in the clay mineral assemblage would be greatly minimised, or possibly that no great shift occurred in the clay mineral composition in the first place. However, the mostly likely explanation, again, is sample averaging (section 3.1). Therefore, while it is possible that the K/Al and Rb/Al ratios were affected by changing clay mineral assemblages during brief episodes of drier climate, such speculation (expanded upon in sections 4.1 and 4.2) cannot be sufficiently justified by my dataset.

3.5 Organic and isotopic geochemical interpretations

All three pavements show point decreases in TOC. While this is necessarily due in part to the dilution effect of the shell material, it is also the case that the sediments directly associated with the pavement had a lower organic matter content in and of themselves, as shown in thin section (e.g., Figs. 6.12 and 6.13). This implies either a further dilution effect of the silty lenses (when present) on sediment TOC, or that the intervals were more oxidising (both effects are likely to have worked in concert). All three pavements also demonstrate variable decreases in the HI, and corresponding increases in OI. This implies either re-oxidation of organic matter during the formation of the shell pavements (especially in Pseud34), or a switch to an organic matter assemblage more dominated by recalcitrant organic matter. This latter interpretation, is not supported by the palynological data, which shows that the content of phytoclasts (i.e. recalcitrant, woody material), does not change through Bos32, where a significant decrease in the HI occurs (Fig. 6.33). However, the sampling method of the palynological study probably incurred time-averaging many times greater than the duration of this pavement, so determining the true contribution of recalcitrant organic matter to the pavement TOC is not possible based on my datasets.

The C_{35} homohopane index, while higher than in the LSB, shows no appreciable variability through the shell pavements, and neither does the phenanthrene/dibenzothiophene ratio (Figs. 6.36 and 6.41). This indicates that, while organic matter sulphurisation took place in the euxinic porewaters of the sediment post-deposition, no change in the degree of organic matter sulphurisation occurred. There is also no correlation between Σ(methyl)dibenzothiophenes and C_{35} hopanes (Fig. 6.50). As in the LSB (Chapter 5, section 3.5), this implies that fixation of C_{35} hopanoids into the kerogen via side chain sulphurisation was less dominant than the formation of (methyl)dibenzothiophenes, which was, in turn, less dominant than the sequestration of sulphide into pyrite. If the formation of (methyl)dibenzothiophenes was indeed limited by the availability of biphenyl (as speculated in Chapter 5, section 3.5), then the extent of their formation would have been even more pronounced here than in the LSB, since carotenoid biomarkers (a precursor of biphenyls; Grice *et al.*, 1996) were especially abundant in the sediments of the Upper Grey Shale and Mulgrave Shale Members (French *et al.*, 2014).

The consistently low steranes/(hopanes+steranes) ratio (Fig. 6.36) through the shell pavements strongly implies that primary production during both intervals was dominated by (hopanoid-producing) prokaryotes, which is consistent with the frequently anoxic nature of the basin. The lack of a significant excursion in this ratio might also imply that no large changes in primary production occurred (Chapter 5, section 3.3). The upper water column in the Cleveland Basin might have been comparatively oligotrophic, with nutrients only being returned to the surface from beneath the chemocline by episodic upwelling (Sælen *et al.*, 1996).

The slight increases in retene and (methyl)phenanthrenes seen in the shell pavements (Fig. 6.40) may represent an increase in the dominance of the terrestrial land plant community by gymnosperms, since the palynological data support this (compare Figs. 6.23 and 6.40). However, (methyl)phenanthrenes can also be produced by the degradation of aromatic secohopanoids (Chapter 5, section 3.6), and given that there is covariation between this, and the content of (methyl)dibenzothiophenes, I strongly suspect that bacterial degradation exerts a greater influence. It is possible that a component of PAH content of the samples was derived from wildfire charcoals, but there is no palynological evidence to corroborate this (levels of opaque phytoclasts decline in Bos32 from 14.6% to 6%, and only rise by 1.34% in Pseud 41; Appendix 3). As discussed in Chapter 5, section 3.6, wildfires have typically been associated with high atmospheric oxygen content, resulting from the extensive carbon burial during the T-OAE. So the lack of significant charcoal, or PAH content of the shell pavement sediments implies they were not associated with such a change. In other words, improved redox was not due to enhanced oxygen availability in the atmosphere, raising the oxygen content of the basinal water mass by diffusion.

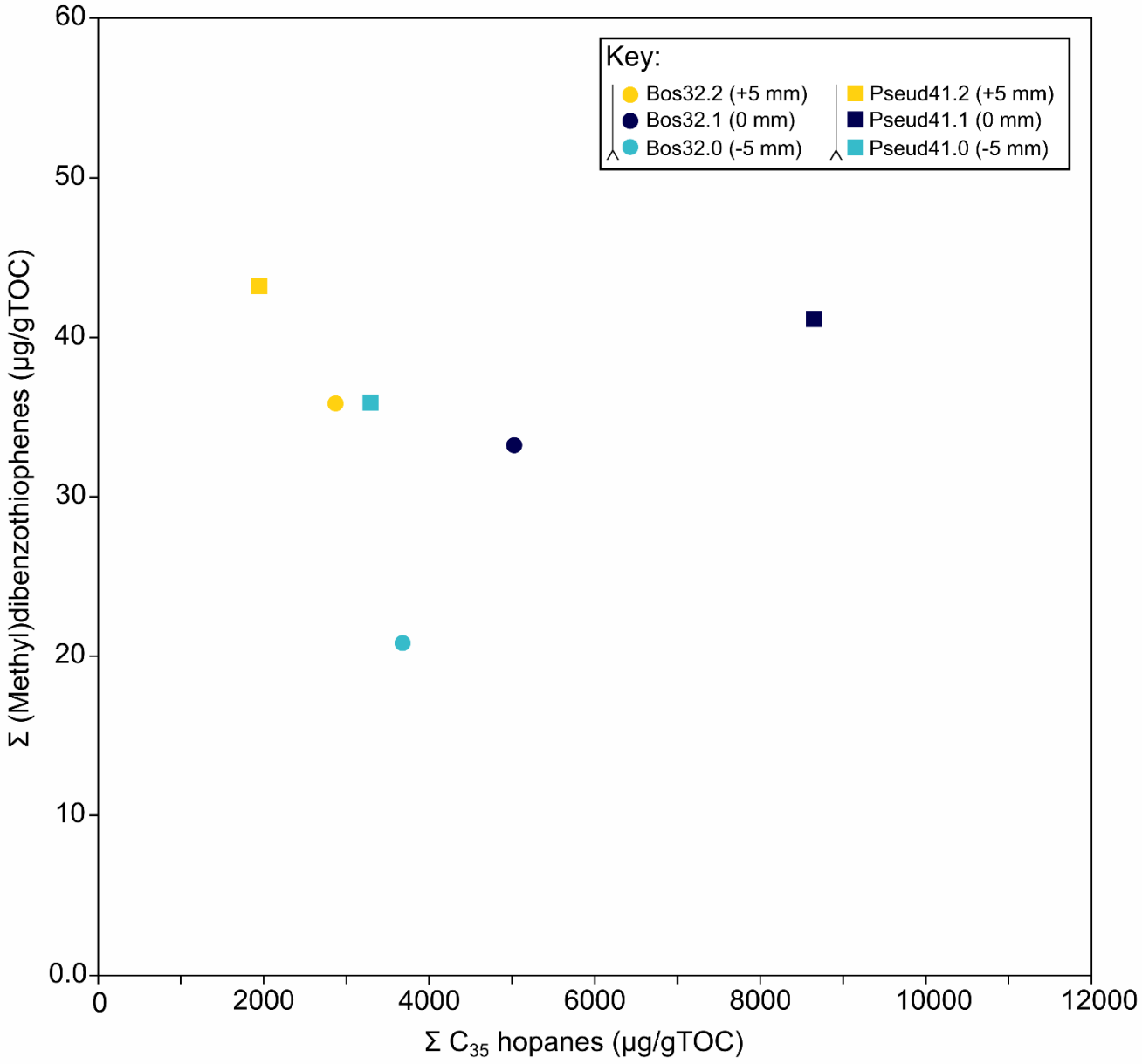

Figure 6.50. Concentration of C_{35} hopanes through Bos32 and Pseud41 compared with that of dibenzothiophene and methyldibenzothiopnehes (grouped together as Σ(methyl)dibenzothiophenes. Concentration of C_{35} hopanes, compared with that of dibenzothiophene and methyldibenzothiopnehes (grouped together as Σ(methyl)dibenzothiophenes), through Bos32 and Pseud41.

Regrettably, all the organic geochemical proxy records, including the TAR, AIR, and isorenieratane content (Figs. 6.35, 6.38 and 6.39), have been greatly corrupted by the sampling methodology (see section 3.1). The required sample weights for efficient extraction (for the TOC content of the shell pavement samples), also mean that the sampling method I selected (averaging approximately 1 cm of stratigraphic height per sample) is about the highest resolution sampling that can currently be performed for a biomarker analysis.

The $\delta^{13}C$ excursions in marine and terrestrial fractions are essentially synchronous in Bos32 (i.e. a negative $\delta^{13}C$ excursion in *n*-C_{17} is matched by a negative excursion in *n*-C_{27}; Figs. 6.42 and 6.43). Taken at face value, this implies that an injection of isotopically depleted carbon into the earth surface system was accompanied by an increase in stratification in the basin (Sælen *et al.*, 1996; French *et al.*, 2014), although an increase in climatic humidity could also influence these isotopic signatures (Chapter 1, section 9.8.7). However, the occurrence of dinoflagellate cysts, equivocal Fe-speciation proxy values, and partial reoxygenation of the sediment means that it was unlikely that the Cleveland Basin was highly stratified during the formation of the shell pavements. I therefore highly suspect that these trends are erroneous: as with much of the geochemical data described here, the CSIA data points bear mixed signals from the pavement, and the directly adjacent sediments, and as such, show little to no variability. It is, however, noteworthy that with the exception of *n*-C_{19}, all the CSIA trends are depleted relative to both the bulk $\delta^{13}C$ signal (Kemp *et al.*, 2011), and the m-scale CSIA analysis of French *et al.* (2014; Figs. 6.42 and 6.45). This implies that, although the shell pavement CSIA data is inconclusive, CSIA trends likely varied at a much higher frequency through the upper Grey Shale and Mulgrave Shale members than a m-scale analysis would suggest. A future CSIA study focusing on a constrained interval in these formations, at cm-scale resolution, could, therefore, potentially provide greatly improved records of carbon cycle dynamics, particularly if combined with spectral analysis.

4.0 Discussion

4.1 Model for shell pavement formation

The depositional environments of the upper Grey Shale, and Mulgrave Shale Members were characterised by highly frequent anoxic (euxinic) events. However, this state was interrupted by brief periods where the oxic/anoxic boundary descended onto, or lower than, the sediment-water interface, thereby facilitating the development of an exaerobic biofacies. Savrda and Bottjer (1987) argued that exaerobic conditions were

typified by oxygen concentrations of 0.2-1.0 mL/L (severe to extreme dysoxia; Tyson & Pearson, 1991), and incidentally, my multiproxy comparison of the shell pavements, and the LSB fossil, implies that *P. dubius* grew under these very oxygen concentration values. Del Piero *et al.* (2020) also invoked a model of episodic benthic reoxygenation in their study of *Halobia cordillerana* pavements from the Triassic-aged Quatsino Formation (Vancouver Island, Canada). Here, the presence of both mature pavements, and pavements composed of juveniles, indicates that *Halobia cordillerana* produced planktonic larvae, which were dispersed into both oxic and euxinic environments. If they were not killed by euxinia while still in their juvenile stage, the bivalves grew to form shell pavements.

All the shell pavements, and the individual *P. dubius* shell from the LSB (Chapter 3), correspond with oxygen-limited conditions, as corroborated by a wide suite of redox proxies. However, this does not preclude a benthic mode of life for the bivalves in question. This is because the redox proxy values attained could have been generated under different oxygen concentrations. For example, MoERF values between 1 – 10 are typically associated with dysoxic environments (Algeo & Tribovillard, 2009), which encompass oxygen concentrations as low as 0.2 mL/L and as high as 2.0 mL/L (Tyson & Pearson, 1991). Furthermore, the values of some redox-sensitive proxies, such as Fe_{HR}/Fe_T and Fe_{Py}/Fe_{HR} are also sensitive to rapid sedimentation changes and redox fluctuations, and this is why these two proxy systems use equivocal zones (Chapter 1, section 9.1.4). In order to accurately determine the most probable range of oxygen concentrations coeval with the formation of each pavement (and the individual *P. dubius*), I have therefore compared the values of multiple redox proxies (Tables 6.1 – 6.4). I have then made a qualitative judgement as to what the probable range of oxygen content was. This often involved critically examining the results of some proxy values, such as the small framboid size distributions (implying euxinic conditions via the Wilkins plot). One of the main factors that have complicated the interpretation of the redox proxies I applied has been the frequent occurrence of mm-scale, normally graded silty laminae through the studied intervals, which are likely to be associated with cryptic hiatuses (Kemp *et al.*, 2018). Occasionally, these are concomitant with the shell pavements, implying that any attempt to establish continuous changes in palaeoenvironmental parameters across them is impossible. The interpretation of up-section proxy trends has also been complicated by diagenetic sulphide formation, which has affected the proportion of sedimentary Fe that is highly reactive (Fe_{HR}/Fe_T), the proportion of highly reactive Fe hosted in pyrite (Fe_{Py}/Fe_T), and the distributions of sulphide associated trace elements (particularly As, Cd, Ni and Zn).

As discussed in Chapter 1, section 6.0, some workers have been reluctant to accept the in situ growth of bivalves within black shale sequences, instead suggesting non-benthic life modes (see review in Chapter 1, section 6.0). It could be argued that the apparent contradictions between the presence of shell

pavements, and the proxy data implying anoxic or euxinic conditions, is further evidence that the shells did not grow in situ, and were transported into the frequently anoxic/euxinic basin depocenter during episodes of shelf-to-basin transport. However, the occurrence of geochemical proxy data indicating anoxia or euxinia in the shell pavements, is likely to be largely due to the inherent time-averaging introduced my sampling methodology. As discussed in section 3.1, the aim of this work was to attempt to evaluate the redox history of the shell pavements with the same methods applied to the LSB, so that the results could be directly comparable. However, the nature of the results seems to indicate that these methods are inappropriate for mm-scale features, such as shell pavements. Despite the limitations of the geochemical data, it can still be argued that the shell pavements I studied grew in situ, during a brief period of benthic reoxygenation. A key argument in favour of this is that none of the shell pavements I studied display any evidence of post-mortem transport: none of the shells display fracture due to abrasion or saltation, and no evidence of imbrication was found either. While the shells appear to be disarticulated, the sediments have been subjected to compaction (*P. dubius* valves were originally convex; Chapter 1, section 6.0), so the initial space between the valves is often no longer present. Disarticulation commonly occurs during the in situ decay of bivalves, and does not necessarily mean that the disarticulated shells will be transported. Additionally, most of the valves in the shell pavements are concave-up – which is hydrodynamically unfavourable, and therefore, evidence against transport (Del Piero *et al.*, 2020). Moreover, the taphanomically-controlled sulphide generation described in section 3.3, not only reconciles the high pyrite content of the pavements (specifically Bos32) with the presence of macrofauna, but serves as additional evidence in favour of in situ growth. It is clear, however, that *P. dubius* could also adopt a pseudoplanktonic mode of life, encrusting floating macrophyte debris (the fossil wood assemblages of the Posidonia Shale are impressive examples of this mode of life). It is, therefore, possible that the individual *P. dubius* recovered from the LSB dropped off a floating log or ammonite, and, therefore, does not represent in situ growth on the sediment-water interface. However, this explanation cannot reasonably explain the high number of individuals comprising a shell pavement (Kauffman; 1978, 1982). I have demonstrated that the pavement-forming bivalves could tolerate oxygen levels just as low, if not lower, than the individual recovered from the LSB. It is still possible that the individual shell dropped onto the seafloor, but it is equally likely that it grew in situ. These two models are impossible to test based on the geological data available. However, the in situ growth of *P. dubius* under a brief period of extreme dysoxia is supported by the evidence for in situ pavement development I present here, while the model invoking deposition of a *P. dubius* shell that dropped from floating macrophyte debris runs the risk of being unfalsifiable.

P. dubius-individual (LSB)	VALUE	IMPLIED WATER COLLUMN REDOX STATE	POSSIBLE O_2 LEVEL
Bioturbation (%)	0 – 5.31	ORB 3 – 4 (lower dysaerobic)- probably severe to extreme dysoxic (Tyson & Pearson,1991)	1.0 – 0.2 mL/L
Framboid distribution	Right of Wilkins Plot	Severe dysoxic	
Fe_{HR}/Fe_T	0.457–0.704	Anoxic	0 mL/L
Fe_{Py}/Fe_{HR}	0.485 –0.673	Ferruginous	
Mn/Al (ppm/wt%)	85.1 – 116	Oxygen depletion and stratification, but some O_2 present	1.1 – 0.0 mL/L
Mo/Al (ppm/wt%)	1.69 – 2.41 (ERF =11.2 – 16.0)	Anoxic (Algeo & Tribovillard, 2009)	0 mL/L
Isorenieratane (µg/gTOC)	2.189 – 3.91	Episodic euxinia in bioturbated interval	≥0 mL/L
AIR	2.14 – 2.38	Somewhat episodic euxinia	
OVERALL:		**Extreme dysoxic/suboxic**	**1.1 – 0.2 mL/L**

Table 6.2. Key redox proxy values concomitant with the *P. dubius* individual found in the LSB, along with an interpretation of redox state, and range of O_2 values based on each proxy. Overall, it is likely that the individual *P. dubius* grew under extreme dysoxic/suboxic conditions (O_2 = 0.2 mL/L; Tyson & Pearson, 1991). Oxygen concentration based on sedimentary Mn loss is based on the observation that dissolved Mn content increases when O_2 concentration drops below 50µM (Klinkhamer & Bender, 1980)

P. dubius, B. radiata together (Bos32)	*VALUE*	*IMPLIED WATER COLLUMN REDOX STATE*	*POSSIBLE O_2 LEVEL*
Bioturbation (%)	0	ORB 1 – 3(anaerobic -lower dysaerobic)- probably extreme dysoxic to anoxic (Tyson & Pearson,1991)	0.2 – 0.0 mL/L
Framboid distribution	Left of Wilkins Plot	Euxinic	0 mL/L
Fe_{HR}/Fe_T	0.911	Anoxic	0 mL/lL
Fe_{Py}/Fe_{HR}	0.759	Equivocal	
D*Mn/Al (ppm/wt%)	38.4	Possible brief entrainment of oxygen	1.1 – 0.0 mL/L
D*Mo/Al (ppm/wt%)	0.580 (ERF=3.47)	Suboxic (Algeo & Tribovillard, 2009)	0.2 - 0 mL/L
Isorenieratane (µg/gTOC)	6.36	Episodic euxinia (with some isorenieratane supplied via remobilised microbial mat fragments)	≥0 mL/L
AIR	2.26	Somewhat episodic euxinia	
OVERALL:		**Suboxic**	**≤ 0.2, but > 0.0 mL/L**

Table 6.3. Key redox proxy values concomitant with Bos32, along with an interpretation of redox state, and range of O_2 values based on each proxy. Overall, it is likely that Bos32 pavement represents suboxic conditions ($O_2 \leq 0.2$ mL/L; Tyson & Pearson, 1991).

P. dubius – many small shells (Pseud34)	***VALUE***	***IMPLIED WATER COLLUMN REDOX STATE***	***POSSIBLE O_2 LEVEL***
Bioturbation (%)	0	ORB 1 – 3(anaerobic -lower dysaerobic)- probably extreme dysoxic to anoxic (Tyson & Pearson,1991)	0.2 – 0.0 mL/L
Framboid distribution	Left of Wilkins Plot	Euxinic	0 mL/L
Fe_{HR}/Fe_T	0.382	Anoxic	0 mL/L
Fe_{Py}/Fe_{HR}	0.160	Equivocal	
D*Mn/Al (ppm/wt%)	89.4	Possible brief entrainment of oxygen	1.1 – 0.0 mL/L
D*Mo/Al (ppm/wt%)	1.01 (ERF=4.96)	Suboxic (Algeo & Tribovillard, 2009)	0.2 – 0 mL/L
Isorenieratane (µg/gTOC)	n/a	n/a	n/a
AIR	n/a	n/a	n/a
<u>OVERALL:</u>		**Suboxic**	**≤ 0.2, but > 0.0 mL/L**

Table 6.4. Key redox proxy values concomitant with Pseud34, along with an interpretation of redox state, and range of O_2 values based on each proxy. Overall, it is likely that the Pseud34 pavement represents suboxic conditions ($O_2 \leq 0.2$ mL/L; Tyson & Pearson, 1991).

P. dubius – few large shells (Pseud41)	***VALUE***	***IMPLIED WATER COLLUMN REDOX STATE***	***POSSIBLE O_2 LEVEL***
Bioturbation (%)	0	ORB 1 – 3(anaerobic -lower dysaerobic)- probably extreme dysoxic to anoxic (Tyson & Pearson,1991)	0.2 – 0.0 mL/L
Framboid distribution	Left of Wilkins Plot	Euxinic	0 mL/L
Fe_{HR}/Fe_T	0.886	Anoxic	0 mL/lL
Fe_{Py}/Fe_{HR}	0.750	Equivocal	
D*Mn/Al (ppm/wt%)	31.3	No change in redox through the pavement – persistently dysoxic	1.1 – 0.0 mL/L
D*Mo/Al (ppm/wt%)	2.65 (ERF=14.3)	Anoxic (Algeo & Tribovillard, 2009)	0 mL/L
Isorenieratane (µg/gTOC)	8.52	Episodic euxinia (with some isorenieratane supplied via remobilised microbial mat fragments)	≥0 mL/L
AIR	2.07	Somewhat episodic euxinia	
OVERALL:		**Suboxic**	**≤ 0.2, but > 0.0 mL/L**

Table 6.5. Key redox proxy values concomitant with Pseud41, along with an interpretation of redox state, and range of O_2 values based on each proxy. Overall, it is likely that the Pseud41 pavement represents suboxic conditions ($O_2 \leq 0.2$ mL/L; Tyson & Pearson, 1991).

The small, juvenile, individual *P. dubius* recovered from the LSB probably grew under extreme dysoxic/suboxic conditions (1.1 – 0.2 mL/L; Table 6.1), but my multiproxy analysis of the shell pavements has shown that this species could tolerate even lower oxygen levels (≤ 0.2 mL/L, but > 0 mL/L; Tables 6.2 – 6.4). Some extant epibenthic bivalves are known to tolerate oxygen levels of 0.2 mLL or below. For example, *Jupiteria callimene* is an epibenthic bivalve (and a member of the family Nuculanidae) that has been recovered from the oxygen minimum zone off Baja California, from a site with a dissolved oxygen content of around 0.1 mL/L (Dall, 1908; Hendrickx *et al.*, 2016; Suarez-Monzo *et al.*, 2018). Recent incubation and genetic sequencing of the nuculanid bivalve *Lembulus bicuspidatus* has also shown that, under dysoxic conditions, genes involved in the production of enzymes regulating anaerobic glycolysis become active (Amorim *et al.*, 2021). It is possible that *P. dubius* and *B. radiata* possessed similar adaptations to the extant Nuculanidae, and, therefore, could inhabit extreme dysoxic/suboxic environments.

Despite the development of shell pavements at benthic oxygen concentrations of less than 0.2 mL/L, the LSB does not contain any, even though the redox state in the upper part of Lithofacies A was not only favourable for pavement development (1.1 – 0.2 mL/L), but contains in situ fossils of (juvenile) *P. dubius*. As for the thin laminae near the shell pavements (see section 3.1.1), the reason for this absence is probably the lack of mass colonisation of the sediment by *P. dubius* spat. One possible reason for this is that the spawning event wherein this individual was conceived did not result in a very wide spread of viable spat outside of the basin margins, due to low energy conditions (this individual being a rare exception). However, shelf-to-basin transport occurred during the deposition of the LSB (Chapter 3, section 3.1), and I did invoke the occurrence of intermittent storms to account for the sedimentary structures observed here. Even so, I have suggested that the dispersal of *P. dubius* spat, and shelf-to-basin transport episodes are not necessarily related. It might be the case that the period of bottom-water dysoxia represented by the individual *P. dubius* was much shorter than 15 years, so there was no opportunity for a pavement to form. It is also possible (as mentioned above) that this individual *P. dubius* fell off a floating log and floated down onto the sediment, but this would be difficult to prove.

Outside the shell pavements, the palaeoenvironment was dominated by water column stratification, with severe oxygen depletion beneath the chemocline, and episodic upwelling of nutrients into the photic zone (Sælen *et al.*, 2000). Nutrient stimulation through enhanced fluvial flux would have assisted in maintaining an anoxic state in the bottom waters, and (as discussed in Chapter 5, section 4.1) was instrumental in triggering system shifts in the redox state of the basin. However, prolonged oxygen depletion is unlikely to have been solely due to eutrophication. Instead, the key factor in the maintenance of frequently anoxic conditions was the moderately restricted nature of the basin, and its susceptibility to

stratification under a warm, humid climate. The shell pavements mark points where this system state was momentarily perturbed, with the return of higher benthic redox accompanying the temporary destruction of stratification (possibly accompanied by a drier climate – see section 4.2).

4.2 Wider implications for the Lower Toarcian world

Overall, this dataset reveals that the marine environment in the Cleveland Basin was generally anoxic and sulphidic across each of the three studied intervals. There might have been occasional brief episodes of re-oxygenation either side of the pavements, on a scale too fine to be captured by the sampling procedure used (see Chapter 3; section 4.3; Chapter 4; section 3.2.1; Chapter 5; section 4.2), but the frequency of periods of anoxia and euxinia were generally far greater. Major factors contributing to the maintenance of this high frequency of anoxia were the hydrographically isolated nature of the basin (Baroni *et al.*, 2018), and the generally hot, humid climate (Rees *et al.* 2000, Ruebsam *et al.*, 2020a) – forced by a massive injection of carbon dioxide into the ocean-atmosphere system (Hesselbo *et al.*, 2000; French *et al.*, 2014; Ruebsam *et al.*, 2020a).

The modelling work of Baroni *et al.* (2018) suggests that circulation in the EES was dominated by a clockwise gyre of warm water from the Tethys (Fig. 6.51), and that the rough bathymetry of the EES resulted in sluggish circulation in the Cleveland and SW German basins. By contrast, flow through the Viking Corridor was weaker, and ran in a southward direction. This circulation model is supported by higher TOC/P and Fe_T/Al values of lower Toarcian sediments from the UK and Germany compared with those further south (e.g. in Spain). The Baroni *et al.* (2018) model, however, conflicts with a model of northward-flowing warm waters through the Viking Corridor proposed by Korte *et al.* (2015). Based on a positive shift in the $\delta^{18}O$ of belemnite calcite from northern EES localities (particularly Yorkshire and Scotland), these workers suggested an origin of the Pliensbachian icehouse involving the partial obstruction of this northward current of warm water by uplift in the northern EES, forced by the emplacement of a thermal dome in the underlying lithosphere. However, others have suggested that Korte *et al.* (2015) underestimated the masking effect of enhanced salinity on belemnite $\delta^{18}O$ (van de Schootbrugge *et al.*, 2019).

The clockwise warm current would have created a low-pressure zone over the northern EES, resulting in a more humid climate, and possibly setting up an atmospheric convection cell, with a low-pressure zone located over Laurasia (Fig. 6.51). The resulting humid conditions would enhance runoff (and weathering rates; Cohen *et al.*, 2004), raising the likelihood of salinity stratification in restricted settings. As implied

by my model for the formation of the shell pavements, this current regime was not constant, and episodic cooling of the northern hemisphere (Baroni *et al.*, 2018) is likely to have, in turn, weakened the clockwise gyre (Fig. 6.52). This would have resulted in the low-pressure zone being restricted to Gondwana, with a high-pressure zone moving southward from the boreal region, resulting in a drier climate. As in the model of Röhl *et al.* (2001), such brief episodes of drier climate would have been accompanied by more intense ventilation of the water column during the winter months. The stronger circulation would have temporarily disrupted water column stratification, and could have induced episodes of shelf-to-basin transport (Ghadeer & MacQuaker, 2011; 2012). While the change in circulation was sufficient to oxygenate the water column, the sediment porewaters remained anoxic and sulphidic, with the oxic/euxinic chemocline positioned precisely on the sediment-water interface.

The timescales of these periods of circulation state change were likely to have been on the order of decades to centuries, although precise estimates are not possible (see Chapter 1, section 6.0).

The interannual variability model I propose here is somewhat analogous to the modern El Niño Southern Oscillation (ENSO). ENSO is also characterised by a spatio-temporal shift in the distribution of warm water masses, and is coupled via positive feedback to changes in atmospheric pressure and equatorial wind direction. ENSO oscillations have also been tied to the local amelioration of dysoxic conditions in shelfal marine environments: during the 1997/98 El Niño, for example, suppression of the normal upwelling of nutrient-rich waters resulted in the O_2 concentration in the lower water column off the Chilean coast rising by 3-6 mL/L (Sellanes, 2002; Escribano *et al.*, 2004). However, an essential feature of ENSO that distinguishes it from my model, is the upwelling of cold, deep water of the western margin of South America - upwelling does not play a major role in my model of the interannual variability of the clockwise gyre. The causes of ENSO are still unclear, although anomalous equatorial zonal winds may be involved (Chen *et al.*, 2019). Similar stochastic behaviour in wind patterns might have also modulated the interannual variability in the strength of the clockwise gyre, which took place over a time period too long to have been influenced by the seasons, and too short to have been influenced by Milankovitch cycles.

Another possible trigger for the shifts in circulation mode could be episodic declines in the flux of (isotopically light) CO_2 to the atmosphere (as implied in section 3.4). The reasons for such declines in carbon injection would depend on the suggested cause for the Toarcian CIE. Episodic declines in the dissociation of methane hydrate deposits (Hesselbo *et al.*, 2000; Kemp *et al.*, 2005), lulls in the intensity of volcanism in the Karoo-Ferrar LIP, exhaustion of the carbon content of coal deposits cut by Karoo-Ferrar-related intrusions (McElwain *et al.*, 2005; Svensen *et al.*; 2007), and breaks in the rate of permafrost destabilisation in the high latitudes (Ruebsam *et al.* 2019; 2020a), are all possible explanations.

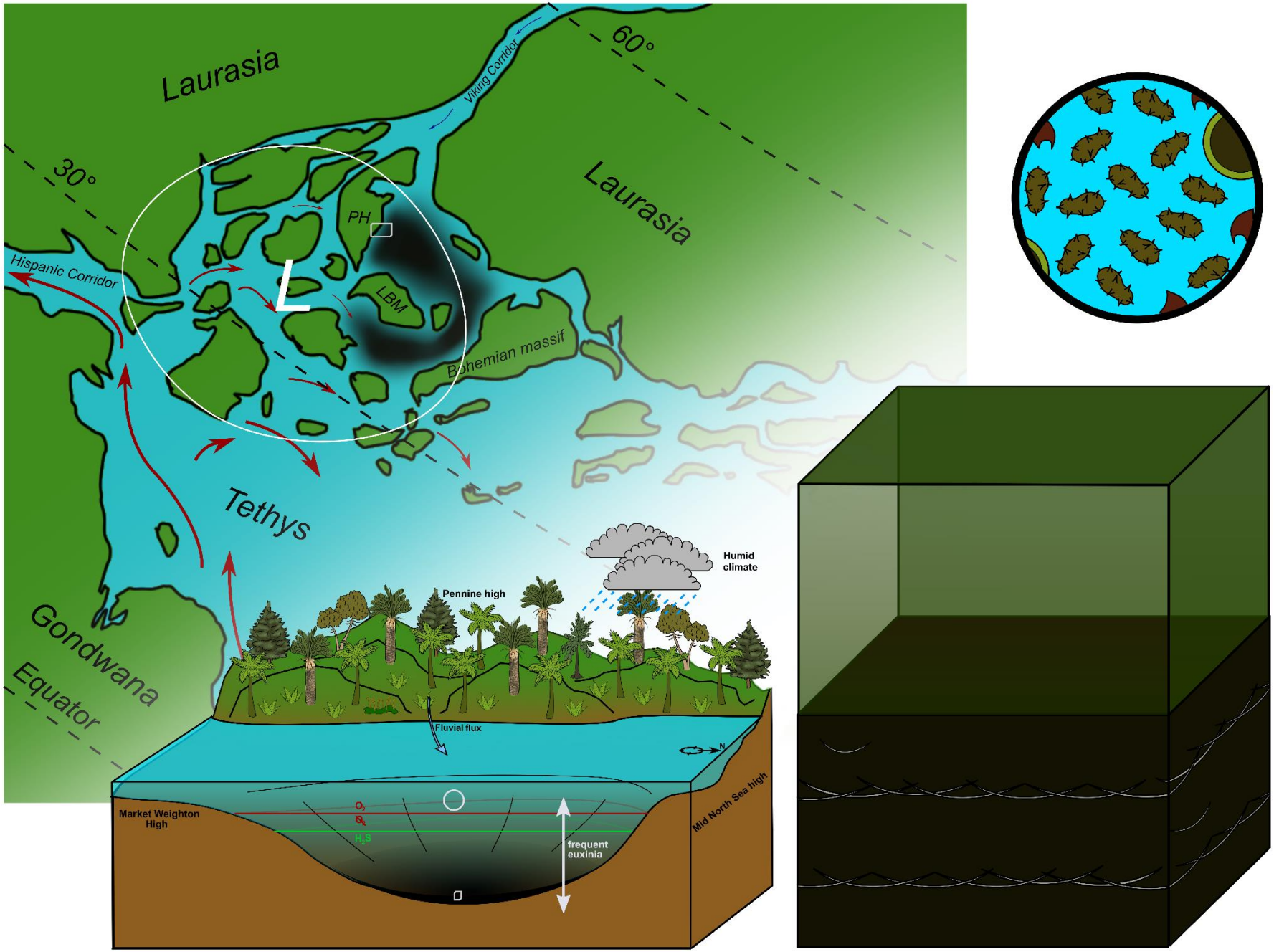
Laurasia
Viking Corridor
60°
30°
Laurasia
PH
Hispanic Corridor
L
LBM
Bohemian massif
Tethys
Gondwana
Equator
Humid climate
Pennine high
Fluvial flux
N
Market Weighton High
O_2
NO_3
H_2S
frequent euxinia
Mid North Sea high

Figure 6.51

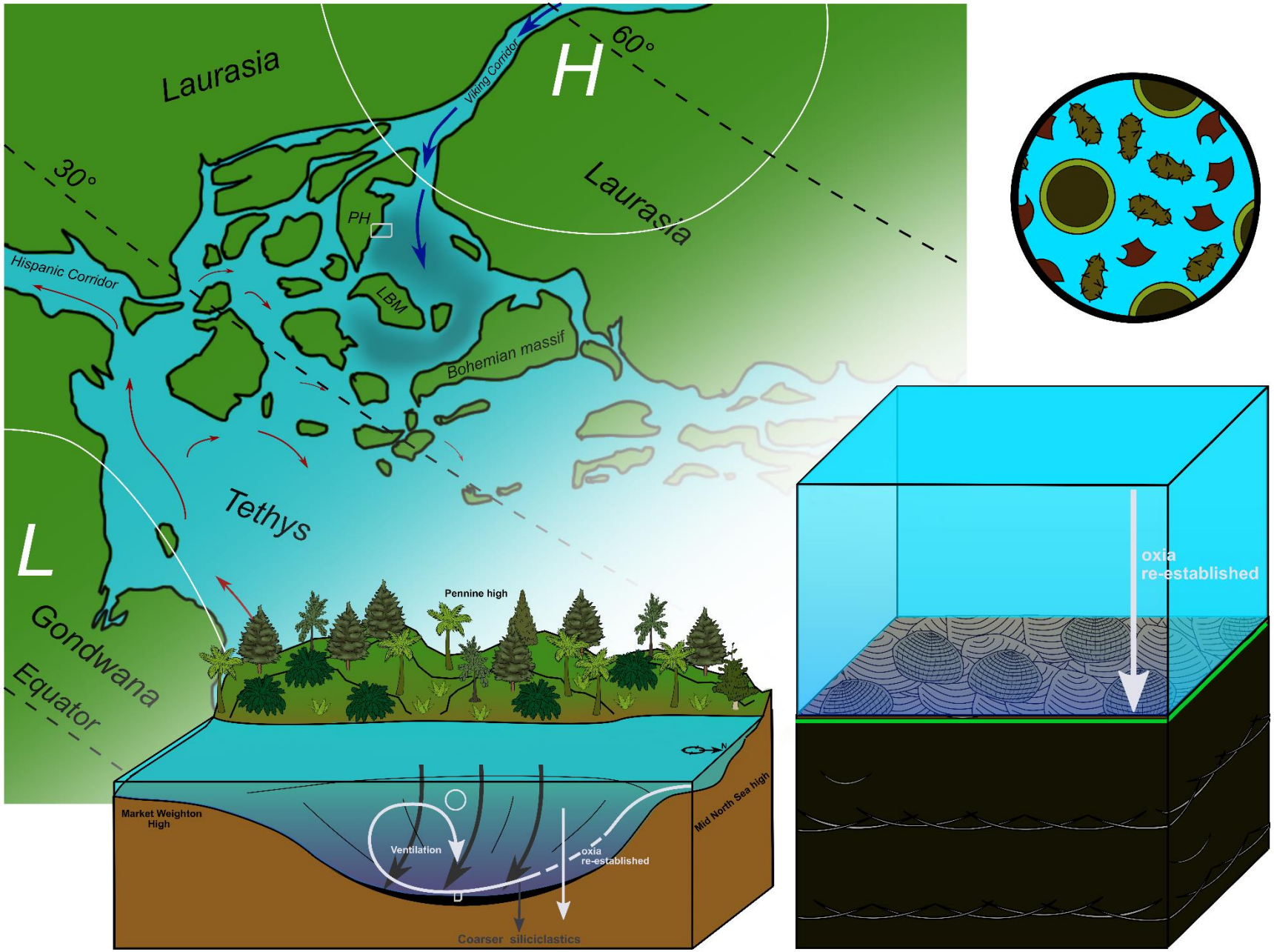
Laurasia
H
60°
Viking Corridor
Laurasia
30°
PH
Hispanic Corridor
LBM
Bohemian massif
Tethys
L
Gondwana
Equator
Pennine high
Market Weighton High
Ventilation
oxia re-established
Mid North Sea high
Coarser siliciclastics
oxia re-established

Figure 6.52

Figure 6.50 (page 287). Summary diagram of the paleoenvironment of the Cleveland Basin during the deposition of the Mulgrave Shale Member, and its relationship with the wider palaeogeography of Europe. As discussed in the text, the EES is dominated by the clockwise flow of warm Tethyan waters (red arrows), and the development of a low pressure system (*L*). Southward flow of cool, ventilating water from the Viking corridor (blue arrows) is greatly diminished, and the northern EES becomes dominated by low redox and the burial of organic carbon (shaded black). The Cleveland Basin (bottom left) is charcaterised by a highly stratified water column, with frequently euxinic bottom waters. The warm, humid climate also leads to a land plant community dominated by ferns (key for plant symbols in Chapter 5, Fig. 5.23). The benthic environment is sterile, and acritarchs dominate the phytoplankton community.

Figure 6.51 (page 288). Summary diagram of the palaeoenvironment of the Cleveland Basin during the formation of the shell pavements, and its relationship with the wider palaeogeography of Europe. Due to a decrease in northern hemisphere temperatures, the strength of the clockwise gyre is decreased. Low pressure shifts southward to Gondwana, and a high pressure zone (*H*) moves southward from the boreal region (beyond the top of the diagram). The southward cool water current through Viking Corridor is enhanced, resulting in better ventilation of the northern EES, and a brief reduction in the rate of organic carbon burial. The lack of a low pressure zone over Europe leads to a cooler, drier climate, and bisaccate producers and cycads dominate the land plant community at the expense of ferns. Periods of bottom-water dysoxia lasting decades (perhaps even centuries) facilitate the development of a shell pavement, and the more oxygenated (possibly nitrogenous) upper water column means the phytoplankton community becomes more dominated by prasinophytes, and some dinoflagellate genera. Intermittent storms, before and after (and possibly during) the formation of the pavement lead to shelf-to-basin transport.

4.3 Suggestions for future work

I argue that my model needs further testing, and that the selection of 2-3 shell pavements means that this data is rather noisy and low-resolution. An essential requirement in any future study of the shell pavements would be the utilisation of non-destructive sampling methods, capable of generating redox proxy records of sub-mm scale resolution (e.g. Dahl *et al.*, 2019). Unfortunately this exceeds the resolution of palynological and organic geochemical analysis, and so determining the change in palaeoenvironmental parameters such as the influence of marine verses terrestrial organic matter, and the composition of the planktonic and terrestrial plant communities (among others), are not possible with current analytical methods. Proxies such as the dominance of dinoflagellates and prasinophytes, and the relationship between shell size frequency and pavement duration, would greatly benefit from a wider survey of the shell pavements, which frequently occur throughout the Whitby Mudstone Formation (Caswell & Coe, 2013; Danise *et al.* 2013). However, such a study would have to overcome the issues of sampling averaging encountered in this study, and are therefore more likely to take a time-invariant approach (i.e. are shell pavements associated with a higher prasinophyte content of the palynological assemblage compared to proximal sediments).

Based on the work presented here, I also predict that periods of drier climate in the EES were generally accompanied by brief exaerobic spells in dominantly euxinic shallow marine settings, and this facilitated 'paper pecten' pavement formation. I have speculated that these periods of drier climate are related to interannual variability in the circulation regime through the EES, and that this, in turn, could have been due to decadal to centennial changes in the dynamics of the global carbon cycle. A high-resolution, compound-specific isotopic analysis through multiple shell pavements, and comparison with a globally integrated carbon isotope record, would be an ideal way to test this. However, such a method would need to overcome two key difficulties:

- The thin profile of the shell pavements makes it very difficult to avoid time averaging during sampling. This is exacerbated by the need for a relatively high sample weight of 2.5 g (for a TOC of 8.0 wt.%) for an efficient TLE, which is the method I have used to obtain long-chain *n*-alkane fractions for CSIA. An analytical method utilising raw samples may require a smaller weight, and, therefore, be able to avoid sample averaging (at the possible expense of analytical precision).

- The pavements occur very frequently through the Whitby Mudstone Formation, and may not have been continuous across the sediment surface. The samples I studied were very spatially limited

(blocks on the order of 10 cm in diameter), and so the possibility of large gaps between shells that are only evident when studied at a metre scale remains. If this is the case, it is possible that many pavements are not visible at the exposure surface. Coring would also risk missing shell pavements entirely.

However, if the shell pavements are generally correlated with carbon isotope evidence for a drier climate, and improved circulation in the Cleveland Basin (positive excursions in the $\delta^{13}C$ of *n*-$C_{27\text{-}29}$ alkanes), and if these excursions can be compared to a global $\delta^{13}C$ stack (impossible with my limited dataset; Figs. 6.42 and 6.43), with reference to an accurate age model, than it may be possible to further constrain the origin and nature of the T-OAE CIE, as well as finely resolve the dynamic relationship between ^{12}C injection, and the earth surface system of the Lower Jurassic.

5.0 Conclusions

- The bivalves *P. dubius* and *B. radiata* could tolerate oxygen levels lower than 0.2 mL/L, and had a predominantly epibenthic mode of life. When oxygen levels improved sufficiently, the spat of these bivalves was not immediately killed while attempting to colonise the seafloor of a distal basin. Furthermore, if favourable conditions persisted for at least a decade, multiple generations of bivalves could grow, with the shells interlinking to form a shell pavement.

- The generally euxinic redox state of the Cleveland Basin was frequently interrupted by periods of dysoxia lasting decades to centuries, during the deposition of the upper Grey Shale and Mulgrave Shale Members of the Whitby Mudstone Formation. These are often marked by shell pavements, and occasionally (but not necessarily) coincide with episodes of shelf-to-basin transport of silty material. The oxic/euxinic chemocline descended to at least the depth of the sediment-water interface during these episodes ,facilitating the development of an exaerobic biofacies. and sometimes descended slightly deeper. This possibly resulted in the reprecipitation of redox-sensitive trace elements within diagenetic pyrite (a process aided by the in-situ decay of bivalve tissues).

- Shelf-to-basin transport under anoxic conditions resulted in the preservation of lags of small, reworked pyrite framboids. This further highlights the importance of careful interpretation of redox proxy records with reference to sub-mm scale lithology, particularly in condensed sequences.

- The episodes of dysoxia marked by shell pavement formation were possibly developed under relatively dry climatic conditions. A timescale of decades to centuries for these putative dry episodes implies they were primarily controlled by interannual climate variability over the EES. Recent modelling work suggests the presence of a clockwise gyre of warm water-dominated circulation in the EES during the Toarcian. Episodic weakening of this current system due to intermittent cooling in the northern hemisphere could have resulted in better ventilation of the Cleveland Basin, with a corresponding shift in atmospheric pressure systems leading to a drier climate.

- The declines in northern hemisphere palaeotemperature (if present) could be related to episodic declines in the rate of ^{12}C injection during the T-OAE. The proxy records I have presented here, however, are insufficient to test this, and I, therefore, recommend a more extensive CSIA of shell pavements recovered from core material in the Cleveland Basin: A sufficiently high-resolution record could be better tied to a global $\delta^{13}C$ stack.

- Regardless of major limitations related to sample averaging, this study has demonstrated the highly dynamic nature of the redox state of the Cleveland Basin – even at the height of the T-OAE – and the ability of thin-shelled bivalves to thrive, albeit briefly, during the very geologically brief intervals of improved redox within a predominantly inhospitable environment.

Chapter 7 – Conclusion

At the beginning of this project, I aimed to reconstruct the redox dynamics, reactive Fe enrichment, and causal mechanisms of the LSB, and, more specifically, to investigate whether the LSB could be considered a bellwether for the intense oxygen depletion that would come to characterise the Cleveland Basin during the T-OAE. To this end, I employed a wide range of sedimentological, (micro)palaeontological, inorganic geochemical, organic geochemical, and isotopic analysis techniques, to derive 13 palaeontological, 4 pyrite framboid, 54 inorganic geochemical, 31 organic geochemical, and 6 isotopic geochemical proxy records either for redox, or for complementary palaeoenvironmental variables (nutrient stimulation, palaeoshoreline distance, biological community structures, etc.), in what is, to my knowledge, the highest resolution study of a thin black shale to date.

Above all, my study has highlighted the dynamic nature of redox changes in restricted shallow marine settings, and black shale deposition in these environments. This is of great relevance not just to the understanding of the geological history of the Cleveland Basin, but to the interpretation of proxy records from black shale sequences in general. The occurrence of sedimentary structures within the LSB and Mulgrave Shale Member indicative of reletivley energetic shelf-to-basin transport, that bear proxy indicators for low oxygen levels (e.g. small framboid sizes; Chapter), further highlights how high-energy events such as shelf-to-basin transport do not necessarily change the redox state of the basins in which they occur, and is consistent with the work of Ghadeer & MacQuaker (2011, 2012), who arrived at the same conclusion. My Fe-speciation and biomarker studies of the bioturbated portions of the LSB have demonstrated that biological reworking of the sediment can greatly homogenise redox proxy signals, to the point of generating simultaneous, and apparently incompatible biological and geochemical records of redox state (chapters 3 and 5). My palynological investigation of the LSB revealed a small population of dinoflagellates even during the period of the deposition of the LSB characterised by the most intense anoxia (chapter 4), and I have argued that the shell pavements of the Grey Shale and Mulgrave Shale Members are indicative of brief spells of higher bottom water oxygen concentration, lasting decades to centuries (chapter 6). These findings demonstrate how dynamic the redox state concomitant with black shale deposition can be – a property not recognised in many older studies. The observation of the highly dynamic, often seasonal nature of redox change in modern dysoxic environments (Tyson & Pearson, 1991; Rabalais *et al.*; 2010), when combined with the principle that the present is the key to the past, provides further support for this model of black shale formation. This realisation, however, does raise the important question of how much we can ever really know about the deposition of black shales in the deep past, given the limitations of our current analytical procedures and technology, combined with the widespread incompleteness of the geological record. In chapters 3 and 5, I suggested that in samples that are

known to contain a time-averaged signal (due to bioturbation, for example), proxy values should be thought of as representing anoxia frequency instead of being an absolute function of anoxia through time. However, the true value for anoxia frequency for any given interval may be impossible to establish, even at the highest possible sampling resolution, depending on how frequently the redox state oscillated, or how thoroughly the sediment was mixed by bioturbation. Therefore, if this approach were to be adopted in future work on black shales, an estimate for the true frequency of anoxia may have to be calculated as a function of the proxy data, plus the limit of sampling resolution (perhaps utilising models based on Baysian statistics).

In addition to highlighting one of the most fundamental challenges in accurate palaeoenvironmental reconstruction, my work has provided excellent constraints on the palaeoenvironmental processes responsible for the formation of the LSB, and an attempt at providing similar constraints for the shell pavements of the Whitby Mudstone Formation. The relative sea level lowstand in the Cleveland Basin towards the end of the Pliensbachian (possibly due to glaciation in the high latitudes; Hesselbo & Korte, 2011; Ruebsam *et al.*, 2019), resulted in a highly restricted system, and therefore, its oxygen inventory was vulnerable to rapid depletion. This did not occur throughout the upper Pliensbachinan, due to the absence of major warming episodes in the global climate, so the Cleveland Basin became characterised by the deposition of Fe-rich sediments. However, as soon as a brief period of warming occurred (probably concomitant with the Pl-To boundary), the resulting rapid shift to a humid climate – characterised by high nutrient flux from the hinterland – shifted the Cleveland Basin into a redox state characterised by highly frequent anoxia. While anoxia was not persistent (probably due to seasonal fluctuations in primary production and stratification strength; Tyson & Pearson 1991), it was frequent enough to eliminate all benthos and most metazoans from the Cleveland Basin. Even after the nutrient pulse subsided, the highly frequent anoxia persisted due to the lack of renewal of the oxygen inventory by ocean currents - in other words, the redox state demonstrated a hysteresis-like response. This state persisted for several kyr after the nutrient pulse, and was ended by a transgression that improved the connectivity of the Cleveland Basin to oxygenated water masses. My inorganic geochemical study of the LSB (chapter 3) showed how reactive Fe was enriched throughout the LSB, and reached its highest level of enrichment during the interval characterised by the greatest TOC content (the up-section profile being later homogenised by bioturbation). While there is also lithological evidence for shelf-to-basin transport (in the form of coarser-grained layers), developed during periods of humid climate, these are not correlated with a high increase in the enrichment of highly reactive Fe, and if anything, show a decrease in total Fe. Therefore, of the two modes of Fe_{HR} enrichment in the LSB proposed by Newton (2001, p.143), the mode invoking lateral diffusion of Fe^{2+} in basinal bottom waters, following the dissolution of a steady supply of reworked Fe oxides, is likely to have been the most dominant.

While my study of the LSB establishes a link between temporally constrained periods of anoxia, and nutrient stimulation in restricted settings, my work on the shell pavements of the Whitby Mudstone Formation suggests that episodic ventilation of restricted settings is responsible for periods of oxygenation, which are geologically brief, but none-the-less long enough to be exploited by dysoxia-tolerant bivalves. Moreover, the timescales of shell pavement deposition, and their possible link with changes in the local climate, imply a link between episodes of reoxygenation, and interannual variability in the early Toarcian climate (a similar conclusion was drawn by Röhl *et al.*, 2001, for the Inoceramenbank of the Posidonia Shale). The speculations I made in chapter 6, if correct, have important implications for our understanding of the T-OAE. Episodic weakening of the clockwise gyre (a circulation pattern proposed by Baroni *et al.*, 2018), combined with a shift in the distribution of atmospheric pressure systems, implies that episodes of cooler climate in the northern hemisphere occurred during the T-OAE. However, given that the shell pavements themselves represent reoxygenation periods decades to centuries in duration, it is not likely that Milankovich cycles are the cause of this variability in palaeotemperature. As discussed in chapter 6, the nearest modern equivalent to the interannual variability I propose is ENSO, the causes of which are still not clearly understood. What is well understood, however, is that the T-OAE was accompanied by a massive injection of isotopically depleted carbon dioxide into the earth surface system. Given the profound effect this had on the global climate of the early Jurassic, I believe it is reasonable to suggest that the episodic declines in northern hemisphere palaeotemperature I invoked in my work (and suggested by Baroni *et al.*, 2018), are linked to variability in the rate of carbon dioxide injection. My purpose with this work is not to argue for or against any of the many suggested pathways for ^{12}C injection into the earth surface system during the T-OAE, only to suggest that the primary mechanism(s) for the release of carbon dioxide experienced fluctuations in its intensity through the CIE interval. Regrettably, my study of the shell pavements exceeds the maximum resolution that can be geochemically analysed with acceptable precision, due the frequent occurrence of cryptic hiatal surfaces in the surrounding lithology, and possibly on the pavements themselves.

It can also be inferred from the model of oxygen depletion I invoked for the LSB, that the crossing of environmental thresholds (due to nutrient stimulation) can shift shallow seas vulnerable to oxygen depletion into a state of highly frequent anoxia. Many such regions in the modern ocean are predicted to suffer prolonged anoxia as global temperatures rise, and surface runoff and nitrate loading of river catchment systems increases (Sinha *et al.*, 2017). Modelling by Conley *et al.* (2009) predicts that (due to reduced O_2 solubility) a 4^{o}C rise in SST by the end of the century will lead to a doubling in the area of the seafloor of the Danish Straits exposed to "hypoxia". The age model adopted here implies that these frequently anoxic states demonstrate hysteresis-like behaviour and can persist for a timescale on the order of 10^{3-4} years. This further highlights the vulnerability of coastal marine ecosystems to anthropogenic activity, and emphasises the need for appropriate safeguarding and mitigation of

ecosystem-related impacts (Breitburg *et al.*, 2018). Given the position of the LSB during the *P. paltum* subzone (at the top of the Pliensbachian-aged Cleveland Ironstone Formation), and the concomitant (possibly carbon-cycle influenced) $\delta^{13}C_{Org}$ excursion (Littler *et al.*, 2010), it is possible that it is coeval with the Pl-To boundary in the Cleveland Basin. Given the similarity of the Pl-To event to modern climate change (both are concomitant with a relatively short duration of carbon emission, but at a high rate; cf. Clapham & Renne, 2019 – their Fig.6), my research is of potential relevance to the study of modern environments. Specifically, I showed how benthic environments repeatedly exposed to dysoxia become inamicable to an increasing number of organisms, the more frequently the exposure occurs. My models for the formation of the LSB and the shell pavements show how even relatively brief periods of reoxygenation, driven by improvements in hydrographic connectivity and current intensity, can provide an opportunity for the partial recovery of benthic communities. However, only a few groups of highly specialised organisms can exploit these re-established niches as they form, and are usually unable to act as ecosystem engineers, especially if the return to dysoxic conditions is very brief. In the Cleveland Basin, despite the intermittent occurrence of shell pavement and *Chondrites* trace-makers throughout the Mulgrave Shale Member, full ecosystem recovery did not start until the *Dumortieria pseudoradiosa* zone (Atkinson *et al.*, 2022). This was probably driven by the colonisation of the sediment by infaunal bivalves such as *Dacryomya ovum* (Caswell & Dawn, 2019), which could rework the sediment more extensively, and lead to deeper oxygen penetration than *Chondrites* trace-makers could. This might mean that modern shallow marine ecosystems, in addition to being greatly disturbed by the occurrence of dysoxia, may take thousands of years to recover to a state of biodiversity comparable to before the initial oxygen depletion, with the species composition of the environment often being radically different.

In closing, my study of the LSB has shown that it represents a period of highly frequent anoxia, triggered by a nutrient pulse into a restricted system, and my study of the shell pavements suggests that episodic ventilation of the Cleveland Basin during the T-OAE was linked to interannual variability in the lower Toarcian climate. A careful and critical examination of high-resolution, multiproxy datasets, while bearing in mind the dynamic nature of deposition in shallow marine environments, is the key to the reconciliation of palaeontology and geochemistry, in the solving of oceanic anoxic event conundrums.

Appendix 1 – References

Ærtebjerg, G., Carstensen, J., Axe, P., Duron, J.-N. and Stips, A. 2003. Helsinki Commission.

Adegoke, A.K., Sarki Yandoka, B.M., Abdullah, W.H. and Akaegbobi, I.M. 2014. Molecular geochemical evaluation of late cretaceous sediments from Chad (Bornu) basin, Ne Nigeria: Implications for paleodepositional conditions, source input and thermal maturation. *Arabian Journal of Geosciences*. **8**(3),pp.1591–1609.

Adelson, J.M., Helz, G.R. and Miller, C.V. 2001. Reconstructing the rise of recent coastal anoxia; molybdenum in Chesapeake Bay Sediments. *Geochimica et Cosmochimica Acta*. **65**(2),pp.237–252.

Agbi, I., Ozibo, B. and Newton, R.J. 2015. Pyrite framboid size distribution of the Grey Shales (Yorkshire UK) as an indication of redox conditions. *IOSR Journal of Applied Geology and Geophysics*. **3**(5),pp.36–42.

Ait-Itto, F.-Z., Martinez, M., Price, G.D. and Ait Addi, A. 2018. Synchronization of the astronomical time scales in the early Toarcian: A link between anoxia, carbon-cycle perturbation, mass extinction and volcanism. *Earth and Planetary Science Letters*. **493**,pp.1–11.

Alcott, L.J., Krause, A.J., Hammarlund, E.U., Bjerrum, C.J., Scholz, F., Xiong, Y., Hobson, A.J., Neve, L., Mills, B.J., März, C., Schnetger, B., Bekker, A. and Poulton, S.W. 2020. Development of iron speciation reference materials for palaeoredox analysis. *Geostandards and Geoanalytical Research*. **44**(3),pp.581–591.

Algeo, T.J. and Lyons, T.W. 2006. Mo-total organic carbon covariation in modern anoxic marine environments: Implications for analysis of paleoredox and paleohydrographic conditions. *Paleoceanography*. **21**(1),pp.n/a-n/a.

Algeo, T.J. and Maynard, J.B. 2004. Trace-element behavior and redox facies in core shales of Upper Pennsylvanian Kansas-Type cyclothems. *Chemical Geology*. **206**(3-4),pp.289–318.

Algeo, T.J. and Tribovillard, N. 2009. Environmental analysis of paleoceanographic systems based on molybdenum–uranium covariation. *Chemical Geology*. **268**(3-4),pp.211–225.

Allen, J.A. and Scheltema, R.S. 1972. The functional morphology and geographical distribution of *planktomya henseni*, a supposed neotenous pelagic bivalve1. *Journal of the Marine Biological Association of the United Kingdom*. **52**(1),pp.19–31.

Amorim, K., Piontkivska, H., Zettler, M.L., Sokolov, E., Hinzke, T., Nair, A.M. and Sokolova, I.M. 2021. Transcriptional response of key metabolic and stress response genes of a nuculanid bivalve, Lembulus bicuspidatus from an oxygen minimum zone exposed to hypoxia-reoxygenation. *Comparative Biochemistry and Physiology Part B: Biochemistry and Molecular Biology*. **256**,p.110617.

Anderson, D.M., Aubrey, D.G., Tyler, M.A. and Coats, D.W. 1982. Vertical and horizontal distributions of dinoflagellate cysts in sediments1. *Limnology and Oceanography*. **27**(4),pp.757–765.

Anderson, D.M., Taylor, C.D. and Armbrust, E.V. 1987. The effects of darkness and anaerobiosis on dinoflagellate cyst germination1,2. *Limnology and Oceanography*. **32**(2),pp.340–351.

Anderson, T.F. and Raiswell, R. 2004. Sources and mechanisms for the enrichment of highly reactive iron in euxinic Black Sea sediments. *American Journal of Science*. **304**(3),pp.203–233.

Andrews, J.E. and Walton, W. 1990. Depositional environments within Middle Jurassic oyster-dominated lagoons: An integrated litho-, bio- and palynofacies study of the Duntulm Formation (great estuarine group, Inner Hebrides). *Transactions of the Royal Society of Edinburgh: Earth Sciences*. **81**(1),pp.1–22.

Anita, D.D.J. and Wood, B.A. 1977. Some aspects of the palaeoecology of the E1b zone of the Edale Shales (Namurian) in the Edale Valley, Derbyshire. *The Mercian Geologist*. **6**(3),pp.179–196.

Anon n.d. Hopanoids. *The Summons Lab*. [Online]. [Accessed 12 October 2022]. Available from: https://summons.mit.edu/biomarkers/biomarker-

classification/lipids/isoprenoids/polycyclic-isoprenoids-with-concatenated-ring-system/hopanoids/.

Anon n.d. Paleobiology database. *paleobiodb.org*. [Online]. [Accessed 1 September 2022]. Available from: https://paleobiodb.org/navigator/.

Armstrong, H.A. and Brasier, M.D. 2005. *Microfossils* 2nd ed. Oxford: Blackwell.

Armstrong, H.A., Wagner, T., Herringshaw, L.G., Farnsworth, A.J., Lunt, D.J., Harland, M., Imber, J., Loptson, C. and Atar, E.F.L. 2016. Hadley circulation and precipitation changes controlling black shale deposition in the Late Jurassic Boreal Seaway. *Paleoceanography*. **31**(8),pp.1041–1053.

Arntz, W.E. and Rumohr, H. 1986. Fluctuations of benthic macrofauna during succession and in an established community. *Meeresforschung - Reports on Marine Research*. **31**(2),pp.97–114.

Asif, M., Alexander, R., Fazeelat, T. and Pierce, K. 2009. Geosynthesis of dibenzothiophene and alkyl dibenzothiophenes in crude oils and sediments by carbon catalysis. *Organic Geochemistry*. **40**(8),pp.895–901.

Atar, E., Aplin, A.C., Lamoureux-Var, V., März, C. and Wagner, T. 2020. Sedimentation of the Kimmeridge Clay Formation in the Cleveland Basin (Yorkshire, UK). *Minerals*. **10**(11),p.977.

Atar, E., März, C., Aplin, A.C., Dellwig, O., Herringshaw, L.G., Lamoureux-Var, V., Leng, M.J., Schnetger, B. and Wagner, T. 2019. Dynamic climate-driven controls on the deposition of the Kimmeridge Clay Formation in the Cleveland Basin, Yorkshire, UK. *Climate of the Past*. **15**(4),pp.1581–1601.

Atkinson, J.W., Wignall, P.B. and Page, K.N. 2020. The Hettangian–Sinemurian (Lower Jurassic) strata of Redcar, Cleveland Basin, NE England: facies and palaeoecology. *Proceedings of the Yorkshire Geological Society*. **63**(2),pp.77–87.

Baker, S.J., Hesselbo, S.P., Lenton, T.M., Duarte, L.V. and Belcher, C.M. 2017. Charcoal evidence that rising atmospheric oxygen terminated early jurassic ocean anoxia. *Nature Communications*. **8**(1).

Bam, L.C., Miller, J.A., Becker, M., De Beer, F.C. and Basson, I. 2016. The Third Ausimm International Geometallergy Conference (15th-16th June 2016) *In*: Perth, pp. 209–219.

Bang, E., Nakrem, H.A., Little, C.T.S., Kürschner, W., Kelly, S.R.A. and Smelror, M. 2022. Palynology of Early Cretaceous (Barremian to aptian) hydrocarbon (methane) seep carbonates and associated mudstones, Wollaston Forland, Northeast Greenland. *Acta Palaeobotanica*. **62**(1),pp.11–23.

Baroni, I.R., Pohl, A., van Helmond, N.A.G.M., Papadomanolaki, N.M., Coe, A.L., Cohen, A.S., van de Schootbrugge, B., Donnadieu, Y. and Slomp, C.P. 2018. Ocean Circulation in the Toarcian (Early Jurassic): A Key Control on Deoxygenation and Carbon Burial on the European Shelf. *Paleoceanography and Paleoclimatology*. **33**(9),pp.994–1012.

Baucon, A., Bednarz, M., Dufour, S., Felletti, F., Malgesini, G., Neto de Carvalho, C., Niklas, K.J., Wehrmann, A., Batstone, R., Bernardini, F., Briguglio, A., Cabella, R., Cavalazzi, B., Ferretti, A., Zanzerl, H. and McIlroy, D. 2020. Ethology of the trace fossil Chondrites: Form, function and environment. *Earth-Science Reviews*. **202**,p.102989.

Beatty, J.T., Overmann, J., Lince, M.T., Manske, A.K., Lang, A.S., Blankenship, R.E., Van Dover, C.L., Martinson, T.A. and Plumley, F.G. 2005. An obligately photosynthetic bacterial anaerobe from a deep-sea hydrothermal vent. *Proceedings of the National Academy of Sciences*. **102**(26),pp.9306–9310.

Belcher, C.M., Mander, L., Rein, G., Jervis, F.X., Haworth, M., Hesselbo, S.P., Glasspool, I.J. and McElwain, J.C. 2010. Increased fire activity at the triassic/jurassic boundary in Greenland due to climate-driven floral change. *Nature Geoscience*. **3**(6),pp.426–429.

Berner, R.A. 1970. Sedimentary Pyrite Formation. *American Journal of Science*. **268**(1),pp.1–23.

Berner, R.A. 1984. Sedimentary pyrite formation: An update. *Geochimica et Cosmochimica Acta*. **48**(4),pp.605–615.

Bertine, K.K. and Turekian, K.K. 1973. Molybdenum in marine deposits. *Geochimica et Cosmochimica Acta*. **37**(6),pp.1415–1434.

Bishop, A.N. and Abbott, G.D. 1995. Vitrinite reflectance and molecular geochemistry of Jurassic sediments: the influence of heating by Tertiary dykes (northwest Scotland). *Organic Geochemistry*. **22**(1),pp.165–177.

Bodin, S., Mattioli, E., Fröhlich, S., Marshall, J.D., Boutib, L., Lahsini, S. and Redfern, J. 2010. Toarcian carbon isotope shifts and nutrient changes from the northern margin of Gondwana (high atlas, Morocco, Jurassic): Palaeoenvironmental implications. *Palaeogeography, Palaeoclimatology, Palaeoecology*. **297**(2),pp.377–390.

Bogus, K., Mertens, K.N., Lauwaert, J., Harding, I.C., Vrielinck, H., Zonneveld, K.A. and Versteegh, G.J. 2014. Differences in the chemical composition of organic-walled dinoflagellate resting cysts from phototrophic and heterotrophic dinoflagellates. *Journal of Phycology*. **50**(2),pp.254–266.

Bonis, N.R., Ruhl, M. and Kürschner, W.M. 2010. Milankovitch-scale palynological turnover across the Triassic–Jurassic transition at St. Audrie's Bay, SW UK. *Journal of the Geological Society*. **167**(5),pp.877–888.

Boulila, S. and Hinnov, L.A. 2015. Comment on “Chronology of the early Toarcian Environmental Crisis in the Lorraine Sub-basin (Ne Paris Basin)” by W. Ruebsam, P. Münzberger, and L. Schwark [earth and planetary science letters 404 (2014) 273–282]. *Earth and Planetary Science Letters*. **416**,pp.143–146.

Bourbonniere, R.A. and Meyers, P.A. 1996. Sedimentary geolipid records of historical changes in the watersheds and productivities of Lakes Ontario and Erie. *Limnology and Oceanography*. **41**(2),pp.352–359.

Breitburg, D., Levin, L.A., Oschlies, A., Grégoire, M., Chavez, F.P., Conley, D.J., Garçon, V., Gilbert, D., Gutiérrez, D., Isensee, K., Jacinto, G.S., Limburg, K.E., Montes, I., Naqvi, S.W.A., Pitcher, G.C., Rabalais, N.N., Roman, M.R., Rose, K.A., Seibel, B.A.,

Telszewski, M., Yasuhara, M. and Zhang, J. 2018. Declining oxygen in the global ocean and coastal waters. *Science*. **359**(6371),p.eaam7240.

Briggs, D.E., Raiswell, R., Bottrell, S.H., Hatfield, D. and Bartels, C. 1996. Controls on the pyritization of exceptionally preserved fossils; an analysis of the Lower Devonian Hunsrueck slate of Germany. *American Journal of Science*. **296**(6),pp.633–663.

Brocks, J.J. and Schaeffer, P. 2008. Okenane, a biomarker for purple sulfur bacteria (Chromatiaceae), and other new carotenoid derivatives from the 1640ma barney creek formation. *Geochimica et Cosmochimica Acta*. **72**(5),pp.1396–1414.

BROOKS, J.D., GOULD, K. and SMITH, J.W. 1969. Isoprenoid Hydrocarbons in Coal and Petroleum. *Nature*. **222**(5190),pp.257–259.

Brown, J.W. and Sorhannus, U. 2010. A Molecular Genetic Timescale for the Diversification of Autotrophic Stramenopiles (Ochrophyta): Substantive Underestimation of Putative Fossil Ages. *PLoS ONE*. **5**(9),p.e12759.

Brumsack, H.-J. 2006. The trace metal content of recent organic carbon-rich sediments: Implications for Cretaceous black shale formation. *Palaeogeography, Palaeoclimatology, Palaeoecology*. **232**(2-4),pp.344–361.

Bryan, A.L., Dickson, A.J., Dowdall, F., Homoky, W.B., Porcelli, D. and Henderson, G.M. 2021. Controls on the cadmium isotope composition of modern marine sediments. *Earth and Planetary Science Letters*. **565**,p.116946.

Bühring, S.I., Sievert, S.M., Jonkers, H.M., Erterai, T., Elshahed, M.S., Krumholz, L.R. and Hinrichs, K.-U. 2011. Insights into chemotaxonomic composition and carbon cycling of phototrophic communities in an artesian sulfur-rich spring (Zodletone, Oklahoma, USA), a possible analog for ancient microbial Mat Systems. *Geobiology*. **9**,pp.166–179.

Calvert, S.E. and Pedersen, T.F. 1993. Geochemistry of Recent oxic and anoxic marine sediments: Implications for the geological record. *Marine Geology*. **113**(1-2),pp.67–88.

Calvert, S.E. and Pedersen, T.F. 1996. Sedimentary geochemistry of manganese; implications for the environment of formation of manganiferous black shales. *Economic Geology*. **91**(1),pp.36–47.

Calvert, S.E. and Pedersen, T.F. 2007. Chapter Fourteen: Elemental Proxies for Palaeoclimatic and Palaeoceanographic Variability in Marine Sediments: Interpretation and Application *In*: C. Hillaire–Marcel and A. De Vernal, eds. *Proxies in Late Cenozoic Paleoceanography*. Developments in Marine Geology. Elsevier, pp. 567–644.

DOI: 10.1016/S1572-5480(07)01019-6

Calvert, S.E. and Piper, D.Z. 1984. Geochemistry of ferromanganese nodules from Domes Site A, northern equatorial Pacific: Multiple diagenetic metal sources in the Deep Sea. *Geochimica et Cosmochimica Acta*. **48**(10),pp.1913–1928.

Campbell, H.J. 1985. The stratigraphic significance of the Triassic bivalves Daonella and Halobia in New Zealand and New Caledonia . *New Zealand Geological Survey Record*. **9**,pp.21–23.

Canfield, D.E., Raiswell, R., Westrich, J.T., Reaves, C.M. and Berner, R.A. 1986. The use of chromium reduction in the analysis of reduced inorganic sulfur in sediments and shales. *Chemical Geology*. **54**(1-2),pp.149–155.

Carmichael, M.J., Inglis, G.N., Badger, M.P.S., Naafs, B.D., Behrooz, L., Remmelzwaal, S., Monteiro, F.M., Rohrssen, M., Farnsworth, A., Buss, H.L., Dickson, A.J., Valdes, P.J., Lunt, D.J. and Pancost, R.D. 2017. Hydrological and associated biogeochemical consequences of rapid global warming during the paleocene-eocene thermal maximum. *Global and Planetary Change*. **157**,pp.114–138.

Carrie, J., Sanei, H. and Stern, G. 2012. Standardisation of Rock–Eval pyrolysis for the analysis of recent sediments and soils. *Organic Geochemistry*. **46**,pp.38–53.

Caswell, B.A. and Coe, A.L. 2013. Primary productivity controls on opportunistic bivalves during Early Jurassic oceanic deoxygenation. *Geology*. **41**(11),pp.1163–1166.

Caswell, B.A. and Dawn, S.J. 2019. Recovery of benthic communities following the Toarcian oceanic anoxic event in the Cleveland Basin, UK. *Palaeogeography, Palaeoclimatology, Palaeoecology*. **521**,pp.114–126.

Caswell, B.A., Coe, A.L. and Cohen, A.S. 2009. New range data for marine invertebrate species across the early Toarcian (Early Jurassic) mass extinction. *Journal of the Geological Society*. **166**(5),pp.859–872.

Cernusak, L.A., Ubierna, N., Winter, K., Holtum, J.A., Marshall, J.D. and Farquhar, G.D. 2013. Environmental and physiological determinants of carbon isotope discrimination in terrestrial plants. *New Phytologist*. **200**(4),pp.950–965.

Chappe, B., Albrecht, P. and Michaelis, W. 1982. Polar Lipids of Archaebacteria in Sediments and Petroleums. *Science*. **217**(4554),pp.65–66.

Chen, N., Thual, S. and Stuecker, M.F. 2019. El Niño and the southern oscillation: Theory. *Reference Module in Earth Systems and Environmental Sciences*.

Chih, C.P. and Ellington, W.R. 1983. Energy metabolism during contractile activity and environmental hypoxia in the phasic adductor muscle of the bay scallop Argopecten Irradians concentricus. *Physiological Zoology*. **56**(4),pp.623–631.

Chowns, T.M. 1968. ENVIRONMENTAL AND DIAGENETIC STUDIES OF THE CLEVELAND IRONSTONE FORMATION OF NORTH EAST YORKSHIRE.

Clapham, M.E. and Renne, P.R. 2019. Flood Basalts and Mass Extinctions. *Annual Review of Earth and Planetary Sciences*. **47**(1),pp.275–303.

Coates, J.D., Anderson, R.T. and Lovley, D.R. 1996. Oxidation of polycyclic aromatic hydrocarbons under sulfate-reducing conditions. *Applied and Environmental Microbiology*. **62**(3),pp.1099–1101.

Cochran, J.R., Stow, D.A.V., Stow, D.A.V. and Wetzel, A. 1990. Hemiturbidite: A New Type of Deep-Water Sediment *In*: *Proceedings of the Ocean Drilling Program, Scientific Results, 116*.

Cohen, A.S., Coe, A.L., Harding, S.M. and Schwark, L. 2004. Osmium isotope evidence for the regulation of atmospheric CO2 by Continental Weathering. *Geology*. **32**(2),p.157.

Cole, J.J., Lane, J.M., Marino, R. and Howarth, R.W. 1993. Molybdenum assimilation by cyanobacteria and phytoplankton in freshwater and salt water. *Limnology and Oceanography*. **38**(1),pp.25–35.

Conley, D.J., Carstensen, J., Vaquer-Sunyer, R. and Duarte, C.M. 2009. Ecosystem thresholds with hypoxia. *Hydrobiologia*. **629**(1),pp.21–29.

Conley, D.J., Carstensen, J., Ærtebjerg, G., Christensen, P.B., Dalsgaard, T., Hansen, J.L.S. and Josefson, A.B. 2007. LONG-TERM CHANGES AND IMPACTS OF HYPOXIA IN DANISH COASTAL WATERS. *Ecological Applications*. **17**(sp5),pp.S165–S184.

Conti, M.A. and Monari, S. 1992. Thin-shelled bivalves from the Jurassic Rosso Ammonitico and Calcari a Posidonia Formations of the Umbrian-Marchean Apennine (Central Italy). *PALEOPELAGOS*. **2**,pp.193–213.

Conway, E. 1949. Xxii.—the autecology of Bracken (pteridium aquilinum (L.) kuhn): The germination of the spore, and the development of the prothallus and the young sporophyte. *Proceedings of the Royal Society of Edinburgh. Section B. Biology*. **63**(3),pp.325–343.

Cornford, C., Gardner, P. and Burgess, C. 1998. Geochemical truths in large data sets. I: Geochemical screening data. *Organic Geochemistry*. **29**(1-3),pp.519–530.

Correia, V.F., Riding, J.B., Duarte, L.V., Fernandes, P. and Pereira, Z. 2017. The palynological response to the Toarcian Oceanic Anoxic Event (Early Jurassic) at Peniche, Lusitanian Basin, western Portugal. *Marine Micropaleontology*. **137**,pp.46–63.

Crowe, S.A., Jones, C., Katsev, S., Magen, C., O'Neill, A.H., Sturm, A., Canfield, D.E., Haffner, G.D., Mucci, A., Sundby, B. and Fowle, D.A. 2008. Photoferrotrophs thrive in an Archean ocean analogue. Proceedings of the National Academy of Sciences. 105(41),pp.15938–15943.

Crusius, J. and Thomson, J. 2000. Comparative behavior of authigenic Re, U, and Mo during reoxidation and subsequent long-term burial in marine sediments. *Geochimica et Cosmochimica Acta*. **64**(13),pp.2233–2242.

Crusius, J., Calvert, S., Pedersen, T. and Sage, D. 1996. Rhenium and molybdenum enrichments in sediments as indicators of oxic, suboxic and sulfidic conditions of deposition. *Earth and Planetary Science Letters*. **145**(1-4),pp.65–78.

Czochanska, Z., Gilbert, T.D., Philp, R.P., Sheppard, C.M., Weston, R.J., Wood, T.A. and Woolhouse, A.D. 1988. Geochemical application of sterane and triterpane biomarkers to a description of oils from the Taranaki Basin in New Zealand. *Organic Geochemistry*. **12**(2),pp.123–135.

Dahl, J.E.P., Moldowan, J.M., Teerman, S.C., McCaffrey, M.A., Sundararaman, P. and Stelting, C.E. 1994. Source rock quality determination from oil biomarkers I: A new geochemical technique. *AAPG Bulletin*. **78**(10),pp.1507–1526.

Dahl, T.W., Siggaard-Andersen, M.-L., Schovsbo, N.H., Persson, D.O., Husted, S., Hougård, I.W., Dickson, A.J., Kjær, K. and Nielsen, A.T. 2019. Brief oxygenation events in locally anoxic oceans during the Cambrian solves the animal breathing paradox. *Scientific Reports*. **9**(1).

Dal Corso, J., Mietto, P., Newton, R.J., Pancost, R.D., Preto, N., Roghi, G. and Wignall, P.B. 2012. Discovery of a major negative 13C spike in the Carnian (late triassic) linked to the eruption of Wrangellia Flood Basalts. *Geology*. **40**(1),pp.79–82.

Dall, W.H. 1908. The Mollusca and the Brachiopoda *In*: *Reports on the scientific results of the expedition to the eastern tropical Pacific, in charge of the Alexander Agassiz, by the U.S. fish commission steamer "Albatross", from October, 1904, to March 1905, Lieit. Commander L. M. Garrett, U.S.C.N commanding*. Boston, Massachusetts: Bulletin of the Museum of Comparative Zoology at Harvard Collage, pp. 372–373.

Dando, P.R. and Southward, A.J. 1986. Chemoautotrophy in Bivalve Molluscs of the Genus Thyasira. *Journal of the Marine Biological Association of the United Kingdom*. **66**(4),pp.915–929.

Danise, S., Twitchett, R.J., Little, C.T.S. and Clémence, M.-E. 2013. The Impact of Global Warming and Anoxia on Marine Benthic Community Dynamics: an Example from the Toarcian (Early Jurassic). *PLoS ONE*. **8**(2),p.e56255.

De Graaf, W., Damsté, J.S.S. and de Leeuw, J.W. 1992. Laboratory simulation of natural sulphurization: I. Formation of monomeric and oligomeric isoprenoid polysulphides by low-temperature reactions of inorganic polysulphides with phytol and phytadienes. *Geochimica et Cosmochimica Acta*. **56**(12),pp.4321–4328.

Deer, W.A., Howie, R.A. and Zussman, J. (2013) *An introduction to the rock-forming minerals*. London: Mineralogical Society of Great Britain & Ireland.

Dekov, V.M., Maynard, J.B., Kamenov, G.D., Rouxel, O., Lalonde, S. and Juranov, S. 2020. Origin of the Oligocene manganese deposit at Obrochishte (Bulgaria): Insights from C, O, Fe, Sr, Nd, and Pb isotopes. *Ore Geology Reviews*. **122**,p.103550.

Del Piero, N., Rigaud, S., Takahashi, S., Poulton, S.W. and Martini, R. 2020. Unravelling the paleoecology of flat clams: New insights from an Upper Triassic halobiid bivalve. *Global and Planetary Change*. **190**,p.103195.

Dera, G., Brigaud, B., Monna, F., Laffont, R., Pucéat, E., Deconinck, J.-F., Pellenard, P., Joachimski, M.M. and Durlet, C. 2011. Climatic ups and downs in a disturbed jurassic world. *Geology*. **39**(3),pp.215–218.

Diaz, R.J. and Rosenberg, R. 2008. Spreading Dead Zones and Consequences for Marine Ecosystems. *Science*. **321**(5891),pp.926–929.

Dickinson, W.R. 1988. Provenance and Sediment Dispersal in Relation to Paleotectonics and Paleogeography of Sedimentary Basins *In*: K. L. Kleinspehn and C. Paola, eds. *New Perspectives in Basin Analysis*. New York: Springer, pp. 3–25.

Doyle, P. and Whitham, A.G. 1991. Palaeoenvironments of the Nordenskjöld Formation: an Antarctic Late Jurassic-Early Cretaceous black shale-tuff sequence *In*: *Geological Society, London, Special Publications Volume 58: Modern and Ancient Continental Shelf Anoxia*. Geological Society of London Special Publications. London: The Geological Society, pp. 397–414.

Dubilier, N., Bergin, C. and Lott, C. 2008. Symbiotic diversity in marine animals: the art of harnessing chemosynthesis. *Nature Reviews Microbiology*. **6**(10),pp.725–740.

Duff, K.L. 1975. Palaeoecology of a bituminous shale - the Lower Oxford Clay of central England. *Palaeontology*. **18**(3),pp.443–482.

Dufour, S.C. and Felbeck, H. 2003. Sulphide mining by the superextensile foot of symbiotic thyasirid bivalves. *Nature*. **426**(6962),pp.65–67.

Dumas, S., Arnott, R.W.C. and Southard, J.B. 2005. Experiments on Oscillatory-Flow and Combined-Flow Bed Forms: Implications for Interpreting Parts of the Shallow-Marine Sedimentary Record. *Journal of Sedimentary Research*. **75**(3),pp.501–513.

Dypvik, H. and Harris, N.B. 2001. Geochemical facies analysis of fine-grained siliciclastics using th/u, Zr/Rb and (Zr+RB)/Sr ratios. *Chemical Geology*. **181**(1-4),pp.131–146.

Einsele, G., Seilacher, A. and Kauffman, E.G. 1988. The Community Structure of "Shell Islands" on Oxygen Depleted Substrates in Mesozoic Dark Shales and Laminated Carbonates (Abstract) *In*: *Cyclic and Event Stratification*. New York: Springer-Verlang, pp. 502–503.

Erickson, B.E. and Helz, G.R. 2000. Molybdenum(VI) speciation in Sulfidic Waters: *Geochimica et Cosmochimica Acta*. **64**(7),pp.1149–1158.

Etheridge, S.M. 2010. Paralytic shellfish poisoning: Seafood Safety and human health perspectives. *Toxicon*. **56**(2),pp.108–122.

Farrell, Ú.C., Martin, M.J., Hagadorn, J.W., Whiteley, T. and Briggs, D.E.G. 2009. Beyond Beecher's trilobite bed: Widespread pyritization of soft tissues in the late ordovician taconic foreland basin. *Geology*. **37**(10),pp.907–910.

Feeley, K.J., Bravo-Avila, C., Fadrique, B., Perez, T.M. and Zuleta, D. 2020. Climate-driven changes in the composition of New World Plant Communities. *Nature Climate Change*. **10**(10),pp.965–970.

Fernex, F., Février, G., Bénaïm, J. and Arnoux, A. 1992. Copper, lead and zinc trapping in Mediterranean deep-sea sediments: probable coprecipitation with Mn and Fe. *Chemical Geology*. **98**(3-4),pp.293–306.

Fox, C.P., Cui, X., Whiteside, J.H., Olsen, P.E., Summons, R.E. and Grice, K. 2020. Molecular and isotopic evidence reveals the end-triassic carbon isotope excursion is not from massive exogenous light carbon. *Proceedings of the National Academy of Sciences*. **117**(48),pp.30171–30178.

French, K.L., Birdwell, J.E. and Whidden, K.J. 2019. Geochemistry of a thermally immature Eagle Ford Group drill core in central Texas. *Organic Geochemistry*. **131**,pp.19–33.

French, K.L., Sepúlveda, J., Trabucho-Alexandre, J., Gröcke, D.R. and Summons, R.E. 2014. Organic geochemistry of the early Toarcian oceanic anoxic event in Hawsker Bottoms, Yorkshire, England. *Earth and Planetary Science Letters*. **390**,pp.116–127.

Fustic, M., Nair, R., Wetzel, A., Siddiqui, R., Matthews, W., Wust, R., Bringue, M. and Radovic, J. 2021. Bioturbation, heavy mineral concentration, and high gamma-ray activity in the Lower Cretaceous McMurray Formation, Canada. *Palaeogeography, Palaeoclimatology, Palaeoecology*. **564**,p.110187.

Galic, N., Hawkins, T. and Forbes, V.E. 2019. Adverse impacts of hypoxia on aquatic invertebrates: A meta-analysis. *Science of The Total Environment*. **652**,pp.736–743.

Ghadeer, S.G. and Macquaker, J.H.S. 2011. Sediment transport processes in an ancient mud-dominated succession: a comparison of processes operating in marine offshore settings and anoxic basinal environments. *Journal of the Geological Society*. **168**(5),pp.1121–1132.

Ghadeer, S.G. and Macquaker, J.H.S. 2012. The role of event beds in the preservation of organic carbon in fine-grained sediments: Analyses of the sedimentological processes operating during deposition of the Whitby Mudstone Formation (Toarcian, Lower Jurassic) preserved in northeast England. *Marine and Petroleum Geology*. **35**(1),pp.309–320.

Giger, W., Schaffner, C. and Wakeham, S.G. 1980. Aliphatic and olefinic hydrocarbons in recent sediments of Greifensee, Switzerland. *Geochimica et Cosmochimica Acta*. **44**(1),pp.119–129.

Giner, J.L. and Djerassi, C. 1991. Biosynthetic studies of marine lipids. 31. Evidence for a protonated cyclopropyl intermediate in the biosynthesis of 24-propylidenecholesterol. *Journal of the American Chemical Society*. **113**(4),pp.1386–1393.

Goldring, R., Pollard, J.E. and Taylor, A.M. 1991. Anconichnus horizontalis: A Pervasive Ichnofabric-Forming Trace Fossil in Post-Paleozoic Offshore Siliciclastic Facies. *PALAIOS*. **6**(3),pp.250–263.

González, M.A. 2015. Aromatic abietane diterpenoids: Their biological activity and synthesis. *Natural Product Reports*. **32**(5),pp.684–704.

Govin, A., Holzwarth, U., Heslop, D., Ford Keeling, L., Zabel, M., Mulitza, S., Collins, J.A. and Chiessi, C.M. 2012. Distribution of major elements in Atlantic surface sediments (36°N-49°S): Imprint of Terrigenous Input and Continental Weathering. *Geochemistry, Geophysics, Geosystems*. **13**(1).

Grabenstatter, J., Méhay, S., McIntyre-Wressnig, A., Giner, J.-L., Edgcomb, V.P., Beaudoin, D.J., Bernhard, J.M. and Summons, R.E. 2013. Identification of 24-n-propylidenecholesterol in a member of the Foraminifera. *Organic Geochemistry*. **63**,pp.145–151.

Grantham, P.J. 1986. The occurence of unusual C27 and C29 Sterane predominances in two types of Oman Crude Oil. *Organic Geochemistry*. **9**(1),pp.1–10.

Grantham, P.J. and Wakefield, L.L. 1988. Variations in the sterane carbon number distributions of marine source rock derived crude oils through geological time. *Organic Geochemistry*. **12**(1),pp.61–73.

Grice, K. and Eiserbeck, C. 2014. 12.3 The Analysis and Application of Biomarkers *In*: P. G. Falkowski, K. H. Freeman, H. D. Holland and K. K. Turekin, eds. *Volume 12: Organic Geochemistry*. Treatise on Geochemistry. Elsevier, pp. 47–78.

DOI: https://doi.org/10.1016/B978-0-08-095975-7.01006-8

Grice, K., Schaeffer, P., Schwark, L. and Maxwell, J. 1996. Molecular indicators of palaeoenvironmental conditions in an immature Permian shale (Kupferschiefer, Lower Rhine Basin, north-West Germany) from free and S-bound lipids. *Organic Geochemistry*. **25**(3-4),pp.131–147.

Griffin, N.J.G. and Aken, M.E. 1993. RHYTHMIC SETTLING BEHAVIOR IN PYRAMIMONAS PARKEAE(PRASINOPHYCEAE)1. *Journal of Phycology*. **29**(1),pp.9–15.

Gómez, J.J., Comas-Rengifo, M.J. and Goy, A. 2016. Palaeoclimatic oscillations in the pliensbachian (early jurassic) of the Asturian Basin (Northern Spain). *Climate of the Past*. **12**(5),pp.1199–1214.

Hagerman, L. 1998. Physiological flexibility; a necessity for life in anoxic and sulphidic habitats. *Hydrobiologia*. **375/376**,pp.241–254.

Hallam, A. 1997. Estimates of the amount and rate of sea-level change across the Rhaetian—Hettangian and Pliensbachian—Toarcian boundaries (latest Triassic to early Jurassic). *Journal of the Geological Society*. **154**(5),pp.773–779.

Harazim, D. and McIlroy, D. 2015. Mud-Rich Density-Driven Flows Along an Early Ordovician Storm-Dominated Shoreline: Implications for Shallow-Marine Facies Models. *Journal of Sedimentary Research*. **85**(5),pp.509–528.

Harazim, D., McIlroy, D., Edwards, N.P., Wogelius, R.A., Manning, P.L., Poduska, K.M., Layne, G.D., Sokaras, D., Alonso-Mori, R. and Bergmann, U. 2015. Bioturbating animals control the mobility of redox-sensitive trace elements in organic-rich mudstone. *Geology*. **43**(11),pp.1007–1010.

Hare, V.J., Loftus, E., Jeffrey, A. and Ramsey, C.B. 2018. Atmospheric CO2 effect on stable carbon isotope composition of Terrestrial Fossil Archives. *Nature Communications*. **9**(1).

Hautevelle, Y., Michels, R., Malartre, F. and Trouiller, A. 2006. Vascular plant biomarkers as proxies for palaeoflora and palaeoclimatic changes at the Dogger/malm transition of the Paris Basin (France). *Organic Geochemistry*. **37**(5),pp.610–625.

Hayes, J.M. 2001. Fractionation of carbon and hydrogen isotopes in biosynthetic processes. *Reviews in Mineralogy and Geochemistry*. **43**(1),pp.225–277.

Hazra, B., Wood, D.A., Mani, D., Singh, P.K. and Singh, A.K. 2019. *In*: *Evaluation of Shale Source Rocks and Reservoirs*. Petroleum Engineering. Cham, Switzerland: Springer Nature, pp. 7–55.

DOI: https://doi.org/10.1007/978-3-030-13042-8

He, T., Wignall, P.B., Newton, R.J., Atkinson, J.W., Keeling, J.F.J., Xiong, Y. and Poulton, S.W. 2022. Extensive marine anoxia in the European epicontinental sea during the end-Triassic mass extinction. *Global and Planetary Change*. **210**,p.103771.

Heier, K.S. and Adams, J.A.S. 1964. The geochemistry of the alkali metals. *Physics and Chemistry of the Earth*. **5**,pp.253–381.

Heindel, K., Foster, W.J., Richoz, S., Birgel, D., Roden, V.J., Baud, A., Brandner, R., Krystyn, L., Mohtat, T., Koşun, E., Twitchett, R.J., Reitner, J. and Peckmann, J. 2018. The formation of microbial-metazoan bioherms and biostromes following the latest Permian Mass Extinction. *Gondwana Research*. **61**,pp.187–202.

Helz, G.R. and Vorlicek, T.P. 2019. Precipitation of molybdenum from euxinic waters and the role of organic matter. *Chemical Geology*. **509**,pp.178–193.

Helz, G.R., Miller, C.V., Charnock, J.M., Mosselmans, J.F.W., Pattrick, R.A.D., Garner, C.D. and Vaughan, D.J. 1996. Mechanism of molybdenum removal from the sea and its concentration in black shales: Exafs Evidence. *Geochimica et Cosmochimica Acta*. **60**(19),pp.3631–3642.

Hendelberg, M. and Jensen, P. 1993. Vertical distribution of the nematode fauna in a coastal sediment influenced by seasonal hypoxia in the bottom water. *Ophelia*. **37**(2),pp.83–94.

Henderson, R.A. 2004. A Mid-Cretaceous Association of Shell Beds and Organic-rich Shale: Bivalve Exploitation of a Nutrient-Rich, Anoxic Sea-floor Environment . *PALAIOS*. **19**(2),pp.156–169.

Hendrickx, M., Valentich-Scott, P. and Suárez-Mozo, N. 2016. Deep-water bivalve mollusks collected during the TALUD XV cruise off the west coast of the southern Baja California Peninsula, Mexico. *Biodiversity Data Journal*. **4**,p.e8661.

Hesselbo, S.P. 2008. Sequence stratigraphy and inferred relative sea-level change from the onshore British jurassic. *Proceedings of the Geologists' Association*. **119**(1),pp.19–34.

Hesselbo, S.P. and Jenkyns, H.C. 1995. A comparison of the Hettangian to Bajocian successions of Dorset and Yorkshire *In*: P. D. Taylor, ed. *Field Geology of the British Jurassic*. London: The Geological Society, pp. 105–150.

Hesselbo, S.P., Gröcke, D.R., Jenkyns, H.C., Bjerrum, C.J., Farrimond, P., Morgans Bell, H.S. and Green, O.R. 2000. Massive dissociation of gas hydrate during a Jurassic oceanic anoxic event. *Nature*. **406**(6794),pp.392–395.

Hesselbo, S.P., Jenkyns, H.C., Duarte, L.V. and Oliveira, L.C.V. 2007. Carbon-isotope record of the Early Jurassic (Toarcian) Oceanic Anoxic Event from fossil wood and marine carbonate (Lusitanian Basin, Portugal). *Earth and Planetary Science Letters*. **253**(3-4),pp.455–470.

Hesselbo, S.P. and Pieńkowski, G. (2011) 'Stepwise atmospheric carbon-isotope excursion during the Toarcian Oceanic anoxic event (early jurassic, polish basin)', *Earth and Planetary Science Letters*, 301(1–2), pp. 365–372. doi:10.1016/j.epsl.2010.11.021.

Hesselbo, S.P., Little, C.T.S., Ruhl, M., Thibault, N. and Ullmann, C.V. 2020. Comments on "Paleosalinity determination in ancient epicontinental seas: A case study of the T-OAE in the Cleveland Basin (UK)" by Remirez, M. N. and Algeo, T. J. *Earth-Science Reviews*. **208**,p.103290.

Heusser, L. and Balsam, W.L. 1977. Pollen distribution in the Northeast Pacific Ocean. *Quaternary Research*. **7**(1),pp.45–62.

Hillaire–Marcel, C., De Vernal, A., Calvert, S.E. and Pedersen, T.F. 2007. Elemental Proxies for Palaeoclimatic and Palaeoceanographic Variability in Marine Sediments: Interpretation and Application *In*: *Developments in Marine Geology 1: Proxies in Late Cenozoic Paleoceanography*. Elsevier, pp. 597–644.

Hollaar, T.P., Hesselbo, S.P., Deconinck, J.-F., Damaschke, M., Ullmann, C.V., Jiang, M. and Belcher, C.M. 2023. Environmental changes during the onset of the late Pliensbachian event (early jurassic) in the Cardigan Bay Basin, Wales. *Climate of the Past*. **19**(5),pp.979–997.

Hollingworth, N.T.J. and Wignall, P.B. 1992. The callovian-oxfordian boundary in Oxfordshire and Wiltshire based on two new temporary sections. *Proceedings of the Geologists' Association*. **103**(1),pp.15–30.

Hopkins, J.S. 1950. Differential Flotation and Deposition of Coniferous and Deciduous Tree Pollen. *Ecology*. **31**(4),pp.633–641.

Howard, A.S. 1984. Palaeoecology, sedimentology and depositional environments of the middle lias of North Yorkshire.

Howard, A.S. 1985. Lithostratigraphy of the Staithes Sandstone and Cleveland Ironstone formations (Lower Jurassic) of north-east Yorkshire. *Proceedings of the Yorkshire Geological Society*. **45**(4),pp.261–275.

Howarth, M.K. 1955. DOMERIAN OF THE YORKSHIRE COAST. *Proceedings of the Yorkshire Geological Society*. **30**(2),pp.147–175.

Howarth, M.K. 1962. THE JET ROCK SERIES AND THE ALUM SHALE SERIES OF THE YORKSHIRE COAST. *Proceedings of the Yorkshire Geological Society*. **33**(4),pp.381–422.

Howarth, M.K. 1973. The stratigraphy and ammonite fauna of the Upper Liassic Grey Shales of the Yorkshire coast. *Bulletin of the British Museum (Natural History): Geology*. **24**(4),pp.237–277.

Huang, C. and Hesselbo, S.P. 2014. Pacing of the toarcian oceanic anoxic event (early jurassic) from astronomical correlation of marine sections. *Gondwana Research*. **25**(4),pp.1348–1356.

Huang, W.-Y. and Meinschein, W.G. 1979. Sterols as ecological indicators. *Geochimica et Cosmochimica Acta*. **43**(5),pp.739–745.

Huckriede, H. and Meischner, D. 1996. Origin and environment of manganese-rich sediments within black-shale basins. *Geochimica et Cosmochimica Acta*. **60**(8),pp.1399–1413.

Hudson, J.D., Clements, R.G., Riding, J.B., Wakefield, M.I. and Walton, W. 1995. Jurassic paleosalinities and brackish-water communities: A case study. *PALAIOS*. **10**(5),p.392.

Huerta-Diaz, M.A. and Morse, J.W. 1992. Pyritization of trace metals in anoxic marine sediments. *Geochimica et Cosmochimica Acta*. **56**(7),pp.2681–2702.

Hughes, W.B., Holba, A.G. and Dzou, L.I.P. 1995. The ratios of dibenzothiophene to phenanthrene and pristane to phytane as indicators of depositional environment and lithology of petroleum source rocks. *Geochimica et Cosmochimica Acta*. **59**(17),pp.3581–3598.

Izumi, K., Kemp, D.B., Itamiya, S. and Inui, M. 2018. Sedimentary evidence for enhanced hydrological cycling in response to rapid carbon release during the early Toarcian Oceanic anoxic event. *Earth and Planetary Science Letters*. **481**,pp.162–170.

Jaraula, C.M.B., Grice, K., Twitchett, R.J., Böttcher, M.E., LeMetayer, P., Dastidar, A.G. and Opazo, L.F. 2013. Elevated PCO2 leading to late triassic extinction, persistent photic zone euxinia, and rising sea levels. *Geology*. **41**(9),pp.955–958.

Jefferies, R.P.S. and Minton, P. 1965. The mode of life of two Jurassic species of 'Posidonia' (Bivalvia). *Palaeontology*. **8**(1),pp.156–185.

Jeffree, C.E. 2006. The fine structure of the plant cuticle *In*: M. Riederer and C. Müller, eds. *Biology of the Plant Cuticle*. Annual Plant Reviews. Oxford: Blackwell, pp. 11–110.

Jenkyns, H.C. 1988. The early Toarcian (Jurassic) anoxic event; stratigraphic, sedimentary and geochemical evidence. *American Journal of Science*. **288**(2),pp.101–151.

Jenkyns, H.C. 2010. Geochemistry of oceanic anoxic events. *Geochemistry, Geophysics, Geosystems*. **11**(3),pp.n/a-n/a.

Jenkyns, H.C., Géczy, B. and Marshall, J.D. 1991. Jurassic Manganese Carbonates of Central Europe and the Early Toarcian Anoxic Event. *The Journal of Geology*. **99**(2),pp.137–149.

Jiang, C., Alexander, R., Kagi, R.I. and Murray, A.P. 1998. Polycyclic aromatic hydrocarbons in ancient sediments and their relationships to palaeoclimate. *Organic Geochemistry*. **29**(5-7),pp.1721–1735.

John, C.M., Banerjee, N.R., Longstaffe, F.J., Sica, C., Law, K.R. and Zachos, J.C. 2012. Clay assemblage and oxygen isotopic constraints on the weathering response to the paleocene-eocene thermal maximum, East Coast of North America. *Geology*. **40**(7),pp.591–594.

Jones, D.L. 1993. *Cycads of the world*. Washington, D.C.: Smithsonian Institution Press.

Jørgensen, B.B. 1980. Seasonal Oxygen Depletion in the Bottom Waters of a Danish Fjord and Its Effect on the Benthic Community. *Oikos*. **34**(1),p.68.

Kasprak, A.H., Sepúlveda, J., Price-Waldman, R., Williford, K.H., Schoepfer, S.D., Haggart, J.W., Ward, P.D., Summons, R.E. and Whiteside, J.H. 2015. Episodic photic zone euxinia in the northeastern Panthalassic Ocean during the end-triassic extinction. *Geology*. **43**(4),pp.307–310.

Kauffman, E.G. 1978. Benthic environments and palaeoecology of the Posidonienschiefer (Toarcian). *Neues Jahrbuch für Geologie und Paläontologie Abhandlungen*. **157**,pp.18–36.

Kauffman, E.G. 1982. The community structure of "shell islands" on oxygen depleted substrates in Mesozoic dark shales and laminated carbonates (abstract) *In*: G. Einsele and A. Seilacher, eds. *Cyclic and Event Stratification*. Berlin Heidelberg New York: Springer-Verlag, pp. 502–503.

Kemp, D.B., Coe, A.L., Cohen, A.S. and Schwark, L. 2005. Erratum: Astronomical pacing of methane release in the Early Jurassic period. *Nature*. **438**(7068),pp.696–696.

Kemp, D.B., Coe, A.L., Cohen, A.S. and Weedon, G.P. 2011. Astronomical forcing and chronology of the early toarcian (early 325urassic) oceanic anoxic event in Yorkshire, UK. Paleoceanography. 26(4).

Kemp, D.B., Fraser, W.T. and Izumi, K. 2018. Stratigraphic completeness and resolution in an ancient Mudrock succession. *Sedimentology*. **65**(6),pp.1875–1890.

Killops, S.D. 1991. Novel aromatic hydrocarbons of probable bacterial origin in a Jurassic lacustrine sequence. *Organic Geochemistry*. **17**(1),pp.25–36.

Kleinspehn, K.L., Paola, C. and Dickinson, W.R. 1988. Provenance and Sediment Dispersal in Relation to Paleotectonics and Paleogeography of Sedimentary Basins *In*: *New Perspectives in Basin Analysis*. New York: Springer-Verlag, pp. 3–25.

Klinkhammer, G.P. and Bender, M.L. 1980. The Distribution of Manganese in the Pacific Ocean. *Earth and Planetary Science Letters*. **46**,pp.361–384.

Klinkhammer, G.P. and Palmer, M.R. 1991. Uranium in the oceans: Where it goes and why. *Geochimica et Cosmochimica Acta*. **55**(7),pp.1799–1806.

Kodner, R.B., Pearson, A., Summons, R.E. and Knoll, A.H. 2008. Sterols in red and green algae: Quantification, phylogeny, and relevance for the interpretation of geologic steranes. *Geobiology*. **6**(4),pp.411–420.

Kohn, M.J. 2010. Carbon isotope compositions of terrestrial C3 plants as indicators of (paleo)ecology and (paleo)climate. *Proceedings of the National Academy of Sciences*. **107**(46),pp.19691–19695.

Kong, X., Jiang, Z., Han, C. and Zhang, R. 2020. Organic matter enrichment and hydrocarbon accumulation models of the marlstone in the Shulu Sag, Bohai Bay Basin, Northern China. *International Journal of Coal Geology*. **217**,p.103350.

Koopmans, M.P., Köster, J., Van Kaam-Peters, H.M.E., Kenig, F., Schouten, S., Hartgers, W.A., de Leeuw, J.W. and Sinninghe Damsté, J.S. 1996. Diagenetic and catagenetic

products of Isorenieratene: Molecular Indicators for Photic Zone Anoxia. *Geochimica et Cosmochimica Acta*. **60**(22),pp.4467–4496.

Koopmans, M.P., Rijpstra, W.I.C., Klapwijk, M.M., de Leeuw, J.W., Lewan, M.D. and Sinninghe Damsté, J.S. 1999. A thermal and chemical degradation approach to decipher pristane and phytane precursors in sedimentary organic matter. *Organic Geochemistry*. **30**(9),pp.1089–1104.

Koppelhus, E.B. and Dam, G. 2003. Palynostratigraphy and palaeoenvironments of the RÆVEKLØFT, Gule Horn and OSTREAELV formations (lower–middle jurassic), Neill Klinter Group, Jameson Land, East Greenland. *Geological Survey of Denmark and Greenland Bulletin*. **1**,pp.723–775.

Korte, C. and Hesselbo, S.P. 2011. Shallow marine carbon and oxygen isotope and elemental records indicate icehouse-greenhouse cycles during the early jurassic. *Paleoceanography*. **26**(4).

Korte, C., Hesselbo, S.P., Ullmann, C.V., Dietl, G., Ruhl, M., Schweigert, G. and Thibault, N. 2015. Jurassic climate mode governed by Ocean Gateway. *Nature Communications*. **6**(1).

Krügel, H., Krubasik, P., Weber, K., Saluz, H.P. and Sandmann, G. 1999. Functional analysis of genes from Streptomyces griseus involved in the synthesis of isorenieratene, a carotenoid with aromatic end groups, revealed a novel type of carotenoid desaturase. *Biochimica et Biophysica Acta (BBA) - Molecular and Cell Biology of Lipids*. **1439**(1),pp.57–64.

Köster, J., Van Kaam-Peters, H.M.E., Koopmans, M.P., De Leeuw, J.W. and Sinninghe Damsté, J.S. 1997. Sulphurisation of homohopanoids: Effects on carbon number distribution, speciation, and epimer ratios. *Geochimica et Cosmochimica Acta*. **61**(12),pp.2431–2452.

Küspert, W. 1982. Environmental Changes During Oil Shale Deposition as Deduced from Stable Isotope Ratios *In*: G. Einsele and A. Seilacher, eds. *Cyclic and Event Stratification*. Berlin Heidelburg New York: Springer-Verlag, pp. 482–501.

Laffoley, D., Baxter, J.M., Pitcher, G.C. and Jacinto, G.S. 2019. Ocean deoxygenation links to harmful algal blooms *In*: *Ocean deoxygenation: Everyone's problem*. Gland, Switzerland: IUCN, pp. 137–153.

Lam, P. and Kuypers, M.M.M. 2011. Microbial Nitrogen Cycling Processes in Oxygen Minimum Zones. *Annual Review of Marine Science*. **3**(1),pp.317–345.

Lange, I.M., Reynolds, R.C. and Lyons, J.B. 1966. K/Rb ratios in coexisting K-feldspars and biotites from some New England granites and metasediments. *Chemical Geology*. **1**,pp.317–322.

Lehndorff, E. and Schwark, L. 2004. Biomonitoring of air quality in the Cologne Conurbation using pine needles as a passive sampler—Part II: polycyclic aromatic hydrocarbons (PAH). *Atmospheric Environment*. **38**(23),pp.3793–3808.

Lehndorff, E. and Schwark, L. 2009. Biomonitoring airborne parent and alkylated three-ring PAHs in the Greater Cologne Conurbation I: Temporal accumulation patterns. *Environmental Pollution*. **157**(4),pp.1323–1331.

Levin, L. 2002. Deep-Ocean Life Where Oxygen Is Scarce. *American Scientist*. **90**(5),p.436.

Lewis, J. 1988. Cysts and sediments: Gonyaulax polyedra (Lingulodinium machaerophorum) in Loch Creran. *Journal of the Marine Biological Association of the United Kingdom*. **68**,pp.701–714.

Li, M., Larter, S.R., Taylor, P., Jones, D.M., Bowler, B. and Bjorøy, M. 1995. Biomarkers or not biomarkers? A new hypothesis for the origin of pristane involving derivation from methyltrimethyltridecylchromans (MTTCs) formed during diagenesis from chlorophyll and alkylphenols. *Organic Geochemistry*. **23**(2),pp.159–167.

Li, M., Lee, Y.J., Testa, J.M., Li, Y., Ni, W., Kemp, W.M. and Di Toro, D.M. 2016. What drives interannual variability of hypoxia in Chesapeake Bay: Climate forcing versus nutrient loading? *Geophysical Research Letters*. **43**(5),pp.2127–2134.

Li, S., Wignall, P.B., Poulton, S.W., Hedhli, M. and Grasby, S.E. 2022. Carbonate shutdown, phosphogenesis and the variable style of marine anoxia in the late Famennian (Late

Devonian) in western Laurentia. *Palaeogeography, Palaeoclimatology, Palaeoecology*. **589**,p.110835.

Liaaen-Jensen, S., Renstrøm, B., Ramdahl, T., Hallenstvet, M. and Bergquist, P. 1982. Carotenoids of marine sponges. *Biochemical Systematics and Ecology*. **10**(2),pp.167–174.

Litchman, E., Klausmeier, C.A., Miller, J.R., Schofield, O.M. and Falkowski, P.G. 2006. Multi-nutrient, multi-group model of present and future oceanic phytoplankton communities. *Biogeosciences*. **3**(4),pp.585–606.

Little, C.T.S. 1995. The Pliensbachian-Toarcian (Lower Jurassic) extinction event.

Little, C.T.S. and Benton, M.J. 1995. Early Jurassic mass extinction: A global long-term event. *Geology*. **23**(6),p.495.

Littler, K., Hesselbo, S.P. and Jenkyns, H.C. 2010. A carbon-isotope perturbation at the Pliensbachian–Toarcian boundary: evidence from the Lias Group, NE England. *Geological Magazine*. **147**(2),pp.181–192.

Liu, F., Peng, H., Bomfleur, B., Kerp, H., Zhu, H. and Shen, S. 2020. Palynology and vegetation dynamics across the Permian–triassic boundary in Southern Tibet. *Earth-Science Reviews*. **209**,p.103278.

Lu, P., Nuhfer, N.T., Kelly, S., Li, Q., Konishi, H., Elswick, E. and Zhu, C. 2011. Lead coprecipitation with iron oxyhydroxide nano-particles. *Geochimica et Cosmochimica Acta*. **75**(16),pp.4547–4561.

Lyons, T.W. and Severmann, S. 2006. A critical look at iron paleoredox proxies: New insights from modern euxinic marine basins. *Geochimica et Cosmochimica Acta*. **70**(23),pp.5698–5722.

Ma, J., French, K.L., Cui, X., Bryant, D.A. and Summons, R.E. 2021. Carotenoid biomarkers in Namibian shelf sediments: Anoxygenic photosynthesis during sulfide eruptions in the Benguela Upwelling System. *Proceedings of the National Academy of Sciences*. **118**(29).

MacLeod, K.G. and Orr, W.N. 1993. The taphonomy of Maastrichtian inoceramids in the Basque region of France and Spain and the pattern of their decline and disappearance. *Paleobiology*. **19**(2),pp.235–250.

MacQuaker, J.H.S., Keller, M.A. and Davies, S.J. 2010. Algal Blooms and "Marine Snow": Mechanisms That Enhance Preservation of Organic Carbon in Ancient Fine-Grained Sediments. *Journal of Sedimentary Research*. **80**(11),pp.934–942.

MacRae, R.A., Fensome, R.A. and Williams, G.L. 1996. Fossil dinoflagellate diversity, originations, and extinctions and their significance. *Canadian Journal of Botany*. **74**(11),pp.1687–1694.

Marynowski, L., Szełęg, E., Jędrysek, M.O. and Simoneit, B.R.T. 2011. Effects of weathering on organic matter Part II: Fossil wood weathering and implications for organic geochemical and petrographic studies. *Organic Geochemistry*. **42**(9),pp.1076–1088.

Mathews, R.P., Singh, B.D., Singh, V.P., Singh, A., Singh, H., Shivanna, M., Dutta, S., Mendhe, V.A. and Chetia, R. 2020. Organo-petrographic and geochemical characteristics of gurha lignite deposits, Rajasthan, India: Insights into the palaeovegetation, palaeoenvironment and hydrocarbon source rock potential. *Geoscience Frontiers*. **11**(3),pp.965–988.

Matthewson, A.P., Shimmield, G.B., Kroon, D. and Fallick, A.E. 1995. A 300 kyr high-resolution aridity record of the North African continent. *Paleoceanography*. **10**(3),pp.677–692.

Maynard, J.B. 2010. The Chemistry of Manganese Ores through Time: A Signal of Increasing Diversity of Earth-Surface Environments. *Economic Geology*. **105**(3),pp.535–552.

McArthur, J.M. 2019. Early Toarcian black shales: A response to an oceanic anoxic event or anoxia in marginal basins? *Chemical Geology*. **522**,pp.71–83.

McArthur, J.M., Algeo, T.J., van de Schootbrugge, B., Li, Q. and Howarth, R.J. 2008. Basinal restriction, black shales, Re-Os dating, and the Early Toarcian (Jurassic) oceanic anoxic event. *Paleoceanography*. **23**(4),pp.n/a-n/a.

McArthur, J.M., Donovan, D.T., Thirlwall, M.F., Fouke, B.W. and Mattey, D. 2000. Strontium isotope profile of the early Toarcian (Jurassic) oceanic anoxic event, the duration of ammonite biozones, and belemnite palaeotemperatures. *Earth and Planetary Science Letters*. **179**(2),pp.269–285.

McElwain, J.C., Wade-Murphy, J. and Hesselbo, S.P. 2005. Changes in carbon dioxide during an oceanic anoxic event linked to intrusion into Gondwana coals. *Nature*. **435**(7041),pp.479–482.

McInerney, F.A. and Wing, S.L. 2011. The paleocene-eocene thermal maximum: A perturbation of carbon cycle, climate, and biosphere with implications for the future. *Annual Review of Earth and Planetary Sciences*. **39**(1),pp.489–516.

McManus, J., Berelson, W.M., Klinkhammer, G.P., Hammond, D.E. and Holm, C. 2005. Authigenic uranium: Relationship to oxygen penetration depth and organic carbon rain. *Geochimica et Cosmochimica Acta*. **69**(1),pp.95–108.

McRoberts, C.A. and Stanley, G.D. 1989. A unique bivalve–algae life assemblage from the Bear Gulch Limestone (Upper Mississippian) of Central Montana. *Journal of Paleontology*. **63**(5),pp.578–581.

Merian, E., Anke, M., Ihnat, M., Stoeppler, M. and Wedepohl, K.H. 2004. The Composition of Earth's Upper Crust, Natural Cycles of Elements, Natural Resources *In*: *Elements and Their Compounds in the Environment: Occurrence, Analysis and Biological Relevance*. Weinheim: WILEY-VCH Verlag GmbH & Co., pp. 3–16.

Mermoud, F., Gülaçar, F.O. and Buchs, A. 1985. 5α(H)-cholestan-3α-ol in sediments: Characterization and geochemical significance. *Geochimica et Cosmochimica Acta*. **49**(2),pp.459–462.

Morford, J.L., Russell, A.D. and Emerson, S. 2001. Trace metal evidence for changes in the redox environment associated with the transition from terrigenous clay to diatomaceous sediment, Saanich Inlet, BC. *Marine Geology*. **174**(1-4),pp.355–369.

Mudie, P.J. 1982. Pollen distribution in recent marine sediments, Eastern Canada. *Canadian Journal of Earth Sciences*. **19**(4),pp.729–747.

Muller, J. 1959. Palynology of Recent Orinoco Delta and Shelf Sediments: Reports of the Orinoco Shelf Expedition; Volume 5. *Micropaleontology*. **5**(1),pp.1–32.

Muramoto, J.A., Honjo, S., Fry, B., Hay, B.J., Howarth, R.W. and Cisne, J.L. 1991. Sulfur, iron and organic carbon fluxes in the Black Sea: Sulfur isotopic evidence for origin of sulfur fluxes. *Deep Sea Research Part A. Oceanographic Research Papers*. **38**.

März, C., Poulton, S.W., Beckmann, B., Küster, K., Wagner, T. and Kasten, S. 2008. Redox sensitivity of P cycling during marine black shale formation: Dynamics of sulfidic and anoxic, non-sulfidic bottom waters. *Geochimica et Cosmochimica Acta*. **72**(15),pp.3703–3717.

März, C., Schnetger, B. and Brumsack, H.-J. 2010. Paleoenvironmental implications of Cenozoic sediments from the central Arctic Ocean (IODP Expedition 302) using inorganic geochemistry. *Paleoceanography*. **25**(3).

März, C., Vogt, C., Schnetger, B. and Brumsack, H.-J. 2011. Variable Eocene-Miocene sedimentation processes and bottom water redox conditions in the Central Arctic Ocean (IODP Expedition 302). *Earth and Planetary Science Letters*. **310**(3-4),pp.526–537.

Naimo, D., Adamo, P., Imperato, M. and Stanzione, D. 2005. Mineralogy and geochemistry of a marine sequence, Gulf of Salerno, Italy. *Quaternary International*. **140-141**,pp.53–63.

Newell, A.J., Vane, C.H., Sorensen, J.P.R., Moss-Hayes, V. and Gooddy, D.C. 2016. Long-term Holocene groundwater fluctuations in a chalk catchment: evidence from Rock-Eval pyrolysis of riparian peats. *Hydrological Processes*. **30**(24),pp.4556–4567.

Newton, R.J. 2001. The Characterisation of Depositional Environments Using Fe, S and C Geochemistry.

O'Brien, N.R. 1990. Significance of lamination in Toarcian (Lower Jurassic) shales from Yorkshire, Great Britain. *Sedimentary Geology*. **67**(1-2),pp.25–34.

Ogg, J.G., Ogg, G.M. and Gradstein, F.M. 2016. *A Concise Geologic Time Scale*. Elsevier.

OLIVER, P.G. 2001. FUNCTIONAL MORPHOLOGY AND DESCRIPTION OF A NEW SPECIES OF AMYGDALUM (MYTILOIDEA) FROM THE OXYGEN MINIMUM ZONE OF THE ARABIAN SEA. *Journal Molluscan Studies*. **67**(2),pp.225–241.

Oschmann, W. 1988. Kimmeridge clay sedimentation — A new cyclic model. *Palaeogeography, Palaeoclimatology, Palaeoecology*. **65**(3-4),pp.217–251.

OSCHMANN, W. 1993. Environmental oxygen fluctuations and the adaptive response of marine benthic organisms. *Journal of the Geological Society*. **150**(1),pp.187–191.

Overmann , J. 2006. Chapter 5.1: The Family Chlorobiaceae *In*: M. Dworkin, S. Falkow, E. Rosenburg, K.-H. Schleifer and E. Stackebrandt, eds. *The Prokaryotes* . New York: Springer, pp. 359–378.

Overnell, J., Brand, T., Bourgeois, W. and Statham, P.J. 2002. Manganese dynamics in the water column of the upper basin of Loch Etive, a Scottish fjord. *Estuarine, Coastal and Shelf Science*. **55**(3),pp.481–492.

Page, K.N. 1995. Biohorizons and zonules: intra-subzonal units in Jurassic ammonite stratigraphy. *Palaeontology*. **38**(4),pp.801–814.

Page, K.N. 2004. A sequence of biohorizons for the subboreal province lower Toarcian in northern Britain and their correlation with a submediterranean standard. *Rivista Italiana di Paleontologia e Stratigrafia*. **110**(1),pp.109–114.

Pan, Y.H., Hu, S.X., Sha, J.G., Zhang, Q.Y., Wang, Y.Q., Zhou, C.Y., Wen, W., Huang, J.Y. and Xie, T. 2014. Early Triassic bivalves from the Feixianguan Formation in Xingyi, Guizhou and the Ximatang Formation in Qiubei, Yunnan (southern China). *Palaeoworld*. **23**(2),pp.143–154.

Pastouret, L., Chamley, H., Delibrias, G., Duplessy, J.C. and Thiede, J. 1978. Late Quaternary climatic changes in western tropical Africa deduced from deep-sea sedimentation off the Niger delta . *Oceanologica Acta*. **1**(2),pp.217–232.

Peacock, C.L. and Sherman, D.M. 2007. Sorption of Ni by birnessite: Equilibrium controls on Ni in seawater. *Chemical Geology*. **238**(1-2),pp.94–106.

Pearce, C.R., Cohen, A.S., Coe, A.L. and Burton, K.W. 2008. Molybdenum isotope evidence for global ocean anoxia coupled with perturbations to the carbon cycle during the Early Jurassic. *Geology*. **36**(3),p.231.

Pedersen, T.F., Shimmield, G.B. and Price, N.B. 1992. Lack of enhanced preservation of organic matter in sediments under the oxygen minimum on the oman margin. *Geochimica et Cosmochimica Acta*. **56**(1),pp.545–551.

Percival, L.M.E., Witt, M.L.I., Mather, T.A., Hermoso, M., Jenkyns, H.C., Hesselbo, S.P., Al-Suwaidi, A.H., Storm, M.S., Xu, W. and Ruhl, M. 2015. Globally Enhanced Mercury deposition during the end-pliensbachian extinction and Toarcian OAE: A link to the Karoo–Ferrar Large Igneous Province. *Earth and Planetary Science Letters*. **428**,pp.267–280.

Peters, K.E. and Moldowan, J.M. 1991. Effects of source, thermal maturity, and biodegradation on the distribution and isomerization of homohopanes in petroleum. *Organic Geochemistry*. **17**(1),pp.47–61.

Peters, K.E., Fraser, T.H., Amris, W., Rustanto, B. and Hermanto, E. 1999. Geochemistry of crude oils from eastern indonesia1. *AAPG Bulletin*. **83**(12),pp.1927–1942.

Peters, K.E., Walters, C.C. and Moldowan, J.M. 2005. *The biomarker guide*. Cambridge: Cambridge University Press.

Piasecki, S. 1986. Palynological analysis of the organic debris in the lower cretaceous jydegård formation, Bornholm, Denmark. *Grana*. **25**(2),pp.119–129.

Pitcher, G.C. and Jacinto, G.S. 2019. 3.3 Ocean deoxygenation links to harmful algal blooms *In*: D. Laffoley and J. M. Baxter, eds. *Ocean deoxygenation: Everyone's problem: Causes, impacts, consequences and solutions*. Gland, Switzerland: IUCN, pp. 137–153.

Plint, A.G. 2013. Mud dispersal across a Cretaceous prodelta: Storm-generated, wave-enhanced sediment gravity flows inferred from mudstone microtexture and microfacies. *Sedimentology*. **61**(3),pp.609–647.

Popp, B.N., Laws, E.A., Bidigare, R.R., Dore, J.E., Hanson, K.L. and Wakeham, S.G. 1998. Effect of phytoplankton cell geometry on carbon isotopic fractionation. *Geochimica et Cosmochimica Acta*. **62**(1),pp.69–77.

Poulton, S.W. 2021. *The iron speciation paleoredox proxy*. Cambridge University Press.

Poulton, S.W. and Canfield, D.E. 2005. Development of a sequential extraction procedure for iron: implications for iron partitioning in continentally derived particulates. *Chemical Geology*. **214**(3-4),pp.209–221.

Poulton, S.W. and Canfield, D.E. 2011. Ferruginous Conditions: A Dominant Feature of the Ocean through Earth's History. *Elements*. **7**(2),pp.107–112.

Poulton, S.W. and Raiswell, R. 2002. The low-temperature geochemical cycle of iron: From continental fluxes to marine sediment deposition. *American Journal of Science*. **302**(9),pp.774–805.

Poulton, S.W., Bottrell, S.H. and Underwood, C.J. 1998. Porewater sulphur geochemistry and fossil preservation during phosphate diagenesis in a Lower Cretaceous Shelf Mudstone. *Sedimentology*. **45**(5),pp.875–887.

Poulton, S.W., Fralick, P.W. and Canfield, D.E. 2010. Spatial variability in oceanic redox structure 1.8 billion years ago. *Nature Geoscience*. **3**(7),pp.486–490.

Poulton, S.W., Krom, M.D. and Raiswell, R. 2004. A revised scheme for the reactivity of iron (oxyhydr)oxide minerals towards dissolved sulfide. *Geochimica et Cosmochimica Acta*. **68**(18),pp.3703–3715.

Powell, J.H. 1984. Lithostratigraphical nomenclature of the Lias Group in the Yorkshire Basin. *Proceedings of the Yorkshire Geological Society*. **45**(1-2),pp.51–57.

Powell, J.H. 2010. Jurassic sedimentation in the Cleveland Basin: a review. *Proceedings of the Yorkshire Geological Society*. **58**(1),pp.21–72.

POWELL, T.G. and McKIRDY, D.M. 1973. Relationship between Ratio of Pristane to Phytane, Crude Oil Composition and Geological Environment in Australia. *Nature Physical Science*. **243**(124),pp.37–39.

Pross, J. 2001. Paleo-oxygenation in Tertiary epeiric seas: evidence from dinoflagellate cysts. *Palaeogeography, Palaeoclimatology, Palaeoecology*. **166**(3-4),pp.369–381.

Quan, T.M., van de Schootbrugge, B., Field, M.P., Rosenthal, Y. and Falkowski, P.G. 2008. Nitrogen isotope and trace metal analyses from the Mingolsheim core (Germany): Evidence for redox variations across the Triassic-Jurassic boundary. *Global Biogeochemical Cycles*. **22**(2),pp.n/a-n/a.

Rabalais, N., Cai, W., Carstensen, J., Conley, D., Fry, B., Hu, X., Quiñones-Rivera, Z., Rosenberg, R., Slomp, C., Turner, E., Voss, M., Wissel, B. and Zhang, J. 2014. Eutrophication-Driven Deoxygenation in the Coastal Ocean. *Oceanography*. **27**(1),pp.172–183.

Rabalais, N.N., Díaz, R.J., Levin, L.A., Turner, R.E., Gilbert, D. and Zhang, J. 2010. Dynamics and distribution of natural and human-caused hypoxia. *Biogeosciences*. **7**(2),pp.585–619.

Radke, M., Welte, D.H. and Willsch, H. 1991. Distribution of alkylated aromatic hydrocarbons and dibenzothiophenes in rocks of the Upper Rhine Graben. *Chemical Geology*. **93**(3-4),pp.325–341.

Raiswell, R. and Anderson, T.F. 2005. Reactive iron enrichment in sediments deposited beneath euxinic bottom waters: constraints on supply by shelf recycling. *Geological Society, London, Special Publications*. **248**(1),pp.179–194.

Raiswell, R. and Berner, R.A. 1985. Pyrite formation in euxinic and semi-euxinic sediments. *American Journal of Science*. **285**(8),pp.710–724.

Raiswell, R. and Canfield, D.E. 1998. Sources of iron for pyrite formation in marine sediments. *American Journal of Science*. **298**(3),pp.219–245.

Raiswell, R. and Canfield, D.E. 2012. The Iron Biogeochemical Cycle Past and Present. *Geochemical Perspectives*. **1**(1),pp.1–220.

Raiswell, R., Buckley, F., Berner, R.A. and Anderson, T.F. 1988. Degree of pyritization of iron as a paleoenvironmental indicator of bottom-water oxygenation. *Journal of Sedimentary Petrology*. **58**(5),pp.812–819.

Raiswell, R., Hardisty, D.S., Lyons, T.W., Canfield, D.E., Owens, J.D., Planavsky, N.J., Poulton, S.W. and Reinhard, C.T. 2018. The iron paleoredox proxies: A guide to the pitfalls, problems and proper practice. *American Journal of Science*. **318**(5),pp.491–526.

Raiswell, R., Newton, R., Bottrell, S.H., Coburn, P.M., Briggs, D.E., Bond, D.P. and Poulton, S.W. 2008. Turbidite depositional influences on the diagenesis of Beecher's trilobite bed and the Hunsruck slate; sites of soft tissue pyritization. *American Journal of Science*. **308**(2),pp.105–129.

Rees, P.M.C.A., Ziegler, A.M. and Valdes, P.J. 2000. 10 - Jurassic phytogeography and climates: new data and model comparisons *In*: B. T. Huber, K. G. MacLeod and S. L. Wing, eds. *Warm Climates in Earth History*. Cambridge University Press, pp. 297–318.

Reinhardt, M., Duda, J.-P., Blumenberg, M., Ostertag-Henning, C., Reitner, J., Heim, C. and Thiel, V. 2018. The taphonomic fate of Isorenieratene in Lower Jurassic shales-controlled by Iron? *Geobiology*. **16**(3),pp.237–251.

Remírez, M.N. and Algeo, T.J. 2020. Paleosalinity determination in ancient epicontinental seas: A case study of the T-OAE in the Cleveland Basin (UK). *Earth-Science Reviews*. **201**,p.103072.

Remírez, M.N. and Algeo, T.J. 2020. Reply to comment on “Remírez, M.N. and Algeo, T.J., 2020. Paleosalinity determination in ancient epicontinental seas: A case study of the T-OAE in the Cleveland Basin (UK). Earth-Science Reviews, 201, 103072” by Stephen P. Hesselbo, Crispin T. S. Little, Micha Ruhl, Nicolas Thibault, and Clemens V. Ullmann. *Earth-Science Reviews*. **208**,p.103291.

RHOADS, D.O.N.A.L.D.C. and MORSE, J.O.H.N.W. 1971. Evolutionary and ecologic significance of oxygen-deficient marine basins. *Lethaia*. **4**(4),pp.413–428.

Rickard, D. 2019. How long does it take a pyrite framboid to form? *Earth and Planetary Science Letters*. **513**,pp.64–68.

Rieley, G., Collier, R.J., Jones, D.M. and Eglinton, G. 1991. The biogeochemistry of Ellesmere Lake, U.K.—I: source correlation of leaf wax inputs to the sedimentary lipid record. *Organic Geochemistry*. **17**(6),pp.901–912.

Ritter, U. 2003. Solubility of petroleum compounds in kerogen. *Organic Geochemistry*. **34**(3),pp.319–326.

Robert, P. and Yapaudjian, L. 1990. Early Cretaceous rift sediments of the Gabon-Congo margin: Lithology and organic matter; tectonic and Paleogeothermal Evolution. *Journal of African Earth Sciences (and the Middle East)*. **10**(1-2),pp.319–330.

Rodrigues, B., Duarte, L.V., Silva, R.L. and Mendonça Filho, J.G. 2020. Sedimentary organic matter and early Toarcian environmental changes in the Lusitanian Basin (Portugal). *Palaeogeography, Palaeoclimatology, Palaeoecology*. **554**,p.109781.

Rohrssen, M., Gill, B.C. and Love, G.D. 2015. Scarcity of the C30 sterane biomarker, 24-n-propylcholestane, in Lower Paleozoic marine paleoenvironments. *Organic Geochemistry*. **80**,pp.1–7.

Rosenthal, Y., Lam, P., Boyle, E.A. and Thomson, J. 1995. Authigenic cadmium enrichments in suboxic sediments: Precipitation and Postdepositional Mobility. *Earth and Planetary Science Letters*. **132**(1-4),pp.99–111.

Ruebsam, W., Mayer, B. and Schwark, L. 2019. Cryosphere carbon dynamics control early Toarcian global warming and sea level evolution. *Global and Planetary Change*. **172**,pp.440–453.

Ruebsam, W., Reolid, M. and Schwark, L. 2020a. δ13C of terrestrial vegetation records Toarcian CO2 and climate gradients. *Nature Scientific Reports*. **10**(1).

Ruebsam, W., Reolid, M., Sabatino, N., Masetti, D. and Schwark, L. 2020b. Molecular paleothermometry of the early Toarcian Climate Perturbation. *Global and Planetary Change*. **195**,p.103351.

Rybicki, M., Marynowski, L., Misz-Kennan, M. and Simoneit, B.R.T. 2016. Molecular tracers preserved in Lower Jurassic “blanowice brown coals” from southern Poland at the onset of coalification: Organic geochemical and Petrological Characteristics. *Organic Geochemistry*. **102**,pp.77–92.

Röhl, H., Schmid-Röhl, A., Oschmann, W., Frimmel, A. and Schwark, L. 2001. The Posidonia Shale (Lower Toarcian) of SW-Germany: an oxygen-depleted ecosystem controlled by sea level and palaeoclimate. *Palaeogeography, Palaeoclimatology, Palaeoecology*. **165**(1-2),pp.27–52.

Saito, M.A., Moffett, J.W., Chisholm, S.W. and Waterbury, J.B. 2002. Cobalt limitation and uptake in prochlorococcus. *Limnology and Oceanography*. **47**(6),pp.1629–1636.

Salem, N.-E. 2013. Geochemical characterisation of the Pliensbachian-Toarcian boundary during the onset of the Toarcian Oceanic Anoxic Event. North Yorkshire, UK.

Sasaki, R. and Shepherd, S.A. 1995. Larval dispersal and recruitment of Haliotis discus hannai and tegula spp. on miyagi coasts, Japan. *Marine and Freshwater Research*. **46**(3),p.519.

Savrda, C.E. and Bottjer, D.J. 1987. The exaerobic zone, a new oxygen-deficient marine biofacies. *Nature*. **327**(6117),pp.54–56.

Savrda, C.E. and Bottjer, D.J. 1991. Oxygen-related biofacies in marine strata: an overview and update. *Geological Society, London, Special Publications*. **58**(1),pp.201–219.

Schatz, W. 2005. Palaeoecology of the Triassic black shale bivalve Daonella—new insights into an old controversy. *Palaeogeography, Palaeoclimatology, Palaeoecology*. **216**(3-4),pp.189–201.

Schieber, J. and Wilson, R.D. 2021. Burrows without a trace—How meioturbation affects rock fabrics and leaves a record of meiobenthos activity in shales and mudstones. *PalZ*. **95**(4),pp.767–791.

Schindel, D.E. 1980. Microstratigraphic sampling and the limits of paleontologic resolution. *Paleobiology*. **6**(4),pp.408–426.

Schmid-Rohl, A. and Rohl, H.-J. 2003. Overgrowth on ammonite conchs: Environmental implications for the lower toarcian posidonia shale. *Palaeontology*. **46**(2),pp.339–352.

Schneider, R.R., Price, B., Müller, P.J., Kroon, D. and Alexander, I. 1997. Monsoon related variations in Zaire (Congo) sediment load and influence of fluvial silicate supply on marine productivity in the east equatorial Atlantic during the last 200,000 years. *Paleoceanography*. **12**(3),pp.463–481.

Schoon, P.L., Heilmann-Clausen, C., Schultz, B.P., Sinninghe Damsté, J.S. and Schouten, S. 2015. Warming and environmental changes in the eastern North Sea basin during the palaeocene–eocene thermal maximum as revealed by biomarker lipids. *Organic Geochemistry*. **78**,pp.79–88.

Schubert, B.A. and Jahren, A.H. 2012. The effect of atmospheric CO2 concentration on Carbon Isotope Fractionation in C3 Land Plants. *Geochimica et Cosmochimica Acta*. **96**,pp.29–43.

Schwark, L. and Empt, P. 2006. Sterane biomarkers as indicators of palaeozoic algal evolution and extinction events. *Palaeogeography, Palaeoclimatology, Palaeoecology*. **240**(1-2),pp.225–236.

Schwark, L. and Frimmel, A. 2004. Chemostratigraphy of the Posidonia Black Shale, SW-Germany II. Assessment of extent and persistence of photic-zone anoxia using aryl isoprenoid distributions. *Chemical Geology*. **206**(3-4),pp.231–248.

Seifert, W.K. and Moldowan, J.M. 1978. Applications of Steranes, terpanes and monoaromatics to the maturation, migration and source of crude oils. *Geochimica et Cosmochimica Acta*. **42**(1),pp.77–95.

Seifert, W. and Kramer, W. 2003. Accessory titanite: An important carrier of zirconium in lamprophyres. *Lithos*. **71**(1),pp.81–98.

Seilacher, A. 1990. Aberrations in bivalve evolution related to photo- and chemosymbiosis. *Historical Biology*. **3**(4),pp.289–311.

Sellanes, J. 2002. sobre los indicadores bioquimicos de la calidad de la materia organica sedimentaria y la meiofauna en un area de surgencia costera de Chile central.

Shang, Y. and Zavada, M.S. 2003. The ultrastructure of cerebropollenites from the jurassic and cretaceous of Asia. Grana. 42(2),pp.102–107.

Shanks, A.L. 1998. Apparent oceanographic triggers to the spawning of the limpet lottia digitalis (Rathke). *Journal of Experimental Marine Biology and Ecology*. **222**(1-2),pp.31–41.

Shen, S.Z., Cao, C.-Q., Henderson, C.M., Wang, X.-D., Shi, G.R., Wang, Y. and Wang, W. 2006. End-permian mass extinction pattern in the Northern Peri-gondwanan region. *Palaeoworld*. **15**(1),pp.3–30.

Silva, R.L., Duarte, L.V., Wach, G.D., Ruhl, M., Sadki, D., Gómez, J.J., Hesselbo, S.P., Xu, W., O'Connor, D., Rodrigues, B. and Filho, J.G.M. 2021. An Early Jurassic (Sinemurian–Toarcian) stratigraphic framework for the occurrence of Organic Matter Preservation Intervals (OMPIs). *Earth-Science Reviews*. **221**,p.103780.

Simms, M.J., Page, K.N., Morton, N. and Chidlaw, N. 2004. Chapter 6: the Cleveland Basin *In*: *British Lower Jurassic stratigraphy*. Peterborough: Joint Nature Conservation Committee, pp. 239–304.

Sinha, E., Michalak, A.M. and Balaji, V. 2017. Eutrophication will increase during the 21st century as a result of precipitation changes. *Science*. **357**(6349),pp.405–408.

Sirevåg, R., Buchanan, B.B., Berry, J.A. and Troughton, J.H. 1977. Mechanisms of CO2 fixation in bacterial photosynthesis studied by the carbon isotope fractionation technique. *Archives of Microbiology*. **112**(1),pp.35–38.

Slater, S.M., Twitchett, R.J., Danise, S. and Vajda, V. 2019. Substantial vegetation response to Early Jurassic global warming with impacts on oceanic anoxia. *Nature Geoscience*. **12**(6),pp.462–467.

Sluijs, A. and Brinkhuis, H. 2009. A dynamic climate and ecosystem state during the paleocene-eocene thermal maximum: Inferences from dinoflagellate cyst assemblages on the New Jersey Shelf. *Biogeosciences*. **6**(8),pp.1755–1781.

Song, J., Littke, R., Maquil, R. and Weniger, P. 2014. Organic facies variability in the Posidonia Black Shale from Luxembourg: Implications for thermal maturation and depositional environment. *Palaeogeography, Palaeoclimatology, Palaeoecology*. **410**,pp.316–336.

Stachowitsch, M., Riedel, B., Zuschin, M. and Machan, R. 2007. Oxygen depletion and benthic mortalities: the first in situ experimental approach to documenting an elusive phenomenon. *Limnology and Oceanography: Methods*. **5**(10),pp.344–352.

Stow, D.A.V. and Wetzel, A. 1990. 3. Hemiturbidite: a new type of deep-water sediment *In*: J. R. Cochran and D. A. V. Stow, eds. *Proceedings of the Ocean Drilling Program, Scientific Results, Vol. 116*. Texas A&M University, pp. 25–34.

Strahan , A. 1898. The Geology of the Isle of Purbeck and Weymouth. Memoirs of the Geological Survey, England and Wales, pp. 278

Stukins, S., Jolley, D.W., McIlroy, D. and Hartley, A.J. 2013. Middle Jurassic vegetation dynamics from allochthonous palynological assemblages: An example from a marginal marine depositional setting; Lajas Formation, Neuquén Basin, Argentina. *Palaeogeography, Palaeoclimatology, Palaeoecology*. **392**,pp.117–127.

Suan, G., Pittet, B., Bour, I., Mattioli, E., Duarte, L.V. and Mailliot, S. 2008. Duration of the early Toarcian carbon isotope excursion deduced from Spectral Analysis: Consequence for its possible causes. *Earth and Planetary Science Letters*. **267**(3–4),pp.666–679.

Suan, G., Nikitenko, B.L., Rogov, M.A., Baudin, F., Spangenberg, J.E., Knyazev, V.G., Glinskikh, L.A., Goryacheva, A.A., Adatte, T., Riding, J.B., Föllmi, K.B., Pittet, B., Mattioli, E. and Lécuyer, C. 2011. Polar record of Early Jurassic Massive Carbon Injection. *Earth and Planetary Science Letters*. **312**(1-2),pp.102–113.

Suan, G., van de Schootbrugge, B., Adatte, T., Fiebig, J. and Oschmann, W. 2015. Calibrating the magnitude of the Toarcian carbon cycle perturbation. *Paleoceanography*. **30**(5),pp.495–509.

Sullivan, K.A. and Aller, R.C. 1996. Diagenetic cycling of arsenic in Amazon Shelf sediments. *Geochimica et Cosmochimica Acta*. **60**(9),pp.1465–1477.

Summons, R.E. and Powell, T.G. 1987. Identification of aryl isoprenoids in source rocks and crude oils: Biological markers for the green sulphur bacteria. *Geochimica et Cosmochimica Acta*. **51**(3),pp.557–566.

Sun, Y.-Z. and Püttmann, W. 2000. The role of organic matter during copper enrichment in Kupferschiefer from the Sangerhausen Basin, Germany. *Organic Geochemistry*. **31**(11),pp.1143–1161.

Suárez-Mozo, N.Y., Valentich-Scott, P. and Hendrickx, M.E. 2018. Deep-water bivalves from the oxygen minimum zone area off the western peninsula of Baja California, Mexico. *Molluscan Research*. **39**(2),pp.99–109.

Svensen, H., Planke, S., Chevallier, L., Malthe-Sørenssen, A., Corfu, F. and Jamtveit, B. 2007. Hydrothermal venting of greenhouse gases triggering Early Jurassic global warming. *Earth and Planetary Science Letters*. **256**(3-4),pp.554–566.

Sweere, T.C., Dickson, A.J., Jenkyns, H.C., Porcelli, D., Ruhl, M., Murphy, M.J., Idiz, E., van den Boorn, S.H.J.M., Eldrett, J.S. and Henderson, G.M. 2020. Controls on the CD-isotope composition of Upper Cretaceous (Cenomanian–Turonian) organic-rich mudrocks from South Texas (Eagle Ford Group). *Geochimica et Cosmochimica Acta*. **287**,pp.251–262.

Syvitski, J.P.M., LeBlanc, K.W.G. and Cranston, R.E. 1990. The flux and preservation of organic carbon in Baffin Island fjords *In*: J. A. Dowdeswell and J. D. Scourse, eds.

Geological Society Special Publication No. 53: Glacimarine Environments: Processes and Sediments. Geological Society Special Publications. London: The Geological Society, pp. 177–199.

Sælen, G., Doyle, P. and Talbot, M.R. 1996. Stable-Isotope Analyses of Belemnite Rostra from the Whitby Mudstone Fm., England: Surface Water Conditions during Deposition of a Marine Black Shale. *PALAIOS*. **11**(2),pp.97–117.

Sælen, G., Tyson, R.V., Telnæs, N. and Talbot, M.R. 2000. Contrasting watermass conditions during deposition of the Whitby Mudstone (Lower Jurassic) and Kimmeridge Clay (Upper Jurassic) formations, UK. *Palaeogeography, Palaeoclimatology, Palaeoecology*. **163**(3-4),pp.163–196.

Taylor, P.D., Hesselbo, S.P. and Jenkyns, H.C. 1995. A comparison of the Hettangian to Bajocian successions of Dorset and Yorkshire *In*: *Field Geology of the British Jurassic. Geological Society*. London: Geological Society, pp. 105–150.

Teichert, B.M.A. and Luppold, F.W. 2013. Glendonites from an early jurassic methane seep — climate or methane indicators? *Palaeogeography, Palaeoclimatology, Palaeoecology*. **390**,pp.81–93.

Testa, J.M., Murphy, R.R., Brady, D.C. and Kemp, W.M. 2018. Nutrient- and climate-induced shifts in the phenology of linked biogeochemical cycles in a temperate estuary. *Frontiers in Marine Science*. **5**.

Theede, H., Ponat, A., Hiroki, K. and Schlieper, C. 1969. Studies on the resistance of marine bottom invertebrates to oxygen-deficiency and hydrogen sulphide. *Marine Biology*. **2**(4),pp.325–337.

Them, T.R., Jagoe, C.H., Caruthers, A.H., Gill, B.C., Grasby, S.E., Gröcke, D.R., Yin, R. and Owens, J.D. 2019. Terrestrial sources as the primary delivery mechanism of mercury to the oceans across the Toarcian Oceanic Anoxic Event (Early Jurassic). *Earth and Planetary Science Letters*. **507**,pp.62–72.

Thibault, N., Ruhl, M., Ullmann, C.V., Korte, C., Kemp, D.B., Gröcke, D.R. and Hesselbo, S.P. 2018. The wider context of the Lower Jurassic Toarcian oceanic anoxic event in

Yorkshire coastal outcrops, UK. *Proceedings of the Geologists' Association*. **129**(3),pp.372–391.

Thomas, Y., Flye-Sainte-Marie, J., Chabot, D., Aguirre-Velarde, A., Marques, G.M. and Pecquerie, L. 2019. Effects of hypoxia on metabolic functions in marine organisms: Observed patterns and modelling assumptions within the context of Dynamic Energy Budget (DEB) theory. *Journal of Sea Research*. **143**,pp.231–242.

Tomašových, A., Berensmeier, M., Gallmetzer, I., Haselmair, A. and Zuschin, M. 2021. Pyrite-lined shells as indicators of inefficient bioirrigation in the holocene–anthropocene stratigraphic record. *Biogeosciences*. **18**(22),pp.5929–5965.

Trabucho-Alexandre, J., Dirkx, R., Veld, H., Klaver, G. and de Boer, P.L. 2012. Toarcian Black Shales In the Dutch Central Graben: Record of Energetic, Variable Depositional Conditions During An Oceanic Anoxic Event. *Journal of Sedimentary Research*. **82**(4),pp.258–259.

Traverse, A. 2007. *Palaeopalynology* 2nd ed. Dordrecht (Netherlands): Springer.

Tribovillard, N. 2020. Arsenic in marine sediments: how robust a redox proxy? *Palaeogeography, Palaeoclimatology, Palaeoecology*. **550**,p.109745.

Tribovillard, N., Algeo, T.J., Lyons, T. and Riboulleau, A. 2006. Trace metals as paleoredox and paleoproductivity proxies: An update. *Chemical Geology*. **232**(1-2),pp.12–32.

Tribovillard, N., Koched, H., Baudin, F., Adatte, T., Delattre, M., Abraham, R. and Ferry, J. 2019. Storm-induced concentration of sulfurized, marine-origin, organic matter as a possible mechanism in the formation of petroleum source-rock. *Marine and Petroleum Geology*. **109**,pp.808–818.

Tribovillard, N., Riboulleau, A., Lyons, T. and Baudin, F. 2004. Enhanced trapping of molybdenum by sulfurized Marine Organic matter of marine origin in Mesozoic limestones and shales. *Chemical Geology*. **213**(4),pp.385–401.

Tribovillard, N.-P., Desprairies, A., Lallier-Vergès, E., Bertrand, P., Moureau, N., Ramdani, A. and Ramanampisoa, L. 1994. Geochemical study of organic-matter rich cycles from

the Kimmeridge Clay Formation of Yorkshire (UK): productivity versus anoxia. *Palaeogeography, Palaeoclimatology, Palaeoecology*. **108**(1-2),pp.165–181.

Tyson, R.V. 1989. Late Jurassic palynofacies trends, Piper and Kimmeridge Clay Formations, UK onshore and northern North Sea *In*: D. J. Batten and M. C. Keen, eds. *Northwest European Micropalaeontology and Palynology*. Ellis Horwood, pp. 135–172.

Tyson, R.V. 1995. *Sedimentary organic matter*. Chapman and Hall.

Tyson, R.V., Pearson, T.H., Tyson, R.V. and Pearson, T.H. 1991. Modern and ancient continental shelf anoxia: an overview *In*: *Modern and Ancient Continental Shelf Anoxia, Geological Society Special Publication No 58*. Bath: Geological Society, pp. 1–24.

Vajda, V., Raine, J.I. and Hollis, C.J. 2001. Indication of global deforestation at the cretaceous-tertiary boundary by New Zealand fern spike. *Science*. **294**(5547),pp.1700–1702.

VAN BUCHEM, F.S.P., MELNYK, D.H. and McCAVE, I.N. 1992. Chemical cyclicity and correlation of Lower Lias mudstones using gamma ray logs, Yorkshire, UK. *Journal of the Geological Society*. **149**(6),pp.991–1002.

van de Schootbrugge, B., Bachan, A., Suan, G., Richoz, S. and Payne, J.L. 2013. Microbes, mud and methane: cause and consequence of recurrent Early Jurassic anoxia following the end-Triassic mass extinction. *Palaeontology*. **56**(4),pp.685–709.

van de Schootbrugge, B., Bailey, T.R., Rosenthal, Y., Katz, M.E., Wright, J.D., Miller, K.G., Feist-Burkhardt, S. and Falkowski, P.G. 2005. Early Jurassic climate change and the radiation of organic-walled phytoplankton in the Tethys Ocean. *Paleobiology*. **31**(1),pp.73–97.

van de Schootbrugge, B., Houben, A.J., Ercan, F.E., Verreussel, R., Kerstholt, S., Janssen, N.M., Nikitenko, B. and Suan, G. 2019. Enhanced Arctic-Tethys Connectivity ended the Toarcian oceanic anoxic event in NW Europe. *Geological Magazine*. **157**(10),pp.1593–1611.

Van der Weijden, C.H. 2002. Pitfalls of normalization of marine geochemical data using a common divisor. *Marine Geology*. **184**(3-4),pp.167–187.

Van Kaam-Peters, H.M.E. and Sinninghe Damsté, J.S. 1997. Characterisation of an extremely organic sulphur-rich, 150Ma old carbonaceous rock: palaeoenvironmental implications. *Organic Geochemistry*. **27**(7-8),pp.371–397.

Van Kaam-Peters, H.M.E., Schouten, S., Köster, J. and Sinninghe Damstè, J.S. 1998. Controls on the molecular and carbon isotopic composition of organic matter deposited in a Kimmeridgian euxinic shelf sea: evidence for preservation of carbohydrates through sulfurisation. *Geochimica et Cosmochimica Acta*. **62**(19-20),pp.3259–3283.

Vandenbroucke, M. and Largeau, C. 2007. Kerogen origin, evolution and Structure. *Organic Geochemistry*. **38**(5),pp.719–833.

Wall, D., Dale, B., Lohmann, G.P. and Smith, W.K. 1977. The environmental and climatic distribution of dinoflagellate cysts in modern marine sediments from regions in the north and south Atlantic Oceans and adjacent seas. *Marine Micropaleontology*. **2**,pp.121–200.

Wallace, J.B., Ross, D.H. and Meyer, J.L. 1982. Seston and dissolved organic carbon dynamics in a Southern Appalachian Stream. *Ecology*. **63**(3),pp.824–838.

Wang, W.-X. and Fisher, N.S. 1996. Assimilation of trace elements and carbon by the mussel Mytilus edulis: Effects of food composition. *Limnology and Oceanography*. **41**(2),pp.197–207.

Wanty, R.B. and Goldhaber, M.B. 1992. Thermodynamics and kinetics of reactions involving vanadium in natural systems: Accumulation of vanadium in Sedimentary Rocks. *Geochimica et Cosmochimica Acta*. **56**(4),pp.1471–1483.

Weedon, G.P., Jenkyns, H.C., Coe, A.L. and Hesselbo, S.P. 1999. Astronomical calibration of the jurassic time-scale from cyclostratigraphy in British Mudrock Formations. *Philosophical Transactions of the Royal Society of London. Series A: Mathematical, Physical and Engineering Sciences*. **357**(1757),pp.1787–1813.

Wedephol, K.H. 2004. The Composition of Earth's Upper Crust, Natural Cycles of Elements, Natural Resources *In*: E. Merian, M. Anke, M. Ihnat and M. Stoeppler, eds. *Elements and Their Compounds in the Environment: Occurrence, Analysis and Biological Relevance - 2nd edition*. Weinheim: WILEY-VCH, pp. 3–16.

Wedepohl, K.H. 1971. Environmental influences on the chemical composition of shales and clays. *Physics and Chemistry of the Earth*. **8**,pp.307–333.

Wehrli, B. and Stumm, W. 1989. Vanadyl in natural waters: Adsorption and hydrolysis promote oxygenation. *Geochimica et Cosmochimica Acta*. **53**(1),pp.69–77.

Wheatcroft, R.A. and Drake, D.E. 2003. Post-depositional alteration and preservation of sedimentary event layers on continental margins, I. The role of episodic sedimentation. *Marine Geology*. **199**(1-2),pp.123–137.

White, A.W. and Lewis, C.M. 1982. Resting cysts of the toxic, red tide dinoflagellate Gonyaulax excavata in bay of fundy sediments. *Canadian Journal of Fisheries and Aquatic Sciences*. **39**(8),pp.1185–1194.

Whiteside, J.H. and Grice, K. 2016. Biomarker Records Associated with Mass Extinction Events. *Annual Review of Earth and Planetary Sciences*. **44**(1),pp.581–612.

Wignall, P.B. 1994. *Black shales*. Oxford: Clarendon Press.

Wignall, P.B. and Bond, D.P.G. 2008. The end-Triassic and Early Jurassic mass extinction records in the British Isles. *Proceedings of the Geologists' Association*. **119**(1),pp.73–84.

Wignall, P.B. and Hallam, A. 1991. Biofacies, stratigraphic distribution and depositional models of British onshore Jurassic black shales. *Geological Society, London, Special Publications*. **58**(1),pp.291–309.

Wignall, P.B. and Newton, R. 1998. Pyrite framboid diameter as a measure of oxygen deficiency in ancient mudrocks. *American Journal of Science*. **298**(7),pp.537–552.

Wignall, P.B., Newton, R.J. and Little, C.T.S. 2005. The timing of paleoenvironmental change and cause-and-effect relationships during the early Jurassic mass extinction in Europe. *American Journal of Science*. **305**(10),pp.1014–1032.

Wijsman, J.W.M., Middelburg, J.J. and Heip, C.H.R. 2001. Reactive iron in Black Sea Sediments: implications for iron cycling. *Marine Geology*. **172**(3-4),pp.167–180.

Wilkin, R., Arthur, M. and Dean, W. 1997. History of water-column anoxia in the Black Sea indicated by pyrite framboid size distributions. *Earth and Planetary Science Letters*. **148**(3-4),pp.517–525.

Wilkin, R.T., Barnes, H.L. and Brantley, S.L. 1996. The size distribution of framboidal pyrite in modern sediments: An indicator of redox conditions. *Geochimica et Cosmochimica Acta*. **60**(20),pp.3897–3912.

Williams, G. 1992. Palynology as a palaeoenvironmental indicator in the Brent Group, northern North Sea. *Geological Society, London, Special Publications*. **61**(1),pp.203–212.

Williams, L.A. and Reimers, C. 1983. Role of bacterial mats in oxygen-deficient marine basins and coastal upwelling regimes: Preliminary report. *Geology*. **11**,pp.267–269.

Winter, M.A. and Hamilton, P.V. 1985. Factors influencing swimming in Bay scallops, Argopecten irradians (Lamarck, 1819). *Journal of Experimental Marine Biology and Ecology*. **88**(3),pp.227–242.

Wittkop, C., Swanner, E.D., Grengs, A., Lambrecht, N., Fakhraee, M., Myrbo, A., Bray, A.W., Poulton, S.W. and Katsev, S. 2020. Evaluating a primary carbonate pathway for manganese enrichments in reducing environments. *Earth and Planetary Science Letters*. **538**,p.116201.

Xu, W., Ruhl, M., Jenkyns, H.C., Leng, M.J., Huggett, J.M., Minisini, D., Ullmann, C.V., Riding, J.B., Weijers, J.W.H., Storm, M.S., Percival, L.M.E., Tosca, N.J., Idiz, E.F., Tegelaar, E.W. and Hesselbo, S.P. 2018. Evolution of the Toarcian (Early Jurassic) carbon-cycle and global climatic controls on local sedimentary processes (Cardigan Bay Basin, UK). *Earth and Planetary Science Letters*. **484**,pp.396–411.

Yamaguchi, M. 1958. Chemical Constitution of Isorenieratene. *Bulletin of the Chemical Society of Japan*. **31**(1),pp.51–55.

Yonge, C.M. 1977. Form and evolution in the Anomiacea (Mollusca:Bivalvia) - Pododesmus, Anomica, Patro, Enigmonia (Anomiidae): Placunanomica, Placuna (Placunidae Fam. Nov.). *Philosophical Transactions of the Royal Society of London B. Biological Sciences*. **276**(950),pp.453–527.

Zheng, Y., Anderson, R.F., van Geen, A. and Fleisher, M.Q. 2002. Remobilization of authigenic uranium in marine sediments by bioturbation. *Geochimica et Cosmochimica Acta*. **66**(10),pp.1759–1772.

Appendix 1 – ICPMS methods (by Stephen Reid)

1. ICP-MS Analysis

ICP-MS analysis was used in 2 modes depending on the element analysed. The two modes are Standard (STD) mode and "Kinetic Energy Discrimination (KED) mode. The table below summarises what mass and mode was used for each element.

Standard mode is used when no significant interference was found on the relevant mass.

KED mode uses helium gas in the collision/reaction cell to reduce the effect of polyatomic interferences.

Element	Mass m/z	Instrument mode	Calibration Range
Li	7	STD	10-100 µg L-1
V	51	KED	0.1-10 µg L-1
Cr	52	KED	0.1-10 µg L-1
Co	59	KED	0.1-10 µg L-1
Ni	60	KED	0.1-10 µg L-1
Cu	63	KED	0.1-10 µg L-1
Zn	66	KED	0.1-10 µg L-1
Ga	71	KED	0.1-10 µg L-1
As	75	KED	0.1-10 µg L-1
Rb	85	KED	0.1-10 µg L-1
Zr	90	KED	0.1-10 µg L-1
Mo	95	KED	0.1-10 µg L-1
Cd	111	KED	0.1-10 µg L-1
Tl	205	KED	0.1-10 µg L-1
Pb*	206	KED	0.1-10 µg L-1
Pb	207	KED	0.1-10 µg L-1
Pb	208	KED	0.1-10 µg L-1
Bi	209	KED	0.1-10 µg L-1
U	238	KED	0.1-10 µg L-1
Zr	90	KED	0.1-10 µg L-1

* To account for the natural isotopic variation in Pb found in environmental samples due to it's radiogenic origins, Pb was analysed using three isotopes and the results combined to determine the concentration.

Calibrations

Direct calibration was used for the analysis with the calibration standards matrix matched.

Calibrations ranges are summarised Above.

Instrument Settings

A Thermo Scientific iCAPQc ICP-MS was used for the analysis

	Std mode	**KED mode**
Nebuliser	c-flow PFA concentric neb	
Cones	Ni sample and skimmer with high matrix insert	
Spraychamber	PFA spraychamber	
Plasma Power / kw	1350	1350
Extraction voltage / v	~ -120	~ -120
Nebuliser gas flow / ml min-1	~0.95	~0.95
Cell gas flow / ml min-1	n/a	5.0

Internal Standardisation

Rhodium at a concentration of 1 µg L^{-1} were added to all standards and samples for use as an internal standard.

Sample Preparation

Samples were analysed neat. All sample handling was carried out in a laminar flow cabinet. Low metal content PFA lab ware was used wherever possible. Trace metal grade acids were used in the preparation of all blanks and calibration standards.

2. ICP-OES Analysis

A Thermo Scientific iCAP7400 ICP-OES was used. The analysis was used in radial mode. The table below summarises what wavelength as used for each element.

Element	**Wavelength / nm**	**Calibration Range**
Iron	259.837 234.349	1-100 mg L-1 1-100 mg L-1
Aluminium	396.152 308.215	1-100 mg L-1 1-100 mg L-1
Manganese	257.610 293.930	1-100 mg L-1 1-100 mg L-1
Calcium	393.366 315.887	1-100 mg L-1 1-100 mg L-1
Potassium	766.490	1-100 mg L-1
Magnesium	279.553 285.213	1-100 mg L-1 1-100 mg L-1
Strontium	407.771 346.446	1-100 mg L-1 1-100 mg L-1
Barium	455.403 493.409	1-100 mg L-1 1-100 mg L-1
Titanium	334.941 368.520	0.1-10 mg L-1 0.1-10 mg L-1

Instrument set up

Nebuliser	Quartz Glass Expantion Seaspray
Spraychamber	Quartz cyclonic spraychamber
Torch	Quartz
Injector	1 mm quartz

Sample Preparation

Samples were diluted to ~2 % HNO_3 before analysis. Appropriate internal standard was added to each dilution (outline below).

Calibrations

Direct calibration was used for the analysis using 2% HNO_3 as diluent.

Internal Standardisation

Yttrium (371.030 nm) and lutetium (261.542 nm) at a concentration of 1 mg L^{-1} was added to all standards and samples for use as an internal standard.

Limit of Detection

Limit of Detection was estimated as 3 times the standard deviation of 5 blank measurements.

$$LOD = 3\sigma_{5\ Blanks}$$

Precision

Precision was estimated by calculating the 95% confidence interval of 5 repeated sample measurements.

$$\bar{x} \pm \frac{t_{n-1}s}{\sqrt{n}}$$

Where n = number of measurements
n-1 = degrees of freedom (5)
t = t value (2.78 for 4 degrees of freedom)
s = calculated standard deviation of 5 measurements
x = calculated mean of 5 measurements

Accuracy

Accuracy was estimated by Spiking a sample with a known amount of analyte and measuring the analyte recovery. Sample and Sample + Spike were analysed 5 times.

$$\%\ Recovery = 100 \times \frac{M_{Spike-}M_{Sample}}{C_{spike}}$$

Where M_{spike} = Measured concentration of spiked sample.
M_{Sample} =Measured concentration of sample.
C_{Spike} = Actual concentration of spike.

Appendix 2 – Data

Note: each cell of the following tables only includes one figure, which is often text-wrapped.

Organic geochemistry (LECO & Rock Eval):

Sample Code	Stratigraphic height*	C (wt.%) of acid-treated sample	TOC (via total combustion)	TOC (via Rock Eval 6)	HI	OI	Tmax (oC)	PI	Inorganic C (via Rock Eval 6)	TIC (%)
LSB1.0	2			1.09	150	36	439	0.08	0.17	
LSB1.1	6			1.27	186	18	437	0.07	0.17	
LSB1.2	14			1.41	150	22	437	0.09	0.21	
LSB1.3	18		1.744933	1.51	192	15	436	0.08	0.2	
LSB1.4	22	0.84551	1.509419	1.44	189	15	437	0.08	0.21	-0.66391
LSB1.5	26			1.64	198	13	434	0.08	0.21	
LSB1.6	30	1.6494	2.321012	1.72	235	16	437	0.08	0.17	-0.67161
LSB1.7	34	6.6765	1.184723	1.10	215	32	437	0.08	0.26	5.491777
LSB1.8	38			0.60	113	45	437	0.11	0.34	
LSB1.9	42	0.80844	0.881126	0.70	110	41	435	0.11	0.3	-0.07269
LSB1.10	46	1.3062	1.347097	1.26	148	19	436	0.1	0.27	-0.0409
LSB1.11	50	3.884	4.20393	3.54	200	8	427	0.1	0.3	-0.31993
LSB1.12	54	4.2166	4.078695	3.73	224	8	427	0.1	0.32	0.137905
LSB1.13	59	1.1244	1.059122	0.85	131	55	431	0.11	0.32	0.065278
LSB1.14	62	0.66969	0.185005	0.30	63	83	428	0.13	0.43	0.484685
LSB1.15	66	1.6071	1.117059	0.99	102	31	433	0.13	0.36	0.490041
LSB1.16	70	5.2049	5.050529	3.85	237	10	427	0.09	0.35	0.154371
LSB1.17	74	7.2442	6.597405	5.46	324	5	431	0.08	0.38	0.646795
LSB1.18	78	6.9571	6.892842	5.42	297	4	429	0.08	0.33	0.064258
LSB1.19	82	7.4281	6.688774	5.69	329	5	430	0.07	0.3	0.739326
LSB1.20	86	7.5428	6.781139	5.93	348	6	430	0.07	0.27	0.761661
LSB1.21	90	7.9717	7.251084	5.80	338	9	428	0.07	0.25	0.720616
LSB1.22	98	2.6859	2.349418	3.63	339	11	432	0.07	0.27	0.336482
LSB1.23	102	1.1324	1.316286	1.03	120	37	434	0.23	0.3	-0.18389
LSB1.24	106			1.14	117	36	433	0.09	0.27	
LSB1.25	110	0.59956	0.649523	0.51	67	65	431	0.14	0.32	-0.04996
LSB1.26	114	0.59782	1.226874	1.01	80	36	433	0.11	0.29	-0.62905

LSB1.27	118			1.66	158	24	436	0.1	0.28	
LSB1.28	122			1.14	83	25	431	0.09	0.22	
LSB1.29	126			1.30	175	32	438	0.08	0.29	
LSB1.30	130			1.49	234	26	437	0.08	0.25	
LSB3.0	-57.5	0.76974	0.770445	0.87	128	14	441	0.08	0.16	-0.0007
LSB3.1	-53.5	0.77532	0.853896	0.89	119	10	441	0.08	0.14	-0.07858
LSB3.2	-50			0.90	98	9	437	0.08	0.1	
LSB3.3	-42			1.14	101	9	440	0.08	0.13	
LSB3.4	-38			1.31	236	33	439	0.06	0.15	
LSB3.5	-34			0.84	82	19	433	0.12	0.16	
LSB3.6	-30	0.82171	0.859235	0.87	114	21	440	0.08	0.15	-0.03752
LSB3.7	-26	0.78981	0.758639	0.85	111	21	439	0.08	0.17	0.031171
LSB3.8	-22		0.893328	0.91	122	21	440	0.07	0.13	
LSB3.9	-18		0.721437	0.78	110	29	435	0.09	0.14	
LSB3.10	-14	0.89346	0.9073	0.90	116	27	438	0.08	0.16	-0.01384
LSB3.11	-10	0.90022	0.956997	1.04	113	9	439	0.08	0.12	-0.05678
LSB3.12	-6			1.01	131	9	440	0.07	0.14	
LSB3.13	-2	0.85701	0.974258	1.13	230	46	437	0.06	0.16	-0.11725
LSB3.14	2			0.86	97	26	438	0.08	0.15	
LSB3.15	6	0.96262	1.074152	1.02	133	22	440	0.07	0.16	-0.11153
LSB3.16	10	0.93905	1.051856	1.00	152	21	440	0.07	0.13	-0.11281
LSB3.17	14	1.0182	1.057628	1.13	185	27	440	0.06	0.18	-0.03943
LSB3.18	18			1.03	142	26	439	0.08	0.18	0
LSB3.19	22	0.98646	1.044192	1.06	133	22	442	0.08	0.17	-0.05773
LSB3.20	30	1.4839	1.712802	1.24	184	27	442	0.07	0.17	-0.2289
LSB3.21	34	1.554	1.787751	1.34	181	24	441	0.08	0.17	-0.23375
LSB3.22	38	1.4238	1.694174	2.06	123	14	436	0.08	0.2	-0.27037
LSB3.23	42	1.527	1.668695	1.63	155	22	437	0.07	0.16	-0.1417
LSB3.24	46	1.2941	1.383487	1.44	119	17	435	0.1	0.15	-0.08939
LSB5.0	79	6.7933	7.345086	5.60	280	8	428	0.08	0.54	-0.55179
LSB5.1	82.5	6.6407	7.142033	5.61	318	8	429	0.07	0.51	-0.50133
LSB5.2	87	7.4955	8.358496	5.94	391	6	433	0.06	0.42	-0.863
LSB5.3	91	4.3084	4.671255	3.81	215	8	433	0.1	0.38	-0.36286
LSB5.4	95	5.909	6.69218	4.25	252	9	430	0.08	0.4	-0.78318
LSB5.5	99	1.1478	1.398918	1.07	105	39	434	0.13	0.33	-0.25112
LSB5.6	103	1.1137	1.238636	0.85	78	42	431	0.15	0.34	-0.12494
LSB5.7	107	0.87372	0.94982	0.74	64	53	430	0.1	0.27	-0.0761
LSB5.8	111	1.7562	2.215888	1.64	107	23	431	0.09	0.23	-0.45969
LSB5.9	115	2.1848	2.584807	1.84	101	24	431	0.09	0.28	-0.40001

LSB5.10	119	0.99421	1.102054	0.96	78	39	433	0.09	0.28	-0.10784
LSB5.11	123	1.8831	2.334152	1.38	102	38	434	0.13	0.26	-0.45105
LSB5.12	127	2.3114	2.681938	2.12	140	19	433	0.1	0.23	-0.37054
LSB5.13	131	1.785	1.737747	2.02	122	19	433	0.08	0.26	0.047253
LSB5.14	135	0.94648	1.051764	0.80	76	51	431	0.1	0.23	-0.10528
LSB5.15	139			1.25	70	27	430	0.08	0.19	
LSB5.16	143			1.54	87	23	430	0.08	0.21	
LSB5.17	147			1.59	218	21	438	0.07	0.21	
Bos32.1	-2	6.2766	5.937148	5.56	453	1	433	0.14	0.3	0.339452
Bos32.2	0	6.1354	4.908235	4.76	376	2	431	0.13	0.8	1.227165
Bos32.3	2	7.7097	7.127399	6.65	472	0	434	0.13	0.3	0.582301
Pseud34.1	-2	7.6451	6.169544	5.65	506	6	436	0.12	1.09	1.475556
Pseud34.2	0	7.6142	4.40528	3.90	416	15	436	0.13	2.68	3.20892
Pseud34.3	2	8.5877	7.299382	6.80	507	4	431	0.1	0.72	1.288318
Pseud41.1	-2	6.1203	4.134251	4.17	384	9	431	0.16	1.28	1.986049
Pseud41.2	0	6.1018	3.817735	3.86	396	8	436	0.17	1.64	2.284065
Pseud41.3	2	6.4359	4.54744	4.56	398	9	435	0.15	1.17	1.88846
LSB accuracy:										
		C (wt.%) of acid-treated sample	**TOC (via total combustion)**	**TOC (via Rock Eval 6)**	**HI**	**OI**	**Tmax (oC)**	**PI**	**Inorganic C (via Rock Eval 6)**	**TIC (%)**
Sample		7.2442	6.597405	5.46	324	5	431	0.08	0.38	0.646795
Repeat 1		5.818	6.54174	5.56	297	6	429	0.07	0.41	-0.72374
Repeat 2		5.8931	6.326225	5.56	306	6	430	0.07	0.4	-0.43312
Repeat 3		5.9719	6.380173	5.55	312	7	428	0.07	0.48	-0.40827
Standard (SBC-1 for LECO data, and ifp for RE6 data)		1.5196	0.817342	3.3	392	25	456	0.01	3.27	0.702258
Mean		6.2318	6.461386	5.5325	309.75	6	429.5	0.0725	0.4175	-0.22959
Stan.Dev		0.677852	0.128869	0.048563	11.32475	0.816497	1.290994	0.005	0.043493	0.60155
95% Confidence		1.077446	0.204838	0.07719	18.00069	1.297821	2.052036	0.007948	0.069133	0.956164
as a % of measurement (i.e. precision)		17.28948	3.170184	1.395217	5.811362	21.63036	0.477773	10.96207	16.5587	416.4736
Measured standard - reported standard		0.2896	.	0	9	1	40	0.000415	0.07	-0.14774
Deviation (i.e. accuracy)		19.05765	.	0	2.295918	4	8.77193	4.153355	2.140673	21.03818

Shell pavement accuracy:										
		C (wt.%) of acid-treated sample	**TOC (via total combustion)**	**TOC (via Rock Eval 6)**	**HI**	**OI**	**Tmax (oC)**	**PI**	**Inorganic C (via Rock Eval 6)**	**TIC (%)**
Sample		6.2766	4.134251	5.56	453	1	433	0.14	0.3	1.986049
Repeat 1		6.2751	4.598618	5.84	454	3	432	0.16	0.3	1.046582
Repeat 2		6.3423	.	5.89	457	2	432	0.16	0.28	.
Repeat 3		6.3261	.	5.97	473	3	432	0.16	0.27	.
Standard (SBC-1 for LECO data, and ifp for RE6 data)		2.0883	1.102576	3.28	373	23	414	0.01	3.22	0.9857
Mean		6.305025	4.366435	5.815	442	2.25	432.25	0.126	0.2875	1.516315
Stan.Dev		0.034337	0.328357	0.178232	9.322911	0.957427	0.5	0.01	0.015	0.664303
95% Confidence		0.054578	2.948727	0.2833	14.81877	1.52183	0.79475	0.015895	0.023843	5.965612
as a % of measurement (i.e. precision)		0.865635	67.53169	4.871881	3.352662	67.63691	0.183864	12.61508	8.293043	393.4282
Measured standard - reported standard		0.8583	.	-0.02	-10	-1	-2	0.000415	0.02	0.135724
Deviation (i.e. accuracy)		41.10042	.	0.609756	2.680965	4.347826	0.483092	4.153355	0.621118	13.76896

Bioturbation:

Sample block	**Stratigraphic height***	Bioturnation intensity (%area)
LSB1	134	20.82983
LSB1	124	32.82981
LSB1	114	27.62942
LSB1	104	16.50173
LSB1	94	18.0601
LSB1	84	26.12957
LSB1	74	6.219918
LSB1	64	0
LSB1	54	0
LSB1	44	0
LSB1	34	3.974829
LSB1	24	16.15736
LSB1	14	2.146444
LSB1	4	10.11019
LSB3	49	11.53193
LSB3	39	8.684332
LSB3	29	7.238297
LSB3	19	1.97899
LSB3	9	12.97796

LSB3	-1	88.63235
LSB3	-11	71.49501
LSB3	-21	93.0259
LSB3	-31	88.44486
LSB3	-41	94.14246
LSB3	-51	80.40715
LSB3	-61	85.95575
LSB5	146	50.22071
LSB5	136	38.48497
LSB5	126	37.26967
LSB5	116	37.52871
LSB5	106	21.09569
LSB5	96	34.34592
LSB5	86	21.2678
LSB5	76	2.045881
LSB6	70	2.745055
LSB6	60	0.950307
LSB6	50	5.306801
LSB6	40	5.735958
LSB6	30	15.9008
LSB6	20	22.50707
LSB6	10	44.30395
LSB6	0	63.20682

Shell pavement data 1:

Pavement:	Bed number:	Duration (yr):	Thickness (m):	Sed rate (mm/yr):		Shell pavement thickness (um)	Shell pavement duration (yr):
Pseud41	41	120000	5.1816	0.04318		728.5149	16.87158
Pseud34	34	520000	2.6	0.005		581.8182	116.3636
Bos32	32	20000	1.85	0.0925		1386.047	14.98429

Shell pavement data 2:

	Bos32 Length	Pseud34 Length	Pseud41 length	Bos32 Spacing	Pseud34 Spacing	Pseud41 Spacing
n	**12**	**31**	**8**	**N/A**	**79**	**20**
	9.885154	2.039654	4.665603	N/A	0.276289	0.339261
	12.89115	2.10868	5.367719		0.308891	0.339261
	14.53081	2.144598	6.112205		0.308891	0.42916
	14.91894	2.459567	8.38462		0.414433	0.606908
	16.54503	2.860922	9.785059		0.436858	1.398846

	17.99423	2.874598	12.7176			0.498102	5.050496	
	18.13827	2.936993	14.46272			0.569569	5.134098	
	23.24251	3.116673	14.59776			0.690721	5.312605	
	27.98445	3.530139	15.29096			0.743907	6.191141	
	30.24807	3.634023	27.1837			0.743907	6.99427	
	30.40708	3.877894				0.976818	7.65432	
	33.23585	4.052232				1.105154	8.300715	
		4.300017				1.113765	9.907654	
		4.825149				1.188363	10.95169	
		4.905595				1.188363	11.24213	
		4.950952				1.243298	15.50289	
		5.532678				1.408795	15.63967	
		6.171135				1.468474	15.93061	
		6.204197				1.494261	18.56098	
		8.200704				1.611038	22.93485	
		8.318541				1.663487		
		8.41911				1.795876		
		9.021788				1.801171		
		10.36911				1.801171		
		10.57863				1.919146		
		11.42177				2.15786		
		12.70025				2.214637		
		13.92517				2.248805		
		16.52426				2.447916		
		19.19063				2.762885		
		31.80201				2.927231		
						3.326974		
						3.464658		
						3.538197		
						3.538197		
						3.540914		
						3.670585		
						3.706779		
						3.757939		
						3.890189		
						3.899997		
						3.909759		
						4.02755		
						4.180982		
						4.39681		
						4.455015		
						4.497655		
						4.510364		
						4.510364		
						4.592146		
						4.70501		

						5.113226		
						5.41765		
						5.4998		
						5.51541		
						5.679065		
						5.941815		
						5.946604		
						5.997764		
						6.079913		
						6.458889		
						6.666796		
						6.858679		
						6.908595		
						7.279835		
						7.434142		
						7.732395		
						7.960978		
						8.013565		
						8.22511		
						8.39162		
						8.444897		
						8.569411		
						9.670099		
						9.879019		
						10.49261		
						11.19309		
						11.65988		
						13.29708		

Sulphur data:

Sample Code	Stratigraphic height*		Pyritic Sulphur (wt.%) - Spy	TS (via total combustion)	"OM-hosted sulphur (wt.%)" -Sorg
LSB1.0	2		2.718468		
LSB1.1	6		2.778032		
LSB1.2	14		3.484796		
LSB1.3	18		3.599863		
LSB1.4	22		3.205982	3.7924	0.586418
LSB1.5	26		2.946408		
LSB1.6	30		3.144982	3.6601	0.515118
LSB1.7	34		2.369831	11.255	8.885169
LSB1.8	38		1.823771		
LSB1.9	42		0.645117	3.4983	2.853183
LSB1.10	46		4.208356	5.059	0.850644
LSB1.11	50		6.120013	10.518	4.397987
LSB1.12	54		2.697483	9.5352	6.837717
LSB1.13	59		5.153044	6.4776	1.324556
LSB1.14	62		4.262661	5.6026	1.339939
LSB1.15	66		3.539992	6.083	2.543008
LSB1.16	70		7.772224	9.1976	1.425376
LSB1.17	74		8.57584	10.456	1.88016
LSB1.18	78		10.20941	11.682	1.472593
LSB1.19	82		9.943459	12.008	2.064541
LSB1.20	86		9.269871	11.911	2.641129
LSB1.21	90		8.48493	10.749	2.26407
LSB1.22	98		3.317356	5.9216	2.604244
LSB1.23	102		5.58673	4.8093	-0.77743
LSB1.24	106		5.277875		
LSB1.25	110		4.660646	3.6562	-1.00445
LSB1.26	114		4.773696	5.6182	0.844504
LSB1.27	118		4.274734		
LSB1.28	122		5.121653		
LSB1.29	126		2.411669		
LSB1.30	130		2.35929		
LSB3.0	-57.5		2.514392	2.5896	0.075208
LSB3.1	-53.5		2.43406	2.5717	0.13764
LSB3.2	-50		2.505207		
LSB3.3	-42		2.485885		
LSB3.4	-38		1.579923		
LSB3.5	-34		2.385387		
LSB3.6	-30		2.136353	2.7046	0.568247
LSB3.7	-26		2.227682	2.4848	0.257118
LSB3.8	-22		2.031978		
LSB3.9	-18		1.372622		
LSB3.10	-14		1.662714	2.5555	0.892786

LSB3.11	-10		2.57853	2.7106	0.13207
LSB3.12	-6		2.335972		
LSB3.13	-2		2.591406	2.7431	0.151694
LSB3.14	2		2.238105		
LSB3.15	6		1.84268	2.4913	0.64862
LSB3.16	10		2.360254	2.4985	0.138246
LSB3.17	14		2.583286	2.6687	0.085414
LSB3.18	18		2.653715		
LSB3.19	22		2.612887	2.892	0.279113
LSB3.20	30		2.818537	3.574	0.755463
LSB3.21	34		1.819218	3.3711	1.551882
LSB3.22	38		2.671715	3.3711	0.699385
LSB3.23	42		6.326706	3.4548	-2.87191
LSB3.24	46		2.537479	3.0822	0.544721
LSB5.0	79		1.290012	11.407	10.11699
LSB5.1	82.5		10.71713	12.235	1.517871
LSB5.2	87		9.49159	10.093	0.60141
LSB5.3	91		10.77225	11.875	1.102752
LSB5.4	95		1.067434	8.2253	7.157866
LSB5.5	99		5.340183	6.0897	0.749517
LSB5.6	103		0.640362	6.7298	6.089438
LSB5.7	107		3.739971	5.6595	1.919529
LSB5.8	111		4.766517	5.7766	1.010083
LSB5.9	115		5.41525	7.0363	1.62105
LSB5.10	119		5.288256	6.1045	0.816244
LSB5.11	123		4.825886	5.3204	0.494514
LSB5.12	127		4.827994	5.247	0.419006
LSB5.13	131		2.959673	5.7413	2.781627
LSB5.14	135		3.731819	5.3853	1.653481
LSB5.15	139				
LSB5.16	143				
LSB5.17	147				
Bos32.1	-2		3.916592	6.4983	2.581708
Bos32.2	0		5.679961	6.496	0.816039
Bos32.3	2		5.558905	6.0837	0.524795
Pseud34.1	-2		4.098146	4.3455	0.247354
Pseud34.2	0		0.331421	3.5417	3.210279
Pseud34.3	2		3.72394	4.4893	0.76536
Pseud41.1	-2		4.320454	4.7118	0.391346
Pseud41.2	0		4.533001	5.0367	0.503699
Pseud41.3	2		4.206655	4.5009	0.294245
LSB accuracy:					
			Pyritic Sulphur (wt.%)	**TS (via total combustion)**	**OM-hosted sulphur (wt.%)**

Sample			8.57584	10.456	1.88016
Repeat 1			8.380094	10.556	2.175906
Repeat 2			8.821722	10.516	1.694278
Repeat 3			9.306273	10.522	1.215727
Standard (SBC-1)			.	0.63187	.
Mean			8.770983	10.5125	1.741517
Stan.Dev			0.399994	0.041581	0.402742
95% Confidence			0.63579	0.066093	0.640158
as a % of measurement (i.e. precision)			7.24879	0.628712	36.75862
Measured standard - reported standard			.	-0.08313	.
Deviation (i.e. accuracy)			.	0.08313	.
Shell pavement accuracy:					
			Pyritic Sulphur (wt.%)	**TS (via total combustion)**	**OM-hosted sulphur (wt.%)**
Sample			3.916592	6.4983	2.581708
Repeat 1			6.468845	6.3851	-0.08374
Repeat 2			6.054584	6.2963	0.241716
Repeat 3			6.131791	6.4417	0.309909
Standard (SBC-1)			.	0.11235	.
Mean			5.642953	6.40535	0.762397
Stan.Dev			1.164878	0.086145	1.224977
95% Confidence			1.851574	0.136928	1.947101
as a % of measurement (i.e. precision)			32.81215	2.13771	255.3919
Measured standard - reported standard			.	-0.60265	.
Deviation (i.e. accuracy)			.	0.60265	.

Inorganic geochemistry:

Sample Code	Stratigraphic height*		FeCarb (wt.%)	FeOx (wt.%)	FeMag (wt.%)	FePy (wt.%)	FeT (wt.%)		FeHR/FeT	FePy/FeHR
LSB1.0	2		0.526397	0.074367	0.133417	2.36771	4.88507		0.634974	0.763312
LSB1.1	6		0.575819	0.074315	0.127444	2.419588	5.1253		0.623801	0.756792
LSB1.2	14		0.726735	0.181277	0.128502	3.035161	5.52296		0.737227	0.745433
LSB1.3	18		0.785063	0.099317	0.140612	3.135381	5.542755		0.750597	0.75363
LSB1.4	22		0.752113	0.12294	0.126028	2.792322	4.680812		0.810415	0.736099
LSB1.5	26		0.7342	0.089478	0.114435	2.56624	5.067817		0.691492	0.732301
LSB1.6	30		0.764139	0.102963	0.116588	2.739192	5.315432		0.700391	0.735772
LSB1.7	34		0.668165	0.073744	0.093943	2.064057	4.351582		0.666403	0.711766
LSB1.8	38		0.845825	0.083288	0.07288	1.588454	4.048192		0.639902	0.613197

LSB1.9	42		0.859097	0.135042	0.090898	0.561879	4.277094		0.385055	0.34117
LSB1.10	46		1.14397	0.132567	0.13391	3.665362	6.244466		0.812849	0.722124
LSB1.11	50		1.767789	0.657733	0.163334	5.330362	11.25185		0.703815	0.673092
LSB1.12	54		1.810378	0.510017	0.171167	2.349433	10.58229		0.457462	0.48532
LSB1.13	59		1.775648	0.203314	0.134397	4.488158	7.384563		0.893962	0.679868
LSB1.14	62		1.967228	0.187079	0.132555	3.71266	6.434401		0.932414	0.618826
LSB1.15	66		1.899375	0.270594	0.135004	3.083235	7.463918		0.721901	0.572219
LSB1.16	70		2.096919	0.640404	0.213399	6.769392	10.84632		0.896167	0.696431
LSB1.17	74		2.130407	0.397379	0.204562	7.469319	12.36967		0.824732	0.732167
LSB1.18	78		2.140984	0.537797	0.260155	8.89211	13.08221		0.904361	0.751591
LSB1.19	82		2.075387	0.513096	0.231803	8.660477	13.06641		0.878647	0.754347
LSB1.20	86		1.91525	0.383581	0.195524	8.0738	12.26039		0.861975	0.763974
LSB1.21	90		1.745204	0.782176	0.200016	7.390139	11.73604		0.862091	0.730429
LSB1.22	98		1.598261	0.41575	0.175569	2.889325	7.388276		0.687428	0.568887
LSB1.23	102		1.613401	0.17529	0.155992	4.865887	7.475808		0.911015	0.714461
LSB1.24	106		1.57575	0.330181	0.14014	4.596883	7.168137		0.926734	0.691994
LSB1.25	110		1.503258	0.565276	0.114442	4.059294	6.639286		0.940202	0.650291
LSB1.26	114		1.461365	0.389441	0.136486	4.157757	7.063048		0.870028	0.676603
LSB1.27	118		1.346959	0.252223	0.149131	3.723175	6.883197		0.794905	0.680468
LSB1.28	122		1.407446	0.584988	0.151486	4.460818	7.090976		0.931428	0.675397
LSB1.29	126		0.849922	0.156348	0.12671	2.100497	4.876593		0.663061	0.649609
LSB1.30	130		0.795123	0.091575	0.152577	2.054876	4.75806		0.650297	0.664116
LSB3.0	-57.5		0.536719	0.148565	0.147861	2.189966	4.861711		0.62182	0.724408
LSB3.1	-53.5		0.53932	0.146142	0.162546	2.119999	4.952422		0.599304	0.714284
LSB3.2	-50		0.58874	0.147603	0.163172	2.181966	4.875805		0.631994	0.70809
LSB3.3	-42		0.576165	0.10232	0.122861	2.165137	5.222841		0.567983	0.729867
LSB3.4	-38		0.534362	0.109796	0.112509	1.376069				0.645213
LSB3.5	-34		0.581922	0.085707	0.105374	2.077606				0.728829
LSB3.6	-30		0.594341	0.095324	0.114453	1.860704	4.818813		0.553004	0.698247
LSB3.7	-26		0.61336	0.093155	0.111868	1.940249				0.703338
LSB3.8	-22		0.650529	0.098572	0.123324	1.769797				0.669814
LSB3.9	-18		0.636602	0.10179	0.122302	1.195515	4.447993		0.462278	0.581417
LSB3.10	-14		0.607309	0.099419	0.119456	1.448178				0.63674
LSB3.11	-10		0.572268	0.09716	0.102156	2.245828				0.74429

LSB3.12	-6		0.573799	0.099447	0.11534	2.034567	4.699093		0.600787	0.720672
LSB3.13	-2		0.584272	0.089404	0.101669	2.257043				0.744312
LSB3.14	2		0.591104	0.078067	0.096276	1.949327				0.718044
LSB3.15	6		0.566632	0.074713	0.098581	1.604923				0.684446
LSB3.16	10		0.577324	0.082879	0.10928	2.055716				0.727636
LSB3.17	14		0.572706	0.071447	0.096948	2.24997				0.752229
LSB3.18	18		0.555718	0.072803	0.097756	2.311313	4.655963		0.652408	0.760903
LSB3.19	22		0.556142	0.079774	0.095047	2.275752				0.75689
LSB3.20	30		0.670912	0.121846	0.089835	2.454868				0.73555
LSB3.21	34		0.725527	0.122672	0.071519	1.584489				0.632731
LSB3.22	38		0.72018	0.121851	0.080695	2.32699				0.716059
LSB3.23	42		0.749741	0.121047	0.118657	5.510385				0.847774
LSB3.24	46		0.670418	0.169024	0.097628	2.210074				0.702248
LSB5.0	79		2.494988	0.473832	0.210059	1.123564				0.261146
LSB5.1	82.5		2.369702	0.265131	0.193216	9.334322				0.767475
LSB5.2	87		2.219568	0.18598	0.204208	8.266912				0.760059
LSB5.3	91		2.026372	0.586391	0.182875	9.382329				0.770435
LSB5.4	95		2.057211	0.395073	0.220669	0.929705				0.258061
LSB5.5	99		1.5938	0.198699	0.148858	4.651151				0.705521
LSB5.6	103		1.724667	0.287985	0.150286	0.557738				0.205
LSB5.7	107		1.613339	0.36479	0.143329	3.257411				0.605594
LSB5.8	111		1.811596	0.367215	0.139142	4.151504				0.641708
LSB5.9	115		1.79285	0.414447	0.141884	4.716533				0.667524
LSB5.10	119		1.950122	0.430351	0.124097	4.605925				0.647764
LSB5.11	123		1.625496	0.264529	0.123999	4.203213				0.676058
LSB5.12	127		1.584747	0.328571	0.148768	4.205049				0.670968
LSB5.13	131		1.535385	0.395733	0.137089	2.577793	7.780441		0.597139	0.554841
LSB5.14	135		1.439331	0.324221	0.112258	3.250311				0.634068
LSB5.15	139		1.421847	0.576911	0.116059		8.436172			
LSB5.16	143		1.573246	0.409456	0.142418					
LSB5.17	147		0.868485	0.1351	0.115374		4.298041			
Bos32.1	-2		1.381	0.071044	0.107905	3.411243	7.052342		0.704899	0.686202
Bos32.2	0		1.272004	0.21705	0.084925	4.947089	7.157917		0.911029	0.758632
Bos32.3	2		1.418247	0.066906	0.090857	4.841652	7.011795		0.915267	0.754426

Pseud34.1	-2		1.375481	0.068835	0.064846	3.569371	5.507299		0.922146	0.702835
Pseud34.2	0		1.174778	0.283137	0.058145	0.288658	4.720028		0.382353	0.159947
Pseud34.3	2		1.411683	0.114843	0.097956	3.243449	5.715397		0.851722	0.666289
Pseud41.1	-2		1.332096	0.122639	0.073012	3.762996	5.54745		0.953725	0.711242
Pseud41.2	0		1.114867	0.132936	0.066255	3.948118	5.940996		0.88574	0.750282
Pseud41.3	2		1.219916	0.116865	0.071689	3.66388	5.538466		0.91584	0.722324
LSB accuracy:										
			FeCarb (wt.%)	**FeOx (wt.%)**	**FeMag (wt.%)**	**FePy (wt.%)**	**FeT (wt.%)**		**FeHR/FeT**	**FePy/FeHR**
Sample			0.72018	0.121851	0.080695	7.469319	12.36967		0.824732	0.732167
Repeat 1			0.770983	0.130619	0.120773	7.29883	11.69048		0.865681	0.721212
Repeat 2			0.743797	0.133667	0.12478	7.683476	11.35626		0.911448	0.742319
Repeat 3			0.768179	0.136338	0.118745	8.105506	11.53885		0.950079	0.739363
Standard (Whitby for FeOx, FeCarb, FeMag and FeT, for all else SBC-1)			0.581482	0.073784	2.372951	.	4.613414		.	.
Mean			0.750785	0.130619	0.111248	7.639283	11.73882		0.887985	0.733765
Stan.Dev			0.023777	0.006295	0.020523	0.348383	0.44221		0.054481	0.009392
95% Confidence			0.037793	0.010005	0.032621	0.553756	0.702893		0.086598	0.014929
as a % of measurement (i.e. precision)			5.033779	7.659962	29.32274	7.24879	5.987768		9.752186	2.034544
Measured standard - reported standard			-0.00152	0.011784	2.269951	.	0.073414		.	.
Deviation (i.e. accuracy)			0.001518	0.011784	2.269951	.	0.073414		.	.
Shell pavement accuracy:										
			FeCarb (wt.%)	**FeOx (wt.%)**	**FeMag (wt.%)**	**FePy (wt.%)**	**FeT (wt.%)**		**FeHR/FeT**	**FePy/FeHR**
Sample			1.381	0.071044	0.107905	3.411243	7.052342		0.704899	0.686202
Repeat 1			1.585213	0.075629	0.099566	5.634184	7.385331		1.001254	0.761933
Repeat 2			1.747987	0.073951	0.100659	5.273375	7.371531		0.976184	0.732823
Repeat 3			1.580668	0.076571	0.104983	5.34062	7.392399		0.96083	0.751899
Standard (Whitby)			0.727637	0.063934	0.133784	.	4.431888		.	.
Mean			1.573717	0.074299	0.103278	4.914855	7.300401		0.910792	0.733214
Stan.Dev			0.150211	0.002425	0.003871	1.014577	0.165599		0.138269	0.033587
95% Confidence			0.238761	0.003855	0.006153	1.61267	0.26322		0.219779	0.053386
as a % of measurement (i.e. precision)			15.17179	5.188911	5.957864	32.81215	3.605559		24.13052	7.281077
Measured standard - reported standard			0.144637	0.001934	0.030784	.	-0.10811		.	.

Deviation (i.e. accuracy)	0.144637	0.001934	0.030784	.	0.108112		.	.

Sample Code	Stratigraphic height*	Al (wt.%)	Ti (wt.%)	Mn (wt.%)	Ca (wt.%)	K (wt.%)	Mg (wt.%)	Ti wt.%/wt%	FeTwt.%/wt%	Mn wt.%/wt%	Ca wt.%/wt%	K wt.%/wt%	Mgwt.%/wt%
LSB1.0	2	9.01559	0.45166	0.032789	0.37541	1.878616	0.889653	0.050098	0.541847	0.003637	0.04164	0.208374	0.098679
LSB1.1	6	9.690518	0.467946	0.031363	0.410976	1.956618	0.959446	0.048289	0.528898	0.003236	0.04241	0.201911	0.099009
LSB1.2	14	9.267754	0.451165	0.030418	0.720802	1.786342	0.896872	0.048681	0.595933	0.003282	0.077775	0.192748	0.096773
LSB1.3	18	8.754688	0.449245	0.032257	0.454368	1.721451	0.892677	0.051315	0.633119	0.003685	0.0519	0.196632	0.101966
LSB1.4	22	7.793081	0.403909	0.029527	0.462557	1.514326	0.7737	0.051829	0.600637	0.003789	0.059355	0.194317	0.09928
LSB1.5	26	8.593852	0.452273	0.034092	0.511205	1.688416	0.875913	0.052627	0.589703	0.003967	0.059485	0.196468	0.101923
LSB1.6	30	8.609391	0.472288	0.034598	0.490969	1.78858	0.91353	0.054857	0.617399	0.004019	0.057027	0.207748	0.106109
LSB1.7	34	7.704854	0.401021	0.034253	0.666333	1.436834	0.762217	0.052048	0.564784	0.004446	0.086482	0.186484	0.098927
LSB1.8	38	6.777245	0.283037	0.038892	0.954156	0.986743	0.616362	0.041763	0.597321	0.005739	0.140788	0.145596	0.090946
LSB1.9	42	6.582083	0.302213	0.038959	0.842771	1.026673	0.619258	0.045914	0.649808	0.005919	0.12804	0.155 98	0.094082
LSB1.10	46	7.178685	0.361098	0.049578	0.828167	1.315874	0.754939	0.050301	0.869862	0.006906	0.115365	0.183303	0.105164
LSB1.11	50	7.158115	0.385341	0.060909	0.560784	1.575645	0.826251	0.053833	1.571901	0.008509	0.078342	0.22012	0.115429
LSB1.12	54	7.151974	0.387811	0.08294	0.636035	1.478428	0.819204	0.054224	1.479632	0.011597	0.088931	0.206716	0.114542
LSB1.13	59	6.477243	0.274252	0.076541	0.982368	0.925167	0.616623	0.042341	1.140078	0.011817	0.151665	0.142833	0.095198
LSB1.14	62	5.673031	0.212115	0.077725	1.400761	0.685195	0.568124	0.037039	1.134209	0.013701	0.246916	0.120781	0.100145
LSB1.15	66	6.408721	0.282376	0.076492	1.075359	0.987457	0.658742	0.044061	1.16465	0.011936	0.167796	0.15408	0.102788
LSB1.16	70	7.727819	0.379816	0.095002	0.437324	1.601532	0.888724	0.049149	1.403542	0.012294	0.056591	0.207242	0.115003
LSB1.17	74	9.178176	0.456071	0.112489	0.528588	1.858166	1.060733	0.049691	1.347727	0.012256	0.057592	0.202455	0.115571
LSB1.18	78	8.326353	0.369806	0.091343	0.404591	1.646143	0.88043	0.044414	1.571181	0.01097	0.048592	0.197703	0.10574
LSB1.19	82	8.459478	0.377816	0.091033	0.361005	1.698529	0.890603	0.044662	1.544588	0.010761	0.042675	0.200784	0.105279
LSB1.20	86	8.350937	0.40654	0.083908	0.350539	1.720552	0.872596	0.048682	1.468146	0.010048	0.041976	0.206031	0.104491
LSB1.21	90	8.110286	0.393927	0.07999	0.319328	1.645686	0.818686	0.048571	1.447056	0.009863	0.039373	0.202913	0.100944
LSB1.22	98	7.917072	0.397805	0.063133	0.606505	1.492412	0.813279	0.050246	0.933208	0.007974	0.076607	0.188506	0.102725
LSB1.23	102	7.323013	0.301667	0.07054	0.953496	1.056905	0.682845	0.041194	1.020865	0.009633	0.130205	0.144326	0.093246
LSB1.24	106	7.59585	0.322908	0.069192	0.926452	1.149985	0.710642	0.042511	0.943691	0.009109	0.121968	0.151396	0.093557
LSB1.25	110	6.680511	0.251597	0.076446	1.158813	0.863741	0.597109	0.037661	0.993829	0.011443	0.173462	0.129293	0.089381
LSB1.26	114	7.832624	0.349933	0.07486	1.198539	1.166283	0.712747	0.044676	0.901747	0.009557	0.153019	0.148901	0.090997
LSB1.27	118	8.029327	0.415923	0.066357	0.763827	1.466033	0.839182	0.0518	0.857257	0.008264	0.09513	0.182585	0.104515
LSB1.28	122	7.69828	0.357663	0.06032	0.648798	1.244991	0.708005	0.04646	0.921112	0.007836	0.084278	0.161723	0.091969
LSB1.29	126	8.861963	0.466471	0.044186	0.764807	1.712689	0.898178	0.052637	0.550284	0.004986	0.086302	0.193263	0.101352

LSB1.30	130		8.863886	0.455545	0.038288	0.64574	1.729783	0.896653		0.051393	0.536792	0.004319	0.072851	0.195149	0.101158
LSB3.0	-57.5		9.982714	0.507779	0.032411	0.419188	2.104581	1.030683		0.050866	0.487013	0.003247	0.041991	0.210823	0.103247
LSB3.1	-53.5		10.07785	0.510381	0.032439	0.361159	2.227509	1.053201		0.050644	0.491416	0.003219	0.035837	0.221 03	0.104506
LSB3.2	-50		10.44158	0.50598	0.035189	0.349586	2.217111	1.060258		0.048458	0.46696	0.00337	0.03348	0.212335	0.101542
LSB3.3	-42		10.81708	0.506035	0.035515	0.376045	2.344475	1.095636		0.046781	0.482833	0.003283	0.034764	0.216738	0.101288
LSB3.4	-38														
LSB3.5	-34														
LSB3.6	-30		9.541249	0.489591	0.033732	0.362375	2.062452	1.008096		0.051313	0.505051	0.003535	0.03798	0.216162	0.105657
LSB3.7	-26														
LSB3.8	-22														
LSB3.9	-18		9.39781	0.479015	0.033987	0.314781	1.991332	0.987682		0.050971	0.473301	0.003617	0.033495	0.211893	0.105097
LSB3.10	-14														
LSB3.11	-10														
LSB3.12	-6		9.810387	0.49258	0.033594	0.315334	2.225886	1.073784		0.05021	0.478992	0.003424	0.032143	0.226891	0.109454
LSB3.13	-2														
LSB3.14	2														
LSB3.15	6														
LSB3.16	10														
LSB3.17	14														
LSB3.18	18		9.105505	0.472477	0.031881	0.321101	1.970183	0.981651		0.051889	0.511335	0.003501	0.035264	0.216373	0.107809
LSB3.19	22														
LSB3.20	30														
LSB3.21	34														
LSB3.22	38														
LSB3.23	42														
LSB3.24	46														
LSB5.0	79														
LSB5.1	82.5														
LSB5.2	87														
LSB5.3	91														
LSB5.4	95														
LSB5.5	99														
LSB5.6	103														

LSB5.7	107															
LSB5.8	111															
LSB5.9	115															
LSB5.10	119															
LSB5.11	123															
LSB5.12	127															
LSB5.13	131		7.574382	0.437362	0.062255	0.514458	1.604065	0.890755		0.057742	1.027205	82.19167	0.067921	0.211775	0.117601	
LSB5.14	135															
LSB5.15	139		7.206206	0.399159	0.040277	0.523288	1.508532	0.779372		0.055391	1.170681	55.8915	0.072616	0.209338	0.108153	
LSB5.16	143															
LSB5.17	147		8.29109	0.456271	0.034873	0.645543	1.760928	0.917489		0.055031	0.518393	42.06085	0.07786	0.212388	0.11066	
Bos32.1	-2		8.470476	0.404423	0.027686	1.354203	2.187094	0.926929		0.047745	0.832579	0.003269	0.159873	0.258202	0.109431	
Bos32.2	0		8.597101	0.383756	0.02961	3.72694	1.936719	0.835597		0.044638	0.832597	0.003444	0.433511	0.225276	0.097195	
Bos32.3	2		9.682051	0.440499	0.027632	1.406122	2.349436	0.981274		0.045496	0.724206	0.002854	0.14523	0.242659	0.10135	
Pseud34.1	-2		8.729468	0.348952	0.044237	3.08134	2.204973	1.327481		0.039974	0.630886	0.005068	0.352981	0.252 59	0.152069	
Pseud34.2	0		6.829705	0.260267	0.04474	8.698234	1.629668	1.193723		0.038108	0.691103	0.006551	1.273589	0.238615	0.174784	
Pseud34.3	2		9.259338	0.372427	0.041744	2.27534	2.51462	1.28569		0.040222	0.617258	0.004508	0.245735	0.271577	0.138853	
Pseud41.1	-2		9.316227	0.361652	0.023881	5.508016	2.235905	0.871388		0.03882	0.595461	0.002563	0.591228	0.240001	0.093534	
Pseud41.2	0		9.257311	0.339573	0.023465	6.452342	2.225473	0.880693		0.036682	0.641763	0.002535	0.697	0.240402	0.095135	
Pseud41.3	2		9.681309	0.373703	0.02441	5.209764	2.341328	0.890371		0.0386	0.572078	0.002521	0.538126	0.241 84	0.091968	
LSB accuracy:																
			Al (wt.%)	**Ti (wt.%)**	**Mn (wt.%)**	**Ca (wt.%)**	**K (wt.%)**	**Mg (wt.%)**		**Ti wt.%/wt%**	**FeTwt.%/wt%**	**Mn wt.%/wt%**	**Ca wt.%/wt%**	**K wt.%/wt%**	**Mgwt.%/wt%**	
Sample			9.178176	0.456071	0.112489	0.528588	1.858166	1.060733		0.049691	1.347727	0.012256	0.057592	0.202455	0.115571	
Repeat 1			8.456018	0.426413	0.103654	0.397178	1.744907	0.963805		0.050427	1.382504	0.012258	0.046 97	0.206351	0.113979	
Repeat 2			7.909384	0.420841	0.100243	0.390716	1.6821	0.918107		0.053208	1.435796	0.012674	0.049399	0.212671	0.116078	
Repeat 3			8.104182	0.413243	0.101689	0.405181	1.700733	0.933381		0.050991	1.423815	0.012548	0.049996	0.209859	0.115173	
Standard (Whitby for FeOx, FeCarb, FeMag and FeT, for all else SBC-1)			10.85943	0.383225	0.114973	2.144246	2.88279	1.496455		0.03529	0.633514	0.010587	0.197455	0.265464	0.137802	
Mean			8.41194	0.429142	0.104519	0.430416	1.746476	0.969007		0.051079	1.39746	0.012434	0.050989	0.207834	0.1152	
Stan. Dev			0.558671	0.018747	0.005494	0.065715	0.078981	0.064033		0.001516	0.040255	0.000211	0.004592	0.004421	0.000895	
95% Confidence			0.888007	0.029798	0.008733	0.104454	0.12554	0.101781		0.002409	0.063985	0.000335	0.007299	0.007027	0.001422	

as a % of measurement (i.e. precision)			10.55651	6.943623	8.355576	24.26828	7.188197	10.5036		4.716367	4.578644	2.692464	14.3153	3.381118	1.234497
Measured standard - reported standard			0.067434	-0.12977	-0.00103	0.144246	0.02009	-0.07125		-0.01225	0.62397	-0.00016	0.012132	0.000203	-0.00746
Deviation (i.e. accuracy)			0.067434	0.129775	0.001027	0.144246	0.02009	0.071245		0.012246	0.62397	0.000161	0.012132	0.000203	0.007463
Shell pavement accuracy:															
			Al (wt.%)	**Ti (wt.%)**	**Mn (wt.%)**	**Ca (wt.%)**	**K (wt.%)**	**Mg (wt.%)**		**Ti wt.%/wt%**	**FeTwt.%/wt%**	**Mn wt.%/wt%**	**Ca wt.%/wt%**	**K wt.%/wt%**	**Mgwt.%/wt%**
Sample			8.470476	0.404423	0.027686	1.354203	2.187094	0.926929		0.047745	0.832579	0.003269	0.159873	0.258202	0.109431
Repeat 1			9.051687	0.383615	0.003045	1.512336	2.168151	0.923651		0.042381	0.815907	0.003045	0.167078	0.23953	0.102042
Repeat 2			9.093798	0.410127	0.003058	1.503181	2.200472	0.941227		0.0451	0.810611	0.003058	0.165297	0.241975	0.103502
Repeat 3			9.146474	0.401699	0.003031	1.513434	2.189536	0.932888		0.043918	0.808224	0.003031	0.165466	0.239386	0.101994
Standard (Whitby)			11.69034	0.439262	0.017468	1.031399	2.694114	1.054896							
Mean			8.940609	0.399966	0.009205	1.470788	2.186313	0.931174		0.044786	0.81683	0.003101	0.164429	0.244773	0.104242
Stan. Dev			0.315811	0.011452	0.012321	0.077859	0.013433	0.007716		0.002265	0.010979	0.000112	0.003141	0.009031	0.003529
95% Confidence			0.501982	0.018203	0.019584	0.123757	0.021352	0.012264		0.0036	0.017452	0.000179	0.004993	0.014355	0.005609
as a % of measurement (i.e. precision)			5.61463	4.551203	212.7504	8.41434	0.976613	1.317086		8.039259	2.136492	5.765842	3.036473	5.864513	5.381033
Measured standard - reported standard			-0.20966	-0.11374	-0.00153	0.001399	0.044114	-0.04451							
Deviation (i.e. accuracy)			0.209662	0.113738	0.001532	0.001399	0.044114	0.045104							

Sample Code	**Stratigraphic height***		**Mn ppm/wt.%**	**V ppm/wt.%**	**Zr ppm/wt.%**	**Rb ppm/wt.%**	**Sr ppm/wt.%**	**Ni ppm/wt.%**	**As ppm/wt.%**	**Cr ppm/wt.%**	**Li ppm/wt.%**	**Zn ppm/wt.%**
LSB1.0	2		36.36956	15.03123	6.021362	9.669828	17.08331	18.69702	1.890145	13.21057	9.567683	8.721303
LSB1.1	6		32.36484	14.86567	5.565571	9.635375	13.50666	13.78142	1.843861	13.02203	9.382482	8.340708
LSB1.2	14		32.8211	14.15855	6.007698	9.211226	13.96259	15.28143	2.197709	12.54008	9.04981	8.666307
LSB1.3	18		36.84507	14.95081	6.264597	9.444796	13.58213	33.07257	2.471423	13.32488	9.514031	8.892168
LSB1.4	22		37.88894	14.43243	6.36882	9.305287	14.07994	37.7307	2.433615	13.01957	9.496444	8.450158
LSB1.5	26		39.67027	14.32702	6.600622	9.170615	14.23586	17.14074	2.539923	13.09916	9.158212	8.179684
LSB1.6	30		40.18635	15.53124	6.927138	10.07424	15.24705	17.23015	2.672993	14.43971	9.548824	8.598139
LSB1.7	34		44.45692	13.69125	7.678184	8.522755	14.87579	15.64669	2.358189	12.40593	8.264883	8.201094
LSB1.8	38		57.38581	10.57686	5.29927	6.397729	13.72028	14.89444	2.421339	9.837094	6.637684	7.794458
LSB1.9	42		59.18924	11.48988	6.503512	6.987569	13.28738	16.21318	2.857816	11.04635	7.050181	8.675077
LSB1.10	46		69.0631	13.26228	6.835938	8.365068	21.06915	20.82058	4.516493	12.44078	8.121061	9.896857

LSB1.11	50		85.09097	16.55311	7.119796	10.52671	17.17536	35.16391	11.88099	15.45655	10.35487	12.8949
LSB1.12	54		115.9684	15.90769	6.822456	9.762361	16.9838	48.61515	12.07561	14.92191	9.957867	13.1282
LSB1.13	59		118.1688	10.55343	5.209284	6.159447	13.55727	99.53954	7.021688	10.44692	6.97102	9.938791
LSB1.14	62		137.0074	9.204547	5.136694	5.146127	13.74677	32.20839	7.153416	9.992567	6.090083	10.39846
LSB1.15	66		119.3565	11.54285	6.314261	6.803417	14.29897	40.04466	6.836237	11.88484	7.556638	9.78713
LSB1.16	70		122.9353	17.41856	5.889264	10.04516	13.94024	46.24203	10.63583	15.70534	11.27058	15.97094
LSB1.17	74		122.5613	16.58458	5.459563	9.941363	13.95403	52.8019	10.23147	15.34449	11.01211	14.74379
LSB1.18	78		109.703	16.9382	5.026758	9.626573	13.30925	45.81111	10.45532	15.05323	11.70151	17.32061
LSB1.19	82		107.6111	16.89554	5.477382	9.606276	13.15656	45.48724	9.667507	14.88698	11.93264	17.13859
LSB1.20	86		100.477	18.14482	5.673516	10.28625	16.7818	47.00013	9.499701	16.71757	11.82563	19.1487
LSB1.21	90		98.62735	17.57233	6.078972	10.13436	13.57636	55.17538	9.643549	16.35102	11.70847	18.11333
LSB1.22	98		79.74277	15.20931	7.181024	8.983797	14.26987	60.20907	5.330531	14.20028	9.936847	13.22961
LSB1.23	102		96.32712	11.19267	4.923877	6.432884	12.95329	46.56836	6.298442	10.55502	7.788623	11.81312
LSB1.24	106		91.09176	11.67429	4.796093	6.817878	12.93742	61.98413	6.511067	11.44261	7.906133	11.80858
LSB1.25	110		114.4316	9.894951	4.654329	5.439377	12.29711	59.44233	6.786477	9.87204	6.872419	9.98161
LSB1.26	114		95.57414	10.89207	5.7586	6.428788	13.3517	210.9628	6.508924	10.46221	7.247129	15.59534
LSB1.27	118		82.64373	14.40844	6.02786	8.397495	14.11439	40.82684	6.666728	14.09189	9.631491	13.089
LSB1.28	122		78.35515	12.87834	5.736443	7.467922	12.70215	36.93087	6.859325	12.53457	8.748424	11.63465
LSB1.29	126		49.86051	14.81198	6.595394	8.998964	14.44684	22.4421	3.270772	13.89176	9.994337	10.97281
LSB1.30	130		43.19496	14.63657	6.526553	9.232335	17.88252	23.72904	2.379896	13.32501	9.655832	9.74937
LSB3.0	-57.5		32.46753	15.25974	6.688312	10.15152	13.18182	29.43723	2.186147	13.52814	10.56277	8.593074
LSB3.1	-53.5		32.18884	15.55794	6.695279	10.5794	13.41202	16.90987	2.360515	14.09871	11.11588	8.519313
LSB3.2	-50		33.70044	14.97797	6.431718	10.22026	12.57709	11.1674	1.746696	13.10573	10.50661	8.193833
LSB3.3	-42		32.83262	14.95708	5.536481	10.21459	12.87554	9.785408	1.783262	13.19742	10.60086	7.832618
LSB3.4	-38											
LSB3.5	-34											
LSB3.6	-30		35.35354	15.05051	6.020202	11.0303	13.61616	12.18182	1.876768	13.31313	10.9899	8.464646
LSB3.7	-26											
LSB3.8	-22											
LSB3.9	-18		36.16505	14.90291	5.752427	10.65534	13.42233	10.80097	1.832524	13.30097	11.09223	7.76699
LSB3.10	-14											
LSB3.11	-10											
LSB3.12	-6		34.2437	15.73529	6.113445	11.59664	13.84454	12.31092	1.87395	13.94958	11.51261	8.02521

LSB3.13	-2											
LSB3.14	2											
LSB3.15	6											
LSB3.16	10											
LSB3.17	14											
LSB3.18	18		35.01259	15.31486	6.473552	11.20907	13.92947	11.88917	1.732997	13.60202	11.71285	7.43073
LSB3.19	22											
LSB3.20	30											
LSB3.21	34											
LSB3.22	38											
LSB3.23	42											
LSB3.24	46											
LSB5.0	79											
LSB5.1	82.5											
LSB5.2	87											
LSB5.3	91											
LSB5.4	95											
LSB5.5	99											
LSB5.6	103											
LSB5.7	107											
LSB5.8	111											
LSB5.9	115											
LSB5.10	119											
LSB5.11	123											
LSB5.12	127											
LSB5.13	131		82.19167	15.02549	6.3868	9.78622	15.73267	19.03413	7.414484	14.65339	11.14549	11.86892
LSB5.14	135											
LSB5.15	139		55.8915	14.33699	6.162359	9.247467	15.47253	11.98759	11.24252	13.49531	11.05409	13.55173
LSB5.16	143											
LSB5.17	147		42.06085	15.14919	6.302078	10.40395	15.42231	18.72268	4.967669	14.22356	11.44177	11.40953
Bos32.1	-2		32.68547	15.69848	6.551603	13.49972	17.1887	11.62697	2.486289	12.33976	11.36197	11.16658
Bos32.2	0		34.44152	14.17866	6.071897	11.80835	22.23381	9.677064	2.273498	11.07213	10.10399	14.01207
Bos32.3	2		28.5399	15.66203	7.215881	12.94445	15.881	9.24115	2.1314	12.38531	10.96239	8.63151
Pseud34.1	-2		50.6759	17.50322	6.309106	13.43258	20.32102	10.0586	2.04867	10.63537	7.483171	11.21763
Pseud34.2	0		65.50763	17.20269	6.518036	12.87424	47.09977	16.62086	2.333216	10.29496	6.758247	39.30621
Pseud34.3	2		45.08366	18.51785	5.913294	14.4738	17.58423	12.21382	1.975223	11.1835	7.437486	9.607128

Pseud41.1	-2		25.63347	16.75646	6.043302	13.7974	25.93731	26.97538	3.641799	11.20852	16.34966	13.98363
Pseud41.2	0		25.34781	16.88062	5.879496	13.65127	29.27635	22.39629	4.337844	11.10342	16.05905	12.05978
Pseud41.3	2		25.2134	17.01544	6.543027	13.7033	25.05159	17.13223	3.28038	11.32717	16.71579	11.35957
LSB accuracy:												
			Mn ppm/wt.%	**V ppm/wt.%**	**Zr ppm/wt.%**	**Rb ppm/wt.%**	**Sr ppm/wt.%**	**Ni ppm/wt.%**	**As ppm/wt.%**	**Cr ppm/wt.%**	**Li ppm/wt.%**	**Zn ppm/wt.%**
Sample			122.5613	16.58458	5.459563	9.941363	13.95403	52.8019	10.23147	15.34449	11.01211	14.74379
Repeat 1			122.5806	17.66881	6.1534	10.20765	13.35684	48.69395	10.87923	16.3938	11.50683	16.4018
Repeat 2			126.7388	18.12406	6.38287	9.675844	13.93524	49.87803	11.2513	16.89259	12.39145	17.36129
Repeat 3			125.4776	17.16706	6.052706	9.565438	13.54117	47.55194	10.89555	16.0353	11.4743	16.75232
Standard (Whitby for FeOx, FeCarb, FeMag and FeT, for all else SBC-1)			105.8738	20.65007	8.201339	12.70972	17.29101	7.869213	3.120015	10.15157	17.50215	23.52446
Mean			124.3396	17.38613	6.012135	9.847574	13.69682	49.73145	10.81439	16.16655	11.59617	16.3148
Stan.Dev			2.106196	0.66205	0.393439	0.287254	0.295982	2.256532	0.424844	0.651102	0.576318	1.119853
95% Confidence			3.347798	1.052329	0.62537	0.45659	0.470464	3.586758	0.675289	1.034926	0.916058	1.780006
as a % of measurement (i.e. precision)			2.692464	6.052691	10.4018	4.636537	3.434841	7.212252	6.244362	6.401653	7.899655	10.91038
Measured standard - reported standard			-1.61321	0.264597	-4.21527	-0.91148	0.797309	0.196863	0.738622	0.051492	2.398367	6.289473
Deviation (i.e. accuracy)			1.61321	0.264597	4.215265	0.911483	0.797309	0.196863	0.738622	0.051492	2.398367	6.289473
Shell pavement accuracy:												
			Mn ppm/wt.%	**V ppm/wt.%**	**Zr ppm/wt.%**	**Rb ppm/wt.%**	**Sr ppm/wt.%**	**Ni ppm/wt.%**	**As ppm/wt.%**	**Cr ppm/wt.%**	**Li ppm/wt.%**	**Zn ppm/wt.%**
Sample			32.68547	15.69848	6.551603	13.49972	17.1887	11.62697	2.486289	12.33976	11.36197	11.16658
Repeat 1			30.45127	15.07977	5.271459	12.63302	16.10432	10.58864	2.384059	11.98088	10.94778	12.29271
Repeat 2			30.5808	15.19849	6.125903	12.70709	16.2459	11.22742	2.436956	11.92109	10.25796	11.92466
Repeat 3			30.30882	15.247	5.912177	12.73821	16.03949	11.15181	2.47291	11.98907	10.64054	11.20778
Standard (Whitby)												
Mean			31.00659	15.30593	5.965286	12.89451	16.3946	11.14871	2.445053	12.0577	10.80206	11.64793
Stan.Dev			1.124751	0.27096	0.533473	0.40588	0.536369	0.427634	0.045688	0.190464	0.467924	0.553095
95% Confidence			1.787791	0.43069	0.847956	0.645147	0.852558	0.679725	0.072621	0.302742	0.743765	0.879145
as a % of measurement (i.e. precision)			5.765842	2.813877	14.21484	5.003268	5.200236	6.096891	2.970137	2.510777	6.885403	7.547652

Measured standard - reported standard										
Deviation (i.e. accuracy)										

Sample Code	Stratigraphic height*		Ba ppm/wt.%	U ppm/wt.%	Mo ppm/wt.%	Cu ppm/wt.%	Cd ppm/wt.%	Co ppm/wt.%	Ga ppm/wt.%	Tl ppm/wt.%	Pb ppm/wt.%
LSB1.0	2		40.02399	0.256473	0.180054	4.002859	0	2.938784	2.676949	0.069947	4.981097
LSB1.1	6		35.07625	0.234153	0.202256	4.130919	0	3.135307	2.649047	0.07592	5.660851
LSB1.2	14		40.80611	0.240191	0.290081	4.725745	0	4.154865	2.52644	0.0948	8.065681
LSB1.3	18		43.30734	0.262132	0.364019	5.186699	0	4.11388	2.675796	0.098054	8.582847
LSB1.4	22		50.05551	0.272558	0.359756	4.902043	0	3.835391	2.572357	0.088279	8.369075
LSB1.5	26		52.42913	0.279455	0.3763	5.09061	0	3.710475	2.580254	0.108799	8.48757
LSB1.6	30		48.15455	0.298227	0.39946	5.178831	0	4.066433	2.750962	0.100846	9.308581
LSB1.7	34		75.24061	0.306827	0.429198	4.883191	0	3.7061	2.416329	0.099551	8.09737
LSB1.8	38		116.7797	0.247813	0.625571	5.122687	0	3.606926	1.992906	0.118377	7.103456
LSB1.9	42		105.5231	0.27423	0.683454	5.468576	0	4.388213	2.118347	0.124124	8.457012
LSB1.10	46		76.46964	0.293373	0.870797	6.196708	0	5.500004	2.414501	0.170615	12.44111
LSB1.11	50		39.89592	0.308264	1.686389	11.842	0.018383	11.3485	2.884203	0.338903	33.44673
LSB1.12	54		37.33792	0.33505	2.405452	13.24506	0.020973	10.50095	2.783909	0.33432	37.13252
LSB1.13	59		57.63608	0.295324	2.007586	9.996239	0.025073	5.395226	2.017421	0.237206	17.55472
LSB1.14	62		98.11013	0.278595	1.721601	10.4995	0.022826	4.904016	1.760311	0.265692	12.704
LSB1.15	66		71.29911	0.302005	1.866426	10.4265	0.023386	5.602692	2.13076	0.270489	18.09707
LSB1.16	70		26.21621	0.311637	3.305291	16.0551	0.033342	8.046418	2.920879	0.348492	39.37668
LSB1.17	74		29.61148	0.32135	3.426488	14.6187	0.028986	7.969649	2.934017	0.303872	36.72136
LSB1.18	78		23.74211	0.283923	2.547527	17.30349	0.046787	8.526899	2.814173	0.368059	33.91906
LSB1.19	82		23.22342	0.288535	2.361779	16.45468	0.042869	8.399022	2.75549	0.356092	34.03985
LSB1.20	86		27.74704	0.284621	2.100211	17.2391	0.041045	9.691762	2.94666	0.306616	31.17769
LSB1.21	90		26.55135	0.286196	2.348884	17.31932	0.039826	9.292677	2.892144	0.298839	33.88605
LSB1.22	98		39.30685	0.306624	1.386784	11.00114	0.020856	6.264141	2.62098	0.153543	23.99062
LSB1.23	102		53.16573	0.25692	1.460562	11.10508	0.0251	6.489815	2.150787	0.191991	17.65256
LSB1.24	106		54.5505	0.260266	1.51865	11.37155	0.024621	5.738195	2.217743	0.200877	17.87074
LSB1.25	110		70.01655	0.247001	1.510447	11.0548	0.027759	5.737902	1.93633	0.184892	17.07308
LSB1.26	114		59.20578	0.277446	1.597425	11.39508	0.033539	5.870398	2.130896	0.204223	20.34514
LSB1.27	118		47.14197	0.295976	1.667198	11.29474	0.025682	7.137604	2.670324	0.170294	21.67966
LSB1.28	122		49.10004	0.270392	1.181938	10.96794	0.023272	6.115519	2.388231	0.177249	17.25657

LSB1.29	126		49.39891	0.283084	0.50218	5.903552	0.016211	4.604622	2.611377	0.103561	9.438838
LSB1.30	130		49.96023	0.255942	0.354711	5.00147	0.018362	3.789384	2.605342	0.08828	8.171078
LSB3.0	-57.5		30.73593	0.25974	0.135714	3.138528	0	2.922078	2.705628	0.067749	3.354978
LSB3.1	-53.5		30.04292	0.227468	0.135622	3.133047	0.000839	2.896996	2.7897	0.07382	3.626609
LSB3.2	-50		27.7533	0.222467	0.122687	2.819383	0	2.599119	2.687225	0.049339	3.303965
LSB3.3	-42		27.46781	0.209227	0.11824	2.939914	0	2.532189	2.660944	0.058155	3.519313
LSB3.4	-38										
LSB3.5	-34										
LSB3.6	-30		35.15152	0.190505	0.149091	3.151515	0.000588	2.929293	2.727273	0.05899	3.89899
LSB3.7	-26										
LSB3.8	-22										
LSB3.9	-18		35.19417	0.178155	0.153155	2.839806	0.000772	2.645631	2.742718	0.067718	3.956311
LSB3.10	-14										
LSB3.11	-10										
LSB3.12	-6		31.93277	0.195588	0.131303	3.130252	0.000851	2.62605	2.941176	0.068487	4.159664
LSB3.13	-2										
LSB3.14	2										
LSB3.15	6										
LSB3.16	10										
LSB3.17	14										
LSB3.18	18		39.5466	0.199748	0.162972	3.929471	0.000798	2.846348	2.947103	0.062469	5.088161
LSB3.19	22										
LSB3.20	30										
LSB3.21	34										
LSB3.22	38										
LSB3.23	42										
LSB3.24	46										
LSB5.0	79										
LSB5.1	82.5										
LSB5.2	87										
LSB5.3	91										
LSB5.4	95										
LSB5.5	99										
LSB5.6	103										
LSB5.7	107										
LSB5.8	111										
LSB5.9	115										
LSB5.10	119										
LSB5.11	123										

LSB5.12	127										
LSB5.13	131		39.55377	0.250525	1.116213	13.16753	0.290419	6.832718	2.968374	0.191412	23.21329
LSB5.14	135										
LSB5.15	139		35.89506	0.221995	0.622567	11.41568	0.242061	6.376889	2.768918	0.157318	15.15226
LSB5.16	143										
LSB5.17	147		26.82864	0.24381	0.293675	7.120772	0.227071	6.610128	2.929843	0.093936	11.20744
Bos32.1	-2		30.90138	0.468282	0.508688	5.011662	0.00336	2.602243	3.094037	0.029891	3.451083
Bos32.2	0		31.48947	0.409293	0.520738	4.465258	0.005004	2.244159	2.785802	0.023621	3.10822
Bos32.3	2		26.70154	0.441517	0.369974	5.140868	0.002262	2.445467	3.072365	0.027599	3.409355
Pseud34.1	-2		33.26527	0.50756	0.70099	8.424203	0.004678	3.075474	3.022306	0.023447	2.943194
Pseud34.2	0		38.30917	0.581492	0.741872	7.26408	0.023446	2.813331	2.99462	0.020961	2.664252
Pseud34.3	2		30.46298	0.535457	0.61714	8.657438	0.003392	3.170548	3.034907	0.022967	2.990431
Pseud41.1	-2		25.6242	0.521205	2.125623	4.346001	0.004931	3.387668	2.79229	0.035844	2.957034
Pseud41.2	0		27.37858	0.586714	2.145339	4.410548	0.002492	3.314003	2.918181	0.032061	2.813346
Pseud41.3	2		25.79192	0.480218	2.011024	4.457751	0.002602	3.475659	2.801159	0.037889	2.792609
LSB accuracy:											
			Ba ppm/wt.%	**U ppm/wt.%**	**Mo ppm/wt.%**	**Cu ppm/wt.%**	**Cd ppm/wt.%**	**Co ppm/wt.%**	**Ga ppm/wt.%**	**Tl ppm/wt.%**	**Pb ppm/wt.%**
Sample			29.61148	0.32135	3.426488	14.6187	0.028986	7.969649	2.934017	0.303872	36.72136
Repeat 1			26.03625	0.303488	3.365547	16.28521	0.034912	8.25517	2.947733	0.321562	38.75979
Repeat 2			26.10489	0.331064	3.302784	16.8789	0.03845	8.435102	2.988626	0.322696	39.39465
Repeat 3			25.55367	0.313492	3.251744	16.42451	0.040103	8.165995	2.88471	0.33255	39.86951
Standard (Whitby for FeOx, FeCarb, FeMag and FeT, for all else SBC-1)			67.28843	0.511754	0.203765	2.754582	0.047139	2.085744	2.706327	0.085409	3.212419
Mean			26.82657	0.317349	3.336641	16.05185	0.035613	8.206479	2.938772	0.32017	38.68633
Stan.Dev			1.872735	0.011706	0.075855	0.988496	0.00492	0.193534	0.04286	0.011933	1.386617
95% Confidence			2.976713	0.018607	0.120572	1.571214	0.00782	0.307623	0.068127	0.018968	2.204028
as a % of measurement (i.e. precision)			11.09613	5.863316	3.613562	9.788372	21.95796	3.748536	2.318197	5.924333	5.697177
Measured standard - reported standard			-5.72862	-0.02197	-0.01862	-0.11792	0.010075	-0.01767	0.204474	0.00294	-0.03072
Deviation (i.e. accuracy)			5.728618	0.021975	0.018622	0.117916	0.010075	0.017666	0.204474	0.00294	0.030724
Shell pavement accuracy:											

			Ba ppm/wt.%	U ppm/wt.%	Mo ppm/wt.%	Cu ppm/wt.%	Cd ppm/wt.%	Co ppm/wt.%	Ga ppm/wt.%	Tl ppm/wt.%	Pb ppm/wt.%
Sample			30.90138	0.468282	0.508688	5.011662	0.00336	2.602243	3.094037	0.029891	3.451083
Repeat 1			28.88998	0.404847	0.478149	4.71622	0.003655	2.523195	2.920563	0.025953	3.132755
Repeat 2			28.90691	0.427911	0.478201	4.953592	0.002918	2.538681	2.957412	0.025993	3.18879
Repeat 3			28.56028	0.413044	0.47282	4.860795	0.002731	2.550418	3.049232	0.026561	3.195872
Standard (Whitby)											
Mean			29.31464	0.428521	0.484465	4.885567	0.003166	2.553634	3.005311	0.027099	3.242125
Stan.Dev			1.069795	0.028174	0.016345	0.128866	0.000419	0.03427	0.080162	0.001882	0.142137
95% Confidence			1.700439	0.044782	0.02598	0.204833	0.000667	0.054472	0.127418	0.002991	0.225927
as a % of measurement (i.e. precision)			5.800647	10.45046	5.362658	4.192607	21.05585	2.133103	4.239748	11.03714	6.968498
Measured standard - reported standard											
Deviation (i.e. accuracy)											

Sample Code	Stratigraphic height*		K/Rb		TIC	CaCO3 (wt.%)	D		D*Ti wt.%/wt%	D*FeTwt.%/wt%	D*Mn wt.%/wt%	D*Ca wt.%/wt%	D*K wt.%/wt%	D*Mgwt.%/wt%
LSB1.0	2		215.489											
LSB1.1	6		209.5513											
LSB1.2	14		209.2534											
LSB1.3	18		208.1908											
LSB1.4	22		208.824		0	0	1		0.051829	0.600637	0.003789	0.059355	0.194317	0.09928
LSB1.5	26		214.2363											
LSB1.6	30		206.2165		0	0	1		0.054857	0.617399	0.004019	0.057027	0.207748	0.106109
LSB1.7	34		218.8074		5.491777	45.76481	1.843821		0.095967	1.041362	0.008197	0.159458	0.343844	0.182403
LSB1.8	38		227.5753											
LSB1.9	42		223.2249		0	0	1		0.045914	0.649808	0.005919	0.12804	0.15598	0.094082
LSB1.10	46		219.1291		0	0	1		0.050301	0.869862	0.006906	0.115365	0.183303	0.105164
LSB1.11	50		209.1064		0	0	1		0.053833	1.571901	0.008509	0.078342	0.22012	0.115429
LSB1.12	54		211.748		0.137905	1.149209	1.011626		0.054855	1.496833	0.011732	0.089965	0.209119	0.115874
LSB1.13	59		231.8932		0.065278	0.543985	1.00547		0.042572	1.146314	0.011882	0.152494	0.143615	0.095719
LSB1.14	62		234.7029		0.484685	4.039041	1.04209		0.038964	1.181948	0.014277	0.257309	0.125865	0.10436
LSB1.15	66		226.4748		0.490041	4.083672	1.042575		0.045937	1.214236	0.012444	0.17494	0.16064	0.107165
LSB1.16	70		206.3108		0.154371	1.286425	1.013032		0.04979	1.421833	0.012454	0.057328	0.209943	0.116502

LSB1.17	74		203.649		0.646795	5.389956	1.05697		0.052522	1.424507	0.012954	0.060873	0.213989	0.122155
LSB1.18	78		205.3719		0.064258	0.535486	1.005384		0.044653	1.57964	0.011029	0.048853	0.198767	0.106309
LSB1.19	82		209.0135		0.739326	6.161053	1.065656		0.047594	1.645999	0.011468	0.045476	0.213967	0.112191
LSB1.20	86		200.2975		0.761661	6.347171	1.067773		0.051981	1.567647	0.010729	0.044821	0.219994	0.111573
LSB1.21	90		200.2232		0.720616	6.005133	1.063888		0.051674	1.539506	0.010493	0.041889	0.215877	0.107393
LSB1.22	98		209.8284		0.336482	2.80402	1.028849		0.051696	0.96013	0.008204	0.078817	0.193944	0.105688
LSB1.23	102		224.3574		0	0	1		0.041194	1.020865	0.009633	0.130205	0.144326	0.093246
LSB1.24	106		222.0581											
LSB1.25	110		237.6975		0	0	1		0.037661	0.993829	0.011443	0.173462	0.129293	0.089381
LSB1.26	114		231.6156		0	0	1		0.044676	0.901747	0.009557	0.153019	0.148901	0.090997
LSB1.27	118		217.4277											
LSB1.28	122		216.5573											
LSB1.29	126		214.7613											
LSB1.30	130		211.376											
LSB3.0	-57.5		207.6759		0	0	1		0.050866	0.487013	0.003247	0.041991	0.210823	0.103247
LSB3.1	-53.5		208.9249		0	0	1		0.050644	0.491416	0.003219	0.035837	0.22103	0.104506
LSB3.2	-50		207.7586											
LSB3.3	-42		212.1849											
LSB3.4	-38													
LSB3.5	-34													
LSB3.6	-30		195.9707		0	0	1		0.051313	0.505051	0.003535	0.03798	0.216162	0.105657
LSB3.7	-26													
LSB3.8	-22													
LSB3.9	-18		198.861											
LSB3.10	-14													
LSB3.11	-10													
LSB3.12	-6		195.6522											
LSB3.13	-2													
LSB3.14	2													
LSB3.15	6													
LSB3.16	10													
LSB3.17	14													
LSB3.18	18		193.0337		0	0	1							
LSB3.19	22													

LSB3.20	30													
LSB3.21	34													
LSB3.22	38													
LSB3.23	42													
LSB3.24	46													
LSB5.0	79													
LSB5.1	82.5													
LSB5.2	87													
LSB5.3	91													
LSB5.4	95													
LSB5.5	99													
LSB5.6	103													
LSB5.7	107													
LSB5.8	111													
LSB5.9	115													
LSB5.10	119													
LSB5.11	123													
LSB5.12	127													
LSB5.13	131		216.4013		0.047253	0.393774	1.003953		0.05797	1.031265	82.51659	0.068189	0.212612	0.118066
LSB5.14	135													
LSB5.15	139		226.3733											
LSB5.16	143													
LSB5.17	147		204.1418											
Bos32.1	-2		191.2647		0.339452	2.828763	1.029111		0.049135	0.856816	0.003364	0.164527	0.265719	0.112616
Bos32.2	0		190.7767		1.227165	10.22638	1.113913		0.049723	0.92744	0.003836	0.482894	0.250938	0.108267
Bos32.3	2		187.4617		0.582301	4.852512	1.051		0.047817	0.76114	0.003	0.152636	0.255034	0.106519
Pseud34.1	-2		188.0426		1.475556	12.2963	1.140203		0.045578	0.719338	0.005778	0.40247	0.288003	0.173389
Pseud34.2	0		185.3427		3.20892	26.741	1.36502		0.052018	0.943369	0.008942	1.738474	0.325714	0.238584
Pseud34.3	2		187.6333		1.288318	10.73598	1.120272		0.045059	0.691497	0.005051	0.27529	0.30424	0.155554
Pseud41.1	-2		173.9466		1.986049	16.5504	1.198328		0.046519	0.713558	0.003072	0.708485	0.2876	0.112085
Pseud41.2	0		176.1021		2.284065	19.03387	1.235084		0.045305	0.792631	0.003131	0.860853	0.296916	0.1175
Pseud41.3	2		176.4831		1.88846	15.73717	1.186763		0.04581	0.678921	0.002992	0.638628	0.287007	0.109144

LSB accuracy:														
			K/Rb		TIC	CaCO3 (wt. %)	D		D*Ti wt.%/ wt%	D*FeTwt. %/wt%	D*Mn wt.%/ wt%	D*Ca wt.%/ wt%	D*K wt.%/ wt%	D*Mgwt. %/wt%
Sample			203.649		0.646795	5.389956	1.05697		0.052522	1.424507	0.012954	0.060873	0.213989	0.122155
Repeat 1			202.1531		0	0	1		0.050427	1.382504	0.012258	0.04697	0.206351	0.113979
Repeat 2			219.7962		0	0	1		0.053208	1.435796	0.012674	0.049399	0.212671	0.116078
Repeat 3			219.3926		0	0	1		0.050991	1.423815	0.012548	0.049996	0.209859	0.115173
Standard (Whitby for FeOx, FeCarb, FeMag and FeT, for all else SBC-1)			208.867		0.702258	1.702258	2.702258		4.702258	5.702258	6.702258	7.702258	8.702258	9.702258
Mean			211.2477		0.161699	1.347489	1.014243		0.051787	1.416656	0.012609	0.05181	0.210717	0.116846
Stan. Dev			9.658659		0.323397	2.694978	0.028485		0.001296	0.023421	0.000289	0.006182	0.003383	0.003642
95% Confidence			15.35244		0.51404	4.283667	0.045277		0.00206	0.037227	0.000459	0.009827	0.005377	0.00579
as a % of measurement (i.e. precision)			7.267504		317.9	317.9	4.464128		3.978572	2.627822	3.642076	18.96725	2.551523	4.954804
Measured standard - reported standard														
Deviation (i.e. accuracy)														
Shell pavement accuracy:														
			K/Rb		TIC	CaCO3 (wt. %)	D		D*Ti wt.%/ wt%	D*FeTwt. %/wt%	D*Mn wt.%/ wt%	D*Ca wt.%/ wt%	D*K wt.%/ wt%	D*Mgwt. %/wt%
Sample			191.2647		1.986049	16.5504	1.198328		0.057214	0.997703	0.003917	0.191581	0.309411	0.131134
Repeat 1			189.6063		1.046582	8.721517	1.095548		0.04643	0.893865	0.003336	0.183042	0.262417	0.111792
Repeat 2			190.4252		.	.	.							
Repeat 3			187.9275		.	.	.							
Standard (Whitby)					0.985724	8.214366	1.089495		0	0	0	0	0	0
Mean			189.8059		1.516315	12.63596	1.146938		0.051822	0.945784	0.003626	0.187311	0.285914	0.121463
Stan. Dev			1.423593		0.664303	5.53586	0.072676		0.007626	0.073424	0.000411	0.006038	0.03323	0.013677
95% Confidence			2.262801		5.965612	49.71344	0.652651		0.06848	0.65937	0.003687	0.054222	0.298412	0.12282
as a % of measurement (i.e. precision)			1.192166		393.4282	393.4282	56.90378		132.1441	69.7168	101.6835	28.94768	104.3712	101.1178
Measured standard - reported standard														
Deviation (i.e. accuracy)														

Sample Code	Stratigraphic height*		D*Mn ppm/wt.%	D*V ppm/wt.%	D*Zr ppm/wt.%	D*Rb ppm/wt.%	D*Sr ppm/wt.%	D*Ni ppm/wt.%	D*As ppm/wt.%	D*Cr ppm/wt.%
LSB1.0	2									
LSB1.1	6									
LSB1.2	14									
LSB1.3	18									
LSB1.4	22		37.88894	14.43243	6.36882	9.305287	14.07994	37.7307	2.433615	13.01957
LSB1.5	26									
LSB1.6	30		40.18635	15.53124	6.927138	10.07424	15.24705	17.23015	2.672993	14.43971
LSB1.7	34		81.9706	25.24421	14.1572	15.71444	27.42829	28.8497	4.348079	22.87431
LSB1.8	38									
LSB1.9	42		59.18924	11.48988	6.503512	6.987569	13.28738	16.21318	2.857816	11.04635
LSB1.10	46		69.0631	13.26228	6.835938	8.365068	21.06915	20.82058	4.516493	12.44078
LSB1.11	50		85.09097	16.55311	7.119796	10.52671	17.17536	35.16391	11.88099	15.45655
LSB1.12	54		117.3166	16.09263	6.901772	9.875855	17.18124	49.18033	12.21599	15.09539
LSB1.13	59		118.8151	10.61116	5.237776	6.193137	13.63142	100.084	7.060094	10.50406
LSB1.14	62		142.7741	9.591971	5.3529	5.36273	14.32538	33.56405	7.454507	10.41316
LSB1.15	66		124.4382	12.03429	6.583093	7.093075	14.90775	41.74958	7.127292	12.39084
LSB1.16	70		124.5374	17.64556	5.966012	10.17607	14.12191	46.84465	10.77444	15.91001
LSB1.17	74		129.5436	17.52941	5.770596	10.50772	14.749	55.81003	10.81436	16.21867
LSB1.18	78		110.2936	17.02939	5.053821	9.6784	13.3809	46.05774	10.5116	15.13427
LSB1.19	82		114.6764	18.00482	5.837002	10.23698	14.02037	48.47373	10.30223	15.8644
LSB1.20	86		107.2867	19.37455	6.05803	10.98338	17.91916	50.18549	10.14353	17.85058
LSB1.21	90		104.9284	18.69499	6.467345	10.78183	14.44372	58.70042	10.25965	17.39566
LSB1.22	98		82.04328	15.64808	7.38819	9.242972	14.68155	61.94605	5.484312	14.60995
LSB1.23	102		96.32712	11.19267	4.923877	6.432884	12.95329	46.56836	6.298442	10.55502
LSB1.24	106									
LSB1.25	110		114.4316	9.894951	4.654329	5.439377	12.29711	59.44233	6.786477	9.872047
LSB1.26	114		95.57414	10.89207	5.7586	6.428788	13.3517	210.9628	6.508924	10.46221
LSB1.27	118									
LSB1.28	122									
LSB1.29	126									
LSB1.30	130									
LSB3.0	-57.5		32.46753	15.25974	6.688312	10.15152	13.18182	29.43723	2.186147	13.52814
LSB3.1	-53.5		32.18884	15.55794	6.695279	10.5794	13.41202	16.90987	2.360515	14.09871
LSB3.2	-50									
LSB3.3	-42									
LSB3.4	-38									
LSB3.5	-34									

LSB3.6	-30		35.35354	15.05051	6.020202	11.0303	13.61616	12.18182	1.876768	13.31313
LSB3.7	-26									
LSB3.8	-22									
LSB3.9	-18									
LSB3.10	-14									
LSB3.11	-10									
LSB3.12	-6									
LSB3.13	-2									
LSB3.14	2									
LSB3.15	6									
LSB3.16	10									
LSB3.17	14									
LSB3.18	18									
LSB3.19	22									
LSB3.20	30									
LSB3.21	34									
LSB3.22	38									
LSB3.23	42									
LSB3.24	46									
LSB5.0	79									
LSB5.1	82.5									
LSB5.2	87									
LSB5.3	91									
LSB5.4	95									
LSB5.5	99									
LSB5.6	103									
LSB5.7	107									
LSB5.8	111									
LSB5.9	115									
LSB5.10	119									
LSB5.11	123									
LSB5.12	127									
LSB5.13	131		82.51659	15.08489	6.412049	9.824908	15.79486	19.10938	7.443796	14.71132
LSB5.14	135									
LSB5.15	139									
LSB5.16	143									
LSB5.17	147									
Bos32.1	-2		33.63698	16.15548	6.742327	13.89271	17.68908	11.96545	2.558667	12.69898
Bos32.2	0		38.36486	15.7938	6.763565	13.15348	24.76653	10.77941	2.532479	12.33339
Bos32.3	2		29.99543	16.46079	7.58389	13.60462	16.69093	9.712448	2.240101	13.01696
Pseud34.1	-2		57.78081	19.95722	7.19366	15.31586	23.17009	11.46884	2.335899	12.12648
Pseud34.2	0		89.41922	23.48202	8.89725	17.5736	64.29212	22.68781	3.184887	14.05283
Pseud34.3	2		50.50597	20.74504	6.624498	16.2146	19.69913	13.6828	2.212788	12.52856

Pseud41.1	-2		30.71731	20.07973	7.241859	16.53382	31.08141	32.32536	4.364071	13.43149
Pseud41.2	0		31.30669	20.84899	7.261674	16.86047	36.15876	27.6613	5.357604	13.71366
Pseud41.3	2		29.92233	20.1933	7.765021	16.26257	29.7303	20.3319	3.893033	13.44266
LSB accuracy:										
			D*Mn ppm/wt.%	**D*V ppm/wt.%**	**D*Zr ppm/wt.%**	**D*Rb ppm/wt.%**	**D*Sr ppm/wt.%**	**D*Ni ppm/wt.%**	**D*As ppm/wt.%**	**D*Cr ppm/wt.%**
Sample			129.5436	17.52941	5.770596	10.50772	14.749	55.81003	10.81436	16.21867
Repeat 1			122.5806	17.66881	6.1534	10.20765	13.35684	48.69395	10.87923	16.3938
Repeat 2			126.7388	18.12406	6.38287	9.675844	13.93524	49.87803	11.2513	16.89259
Repeat 3			125.4776	17.16706	6.052706	9.565438	13.54117	47.55194	10.89555	16.0353
Standard (Whitby for FeOx, FeCarb, FeMag and FeT, for all else SBC-1)			11.70226	12.70226	13.70226	14.70226	15.70226	16.70226	17.70226	18.70226
Mean			126.0852	17.62234	6.089893	9.989164	13.89556	50.48349	10.96011	16.38509
Stan.Dev			2.889033	0.395727	0.253773	0.445105	0.617992	3.675827	0.197267	0.368641
95% Confidence			4.592118	0.629009	0.403372	0.707494	0.982298	5.842726	0.313556	0.585955
as a % of measurement (i.e. precision)			3.642076	3.569384	6.623633	7.082618	7.069154	11.57354	2.860888	3.576147
Measured standard - reported standard										
Deviation (i.e. accuracy)										
Shell pavement accuracy:										
			D*Mn ppm/wt.%	**D*V ppm/wt.%**	**D*Zr ppm/wt.%**	**D*Rb ppm/wt.%**	**D*Sr ppm/wt.%**	**D*Ni ppm/wt.%**	**D*As ppm/wt.%**	**D*Cr ppm/wt.%**
Sample			39.16792	18.81193	7.85097	16.1771	20.5977	13.93293	2.97939	14.78708
Repeat 1			33.36085	16.52062	5.775139	13.84008	17.64306	11.60037	2.611852	13.12564
Repeat 2										
Repeat 3										
Standard (Whitby)			0	0	0	0	0	0	0	0
Mean			36.26438	17.66627	6.813055	15.00859	19.12038	12.76665	2.795621	13.95636
Stan.Dev			4.106219	1.620199	1.467834	1.652518	2.089247	1.649366	0.259888	1.174817
95% Confidence			36.8749	14.5498	13.18153	14.84004	18.76198	14.81173	2.333864	10.55015
as a % of measurement (i.e. precision)			101.6835	82.3592	193.4746	98.87695	98.12553	116.0189	83.48284	75.59389
Measured standard - reported standard										

Deviation (i.e. accuracy)								

Sample Code	Stratigraphic height*		D*Li ppm/ wt.%	D*Zn ppm/ wt.%	D*Ba ppm/ wt.%	D*U ppm/ wt.%	D*Mo ppm/ wt.%	D*Cu ppm/ wt.%	D*Cd ppm/ wt.%	D*Co ppm/ wt.%	D*Ga ppm/ wt.%	D*Tl ppm/ wt.%	D*Pb ppm/ wt.%
LSB1.0	2												
LSB1.1	6												
LSB1.2	14												
LSB1.3	18												
LSB1.4	22		9.496444	8.450158	50.05551	0.272558	0.359756	4.902043	0	3.835391	2.572357	0.088279	8.369075
LSB1.5	26												
LSB1.6	30		9.548824	8.598139	48.15455	0.298227	0.39946	5.178831	0	4.066433	2.750962	0.100846	9.308581
LSB1.7	34		15.23897	15.12135	138.7302	0.565734	0.791364	9.00373	0	6.833386	4.455278	0.183554	14.9301
LSB1.8	38												
LSB1.9	42		7.050181	8.675077	105.5231	0.27423	0.683454	5.468576	0	4.388213	2.118347	0.124124	8.457012
LSB1.10	46		8.121061	9.896857	76.46964	0.293373	0.870797	6.196708	0	5.500004	2.414501	0.170615	12.44111
LSB1.11	50		10.35487	12.8949	39.89592	0.308264	1.686389	11.842	0.018383	11.3485	2.884203	0.338903	33.44673
LSB1.12	54		10.07363	13.28082	37.772	0.338945	2.433417	13.39905	0.021217	10.62303	2.816274	0.338206	37.56421
LSB1.13	59		7.009149	9.993152	57.95132	0.296939	2.018566	10.05091	0.02521	5.424735	2.028456	0.238503	17.65073
LSB1.14	62		6.346418	10.83614	102.2396	0.290321	1.794064	10.94151	0.023787	5.110428	1.834404	0.276875	13.23872
LSB1.15	66		7.878365	10.20382	74.33469	0.314863	1.94589	10.87041	0.024381	5.841228	2.221478	0.282005	18.86756
LSB1.16	70		11.41745	16.17907	26.55786	0.315698	3.348365	16.26433	0.033777	8.151278	2.958944	0.353033	39.88984
LSB1.17	74		11.63947	15.58374	31.29845	0.339657	3.621696	15.45153	0.030638	8.423682	3.101169	0.321184	38.81339
LSB1.18	78		11.76451	17.41386	23.86993	0.285452	2.561242	17.39665	0.047039	8.572805	2.829324	0.370041	34.10167
LSB1.19	82		12.71608	18.26384	24.74816	0.307479	2.516843	17.53502	0.045684	8.950465	2.936404	0.379471	36.27476
LSB1.20	86		12.62709	20.44647	29.62756	0.303911	2.242549	18.40746	0.043827	10.34861	3.146366	0.327396	33.29071
LSB1.21	90		12.4565	19.27056	28.24766	0.30448	2.49895	18.42582	0.042371	9.886366	3.076917	0.317931	36.05096
LSB1.22	98		10.22352	13.61127	40.44081	0.315469	1.426791	11.31851	0.021458	6.444857	2.696593	0.157972	24.68273
LSB1.23	102		7.788623	11.81312	53.16573	0.25692	1.460562	11.10508	0.0251	6.489815	2.150787	0.191991	17.65256
LSB1.24	106												
LSB1.25	110		6.872419	9.98161	70.01655	0.247001	1.510447	11.0548	0.027759	5.737902	1.93633	0.184892	17.07308
LSB1.26	114		7.247129	15.59534	59.20578	0.277446	1.597425	11.39508	0.033539	5.870398	2.130896	0.204223	20.34514
LSB1.27	118												
LSB1.28	122												
LSB1.29	126												
LSB1.30	130												

LSB3.0	-57.5		10.56277	8.593074	30.73593	0.25974	0.135714	3.138528	0	2.922078	2.705628	0.067749	3.354978
LSB3.1	-53.5		11.11588	8.519313	30.04292	0.227468	0.135622	3.133047	0.000839	2.896996	2.7897	0.07382	3.626609
LSB3.2	-50												
LSB3.3	-42												
LSB3.4	-38												
LSB3.5	-34												
LSB3.6	-30		10.9899	8.464646	35.15152	0.190505	0.149091	3.151515	0.000588	2.929293	2.727273	0.05899	3.898999
LSB3.7	-26												
LSB3.8	-22												
LSB3.9	-18												
LSB3.10	-14												
LSB3.11	-10												
LSB3.12	-6												
LSB3.13	-2												
LSB3.14	2												
LSB3.15	6												
LSB3.16	10												
LSB3.17	14												
LSB3.18	18												
LSB3.19	22												
LSB3.20	30												
LSB3.21	34												
LSB3.22	38												
LSB3.23	42												
LSB3.24	46												
LSB5.0	79												
LSB5.1	82.5												
LSB5.2	87												
LSB5.3	91												
LSB5.4	95												
LSB5.5	99												
LSB5.6	103												
LSB5.7	107												
LSB5.8	111												
LSB5.9	115												

LSB5.10	119												
LSB5.11	123												
LSB5.12	127												
LSB5.13	131		11.18955	11.91584	39.71014	0.251515	1.120625	13.21959	0.291567	6.85973	2.980109	0.192169	23.30506
LSB5.14	135												
LSB5.15	139												
LSB5.16	143												
LSB5.17	147												
Bos32.1	-2		11.69273	11.49165	31.80095	0.481914	0.523496	5.157557	0.003458	2.677997	3.184108	0.030761	3.551548
Bos32.2	0		11.25497	15.60823	35.07652	0.455917	0.580057	4.973908	0.005574	2.499798	3.103141	0.026311	3.462286
Bos32.3	2		11.52147	9.071717	28.06331	0.464034	0.388842	5.403051	0.002377	2.570186	3.229055	0.029006	3.583232
Pseud34.1	-2		8.532332	12.79038	37.92915	0.578722	0.799271	9.6053	0.005334	3.506664	3.446042	0.026734	3.355838
Pseud34.2	0		9.225142	53.65376	52.29279	0.793749	1.012669	9.915615	0.032004	3.840253	4.087716	0.028613	3.636757
Pseud34.3	2		8.332008	10.7626	34.12683	0.599858	0.691364	9.698687	0.0038	3.551877	3.399922	0.02573	3.350097
Pseud41.1	-2		19.59225	16.75697	30.70619	0.624574	2.547194	5.207935	0.005909	4.059538	3.34608	0.042953	3.543497
Pseud41.2	0		19.83428	14.89485	33.81486	0.724642	2.649675	5.447399	0.003077	4.093074	3.6042	0.039597	3.47472
Pseud41.3	2		19.83768	13.48112	30.6089	0.569905	2.386609	5.290294	0.003088	4.124783	3.324311	0.044965	3.314165
LSB accuracy:													
			D*Li ppm/ wt.%	**D*Zn ppm/ wt.%**	**D*Ba ppm/ wt.%**	**D*U ppm/ wt.%**	**D*Mo ppm/ wt.%**	**D*Cu ppm/ wt.%**	**D*Cd ppm/ wt.%**	**D*Co ppm/ wt.%**	**D*Ga ppm/ wt.%**	**D*Tl ppm/ wt.%**	**D*Pb ppm/ wt.%**
Sample			11.63947	15.58374	31.29845	0.339657	3.621696	15.45153	0.030638	8.423682	3.101169	0.321184	38.81339
Repeat 1			11.50683	16.4018	26.03625	0.303488	3.365547	16.28521	0.034912	8.25517	2.947733	0.321562	38.75979
Repeat 2			12.39145	17.36129	26.10489	0.331064	3.302784	16.87897	0.03845	8.435102	2.988626	0.322696	39.39465
Repeat 3			11.4743	16.75232	25.55367	0.313492	3.251744	16.42451	0.040103	8.165995	2.88471	0.33255	39.86951
Standard (Whitby for FeOx, FeCarb, FeMag and FeT, for all else SBC-1)			19.70226	20.70226	21.70226	22.70226	23.70226	24.70226	25.70226	26.70226	27.70226	28.70226	29.70226
Mean			11.75301	16.52479	27.24832	0.321926	3.385443	16.26005	0.036026	8.319987	2.98056	0.324498	39.20933
Stan.Dev			0.431577	0.742112	2.711207	0.016421	0.164235	0.595663	0.004194	0.131553	0.091061	0.005407	0.525686
95% Confidence			0.685992	1.179588	4.309464	0.026102	0.261052	0.946806	0.006666	0.209104	0.144741	0.008594	0.835579
as a % of measurement (i.e. precision)			5.836731	7.138292	15.81552	8.10806	7.711001	5.822894	18.50467	2.513267	4.856174	2.648361	2.131071
Measured standard - reported standard													
Deviation (i.e. accuracy)													

Shell pavement accuracy:													
			D*Li ppm/ wt.%	**D*Zn ppm/ wt.%**	**D*Ba ppm/ wt.%**	**D*U ppm/ wt.%**	**D*Mo ppm/ wt.%**	**D*Cu ppm/ wt.%**	**D*Cd ppm/ wt.%**	**D*Co ppm/ wt.%**	**D*Ga ppm/ wt.%**	**D*Tl ppm/ wt.%**	**D*Pb ppm/ wt.%**
Sample			13.61536	13.38123	37.02999	0.561156	0.609575	6.005615	0.004027	3.11834	3.707672	0.035819	4.13553
Repeat 1			11.99382	13.46725	31.65037	0.44353	0.523836	5.166847	0.004004	2.764283	3.199618	0.028432	3.432085
Repeat 2													
Repeat 3													
Standard (Whitby)			0	0	0	0	0	0	0	0	0	0	0
Mean			12.80459	13.42424	34.34018	0.502343	0.566705	5.586231	0.004016	2.941312	3.453645	0.032126	3.783807
Stan.Dev			1.146607	0.060828	3.803965	0.083174	0.060627	0.593098	1.58E-05	0.250357	0.359248	0.005223	0.49741
95% Confidence			10.29682	0.546254	34.16058	0.746926	0.544444	5.326176	0.000142	2.248266	3.226139	0.046907	4.466872
as a % of measurement (i.e. precision)			80.41507	4.069159	99.47699	148.6886	96.07184	95.34472	3.526284	76.43752	93.4126	146.0094	118.0523
Measured standard - reported standard													
Deviation (i.e. accuracy)													

Palynology:

Sample Code:	**Stratigraphic height***		**Spores (%) = A**	**Pollen (%)= B**	**Dinoflagellages (%) = E**	**Phytoclasts (%) = C**	**Acritarchs (%) = F**	**Prasinophytes (%) = G**	**Foraminiferal test linings (%)**	**AOM (%)**	**Botryococcus (%) = D**
LSB1.0 Pal	28.5		19.66667	10.66667	5.666667	24.66667	1.333333	0.333333	0	35.66667	2
LSB1.1 Pal	38.5		22	10.33333	5.333333	30	2.333333	0.666667	0	23	6.333333
LSB1.2 Pal	48.5		19	6.333333	3	19.33333	1.666667	0.666667	0	40	10
LSB1.3 Pal	56.8		10.33333	2.666667	8	40.33333	1.666667	3.333333	0	22.66667	11
LSB1.4 Pal	63.3		9.666667	5.666667	3.666667	47.66667	2.333333	1	0	22.33333	7.666667
LSB1.5 Pal	71.1		4	2.666667	3.333333	30	2.666667	1.666667	0	46.66667	9
LSB1.6 Pal	80.3		2.666667	3.333333	1.333333	20.66667	3.333333	1	0	64.66667	3
LSB1.7 Pal	89.4		3.666667	1.333333	3	36.66667	6	1	0	40.33333	7.666667
LSB1.8 Pal	99		2.666667	2.333333	1	37	7.333333	1.666667	0	40.66667	7.333333
LSB1.9 Pal	109		5.333333	3.333333	2.333333	36.33333	3	1	0	42.66667	6
LSB3.0 Pal	-28		11	8	5.666667	37.66667	2	6.666667	0	22.66667	6.333333
LSB3.1 Pal	-3		8.666667	6.333333	12	38	3.666667	1.333333	0	21.33333	8.666667

LSB3.2 Pal	7		10.66667	10.33333	2.333333	33	2.333333	1.666667	0	36.33333	3.333333
LSB3.3 Pal	17		10.33333	7.333333	6.333333	28.66667	3	1	0	39	4.333333
LSB3.4 Pal	27		8.666667	6	3.666667	20.33333	4.333333	1.333333	0	53.66667	2
LSB3.5 Pal	37		6	3.333333	1.666667	24.66667	5	0.333333	0	55.33333	3.666667
LSB5.0 Pal	93.5		2.333333	2.666667	1.333333	23.66667	3.666667	1	0	62.33333	3
LSB5.1 Pal	99		6.333333	1.333333	2.666667	31.33333	4.333333	0.666667	0	49	4.333333
LSB5.2 Pal	109		1.666667	1.666667	2.666667	34.33333	3.666667	1.333333	0	51.33333	3.333333
LSB5.3 Pal	119		3.666667	4	4.666667	30.66667	2.666667	0	0	49.66667	4.666667
LSB5.4 Pal	129		4	5	3.333333	33.33333	3	3.333333	0	45	3
LSB5.5 Pal	139		8.666667	6	2.666667	48.33333	1.666667	0.333333	0	30.66667	1.666667
LSB5.6 Pal	149		7	5.666667	6	32.66667	2.666667	2	0	40	4
Bos32.1 Pal	-5		0.333333	0	1.666667	22.66667	2	0.666667	0	70.66667	2
Bos32.2 Pal	0		0.666667	1.333333	4	21	1	1.333333	0	70	0.666667
Bos32.3 Pal	5		0.666667	0	1	19.66667	1.333333	0.333333	0	76.66667	0.333333
Pseud41.1 Pal	-5		3	2	0	16	5.666667	2.333333	0	70.33333	0.666667
Pseud41.2 Pal	0		2.333333	2.333333	1.333333	15.66667	7.333333	1.666667	0	68.33333	1
Pseud41.3 Pal	5		3	1	0.333333	17.66667	7.333333	1	0	68.66667	1

Sample Code:	**Stratigraphic height***		**Dinoflagellate predominance**	**Acritarch predominance**	**Prasinophyte predominance**		**Terrestrial/Marine = (A+B+C+D)/(E+F+G)**		**Palynomorphs (for tyson's ternary)%**
LSB1.0 Pal	28.5		0.772727	0.181818	0.045455		7.772727		39.66667
LSB1.1 Pal	38.5		0.64	0.28	0.08		8.24		47
LSB1.2 Pal	48.5		0.5625	0.3125	0.125		10.25		40.66667
LSB1.3 Pal	56.8		0.615385	0.128205	0.25641		4.948718		37
LSB1.4 Pal	63.3		0.52381	0.333333	0.142857		10.09524		30
LSB1.5 Pal	71.1		0.434783	0.347826	0.217391		5.956522		23.33333
LSB1.6 Pal	80.3		0.235294	0.588235	0.176471		5.235294		14.66667
LSB1.7 Pal	89.4		0.3	0.6	0.1		4.933333		22.66667
LSB1.8 Pal	99		0.1	0.733333	0.166667		4.933333		22.33333
LSB1.9 Pal	109		0.368421	0.473684	0.157895		8.052632		21
LSB3.0 Pal	-28		0.395349	0.139535	0.465116		4.395349		39.66667
LSB3.1 Pal	-3		0.705882	0.215686	0.078431		3.627451		40.66667
LSB3.2 Pal	7		0.368421	0.368421	0.263158		9.052632		30.66667
LSB3.3 Pal	17		0.612903	0.290323	0.096774		4.903226		32.33333
LSB3.4 Pal	27		0.392857	0.464286	0.142857		3.964286		26
LSB3.5 Pal	37		0.238095	0.714286	0.047619		5.380952		20
LSB5.0 Pal	93.5		0.222222	0.611111	0.166667		5.277778		14
LSB5.1 Pal	99		0.347826	0.565217	0.086957		5.652174		19.66667
LSB5.2 Pal	109		0.347826	0.478261	0.173913		5.347826		14.33333

LSB5.3 Pal	119		0.636364	0.363636	0		5.863636		19.66667
LSB5.4 Pal	129		0.344828	0.310345	0.344828		4.689655		21.66667
LSB5.5 Pal	139		0.571429	0.357143	0.071429		13.85714		21
LSB5.6 Pal	149		0.5625	0.25	0.1875		4.625		27.33333
Bos32.1 Pal	-5		0.384615	0.461538	0.153846		5.769231		6.666667
Bos32.2 Pal	0		0.631579	0.157895	0.210526		3.736842		9
Bos32.3 Pal	5		0.375	0.5	0.125		7.75		3.666667
Pseud41.1 Pal	-5		0	0.708333	0.291667		2.708333		13.66667
Pseud41.2 Pal	0		0.129032	0.709677	0.16129		2.064516		16
Pseud41.3 Pal	5		0.038462	0.846154	0.115385		2.615385		13.66667

Sample Code:	**Stratigraphic height***		Spore indet.	Bryophyte indet.	*Anapiculatisporites spp.*	*Polycingulatisporites crenulatus*	*Polycingulatisporites liassicus*	*Polycingulatisporites sp.*	*Rogalskaisporites cicatricosus*	*Stereisporites antiquaspores*	*Stereisporites psilatus*	*Stereisporites seebergensis*	*Stereisporites sp.*	**Bryophyte total**
LSB1.0 Pal	28.5		4	0	0	0	0	0	1	0	2	0	6	9
LSB1.1 Pal	38.5		6	0	0	0	0	0	0	0	0	0	5	5
LSB1.2 Pal	48.5		2	0	0	0	0	0	0	0	0	0	6	6
LSB1.3 Pal	56.8		5	0	0	0	0	0	0	0	0	1	3	4
LSB1.4 Pal	63.3		4	0	0	0	0	0	0	0	0	0	2	2
LSB1.5 Pal	71.1		0	0	0	0	0	0	0	0	0	0	1	1
LSB1.6 Pal	80.3		1	0	0	0	0	0	0	0	0	0	1	1
LSB1.7 Pal	89.4		0	0	0	0	0	0	0	0	0	0	2	2
LSB1.8 Pal	99		2	0	0	0	0	0	0	0	0	0	2	2
LSB1.9 Pal	109		1	0	0	0	0	0	0	1	0	0	1	2
LSB3.0 Pal	-28		0	0	0	0	0	0	0	0	0	0	2	2
LSB3.1 Pal	-3		0	0	0	0	0	0	0	1	0	0	2	3
LSB3.2 Pal	7		1	0	0	0	0	0	1	0	0	0	1	2
LSB3.3 Pal	17		0	0	0	0	0	0	1	0	0	0	2	3
LSB3.4 Pal	27		1	0	0	0	0	0	0	0	0	0	2	2
LSB3.5 Pal	37		0	0	0	0	0	0	0	0	0	0	2	2
LSB5.0 Pal	93.5		0	0	0	0	0	0	0	0	0	0	0	0
LSB5.1 Pal	99		1	0	0	0	0	0	0	0	0	0	0	0
LSB5.2 Pal	109		0	0	0	0	0	0	0	0	0	0	0	0
LSB5.3 Pal	119		0	0	0	0	0	0	0	0	0	0	1	1
LSB5.4 Pal	129		1	0	0	0	0	0	0	0	0	0	0	0

LSB5.5 Pal	139		0	0	0	0	0	0	0	0	0	0	1	1
LSB5.6 Pal	149		1	0	0	0	0	0	0	0	0	0	3	3
Bos32.1 Pal	-5		0	0	0	0	0	0	0	0	0	0	0	0
Bos32.2 Pal	0		0	0	0	0	0	0	0	0	0	0	0	0
Bos32.3 Pal	5		0	0	0	0	0	0	0	0	0	0	0	0
Pseud41.1 Pal	-5		0	0	0	0	0	0	0	0	0	0	4	4
Pseud41.2 Pal	0		0	0	0	0	0	0	0	0	0	0	0	0
Pseud41.3 Pal	5		0	0	0	0	0	0	0	0	0	0	0	0

Sample Code:	**Stratigraphic height***		Lycophyte indet.	*Camarozonosporites rudis*	*Ceratosporites spinosus*	*Densoisporites velatus*	*Densoisporites crassus*	*Kekryphalospora distincta*	*Kraeuselisporites reissingeri*	*Leptolepidites equatibossus*	*Leptolepidites major*	*Lycopodiacidites rugulatus*	*Neoraistrickia truncata*
LSB1.0 Pal	28.5		0	1	0	3	0	0	0	0	1	0	0
LSB1.1 Pal	38.5		0	1	0	3	0	0	0	0	1	0	0
LSB1.2 Pal	48.5		0	3	0	2	0	0	0	0	2	0	0
LSB1.3 Pal	56.8		0	1	0	0	0	0	0	0	0	0	0
LSB1.4 Pal	63.3		0	0	0	1	0	0	0	0	1	0	0
LSB1.5 Pal	71.1		0	1	0	0	0	0	0	0	1	0	0
LSB1.6 Pal	80.3		0	0	0	0	0	0	0	0	1	0	0
LSB1.7 Pal	89.4		0	0	0	0	0	0	0	0	0	0	0
LSB1.8 Pal	99		0	0	0	0	0	0	0	0	1	0	0
LSB1.9 Pal	109		0	0	0	0	0	0	0	0	3	0	0
LSB3.0 Pal	-28		0	0	0	1	0	0	0	0	0	1	0
LSB3.1 Pal	-3		0	0	0	0	0	0	0	0	0	0	0
LSB3.2 Pal	7		0	0	0	2	0	0	0	0	0	0	0
LSB3.3 Pal	17		0	0	0	0	0	0	0	0	1	0	0
LSB3.4 Pal	27		0	0	0	0	0	0	0	0	1	0	0
LSB3.5 Pal	37		0	0	0	0	0	0	0	0	0	0	0
LSB5.0 Pal	93.5		0	0	0	0	0	0	0	0	0	0	0
LSB5.1 Pal	99		0	0	0	0	0	0	0	0	0	0	0
LSB5.2 Pal	109		0	0	0	0	0	0	0	0	0	0	0

LSB5.3 Pal	119		0	0	0	0	0	0	0	0	0	0	1
LSB5.4 Pal	129		0	0	0	0	0	0	0	0	1	0	0
LSB5.5 Pal	139		0	1	0	0	0	0	0	1	0	0	0
LSB5.6 Pal	149		0	0	0	0	0	0	0	0	0	0	1
Bos32.1 Pal	-5		0	0	0	0	0	0	0	0	0	0	0
Bos32.2 Pal	0		0	0	0	0	0	0	0	0	0	0	0
Bos32.3 Pal	5		0	0	0	0	0	0	0	0	0	0	0
Pseud41.1 Pal	-5		0	0	0	0	0	0	0	0	0	0	0
Pseud41.2 Pal	0		0	0	0	0	0	0	0	0	0	0	0
Pseud41.3 Pal	5		0	0	0	0	0	0	0	0	0	0	0

Sample Code:	**Stratigraphic height***		*Retitriletes austroclavatidites*	*Retitriletes clavatoides*	*Retitriletes semimuris*	*Retitriletes sp.*	*cf. Sestrosporites pseudoalveolatus*	*Staplinisporites telatus*	*Staplinisporites caminus*	*Uvaesporites argentaeformis*	*Zebraspsporites laevigatus*	**Lycophyte total**
LSB1.0 Pal	28.5		0	0	0	0	1	0	0	4	0	10
LSB1.1 Pal	38.5		0	0	0	0	1	0	0	4	0	10
LSB1.2 Pal	48.5		0	0	0	0	2	0	0	4	0	13
LSB1.3 Pal	56.8		0	0	0	0	0	0	0	1	0	2
LSB1.4 Pal	63.3		0	0	0	0	0	0	0	2	0	4
LSB1.5 Pal	71.1		0	0	0	0	0	0	0	0	0	2
LSB1.6 Pal	80.3		0	0	0	0	0	0	0	0	0	1
LSB1.7 Pal	89.4		0	0	0	0	0	0	0	2	0	2
LSB1.8 Pal	99		0	0	0	0	0	0	0	0	0	1
LSB1.9 Pal	109		0	0	0	0	0	0	0	0	0	3
LSB3.0 Pal	-28		0	0	0	0	0	0	0	1	0	3
LSB3.1 Pal	-3		0	0	0	0	0	0	0	2	0	2
LSB3.2 Pal	7		0	0	0	0	0	0	0	1	0	3
LSB3.3 Pal	17		0	0	0	0	0	0	0	0	0	1
LSB3.4 Pal	27		0	0	0	0	0	0	0	1	0	2
LSB3.5 Pal	37		0	0	0	0	1	0	0	0	0	1
LSB5.0 Pal	93.5		0	0	0	0	0	0	0	0	0	0
LSB5.1 Pal	99		0	0	0	0	2	0	0	1	0	3
LSB5.2 Pal	109		0	0	0	0	0	0	0	0	0	0

LSB5.3 Pal	119		0	0	0	0	0	0	0	1	0	2
LSB5.4 Pal	129		0	0	0	0	0	0	0	0	0	1
LSB5.5 Pal	139		0	0	0	0	0	0	0	2	0	4
LSB5.6 Pal	149		0	0	0	0	0	0	0	0	0	1
Bos32.1 Pal	-5		0	0	0	0	0	0	0	0	0	0
Bos32.2 Pal	0		0	0	0	0	0	0	0	0	0	0
Bos32.3 Pal	5		0	0	0	0	0	0	0	0	0	0
Pseud41.1 Pal	-5		0	0	0	0	0	0	0	0	0	0
Pseud41.2 Pal	0		0	0	0	0	0	0	0	0	0	0
Pseud41.3 Pal	5		0	0	0	0	0	0	0	0	0	0

Sample Code:	**Stratigraphic height***		Fern ind et.	*Calamospora mesozoica*	*Laevigatosporites spp.*	*Baculatisporites comaumensis*	*Cibotiumspora jurienensis*	*Conbaculatisporites mesozoicus*	*Concavispori tes toralis*	*Concavissimispori tes variverrucatus*	*Contignispori tes cooksoniae*	*Crassitudisporites problematicus*	*Deltoidospora australis*
LSB1.0 Pal	28.5		0	0	8	0	0	0	0	0	0	0	4
LSB1.1 Pal	38.5		0	0	8	0	0	0	1	0	0	0	4
LSB1.2 Pal	48.5		0	1	4	1	0	0	2	0	0	0	1
LSB1.3 Pal	56.8		0	1	3	1	0	0	1	0	0	0	2
LSB1.4 Pal	63.3		0	0	3	0	0	0	2	0	0	0	0
LSB1.5 Pal	71.1		0	0	2	0	0	1	0	0	0	0	0
LSB1.6 Pal	80.3		0	0	1	0	0	0	0	0	0	0	1
LSB1.7 Pal	89.4		0	1	0	0	0	0	0	0	0	0	0
LSB1.8 Pal	99		0	0	3	1	0	0	0	0	0	0	0
LSB1.9 Pal	109		0	0	1	0	1	0	0	0	0	0	0
LSB3.0 Pal	-28		0	0	8	2	0	1	0	1	0	0	2
LSB3.1 Pal	-3		0	0	2	2	2	0	0	0	0	0	1
LSB3.2 Pal	7		0	0	5	4	1	2	0	1	0	0	0
LSB3.3 Pal	17		0	0	5	2	0	0	0	0	0	0	2
LSB3.4 Pal	27		0	0	4	3	0	0	0	0	0	0	3
LSB3.5 Pal	37		0	0	4	1	0	0	0	0	0	0	1
LSB5.0 Pal	93.5		0	0	1	0	0	0	1	0	0	0	0
LSB5.1 Pal	99		0	0	3	2	0	0	0	0	0	0	1

LSB5.2 Pal	109		0	0	3	0	0	0	0	0	0	0	0
LSB5.3 Pal	119		0	0	4	0	0	0	1	0	0	0	0
LSB5.4 Pal	129		0	1	4	0	0	0	0	0	0	0	0
LSB5.5 Pal	139		0	0	4	1	0	0	0	0	0	0	0
LSB5.6 Pal	149		0	0	4	2	1	0	0	0	0	0	0
Bos32.1 Pal	-5		0	0	0	0	1	0	0	0	0	0	0
Bos32.2 Pal	0		0	0	1	0	1	0	0	0	0	0	0
Bos32.3 Pal	5		0	0	0	1	0	0	0	0	0	0	0
Pseud41.1 Pal	-5		0	0	1	1	0	0	0	0	0	0	1
Pseud41.2 Pal	0		0	0	3	1	0	0	0	0	0	0	1
Pseud41.3 Pal	5		0	0	3	0	0	0	0	0	0	0	0

Sample Code:	**Stratigraphic height***		*Deltoidospora minor*	*Dictyophyllidites equiexinus*	*Dictyophyllidites harrisii*	*Gleicheniidites senonicus*	*Ischyosporites variegatus*	*Marattisporites scabratus*	*Matonisporites phlebopteroides*	*Obtusisporis canadensis*	*Osmundacidites wellmanii*	*Todisporites major*	**Fern total**
LSB1.0 Pal	28.5		0	2	3	1	0	2	0	0	0	1	21
LSB1.1 Pal	38.5		0	2	3	1	0	2	0	0	0	1	22
LSB1.2 Pal	48.5		0	1	5	1	0	1	0	0	0	0	17
LSB1.3 Pal	56.8		0	0	3	2	0	1	0	0	0	0	14
LSB1.4 Pal	63.3		0	0	3	3	0	0	0	0	0	0	11
LSB1.5 Pal	71.1		0	1	0	0	0	0	0	0	0	0	4
LSB1.6 Pal	80.3		0	0	0	0	0	2	0	0	0	0	4
LSB1.7 Pal	89.4		0	0	0	1	0	0	0	0	0	0	2
LSB1.8 Pal	99		0	0	0	0	0	0	0	0	0	0	4
LSB1.9 Pal	109		0	0	1	0	0	0	0	0	1	0	4
LSB3.0 Pal	-28		0	0	2	1	0	0	0	0	0	1	18
LSB3.1 Pal	-3		0	3	0	1	0	3	0	0	0	0	14
LSB3.2 Pal	7		0	2	2	0	0	1	0	0	1	0	19
LSB3.3 Pal	17		0	0	4	2	0	3	1	0	0	0	19
LSB3.4 Pal	27		0	0	1	0	0	4	0	0	0	1	16
LSB3.5 Pal	37		0	0	1	0	0	2	0	0	0	0	9
LSB5.0 Pal	93.5		0	0	0	1	0	2	0	0	1	0	6
LSB5.1 Pal	99		0	0	0	0	0	2	0	0	0	0	8

LSB5.2 Pal	109		0	0	0	0	0	0	0	0	0	0	3
LSB5.3 Pal	119		0	0	0	0	0	1	0	0	0	0	6
LSB5.4 Pal	129		0	0	1	0	0	0	0	0	0	1	7
LSB5.5 Pal	139		0	1	1	1	0	0	0	0	0	0	8
LSB5.6 Pal	149		0	1	2	1	0	1	0	0	0	0	12
Bos32.1 Pal	-5		0	0	0	0	0	0	0	0	0	0	1
Bos32.2 Pal	0		0	0	0	0	0	0	0	0	0	0	2
Bos32.3 Pal	5		0	0	0	0	0	0	0	0	0	0	1
Pseud41.1 Pal	-5		0	0	1	0	0	0	0	0	0	0	4
Pseud41.2 Pal	0		0	1	0	0	0	1	0	0	0	0	7
Pseud41.3 Pal	5		0	0	0	0	0	5	0	0	0	0	8

Sample Code:	**Stratigraphic height***		Chasmatosporites indet.	*Chasmatosporites apertus*	*Chasmatosporites hians*	*Chasmatosporites major*	*Chasmatosporites canadensis*	**Chasmatosporites total**	Psilatriletes	**Sporetotal**	Pollen indet.	Bisaccate indet.
LSB1.0 Pal	28.5		0	9	7	6	1	23	0	59	0	0
LSB1.1 Pal	38.5		0	9	7	6	1	23	0	66	0	0
LSB1.2 Pal	48.5		0	2	5	8	3	18	1	57	2	0
LSB1.3 Pal	56.8		0	1	2	1	0	4	2	31	0	0
LSB1.4 Pal	63.3		0	2	0	1	2	5	3	29	1	0
LSB1.5 Pal	71.1		0	0	1	0	1	2	3	12	0	0
LSB1.6 Pal	80.3		0	0	1	0	0	1	0	8	0	0
LSB1.7 Pal	89.4		0	0	2	0	1	3	1	11	0	0
LSB1.8 Pal	99		0	0	1	0	1	2	0	8	0	0
LSB1.9 Pal	109		0	0	0	2	3	5	1	16	0	1
LSB3.0 Pal	-28		2	2	1	1	2	8	2	33	0	0
LSB3.1 Pal	-3		1	3	1	1	1	7	0	26	0	0
LSB3.2 Pal	7		0	2	2	2	0	6	1	32	0	0
LSB3.3 Pal	17		0	2	1	2	2	7	1	31	0	0
LSB3.4 Pal	27		0	1	0	1	1	3	2	26	0	0
LSB3.5 Pal	37		0	0	0	0	4	4	2	18	0	0

LSB5.0 Pal	93.5		0	0	0	0	1	1	0	7	0	0
LSB5.1 Pal	99		0	2	0	1	3	6	1	19	0	0
LSB5.2 Pal	109		1	1	0	0	0	2	0	5	0	0
LSB5.3 Pal	119		0	1	0	1	0	2	0	11	0	0
LSB5.4 Pal	129		1	0	1	0	0	2	1	12	0	0
LSB5.5 Pal	139		1	6	1	3	2	13	0	26	0	0
LSB5.6 Pal	149		0	1	0	1	1	3	1	21	0	0
Bos32.1 Pal	-5		0	0	0	0	0	0	0	1	0	0
Bos32.2 Pal	0		0	0	0	0	0	0	0	2	0	0
Bos32.3 Pal	5		0	0	0	0	1	1	0	2	0	0
Pseud41.1 Pal	-5		0	0	0	1	0	1	0	9	0	0
Pseud41.2 Pal	0		0	0	0	0	0	0	0	7	0	0
Pseud41.3 Pal	5		0	1	0	0	0	1	0	9	0	0

Sample Code:	**Stratigraphic height***		*Alisporites microsaccus*	*Alisporites thomasii*	*Alisporites sp.*	*Pinuspollenites sp.*	*Podocarpidites ellipticus*	*Protopinus sp.*	*Podocarpidites sp.*	*Quadraeculina anellaeformis*	*Vitreisporites pallidus*	**Bisaccate total**	Classopollis
LSB1.0 Pal	28.5		0	2	0	0	1	2	4	2	3	14	3
LSB1.1 Pal	38.5		0	2	0	0	1	2	4	2	3	14	3
LSB1.2 Pal	48.5		0	1	0	1	1	0	3	1	0	7	1
LSB1.3 Pal	56.8		0	0	1	1	1	1	0	0	0	4	0
LSB1.4 Pal	63.3		0	2	3	0	1	1	0	1	2	10	0
LSB1.5 Pal	71.1		0	0	2	0	1	0	2	0	0	5	0
LSB1.6 Pal	80.3		0	0	1	1	0	1	0	1	2	6	0
LSB1.7 Pal	89.4		0	1	0	0	0	0	0	0	0	1	0
LSB1.8 Pal	99		0	0	0	0	0	0	0	0	0	0	0
LSB1.9 Pal	109		0	2	0	0	0	0	0	0	0	3	0
LSB3.0 Pal	-28		0	0	0	0	3	1	0	0	2	6	3
LSB3.1 Pal	-3		0	0	1	0	3	1	1	1	0	7	1
LSB3.2 Pal	7		0	3	0	3	5	2	1	1	1	16	2
LSB3.3 Pal	17		0	0	0	0	1	1	2	1	0	5	5
LSB3.4 Pal	27		0	1	1	0	2	1	1	1	0	7	0
LSB3.5 Pal	37		0	0	1	0	0	0	1	1	0	3	1

LSB5.0 Pal	93.5		0	0	1	0	0	0	3	1	0	5	0
LSB5.1 Pal	99		0	1	1	0	0	0	0	0	1	3	0
LSB5.2 Pal	109		0	0	0	0	0	1	1	0	0	2	1
LSB5.3 Pal	119		0	0	1	0	0	0	2	1	0	4	0
LSB5.4 Pal	129		0	0	1	3	1	0	0	2	1	8	1
LSB5.5 Pal	139		0	0	0	0	2	1	0	2	1	6	1
LSB5.6 Pal	149		0	0	0	0	0	1	2	0	0	3	2
Bos32.1 Pal	-5		0	0	0	0	0	0	0	0	0	0	0
Bos32.2 Pal	0		0	1	0	0	0	0	0	1	0	2	0
Bos32.3 Pal	5		0	0	0	0	0	0	0	0	0	0	0
Pseud41.1 Pal	-5		0	0	1	1	0	0	0	0	1	3	1
Pseud41.2 Pal	0		0	0	0	0	0	0	0	0	1	1	3
Pseud41.3 Pal	5		0	0	0	0	0	0	1	0	0	1	1

Sample Code:	**Stratigraphic height***		Cerebropollenites	Perinopollenites	Mutant Bisaccate	Cycadopites sp.	*Cycadopites minimus*	*Cycadopites subgranulosus*	**Cycadopites total**	*Araucariacites australis*	*Callialasporites turbatus*	**Pollen total**	Dinolagellate indet.	Nanoceratopsis sp.
LSB1.0 Pal	28.5		0	5	0	5	0	2	7	1	1	32	0	3
LSB1.1 Pal	38.5		0	5	0	5	0	2	7	1	1	31	0	3
LSB1.2 Pal	48.5		2	0	0	5	0	1	6	0	1	19	0	3
LSB1.3 Pal	56.8		0	1	0	1	0	1	2	0	1	8	0	10
LSB1.4 Pal	63.3		0	1	0	4	0	1	5	0	0	17	0	4
LSB1.5 Pal	71.1		1	0	0	2	0	0	2	0	0	8	0	6
LSB1.6 Pal	80.3		0	1	0	2	0	1	3	0	0	10	0	3
LSB1.7 Pal	89.4		0	1	0	2	0	1	3	1	0	4	0	4
LSB1.8 Pal	99		1	0	0	1	0	2	3	0	0	7	0	0
LSB1.9 Pal	109		0	4	0	3	0	0	3	0	0	10	1	5
LSB3.0 Pal	-28		2	6	0	3	0	4	7	0	0	24	3	5
LSB3.1 Pal	-3		2	4	0	1	0	1	2	2	1	19	6	18
LSB3.2 Pal	7		0	4	0	3	0	3	6	3	0	31	0	5
LSB3.3 Pal	17		1	7	0	2	0	1	3	0	1	22	2	16

LSB3.4 Pal	27		0	3	0	1	0	3	4	2	2	18	0	8
LSB3.5 Pal	37		0	3	0	1	0	1	2	1	0	10	0	2
LSB5.0 Pal	93.5		0	1	0	0	0	1	1	1	0	8	1	3
LSB5.1 Pal	99		0	0	0	0	0	1	1	0	0	4	0	4
LSB5.2 Pal	109		0	0	0	0	0	1	1	1	0	5	1	4
LSB5.3 Pal	119		2	1	0	0	0	3	3	1	1	12	0	12
LSB5.4 Pal	129		2	0	0	1	0	2	3	1	0	15	1	5
LSB5.5 Pal	139		0	2	0	2	0	5	7	2	0	18	1	6
LSB5.6 Pal	149		0	1	0	2	0	6	8	3	0	17	1	14
Bos32.1 Pal	-5		0	0	0	0	0	0	0	0	0	0	0	5
Bos32.2 Pal	0		0	0	0	1	0	0	1	0	1	4	0	11
Bos32.3 Pal	5		0	0	0	0	0	0	0	0	0	0	0	3
Pseud41.1 Pal	-5		0	2	0	0	0	0	0	0	0	6	0	0
Pseud41.2 Pal	0		1	0	0	0	0	2	2	0	0	7	0	4
Pseud41.3 Pal	5		0	1	0	0	0	0	0	0	0	3	0	1

Sample Code:	**Stratigraphic height***		Liasidium sp.	Luehndea sp.	Mancodinium sp.	**Dinoflagellate total**	Phytoclast indet.	Opaque	Cuticle	Biostructured	Pseudoamorphous	Fungal	Acritarch indet.	Acanthomorph
LSB1.0 Pal	28.5		2	0	11	16	0	41	6	24	2	1	0	1
LSB1.1 Pal	38.5		2	0	11	16	0	25	21	35	8	1	0	1
LSB1.2 Pal	48.5		1	0	5	9	0	8	23	23	2	2	0	0
LSB1.3 Pal	56.8		3	0	11	24	1	33	68	15	1	3	0	0
LSB1.4 Pal	63.3		3	0	4	11	0	38	93	7	3	2	0	1
LSB1.5 Pal	71.1		1	0	3	10	0	32	41	7	8	2	0	0
LSB1.6 Pal	80.3		1	0	0	4	0	23	27	4	5	3	0	0
LSB1.7 Pal	89.4		0	0	5	9	0	36	59	8	7	0	0	3
LSB1.8 Pal	99		1	0	2	3	0	39	62	5	5	0	0	1
LSB1.9 Pal	109		0	0	1	7	0	21	76	9	3	0	0	0
LSB3.0 Pal	-28		1	0	8	17	0	42	29	27	12	3	0	1
LSB3.1 Pal	-3		0	0	12	36	0	51	22	24	15	2	0	0
LSB3.2 Pal	7		1	0	1	7	0	33	25	27	13	1	0	0
LSB3.3 Pal	17		0	0	1	19	0	29	28	17	12	0	0	2

LSB3.4 Pal	27		1	0	2	11	0	23	20	10	7	1	0	0
LSB3.5 Pal	37		1	0	2	5	0	32	18	14	9	1	0	0
LSB5.0 Pal	93.5		0	0	0	4	0	25	31	9	6	0	0	1
LSB5.1 Pal	99		1	0	3	8	0	23	52	11	7	1	0	1
LSB5.2 Pal	109		0	0	3	8	0	25	63	11	3	1	0	0
LSB5.3 Pal	119		2	0	0	14	0	31	42	8	10	1	0	0
LSB5.4 Pal	129		2	0	2	10	0	43	41	4	12	0	0	1
LSB5.5 Pal	139		0	0	1	8	0	62	51	22	7	3	0	2
LSB5.6 Pal	149		2	0	1	18	0	32	42	13	9	2	0	3
Bos32.1 Pal	-5		0	0	0	5	0	43	17	2	6	0	0	0
Bos32.2 Pal	0		0	0	1	12	0	18	30	5	10	0	0	0
Bos32.3 Pal	5		0	0	0	3	0	28	15	6	10	0	0	0
Pseud41.1 Pal	-5		0	0	0	0	0	22	8	9	9	0	0	1
Pseud41.2 Pal	0		0	0	0	4	0	26	10	6	5	0	0	0
Pseud41.3 Pal	5		0	0	0	1	0	22	7	6	17	1	0	1

Sample Code:	**Stratigraphic height***		Polygonomorph	Netromorph	Diacromorph	Prismatomorph	Oomorph	Herkomorph	Petromorph	Sphaeromorph
LSB1.0 Pal	28.5		1	0	1	0	1	1	0	2
LSB1.1 Pal	38.5		1	0	1	0	1	1	0	2
LSB1.2 Pal	48.5		1	0	1	0	0	0	0	3
LSB1.3 Pal	56.8		1	0	1	0	1	0	0	2
LSB1.4 Pal	63.3		0	0	1	0	1	0	0	4
LSB1.5 Pal	71.1		0	0	1	1	1	0	0	5
LSB1.6 Pal	80.3		0	0	1	0	2	0	0	7
LSB1.7 Pal	89.4		0	1	1	0	0	2	0	11
LSB1.8 Pal	99		0	0	1	0	2	3	0	15
LSB1.9 Pal	109		0	0	3	0	2	2	0	2
LSB3.0 Pal	-28		0	0	0	0	0	1	0	4
LSB3.1 Pal	-3		0	0	0	0	2	1	0	8
LSB3.2 Pal	7		0	0	0	0	0	1	0	6
LSB3.3 Pal	17		0	0	0	0	1	1	0	5

LSB3.4 Pal	27		0	2	0	0	0	1	0	10
LSB3.5 Pal	37		0	1	0	0	2	1	0	11
LSB5.0 Pal	93.5		0	0	1	0	1	0	0	8
LSB5.1 Pal	99		0	0	0	0	2	4	0	6
LSB5.2 Pal	109		0	1	0	0	0	2	0	8
LSB5.3 Pal	119		0	0	1	0	1	1	0	5
LSB5.4 Pal	129		0	0	0	0	1	0	0	7
LSB5.5 Pal	139		0	2	0	0	0	0	0	1
LSB5.6 Pal	149		0	0	0	0	1	0	0	4
Bos32.1 Pal	-5		0	1	0	0	1	0	0	4
Bos32.2 Pal	0		0	1	0	0	1	0	0	1
Bos32.3 Pal	5		0	0	0	0	0	0	0	4
Pseud4 1.1 Pal	-5		0	0	0	0	0	0	0	16
Pseud4 1.2 Pal	0		0	0	0	0	0	0	0	22
Pseud4 1.3 Pal	5		0	0	0	0	0	0	0	21

Sample Code:	**Stratigraphic height***		**Acritarch total**	**Prasinophytes**	AOM indet.	Translucent AOM	Opaque AOM	**AOM total**	**Botryoccocos**
LSB1.0 Pal	28.5		7	1	0	56	13	69	6
LSB1.1 Pal	38.5		7	2	0	56	13	69	19
LSB1.2 Pal	48.5		5	2	80	40	0	120	30
LSB1.3 Pal	56.8		5	10	0	45	23	68	33
LSB1.4 Pal	63.3		7	3	0	50	17	67	23
LSB1.5 Pal	71.1		8	5	1	101	38	140	27
LSB1.6 Pal	80.3		10	3	2	124	68	194	9
LSB1.7 Pal	89.4		18	3	1	79	41	121	23
LSB1.8 Pal	99		22	5	0	108	14	122	22
LSB1.9 Pal	109		9	3	0	124	4	128	18
LSB3.0 Pal	-28		6	20	0	60	8	68	19
LSB3.1 Pal	-3		11	4	0	62	2	64	26
LSB3.2 Pal	7		7	5	0	105	4	109	10
LSB3.3 Pal	17		9	3	0	104	13	117	13
LSB3.4 Pal	27		13	4	0	138	23	161	6
LSB3.5 Pal	37		15	1	0	132	34	166	11
LSB5.0 Pal	93.5		11	3	0	146	41	187	9
LSB5.1 Pal	99		13	2	1	118	28	147	13
LSB5.2 Pal	109		11	4	0	115	39	154	10
LSB5.3 Pal	119		8	0	0	116	33	149	14
LSB5.4 Pal	129		9	10	0	119	16	135	9
LSB5.5 Pal	139		5	1	0	76	16	92	5

LSB5.6 Pal	149		8	6	0	101	19	120	12
Bos32.1 Pal	-5		6	2	0	179	33	212	6
Bos32.2 Pal	0		3	4	0	174	36	210	2
Bos32.3 Pal	5		4	1	3	188	39	230	1
Pseud41.1 Pal	-5		17	7	0	159	52	211	2
Pseud41.2 Pal	0		22	5	0	172	33	205	3
Pseud41.3 Pal	5		22	3	0	156	50	206	3

Sample Code:	**Stratigraphic height***		**Bryophyte dominance**	**Lycophyte dominance**	**Fern dominance**	**Chasmatosporites dominance**	**Psilatrilites dominance**	**Bisaccate dominance**	**Classopollis dominance**
LSB1.0 Pal	28.5		0.094737	0.105263	0.231579	0.242105	0	0.147368	0.031579
LSB1.1 Pal	38.5		0.054945	0.10989	0.241758	0.252747	0	0.153846	0.032967
LSB1.2 Pal	48.5		0.085714	0.185714	0.214286	0.257143	0.014286	0.1	0.014286
LSB1.3 Pal	56.8		0.121212	0.060606	0.393939	0.121212	0.060606	0.121212	0
LSB1.4 Pal	63.3		0.04878	0.097561	0.268293	0.121951	0.073171	0.243902	0
LSB1.5 Pal	71.1		0.05	0.1	0.2	0.1	0.15	0.25	0
LSB1.6 Pal	80.3		0.058824	0.058824	0.235294	0.058824	0	0.352941	0
LSB1.7 Pal	89.4		0.125	0.125	0.125	0.1875	0.0625	0.0625	0
LSB1.8 Pal	99		0.153846	0.076923	0.307692	0.153846	0	0	0
LSB1.9 Pal	109		0.08	0.12	0.16	0.2	0.04	0.12	0
LSB3.0 Pal	-28		0.035088	0.052632	0.315789	0.140351	0.035088	0.105263	0.052632
LSB3.1 Pal	-3		0.066667	0.044444	0.311111	0.155556	0	0.155556	0.022222
LSB3.2 Pal	7		0.032258	0.048387	0.306452	0.096774	0.016129	0.258065	0.032258
LSB3.3 Pal	17		0.056604	0.018868	0.358491	0.132075	0.018868	0.09434	0.09434
LSB3.4 Pal	27		0.046512	0.046512	0.372093	0.069767	0.046512	0.162791	0
LSB3.5 Pal	37		0.071429	0.035714	0.321429	0.142857	0.071429	0.107143	0.035714
LSB5.0 Pal	93.5		0	0	0.4	0.066667	0	0.333333	0
LSB5.1 Pal	99		0	0.136364	0.363636	0.272727	0.045455	0.136364	0
LSB5.2 Pal	109		0	0	0.3	0.2	0	0.2	0.1
LSB5.3 Pal	119		0.043478	0.086957	0.26087	0.086957	0	0.173913	0
LSB5.4 Pal	129		0	0.038462	0.269231	0.076923	0.038462	0.307692	0.038462
LSB5.5 Pal	139		0.022727	0.090909	0.181818	0.295455	0	0.136364	0.022727
LSB5.6 Pal	149		0.081081	0.027027	0.324324	0.081081	0.027027	0.081081	0.054054
Bos32.1 Pal	-5		0	0	1	0	0	0	0
Bos32.2 Pal	0		0	0	0.333333	0	0	0.333333	0
Bos32.3 Pal	5		0	0	0.5	0.5	0	0	0
Pseud41.1 Pal	-5		0.266667	0	0.266667	0.066667	0	0.2	0.066667
Pseud41.2 Pal	0		0	0	0.5	0	0	0.071429	0.214286
Pseud41.3 Pal	5		0	0	0.666667	0.083333	0	0.083333	0.083333

Sample Code:	Stratigraphic height*		Cerebropollenites dominance	Perinopollenites dominance	Cycadopites dominance	Araucariacites australis dominance	Callialasporites turbatus dominance		Number of genera
LSB1.0 Pal	28.5		0	0.052632	0.073684	0.010526	0.010526		25
LSB1.1 Pal	38.5		0	0.054945	0.076923	0.010989	0.010989		24
LSB1.2 Pal	48.5		0.028571	0	0.085714	0	0.014286		23
LSB1.3 Pal	56.8		0	0.030303	0.060606	0	0.030303		19
LSB1.4 Pal	63.3		0	0.02439	0.121951	0	0		17
LSB1.5 Pal	71.1		0.05	0	0.1	0	0		12
LSB1.6 Pal	80.3		0	0.058824	0.176471	0	0		13
LSB1.7 Pal	89.4		0	0.0625	0.1875	0.0625	0		10
LSB1.8 Pal	99		0.076923	0	0.230769	0	0		7
LSB1.9 Pal	109		0	0.16	0.12	0	0		11
LSB3.0 Pal	-28		0.035088	0.105263	0.122807	0	0		21
LSB3.1 Pal	-3		0.044444	0.088889	0.044444	0.044444	0.022222		20
LSB3.2 Pal	7		0	0.064516	0.096774	0.048387	0		24
LSB3.3 Pal	17		0.018868	0.132075	0.056604	0	0.018868		20
LSB3.4 Pal	27		0	0.069767	0.093023	0.046512	0.046512		19
LSB3.5 Pal	37		0	0.107143	0.071429	0.035714	0		16
LSB5.0 Pal	93.5		0	0.066667	0.066667	0.066667	0		12
LSB5.1 Pal	99		0	0	0.045455	0	0		11
LSB5.2 Pal	109		0	0	0.1	0.1	0		7
LSB5.3 Pal	119		0.086957	0.043478	0.130435	0.043478	0.043478		15
LSB5.4 Pal	129		0.076923	0	0.115385	0.038462	0		16
LSB5.5 Pal	139		0	0.045455	0.159091	0.045455	0		17
LSB5.6 Pal	149		0	0.027027	0.216216	0.081081	0		16
Bos32.1 Pal	-5		0	0	0	0	0		1
Bos32.2 Pal	0		0	0	0.166667	0	0.166667		6
Bos32.3 Pal	5		0	0	0	0	0		2
Pseud41.1 Pal	-5		0	0.133333	0	0	0		11
Pseud41.2 Pal	0		0.071429	0	0.142857	0	0		9
Pseud41.3 Pal	5		0	0.083333	0	0	0		6

Organic geochemistry (Biomarkers):

Accuracy checks:

Sample Code:	Stratigraphic height*		TOC for normalisation (wt.%)	gTOC/gSediment		n-alkanes and branched isoprenoids accuracy check (98peak/66peak) - D50 tetracosane
LSB1.0B	5		0.853896	0.008539		0.617842
LSB1.1B	13		1.744933	0.017449		0.553931
LSB1.2B	22		1.509419	0.015094		0.820395
LSB1.3B	29		2.321012	0.02321		0.696737
LSB1.4B	37		0.881126	0.008811		0.774519
LSB1.5B	46		1.347097	0.013471		0.760146
LSB1.6B	55		4.078695	0.040787		0.534256
LSB1.7B	62		0.185005	0.00185		0.644044
LSB1.8B	69		5.050529	0.050505		0.619221
LSB1.9B	78		6.892842	0.068928		0.670596
LSB1.10B	86		6.781139	0.067811		0.649217
LSB1.11B	94		7.251084	0.072511		0.752246
LSB1.12B	102		1.316286	0.013163		0.819499
LSB1.13B	110		0.649523	0.006495		0.572957
LSB1.14B	118		1.226874	0.012269		0.658645
LSB3.0B	-22		0.893328	0.008933		0.684821
LSB5.0B	84		7.142033	0.07142		0.582614
LSB5.1B	93		4.671255	0.046713		0.789747
LSB5.2B	102		1.398918	0.013989		0.606845
LSB5.3B	111		2.215888	0.022159		0.799124
LSB5.4B	120		1.102054	0.011021		0.69157
LSB5.5B	129		1.737747	0.017377		0.706288
LSB5.6B	138		1.051764	0.010518		0.611965
LSB5.7B	145		1.051764	0.010518		0.517689
LSB6.0B	-24		0.758639	0.007586		0.663412
LSB6.1B	-11		0.956997	0.00957		0.56808
LSB6.2B	2		1.285703	0.012857		0.685549
LSB6.3B	14		1.568846	0.015688		0.656425
LSB6.4B	26		1.955786	0.019558		0.667561
LSB6.5B	49		2.096112	0.020961		0.67306
LSB6.6B	51		2.096112	0.020961		0.586284
LSB6.7B	63		0.249404	0.002494		0.607422
Bos32.1B	-5		5.937148	0.059371		0.705512
Bos32.2B	0		4.908235	0.049082		0.709888
Bos32.3B	5		7.127399	0.071274		0.714724
Pseud41.1B	-5		4.134251	0.041343		0.781766
Pseud41.2B	0		3.817735	0.038177		0.622932
Pseud41.3B	5		4.54744	0.045474		0.758566

Sample Code:	Stratigraphic height*		hopanes/steranes accuracy check (Lorenz Schwark):	C27aaS	ug/kg	peak	Standard (deuterated nC24) m/z=66	rat.	CONST.	Check:	C30aaR peak	ug/kg	ug/g	C30aaR
LSB1.0B	5			0.009678	9.678391	1519732	1100441	1.381021	7.008142		411071	2.6179	0.002618	0.002618
LSB1.1B	13			0.033873	33.87331	1223524	1234788	0.990878	34.18515		308721	8.546953	0.008547	0.008547
LSB1.2B	22			0.048001	48.00 08	3154460	1166705	2.703734	17.75352		681151	10.36494	0.010365	0.010365
LSB1.3B	29			0.033874	33.87353	1631692	1025822	1.590619	21.29581		439007	9.113678	0.009114	0.009114
LSB1.4B	37			0.023407	23.40679	2262357	1047354	2.160069	10.83613		441078	4.563479	0.004563	0.004563
LSB1.5B	46			0.085847	85.84749	6105176	1056449	5.778 96	14.85518		1098007	15.43955	0.015 44	0.015 44
LSB1.6B	55			0.165234	165.2342	2522040	1565445	1.611069	102.5618		493356	32.32276	0.032323	0.032323
LSB1.7B	62			0.042182	42.18179	3143111	915601	3.432839	12.28773		551653	7.403401	0.007403	0.007403
LSB1.8B	69			0.097986	97.98646	5086181	1091029	4.661 82	21.01893		989372	19.06048	0.019 06	0.019 06
LSB1.9B	78			0.210439	210.4394	4723603	1210417	3.902459	53.92482		777419	34.63449	0.034634	0.034634
LSB1.10B	86			0.224282	224.2825	4201766	1067954	3.934407	57.0054		563793	30.09422	0.030094	0.030094
LSB1.11B	94			0.187882	187.8824	2984190	907189	3.289491	57.11595		523885	32.98341	0.032983	0.032983
LSB1.12B	102			0.078404	78.40438	5549300	1096022	5.063128	15.48536		894010	12.6312	0.012631	0.012631
LSB1.13B	110			0.019162	19.16227	1306293	1253347	1.042244	18.3856		151623	2.224188	0.002224	0.002224
LSB1.14B	118			0.033342	33.34171	1112886	632962	1.758219	18.96334		144203	4.320276	0.004 32	0.004 32
LSB3.0B	-22			0.012266	12.26631	1762605	908879	1.939318	6.325067		569744	3.964 96	0.003965	0.003965
LSB5.0B	84			0.148116	148.1164	4657944	1089531	4.275183	34.64562		726571	23.10398	0.023104	0.023104
LSB5.1B	93			0.185947	185.9466	4915360	1129094	4.353367	42.71328		751034	28.41139	0.028411	0.028411
LSB5.2B	102			0.058253	58.25283	5304372	1148953	4.616701	12.61785		942454	10.35007	0.010 35	0.010 35
LSB5.3B	111			0.044219	44.21941	4711732	1283068	3.672239	12.04154		681087	6.391973	0.006392	0.006392
LSB5.4B	120			0.027666	27.66631	3152419	1201446	2.623854	10.54415		409339	3.592447	0.003592	0.003592
LSB5.5B	129			0.035142	35.14244	2819846	1125107	2.506291	14.02169		513521	6.399775	0.006 4	0.006 4
LSB5.6B	138			0.023583	23.58271	1564974	887646	1.763061	13.37601		319302	4.811586	0.004812	0.004812
LSB5.7B	145			0.023058	23.05847	975702	910673	1.071408	21.52166		212290	5.016986	0.005017	0.005017
LSB6.0B	-24			0.014133	14.13339	1583820	1032733	1.533 62	9.215706		542057	4.837105	0.004837	0.004837
LSB6.1B	-11			0.020641	20.64076	2134321	861657	2.476996	8.332981		672871	6.507255	0.006507	0.006507
LSB6.2B	2			0.028838	28.83803	2610445	878057	2.972979	9.700044		768061	8.484899	0.008485	0.008485
LSB6.3B	14			0.024159	24.15878	2758754	1052619	2.620848	9.217928		712696	6.241176	0.006241	0.006241

LSB6.4B	26			0.018209	18.20853	2884822	937485	3.077193	5.917252		835331	5.272473	0.005272	0.005272
LSB6.5B	49			0.036009	36.00935	4978516	1453905	3.424237	10.51602		826208	5.975921	0.005976	0.005976
LSB6.6B	51			0.107329	107.3293	4152734	1150135	3.610649	29.72576		822206	21.25028	0.02125	0.02125
LSB6.7B	63			0.017527	17.52665	2547659	1006746	2.530588	6.925922		367215	2.52626	0.002526	0.002526
Bos32.1B	-5			0.691761	691.7614	8296214	1036118	8.007017	86.3944		1749335	145.8644	0.145864	0.145864
Bos32.2B	0			0.827496	827.4965	8426587	2811149	2.99756	276.0567		1820998	178.8232	0.178823	0.178823
Bos32.3B	5			0.812546	812.5456	7848809	1185723	6.619429	122.7516		1557672	161.2575	0.161258	0.161258
Pseud41.1B	-5			0.80384	803.8401	6554619	1065157	6.153665	130.6279		1663235	203.9745	0.203974	0.203974
Pseud41.2B	0			0.574369	574.3686	6624664	1364495	4.85503	118.3038		1465102	127.0266	0.127027	0.127027
Pseud41.3B	5			0.866514	866.514	7498585	1199360	6.252155	138.5945		1690346	195.3313	0.195331	0.195331

Sample Code:	**Stratigraphic height***		**Armomatics accuracy check:**
LSB1.0B	5		5388300
LSB1.1B	13		4115215
LSB1.2B	22		4367391
LSB1.3B	29		4504150
LSB1.4B	37		3838480
LSB1.5B	46		5221968
LSB1.6B	55		3861708
LSB1.7B	62		4419266
LSB1.8B	69		4867237
LSB1.9B	78		4470519
LSB1.10B	86		4706399
LSB1.11B	94		6129881
LSB1.12B	102		4739755
LSB1.13B	110		6909884
LSB1.14B	118		3456499
LSB3.0B	-22		3889092
LSB5.0B	84		4097516
LSB5.1B	93		4943702
LSB5.2B	102		4077958
LSB5.3B	111		3832639
LSB5.4B	120		4345848
LSB5.5B	129		4198174
LSB5.6B	138		4353582
LSB5.7B	145		4003581
LSB6.0B	-24		3997418
LSB6.1B	-11		3928309

LSB6.2B	2		2818601
LSB6.3B	14		4304372
LSB6.4B	26		3935003
LSB6.5B	49		4223420
LSB6.6B	51		3870430
LSB6.7B	63		4244907
Bos32.1B	-5		3890633
Bos32.2B	0		3940692
Bos32.3B	5		5045571
Pseud41.1B	-5		4212297
Pseud41.2B	0		5366051
Pseud41.3B	5		4777821

µg/g sediment (alkanes and branched isoprenoids):

Sample Code:	**Stratigraphic height***		µg/g nor-pristane (TIC)	µg/g nC17 (TIC)	µg/g Pristane (TIC)	µg/g nC18 (TIC)	µg/g Phytane (TIC)		µg/g nC12 (m/z=85)	C13	C14
LSB1.0B	5		0.606184	1.107348	1.577603	0.890635	0.501055		0.781826	0.947987	1.081343
LSB1.1B	13		1.750646	2.819267	4.531796	2.308438	1.608727		2.102894	2.849095	2.913257
LSB1.2B	22		3.04848	4.795131	7.418617	4.091303	3.018529		3.753738	4.066438	4.615856
LSB1.3B	29		3.041696	4.118706	7.398286	3.582739	2.891086		2.681269	3.544151	4.100121
LSB1.4B	37		1.657426	2.515574	4.542406	2.116279	1.937774		1.146571	1.794431	2.128381
LSB1.5B	46		3.259473	3.838079	8.143914	3.659823	3.863527		1.695999	2.863889	3.696498
LSB1.6B	55		6.840647	9.458768	18.89823	7.634654	8.023906		6.892294	8.339565	8.737107
LSB1.7B	62		1.033005	1.317128	3.143638	1.259244	1.424484		0.1019	0.319112	0.553511
LSB1.8B	69		4.070424	5.281307	10.49521	4.496292	4.237052		5.079311	5.704024	5.824555
LSB1.9B	78		12.31371	16.21642	27.89711	13.57761	11.59991		16.31584	18.09354	18.88398
LSB1.10B	86		12.58674	19.85204	34.83724	16.02194	13.08828		18.38472	20.82897	21.49909
LSB1.11B	94		11.25966	17.19251	28.52653	13.89272	11.71889		13.59358	15.39193	16.47003
LSB1.12B	102		1.543446	2.044248	4.951758	1.716053	2.128216		0.391776	0.827934	1.499925
LSB1.13B	110		1.151302	1.396755	2.813397	1.109232	1.183411		0.409889	0.896682	1.072024
LSB1.14B	118		3.032184	3.719511	8.49213	3.427899	3.52405		1.288649	3.821603	5.120181
LSB3.0B	-22		0.575814	1.699838	1.339078	1.655401	0.434795		0.901865	1.411157	1.495899
LSB5.0B	84		7.841409	14.10515	22.04279	10.58694	8.703257		9.325817	12.07623	13.79979
LSB5.1B	93		7.268763	9.692398	22.13158	8.219877	6.814256		9.737325	10.96832	11.45826
LSB5.2B	102		1.603287	2.276217	5.26807	2.090969	2.196445		0.792105	1.406933	2.30786
LSB5.3B	111		2.299888	3.097267	5.924608	2.579128	2.409261		1.717067	2.53327	2.911732

LSB5.4B	120		2.093717	2.672613	5.254856	2.233352	2.030637		1.329334	1.993562	2.639345
LSB5.5B	129		3.35382	4.389524	9.0997	3.573964	3.547899		3.533909	4.917309	5.844142
LSB5.6B	138		2.428395	3.028037	6.268825	2.620993	2.405661		1.223938	2.118499	2.929483
LSB5.7B	145		2.235094	3.045514	6.071996	2.608325	2.185536		1.288205	2.170391	2.733501
LSB6.0B	-24		0.949958	2.017366	2.228142	1.728094	0.676638		1.360819	1.752699	1.799534
LSB6.1B	-11		1.755771	2.783217	3.928801	2.300353	1.372463		1.486709	2.186828	2.466579
LSB6.2B	2		2.852409	3.736871	6.21947	3.105592	2.158255		2.697141	3.503294	3.912539
LSB6.3B	14		1.967461	3.203373	5.560601	2.652955	1.953232		1.857243	2.912222	3.21021
LSB6.4B	26		1.662503	2.870089	4.986077	2.363831	1.942044		1.57677	2.006109	2.513188
LSB6.5B	49		1.322226	2.029434	3.769122	1.601841	1.574021		1.403071	1.558291	1.794588
LSB6.6B	51		5.669085	7.489256	13.52839	6.427274	7.489429		6.457105	8.27341	9.414549
LSB6.7B	63		0.399056	0.640391	1.411389	0.607826	0.888225		0.056591	0.170236	0.383534
Bos32.1B	-5		13.21551	21.3529	27.03992	18.04181	20.54959		11.04015	14.86585	17.80993
Bos32.2B	0		13.68043	22.9844	26.15351	18.60945	21.26913		11.12879	14.40163	16.32091
Bos32.3B	5		17.40879	34.5811	38.14266	28.29449	30.29348		18.74581	22.63248	26.04529
Pseud41.1B	-5		21.25667	33.08084	40.03457	31.13024	31.48167		27.06473	25.72736	30.89369
Pseud41.2B	0		8.174848	17.91233	22.51716	18.03645	18.77196		17.96097	23.46154	17.18278
Pseud41.3B	5		18.10864	31.51303	36.35802	27.38033	32.85011		24.15727	24.51026	28.26121

Sample Code:	**Stratigraphic height***		C15	C16	C17	C18	C19	C20	C21	C22	C23	C24
LSB1.0B	5		1.174849	1.073067	1.057353	0.921257	0.923361	0.894411	0.883671	0.909634	0.955405	0.89763
LSB1.1B	13		3.055915	2.859426	2.846954	2.391424	2.321357	2.557851	2.589824	2.36894	2.399071	2.129476
LSB1.2B	22		5.166782	4.820066	4.761704	3.869911	3.768401	3.597192	3.352818	3.22686	3.396137	3.265777
LSB1.3B	29		4.471045	4.078158	4.133022	3.299083	2.996304	2.877367	2.692159	2.480921	2.539927	2.269613
LSB1.4B	37		2.650385	2.513192	2.517219	1.995526	1.910388	1.728306	1.668016	1.535211	1.547787	1.453569
LSB1.5B	46		4.286589	4.083679	3.976171	3.489432	3.371734	3.135571	2.820148	2.606844	2.602969	2.508262
LSB1.6B	55		10.00244	9.528526	9.102053	7.485787	7.286988	6.679106	5.996355	5.470884	5.349733	5.168139
LSB1.7B	62		0.933152	1.075803	1.289289	1.161897	1.220302	1.158357	1.096744	1.086847	1.085466	1.118145
LSB1.8B	69		6.221899	5.37146	5.421187	4.328285	4.155141	3.791382	3.30224	3.060216	2.953709	2.872195
LSB1.9B	78		19.67493	17.27693	17.4323	13.24291	12.43674	11.08218	9.752907	8.780327	8.395036	7.641988
LSB1.10B	86		23.34576	20.73854	20.54995	15.88146	14.78379	13.26837	11.69034	10.48077	8.644797	9.060301
LSB1.11B	94		18.69074	16.05556	16.32534	12.57449	12.0548	10.10938	8.886557	7.869098	7.759785	6.625865

LSB1.12B	102		1.798864	1.879377	2.02114	1.876315	1.973062	1.840289	1.750525	1.666794	1.776425	1.768221
LSB1.13B	110		1.400004	1.334777	1.272632	1.080044	0.981056	0.922835	0.804364	0.79414	0.75675	0.738657
LSB1.14B	118		4.169861	3.969703	3.682415	3.195803	3.074508	2.77022	2.467162	2.277772	2.319354	2.219209
LSB3.0B	-22		1.65027	1.614112	1.716375	1.638306	1.736448	1.636118	1.715701	1.677059	1.828191	1.609521
LSB5.0B	84		15.88704	14.05582	13.89017	11.04121	13.40676	10.62967	7.812089	7.011672	6.85152	5.849383
LSB5.1B	93		12.12463	11.80149	10.04387	8.171499	8.70109	7.189161	6.12818	6.006422	5.859261	4.964037
LSB5.2B	102		2.183075	2.358501	2.336533	2.021749	1.953103	1.856464	1.734567	1.594948	1.55128	1.622261
LSB5.3B	111		3.370646	3.159845	3.22447	2.611272	2.469755	2.29599	2.068328	1.913193	1.94061	1.795309
LSB5.4B	120		3.777882	3.092225	2.929291	2.208123	2.055333	1.808703	1.6164	1.495727	1.468839	1.329192
LSB5.5B	129		7.382347	4.962948	4.679614	3.658535	3.655683	3.143529	2.839854	2.681535	2.602951	2.466751
LSB5.6B	138		3.568405	3.39648	3.380358	2.665735	2.490154	2.295812	2.722931	1.846851	1.911844	1.84865
LSB5.7B	145		3.518693	3.258895	3.123626	2.566346	2.404705	2.006823	2.077618	1.916301	1.961486	2.038004
LSB6.0B	-24		2.043503	1.936772	1.987152	1.716459	1.826366	1.902415	1.971182	1.956611	2.040991	1.809107
LSB6.1B	-11		3.439672	2.857287	2.675046	2.190767	2.222224	2.008032	2.044591	2.082282	2.272462	2.259473
LSB6.2B	2		4.148501	3.820595	3.727811	3.068296	2.926754	2.803714	2.643144	2.515262	2.563331	2.438174
LSB6.3B	14		3.507439	3.200245	2.990805	2.533928	2.420726	2.217696	2.096927	1.938815	1.990491	1.934353
LSB6.4B	26		2.479576	2.974873	2.929204	2.175816	1.719483	1.625121	1.680231	1.510381	1.547882	1.318104
LSB6.5B	49		2.149697	1.959382	1.91978	1.547792	1.551142	1.360121	1.482072	1.538078	1.372553	1.435428
LSB6.6B	51		8.556731	7.384126	7.559389	6.096267	6.028153	6.243094	4.38324	4.085181	3.985505	3.697575
LSB6.7B	63		0.579787	0.489878	0.614505	0.620792	0.831976	0.713656	0.531535	0.506259	0.501205	0.477651
Bos32.1B	-5		21.14797	21.46343	21.64884	17.73198	15.68263	14.81126	12.19623	10.64174	9.940265	9.16796
Bos32.2B	0		25.91901	22.88224	22.65132	17.11963	16.05745	13.99226	11.83055	11.77997	10.15608	9.440084
Bos32.3B	5		31.0111	30.83528	31.23594	24.82435	21.08083	20.01176	17.27494	15.20893	14.00245	12.69812
Pseud41.1B	-5		34.04862	33.72557	32.67498	25.43831	24.55611	22.07036	18.9301	16.37527	16.04724	14.41137
Pseud41.2B	0		20.12467	17.82508	18.08617	14.82053	12.37012	11.85165	10.17225	10.61539	12.54225	10.6731
Pseud41.3B	5		32.4434	32.42672	31.67753	26.69516	23.0852	26.70096	18.53804	14.60128	13.83886	13.15326

Sample Code:	**Stratigraphic height***		C25	C26	C27	C28	C29	C30	C31	C32	C33	C34	C35
LSB1.0B	5		0.970548	0.800047	0.861465	0.615993	0.655816	0.433232	0.4372	0.277464	0.36813	0.188739	0.167136
LSB1.1B	13		2.250602	1.90575	1.901481	1.376213	1.417796	0.979501	0.857527	0.512501	0.611569	0.412327	0.288444
LSB1.2B	22		3.426465	2.553939	2.916614	2.063065	2.189428	1.367661	1.423158	0.843823	1.062481	0.603588	0.562551
LSB1.3B	29		2.372539	1.977018	2.045841	1.457551	1.537219	0.970993	0.952002	0.551058	0.706098	0.437843	0.384689

LSB1.4B	37		1.532913	1.199844	1.269133	0.933518	0.944021	0.626623	0.569836	0.381712	0.421853	0.24887	0.231738
LSB1.5B	46		2.648386	2.343324	2.068771	1.586896	1.555812	1.095196	0.987511	0.53643	0.617889	0.527246	0.425091
LSB1.6B	55		5.107532	4.355169	4.133589	3.011483	2.269697	1.232137	1.107253	0.555864	0.625356	0.518963	0.369572
LSB1.7B	62		1.212726	1.073787	1.042024	0.822805	0.867839	0.647311	0.591986	0.341979	0.408914	0.339517	0.316249
LSB1.8B	69		2.936369	2.459207	2.282363	1.811883	1.771682	1.182175	1.090484	0.626311	0.718004	0.531577	0.484699
LSB1.9B	78		7.365519	6.175775	5.625946	4.120763	3.938358	2.575715	2.268369	1.242556	1.232728	0.783764	0.666183
LSB1.10B	86		8.979933	7.42855	6.849602	5.022598	4.734564	3.23328	2.76739	1.41337	1.424016	1.074743	0.878492
LSB1.11B	94		6.831049	5.415729	4.912275	3.71942	3.418244	2.032961	1.868883	1.073724	1.048214	0.674778	0.541951
LSB1.12B	102		2.009937	1.77911	1.863305	1.576369	1.606273	1.17564	1.169666	0.729238	0.905414	0.752519	0.574909
LSB1.13B	110		0.750892	0.661245	0.592902	0.461925	0.471584	0.321731	0.288547	0.157249	0.196939	0.152133	0.12432
LSB1.14B	118		2.313422	1.939642	1.895353	1.341346	1.392386	0.893459	0.814684	0.393324	0.393128	0.205184	0.182012
LSB3.0B	-22		1.775379	1.350832	1.558345	1.0703	1.118981	0.774359	0.721038	0.44305	0.584933	0.234907	0.212657
LSB5.0B	84		5.977018	4.927637	4.523419	3.408404	3.343211	2.115588	1.689501	1.014467	1.007324	0.614362	0.460858
LSB5.1B	93		4.537216	3.889589	3.399933	2.591435	2.344707	1.633007	1.376995	0.727772	0.840708	0.596349	0.411839
LSB5.2B	102		1.613864	1.517602	1.435106	1.148459	1.187745	0.854919	0.826994	0.507045	0.667439	0.519031	0.467424
LSB5.3B	111		1.830696	1.5791	1.532313	1.165183	1.202083	0.853502	0.760878	0.491297	0.521331	0.33301	0.312773
LSB5.4B	120		1.404389	1.177901	1.15991	0.88461	0.90102	0.644862	0.609087	0.351253	0.399933	0.24482	0.193853
LSB5.5B	129		2.521532	2.177581	2.124928	1.629344	1.719017	1.126631	1.051503	0.615043	0.703155	0.432613	0.366138
LSB5.6B	138		1.848816	1.634403	1.615954	1.192589	1.249871	0.873657	0.765855	0.421178	0.557854	0.309229	0.250559
LSB5.7B	145		2.007918	1.692795	1.775667	1.306142	1.378765	0.90343	0.829096	0.42286	0.596386	0.288781	0.224963
LSB6.0B	-24		2.053458	1.529431	1.713919	1.11691	1.232386	0.79299	0.749233	0.46843	0.571078	0.301814	0.2496
LSB6.1B	-11		2.467038	1.882999	2.108005	1.382936	1.563413	1.002558	1.041203	0.582896	0.775155	0.341001	0.322273
LSB6.2B	2		2.666864	2.07615	2.227874	1.538754	1.619676	1.074029	1.017703	0.585307	0.751259	0.426437	0.4021
LSB6.3B	14		1.99488	1.668	1.744813	1.214517	1.317822	0.879845	0.87172	0.522608	0.661294	0.405348	0.331131
LSB6.4B	26		1.37436	1.137391	1.132496	0.815018	0.857026	0.568142	0.54361	0.302574	0.387041	0.262099	0.243272
LSB6.5B	49		1.328556	1.060281	0.934102	0.699894	0.698569	0.470071	0.424118	0.238873	0.303642	0.225209	0.175436
LSB6.6B	51		3.696296	3.181201	2.908152	2.173074	2.127355	1.414679	1.201558	0.690861	0.790919	0.539236	0.473351
LSB6.7B	63		0.499059	0.423427	0.400951	0.320263	0.316759	0.231416	0.204514	0.129668	0.154957	0.129584	0.107254
Bos32.1B	-5		8.668859	7.930154	5.57963	4.918565	4.588135	4.383339	4.493695	3.452748	2.851772	2.081684	1.945748
Bos32.2B	0		8.178246	7.590316	5.621555	4.606524	4.556054	3.758279	3.847267	3.062994	2.363292	2.10411	2.079215
Bos32.3B	5		11.87154	10.27821	7.457679	5.589518	5.657049	4.650082	4.550079	2.911809	2.620283	2.186506	1.818248
Pseud41.1B	-5		12.80289	11.45756	8.641977	7.624436	7.705631	6.652969	6.746673	4.960142	4.346514	3.557364	3.023505
Pseud41.2B	0		10.26337	9.013673	6.619668	5.928309	5.98292	4.936179	5.043465	3.901904	3.235713	2.702082	2.139133
Pseud41.3B	5		12.36492	10.58327	8.207247	6.630625	6.874711	6.039661	6.339116	4.843038	3.928743	2.585978	2.381831

Sample Code:	**Stratigraphic height***		C36	C37	C38	C39	C40	µg/g sum n-alkanes
LSB1.0B	5		0.06033	0.047027	0.027798	0.025948	0.025319	18.46398
LSB1.1B	13		0.105225	0.10413	0.042988	0.076575	0.065348	46.29346
LSB1.2B	22		0.174311	0.197225	0.09549	0.09352	0.087691	71.32269
LSB1.3B	29		0.132494	0.126299	0.091081	0.057669	0.037972	56.0015
LSB1.4B	37		0.08305	0.057551	0.049331	0.037406	0.035749	33.21213
LSB1.5B	46		0.159083	0.128586	0.087874	0.062286	0.037169	56.00534
LSB1.6B	55		0.160984	0.08327	0	0	0	119.5698
LSB1.7B	62		0.092624	0.102701	0.084125	0.061205	0.037653	20.24397
LSB1.8B	69		0.181252	0.142231	0.096256	0.110338	0.121142	74.63158
LSB1.9B	78		0.302264	0.21298	0.122322	0.059063	0.055417	215.7573
LSB1.10B	86		0.331679	0.310144	0.232053	0.165207	0.082419	254.0849
LSB1.11B	94		0.134551	0.061731	0	0	0	194.1407
LSB1.12B	102		0.252021	0.205582	0.180975	0.166787	0.14486	36.16325
LSB1.13B	110		0.033159	0.023294	0.019261	0.01526	0.017455	16.75175
LSB1.14B	118		0.064487	0	0	0	0	52.20487
LSB3.0B	-22		0.075583	0.065408	0.040182	0.0317	0.028593	30.71727
LSB5.0B	84		0.176489	0.131397	0.078428	0.055718	0	171.161
LSB5.1B	93		0.202868	0.133511	0.106064	0.077421	0.053563	136.0765
LSB5.2B	102		0.150638	0.179779	0.134595	0.113684	0.102469	35.14617
LSB5.3B	111		0.114525	0.093575	0.066615	0.047789	0.046274	42.96243
LSB5.4B	120		0.07997	0.068312	0.047094	0.036497	0.020177	35.96764
LSB5.5B	129		0.13881	0.103932	0.062706	0	0	67.14204
LSB5.6B	138		0.095015	0.090876	0.064824	0	0	43.36982
LSB5.7B	145		0.099317	0.048664	0	0.031989	0.023362	42.69473
LSB6.0B	-24		0.082455	0.066095	0.051329	0.032532	0.027684	35.14296
LSB6.1B	-11		0.095662	0.084989	0.054169	0.041739	0.031775	43.96976
LSB6.2B	2		0.132479	0.085643	0.068749	0.054483	0.043417	55.53948
LSB6.3B	14		0.089584	0.072989	0.055421	0.053183	0.035861	44.73012
LSB6.4B	26		0.066779	0.066282	0.035564	0.024702	0.023672	33.89677
LSB6.5B	49		0.06999	0.063595	0.033574	0.023872	0.024806	27.84658
LSB6.6B	51		0.135427	0.100047	0.057856	0.056685	0.056354	101.7674
LSB6.7B	63		0.041101	0.035876	0.016129	0.010375	0.012853	9.511792
Bos32.1B	-5		1.036648	0.619731	0.318237	0.265892	0.280235	251.5633
Bos32.2B	0		0.752472	0.543625	0.273624	0.226842	0.133588	253.3779
Bos32.3B	5		0.831794	0.488123	0.203125	0.245084	0	346.9664
Pseud41.1B	-5		1.633558	1.238992	0.988084	0	0.433975	403.778
Pseud41.2B	0		1.146135	0.702418	0	0	0	259.3015
Pseud41.3B	5		0.955144	0.759272	0.755227	0	0	383.3379

µg/g sediment (hopanes and steranes):

Sample Code:	Stratigraphic height*		SUM Hopanes		C19/3	C20/3	C21/3	C22/3	C23/3	C24/3	C25/3 S	C25/3 R	C24/4
LSB1.0B	5		1.084499		0.008403	0.007379	0.007327	0.001063	0.007053	0.003952	0.001318	0.002289	0.017649
LSB1.1B	13		3.530942		0.031752	0.028766	0.028409	0.006123	0.029992	0.017002	0.007975	0.006447	0.062697
LSB1.2B	22		5.402593		0.042221	0.036523	0.036195	0.005944	0.035568	0.019304	0.009202	0.005803	0.080093
LSB1.3B	29		4.178125		0.034714	0.030892	0.031396	0.006366	0.032998	0.018976	0.008651	0.006783	0.064326
LSB1.4B	37		2.588549		0.023164	0.019476	0.020129	0.003 14	0.021813	0.013017	0.005487	0.005581	0.038571
LSB1.5B	46		4.882 82		0.043289	0.034414	0.035904	0.005957	0.038077	0.024199	0.013997	0.009654	0.059066
LSB1.6B	55		9.971964		0.081043	0.070235	0.069908	0.012468	0.081669	0.054742	0.030714	0.021633	0.124981
LSB1.7B	62		2.697629		0.014453	0.014 5	0.016084	0.003751	0.019793	0.012794	0.007439	0.005558	0.026233
LSB1.8B	69		6.384711		0.049919	0.043353	0.044539	0.005 84	0.045223	0.030168	0.014438	0.012 5	0.070439
LSB1.9B	78		11.32276		0.143078	0.111244	0.110997	0.017647	0.109067	0.070934	0.037004	0.024413	0.172876
LSB1.10B	86		12.40685		0.146014	0.128 04	0.119617	0.019738	0.119542	0.073404	0.038597	0.029853	0.191358
LSB1.11B	94		10.65401		0.123262	0.106312	0.099462	0.015377	0.094347	0.060353	0.032538	0.022373	0.160143
LSB1.12B	102		5.413194		0.026224	0.026061	0.028686	0.004661	0.033359	0.023015	0.013672	0.010219	0.047485
LSB1.13B	110		1.257809		0.011 18	0.010761	0.010203	0.002389	0.011424	0.007149	0.003798	0.003069	0.018058
LSB1.14B	118		2.537409		0.028791	0.025752	0.024671	0.004385	0.026369	0.016 41	0.007764	0.006008	0.047 58
LSB3.0B	-22		1.662742		0.012691	0.010413	0.008959	0.001108	0.007515	0.003704	0.001459	0.001573	0.034655
LSB5.0B	84		7.291257		0.090675	0.075892	0.070439	0.010163	0.067979	0.043677	0.021268	0.015487	0.115027
LSB5.1B	93		10.15892		0.096 76	0.078315	0.077224	0.011591	0.080178	0.050061	0.028326	0.019268	0.125862
LSB5.2B	102		3.567 17		0.024154	0.019917	0.020902	0.002589	0.024998	0.015647	0.008657	0.007014	0.036 57
LSB5.3B	111		2.645197		0.026784	0.022 51	0.023785	0.003409	0.023738	0.014755	0.003372	0.007353	0.038947
LSB5.4B	120		2.007 51		0.020507	0.018308	0.018118	0.003114	0.019208	0.011082	0.005673	0.003846	0.032656
LSB5.5B	129		3.580961		0.038 25	0.032462	0.031 21	0.005236	0.031215	0.017587	0.008574	0.006797	0.058107
LSB5.6B	138		2.537065		0.024582	0.022616	0.021198	0.002745	0.019275	0.010781	0.005324	0.003605	0.041999
LSB5.7B	145		2.190 81		0.024489	0.021197	0.019896	0.004193	0.017294	0.010 82	0.005326	0.002536	0.040 8
LSB6.0B	-24		1.684955		0.012243	0.010637	0.009771	0.001755	0.008437	0.004551	0.002097	0.001342	0.030 4
LSB6.1B	-11		2.422239		0.018073	0.015866	0.014803	0.002116	0.013412	0.007033	0.003564	0.002 21	0.037811
LSB6.2B	2		3.445681		0.027886	0.024641	0.023657	0.003768	0.022629	0.012783	0.006322	0.004395	0.054802
LSB6.3B	14		2.981262		0.024692	0.021365	0.021079	0.002896	0.020328	0.010973	0.005733	0.003376	0.043678
LSB6.4B	26		2.200696		0.020 21	0.017029	0.017346	0.002705	0.016326	0.009584	0.004335	0.002989	0.031548
LSB6.5B	49		2.451357		0.021622	0.019422	0.018 79	0.002698	0.019848	0.012374	0.005487	0.005025	0.034434

LSB6.6B	51		6.156334		0.060763	0.052096	0.050607	0.008448	0.053293	0.033782	0.016566	0.012496	0.088318
LSB6.7B	63		0.951616		0.006348	0.006387	0.006619	0.0015	0.007904	0.005156	0.002479	0.001957	0.01033
Bos32.1B	-5		5035.488		13.34722	38.82588	82.008	17.23181	134.3376	91.03021	86.05039	69.11382	36.64537
Bos32.2B	0		5280.641		12.65846	40.29298	81.4583	16.51191	139.1367	93.13445	72.13074	72.17191	37.41106
Bos32.3B	5		4655.191		12.89519	37.8085	77.38497	17.20026	126.3608	83.97881	65.99232	62.48756	32.85776
Pseud41.1B	-5		3220.434		8.056311	25.49359	51.39164	11.15948	88.44903	58.60189	46.50299	44.18499	21.71284
Pseud41.2B	0		7936.182		18.63171	66.06526	133.9399	26.39789	229.3574	155.2969	124.8832	112.0418	48.42134
Pseud41.3B	5		2054.762		4.868153	16.09478	34.21821	6.239771	59.19432	40.12245	30.06191	30.60275	13.58663

Sample Code:	**Stratigraphic height***		C26/3S	C26/3R	C28/3S	C28/3R	C29/3S	C29/3R	Ts	Tm	C30/3S	C30/3R
LSB1.0B	5		0.001523	0.001507	0.001974	0.001171	0.002419	0.001749	0.03162	0.039624	0.013269	0.009538
LSB1.1B	13		0.008455	0.00876	0.006124	0.005079	0.011007	0.008279	0.111976	0.123749	0.044065	0.035585
LSB1.2B	22		0.008523	0.008954	0.007048	0.006802	0.011782	0.009442	0.156	0.176305	0.05776	0.048186
LSB1.3B	29		0.007799	0.007939	0.006578	0.004855	0.01032	0.007213	0.122393	0.133385	0.043558	0.038127
LSB1.4B	37		0.004581	0.004586	0.003898	0.003632	0.006463	0.004853	0.082953	0.082987	0.027917	0.0246
LSB1.5B	46		0.010602	0.011209	0.009488	0.009646	0.016212	0.013174	0.16096	0.13589	0.047171	0.043829
LSB1.6B	55		0.025857	0.026586	0.022231	0.02178	0.05089	0.034919	0.324221	0.265396	0.100537	0.093773
LSB1.7B	62		0.00625	0.006243	0.004022	0.005423	0.011951	0.007432	0.07027	0.057933	0.02248	0.022177
LSB1.8B	69		0.015198	0.015107	0.010968	0.012688	0.02324	0.015781	0.190427	0.149825	0.058583	0.054054
LSB1.9B	78		0.030166	0.031413	0.025836	0.025786	0.044131	0.026966	0.425852	0.331995	0.119324	0.102279
LSB1.10B	86		0.033431	0.036541	0.023123	0.023004	0.050078	0.03278	0.470703	0.368964	0.123092	0.110289
LSB1.11B	94		0.029159	0.029947	0.020566	0.021941	0.037191	0.030127	0.388621	0.300878	0.106456	0.095316
LSB1.12B	102		0.012331	0.012728	0.010834	0.012395	0.021158	0.018415	0.132811	0.110564	0.046964	0.042349
LSB1.13B	110		0.003533	0.003648	0.003014	0.002947	0.005615	0.00349	0.042794	0.032178	0.013857	0.013189
LSB1.14B	118		0.00695	0.006926	0.004578	0.004328	0.008278	0.007673	0.106657	0.071918	0.031443	0.025271
LSB3.0B	-22		0.001123	0.00107	0.001485	0.00162	0.002949	0.00149	0.039984	0.068404	0.023929	0.013827
LSB5.0B	84		0.020241	0.020307	0.011237	0.012455	0.027306	0.017423	0.273119	0.214625	0.072345	0.058786
LSB5.1B	93		0.025802	0.027214	0.015855	0.017775	0.039661	0.025839	0.320696	0.252241	0.094043	0.080023
LSB5.2B	102		0.008123	0.008526	0.006466	0.007767	0.012794	0.010083	0.097374	0.080756	0.031479	0.028674
LSB5.3B	111		0.006244	0.006414	0.004844	0.005228	0.009212	0.006291	0.102069	0.074988	0.028034	0.02307
LSB5.4B	120		0.004205	0.004251	0.003162	0.002763	0.007209	0.00545	0.077842	0.056183	0.022726	0.018383
LSB5.5B	129		0.006961	0.00728	0.005529	0.005491	0.009753	0.008259	0.131572	0.094893	0.040149	0.030866

LSB5.6B	138		0.00392	0.003988	0.003467	0.002821	0.007195	0.005261	0.088639	0.069559	0.032391	0.023303
LSB5.7B	145		0.004031	0.004126	0.002717	0.0021	0.006663	0.00469	0.080612	0.066639	0.02866	0.020228
LSB6.0B	-24		0.001936	0.002007	0.001968	0.001835	0.003885	0.002273	0.043099	0.065959	0.021912	0.013793
LSB6.1B	-11		0.003171	0.003614	0.002986	0.001902	0.004857	0.002724	0.061465	0.082434	0.031018	0.021514
LSB6.2B	2		0.006109	0.00699	0.004183	0.003358	0.00774	0.005005	0.100091	0.117921	0.039735	0.031671
LSB6.3B	14		0.005088	0.005204	0.004108	0.003083	0.006199	0.004514	0.08405	0.097052	0.032723	0.027014
LSB6.4B	26		0.003957	0.004646	0.00329	0.002827	0.004845	0.003381	0.06296	0.067026	0.023864	0.020259
LSB6.5B	49		0.004977	0.004927	0.004048	0.004037	0.007489	0.004962	0.077874	0.071843	0.023004	0.020915
LSB6.6B	51		0.014855	0.015488	0.012888	0.012865	0.023624	0.014939	0.214292	0.177044	0.059327	0.052099
LSB6.7B	63		0.002789	0.002784	0.001924	0.001862	0.004442	0.00235	0.027742	0.021965	0.008789	0.007562
Bos32.1B	-5		37.65759	38.01856	43.52453	48.49552	75.87948	60.63685	113.1605	108.7616	67.18305	59.06476
Bos32.2B	0		38.89913	39.30711	41.59317	46.24787	71.32158	56.78839	116.0552	118.2584	69.1642	61.05714
Bos32.3B	5		34.19773	34.91568	40.40806	44.39552	72.58422	56.24251	107.9087	103.6753	62.1635	56.07132
Pseud41.1B	-5		24.63381	24.8917	32.74048	35.13265	50.9654	39.99855	65.75191	67.13722	48.1271	43.57641
Pseud41.2B	0		66.73447	65.02219	78.93494	76.52823	122.187	99.84375	187.4819	184.4123	129.5066	120.3628
Pseud41.3B	5		17.53352	17.25483	20.27796	23.08294	31.65767	26.35738	44.73499	43.3851	30.30025	27.77973

Sample Code:	**Stratigraphic height***		C29ab	C29Ts	C30*	C29ba	C30ab	C30ba	C31abS	C31abR	C31ba	C32abS
LSB1.0B	5		0.10953	0.049711	0	0.018541	0.150414	0.043904	0.114869	0.082744	0.024851	0.069338
LSB1.1B	13		0.363064	0.169464	0	0.063798	0.484247	0.137167	0.350554	0.25778	0.076772	0.21432
LSB1.2B	22		0.551028	0.240185	0	0.098722	0.744655	0.208021	0.562557	0.401337	0.135926	0.346642
LSB1.3B	29		0.407395	0.181311	0	0.071746	0.557751	0.159384	0.430958	0.317534	0.095778	0.268273
LSB1.4B	37		0.262253	0.118827	0	0.043213	0.365089	0.093974	0.270462	0.194949	0.058852	0.163031
LSB1.5B	46		0.449355	0.228451	0	0.070745	0.703242	0.17201	0.48928	0.35843	0.086511	0.326575
LSB1.6B	55		0.903601	0.449391	0	0.146049	1.372162	0.319834	0.97748	0.725632	0.212009	0.658877
LSB1.7B	62		0.226109	0.110758	0	0.038467	0.381355	0.086761	0.274542	0.199627	0.044836	0.202748
LSB1.8B	69		0.555482	0.270449	0	0.103711	0.906241	0.208483	0.626063	0.461831	0.107237	0.451013
LSB1.9B	78		1.082985	0.552888	0	0.183438	1.651076	0.388861	1.077444	0.819785	0.21481	0.714104
LSB1.10B	86		1.160542	0.602198	0	0.199205	1.794974	0.423885	1.187287	0.901711	0.230673	0.770901
LSB1.11B	94		0.977293	0.509662	0	0.179008	1.585457	0.366812	1.029548	0.763544	0.202892	0.701155
LSB1.12B	102		0.443578	0.223424	0	0.067253	0.742837	0.178271	0.535468	0.386224	0.106054	0.399037
LSB1.13B	110		0.116918	0.06328	0	0.021341	0.17318	0.041972	0.119353	0.090149	0.026151	0.079813

LSB1.14B	118		0.242447	0.14226	0	0.029222	0.360026	0.082053	0.244683	0.174673	0.046217	0.162378
LSB3.0B	-22		0.179636	0.072792	0	0.03176	0.216006	0.073947	0.169782	0.123198	0.04176	0.109296
LSB5.0B	84		0.695018	0.345726	0	0.110237	1.077225	0.249714	0.702652	0.525372	0.126569	0.465001
LSB5.1B	93		0.913386	0.449947	0	0.152658	1.485973	0.343164	0.999387	0.724162	0.164269	0.691798
LSB5.2B	102		0.306627	0.150007	0	0.044876	0.511443	0.117437	0.357903	0.257723	0.06093	0.264161
LSB5.3B	111		0.248142	0.135029	0	0.04185	0.387441	0.087687	0.257759	0.18917	0.043579	0.178545
LSB5.4B	120		0.184156	0.10038	0	0.028574	0.29491	0.06905	0.196486	0.14392	0.034473	0.133333
LSB5.5B	129		0.320152	0.186623	0	0.048819	0.511653	0.115376	0.353853	0.263036	0.063557	0.24357
LSB5.6B	138		0.228216	0.135321	0	0.040074	0.374382	0.08896	0.254715	0.186514	0.04664	0.167113
LSB5.7B	145		0.204336	0.124962	0	0.033716	0.304337	0.0755	0.21249	0.159619	0.040643	0.145153
LSB6.0B	-24		0.172401	0.073662	0	0.032561	0.222698	0.071445	0.173697	0.124828	0.045982	0.106778
LSB6.1B	-11		0.238391	0.109876	0	0.045276	0.320489	0.107574	0.24581	0.179912	0.060107	0.166192
LSB6.2B	2		0.361824	0.160293	0	0.06201	0.479072	0.130836	0.358093	0.262533	0.069802	0.223857
LSB6.3B	14		0.295837	0.132105	0	0.050324	0.408812	0.116843	0.314375	0.228345	0.062794	0.197621
LSB6.4B	26		0.208749	0.09281	0	0.035401	0.296779	0.08211	0.231069	0.170206	0.047128	0.146311
LSB6.5B	49		0.232252	0.103945	0	0.036469	0.351179	0.093018	0.251014	0.184669	0.051744	0.163404
LSB6.6B	51		0.590253	0.281603	0	0.09531	0.871788	0.214353	0.608205	0.454395	0.107607	0.403563
LSB6.7B	63		0.085136	0.041824	0	0.012977	0.132787	0.03087	0.095155	0.070546	0.015856	0.066382
Bos32.1B	-5		307.4989	149.1124	22.05395	46.83793	533.5039	133.3156	404.3139	318.6569	83.85087	308.5198
Bos32.2B	0		325.781	146.5281	21.99245	38.03129	571.5522	141.1996	441.9669	345.4246	75.74914	326.03
Bos32.3B	5		290.9666	137.2274	16.05153	23.53611	507.0283	127.597	375.4919	293.429	72.88261	283.4861
Pseud41.1B	-5		198.4072	86.24515	19.0476	25.48804	334.8492	83.08949	261.1604	207.5729	54.17773	196.7799
Pseud41.2B	0		479.4711	213.9997	39.52481	71.65407	808.3063	214.3099	640.9606	507.2626	118.7803	473.9875
Pseud41.3B	5		130.7857	57.20304	11.91945	17.80234	214.4234	53.60886	167.2263	131.8397	29.40472	123.6436

Sample Code:	**Stratigraphic height***		C32abR	C32baS	C32baR	C33abS	C33abR	C33baS	C33baR	C34abS
LSB1.0B	5		0.04581	0.005849	0.007264	0.047443	0.032671	0.005129	0.006028	0.034515
LSB1.1B	13		0.150352	0.019234	0.022278	0.149839	0.107283	0.017697	0.018116	0.106458
LSB1.2B	22		0.25014	0.041287	0.043511	0.237052	0.162422	0.02847	0.029265	0.168737
LSB1.3B	29		0.190191	0.026006	0.029331	0.18979	0.134165	0.020687	0.025165	0.138045
LSB1.4B	37		0.112049	0.015475	0.01706	0.112669	0.07812	0.009794	0.013326	0.077467
LSB1.5B	46		0.23085	0.026343	0.02734	0.246977	0.172553	0.020631	0.025067	0.151708

LSB1.6B	55		0.470601	0.077638	0.084591	0.492095	0.347816	0.044611	0.062476	0.318942
LSB1.7B	62		0.14048	0.015887	0.016405	0.160537	0.110243	0.011923	0.016036	0.097213
LSB1.8B	69		0.31858	0.048292	0.051645	0.348919	0.24229	0.02868	0.037037	0.21872
LSB1.9B	78		0.49436	0.056888	0.05976	0.523305	0.366459	0.044473	0.058274	0.31145
LSB1.10B	86		0.553552	0.076966	0.085102	0.574187	0.407391	0.053118	0.071984	0.337101
LSB1.11B	94		0.498739	0.04717	0.051752	0.504295	0.352365	0.039774	0.050785	0.3064
LSB1.12B	102		0.275782	0.045319	0.048265	0.323087	0.218436	0.034863	0.035458	0.203915
LSB1.13B	110		0.056197	0.008972	0.009961	0.059782	0.042141	0.005076	0.007747	0.036995
LSB1.14B	118		0.108283	0.012142	0.013218	0.115136	0.081897	0.00912	0.014205	0.071404
LSB3.0B	-22		0.075895	0.012003	0.014231	0.07234	0.050297	0.007999	0.010913	0.051314
LSB5.0B	84		0.332843	0.041526	0.043064	0.343559	0.241865	0.024197	0.036221	0.203813
LSB5.1B	93		0.482655	0.049667	0.052268	0.545215	0.375372	0.050739	0.066099	0.330217
LSB5.2B	102		0.181773	0.018529	0.018843	0.206598	0.14028	0.018585	0.021005	0.130921
LSB5.3B	111		0.125637	0.013591	0.013802	0.126628	0.089641	0.009106	0.012749	0.076049
LSB5.4B	120		0.094545	0.009254	0.009745	0.094815	0.066243	0.006583	0.008572	0.059646
LSB5.5B	129		0.173798	0.01683	0.017682	0.174613	0.123361	0.011516	0.016363	0.11012
LSB5.6B	138		0.115905	0.013082	0.015237	0.120138	0.084474	0.009891	0.012115	0.077239
LSB5.7B	145		0.101798	0.010787	0.013018	0.098879	0.070992	0.008241	0.012037	0.064243
LSB6.0B	-24		0.07591	0.010042	0.012536	0.076169	0.052397	0.009895	0.012333	0.05207
LSB6.1B	-11		0.118167	0.013299	0.016452	0.109941	0.076759	0.013531	0.017152	0.078608
LSB6.2B	2		0.15483	0.017329	0.019934	0.15024	0.104042	0.015225	0.020219	0.10943
LSB6.3B	14		0.14058	0.015671	0.017704	0.136509	0.094975	0.012204	0.017759	0.096017
LSB6.4B	26		0.103779	0.011941	0.013308	0.10242	0.071952	0.010611	0.013375	0.073058
LSB6.5B	49		0.115662	0.011916	0.013126	0.113355	0.07966	0.011112	0.013557	0.07888
LSB6.6B	51		0.291597	0.032461	0.035185	0.291759	0.206666	0.025917	0.036381	0.186076
LSB6.7B	63		0.047148	0.004568	0.005116	0.051433	0.035888	0.004541	0.006373	0.03261
Bos32.1B	-5		219.9389	33.00591	32.82335	306.2062	222.5204	25.00003	36.20436	170.5107
Bos32.2B	0		233.4836	36.65605	37.93348	327.4341	236.2787	28.42931	34.18684	186.8125
Bos32.3B	5		210.5225	25.87859	24.90024	280.537	206.8862	26.51525	33.33666	157.1507
Pseud41.1B	-5		152.0706	22.70724	22.82112	194.1012	144.0245	15.08429	17.23456	108.1867
Pseud41.2B	0		353.9829	50.25152	54.29942	462.752	355.2179	37.94675	59.12088	252.1227
Pseud41.3B	5		91.63127	13.30567	13.06613	118.44	89.74354	10.35163	13.80646	66.70737

Sample Code:	**Stratigraphic height***		C34abR	C34baS	C34baR	C35abS	C35abR	C36abS	C36abR
LSB1.0B	5		0.022623	0.003424	0.003377	0.018505	0.01332	0.007177	0.006636
LSB1.1B	13		0.072822	0.01278	0.011183	0.061558	0.045193	0.022097	0.014644
LSB1.2B	22		0.116191	0.020475	0.022508	0.100293	0.074494	0.031688	0.025332
LSB1.3B	29		0.095576	0.018601	0.018038	0.080266	0.058275	0.027562	0.019026
LSB1.4B	37		0.053213	0.009706	0.010572	0.048101	0.035571	0.016306	0.01162
LSB1.5B	46		0.104306	0.018942	0.015601	0.097387	0.06963	0.039183	0.028947
LSB1.6B	55		0.220298	0.04457	0.040923	0.198511	0.14871	0.080495	0.061069
LSB1.7B	62		0.066635	0.010929	0.009603	0.059775	0.042931	0.023204	0.015841
LSB1.8B	69		0.149235	0.023279	0.021849	0.141603	0.100701	0.059052	0.04203
LSB1.9B	78		0.22227	0.031006	0.031052	0.194809	0.136729	0.083739	0.061784
LSB1.10B	86		0.232219	0.04497	0.046303	0.212046	0.161104	0.083738	0.057521
LSB1.11B	94		0.208863	0.034675	0.032187	0.184897	0.128478	0.071851	0.052041
LSB1.12B	102		0.132526	0.017576	0.019801	0.144424	0.102405	0.056512	0.038745
LSB1.13B	110		0.026247	0.00582	0.006087	0.024006	0.01783	0.00946	0.007034
LSB1.14B	118		0.051409	0.006858	0.005846	0.041983	0.032403	0.016311	0.011485
LSB3.0B	-22		0.034303	0.005389	0.006152	0.026807	0.021041	0.010383	0.007538
LSB5.0B	84		0.13899	0.019239	0.020367	0.12851	0.09723	0.049312	0.034557
LSB5.1B	93		0.216508	0.03173	0.032077	0.217306	0.154325	0.093309	0.069958
LSB5.2B	102		0.088553	0.008794	0.009952	0.084605	0.061033	0.03253	0.02157
LSB5.3B	111		0.052308	0.005847	0.005995	0.047565	0.036462	0.017498	0.012068
LSB5.4B	120		0.040853	0.005418	0.004796	0.036952	0.026714	0.014001	0.009408
LSB5.5B	129		0.074864	0.011589	0.011702	0.067393	0.050278	0.026362	0.017658
LSB5.6B	138		0.053114	0.006183	0.006472	0.044762	0.034615	0.016846	0.012387
LSB5.7B	145		0.045726	0.0047	0.005306	0.036194	0.027511	0.013636	0.009973
LSB6.0B	-24		0.035165	0.008151	0.007772	0.028658	0.021302	0.010938	0.007667
LSB6.1B	-11		0.052669	0.01024	0.010515	0.042808	0.031824	0.015787	0.010284
LSB6.2B	2		0.073928	0.00969	0.011718	0.062821	0.044859	0.022051	0.017361
LSB6.3B	14		0.065684	0.009578	0.010064	0.056849	0.041536	0.020446	0.015479
LSB6.4B	26		0.04988	0.008911	0.009062	0.044848	0.032035	0.015001	0.010824
LSB6.5B	49		0.054078	0.008183	0.007341	0.048122	0.035229	0.017408	0.012259
LSB6.6B	51		0.127591	0.021474	0.022165	0.118382	0.086738	0.044232	0.028843
LSB6.7B	63		0.022261	0.004256	0.003898	0.021158	0.015656	0.008087	0.006198
Bos32.1B	-5		118.1284	22.38006	19.86316	130.7505	87.45899	43.0403	39.0195
Bos32.2B	0		126.3125	20.39154	21.99944	145.7807	101.0727	42.24516	43.77
Bos32.3B	5		108.0737	19.55951	19.02915	120.1461	84.42795	42.22564	38.77615
Pseud41.1B	-5		73.35773	15.1206	12.39486	80.29833	56.25441	23.35993	28.0924
Pseud41.2B	0		176.7718	33.6346	31.31933	192.3668	137.9427	56.48748	67.65861
Pseud41.3B	5		44.49505	8.825174	7.501663	51.79075	36.83438	14.69756	18.35523

Sample Code:	**Stratigraphic height***		SUM Steranes		C21ba	C21aa	C22ab	C22aa		C27baS	C27baR
LSB1.0B	5		0.446564		0.020734	0.024661	0.012535	0.014241		0.036208	0.025113
LSB1.1B	13		1.592594		0.080382	0.092327	0.047419	0.056152		0.149895	0.100123
LSB1.2B	22		1.92769		0.0981	0.113049	0.056131	0.066644		0.179268	0.122682
LSB1.3B	29		1.609715		0.086776	0.10245	0.052777	0.061992		0.152431	0.103718
LSB1.4B	37		1.086886		0.056373	0.06693	0.03551	0.039581		0.115557	0.077595
LSB1.5B	46		3.019256		0.095998	0.11376	0.0577	0.067522		0.307758	0.210634
LSB1.6B	55		6.175405		0.205203	0.232342	0.130561	0.14865		0.651117	0.438103
LSB1.7B	62		1.587038		0.041572	0.044601	0.027833	0.031068		0.170362	0.114526
LSB1.8B	69		3.590349		0.117428	0.131488	0.069179	0.080478		0.36793	0.249819
LSB1.9B	78		7.062059		0.306142	0.342707	0.170926	0.201102		0.723595	0.498279
LSB1.10B	86		8.24308		0.32072	0.399944	0.194779	0.22733		0.817353	0.556546
LSB1.11B	94		6.877248		0.289425	0.329044	0.17244	0.198446		0.718991	0.482056
LSB1.12B	102		2.9499		0.077246	0.078895	0.046827	0.051722		0.307894	0.214282
LSB1.13B	110		0.720107		0.028649	0.032148	0.017432	0.019848		0.079644	0.053487
LSB1.14B	118		1.458756		0.071542	0.083215	0.047529	0.049871		0.161951	0.10832
LSB3.0B	-22		0.555638		0.023517	0.027783	0.013407	0.016993		0.04593	0.031738
LSB5.0B	84		5.056084		0.206155	0.254201	0.128152	0.142046		0.506053	0.342703
LSB5.1B	93		6.18315		0.221526	0.264172	0.142018	0.152404		0.631618	0.427155
LSB5.2B	102		2.189203		0.062353	0.067534	0.03821	0.042543		0.229478	0.156169
LSB5.3B	111		1.646635		0.0638	0.076068	0.040827	0.043217		0.182774	0.123744
LSB5.4B	120		1.058155		0.050859	0.060794	0.032434	0.036083		0.118671	0.078936
LSB5.5B	129		1.676864		0.087905	0.106319	0.057639	0.060194		0.182069	0.121449
LSB5.6B	138		1.146541		0.062143	0.07211	0.037163	0.042139		0.117168	0.078447
LSB5.7B	145		1.078165		0.058797	0.06757	0.035991	0.039067		0.104792	0.071924
LSB6.0B	-24		0.677834		0.027136	0.032712	0.017566	0.019659		0.055022	0.038966
LSB6.1B	-11		0.911565		0.039154	0.047434	0.024042	0.027576		0.076249	0.052847
LSB6.2B	2		1.374727		0.063597	0.075927	0.039383	0.044282		0.123308	0.08532
LSB6.3B	14		1.10066		0.054351	0.06589	0.034349	0.038566		0.103395	0.069912
LSB6.4B	26		0.886327		0.044291	0.053715	0.027738	0.030809		0.084796	0.057295
LSB6.5B	49		1.284641		0.052227	0.06232	0.033386	0.035568		0.135644	0.092456
LSB6.6B	51		3.957955		0.1423	0.169084	0.088663	0.096103		0.406562	0.274025
LSB6.7B	63		0.61161		0.018112	0.020396	0.012742	0.013298		0.066953	0.04542

Bos32.1B	-5		19.93069		0.564197	0.629866	0.310223	0.432021		1.569911	1.068518
Bos32.2B	0		24.56467		0.670026	0.781284	0.38603	0.51306		1.93119	1.345012
Bos32.3B	5		24.68331		0.725518	0.832962	0.394512	0.541361		1.972669	1.366296
Pseud41.1B	-5		25.25038		0.648087	0.723728	0.348269	0.503119		1.990758	1.385682
Pseud41.2B	0		16.77969		0.458555	0.512913	0.236544	0.333729		1.322134	0.942077
Pseud41.3B	5		26.1486		0.717385	0.79382	0.377746	0.517181		2.062019	1.474564

Sample Code:	**Stratigraphic height***		C27abS	C27abR	C28baS 1	C28baS 2	C28baR	C27aaS	C27bbR	C29baS	C27bbS	C27aaR
LSB1.0B	5		0.013636	0.012351	0.012463	0.014652	0.010362	0.009678	0.00595	0.042968	0.005062	0.007435
LSB1.1B	13		0.051391	0.04973	0.048409	0.057466	0.042147	0.033873	0.015429	0.133259	0.014482	0.033808
LSB1.2B	22		0.057778	0.06208	0.057048	0.065664	0.048232	0.048001	0.027049	0.160081	0.024774	0.043291
LSB1.3B	29		0.047603	0.049998	0.046016	0.054806	0.038518	0.033874	0.020103	0.132454	0.018447	0.037155
LSB1.4B	37		0.036376	0.037732	0.034496	0.03806	0.026723	0.023407	0.018804	0.084447	0.016286	0.022679
LSB1.5B	46		0.098845	0.099005	0.103795	0.116775	0.084315	0.085847	0.053435	0.24994	0.047554	0.063308
LSB1.6B	55		0.207815	0.202945	0.21078	0.245755	0.183883	0.165234	0.103345	0.530939	0.088342	0.166749
LSB1.7B	62		0.051423	0.049105	0.0567	0.066735	0.049848	0.042182	0.015927	0.153841	0.014437	0.025147
LSB1.8B	69		0.112748	0.113814	0.119948	0.13887	0.104223	0.097986	0.049691	0.328899	0.044276	0.076927
LSB1.9B	78		0.245726	0.243035	0.232791	0.265444	0.188005	0.210439	0.089837	0.53649	0.078808	0.152768
LSB1.10B	86		0.264326	0.271631	0.258425	0.294755	0.227947	0.224282	0.171332	0.614193	0.14626	0.247058
LSB1.11B	94		0.235692	0.227139	0.226365	0.261952	0.189315	0.187882	0.138537	0.552226	0.128154	0.151362
LSB1.12B	102		0.101739	0.091161	0.106737	0.124392	0.08689	0.078404	0.049266	0.314045	0.044936	0.058616
LSB1.13B	110		0.027246	0.024851	0.025839	0.029657	0.021855	0.019162	0.012772	0.054471	0.011224	0.013855
LSB1.14B	118		0.055208	0.054056	0.046469	0.051555	0.039035	0.033342	0.027982	0.111278	0.026219	0.03817
LSB3.0B	-22		0.015762	0.015885	0.016707	0.01995	0.013431	0.012266	0.005842	0.056319	0.004901	0.012617
LSB5.0B	84		0.166856	0.174537	0.163942	0.188573	0.145385	0.148116	0.092108	0.37408	0.084945	0.119224
LSB5.1B	93		0.203617	0.199801	0.209962	0.24328	0.183727	0.185947	0.109822	0.539765	0.098211	0.139126
LSB5.2B	102		0.070875	0.070293	0.080975	0.091552	0.062744	0.058253	0.040122	0.204784	0.036071	0.036868
LSB5.3B	111		0.055218	0.060045	0.055707	0.060544	0.045948	0.044219	0.031753	0.122878	0.027902	0.036264
LSB5.4B	120		0.038305	0.040212	0.034671	0.040738	0.031564	0.027666	0.021088	0.076512	0.019774	0.025969
LSB5.5B	129		0.057722	0.059822	0.054357	0.061483	0.041794	0.035142	0.029895	0.135613	0.026963	0.039153
LSB5.6B	138		0.037732	0.038087	0.035905	0.042283	0.028476	0.023583	0.013623	0.101897	0.012376	0.023916
LSB5.7B	145		0.036383	0.03539	0.033515	0.039993	0.028305	0.023058	0.01365	0.095962	0.012287	0.027535

LSB6.0B	-24		0.018907	0.01844	0.020044	0.024969	0.016674	0.014133	0.004922	0.074543	0.004291	0.018615
LSB6.1B	-11		0.025966	0.026163	0.025772	0.031653	0.018389	0.020641	0.009033	0.088887	0.007471	0.021322
LSB6.2B	2		0.039156	0.040797	0.039945	0.047264	0.034687	0.028838	0.018466	0.126995	0.016134	0.030275
LSB6.3B	14		0.03247	0.034551	0.033621	0.0391	0.026267	0.024159	0.016239	0.088558	0.013661	0.024842
LSB6.4B	26		0.026721	0.027829	0.025006	0.029084	0.020446	0.018209	0.014705	0.070071	0.013397	0.019326
LSB6.5B	49		0.043086	0.045205	0.042811	0.047618	0.0362	0.036009	0.022952	0.108027	0.020209	0.028217
LSB6.6B	51		0.130964	0.132562	0.129423	0.145549	0.11449	0.107329	0.082013	0.315088	0.075322	0.085517
LSB6.7B	63		0.021522	0.019406	0.021333	0.024653	0.018105	0.017527	0.011054	0.055691	0.010237	0.011535
Bos32.1B	-5		0.476245	0.55452	0.572093	0.665242	0.510391	0.691761	0.572569	1.540616	0.497271	0.495706
Bos32.2B	0		0.613542	0.661945	0.671836	0.763594	0.588885	0.827496	0.784113	1.857803	0.694221	0.645539
Bos32.3B	5		0.600811	0.654203	0.697082	0.774101	0.581748	0.812546	0.688859	1.705824	0.624026	0.574421
Pseud41.1B	-5		0.629717	0.677145	0.696674	0.774275	0.618629	0.80384	0.735694	1.88083	0.672614	0.65849
Pseud41.2B	0		0.408101	0.453028	0.486091	0.521539	0.451578	0.574369	0.52303	1.283413	0.463037	0.426699
Pseud41.3B	5		0.6604	0.686889	0.751867	0.827663	0.621804	0.866514	0.826802	1.951192	0.754803	0.667264

Sample Code:	**Stratigraphic height***		C29baR	C29abR	C28aaS	C29abS	C30baS	C28bbS	C28bbS	C30baR	C28aaR	C30abR
LSB1.0B	5		0.031978	0.009548	0.00399	0.005559	0.024972	0.009278	0.007525	0.014951	0.006876	0.0054
LSB1.1B	13		0.11139	0.026838	0.014492	0.018378	0.086118	0.033899	0.028663	0.037135	0.016368	0.014348
LSB1.2B	22		0.139076	0.03559	0.017877	0.022876	0.106085	0.035915	0.031841	0.042468	0.022042	0.0188
LSB1.3B	29		0.108621	0.034041	0.014323	0.020859	0.084695	0.02816	0.024597	0.042233	0.016413	0.013391
LSB1.4B	37		0.071529	0.017613	0.011561	0.014434	0.054507	0.021107	0.018239	0.022994	0.011885	0.009556
LSB1.5B	46		0.215449	0.069173	0.038911	0.034915	0.174848	0.06999	0.05993	0.079535	0.036311	0.018529
LSB1.6B	55		0.423471	0.142615	0.066931	0.058831	0.354506	0.110242	0.095876	0.16553	0.070264	0.03436
LSB1.7B	62		0.132963	0.030951	0.016486	0.021602	0.098357	0.036984	0.031651	0.044501	0.01958	0.010831
LSB1.8B	69		0.258002	0.067863	0.037942	0.041098	0.211481	0.081346	0.069295	0.09721	0.049394	0.026864
LSB1.9B	78		0.462872	0.11521	0.081656	0.095317	0.399285	0.164901	0.142565	0.132257	0.085834	0.051942
LSB1.10B	86		0.542171	0.152525	0.096274	0.109439	0.468551	0.187457	0.161019	0.194781	0.110269	0.050777
LSB1.11B	94		0.441874	0.109527	0.074392	0.0858	0.389555	0.148681	0.129653	0.148076	0.078668	0.050478
LSB1.12B	102		0.230103	0.068193	0.034201	0.035574	0.174451	0.059435	0.049845	0.077111	0.030444	0.017398
LSB1.13B	110		0.04915	0.011266	0.005996	0.008994	0.039887	0.017126	0.0150 2	0.015806	0.007715	0.005405
LSB1.14B	118		0.087843	0.030589	0.01637	0.01517	0.071827	0.02476	0.021378	0.028231	0.016936	0.011199
LSB3.0B	-22		0.04421	0.014518	0.004738	0.006983	0.033123	0.009323	0.007911	0.013916	0.005916	0.006957

LSB5.0B	84		0.332009	0.090992	0.059796	0.064527	0.279568	0.11721	0.100921	0.125612	0.06221	0.033786
LSB5.1B	93		0.422296	0.128193	0.076112	0.07972	0.348587	0.144549	0.122963	0.131501	0.068792	0.037208
LSB5.2B	102		0.173339	0.039192	0.022616	0.033158	0.13103	0.053274	0.045699	0.049596	0.022641	0.013847
LSB5.3B	111		0.112855	0.02563	0.016822	0.019204	0.091793	0.038569	0.033075	0.029773	0.018034	0.009841
LSB5.4B	120		0.069933	0.015315	0.009839	0.01201	0.055623	0.018707	0.016194	0.018211	0.01026	0.008561
LSB5.5B	129		0.114204	0.02812	0.012625	0.018118	0.08728	0.0311	0.02621	0.033439	0.016316	0.0112
LSB5.6B	138		0.082815	0.019595	0.008254	0.013267	0.062271	0.023361	0.0185	0.023114	0.01094	0.009522
LSB5.7B	145		0.072577	0.02782	0.009217	0.009393	0.054368	0.01899	0.015514	0.026122	0.01263	0.009973
LSB6.0B	-24		0.054	0.013903	0.006399	0.00595	0.039004	0.014198	0.011885	0.019725	0.007947	0.006569
LSB6.1B	-11		0.073211	0.024342	0.008222	0.011706	0.052116	0.017558	0.01503	0.027869	0.010797	0.008482
LSB6.2B	2		0.098907	0.028318	0.010757	0.015673	0.076308	0.028159	0.023645	0.031519	0.012992	0.011306
LSB6.3B	14		0.080767	0.019322	0.009111	0.012613	0.060588	0.021627	0.018378	0.021508	0.01122	0.010141
LSB6.4B	26		0.059752	0.014454	0.007405	0.009496	0.047772	0.016534	0.014141	0.023385	0.008515	0.007792
LSB6.5B	49		0.084179	0.023727	0.011275	0.015798	0.07146	0.025153	0.021666	0.028461	0.014308	0.008448
LSB6.6B	51		0.280145	0.070388	0.045114	0.046739	0.222714	0.089193	0.077419	0.089313	0.044849	0.021831
LSB6.7B	63		0.046295	0.017158	0.007661	0.007408	0.032831	0.012572	0.010928	0.016313	0.007202	0.00434
Bos32.1B	-5		1.207342	0.496311	0.365089	0.257589	1.163756	0.549712	0.509719	0.586373	0.277535	0.069203
Bos32.2B	0		1.488417	0.624006	0.455396	0.319336	1.502813	0.659859	0.623137	0.637443	0.387327	0.077538
Bos32.3B	5		1.546708	0.659666	0.458561	0.332765	1.46757	0.722674	0.656294	0.736895	0.371138	0.080322
Pseud41.1B	-5		1.651515	0.685521	0.483255	0.372672	1.544196	0.644304	0.594132	0.697907	0.431943	0.100519
Pseud41.2B	0		1.040812	0.444858	0.295334	0.215478	0.99219	0.471023	0.417735	0.397675	0.28882	0.053885
Pseud41.3B	5		1.551855	0.691198	0.46162	0.335596	1.577626	0.665842	0.603785	0.767782	0.425571	0.13306

Sample Code:	**Stratigraphic height***		C29aaS	C29bbR	C29bbS	C29aaR	C30aaS	C30bbR	C30bbS	C30aaR
LSB1.0B	5		0.011671	0.011438	0.011509	0.011281	0.001447	0.004734	0.003739	0.002618
LSB1.1B	13		0.032436	0.03991	0.040414	0.03404	0.0068	0.016836	0.019691	0.008547
LSB1.2B	22		0.041945	0.046498	0.044495	0.039582	0.005489	0.021597	0.015276	0.010365
LSB1.3B	29		0.034701	0.035445	0.035302	0.032582	0.005578	0.015872	0.014673	0.009114
LSB1.4B	37		0.019832	0.017388	0.017029	0.019889	0.003251	0.010831	0.010123	0.004563
LSB1.5B	46		0.061124	0.074987	0.073593	0.069031	0.015378	0.031715	0.024207	0.01544
LSB1.6B	55		0.122425	0.156797	0.152285	0.135373	0.028979	0.063777	0.049056	0.032323
LSB1.7B	62		0.029092	0.037667	0.036424	0.03727	0.007004	0.017379	0.015587	0.007403

LSB1.8B	69		0.08282	0.087452	0.08457	0.076199	0.019197	0.039047	0.037804	0.01906
LSB1.9B	78		0.133581	0.178026	0.171467	0.153439	0.032031	0.065814	0.075133	0.034634
LSB1.10B	86		0.156477	0.176221	0.169356	0.18776	0.042563	0.073952	0.096511	0.030094
LSB1.11B	94		0.133912	0.142978	0.14524	0.130677	0.027637	0.068194	0.049899	0.032983
LSB1.12B	102		0.054611	0.070533	0.068089	0.06172	0.013308	0.030178	0.029025	0.012631
LSB1.13B	110		0.012127	0.016251	0.015617	0.012362	0.002899	0.005593	0.004528	0.002224
LSB1.14B	118		0.021902	0.025782	0.025335	0.023866	0.006069	0.009426	0.01201	0.00432
LSB3.0B	-22		0.012426	0.014943	0.014494	0.015137	0.00136	0.006269	0.006402	0.003965
LSB5.0B	84		0.093067	0.103851	0.104253	0.105574	0.022488	0.045641	0.0544	0.023104
LSB5.1B	93		0.116173	0.138636	0.133298	0.115803	0.023556	0.061431	0.053771	0.028411
LSB5.2B	102		0.033411	0.057995	0.05704	0.04239	0.007764	0.022723	0.024317	0.01035
LSB5.3B	111		0.030032	0.039136	0.038003	0.030624	0.006335	0.014541	0.015067	0.006392
LSB5.4B	120		0.014421	0.019166	0.019395	0.016681	0.003177	0.006581	0.006214	0.003592
LSB5.5B	129		0.02201	0.031248	0.031126	0.024936	0.004499	0.010421	0.010091	0.0064
LSB5.6B	138		0.016344	0.023909	0.023583	0.01721	0.003469	0.00901	0.009517	0.004812
LSB5.7B	145		0.019219	0.018966	0.018364	0.01651	0.003102	0.008096	0.008066	0.005017
LSB6.0B	-24		0.014899	0.018611	0.018306	0.017239	0.001973	0.007003	0.008785	0.004837
LSB6.1B	-11		0.019561	0.022783	0.022635	0.022202	0.00357	0.012098	0.010278	0.006507
LSB6.2B	2		0.028563	0.037369	0.037976	0.029054	0.0043	0.016921	0.0201	0.008485
LSB6.3B	14		0.02248	0.02584	0.0261	0.025747	0.002984	0.012385	0.013677	0.006241
LSB6.4B	26		0.021094	0.021473	0.021248	0.019847	0.002849	0.010247	0.011614	0.005272
LSB6.5B	49		0.023007	0.028464	0.028084	0.023026	0.004532	0.011326	0.01382	0.005976
LSB6.6B	51		0.066904	0.104001	0.100351	0.077271	0.015626	0.04047	0.049382	0.02125
LSB6.7B	63		0.0104	0.010818	0.010591	0.011443	0.002772	0.005789	0.006577	0.002526
Bos32.1B	-5		0.511639	0.692865	0.708615	0.577287	0.07942	0.252146	0.329076	0.145864
Bos32.2B	0		0.665206	0.834751	0.870154	0.736233	0.107307	0.289738	0.371613	0.178823
Bos32.3B	5		0.714933	0.860159	0.877061	0.732512	0.105414	0.29994	0.352507	0.161258
Pseud41.1B	-5		0.711102	0.857575	0.857204	0.784948	0.118432	0.333347	0.430283	0.203974
Pseud41.2B	0		0.494678	0.546273	0.541908	0.498401	0.076522	0.209352	0.270881	0.127027
Pseud41.3B	5		0.747897	0.878705	0.888533	0.776611	0.110017	0.321874	0.457784	0.195331

µg/g sediment (aromatics):

Sample Code:	Stratigraphic height*		AI 176	AI 190	AI 204	AI 218	AI 246	AI 260	AI 274	AI 288	Biphenylic iso-reniera tane	Isore nie-ratane	µg/g sum		AI sum
LSB1.0B	5		0.032109	0.020054	0.02099	0.008276	0.008286	0.008269	0.008286	0.003635	0.003398	0.010975	0.12428		0.109906
LSB1.1B	13		0.084097	0.054554	0.055859	0.022909	0.021086	0.021202	0.021086	0.009867	0.009453	0.027459	0.327572		0.29066
LSB1.2B	22		0.114351	0.072403	0.076915	0.030365	0.030996	0.030545	0.030996	0.013586	0.013751	0.058808	0.472716		0.400157
LSB1.3B	29		0.0903	0.055042	0.058293	0.024412	0.024439	0.023605	0.024439	0.009866	0.010227	0.045292	0.365913		0.310395
LSB1.4B	37		0.050892	0.034534	0.038693	0.01767	0.016086	0.016121	0.016086	0.007177	0.006866	0.038745	0.24287		0.197259
LSB1.5B	46		0.080645	0.057553	0.063538	0.029212	0.031626	0.029121	0.031626	0.015421	0.014681	0.05265	0.406073		0.338743
LSB1.6B	55		0.176868	0.115307	0.133164	0.064294	0.060288	0.055897	0.060288	0.029123	0.030403	0.089195	0.814828		0.69523
LSB1.7B	62		0.007578	0.006261	0.008125	0.005183	0.007034	0.00632	0.007034	0.004506	0.004155	0.012044	0.06824		0.05204
LSB1.8B	69		0.127958	0.08801	0.087709	0.04072	0.036759	0.037633	0.036759	0.017616	0.016037	0.051788	0.540987		0.473162
LSB1.9B	78		0.470887	0.308625	0.306258	0.135339	0.113097	0.108858	0.113097	0.052934	0.047521	0.129795	1.78641		1.609094
LSB1.10B	86		0.566763	0.365752	0.367833	0.144985	0.132732	0.13777	0.132732	0.058359	0.055375	0.161031	2.123332		1.906926
LSB1.11B	94		0.418644	0.288412	0.28797	0.130403	0.100123	0.101457	0.100123	0.04176	0.04026	0.106692	1.615845		1.468892
LSB1.12B	102		0.020849	0.014093	0.018318	0.009999	0.016206	0.014277	0.016206	0.00902	0.008237	0.025385	0.15259		0.118969
LSB1.13B	110		0.022519	0.016589	0.021369	0.01052	0.010564	0.009504	0.010564	0.004607	0.004916	0.019851	0.131001		0.106235
LSB1.14B	118		0.065804	0.046454	0.047917	0.021	0.020814	0.019091	0.020814	0.00946	0.009288	0.021117	0.281761		0.251356
LSB3.0B	-22		0.03567	0.022378	0.0201	0.009101	0.005639	0.006415	0.005639	0.001992			0.106934		0.106934
LSB5.0B	84		0.334969	0.207321	0.211933	0.087472	0.080955	0.08372	0.080955	0.035914	0.031983	0.08408	1.239303		1.12324
LSB5.1B	93		0.284897	0.178897	0.182361	0.075379	0.072514	0.069553	0.072514	0.032933	0.027773	0.077561	1.074381		0.969047
LSB5.2B	102		0.028969	0.019653	0.024609	0.011808	0.015634	0.013803	0.015634	0.00755	0.007321	0.020713	0.165696		0.137662
LSB5.3B	111		0.058436	0.0415	0.045995	0.022058	0.022114	0.021481	0.022114	0.010818	0.01043	0.038959	0.293907		0.244518
LSB5.4B	120		0.05392	0.039623	0.047211	0.019227	0.017814	0.016299	0.017814	0.0075	0.007445	0.027195	0.254048		0.219408
LSB5.5B	129		0.09699	0.06992	0.079801	0.034778	0.030629	0.030719	0.030629	0.013846	0.012732	0.032423	0.432466		0.387312
LSB5.6B	138		0.062391	0.040833	0.044424	0.019862	0.017799	0.017109	0.017799	0.007769	0.007485	0.019897	0.255369		0.227987
LSB5.7B	145		0.067495	0.044644	0.047733	0.017891	0.01726	0.015888	0.01726	0.008031	0.006621	0.011824	0.254648		0.236202
LSB6.0B	-24		0.045015	0.02874	0.029336	0.013568	0.010764	0.010685	0.010764	0.004484			0.153356		0.153356
LSB6.1B	-11		0.047628	0.03199	0.032161	0.015151	0.012403	0.012545	0.012403	0.005426			0.169708		0.169708
LSB6.2B	2		0.081501	0.053486	0.053828	0.023033	0.021611	0.021134	0.021611	0.009605	0.009143	0.068052	0.363005		0.28581
LSB6.3B	14		0.098516	0.065335	0.068268	0.027635	0.027109	0.025116	0.027109	0.012015	0.011278	0.059871	0.422252		0.351103
LSB6.4B	26		0.051597	0.033651	0.035353	0.015124	0.014653	0.01401	0.014653	0.006327	0.00628	0.043363	0.235011		0.185368

LSB6.5B	49		0.056077	0.035189	0.04042	0.017765	0.017263	0.016543	0.017263	0.008591	0.007391	0.02848	0.24498		0.20911
LSB6.6B	51		0.16822	0.114592	0.117626	0.051515	0.050132	0.047866	0.050132	0.023288	0.021876	0.070431	0.715678		0.623371
LSB6.7B	63		0.005647	0.004368	0.005522	0.003341	0.003563	0.003228	0.003563	0.001858	0.00167	0.006255	0.039015		0.03109
Bos32.1B	-5		0.715105	0.496079	0.228624	0.264801	0.212066	0.196679	0.212066	0.104189	0.094032	0.243211	2.76804		2.430797
Bos32.2B	0		0.925577	0.627703	0.306015	0.281313	0.277444	0.264793	0.277444	0.12789	0.123616	0.312056	3.523178		3.087505
Bos32.3B	5		1.101549	0.751224	0.355568	0.299122	0.298512	0.287836	0.298512	0.142086	0.125783	0.310563	3.970756		3.534441
Pseud41.1B	-5		0.919258	0.644883	0.306241	0.299609	0.260545	0.257504	0.260545	0.148198	0.135361	0.28344	3.515582		3.096781
Pseud41.2B	0		0.780357	0.535795	0.267623	0.238465	0.255549	0.241996	0.255549	0.12514	0.118786	0.325346	3.144606		2.700474
Pseud41.3B	5		1.01584	0.702446	0.348091	0.361876	0.304526	0.293759	0.304526	0.16207	0.152601	0.548491	4.194224		3.493133

Sample Code:	**Stratigraphic height***		Phen-anthrene	3-Methyl-Phen-anthrene	2-Methyl-Phen-anthrene	9-Methyl-Phen-anthrene	1-Methyl-Phen-anthrene	sum MP	Retene	Diben-zo-thiophene	4-Methyl-Diben-zo-thiophene	2+3-Methyl-Diben-zo-thiophene	1-Methyl-Diben-zo-thiophene	Sum MDBT
LSB1.0B	5		0.690084	0.207729	0.218998	0.318663	0.274496	1.019886	0.066637	0.039774	0.024933	0.035211	0.014887	0.07503
LSB1.1B	13		1.247261	0.374762	0.399792	0.582125	0.498174	1.854853	0.117861	0.071503	0.047029	0.0583	0.026836	0.132165
LSB1.2B	22		1.891678	0.580595	0.603918	0.884668	0.76667	2.835851	0.182991	0.105889	0.067387	0.09362	0.043046	0.204053
LSB1.3B	29		1.487434	0.451027	0.463581	0.685084	0.588593	2.188285	0.142495	0.08418	0.055666	0.069485	0.032859	0.15801
LSB1.4B	37		0.734281	0.232237	0.245582	0.349667	0.303164	1.130652	0.08102	0.044692	0.02968	0.039989	0.017989	0.087658
LSB1.5B	46		1.632607	0.515302	0.538564	0.78362	0.682847	2.520333	0.191929	0.103734	0.064321	0.09474	0.040825	0.199885
LSB1.6B	55		2.125774	0.655808	0.690447	1.025877	0.888816	3.260948	0.244256	0.14091	0.086631	0.126862	0.056753	0.270245
LSB1.7B	62		0.21455	0.057747	0.061328	0.093954	0.081069	0.294098	0.022964	0.007307	0.005621	0.007488	0.003596	0.016705
LSB1.8B	69		1.933182	0.580092	0.610288	0.898906	0.773842	2.863128	0.224629	0.128677	0.081802	0.122509	0.050916	0.255226
LSB1.9B	78		6.747893	2.05174	2.126482	3.137269	2.679151	9.994642	0.736965	0.4491	0.267253	0.422793	0.177348	0.867394
LSB1.10B	86		8.203121	2.522474	2.624033	3.801174	3.308869	12.25655	0.843771	0.584641	0.334092	0.540804	0.218594	1.09349
LSB1.11B	94		8.069586	2.521797	2.594116	3.760882	3.286601	12.16 34	0.936508	0.560387	0.332036	0.516287	0.214543	1.062866
LSB1.12B	102		0.491103	0.137579	0.148666	0.219256	0.187504	0.693004	0.054926	0.027028	0.017122	0.022383	0.010168	0.049673
LSB1.13B	110		0.708329	0.215723	0.229084	0.344946	0.295327	1.085 08	0.086849	0.039765	0.025217	0.032113	0.015172	0.072502
LSB1.14B	118		0.802914	0.247951	0.25535	0.387368	0.328527	1.219196	0.084101	0.046942	0.028622	0.036073	0.017869	0.082563
LSB3.0B	-22		0.576229	0.168597	0.174832	0.257866	0.22458	0.825876	0.046453	0.02923	0.018929	0.027807	0.011002	0.057738
LSB5.0B	84		4.299716	1.260349	1.341345	1.959434	1.672041	6.233168	0.427566	0.290551	0.176813	0.283543	0.112441	0.572797
LSB5.1B	93		4.400821	1.340606	1.38142	2.025529	1.772368	6.519923	0.455014	0.291664	0.177882	0.265695	0.107502	0.551078
LSB5.2B	102		0.494965	0.146912	0.156591	0.229464	0.199513	0.732479	0.058285	0.028407	0.018886	0.026119	0.011573	0.056578
LSB5.3B	111		0.872023	0.27111	0.284494	0.410421	0.356827	1.322852	0.09503	0.052652	0.035288	0.048591	0.022193	0.106072

LSB5.4B	120		0.891056	0.271542	0.285819	0.413641	0.356702	1.327705	0.093111	0.056773	0.036368	0.048305	0.02208	0.106753
LSB5.5B	129		1.544681	0.473421	0.49388	0.719682	0.621625	2.308608	0.161276	0.104166	0.063475	0.091975	0.039335	0.194784
LSB5.6B	138		0.997371	0.307617	0.324295	0.470767	0.410541	1.51322	0.107672	0.063799	0.039641	0.055566	0.025633	0.120841
LSB5.7B	145		1.005383	0.297514	0.311859	0.464683	0.400757	1.474812	0.096032	0.060559	0.035524	0.055341	0.023113	0.113978
LSB6.0B	-24		0.760633	0.219478	0.240019	0.347643	0.29518	1.102321	0.064171	0.038871	0.023984	0.037164	0.014609	0.075758
LSB6.1B	-11		0.804708	0.235107	0.252471	0.360799	0.315681	1.164059	0.069696	0.042303	0.026577	0.037591	0.01535	0.079519
LSB6.2B	2		0.888614	0.262173	0.275841	0.404671	0.351523	1.294208	0.072803	0.047838	0.031641	0.04159	0.018445	0.091675
LSB6.3B	14		1.110845	0.327299	0.345202	0.500854	0.440131	1.613486	0.104418	0.059928	0.037492	0.054683	0.023092	0.115267
LSB6.4B	26		0.805969	0.234802	0.241685	0.355062	0.301675	1.133224	0.074353	0.042597	0.026701	0.041669	0.016599	0.084969
LSB6.5B	49		0.935429	0.277555	0.287816	0.421836	0.364827	1.352035	0.092276	0.057301	0.033843	0.048789	0.020732	0.103364
LSB6.6B	51		2.182516	0.674387	0.702403	1.034481	0.882118	3.29339	0.227389	0.142365	0.089112	0.132374	0.057626	0.279113
LSB6.7B	63		0.1274	0.035264	0.038632	0.057025	0.04959	0.180511	0.016003	0.004663	0.003633	0.004422	0.00191	0.009965
Bos32.1B	-5		3.964619	1.482368	1.554829	2.709886	2.517259	8.264343	0.52165	0.16115	0.696515	0.201602	0.176354	1.07447
Bos32.2B	0		5.341357	1.933063	2.077062	3.573069	3.328144	10.91134	0.696167	0.218677	0.935641	0.242792	0.230624	1.409057
Bos32.3B	5		7.66932	2.813019	2.974059	5.11144	4.741018	15.63954	1.004554	0.341171	1.422172	0.422318	0.365349	2.209839
Pseud41.1B	-5		4.271695	1.587761	1.674528	2.931764	2.690068	8.884121	0.636881	0.18947	0.832244	0.245737	0.210401	1.288381
Pseud41.2B	0		4.671206	1.772241	1.806221	3.19054	2.936969	9.705972	0.680623	0.211929	0.884551	0.24876	0.220665	1.353975
Pseud41.3B	5		5.61757	2.164858	2.179834	3.757427	3.471961	11.57408	0.827946	0.258803	1.093029	0.326549	0.280789	1.700367

µg/gTOC (alkanes and branched isoprenoids):

Sample Code:	**Stratigraphic height***		nor-pristane (TIC)	nC17 (TIC)	Pristane (TIC)	nC18 (TIC)	Phytane (TIC)		nC12 (m/z=85)	C13	C14
LSB1.0B	5		70.99034	129.6818	184.7535	104.3025	58.6787	0	91.55982	111.019	126.6363
LSB1.1B	13		100.3274	161.5688	259.7118	132.2938	92.19423	0	120.5143	163.2782	166.9553
LSB1.2B	22		201.9639	317.6807	491.4884	271.0516	199.9796	0	248.6877	269.4043	305.8036
LSB1.3B	29		131.0504	177.4531	318.7526	154.3611	124.5614	0	115.5215	152.6985	176.6523
LSB1.4B	37		188.1033	285.4955	515.523	240.179	219.9203	0	130.1257	203.6521	241.5524
LSB1.5B	46		241.9627	284.9147	604.5527	271.6821	286.8038	0	125.9002	212.597	274.4047
LSB1.6B	55		167.7166	231.9067	463.3401	187.1838	196.7273	0	168.9828	204.4665	214.2133
LSB1.7B	62		558.3655	711.9417	1699.217	680.6539	769.9704	0	55.07977	172.4884	299.187
LSB1.8B	69		80.59402	104.5694	207.8041	89.02615	83.89324	0	100.5699	112.9391	115.3256
LSB1.9B	78		178.6449	235.2646	404.7258	196.9813	168.2892	0	236.707	262.4975	273.9651

LSB1.10B	86		185.614	292.7538	513.7373	236.272	193.01	0	271.1155	307.1604	317.0424
LSB1.11B	94		155.2825	237.1027	393.4106	191.5951	161.6156	0	187.4696	212.2707	227.1389
LSB1.12B	102		117.2576	155.3042	376.1915	130.3708	161.6833	0	29.76376	62.89924	113.9513
LSB1.13B	110		177.2536	215.0434	433.1485	170.7765	182.197	0	63.10616	138.0525	165.048
LSB1.14B	118		247.1471	303.1697	692.1761	279.401	287.2381	0	105.0351	311.491	417.3354
LSB3.0B	-22		64.45717	190.2815	149.8977	185.3071	48.67136	0	100.9556	157.9663	167.4523
LSB5.0B	84		109.7924	197.4948	308.6347	148.2342	121.8596	0	130.5765	169.0868	193.2193
LSB5.1B	93		155.6062	207.4902	473.7823	175.9672	145.8763	0	208.452	234.8047	245.293
LSB5.2B	102		114.6091	162.7127	376.5817	149.4704	157.0103	0	56.62268	100.5729	164.9746
LSB5.3B	111		103.7908	139.7754	267.3694	116.3925	108.7267	0	77.48887	114.323	131.4025
LSB5.4B	120		189.9831	242.5119	476.8237	202.6535	184.2592	0	120.6233	180.895	239.4932
LSB5.5B	129		192.9981	252.5986	523.6493	205.6665	204.1666	0	203.3616	282.9704	336.3057
LSB5.6B	138		230.8878	287.9007	596.0296	249.1997	228.7263	0	116.37	201.4234	278.5304
LSB5.7B	145		212.509	289.5624	577.3154	247.9952	207.7972	0	122.4804	206.3572	259.8968
LSB6.0B	-24		125.2186	265.9189	293.7023	227.7886	89.19103	0	179.3763	231.0319	237.2054
LSB6.1B	-11		183.4666	290.8281	410.5342	240.3719	143.4135	0	155.3515	228.5093	257.7414
LSB6.2B	2		221.856	290.6481	483.7408	241.5482	167.8658	0	209.7795	272.4808	304.3113
LSB6.3B	14		125.4082	204.1866	354.4389	169.1023	124.5012	0	118.3827	185.6283	204.6224
LSB6.4B	26		85.00439	146.7487	254.9398	120.8635	99.2974	0	80.6208	102.5731	128.5002
LSB6.5B	49		63.07994	96.81897	179.8149	76.41963	75.0924	0	66.93684	74.34196	85.61509
LSB6.6B	51		270.4572	357.2928	645.4039	306.6284	357.301	0	308.0516	394.7027	449.1434
LSB6.7B	63		160.0034	256.768	565.9038	243.7108	356.1382	0	22.69061	68.25706	153.7798
Bos32.1B	-5		222.5903	359.6491	455.4361	303.8801	346.1189	0	185.9503	250.387	299.9744
Bos32.2B	0		278.724	468.2823	532.8495	379.1474	433.3357	0	226.737	293.4178	332.521
Bos32.3B	5		244.2516	485.1854	535.1554	396.982	425.0286	0	263.0106	317.542	365.425
Pseud41.1B	-5		514.1601	800.1652	968.3633	752.9838	761.4841	0	654.6463	622.2979	747.262
Pseud41.2B	0		214.1282	469.1872	589.8043	472.4384	491.704	0	470.4613	614.5408	450.0777
Pseud41.3B	5		398.2162	692.9839	799.5274	602.1042	722.387	0	531.228	538.9903	621.4751

Sample Code:	**Stratigraphic height***		C15	C16	C17	C18	C19	C20	C21	C22	C23
LSB1.0B	5		137.5868	125.6671	123.8269	107.8886	108.1351	104.7447	103.487	106.5275	111.8878
LSB1.1B	13		175.1309	163.8703	163.1555	137.0497	133.0342	146.5874	148.4197	135.7611	137.4879

LSB1.2B	22		342.3028	319.3326	315.4661	256.3842	249.6591	238.3164	222.1265	213.7816	224.9963
LSB1.3B	29		192.6335	175.7061	178.0698	142.1399	129.0947	123.9704	115.9908	106.8896	109.4319
LSB1.4B	37		300.7953	285.2251	285.6821	226.4746	216.8122	196.1475	189.3052	174.2329	175.6602
LSB1.5B	46		318.2092	303.1465	295.1658	259.0334	250.2962	232.7649	209.35	193.5156	193.2279
LSB1.6B	55		245.2362	233.617	223.1609	183.5339	178.6598	163.756	147.0165	134.1332	131.1629
LSB1.7B	62		504.3928	581.4993	696.8937	628.035	659.6046	626.1217	592.8183	587.469	586.7222
LSB1.8B	69		123.193	106.3544	107.339	85.69964	82.27139	75.06901	65.38404	60.592	58.48317
LSB1.9B	78		285.4401	250.6503	252.9044	192.1256	180.4298	160.7781	141.4933	127.3833	121.7935
LSB1.10B	86		344.2749	305.8268	303.0457	234.2005	218.0134	195.6657	172.395	154.5576	127.483
LSB1.11B	94		257.7647	221.4229	225.1434	173.4153	166.2482	139.4188	122.5549	108.5231	107.0155
LSB1.12B	102		136.6621	142.7787	153.5487	142.5461	149.8961	139.8092	132.9896	126.6285	134.9573
LSB1.13B	110		215.5435	205.5012	195.9335	166.2827	151.0427	142.0789	123.8392	122.2651	116.5087
LSB1.14B	118		339.8769	323.5624	300.1461	260.4833	250.5969	225.7949	201.0933	185.6565	189.0458
LSB3.0B	-22		184.7328	180.6852	192.1327	183.3936	194.3796	183.1487	192.0573	187.7316	204.6494
LSB5.0B	84		222.4442	196.8041	194.4849	154.5948	187.7163	148.8325	109.3819	98.17473	95.93234
LSB5.1B	93		259.5583	252.6408	215.0144	174.9316	186.2688	153.9021	131.1891	128.5826	125.4323
LSB5.2B	102		156.0545	168.5947	167.0243	144.5223	139.6153	132.7072	123.9934	114.013	110.8914
LSB5.3B	111		152.1126	142.5995	145.5159	117.8431	111.4567	103.6149	93.3408	86.33979	87.57706
LSB5.4B	120		342.8036	280.5873	265.8028	200.3643	186.5001	164.121	146.6716	135.7217	133.2819
LSB5.5B	129		424.8229	285.5967	269.292	210.5332	210.3691	180.8968	163.4216	154.311	149.7888
LSB5.6B	138		339.2781	322.9318	321.3989	253.4537	236.7597	218.282	258.8918	175.5955	181.7755
LSB5.7B	145		334.5515	309.8503	296.9892	244.0039	228.6354	190.8054	197.5365	182.1988	186.4949
LSB6.0B	-24		269.3642	255.2955	261.9362	226.255	240.7423	250.7667	259.8312	257.9106	269.0331
LSB6.1B	-11		359.4233	298.5679	279.5249	228.9209	232.208	209.8262	213.6465	217.5849	237.4575
LSB6.2B	2		322.6641	297.16	289.9434	238.6473	227.6384	218.0686	205.5797	195.6332	199.372
LSB6.3B	14		223.5681	203.9872	190.6372	161.5154	154.2998	141.3584	133.6605	123.5823	126.8761
LSB6.4B	26		126.7816	152.1063	149.7712	111.2502	87.91776	83.093	85.9108	77.22633	79.14376
LSB6.5B	49		102.5564	93.47697	91.58767	73.84112	74.00093	64.88779	70.70579	73.37767	65.48089
LSB6.6B	51		408.2192	352.2773	360.6386	290.8369	287.5874	297.8416	209.1129	194.8933	190.1383
LSB6.7B	63		232.4684	196.4192	246.3888	248.9097	333.5852	286.1442	213.1215	202.9871	200.9607
Bos32.1B	-5		356.1974	361.5108	364.6336	298.6616	264.1442	249.4676	205.4224	179.2399	167.4249
Bos32.2B	0		528.072	466.2011	461.4962	348.794	327.1531	285.0772	241.0347	240.0041	206.9191
Bos32.3B	5		435.097	432.6302	438.2516	348.2947	295.7717	280.7723	242.3737	213.3869	196.4595
Pseud41.1B	-5		823.574	815.7601	790.3481	615.3064	593.9676	533.8418	457.8845	396.088	388.1535

Pseud41.2B	0		527.1364	466.9021	473.7409	388.2021	324.0173	310.4366	266.4472	278.0547	328.5258
Pseud41.3B	5		713.4431	713.0763	696.6015	587.0372	507.6527	587.1646	407.6589	321.0879	304.3221

Sample Code:	**Stratigraphic height***		C24	C25	C26	C27	C28	C29	C30	C31	C32	C33	C34
LSB1.0B	5		105.1216	113.6611	93.69376	100.8864	72.13904	76.80276	50.73587	51.20057	32.49383	43.11181	22.10331
LSB1.1B	13		122.0377	128.9793	109.2163	108.9716	78.86914	81.25222	56.13405	49.14387	29.37085	35.04826	23.62997
LSB1.2B	22		216.3599	227.0056	169.2002	193.2276	136.6795	145.0511	90.60844	94.28519	55.90382	70.39009	39.98808
LSB1.3B	29		97.78549	102.22	85.17916	88.14435	62.79809	66.23054	41.83488	41.01667	23.74214	30.42197	18.86431
LSB1.4B	37		164.9673	173.9721	136.1717	144.0354	105.9461	107.138	71.11614	64.67134	43.32091	47.87661	28.24456
LSB1.5B	46		186.1975	196.5995	173.9536	153.5725	117.8012	115.4937	81.3004	73.30655	39.82114	45.86819	39.13942
LSB1.6B	55		126.7106	125.2247	106.7785	101.3459	73.83447	55.64762	30.20909	27.14724	13.62847	15.33227	12.72375
LSB1.7B	62		604.3859	655.5095	580.4094	563.2405	444.7471	469.0891	349.8881	319.9836	184.8485	221.0283	183.5177
LSB1.8B	69		56.86919	58.13982	48.69207	45.19058	35.87511	35.07914	23.40695	21.59147	12.40089	14.21641	10.52518
LSB1.9B	78		110.8685	106.8575	89.59694	81.62013	59.78323	57.13693	37.36796	32.90906	18.02676	17.88418	11.3707
LSB1.10B	86		133.6103	132.4251	109.5472	101.0096	74.06716	69.81959	47.68048	40.8101	20.84267	20.99965	15.849
LSB1.11B	94		91.37758	94.20728	74.68854	67.74538	51.29468	47.14114	28.03665	25.77385	14.80777	14.45597	9.305893
LSB1.12B	102		134.3341	152.6975	135.1613	141.5577	119.7588	122.0306	89.31493	88.86107	55.40119	68.78545	57.16988
LSB1.13B	110		113.7231	115.6067	101.8048	91.28273	71.11757	72.60469	49.53342	44.42447	24.2099	30.32051	23.42226
LSB1.14B	118		180.8832	188.5623	158.0963	154.4864	109.3304	113.4906	72.82402	66.40325	32.05902	32.04306	16.72411
LSB3.0B	-22		180.1713	198.7376	151.2134	174.4427	119.8104	125.2598	86.68253	80.71368	49.59547	65.47801	26.29576
LSB5.0B	84		81.90081	83.68791	68.99487	63.33517	47.72316	46.81035	29.62165	23.65574	14.20417	14.10416	8.602065
LSB5.1B	93		106.2677	97.13056	83.26647	72.78415	55.47621	50.19438	34.95863	29.47806	15.57979	17.99749	12.76635
LSB5.2B	102		115.9654	115.3651	108.484	102.5869	82.09626	84.90456	61.11285	59.11667	36.24551	47.71106	37.10231
LSB5.3B	111		81.01985	82.61679	71.26262	69.15119	52.58309	54.24835	38.51738	34.33738	22.17156	23.52694	15.02827
LSB5.4B	120		120.6104	127.4338	106.8823	105.2498	80.26917	81.75826	58.51457	55.2683	31.87255	36.28977	22.2149
LSB5.5B	129		141.9511	145.1035	125.3106	122.2806	93.76186	98.92218	64.83284	60.50954	35.39313	40.46363	24.89504
LSB5.6B	138		175.7666	175.7824	155.3963	153.6423	113.3894	118.8357	83.06586	72.81623	40.04496	53.03986	29.40103
LSB5.7B	145		193.7701	190.9095	160.9481	168.8275	124.1858	131.0907	85.89662	78.82904	40.20486	56.70336	27.45686
LSB6.0B	-24		238.4673	270.6764	201.6018	225.9201	147.2254	162.4469	104.5279	98.76009	61.74613	75.27661	39.78362
LSB6.1B	-11		236.1003	257.7894	196.7611	220.2728	144.5078	163.3665	104.7608	108.7989	60.90887	80.99863	35.63243
LSB6.2B	2		189.6374	207.4246	161.4797	173.2807	119.6819	125.9759	83.53632	79.15537	45.52425	58.4318	33.16759
LSB6.3B	14		123.2978	127.1559	106.3202	111.2163	77.41465	83.99947	56.08229	55.56442	33.31162	42.15162	25.83736

LSB6.4B	26		67.39511	70.27151	58.15521	57.90492	41.67215	43.82002	29.04932	27.79498	15.47071	19.78952	13.40121
LSB6.5B	49		68.48051	63.3819	50.58324	44.56358	33.39009	33.3269	22.42587	20.23357	11.39599	14.48595	10.74412
LSB6.6B	51		176.4016	176.3406	151.7668	138.7403	103.6717	101.4905	67.49064	57.32317	32.95915	37.73267	25.72556
LSB6.7B	63		191.5167	200.1002	169.7754	160.7634	128.4112	127.006	92.78757	82.00112	51.99115	62.13063	51.95738
Bos32.1B	-5		154.4169	146.0105	133.5684	93.97828	82.84389	77.27843	73.82903	75.68776	58.15499	48.03269	35.06201
Bos32.2B	0		192.3315	166.623	154.6445	114.5331	93.85297	92.8247	76.57089	78.38392	62.4052	48.14954	42.86898
Bos32.3B	5		178.1593	166.562	144.2071	104.634	78.42297	79.37046	65.24235	63.83927	40.85374	36.76352	30.67747
Pseud41.1B	-5		348.5848	309.6786	277.1374	209.0337	184.4212	186.3852	160.9232	163.1897	119.9768	105.1342	86.04616
Pseud41.2B	0		279.5663	268.834	236.1	173.3925	155.2834	156.7139	129.296	132.1062	102.2047	84.75479	70.77709
Pseud41.3B	5		289.2454	271.9096	232.7304	180.4806	145.8101	151.1776	132.8145	139.3997	106.5003	86.39462	56.86669

Sample Code:	**Stratigraphic height***		C35	C36	C37	C38	C39	C40	sum n-alkanes
LSB1.0B	5		19.57332	7.065214	5.507391	3.255411	3.038824	2.965064	2162.322
LSB1.1B	13		16.5304	6.030302	5.967541	2.463611	4.388398	3.745014	2653.023
LSB1.2B	22		37.26941	11.54824	13.06626	6.326297	6.195793	5.809577	4725.176
LSB1.3B	29		16.5742	5.708448	5.441534	3.924185	2.484648	1.636032	2412.806
LSB1.4B	37		26.3002	9.42547	6.53154	5.598675	4.24521	4.057203	3769.284
LSB1.5B	46		31.5561	11.80934	9.545444	6.523195	4.623727	2.759185	4157.482
LSB1.6B	55		9.061026	3.946954	2.041574	0	0	0	2931.571
LSB1.7B	62		170.9409	50.06572	55.51252	45.47156	33.08266	20.35242	10942.39
LSB1.8B	69		9.596992	3.588775	2.816164	1.905851	2.18469	2.398595	1477.698
LSB1.9B	78		9.664853	4.38518	3.089865	1.774625	0.856868	0.80398	3130.165
LSB1.10B	86		12.95493	4.891194	4.573628	3.422028	2.43627	1.215409	3746.935
LSB1.11B	94		7.474074	1.8556	0.851337	0	0	0	2677.402
LSB1.12B	102		43.67661	19.14639	15.61831	13.74887	12.67104	11.00517	2747.369
LSB1.13B	110		19.1402	5.105169	3.586336	2.965388	2.3494	2.687353	2579.086
LSB1.14B	118		14.83539	5.256211	0	0	0	0	4255.112
LSB3.0B	-22		23.805	8.460866	7.321785	4.497964	3.548546	3.200771	3438.521
LSB5.0B	84		6.452753	2.471136	1.839777	1.098118	0.780144	0	2396.53
LSB5.1B	93		8.816444	4.342894	2.858147	2.270557	1.657396	1.146645	2913.062
LSB5.2B	102		33.41325	10.76816	12.85129	9.621368	8.126538	7.3249	2512.383
LSB5.3B	111		14.11504	5.168343	4.222923	3.006257	2.156664	2.088299	1938.836
LSB5.4B	120		17.59018	7.256424	6.198562	4.273299	3.311746	1.830898	3263.691
LSB5.5B	129		21.06968	7.987945	5.98083	3.608451	0	0	3863.741
LSB5.6B	138		23.82275	9.033858	8.640307	6.163352	0	0	4123.531
LSB5.7B	145		21.3891	9.442866	4.626912	0	3.04145	2.221241	4059.344
LSB6.0B	-24		32.90105	10.86886	8.712346	6.765889	4.288167	3.649156	4632.366
LSB6.1B	-11		33.6754	9.996008	8.880778	5.660282	4.361441	3.320325	4594.554
LSB6.2B	2		31.27475	10.30399	6.661195	5.347219	4.237619	3.3769	4319.776

LSB6.3B	14		21.10667	5.710169	4.652411	3.532582	3.389969	2.285805	2851.148
LSB6.4B	26		12.43859	3.414416	3.388999	1.818387	1.263034	1.210368	1733.154
LSB6.5B	49		8.369598	3.339039	3.033947	1.601739	1.138859	1.18344	1328.487
LSB6.6B	51		22.58234	6.460858	4.772989	2.760165	2.7043	2.688507	4855.055
LSB6.7B	63		43.00411	16.47965	14.38451	6.467071	4.159939	5.153515	3813.802
Bos32.1B	-5		32.77243	17.46037	10.43819	5.3601	4.478445	4.720022	4237.106
Bos32.2B	0		42.36177	15.3308	11.07577	5.574794	4.62167	2.721707	5162.302
Bos32.3B	5		25.51068	11.67037	6.848543	2.849924	3.438613	0	4868.065
Pseud41.1B	-5		73.13306	39.51278	29.96897	23.89995	0	10.49706	9766.653
Pseud41.2B	0		56.03146	30.02133	18.39882	0	0	0	6792.023
Pseud41.3B	5		52.37742	21.004	16.69668	16.60774	0	0	8429.753

Sample Code:	**Stratigraphic height***		2*C29/(C28+C30)	(C15+`17+`19)/(C27+`29+`31)		Pr/17	Phy/18	Pr/Phy	Pr/(Pr+Phy)		TAR
LSB1.0B	5		1.250097	1.614528		1.424668	0.562582	3.148562	0.758953		0.619376
LSB1.1B	13		1.203708	1.969023		1.607437	0.69689	2.817007	0.738015		0.507866
LSB1.2B	22		1.276364	2.097789		1.547115	0.737792	2.457693	0.71079		0.476692
LSB1.3B	29		1.265959	2.55793		1.796264	0.806948	2.558999	0.719022		0.390941
LSB1.4B	37		1.210174	2.543305		1.805714	0.915652	2.344136	0.700969		0.393189
LSB1.5B	46		1.160148	2.522606		2.121872	1.05566	2.107896	0.678239		0.396415
LSB1.6B	55		1.069699	3.513926		1.997959	1.050985	2.355241	0.701959		0.284582
LSB1.7B	62		1.18064	1.37608		2.386736	1.131222	2.20686	0.688169		0.726702
LSB1.8B	69		1.183466	3.070879		1.987237	0.942344	2.477007	0.712396		0.32564
LSB1.9B	78		1.176248	4.187048		1.7203	0.854341	2.404942	0.706309		0.238832
LSB1.10B	86		1.146956	4.088721		1.754844	0.816898	2.661713	0.726904		0.244575
LSB1.11B	94		1.188462	4.615062		1.659242	0.843527	2.434236	0.708814		0.216682
LSB1.12B	102		1.167345	1.248709		2.422288	1.240181	2.326718	0.699403		0.800827
LSB1.13B	110		1.203549	2.700372		2.014238	1.066874	2.377364	0.703911		0.370319
LSB1.14B	118		1.246092	2.663495		2.283131	1.02805	2.409764	0.706725		0.375447
LSB3.0B	-22		1.213212	1.501632		0.787768	0.262652	3.079793	0.75489		0.665942
LSB5.0B	84		1.210433	4.518981		1.562748	0.822075	2.532706	0.716931		0.221289
LSB5.1B	93		1.110067	4.334621		2.283396	0.828997	3.247836	0.764586		0.230701
LSB5.2B	102		1.185742	1.876232		2.314397	1.050444	2.398453	0.705748		0.532983
LSB5.3B	111		1.190957	2.593465		1.91285	0.934138	2.459097	0.710907		0.385585
LSB5.4B	120		1.178211	3.281817		1.966187	0.909233	2.587787	0.721277		0.304709

LSB5.5B	129		1.247484	3.210665		2.073049	0.992707	2.564814	0.71948		0.311462
LSB5.6B	138		1.209799	2.599049		2.070261	0.917843	2.605864	0.722674		0.384756
LSB5.7B	145		1.247993	2.271109		1.993751	0.837908	2.778264	0.735328		0.440314
LSB6.0B	-24		1.290525	1.58489		1.104481	0.391552	3.292958	0.76706		0.630959
LSB6.1B	-11		1.310767	1.769067		1.411604	0.596632	2.862591	0.741106		0.56527
LSB6.2B	2		1.23981	2.220453		1.664352	0.694958	2.881712	0.742382		0.450359
LSB6.3B	14		1.258448	2.266946		1.735858	0.736248	2.846872	0.740049		0.441122
LSB6.4B	26		1.239228	2.814012		1.737255	0.821567	2.567437	0.719687		0.355365
LSB6.5B	49		1.194171	2.732715		1.857228	0.982632	2.394582	0.705413		0.365936
LSB6.6B	51		1.185898	3.550432		1.806373	1.165257	1.806331	0.643663		0.281656
LSB6.7B	63		1.148343	2.197153		2.20395	1.461315	1.589	0.613751		0.455134
Bos32.1B	-5		0.986494	3.988651		1.266335	1.138998	1.315837	0.568191		0.250711
Bos32.2B	0		1.089339	4.608082		1.137881	1.142921	1.229646	0.551498		0.21701
Bos32.3B	5		1.104936	4.717168		1.102991	1.07065	1.259104	0.557347		0.211992
Pseud41.1B	-5		1.079416	3.952481		1.210204	1.011289	1.271679	0.559797		0.253006
Pseud41.2B	0		1.101372	2.866418		1.257077	1.040779	1.199511	0.545353		0.348867
Pseud41.3B	5		1.085171	4.071043		1.153746	1.199771	1.106785	0.525343		0.245637

µg/gTOC (hopanes and steranes):

Sample Code:	**Stratigraphic height***		SUM Hopanes		C19/3	C20/3	C21/3	C22/3	C23/3	C24/3	C25/3 S	C25/3 R	C24/4
LSB1.0B	5		127.0059	0	0.984058	0.864153	0.858063	0.124494	0.825933	0.462835	0.154387	0.268069	2.066827
LSB1.1B	13		202.3541	0	1.819653	1.648527	1.628109	0.350927	1.718813	0.974 36	0.457 05	0.369451	3.593072
LSB1.2B	22		357.9255	0	2.797178	2.419664	2.397965	0.393824	2.356382	1.278902	0.609671	0.384429	5.306196
LSB1.3B	29		180.0131	0	1.495633	1.330 98	1.352692	0.274277	1.421724	0.817567	0.372717	0.292 24	2.771469
LSB1.4B	37		293.7775	0	2.628922	2.210306	2.284 42	0.356387	2.475627	1.477345	0.622691	0.633441	4.377488
LSB1.5B	46		362.4697	0	3.213479	2.554682	2.665313	0.442173	2.826629	1.796392	1.039012	0.716635	4.384 65
LSB1.6B	55		244.4891	0	1.986977	1.721997	1.713986	0.305683	2.002333	1.342152	0.753032	0.530401	3.064236
LSB1.7B	62		1458.137	0	7.812 22	7.837388	8.693812	2.027493	10.69865	6.915739	4.020968	3.004 16	14.17969
LSB1.8B	69		126.4167	0	0.988395	0.858378	0.881867	0.115625	0.895414	0.597328	0.285875	0.247507	1.394686
LSB1.9B	78		164.2684	0	2.075751	1.613903	1.610322	0.256026	1.582327	1.029103	0.536852	0.354173	2.508053
LSB1.10B	86		182.9611	0	2.153234	1.888184	1.763965	0.291067	1.762859	1.082468	0.569182	0.440237	2.821 92

LSB1.11B	94		146.9299	0	1.699916	1.466147	1.371691	0.212067	1.301149	0.832337	0.448729	0.308544	2.20854
LSB1.12B	102		411.2474	0	1.992269	1.979857	2.179339	0.35413	2.534311	1.748491	1.038661	0.776376	3.607462
LSB1.13B	110		193.6512	0	1.721243	1.656744	1.57088	0.367859	1.758867	1.100599	0.58472	0.472442	2.780218
LSB1.14B	118		206.819	0	2.34666	2.098969	2.010886	0.357385	2.149296	1.337505	0.632844	0.489705	3.878141
LSB3.0B	-22		186.129	0	1.420687	1.165626	1.002904	0.124071	0.841222	0.414611	0.163368	0.176108	3.879361
LSB5.0B	84		102.0894	0	1.26959	1.062605	0.986255	0.142301	0.951817	0.611546	0.297784	0.216845	1.610569
LSB5.1B	93		217.4774	0	2.071389	1.676526	1.653164	0.248141	1.716407	1.071689	0.606382	0.412481	2.694404
LSB5.2B	102		254.9949	0	1.726641	1.423737	1.494169	0.185082	1.786953	1.118473	0.618865	0.501376	2.614178
LSB5.3B	111		119.3741	0	1.208742	1.015855	1.073371	0.153861	1.071264	0.665858	0.152154	0.331835	1.75762
LSB5.4B	120		182.1607	0	1.860809	1.661271	1.644037	0.282561	1.742894	1.005543	0.51473	0.349007	2.963208
LSB5.5B	129		206.0692	0	2.201109	1.868033	1.796003	0.301323	1.79628	1.012073	0.49342	0.391167	3.343809
LSB5.6B	138		241.22	0	2.337191	2.150249	2.015486	0.260985	1.832668	1.025068	0.5062	0.342753	3.993233
LSB5.7B	145		208.2986	0	2.328337	2.015356	1.891718	0.398655	1.644261	1.028784	0.506351	0.241129	3.879155
LSB6.0B	-24		222.1023	0	1.613779	1.402174	1.28798	0.231369	1.11212	0.599928	0.276426	0.176858	4.007156
LSB6.1B	-11		253.1082	0	1.88852	1.657919	1.546819	0.221075	1.401416	0.734863	0.372411	0.230953	3.951024
LSB6.2B	2		267.9998	0	2.168916	1.916521	1.840042	0.293042	1.760013	0.994264	0.491743	0.341849	4.262398
LSB6.3B	14		190.029	0	1.573882	1.361859	1.3436	0.184608	1.295742	0.699408	0.365397	0.215195	2.784062
LSB6.4B	26		112.5223	0	1.033348	0.870696	0.886905	0.13829	0.834758	0.490 03	0.221657	0.152817	1.613046
LSB6.5B	49		116.9478	0	1.031516	0.926559	0.896419	0.128697	0.946898	0.590332	0.261748	0.239709	1.642738
LSB6.6B	51		293.7025	0	2.898835	2.485348	2.414306	0.403035	2.542478	1.611668	0.790331	0.596151	4.213432
LSB6.7B	63		381.5552	0	2.545226	2.560905	2.653972	0.601335	3.169147	2.067498	0.994064	0.784713	4.141887
Bos32.1B	-5		84813.23	0	224.8086	653.9483	1381.269	290.2372	2262.663	1533.231	1449.355	1164.091	617.2217
Bos32.2B	0		107587.4	0	257.9026	820.9261	1659.625	336.4124	2834.76	1897.514	1469.586	1470.425	762.21
Bos32.3B	5		65314.02	0	180.9242	530.4671	1085.739	241.326	1772.889	1178.253	925.8963	876.7233	461.0064
Pseud41.1B	-5		77896.43	0	194.8675	616.6435	1243.07	269.9275	2139.421	1417.473	1124.822	1068.754	525.1939
Pseud41.2B	0		207876.7	0	488.0305	1730.483	3508.359	691.4541	6007.682	4067.776	3271.132	2934.772	1268.326
Pseud41.3B	5		45185.04	0	107.0526	353.9307	752.472	137.215	1301.707	882.3085	661.0734	672.9666	298.7755

Sample Code:	**Stratigraphic height***		C26/3S	C26/3R	C28/3S	C28/3R	C29/3S	C29/3R	Ts	Tm	C30/3S	C30/3R	C29ab
LSB1.0B	5		0.178312	0.176439	0.231182	0.13718	0.283314	0.204786	3.702991	4.64035	1.553887	1.117032	12.82713
LSB1.1B	13		0.48455	0.502013	0.350987	0.291073	0.630794	0.474461	6.417199	7.091902	2.52531	2.039324	20.80674
LSB1.2B	22		0.564678	0.593201	0.46695	0.45067	0.780572	0.625558	10.33509	11.68029	3.826656	3.192344	36.50598

LSB1.3B	29		0.33602	0.342068	0.283418	0.209172	0.444655	0.310774	5.273263	5.746856	1.876662	1.642706	17.55249
LSB1.4B	37		0.519952	0.520436	0.442441	0.412199	0.733467	0.550811	9.414468	9.418282	3.168355	2.791 83	29.76343
LSB1.5B	46		0.788 35	0.832 06	0.704363	0.716029	1.203445	0.977932	11.94868	10.08764	3.501681	3.253569	33.35728
LSB1.6B	55		0.633947	0.651833	0.545047	0.533992	1.247706	0.856122	7.949145	6.506873	2.464 93	2.299085	22.15418
LSB1.7B	62		3.378281	3.374239	2.174002	2.931346	6.459586	4.017258	37.98295	31.31417	12.15087	11.98707	122.2 18
LSB1.8B	69		0.300913	0.299115	0.217172	0.251217	0.460154	0.312462	3.770434	2.966519	1.159936	1.070262	10.99848
LSB1.9B	78		0.437639	0.455736	0.374818	0.374102	0.640243	0.391212	6.178181	4.816525	1.731125	1.483843	15.71174
LSB1.10B	86		0.492994	0.538868	0.340984	0.339237	0.738496	0.483396	6.941354	5.441 03	1.815218	1.626413	17.11426
LSB1.11B	94		0.402 14	0.413	0.283627	0.302594	0.512 9	0.415478	5.359482	4.149 42	1.468 14	1.314505	13.47789
LSB1.12B	102		0.936784	0.966953	0.823065	0.941699	1.607437	1.399009	10.08985	8.399 69	3.567909	3.217288	33.69922
LSB1.13B	110		0.543952	0.561626	0.464099	0.453726	0.864545	0.537352	6.588518	4.954068	2.133426	2.030618	18.00057
LSB1.14B	118		0.566476	0.564507	0.373111	0.352777	0.674739	0.625424	8.693372	5.861 91	2.562877	2.059773	19.76134
LSB3.0B	-22		0.125 69	0.119738	0.166 26	0.181398	0.330135	0.166783	4.475877	7.657 21	2.678643	1.547812	20.10868
LSB5.0B	84		0.283401	0.284337	0.157336	0.174397	0.382331	0.243949	3.824 11	3.005095	1.012941	0.823097	9.731 37
LSB5.1B	93		0.552348	0.582576	0.339413	0.380521	0.849043	0.553154	6.865305	5.399856	2.013228	1.713089	19.55334
LSB5.2B	102		0.580661	0.609481	0.462243	0.555 21	0.914585	0.720776	6.960 69	5.772772	2.250204	2.049759	21.91889
LSB5.3B	111		0.281769	0.289448	0.218611	0.235949	0.415739	0.283 91	4.606211	3.384117	1.265115	1.041136	11.19832
LSB5.4B	120		0.381597	0.385717	0.286876	0.250741	0.654106	0.494501	7.063338	5.098038	2.062158	1.668105	16.71029
LSB5.5B	129		0.400569	0.418911	0.318168	0.315965	0.561246	0.475 29	7.571431	5.460695	2.310417	1.776221	18.42338
LSB5.6B	138		0.372707	0.379144	0.329 67	0.268215	0.684101	0.500248	8.427677	6.613578	3.079 72	2.215615	21.69836
LSB5.7B	145		0.383233	0.392272	0.258299	0.199625	0.633481	0.445 9	7.664425	6.335903	2.724908	1.923 21	19.42795
LSB6.0B	-24		0.255155	0.264614	0.259372	0.241879	0.512146	0.299571	5.681035	8.694427	2.888 37	1.818161	22.72503
LSB6.1B	-11		0.331343	0.377 69	0.312057	0.198739	0.507 57	0.284652	6.422724	8.613828	3.241208	2.248 08	24.91027
LSB6.2B	2		0.475164	0.543644	0.325331	0.261152	0.602032	0.389257	7.784935	9.171693	3.090528	2.463321	28.14209
LSB6.3B	14		0.324 32	0.331714	0.261825	0.196491	0.395159	0.287722	5.357411	6.186189	2.085793	1.721892	18.85697
LSB6.4B	26		0.202336	0.237545	0.168215	0.144551	0.247 71	0.172852	3.219161	3.427045	1.220194	1.035841	10.67341
LSB6.5B	49		0.237454	0.235056	0.193097	0.192575	0.357289	0.236727	3.715182	3.427419	1.097467	0.997 8	11.08014
LSB6.6B	51		0.708716	0.738904	0.614869	0.613748	1.127023	0.712712	10.22332	8.446325	2.830353	2.485483	28.15942
LSB6.7B	63		1.118305	1.116124	0.771399	0.746597	1.781092	0.942 09	11.12343	8.806938	3.524183	3.032156	34.13575
Bos32.1B	-5		634.2707	640.3505	733.0882	816.815	1278.046	1021.313	1905.974	1831.882	1131.571	994.8339	5179.235
Bos32.2B	0		792.5279	800.8401	847.4161	942.2506	1453.1	1157.002	2364.5	2409.388	1409.146	1243.974	6637.437
Bos32.3B	5		479.8067	489.8798	566.9399	622.8853	1018.383	789.103	1513.999	1454.602	872.1765	786.7011	4082.367
Pseud41.1B	-5		595.8469	602.0848	791.9325	849.7946	1232.76	967.492	1590.419	1623.927	1164.107	1054.034	4799.108
Pseud41.2B	0		1748.012	1703.161	2067.586	2004.545	3200.511	2615.261	4910.814	4830.411	3392.236	3152.729	12559 .05

Pseud41.3B	5		385.569	379.4405	445.9205	507.6029	696.1646	579.6093	983.7402	954.0555	666.3145	610.8873	2876.028

Sample Code:	**Stratigraphic height***		C29Ts	C30*	C29ba	C30ab	C30ba	C31abS	C31abR	C31ba	C32abS	C32abR	C32baS
LSB1.0B	5		5.821694	0	2.171311	17.61507	5.141597	13.45233	9.690166	2.910317	8.12014	5.364867	0.685022
LSB1.1B	13		9.711792	0	3.656201	27.75162	7.860882	20.08981	14.77306	4.399732	12.28241	8.616476	1.102285
LSB1.2B	22		15.91244	0	6.540399	49.33389	13.78153	37.26978	26.58886	9.005159	22.96525	16.57193	2.735312
LSB1.3B	29		7.811706	0	3.091142	24.03053	6.866 99	18.56768	13.68086	4.126 57	11.55847	8.194305	1.120471
LSB1.4B	37		13.48586	0	4.904287	41.43439	10.66519	30.69506	22.12501	6.679195	18.5026	12.71662	1.756276
LSB1.5B	46		16.95878	0	5.251679	52.20426	12.76895	36.32104	26.60761	6.421997	24.24287	17.13681	1.955552
LSB1.6B	55		11.01801	0	3.580772	33.64218	7.841573	23.96552	17.79079	5.197962	16.15412	11.53802	1.903501
LSB1.7B	62		59.86744	0	20.79251	206.1322	46.89631	148.397	107.9035	24.23514	109.5902	75.93281	8.587137
LSB1.8B	69		5.354856	0	2.053475	17.9435	4.127947	12.39598	9.14422	2.123279	8.930012	6.30786	0.956173
LSB1.9B	78		8.02119	0	2.661283	23.95349	5.641525	15.63134	11.89329	3.116427	10.36008	7.172081	0.825326
LSB1.10B	86		8.880482	0	2.937634	26.4701	6.25094	17.50866	13.29734	3.401685	11.36831	8.163108	1.134999
LSB1.11B	94		7.028771	0	2.468705	21.8651	5.058721	14.19855	10.53007	2.798085	9.669659	6.878137	0.650522
LSB1.12B	102		16.9738	0	5.109261	56.4343	13.54351	40.68019	29.34197	8.057069	30.31538	20.95153	3.442968
LSB1.13B	110		9.742613	0	3.285714	26.66262	6.462025	18.37557	13.87923	4.026256	12.28795	8.652021	1.381271
LSB1.14B	118		11.59533	0	2.381829	29.34497	6.688012	19.94359	14.23722	3.767035	13.2351	8.82595	0.989645
LSB3.0B	-22		8.148432	0	3.555233	24.17987	8.2777	19.00558	13.79085	4.674605	12.23468	8.495781	1.343654
LSB5.0B	84		4.840728	0	1.543498	15.08288	3.496404	9.838259	7.356053	1.772165	6.510759	4.660346	0.581435
LSB5.1B	93		9.632247	0	3.268034	31.81099	7.346289	21.39439	15.50252	3.516598	14.80967	10.33245	1.063249
LSB5.2B	102		10.72308	0	3.207912	36.55993	8.394851	25.58424	18.42304	4.355495	18.88322	12.99381	1.324541
LSB5.3B	111		6.09366	0	1.888653	17.48466	3.957213	11.6323	8.536997	1.966658	8.057487	5.669841	0.613331
LSB5.4B	120		9.108422	0	2.592774	26.76001	6.265566	17.82908	13.05923	3.128022	12.09861	8.578969	0.839714
LSB5.5B	129		10.73937	0	2.80933	29.44347	6.63943	20.36275	15.13658	3.657445	14.01642	10.00136	0.968508
LSB5.6B	138		12.86608	0	3.810212	35.59558	8.458205	24.21784	17.73349	4.434439	15.8888	11.02002	1.243832
LSB5.7B	145		11.88115	0	3.205635	28.93587	7.178446	20.20315	15.17627	3.86429	13.80095	9.678764	1.025611
LSB6.0B	-24		9.70973	0	4.292013	29.35487	9.41749	22.89588	16.45415	6.061103	14.07489	10.00602	1.323647
LSB6.1B	-11		11.48136	0	4.730999	33.48906	11.24083	25.6855	18.79964	6.280808	17.36595	12.34764	1.389674
LSB6.2B	2		12.46736	0	4.823006	37.26151	10.17619	27.85196	20.41942	5.429112	17.41126	12.0424	1.34784
LSB6.3B	14		8.420522	0	3.2077	26.05816	7.447677	20.03863	14.55494	4.002534	12.59661	8.960747	0.998915
LSB6.4B	26		4.745384	0	1.810091	15.1744	4.198298	11.81465	8.702708	2.409678	7.480942	5.306272	0.610571

LSB6.5B	49		4.958949	0	1.739822	16.75381	4.437664	11.97523	8.81008	2.468593	7.795591	5.517934	0.568467
LSB6.6B	51		13.43454	0	4.547002	41.5907	10.22623	29.01587	21.67797	5.133627	19.25294	13.91135	1.548624
LSB6.7B	63		16.7695	0	5.203199	53.24179	12.37757	38.15279	28.28585	6.357698	26.61618	18.90425	1.831616
Bos32.1B	-5		2511.515	371.457	788.8961	8985.86	2245.449	6809.901	5367.17	1412.309	5196.431	3704.453	555.9219
Bos32.2B	0		2985.352	448.0726	774.8465	11644.76	2876.79	9004.6	7037.654	1543.307	6642.509	4756.977	746.8275
Bos32.3B	5		1925.351	225.2088	330.2202	7113.791	1790.232	5268.288	4116.916	1022.57	3977.413	2953.708	363.0861
Pseud41.1B	-5		2086.113	460.7267	616.5091	8099.391	2009.783	6316.994	5020.81	1310.461	4759.748	3678.311	549.2468
Pseud41.2B	0		5605.411	1035.295	1876.874	21172.4	5613.536	16789.03	13287	3111.278	12415.41	9272.066	1316.265
Pseud41.3B	5		1257.918	262.1134	391.4805	4715.255	1178.88	3677.373	2899.207	646.6214	2718.973	2015.008	292.597

Sample Code:	**Stratigraphic height***		C32baR	C33abS	C33abR	C33baS	C33baR	C34abS	C34abR	C34baS
LSB1.0B	5		0.850717	5.556112	3.826061	0.60068	0.705991	4.042015	2.649329	0.401011
LSB1.1B	13		1.276722	8.587122	6.148237	1.014193	1.038222	6.100961	4.173353	0.732427
LSB1.2B	22		2.88266	15.70483	10.76056	1.886166	1.938804	11.17894	7.69776	1.356479
LSB1.3B	29		1.263714	8.177056	5.780472	0.891278	1.084239	5.947624	4.117843	0.801403
LSB1.4B	37		1.936208	12.78695	8.86594	1.111523	1.512416	8.791766	6.039202	1.10154
LSB1.5B	46		2.02955	18.33404	12.80924	1.531512	1.860844	11.26184	7.743003	1.406121
LSB1.6B	55		2.073966	12.06502	8.527638	1.093748	1.531759	7.819698	5.401178	1.092755
LSB1.7B	62		8.867233	86.77432	59.58926	6.444487	8.667709	52.54626	36.01799	5.907201
LSB1.8B	69		1.022568	6.908567	4.797322	0.567855	0.733336	4.330635	2.954834	0.460919
LSB1.9B	78		0.866992	7.592012	5.316509	0.645202	0.845424	4.518453	3.224654	0.449822
LSB1.10B	86		1.254975	8.467418	6.007708	0.783326	1.061538	4.971151	3.424482	0.663158
LSB1.11B	94		0.71372	6.954755	4.859476	0.548526	0.70038	4.225581	2.880436	0.478203
LSB1.12B	102		3.666789	24.54538	16.59487	2.648573	2.693813	15.49166	10.06814	1.33528
LSB1.13B	110		1.533549	9.203956	6.487998	0.781505	1.192711	5.695759	4.040891	0.896065
LSB1.14B	118		1.077405	9.384496	6.675236	0.743319	1.157824	5.820019	4.190246	0.559015
LSB3.0B	-22		1.593041	8.097839	5.63027	0.89536	1.221631	5.744103	3.839945	0.60325
LSB5.0B	84		0.602965	4.810379	3.386497	0.338792	0.507159	2.853706	1.94609	0.269384
LSB5.1B	93		1.118925	11.67171	8.035795	1.086197	1.415021	7.069135	4.634893	0.679255
LSB5.2B	102		1.346936	14.76845	10.02775	1.328531	1.501544	9.358752	6.330087	0.628624
LSB5.3B	111		0.622879	5.714546	4.045387	0.410951	0.575338	3.431967	2.36061	0.263876
LSB5.4B	120		0.884231	8.603462	6.010837	0.597311	0.777835	5.412259	3.706973	0.491613

LSB5.5B	129		1.017546	10.04822	7.098927	0.662676	0.941609	6.336947	4.30813	0.666886
LSB5.6B	138		1.448747	11.42253	8.031664	0.940439	1.151854	7.343779	5.049972	0.587858
LSB5.7B	145		1.237705	9.401274	6.749778	0.783565	1.144457	6.108154	4.347527	0.446894
LSB6.0B	-24		1.652496	10.04018	6.906661	1.304255	1.625663	6.863547	4.635335	1.074438
LSB6.1B	-11		1.719175	11.48811	8.020838	1.41388	1.792256	8.214075	5.503569	1.070049
LSB6.2B	2		1.550465	11.68543	8.092238	1.184147	1.57257	8.51129	5.749977	0.753705
LSB6.3B	14		1.128447	8.701208	6.053787	0.777886	1.131984	6.120229	4.186742	0.610504
LSB6.4B	26		0.680452	5.236782	3.678918	0.542559	0.683846	3.735477	2.550379	0.455642
LSB6.5B	49		0.626197	5.407887	3.80039	0.530136	0.646755	3.763175	2.579914	0.390404
LSB6.6B	51		1.678585	13.91904	9.859493	1.236446	1.735633	8.877187	6.087039	1.024453
LSB6.7B	63		2.051443	20.62233	14.38967	1.820699	2.555194	13.07522	8.925568	1.706487
Bos32.1B	-5		552.847	5157.462	3747.934	421.0781	609.7937	2871.929	1989.648	376.9496
Bos32.2B	0		772.8538	6671.117	4813.924	579.2165	696.52	3806.103	2573.481	415.4557
Bos32.3B	5		349.3594	3936.037	2902.689	372.0186	467.7255	2204.881	1516.314	274.427
Pseud41.1B	-5		552.0012	4694.954	3483.689	364.8614	416.8726	2616.84	1774.39	365.7398
Pseud41.2B	0		1422.294	12121.11	9304.413	993.9599	1548.585	6603.987	4630.279	881.0093
Pseud41.3B	5		287.3293	2604.543	1973.496	227.6365	303.6095	1466.922	978.4638	194.0691

Sample Code:	**Stratigraphic height***		C34baR	C35abS	C35abR	C36abS	C36abR		C35 homohopane index		Ts/(Ts+Tm) %
LSB1.0B	5		0.395443	2.167117	1.559883	0.84048	0.777126		6.604875		44.38259
LSB1.1B	13		0.640902	3.52782	2.589966	1.266338	0.839213		7.040903		47.50278
LSB1.2B	22		1.491144	6.644464	4.935288	2.099328	1.678271		7.223005		46.94486
LSB1.3B	29		0.777146	3.458218	2.510762	1.1875	0.819739		7.27984		47.85124
LSB1.4B	37		1.199809	5.459018	4.036977	1.850623	1.318733		7.303536		49.98987
LSB1.5B	46		1.158151	7.229412	5.168882	2.908694	2.148864		7.430591		54.22265
LSB1.6B	55		1.003331	4.867031	3.646031	1.973559	1.497259		7.616246		54.98848
LSB1.7B	62		5.190487	32.31008	23.20508	12.54259	8.562675		7.581278		54.81173
LSB1.8B	69		0.432606	2.803734	1.993862	1.169218	0.832183		7.921136		55.96645
LSB1.9B	78		0.450497	2.826249	1.983635	1.214873	0.896357		6.82076		56.19233
LSB1.10B	86		0.682815	3.126992	2.375766	1.234871	0.848247		6.991098		56.0583
LSB1.11B	94		0.443892	2.549918	1.771845	0.990898	0.717696		6.698494		56.36278
LSB1.12B	102		1.504314	10.97211	7.779839	4.293312	2.943521		9.070259		54.57057

LSB1.13B	110		0.937176	3.695884	2.745077	1.456425	1.082907		7.571871		57.08009
LSB1.14B	118		0.476456	3.421936	2.641115	1.329443	0.936136		6.860603		59.72658
LSB3.0B	-22		0.688704	3.000789	2.35539	1.162337	0.843774		6.516412		36.88984
LSB5.0B	84		0.285168	1.79935	1.361371	0.690449	0.483854		7.099104		55.99641
LSB5.1B	93		0.686691	4.651993	3.303722	1.997517	1.497631		7.845387		55.97403
LSB5.2B	102		0.711416	6.047878	4.362844	2.325362	1.541897		8.211639		54.66455
LSB5.3B	111		0.270567	2.146533	1.645486	0.789663	0.54462		7.122346		57.64733
LSB5.4B	120		0.43516	3.352998	2.423999	1.27046	0.853669		7.125374		58.08009
LSB5.5B	129		0.673423	3.878155	2.893275	1.51704	1.016165		7.197464		58.0982
LSB5.6B	138		0.615345	4.255864	3.291122	1.601704	1.177716		6.971484		56.03041
LSB5.7B	145		0.504488	3.441223	2.615687	1.296496	0.948246		6.617927		54.74461
LSB6.0B	-24		1.024442	3.777498	2.807935	1.441845	1.010613		6.688292		39.51897
LSB6.1B	-11		1.098781	4.473167	3.325427	1.649664	1.074648		6.768209		42.71407
LSB6.2B	2		0.911379	4.886125	3.489069	1.715118	1.350288		6.971243		45.91087
LSB6.3B	14		0.641501	3.62359	2.647524	1.303269	0.986617		7.168296		46.41023
LSB6.4B	26		0.463335	2.293104	1.637978	0.767028	0.553425		7.496742		48.43607
LSB6.5B	49		0.350202	2.29576	1.680701	0.830499	0.584843		7.415082		52.01441
LSB6.6B	51		1.057415	5.647703	4.138037	2.110194	1.376		7.391788		54.75904
LSB6.7B	63		1.563001	8.483294	6.277409	3.242683	2.484983		8.033798		55.81147
Bos32.1B	-5		334.5572	2202.243	1473.081	724.9323	657.2095		9.541277		50.9911
Bos32.2B	0		448.2148	2970.124	2059.247	860.6997	891.7667		9.991651		49.52985
Bos32.3B	5		266.9859	1685.694	1184.555	592.4411	544.0435		9.649033		51.00041
Pseud41.1B	-5		299.809	1942.27	1360.692	565.034	679.5039		9.265308		49.47877
Pseud41.2B	0		820.3642	5038.768	3613.207	1479.607	1772.219		9.295675		50.41269
Pseud41.3B	5		164.9645	1138.899	810.0026	323.2053	403.6388		9.608602		50.76594

Sample Code:	**Stratigraphic height***		SUM Steranes		C21ba	C21aa	C22ab	C22aa		C27baS	C27baR
LSB1.0B	5		52.29727	0	2.428139	2.888067	1.468027	1.667747	0	4.240368	2.940969
LSB1.1B	13		91.26969	0	4.606612	5.291133	2.717522	3.218004	0	8.590301	5.737911
LSB1.2B	22		127.7107	0	6.499188	7.489551	3.718724	4.415219	0	11.87663	8.127789
LSB1.3B	29		69.35403	0	3.738718	4.41401	2.273899	2.67091	0	6.567433	4.468671
LSB1.4B	37		123.352	0	6.397842	7.595927	4.030047	4.492042	0	13.11466	8.806334

LSB1.5B	46		224.1305	0	7.126289	8.444805	4.283293	5.012374	0	22.84601	15.63612
LSB1.6B	55		151.4064	0	5.031089	5.696473	3.20104	3.644553	0	15.96385	10.74125
LSB1.7B	62		857.8345	0	22.47058	24.1081	15.04452	16.7931	0	92.085	61.90418
LSB1.8B	69		71.08857	0	2.32507	2.603459	1.369741	1.593451	0	7.284982	4.946387
LSB1.9B	78		102.455	0	4.44145	4.971932	2.479754	2.917546	0	10.49778	7.228931
LSB1.10B	86		121.5589	0	4.729589	5.897881	2.872367	3.352392	0	12.05332	8.207265
LSB1.11B	94		94.84441	0	3.991468	4.537853	2.378121	2.736779	0	9.915634	6.648055
LSB1.12B	102		224.1077	0	5.868445	5.993771	3.557527	3.929383	0	23.3911	16.27925
LSB1.13B	110		110.8671	0	4.410754	4.949488	2.683851	3.055742	0	12.26193	8.234884
LSB1.14B	118		118.9003	0	5.831268	6.782698	3.87396	4.064843	0	13.20033	8.82897
LSB3.0B	-22		62.19871	0	2.632529	3.11002	1.500768	1.902177	0	5.141473	3.552738
LSB5.0B	84		70.79334	0	2.886501	3.559218	1.794342	1.98887	0	7.085553	4.798391
LSB5.1B	93		132.3659	0	4.742328	5.655277	3.04025	3.262595	0	13.52139	9.144332
LSB5.2B	102		156.4926	0	4.457201	4.827583	2.731377	3.041123	0	16.40398	11.16353
LSB5.3B	111		74.31036	0	2.879204	3.432826	1.842447	1.950325	0	8.248341	5.58441
LSB5.4B	120		96.01658	0	4.614892	5.516404	2.943021	3.274196	0	10.76814	7.162609
LSB5.5B	129		96.49642	0	5.058536	6.118205	3.316897	3.463935	0	10.47731	6.988898
LSB5.6B	138		109.0112	0	5.908491	6.856063	3.533395	4.006474	0	11.1401	7.458626
LSB5.7B	145		102.5102	0	5.590323	6.424434	3.421926	3.714411	0	9.963451	6.838429
LSB6.0B	-24		89.34867	0	3.576906	4.311988	2.315399	2.591305	0	7.252786	5.136284
LSB6.1B	-11		95.25258	0	4.091333	4.956584	2.51222	2.881548	0	7.967541	5.522131
LSB6.2B	2		106.9242	0	4.946487	5.905467	3.063164	3.444153	0	9.590744	6.636097
LSB6.3B	14		70.15731	0	3.464417	4.1999	2.189422	2.458271	0	6.590518	4.456274
LSB6.4B	26		45.31822	0	2.264633	2.746468	1.418241	1.575298	0	4.335652	2.929489
LSB6.5B	49		61.28684	0	2.491635	2.97311	1.592763	1.696844	0	6.471243	4.410811
LSB6.6B	51		188.8237	0	6.788774	8.066568	4.229875	4.58484	0	19.39603	13.073
LSB6.7B	63		245.2281	0	7.262084	8.177754	5.108889	5.332068	0	26.84512	18.21157
Bos32.1B	-5		335.6947	0	9.502831	10.6089	5.225124	7.276571	0	26.44217	17.99715
Bos32.2B	0		500.4788	0	13.65105	15.91782	7.864955	10.45304	0	39.34592	27.40317
Bos32.3B	5		346.3159	0	10.17928	11.68675	5.535142	7.595489	0	27.67726	19.16964
Pseud41.1B	-5		610.7605	0	15.67604	17.50566	8.424002	12.16952	0	48.15281	33.51711
Pseud41.2B	0		439.5195	0	12.01119	13.435	6.195932	8.741541	0	34.63138	24.67635
Pseud41.3B	5		575.0181	0	15.77558	17.45642	8.306793	11.37301	0	45.3446	32.42626

Sample Code:	Stratigraphic height*		C27abS	C27abR	C28baS1	C28baS2	C28baR	C27aaS	C27bbR	C29baS	C27bbS
LSB1.0B	5		1.596891	1.446446	1.459491	1.715893	1.213525	1.133439	0.69685	5.031943	0.592838
LSB1.1B	13		2.945175	2.849976	2.774283	3.293295	2.415402	1.941239	0.88419	7.636897	0.829962
LSB1.2B	22		3.827846	4.112873	3.779449	4.350292	3.195405	3.180086	1.792015	10.6055	1.641281
LSB1.3B	29		2.050953	2.154146	1.982582	2.361291	1.659515	1.459429	0.866129	5.706715	0.794762
LSB1.4B	37		4.128331	4.282273	3.915037	4.319431	3.032828	2.656464	2.134056	9.583946	1.848307
LSB1.5B	46		7.337601	7.349498	7.705094	8.668637	6.259046	6.372775	3.966711	18.55398	3.530084
LSB1.6B	55		5.095133	4.975743	5.167833	6.025344	4.508377	4.051154	2.533783	13.01738	2.165942
LSB1.7B	62		27.79549	26.54265	30.64792	36.07178	26.944	22.80034	8.608862	83.15502	7.803788
LSB1.8B	69		2.232404	2.253514	2.37495	2.749608	2.063607	1.940123	0.983868	6.512173	0.876661
LSB1.9B	78		3.564943	3.525909	3.37728	3.851015	2.727534	3.053014	1.303337	7.783291	1.143332
LSB1.10B	86		3.897952	4.005677	3.810937	4.346695	3.361479	3.307445	2.526599	9.057378	2.156864
LSB1.11B	94		3.250444	3.132481	3.121815	3.612586	2.610845	2.591094	1.910563	7.615776	1.76738
LSB1.12B	102		7.729215	6.925583	8.108938	9.450256	6.601153	5.956483	3.742767	23.85841	3.413826
LSB1.13B	110		4.194698	3.826106	3.978195	4.565942	3.364847	2.950209	1.966422	8.386311	1.727988
LSB1.14B	118		4.499895	4.406013	3.787573	4.202162	3.181657	2.717614	2.280722	9.070063	2.137019
LSB3.0B	-22		1.764438	1.778187	1.870226	2.233184	1.503444	1.373103	0.653957	6.304453	0.548592
LSB5.0B	84		2.336259	2.4438	2.295458	2.640325	2.035618	2.073868	1.289654	5.237719	1.189374
LSB5.1B	93		4.358929	4.277254	4.494765	5.208022	3.93313	3.980655	2.351008	11.55504	2.102464
LSB5.2B	102		5.0664	5.024847	5.788386	6.544479	4.485175	4.164134	2.868074	14.63871	2.57848
LSB5.3B	111		2.491902	2.709749	2.513967	2.732252	2.073577	1.995561	1.43298	5.545338	1.259199
LSB5.4B	120		3.475751	3.648796	3.145991	3.696555	2.86415	2.51043	1.913504	6.942639	1.794287
LSB5.5B	129		3.321685	3.442478	3.128035	3.538082	2.405064	2.022299	1.720358	7.803961	1.551617
LSB5.6B	138		3.587523	3.621202	3.41382	4.020201	2.707416	2.242206	1.295218	9.688216	1.176663
LSB5.7B	145		3.459233	3.364852	3.186543	3.802475	2.691151	2.192362	1.297818	9.123951	1.168261
LSB6.0B	-24		2.492226	2.43064	2.642144	3.291326	2.197837	1.862992	0.648746	9.82587	0.565668
LSB6.1B	-11		2.713316	2.733843	2.692978	3.307508	1.921538	2.156825	0.94386	9.288149	0.780642
LSB6.2B	2		3.045503	3.173123	3.106825	3.67615	2.697929	2.242977	1.436277	9.877476	1.254908
LSB6.3B	14		2.069703	2.202331	2.143026	2.492277	1.674262	1.539908	1.035115	5.644758	0.870791
LSB6.4B	26		1.366233	1.422888	1.278589	1.487098	1.045403	0.931008	0.751852	3.582745	0.684995
LSB6.5B	49		2.055505	2.156597	2.042424	2.271708	1.727012	1.717912	1.094961	5.153672	0.964099
LSB6.6B	51		6.24794	6.32419	6.174449	6.943748	5.462025	5.120398	3.912615	15.03202	3.593394
LSB6.7B	63		8.629416	7.780925	8.553477	9.884557	7.259178	7.027402	4.432245	22.3296	4.104695

Bos32.1B	-5		8.02145	9.339839	9.635827	11.20475	8.59656	11.65141	9.643834	25.94875	8.375592
Bos32.2B	0		12.50026	13.48643	13.68793	15.55741	11.99791	16.85935	15.97545	37.85074	14.144
Bos32.3B	5		8.429598	9.17871	9.780321	10.86092	8.162143	11.40031	9.664942	23.93333	8.755308
Pseud41.1B	-5		15.23171	16.3789	16.85126	18.72829	14.9635	19.44342	17.79509	45.49384	16.2693
Pseud41.2B	0		10.68962	11.86641	12.73245	13.66096	11.82842	15.04475	13.70001	33.61712	12.12858
Pseud41.3B	5		14.52246	15.10496	16.53386	18.20063	13.67371	19.05499	18.1817	42.90749	16.59842

Sample Code:	**Stratigraphic height***		C27aaR	C29baR	C29abR	C28aaS	C29abS	C30baS	C28bbR*	C28bbS	C30baR
LSB1.0B	5		0.870701	3.744986	1.11815	0.467326	0.650973	2.924504	1.086591	0.881309	1.750907
LSB1.1B	13		1.937504	6.383607	1.538027	0.830536	1.053218	4.935348	1.942704	1.64266	2.12814
LSB1.2B	22		2.868091	9.213884	2.357894	1.184373	1.515565	7.028189	2.379364	2.109456	2.813513
LSB1.3B	29		1.600808	4.679899	1.466632	0.61711	0.898707	3.649046	1.213251	1.059762	1.819599
LSB1.4B	37		2.573814	8.117886	1.998913	1.312079	1.638141	6.186077	2.395467	2.069993	2.609597
LSB1.5B	46		4.699565	15.99355	5.134933	2.888513	2.591889	12.97965	5.195588	4.448811	5.904139
LSB1.6B	55		4.088295	10.38252	3.496585	1.640993	1.442391	8.69166	2.702876	2.350642	4.0584
LSB1.7B	62		13.59286	71.86974	16.72992	8.910905	11.67621	53.16439	19.99057	17.10809	24.05401
LSB1.8B	69		1.523157	5.108417	1.343684	0.751254	0.813731	4.187314	1.610645	1.372025	1.924748
LSB1.9B	78		2.21633	6.715262	1.671448	1.184644	1.382839	5.79275	2.392355	2.0683	1.918761
LSB1.10B	86		3.643316	7.995279	2.249258	1.419735	1.613873	6.909622	2.76439	2.374508	2.872396
LSB1.11B	94		2.087438	6.093898	1.510486	1.025944	1.183272	5.372371	2.05046	1.788048	2.042121
LSB1.12B	102		4.453099	17.48125	5.180695	2.598304	2.702613	13.25324	4.51535	3.786788	5.858186
LSB1.13B	110		2.13313	7.567028	1.734554	0.923091	1.384728	6.140973	2.636755	2.312472	2.433431
LSB1.14B	118		3.111123	7.159941	2.493218	1.334322	1.236471	5.854477	2.018167	1.742504	2.301021
LSB3.0B	-22		1.412349	4.9489	1.625181	0.530405	0.781663	3.707851	1.043645	0.885511	1.557783
LSB5.0B	84		1.669331	4.648665	1.27403	0.837247	0.903476	3.914407	1.641132	1.413051	1.758776
LSB5.1B	93		2.978335	9.040313	2.744285	1.629362	1.706603	7.462383	3.094428	2.632344	2.815104
LSB5.2B	102		2.635446	12.39091	2.801622	1.616663	2.370271	9.36651	3.808228	3.266753	3.545313
LSB5.3B	111		1.636543	5.092977	1.156638	0.759155	0.866632	4.142476	1.740586	1.492634	1.343618
LSB5.4B	120		2.356439	6.345675	1.389675	0.892785	1.089792	5.047223	1.697443	1.469427	1.652462
LSB5.5B	129		2.253063	6.571978	1.618171	0.726533	1.042632	5.022584	1.789684	1.508287	1.924292
LSB5.6B	138		2.273932	7.873886	1.863093	0.784819	1.261373	5.920639	2.221151	1.75892	2.197619
LSB5.7B	145		2.618019	6.900525	2.645104	0.876368	0.893039	5.169234	1.8055	1.475093	2.483639

LSB6.0B	-24		2.453791	7.117963	1.832617	0.843454	0.784253	5.141336	1.871539	1.566608	2.600082
LSB6.1B	-11		2.227981	7.650022	2.543566	0.859188	1.223152	5.44575	1.834694	1.570528	2.912104
LSB6.2B	2		2.354781	7.692866	2.202519	0.836697	1.218989	5.935108	2.190176	1.839108	2.4515
LSB6.3B	14		1.583469	5.148157	1.231615	0.580725	0.803951	3.861937	1.378517	1.171413	1.370959
LSB6.4B	26		0.988147	3.055139	0.739061	0.37863	0.485516	2.442579	0.845385	0.723059	1.195663
LSB6.5B	49		1.346144	4.015969	1.131931	0.537908	0.753681	3.409161	1.199966	1.033629	1.357785
LSB6.6B	51		4.079806	13.36498	3.358024	2.152264	2.229807	10.62511	4.255183	3.693461	4.260885
LSB6.7B	63		4.625162	18.56238	6.879616	3.071788	2.970267	13.1638	5.040992	4.381455	6.540608
Bos32.1B	-5		8.349232	20.33538	8.359413	6.149236	4.338593	19.60125	9.258857	8.585249	9.876334
Bos32.2B	0		13.15217	30.32488	12.71345	9.278196	6.506125	30.6182	13.44391	12.69574	12.98722
Bos32.3B	5		8.059333	21.70087	9.255352	6.433783	4.668809	20.59054	10.13939	9.208044	10.33891
Pseud41.1B	-5		15.92768	39.94713	16.58151	11.68905	9.014257	37.35128	15.58454	14.37097	16.8811
Pseud41.2B	0		11.17676	27.26256	11.6524	7.735852	5.644129	25.98897	12.33777	10.94196	10.41652
Pseud41.3B	5		14.6734	34.12591	15.19972	10.1512	7.379897	34.69262	14.64212	13.27746	16.88382

Sample Code:	**Stratigraphic height***		C28aaR	C30abR	C29aaS	C29bbR	C29bbS	C29aaR	C30aaS	C30bbR
LSB1.0B	5		0.8052	0.632398	1.366843	1.339503	1.34777	1.321137	0.169483	0.554458
LSB1.1B	13		0.93804	0.822251	1.858879	2.2872	2.316106	1.950766	0.389687	0.964845
LSB1.2B	22		1.460294	1.24554	2.7789	3.080499	2.947813	2.622343	0.363617	1.430793
LSB1.3B	29		0.707168	0.576931	1.495102	1.52714	1.520973	1.40377	0.240327	0.68382
LSB1.4B	37		1.348892	1.08457	2.250775	1.973415	1.932596	2.25728	0.368975	1.229246
LSB1.5B	46		2.695477	1.375448	4.537483	5.56658	5.463114	5.124428	1.141562	2.354294
LSB1.6B	55		1.722716	0.842418	3.001565	3.844297	3.733671	3.319038	0.710486	1.563674
LSB1.7B	62		10.5835	5.854619	15.72478	20.35983	19.68797	20.14546	3.785673	9.39382
LSB1.8B	69		0.977993	0.531906	1.63982	1.731532	1.674481	1.508729	0.380092	0.773127
LSB1.9B	78		1.245262	0.75356	1.937972	2.58277	2.487606	2.226062	0.464698	0.954814
LSB1.10B	86		1.626108	0.748802	2.307534	2.598695	2.497451	2.768858	0.62767	1.090555
LSB1.11B	94		1.084908	0.696144	1.84679	1.971818	2.003013	1.802174	0.381138	0.940464
LSB1.12B	102		2.312907	1.321726	4.148898	5.358458	5.172782	4.688957	1.011024	2.292672
LSB1.13B	110		1.187728	0.832141	1.867115	2.501932	2.404357	1.90328	0.446382	0.861064
LSB1.14B	118		1.380445	0.912792	1.785214	2.101478	2.064999	1.945264	0.494649	0.768296
LSB3.0B	-22		0.662236	0.778798	1.391033	1.67276	1.622446	1.694419	0.152229	0.70172

LSB5.0B	84		0.871039	0.473056	1.303087	1.454083	1.459716	1.478201	0.314863	0.639047
LSB5.1B	93		1.472662	0.796523	2.486985	2.967855	2.853584	2.479051	0.504269	1.315079
LSB5.2B	102		1.618452	0.989823	2.388377	4.145674	4.077452	3.030208	0.554976	1.624322
LSB5.3B	111		0.813841	0.444125	1.355286	1.766176	1.715016	1.38202	0.285908	0.656236
LSB5.4B	120		0.93102	0.776818	1.308544	1.739136	1.759911	1.513626	0.288279	0.59714
LSB5.5B	129		0.938893	0.644495	1.266599	1.798165	1.791161	1.43497	0.258915	0.599658
LSB5.6B	138		1.040176	0.905365	1.553963	2.27321	2.242275	1.636344	0.329873	0.856618
LSB5.7B	145		1.20082	0.948259	1.827314	1.803226	1.745981	1.569757	0.294969	0.769788
LSB6.0B	-24		1.047582	0.865932	1.963947	2.453167	2.413037	2.272423	0.260131	0.923113
LSB6.1B	-11		1.128249	0.886351	2.044009	2.380648	2.365185	2.319962	0.373094	1.264112
LSB6.2B	2		1.010499	0.879335	2.221553	2.906479	2.953743	2.259755	0.334445	1.316069
LSB6.3B	14		0.715179	0.646402	1.43287	1.647085	1.663658	1.641131	0.190233	0.78941
LSB6.4B	26		0.435398	0.398391	1.078527	1.097901	1.086421	1.014799	0.145667	0.523924
LSB6.5B	49		0.682607	0.40301	1.097618	1.357934	1.339799	1.098489	0.216187	0.540321
LSB6.6B	51		2.139615	1.041504	3.191791	4.961602	4.787495	3.6864	0.74546	1.930725
LSB6.7B	63		2.887755	1.740342	4.169961	4.337663	4.246479	4.588269	1.111587	2.321124
Bos32.1B	-5		4.674558	1.165592	8.617588	11.67	11.93527	9.723305	1.337675	4.246921
Bos32.2B	0		7.89138	1.579756	13.55286	17.00715	17.72844	14.99995	2.186259	5.903105
Bos32.3B	5		5.207201	1.126943	10.03077	12.06835	12.30548	10.27741	1.47899	4.208267
Pseud41.1B	-5		10.44792	2.431362	17.20026	20.74316	20.73421	18.98646	2.864659	8.063045
Pseud41.2B	0		7.565212	1.411449	12.95738	14.30882	14.1945	13.05489	2.004373	5.483679
Pseud41.3B	5		9.358478	2.926035	16.44656	19.32307	19.53918	17.07799	2.419307	7.078142

Sample Code:	**Stratigraphic height***		C30bbS	C30aaR	hopanes/(steranes+hopanes) %	steranes/(steranes+hopanes) %	ΣC27/Σ(C27-C30) %	ΣC28/Σ(C27-C30) %	ΣC29/Σ(C27-C30) %	ΣC30/Σ(C27-C30) %	C27/C28
LSB1.0B	5		0.437819	0.306583	70.83305	29.16695	30.83227	17.40058	36.31246	15.45469	1.771911
LSB1.1B	13		1.128449	0.489816	68.91611	31.08389	34.08998	18.34249	33.17324	14.39429	1.858525
LSB1.2B	22		1.01207	0.686684	73.70239	26.29761	35.44588	17.48174	33.26361	13.80877	2.027594
LSB1.3B	29		0.632164	0.39266	72.18798	27.81202	35.48449	17.0659	33.23872	14.21089	2.079262
LSB1.4B	37		1.148824	0.517915	70.42837	29.57163	39.21635	18.24121	29.50624	13.0362	2.149877
LSB1.5B	46		1.797011	1.146134	61.79161	38.20839	36.00172	19.00053	31.59931	13.39844	1.894774
LSB1.6B	55		1.202741	0.792478	61.75597	38.24403	37.07237	18.02152	31.55976	13.34635	2.057117
LSB1.7B	62		8.42515	4.001728	62.96006	37.03994	33.5036	19.27807	33.27468	13.94365	1.737913

LSB1.8B	69		0.748523	0.377396	64.00674	35.99326	34.87689	18.83018	32.17339	14.11954	1.85218
LSB1.9B	78		1.090021	0.50247	61.58755	38.41245	37.12002	19.22132	30.5636	13.09506	1.93119
LSB1.10B	86		1.423229	0.443793	60.08179	39.91821	38.00945	18.81814	29.69087	13.48153	2.01983
LSB1.11B	94		0.688158	0.454876	60.77152	39.22848	38.55051	18.83568	29.59011	13.0237	2.046675
LSB1.12B	102		2.205077	0.959608	64.72717	35.27283	35.11028	18.25256	33.49899	13.13817	1.923581
LSB1.13B	110		0.697163	0.342434	63.59263	36.40737	38.94374	19.80742	28.97577	12.27307	1.966119
LSB1.14B	118		0.978948	0.352137	63.49609	36.50391	41.87366	17.94335	28.32472	11.85828	2.333659
LSB3.0B	-22		0.716649	0.443841	74.95297	25.04703	30.5822	16.45263	37.77501	15.19017	1.858803
LSB5.0B	84		0.761688	0.323493	59.05123	40.94877	37.78825	19.3742	29.32247	13.51508	1.950442
LSB5.1B	93		1.1511	0.608217	62.16423	37.83577	36.92923	19.42214	30.98048	12.66815	1.901398
LSB5.2B	102		1.738244	0.739862	61.96906	38.03094	35.28461	19.1806	32.41286	13.12194	1.839599
LSB5.3B	111		0.679954	0.288461	61.63329	38.36671	39.49609	18.88623	29.40568	12.21199	2.091263
LSB5.4B	120		0.563843	0.325977	65.48368	34.51632	42.21259	18.44826	27.72629	11.61286	2.288161
LSB5.5B	129		0.580699	0.36828	68.10727	31.89273	40.46113	17.8696	29.70204	11.96723	2.264244
LSB5.6B	138		0.904865	0.457478	68.8745	31.1255	36.97064	17.97664	32.00698	13.04574	2.056593
LSB5.7B	145		0.766922	0.477007	67.01825	32.98175	37.07145	18.03996	31.80085	13.08774	2.054963
LSB6.0B	-24		1.157972	0.637603	71.31212	28.68788	29.8396	17.58321	37.44236	15.13482	1.697051
LSB6.1B	-11		1.074002	0.679966	72.65692	27.34308	30.99352	16.47635	36.8944	15.63574	1.881092
LSB6.2B	2		1.563316	0.659942	71.48111	28.51889	33.19874	17.14666	34.984	14.67061	1.936164
LSB6.3B	14		0.871809	0.39782	73.03574	26.96426	35.17677	17.55614	33.21484	14.05226	2.003674
LSB6.4B	26		0.593829	0.269583	71.28861	28.71139	35.93938	16.59869	32.53537	14.92657	2.165194
LSB6.5B	49		0.659305	0.285096	65.61452	34.38548	38.48528	18.07501	30.36044	13.07927	2.129198
LSB6.6B	51		2.355891	1.013795	60.86769	39.13231	37.38784	18.66186	30.64548	13.30481	2.003435
LSB6.7B	63		2.636961	1.012917	60.87514	39.12486	37.22705	18.72793	31.03947	13.00556	1.987783
Bos32.1B	-5		5.542662	2.456809	99.60576	0.394244	32.93529	19.17144	33.30074	14.59254	1.717935
Bos32.2B	0		7.571221	3.64333	99.53697	0.46303	33.77585	18.68184	33.29348	14.24884	1.807951
Bos32.3B	5		4.945805	2.262502	99.47256	0.527435	32.87144	19.20594	33.48344	14.43918	1.711524
Pseud41.1B	-5		10.40775	4.93377	99.22203	0.777968	32.80446	18.42697	33.87896	14.88961	1.780241
Pseud41.2B	0		7.09534	3.327276	99.78901	0.210987	33.55094	19.24222	33.24477	13.96206	1.743611
Pseud41.3B	5		10.06685	4.295413	98.74341	1.256594	33.69176	18.35593	32.94345	15.00886	1.83547

Sample Code:	**Stratigraphic height***		ΣC27βαDia/Σ(C27-C30)βαDia %	ΣC28βαDia/Σ(C27-C30)βαDia %	ΣC29βαDia/Σ(C27-C30)βαDia %	ΣC30βαDia/Σ(C27-C30)βαDia %	ΣC27βαDia/Σ(C27-C30) %	ΣC28βαDia/Σ(C27-C30) %

LSB1.0B	5		28.69942	17.53979	35.07603	18.68476	16.37881	10.00999
LSB1.1B	13		32.64188	19.32554	31.94087	16.09172	18.99376	11.24521
LSB1.2B	22		32.79916	18.56866	32.49577	16.13641	18.94572	10.72578
LSB1.3B	29		33.54974	18.25029	31.57529	16.62467	19.61747	10.67146
LSB1.4B	37		36.72733	18.87768	29.65837	14.73663	21.73923	11.17387
LSB1.5B	46		33.59529	19.75864	30.16034	16.48573	19.31216	11.3582
LSB1.6B	55		33.99472	19.98756	29.7873	16.23041	19.95402	11.73218
LSB1.7B	62		32.08803	19.5175	32.30382	16.09065	19.75694	12.01713
LSB1.8B	69		32.92234	19.34789	31.27835	16.45142	19.3544	11.37425
LSB1.9B	78		35.52974	19.95452	29.05952	15.45622	20.22575	11.35936
LSB1.10B	86		34.5659	19.65237	29.09296	16.68877	19.34985	11.00131
LSB1.11B	94		35.21709	19.86951	29.14899	15.76441	20.39858	11.5089
LSB1.12B	102		31.91968	19.43997	33.26285	15.3775	19.3742	11.79943
LSB1.13B	110		36.00129	20.91734	28.02099	15.06037	21.40273	12.43534
LSB1.14B	118		38.25448	19.39943	28.18385	14.16225	22.39946	11.3591
LSB3.0B	-22		28.20959	18.19223	36.51309	17.08509	16.38772	10.56836
LSB5.0B	84		34.53138	20.25692	28.72703	16.48466	19.62199	11.51072
LSB5.1B	93		33.74157	20.29925	30.65949	15.29969	19.59593	11.7891
LSB5.2B	102		32.69121	19.94384	32.05334	15.31161	19.49126	11.89098
LSB5.3B	111		37.10805	19.63625	28.53858	14.71712	21.54448	11.40056
LSB5.4B	120		37.64951	20.38132	27.90171	14.06745	22.50682	12.18392
LSB5.5B	129		36.49422	18.95349	30.03736	14.51493	22.23894	11.54993
LSB5.6B	138		34.17594	18.63532	32.2711	14.91764	20.96652	11.43254
LSB5.7B	145		33.49697	19.29881	31.94711	15.25711	20.15603	11.61261
LSB6.0B	-24		27.40603	17.98738	37.48169	17.1249	16.18364	10.62179
LSB6.1B	-11		28.88103	16.96085	36.26418	17.89394	16.69289	9.803165
LSB6.2B	2		31.40799	18.35084	34.00841	16.23276	18.11741	10.58551
LSB6.3B	14		33.0919	18.901	32.33138	15.67572	19.09713	10.90765
LSB6.4B	26		34.02501	17.84857	31.08736	17.03907	19.4705	10.21368
LSB6.5B	49		35.2629	19.5761	29.71389	15.44711	20.7149	11.49982
LSB6.6B	51		34.41986	19.69657	30.10318	15.78039	19.6599	11.25027
LSB6.7B	63		34.3027	19.56388	31.132	15.00142	20.54126	11.71531
Bos32.1B	-5		29.69785	19.67221	30.93069	19.69924	14.66251	9.712621
Bos32.2B	0		30.37178	18.76626	31.02087	19.84108	14.74818	9.112678
Bos32.3B	5		30.77701	18.92296	29.98031	20.31972	15.04787	9.252041
Pseud41.1B	-5		30.03826	18.58978	31.42525	19.94671	14.66285	9.074397
Pseud41.2B	0		30.44314	19.61958	31.25004	18.68724	14.85903	9.576145
Pseud41.3B	5		30.52364	18.99934	30.2342	20.24282	14.8956	9.271714

Sample Code:	**Stratigraphic height***		ΣC29βαDia/Σ(C27-C30) %	ΣC30βαDia/Σ(C27-C30) %	ΣC27/Σ(C27-C29) %	ΣC28/Σ(C27-C29) %	ΣC29/Σ(C27-C29) %	ΣC27/ΣC29
LSB1.0B	5		20.01795	10.66343	36.46834	20.58137	42.95029	0.849083
LSB1.1B	13		18.58586	9.363499	39.82209	21.42672	38.7512	1.027635

LSB1.2B	22		18.77048	9.320848	41.12469	20.28251	38.5928	1.065605
LSB1.3B	29		18.46296	9.720913	41.36246	19.89285	38.74468	1.067565
LSB1.4B	37		17.55505	8.72274	45.09502	20.97563	33.92934	1.329086
LSB1.5B	46		17.33759	9.47678	41.57168	21.94017	36.48815	1.13932
LSB1.6B	55		17.48437	9.526826	42.78224	20.79718	36.42057	1.174672
LSB1.7B	62		19.8898	9.907183	38.93217	22.40168	38.66616	1.00688
LSB1.8B	69		18.38793	9.671465	40.61097	21.92604	37.46299	1.084029
LSB1.9B	78		16.5425	8.798647	42.71336	22.11764	35.169	1.214517
LSB1.10B	86		16.28612	9.342305	43.93219	21.75043	34.31738	1.280173
LSB1.11B	94		16.88379	9.131126	44.32301	21.6561	34.02089	1.302817
LSB1.12B	102		20.18946	9.333637	40.42084	21.01333	38.56583	1.0481
LSB1.13B	110		16.65844	8.953374	44.392	22.5785	33.0295	1.344011
LSB1.14B	118		16.50271	8.292534	47.50719	20.35738	32.13543	1.478343
LSB3.0B	-22		21.21145	9.925193	36.05973	19.39944	44.54083	0.809588
LSB5.0B	84		16.32375	9.367189	43.69346	22.40183	33.90472	1.288713
LSB5.1B	93		17.80596	8.885528	42.2861	22.23947	35.47443	1.192016
LSB5.2B	102		19.11094	9.129137	40.61395	22.07761	37.30845	1.088599
LSB5.3B	111		16.56915	8.544578	44.9903	21.51346	33.49624	1.343145
LSB5.4B	120		16.6796	8.409499	47.75875	20.87211	31.36914	1.522475
LSB5.5B	129		18.30424	8.845147	45.96144	20.2988	33.73975	1.362234
LSB5.6B	138		19.79792	9.151788	42.51734	20.67368	36.80898	1.155081
LSB5.7B	145		19.22343	9.18061	42.65388	20.75652	36.5896	1.165738
LSB6.0B	-24		22.13345	10.11249	35.16119	20.719	44.11982	0.796948
LSB6.1B	-11		20.96026	10.34248	36.73773	19.53001	43.73226	0.84006
LSB6.2B	2		19.61744	9.363723	38.90657	20.09467	40.99877	0.948969
LSB6.3B	14		18.65824	9.046363	40.92809	20.42652	38.64539	1.059068
LSB6.4B	26		17.78946	9.750453	42.24512	19.51101	38.24387	1.104625
LSB6.5B	49		17.45518	9.074283	44.27629	20.79482	34.92889	1.267612
LSB6.6B	51		17.1943	9.013426	43.12562	21.52584	35.34854	1.220011
LSB6.7B	63		18.64257	8.9832	42.79245	21.52773	35.67982	1.199346
Bos32.1B	-5		15.27119	9.725969	38.56254	22.44703	38.99043	0.989026
Bos32.2B	0		15.06338	9.634599	39.38821	21.7861	38.82569	1.014488
Bos32.3B	5		14.65833	9.934963	38.4188	22.44712	39.13408	0.981722
Pseud41.1B	-5		15.3399	9.736769	38.54342	21.65067	39.8059	0.968284
Pseud41.2B	0		15.25287	9.121077	38.99552	22.36481	38.63966	1.00921
Pseud41.3B	5		14.75435	9.878535	39.6415	21.59746	38.76104	1.022715

µg/gTOC (aromatics):

Sample Code:	**Stratigraphic height***		AI 176	AI 190	AI 204	AI 218	AI 246	AI 260	AI 274
LSB1.0B	5		3.760306	2.348572	2.458103	0.969207	0.970426	0.968428	0.970426
LSB1.1B	13		4.819492	3.126409	3.201238	1.312895	1.208404	1.215075	1.208404
LSB1.2B	22		7.57584	4.796738	5.095673	2.01171	2.053514	2.023634	2.053514
LSB1.3B	29		3.890532	2.371485	2.511524	1.051768	1.05293	1.016999	1.05293
LSB1.4B	37		5.775789	3.919315	4.391347	2.005348	1.825638	1.82956	1.825638
LSB1.5B	46		5.986563	4.272386	4.716685	2.168536	2.347711	2.161774	2.347711
LSB1.6B	55		4.336382	2.827064	3.264867	1.576338	1.478127	1.370474	1.478127
LSB1.7B	62		4.095888	3.384307	4.391576	2.801495	3.802051	3.416236	3.802051
LSB1.8B	69		2.533564	1.742582	1.736623	0.806243	0.727817	0.745124	0.727817
LSB1.9B	78		6.831532	4.477468	4.443135	1.963477	1.640782	1.579293	1.640782
LSB1.10B	86		8.357934	5.393664	5.424349	2.138056	1.957371	2.031671	1.957371
LSB1.11B	94		5.773535	3.977506	3.971407	1.798389	1.380807	1.399192	1.380807
LSB1.12B	102		1.583906	1.070632	1.391678	0.759655	1.231214	1.084672	1.231214
LSB1.13B	110		3.466955	2.554106	3.289907	1.619626	1.626375	1.463226	1.626375
LSB1.14B	118		5.363579	3.786375	3.905634	1.711691	1.696527	1.556101	1.696527
LSB3.0B	-22		3.992936	2.504969	2.249988	1.018728	0.63126	0.718135	0.63126
LSB5.0B	84		4.690109	2.90283	2.967401	1.224755	1.133502	1.172216	1.133502
LSB5.1B	93		6.09894	3.829744	3.903887	1.613675	1.552336	1.488965	1.552336
LSB5.2B	102		2.070832	1.404894	1.759113	0.844086	1.117612	0.986698	1.117612
LSB5.3B	111		2.637151	1.872856	2.075693	0.995462	0.997985	0.969422	0.997985
LSB5.4B	120		4.892654	3.595383	4.283935	1.744682	1.616421	1.478947	1.616421
LSB5.5B	129		5.58135	4.023577	4.592226	2.001312	1.762598	1.76772	1.762598
LSB5.6B	138		5.932057	3.882372	4.223799	1.888404	1.692291	1.62672	1.692291
LSB5.7B	145		6.417331	4.244678	4.538352	1.701085	1.641008	1.510651	1.641008
LSB6.0B	-24		5.933693	3.788396	3.866884	1.788415	1.418825	1.408505	1.418825
LSB6.1B	-11		4.976832	3.342751	3.36057	1.583222	1.296029	1.310906	1.296029
LSB6.2B	2		6.339061	4.160078	4.186633	1.791507	1.680882	1.643767	1.680882
LSB6.3B	14		6.279547	4.164513	4.351476	1.761481	1.727956	1.600941	1.727956
LSB6.4B	26		2.638196	1.720586	1.807612	0.773274	0.749216	0.716324	0.749216
LSB6.5B	49		2.675267	1.678771	1.928316	0.847513	0.823574	0.789205	0.823574
LSB6.6B	51		8.025317	5.466883	5.611644	2.457649	2.39167	2.283547	2.39167
LSB6.7B	63		2.264026	1.751516	2.214233	1.339588	1.428648	1.294106	1.428648
Bos32.1B	-5		12.04459	8.355504	3.850736	4.460065	3.581852	3.312685	3.581852
Bos32.2B	0		18.85764	12.77506	6.234718	5.731446	5.652622	5.394866	5.652622
Bos32.3B	5		15.45514	10.53995	4.98875	4.196791	4.188235	4.038451	4.188235
Pseud41.1B	-5		22.23516	15.59853	7.407419	7.246991	6.30211	6.22854	6.30211
Pseud41.2B	0		20.44032	14.03437	7.009991	6.246239	6.693731	6.338736	6.693731
Pseud41.3B	5		22.33872	15.44706	7.654657	7.957797	6.69664	6.45988	6.69664

Sample Code:	**Stratigraphic height***		AI 288	Biphenylic isorenieratane	Isorenieratane	µg/g sum	AI sum	AIR
LSB1.0B	5		0.425702	0.397985	1.285293	14.55445	12.87117	2.859443
LSB1.1B	13		0.565481	0.541738	1.573619	18.77275	16.6574	2.968538
LSB1.2B	22		0.900055	0.910991	3.896056	31.31773	26.51068	2.770694
LSB1.3B	29		0.425084	0.440615	1.95138	15.76525	13.37325	2.769298
LSB1.4B	37		0.814542	0.779194	4.39723	27.5636	22.38718	2.556129
LSB1.5B	46		1.144737	1.089837	3.90838	30.14432	25.1461	2.142503
LSB1.6B	55		0.714027	0.745408	2.186848	19.97766	17.04541	2.381518
LSB1.7B	62		2.435521	2.245892	6.510293	36.88531	28.12913	1.090474
LSB1.8B	69		0.3488	0.317535	1.025391	10.7115	9.368571	2.674585
LSB1.9B	78		0.767954	0.689432	1.883035	25.91689	23.34442	3.14731
LSB1.10B	86		0.860607	0.81661	2.374689	31.31232	28.12102	3.13118
LSB1.11B	94		0.575912	0.555231	1.471397	22.28418	20.25755	3.276708
LSB1.12B	102		0.685225	0.625761	1.928533	11.59249	9.038196	1.135516
LSB1.13B	110		0.709281	0.756801	3.056186	20.16884	16.35585	2.01476
LSB1.14B	118		0.771058	0.757055	1.721197	22.96574	20.48749	2.581596
LSB3.0B	-22		0.222965	0	0	11.97024	11.97024	4.432081
LSB5.0B	84		0.50286	0.447817	1.177255	17.35225	15.72718	2.989562
LSB5.1B	93		0.70502	0.594548	1.660379	22.99983	20.7449	2.915125
LSB5.2B	102		0.539725	0.523354	1.480646	11.84457	9.840571	1.616028
LSB5.3B	111		0.488198	0.47069	1.75818	13.26362	11.03475	2.195154
LSB5.4B	120		0.680547	0.675531	2.467696	23.05222	19.90899	2.69209
LSB5.5B	129		0.796787	0.732645	1.865781	24.88659	22.28817	2.659976
LSB5.6B	138		0.738661	0.711688	1.891738	24.28002	21.6766	2.769867
LSB5.7B	145		0.763601	0.629555	1.124206	24.21147	22.45771	3.041871
LSB6.0B	-24		0.591065	0	0	20.21461	20.21461	3.178972
LSB6.1B	-11		0.566993	0	0	17.73333	17.73333	2.967227
LSB6.2B	2		0.747038	0.711133	5.292998	28.23398	22.22985	2.864334
LSB6.3B	14		0.765831	0.71885	3.816246	26.9148	22.3797	2.843537
LSB6.4B	26		0.323495	0.321101	2.217179	12.0162	9.47792	2.734035
LSB6.5B	49		0.409861	0.352592	1.358702	11.68738	9.976081	2.505034
LSB6.6B	51		1.110997	1.043634	3.360095	34.1431	29.73937	2.636562
LSB6.7B	63		0.744826	0.669762	2.507931	15.64329	12.46559	1.545958
Bos32.1B	-5		1.754873	1.583785	4.096429	46.62237	40.94216	2.347337
Bos32.2B	0		2.605621	2.518549	6.357808	71.78095	62.90459	2.258338
Bos32.3B	5		1.993517	1.76478	4.357307	55.71115	49.58906	2.441668
Pseud41.1B	-5		3.584627	3.274124	6.85589	85.03551	74.90549	2.341402
Pseud41.2B	0		3.27786	3.111433	8.521957	82.36837	70.73498	2.074891
Pseud41.3B	5		3.563988	3.355746	12.06153	92.23266	76.81538	2.280305

Sample Code:	Stratigraphic height*		Phenan-threne	3-Methyl-Phenan-threne	2-Methyl-Phenan-threne	9-Methyl-Phenan-threne	1-Methyl-Phenan-threne	sum MP	Retene	Dibenzo-thiophene
LSB1.0B	5		80.81596	24.32719	25.64692	37.31867	32.14631	119.4391	7.80388	4.657926
LSB1.1B	13		71.47904	21.47715	22.91163	33.36091	28.54974	106.2994	6.754458	4.097763
LSB1.2B	22		125.325	38.46483	40.00999	58.60985	50.79239	187.8771	12.12329	7.015216
LSB1.3B	29		64.0856	19.43234	19.97321	29.51662	25.35934	94.28151	6.13933	3.626881
LSB1.4B	37		83.33439	26.35688	27.87144	39.68416	34.40649	128.319	9.195021	5.072189
LSB1.5B	46		121.1945	38.25276	39.97958	58.17101	50.69024	187.0936	14.24762	7.700572
LSB1.6B	55		52.11898	16.07888	16.92813	25.15208	21.79167	79.95076	5.988586	3.454783
LSB1.7B	62		115.9697	31.21373	33.14916	50.78468	43.81993	158.9675	12.41258	3.949451
LSB1.8B	69		38.27682	11.48577	12.08364	17.79825	15.322	56.68966	4.447624	2.54779
LSB1.9B	78		97.89712	29.76624	30.85059	45.51488	38.8686	145.0003	10.69174	6.51545
LSB1.10B	86		120.9697	37.19837	38.69604	56.05509	48.79518	180.7447	12.44291	8.621572
LSB1.11B	94		111.288	34.77821	35.77556	51.86648	45.32564	167.7459	12.91542	7.72832
LSB1.12B	102		37.3097	10.45206	11.29432	16.65716	14.2449	52.64844	4.172778	2.053369
LSB1.13B	110		109.0538	33.21248	35.26959	53.10766	45.46829	167.058	13.37122	6.122226
LSB1.14B	118		65.44391	20.20998	20.81306	31.57361	26.77756	99.37421	6.854927	3.826159
LSB3.0B	-22		64.5036	18.87297	19.57088	28.86577	25.13971	92.44932	5.200029	3.271986
LSB5.0B	84		60.20296	17.64692	18.78099	27.43524	23.41127	87.27442	5.986612	4.068179
LSB5.1B	93		94.21068	28.69905	29.57279	43.36156	37.942	139.5754	9.740715	6.243809
LSB5.2B	102		35.38201	10.50181	11.19371	16.40298	14.26192	52.36042	4.166457	2.030673
LSB5.3B	111		39.35319	12.23482	12.83882	18.52174	16.10311	59.6985	4.288561	2.376113
LSB5.4B	120		80.8541	24.63965	25.93509	37.53365	32.36703	120.4754	8.44883	5.151546
LSB5.5B	129		88.88984	27.24337	28.42071	41.41464	35.77192	132.8506	9.280772	5.994298
LSB5.6B	138		94.82838	29.24769	30.83345	44.75972	39.03357	143.8744	10.23732	6.065919
LSB5.7B	145		95.59019	28.28713	29.65106	44.18126	38.10327	140.2227	9.130609	5.757815
LSB6.0B	-24		100.2627	28.93053	31.63808	45.82458	38.90914	145.3023	8.45864	5.123787
LSB6.1B	-11		84.08672	24.56713	26.38163	37.70118	32.98665	121.6366	7.282768	4.420369
LSB6.2B	2		69.11502	20.39144	21.45447	31.47471	27.34091	100.6615	5.662533	3.720771
LSB6.3B	14		70.80652	20.86243	22.00355	31.925	28.05444	102.8454	6.655704	3.819865
LSB6.4B	26		41.2095	12.0055	12.35742	18.15444	15.42476	57.94213	3.801707	2.177989
LSB6.5B	49		44.62686	13.24142	13.73095	20.12471	17.40495	64.50203	4.402247	2.733663
LSB6.6B	51		104.1221	32.17325	33.50983	49.35239	42.08355	157.119	10.84812	6.791847
LSB6.7B	63		51.08165	14.13931	15.4898	22.86439	19.88332	72.37681	6.41647	1.869689

Bos32.1B	-5		66.77649	24.96768	26.18815	45.64289	42.39846	139.1972	8.786198	2.714273
Bos32.2B	0		108.8244	39.38408	42.3179	72.79743	67.80734	222.3068	14.18365	4.455307
Bos32.3B	5		107.6034	39.46768	41.72713	71.71537	66.51821	219.4284	14.09426	4.786755
Pseud41.1B	-5		103.3245	38.40504	40.50378	70.91402	65.06783	214.8907	15.40499	4.582923
Pseud41.2B	0		122.3554	46.42127	47.31134	83.57155	76.92962	254.2338	17.82792	5.551159
Pseud41.3B	5		123.5326	47.60609	47.93542	82.6273	76.34981	254.5186	18.20686	5.69117

Sample Code:	**Stratigraphic height***		4-Methyl-Dibenzo-thiophene	2+3-Methyl-Dibenzo-thiophene	1-Methyl-Dibenzo-thiophene	Sum MDBT	Phen/DBT	DBT/Phen
LSB1.0B	5		2.919917	4.123535	1.743368	8.78682	17.3502	5.763622
LSB1.1B	13		2.6952	3.341089	1.537931	7.57422	17.44343	5.732817
LSB1.2B	22		4.464429	6.20238	2.851852	13.51866	17.86473	5.597621
LSB1.3B	29		2.398358	2.993736	1.415713	6.807807	17.66962	5.659433
LSB1.4B	37		3.368444	4.538356	2.041586	9.948387	16.42967	6.08655
LSB1.5B	46		4.774749	7.032929	3.030555	14.83823	15.73837	6.353898
LSB1.6B	55		2.123981	3.110361	1.39144	6.625782	15.08603	6.628647
LSB1.7B	62		3.038487	4.047359	1.943756	9.029602	29.36349	3.40559
LSB1.8B	69		1.619663	2.425671	1.008123	5.053458	15.02354	6.656221
LSB1.9B	78		3.877254	6.133795	2.572928	12.58398	15.02538	6.655406
LSB1.10B	86		4.92678	7.975117	3.223565	16.12546	14.03104	7.127054
LSB1.11B	94		4.579121	7.120129	2.958776	14.65803	14.40002	6.944433
LSB1.12B	102		1.300767	1.7005	0.77248	3.773747	18.16999	5.50358
LSB1.13B	110		3.882405	4.944148	2.335803	11.16236	17.81277	5.61395
LSB1.14B	118		2.33289	2.940201	1.45647	6.729562	17.10434	5.84647
LSB3.0B	-22		2.118923	3.11276	1.231557	6.46324	19.7139	5.072563
LSB5.0B	84		2.475666	3.970063	1.574349	8.020077	14.7985	6.75744
LSB5.1B	93		3.808009	5.687862	2.301342	11.79721	15.08865	6.627496
LSB5.2B	102		1.350064	1.867073	0.827305	4.044442	17.42378	5.739283
LSB5.3B	111		1.592494	2.192847	1.001531	4.786872	16.562	6.037918
LSB5.4B	120		3.300022	4.383181	2.003528	9.686732	15.69511	6.37141
LSB5.5B	129		3.652718	5.292758	2.263545	11.20902	14.82907	6.743513
LSB5.6B	138		3.769044	5.283141	2.437178	11.48936	15.63298	6.396734
LSB5.7B	145		3.377606	5.261691	2.197562	10.83686	16.60182	6.023437
LSB6.0B	-24		3.161452	4.898805	1.925712	9.98597	19.56809	5.11036
LSB6.1B	-11		2.777165	3.92806	1.60397	8.309195	19.02256	5.256917
LSB6.2B	2		2.460956	3.234783	1.434605	7.130345	18.57546	5.383447
LSB6.3B	14		2.389767	3.485583	1.471919	7.347269	18.53639	5.394793
LSB6.4B	26		1.365207	2.130565	0.848712	4.344483	18.9209	5.285162
LSB6.5B	49		1.614554	2.327574	0.989074	4.931202	16.32493	6.1256
LSB6.6B	51		4.251307	6.31522	2.749201	13.31573	15.33046	6.522963

LSB6.7B	63		1.456553	1.77319	0.765958	3.995701	27.32093	3.660197
Bos32.1B	-5		11.73147	3.395598	2.970352	18.09742	24.60198	0.040647
Bos32.2B	0		19.06267	4.946625	4.69872	28.70802	24.42579	0.04094
Bos32.3B	5		19.95359	5.925279	5.125985	31.00485	22.47939	0.044485
Pseud41.1B	-5		20.13046	5.943931	5.089206	31.1636	22.54555	0.044355
Pseud41.2B	0		23.16951	6.515907	5.779995	35.46541	22.04142	0.045369
Pseud41.3B	5		24.03615	7.180945	6.174655	37.39175	21.70601	0.04607

Compound-specific isotopic analysis:

CSOK sample code	height (mm)	Dilution (µL)	δ13C17(‰)	δ13C18(‰)	δ13C19(‰)	δ13C27(‰)	δ13C28(‰)	δ13C29(‰)
LSB1.0B	5	500	-34.88	-34.06	-34.89	-32.26	-32.45	-32.3
LSB1.1B	13	500	-35.71	-34.72	-35.69	-33.17	-33.45	-33.17
LSB1.2B	22	1000	-33.84	-33.68	-34.01	-32.5	-32.44	-32.69
LSB1.3B	29	750	-34.91	-34.51	-34.66	-33.51	-33.32	-33.67
LSB1.4B	37	1500	-36.23	-34.09	-35.57	-33.1	-33.76	-33.61
LSB1.5B	46	1500	-35.31	-34.86	-35.15	-33.04	-32.99	-32.83
LSB1.6B	55	250	-34.49	-33.49	-33.14	-32.29	-32.07	-31.99
LSB1.7B	62	250	-33.74	-33.46	-32.94	-32.03	-32.27	-32.25
LSB1.8B	69	1000	-34.71	-34.07	-34.47	-32.32	-32.4	-31.99
LSB1.9B	78	1000	-35.78	-34.86	-35.32	-34.65	-33.88	-34.02
LSB1.10B	86	1000	-35.52	-35.34	-35.5	-35.66	-34.95	-34.32
LSB1.11B	94	1000	-38.36	-35.54	-37.44	-33.85	-33.42	-35.58
LSB1.12B	102	500	-33.21	-32.42	-32.15	-31.68	-31.84	-31.86
LSB1.13B	110	250	-36.39	-35.01	-33.65	-34.68	-34.09	-33.58
LSB1.14B	118	250	-37.93	-36.81	-35.37	-35.65	-35.25	-33.87
LSB3.0B	-22	500	-36.24	-35.31	-34.69	-34.57	-34.02	-33.88
LSB5.0B	84	1500	-36.59	-36.19	-33.88	-33.3	-34.33	-33.78
LSB5.1B	93	1000	-36.29	-34.94	-34.23	-33.53	-34.14	-33.81
LSB5.2B	102	1000	-36.66	-35.25	-34.22	-33	-32.32	-32.21
LSB5.3B	111	1000	-36.51	-36.01	-34.73	-34.35	-33.58	-33.87
LSB5.4B	120	1500	-37.93	-35.99	-33.18	-32.4	-32.74	-32.71
LSB5.5B	129	1500	-39.37	-36.57	-35.45	-36.14	-36.09	-35.06
LSB5.6B	138	1000	-36.66	-35.65	-32.86	-33.93	-33.23	-34.66
LSB5.7B	145	250	-37.53	-36.31	-35.26	-36.83	-35.7	-34.7
LSB6.0B	-24	500	-36.03	-35.8	-34.22	-35.18	-35.03	-34.25
LSB6.1B	-11	500	-33.68	-33.87	-33.98	-33.81	-33.4	-33.88
LSB6.2B	2	1000	-38.3	-37.47	-36.21	-37.16	-36.45	-35.25
LSB6.3B	14	1000	-37.17	-36.43	-35.54	-36.02	-35.33	-34.89
LSB6.4B	26	1500	-38.35	-35.62	-34.34	-33.95	-34.43	-33.81
LSB6.5B	49	1500	-38.43	-36.87	-34.52	-35.33	-34.81	-35.98
LSB6.6B	51	1000	-38.13	-36.54	-36.19	-36.08	-35.98	-35.59
LSB6.7B	63	250	-35.99	-35.03	-34.26	-33.01	-32.84	-33.04

Bos32.1B	-5	1000	-36.98	-35.8	-34.44	-34.67	-34.16	-34.82
Bos32.2B	0	1000	-37.95	-37.83	-35.41	-35.89	-35.15	-35.46
Bos32.3B	5	1000	-36.76	-36.5	-34.74	-35.18	-34.31	-35.73
Pseud41.1B	-5	1000	-37.69	-37.27	-35.19	-35.86	-34.66	-36.28
Pseud41.2B	0	500	-34.65	-34.69	-33.98	-34.04	-33.95	-34.46
Pseud41.3B	5	1000	-37.39	-36.66	-34.42	-34.86	-34.04	-35.86